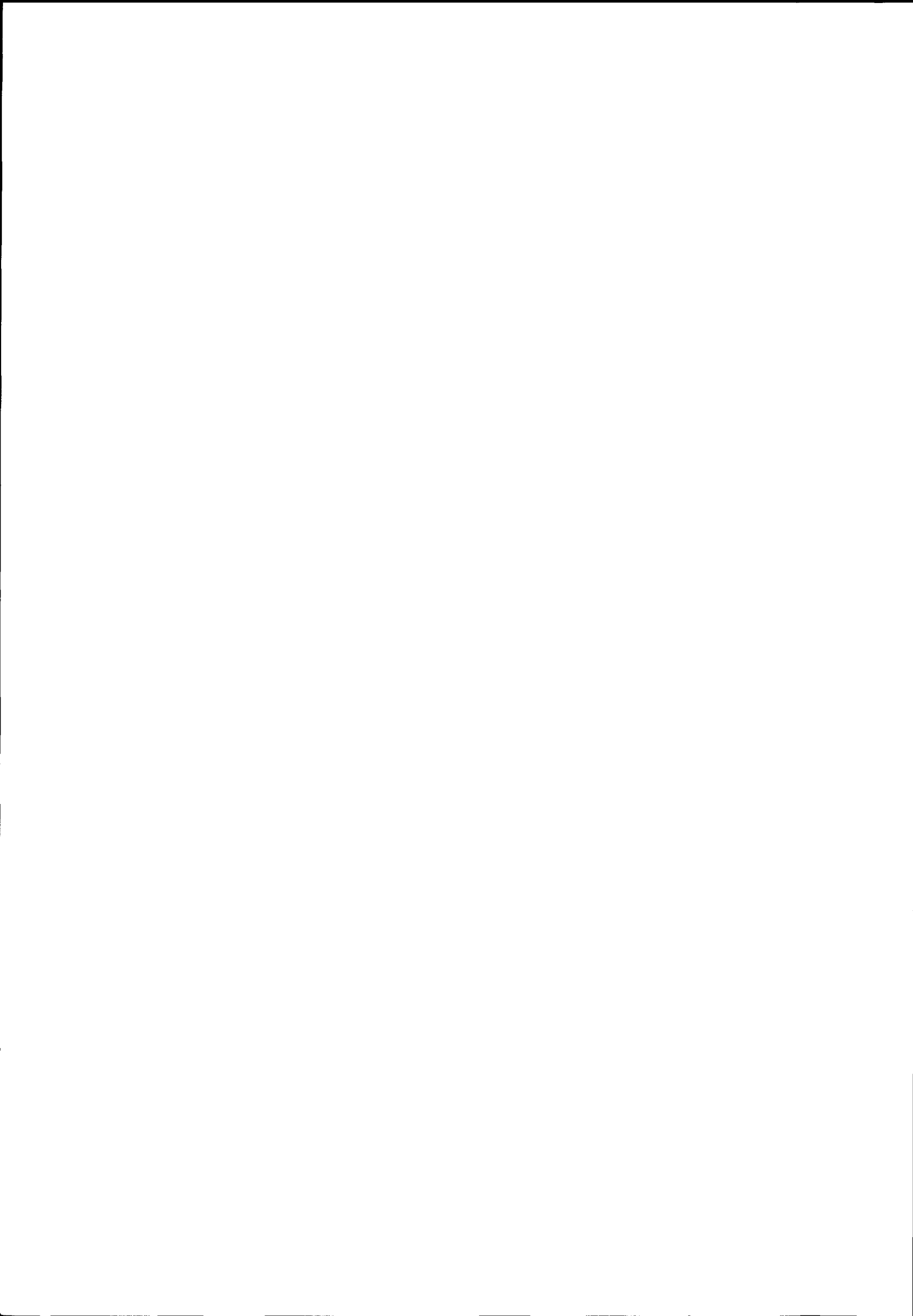


Emerging Scatterometer Applications

*From Research
to Operations*

ESTEC, Noordwijk, The Netherlands
5 - 7 October 1998



esa SP-424

ISBN 92-9092-696-1

November 1998

Workshop on

**Emerging Scatterometer
Applications**

From Research to Operations

ESTEC, Noordwijk, The Netherlands

5-7 October 1998

Co-Sponsors :

ESA & EUMETSAT

**European Space Agency
Agence spatiale européenne**

**SP-424: Proceedings of a Joint ESA-Eumetsat Workshop on
Emerging Scatterometer Applications – From Research to Operations**
ESTEC, Noordwijk, The Netherlands
5-7 October 1998

Proceedings published by: ESA Publications Division
ESTEC, Noordwijk, The Netherlands

Compiled by: Tan-Duc Guyenne

Copyright: © 1998 European Space Agency

Price: 75 Dfl.

ISBN 92-9092-696-1 Printed in The Netherlands

Contents

FOREWORD	7
E. Oriol-Pibernat, <i>ESA</i> & J. Kerkmann, <i>Eumetsat</i>	
THE ERS SCATTEROMETER MISSION	9
G. Duchossois & E. Oriol-Pibernat, <i>ESA</i>	
PERSPECTIVES FOR THE ADVANCED SCATTEROMETER (ASCAT) ON METOP	13
J. Kerkmann & D. Klaes, <i>Eumetsat</i>	
THE SEAWINDS SCATTEROMETER FOR THE QUICKSAT & ADEOS-II MISSIONS (<i>Abstract</i>)	21
M. W. Spencer, <i>JPL, USA</i>	

Land Session

Chair: V. Wismann, IFARS

Rapporteur: C.-C. Lin, ESA/ESTEC

LAND SURFACE MONITORING WITH SPACE-BORNE SCATTEROMETERS	25
V. Wismann, <i>IFARS, Germany</i>	
A COMPARISON OF ERS SCATTEROMETER RETRIEVED SOIL MOISTURE DATA WITH FIELD OBSERVATIONS IN THE UKRAINE	33
W. Wagner, <i>JRC, Italy & Inst. for Photogrammetry & Remote Sensing, Austria</i>	
EVALUATION OF SSM/I DATA FOR IMPROVING SURFACE PARAMETER RETRIEVAL WITH ERS WIND SCATTEROMETER DATA OVER THE SAHEL	39
P.-I. Frison & al., <i>CESBIO, GenCorp Aerojet, ICRISAT</i>	
FEASIBILITY STUDY IN USING SCATTEROMETER DATA FOR WETLAND RICE MAPPING YIELDING METHANE EMISSION INDICATORS FOR GLOBAL APPLICATIONS	45
H.J.C. van Leeuwen & al., <i>Synoptics, NL</i>	
EXTRACTING ERS LANDCOVER SCATTEROMETER DATA USING PRINCIPAL COMPONENTS ANALYSIS & GENERIC ALGORITHMS FOR SOIL MOISTURE ESTIMATION (<i>Abstract</i>)	49
M. Habermeyer & al., <i>DLR, Germany & Univ. Nottingham, UK</i>	
VEGETATION AS OBSERVED WITH AVHRR AND ERS SCATTEROMETER – A CASE STUDY OVER THE IBERIAN PENINSULA	51
W. Wagner, <i>JRC & Inst. for Photogrammetry & Remote Sensing</i>	
RESOLUTION ENHANCEMENT OF ERS SCATTEROMETER DATA	57
J.L. Alvarez Pérez & al., <i>University of Nottingham, UK & DLR, Germany</i>	
GLOBAL VEGETATION MONITORING USING ERS-1 SCATTEROMETER : IMAGE GENERATION AND PROPERTIES	63
M. Abdel Messeh & S. Quegan, <i>University of Sheffield, UK</i>	
RETRIEVAL OF REGIONAL-SCALE GEOPHYSICAL PARAMETERS IN SEMI-ARID AREAS USING DATA FROM ERS WIND SCATTEROMETER	69
I. H. Woodhouse & D. H. Hoekman, <i>University of Dundee & Wageningen Agric. Univ., NL</i>	

Snow & Ice Session



Chair: R. O. Ramseier, Microwave Group, Canada

Rapporteur: J. Johannessen, ESA/ESTEC

SESSION SUMMARY <i>J. Johannessen, ESA/ESTEC</i>	77
FROM RESEARCH WITH SYNERGISM TO OPERATIONS: SCATTEROMETER-PASSIVE MICROWAVE RADIOMETER APPLICATIONS TO SEA-ICE AND SNOW <i>R.O. Ramseier & C. Garrity, MGOR, Canada</i>	79
SNOW ACCUMULATION ON GREENLAND DERIVED FROM NSCAT & AND ERS SCATTEROMETER DATA <i>V. Wismann, IFARS, Germany</i>	87
SEASAT, ERS-1/2 & NSCAT SCATTEROMETER OBSERVED CHANGES ON THE LARGE ICE SHEETS <i>M.R. Drinkwater & D.G. Long, JPL & ECE Dept., USA</i>	91
DIRECTIONAL ANISOTROPY OF C AND KU BAND MW BACKSCATTER FROM THE EAST ANTARCTIC SNOW COVER: DIFFERENCES AND SIMILARITIES (<i>Abstract</i>) <i>N. Young, CRC Hobart</i>	97
AN EMPIRICAL C-BAND BACKSCATTER MODEL OVER ARCTIC SEA ICE FROM AMI WIND DATA <i>A. Cavanie, Ifremer, France</i>	99
POSSIBILITIES FOR A SYNERGETIC USE OF COARSE RESOLUTION ACTIVE AND PASSIVE MICROWAVES FOR SEA ICE RETRIEVALS <i>J. Grandell, Finnish Geodetic Institute, Finland</i>	107
SCATTEROMETER DATA FOR SAF SEA ICE PRODUCTS <i>L.-A. Breivik & H. Schyberg, DNMI</i>	115
INTERANNUAL VARIABILITY IN WEDDELL SEA ICE FROM ERS WIND SCATTEROMETER <i>M.R. Drinkwater & al., JPL & Scott Polar Research Institute</i>	119
ANTARCTIC ICEBERG DRIFT AND OCEAN CURRENTS DERIVED FROM SCATTEROMETER IMAGE SERIES <i>N. W. Young, CRC & Australian Antarctic Division</i>	125

Ocean Session

Chair: P. Courtier, LODYC

Rapporteur: P. Lecomte, ESA/ESRIN

SESSION SUMMARY <i>P. Lecomte, ESA/ESRIN</i>	135
THE MERCATOR MISSION <i>Ph. Courtier, LODYC</i>	139

DETERMINATION OF SATELLITE WIND & WIND-STRESS FIELDS IN AN OCEAN GCM N. Grima, <i>Ifremer & LODYC</i>	143
NSCAT BACKSCATTER COEFFICIENT VARIABILITY N. Tran & al., <i>LODYC & CNAM</i>	149
SCATTEROMETER WINDS OVER THE ARABIAN SEA (<i>Abstract</i>) D. Halpern, <i>JPL</i>	152
SCATTEROMETRY FOR TROPICAL CYCLONES OBSERVATION (<i>Abstract</i>) Y. Quilfen, <i>Ifremer</i>	153
STUDY OF SEA-STATE DEPENDENT ALGORITHM FOR OPERATIONAL PROCESSING OF ERS SCATTEROMETER DATA AT ECMWF (<i>Abstract</i>) D. Le Meur & L. Isaksen, <i>ECMWF</i>	154
CERSAT ACTIVITIES & SCATTEROMETER VALUE-ADDED PRODUCTS S. Pouliquen & al., <i>Ifremer</i>	155
APPLICATIONS OF SCATTEROMETER WINDS TO STUDY EL NIÑO TELECONNECTIONS AND ASIAN MONSOONS (<i>Abstract</i>) T. Liu, <i>JPL</i>	159
OCEANOGRAPHIC APPLICATIONS OF SCATTEROMETER DATA IN THE MEDITERRANEAN SEA S. Zecchetto & C. Cappa, <i>CNR</i>	161

NWP Session

Chair: A. Stoffelen, KNMI

Rapporteur: J. Kerkmann, Eumetsat

SESSION SUMMARY A. Stoffelen, <i>KNMI</i>	169
SCATTEROMETRY AND WEATHER PREDICTION A. Stoffelen, <i>KNMI</i>	171
IMPACT OF ERS SCATTEROMETER WIND DATA ON ECMWF'S ANALYSIS AND FORECASTS OF TROPICAL CYCLONES L. Isaksen & al., <i>ECMWF & KNMI</i>	177
AMBIGUITY REMOVAL BY VARIATIONAL ANALYSIS OF SURFACE WIND FIELDS S.M. Leidner & R.N. Hoffman, <i>Atmospheric & Environmental Research Inc.</i>	185
OPTIMAL AMBIGUITY REMOVAL FOR SCATTEROMETER WINDS H. Schyberg & L.-A. Breivik, <i>DNMI</i>	191
TOWARDS AN IMPROVED Ku-BAND SCATTEROMETER PRODUCT J. Figa & A. Stoffelen, <i>KNMI</i>	197
DEVELOPMENT & APPLICATION OF A VISIBLE-INFRARED RAIN FLAG FOR SCATTEROMETER DATA Chr. Grassotti & al., <i>Atmospheric & Environmental Research Inc.</i>	203

NEURAL NETWORK WIND RETRIEVAL FROM ERS-1 SCATTEROMETER DATA P. Richaume & al., <i>LODYC, Météo-France, CNAM</i>	211
SATELLITE APPLICATION FACILITIES FOR THE SCATTEROMETER A. Stoffelen, <i>KNMI</i>	217
ASSESSMENT OF SCATTEROMETER WIND RETRIEVAL MODEL BY ERS & ADEOS CYCLONE TRACKING L. Saaverdra de Miguel, <i>ESA/ESRIN</i>	221
2-D VARIATIONAL AMBIGUITY REMOVAL J.C.W. de Vries, <i>KNMI</i>	229
EFFECTS OF RESOLUTION & COVERAGE IN HIRLAM DATA ASSIMILATION A. Stoffelen & P. van Beukering, <i>KNMI</i>	233

Instruments & Processing

THE ERS SCATTEROMETER INSTRUMENT AND ITS ON-GROUND DATA PROCESSING P. Lecomte & E. Attema, <i>ESA/ESRIN-ESTEC</i>	241
ERS WIND SCATTEROMETER COMMISSIONING & IN-FLIGHT CALIBRATION P. Lecomte & W. Wagner, <i>ESRIN & JRC</i>	261
ERS WIND PRODUCT SPECIFICATIONS P. Lecomte, <i>ESRIN</i>	271
ROUTINE MONITORING OF SCATTEROMETER DATA R. Crapolicchio & P. Lecomte, <i>ESRIN</i>	285

Participants	301
---------------------	-----

FOREWORD

E. Oriol-Pibernat* & Jochen Kerkmann⁺

**ESA*, 8 rue Mario-Nikis, F-75738 Paris, France

⁺*EUMETSAT*, Am Kavalleriesand 31, D-64295 Darmstadt, Germany

The initial idea of organising a Workshop dedicated to scatterometer applications was triggered by the success of the Third ERS Symposium which took place in March 1997 in Florence, Italy under the auspices of the European Space Agency. The number, quality and novelty of research and applications made possible with the scatterometers on-board ERS-1 and ERS-2 were so unexpected that it was decided to put together the community in an ad-hoc environment.

EUMETSAT – the European Organisation for the Exploitation of Meteorological Satellites, which represents the operational user community for which the scatterometer was first targeted, and which will be operating the new series of European scatterometers – immediately showed high interest in co-organising the Workshop.

The objectives of the Workshop were to review the current applications of scatterometer data products and to promote a dialogue between application development teams and the potential users of new products in the following fields :

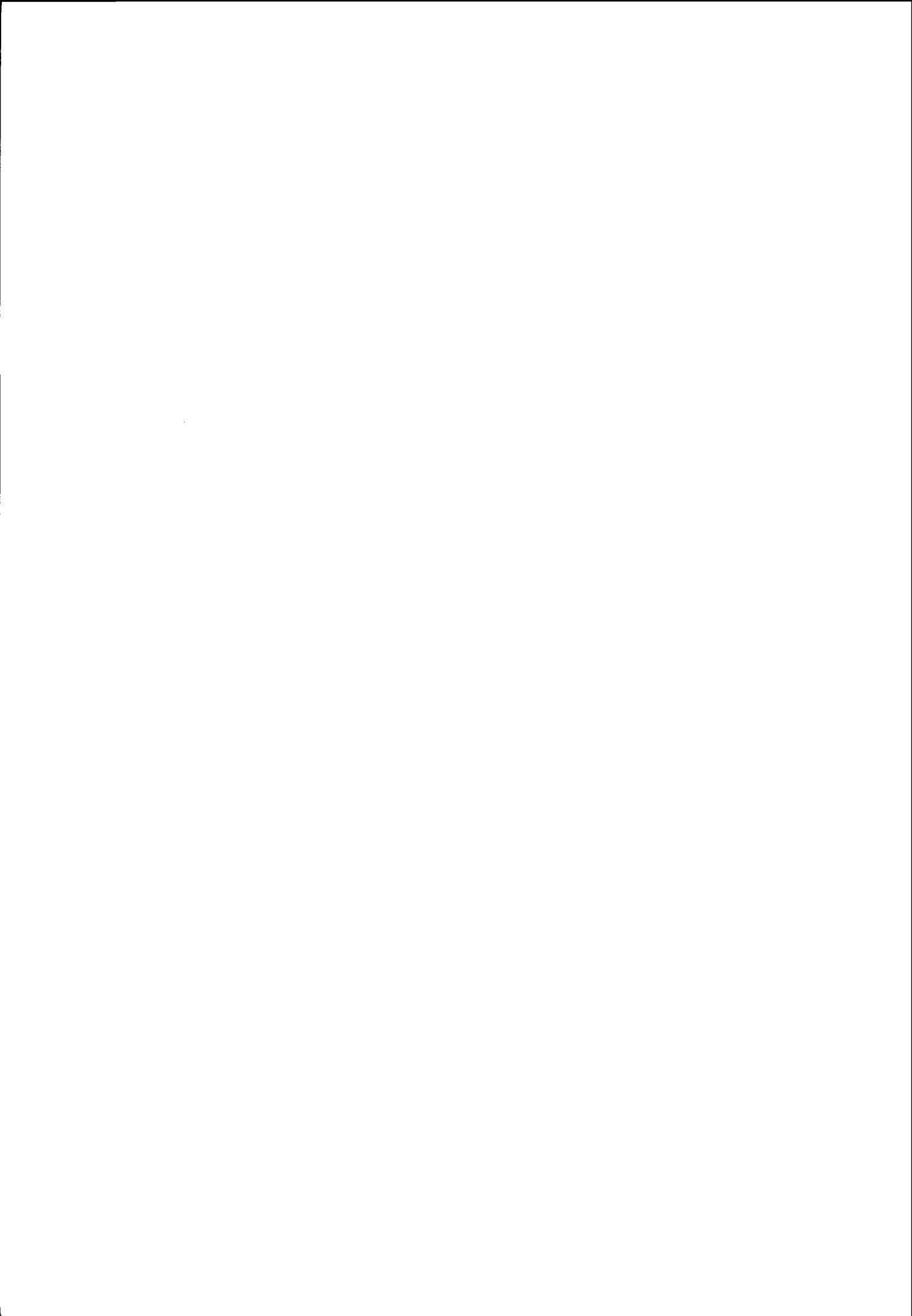
- Land Applications
- Continental & Sea Ice Applications
- Ocean Circulation & Wave Observation
- Numerical Weather Prediction, including Nowcasting & Observation of Extreme Events.

Sessions on the above topics were therefore organised, plus a further session on Instruments and Processing, added to the final programme at the participants' request.

The Workshop raised strong interest among the representatives of the Earth Observation science community working on application development as well as potential users interested in monitoring large-scale land processes, climate change, numerical weather prediction and ocean modeling. Some 70 participants attended the Workshop and followed with interest the presentations of 44 contributed and poster papers which are enclosed in this proceedings.

Discussions were very lively and proved the maturity reached by some of the applications, as well as the potential of many new emerging uses. Details can be found at the beginning of each session.

It is important to stress the unanimous recommendation to continue the scatterometer missions. In particular, there is a need to generate long time series of consistent datasets, and therefore to ensure continuity of the ERS scatterometers until the new generation is flying on Metop.



THE ERS SCATTEROMETER MISSION

G. Duchossois and E. Oriol-Pibernat

European Space Agency

Directorate of Applications, Mission Management Office

8-10 rue Mario Nikis, F-75738 Paris CEDEX 15

Tel: 33-1-5369.7654; fax: ...7674; e-mail: eoriol@hq.esa.fr

Introduction

The launch of the ESA's first European Remote Sensing satellite with a wind scatterometer on board (AMI-wind), opened a new era for wind measurements from space. ERS-1 provided for the first time the wind speed and direction over the ocean's surface globally in near real time, as well as long-term global measurements of the Earth's surface radar backscatter.

A second identical scatterometer was brought into orbit on ERS-2. This means that more than seven years of non-stop measurements are available until present.

The other Earth Observation satellites currently under development at ESA are:

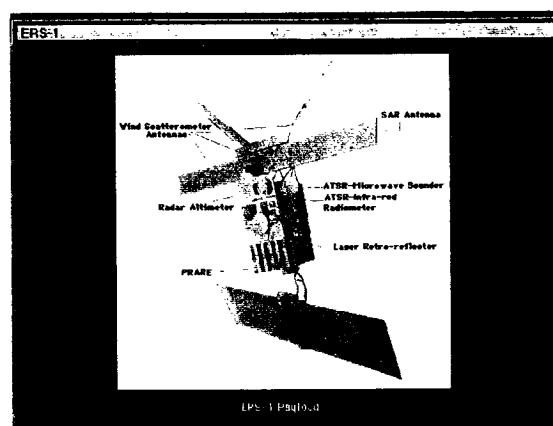
- Envisat, a very ambitious multi-mission platform aimed to serve the needs of the research and applications remote sensing user community as from the year 2000;
- MSG and Metop, two series of satellites prepared in co-operation with EUMETSAT, to fulfill the requirements of the operational meteorological and climate monitoring use community. The prototypes of both series are due for launch in 2000 and 2003, respectively.

Future plans include the Envelope Programme, to be proposed at the ESA's Ministerial Conference in 1999. This should address the Earth Observation market development and mission exploitation, the Earth Explorers and the Earth Watch missions.

The ERS history and objectives

The first European Remote Sensing satellite ERS-1 was launched in July 1991. This satellite, which is still in orbit, was followed by ERS-2 in April 1995, carrying an enhanced payload. Since May 1996, ERS-2 has become the operational satellite while ERS-1 is maintained as a back-up.

Figure 1: ERS-1 artist's view



The Mission objectives of the ERS satellites were originally the following:

- Increase scientific understanding of coastal zones, global ocean processes and polar regions;
- Develop and promote economic and commercial applications;
- Explore the potential of radar data for land studies and applications.

In particular, the key scientific disciplines which were targeted by the original mission were: open oceans, regional seas, polar oceans (including sea ice), and continental ice

The seven years of effective use of the wealth of data provided by both satellites have proven that such mission objectives were not only fulfilled, but largely and unexpectedly overcome.

Historical background

ESA established in 1974 a remote sensing advisory

group to develop the European requirements for a remote sensing mission. The user requirements, with, originally, emphasis on commercial applications, concentrated on land use, coastal zone and open oceans.

The balance of requirements from commercial to science occurred in 1980, with the start of the World Climate Research Program, WCRP. The European contribution would be done through ERS, in particular for the World Ocean Circulation Experiment WOCE, planned to begin in 1990.

NASA developed Seasat in the mid-70s. The Seasat payload can be traced back to the requirements of oceanographers, formulated at a Conference at Woods Hole Oceanographic Institute in 1972. Seasat was launched in 1978, and lost after only 3 months in orbit. The interest generated by the data greatly influenced the selection of the ERS-1 payload.

The interest in microwave observation techniques had already emerged in Europe in early and mid 70s. Studies carried by industry and ESA demonstrated the feasibility of building SARs and multi-frequency microwave radiometers in Europe. Three possible missions emerged: ocean, land and coastal zone monitoring systems.

The precedent of Seasat was a key element for ESA member states to develop in priority the ocean satellite concept. Furthermore, major technological developments were performed in Europe in the period between 1978 and the time of approval of ERS-1.

An initial payload configuration for ERS was selected in 1981, including:

- Active Microwave Instrument (SAR and scatterometer)
- Ocean Color Monitor
- Imaging Passive microwave radiometer
- Radar altimeter

A major change, in 1982, mostly due to financial reasons, led to the final payload: the OCM and IMR were dropped while three AO instruments were accepted: ATSR (UK and Australia), MWS (France) and PRARE (Germany).

The Phase C/D (development) was led by Dornier,

which started in late 1985 for a launch in 1991.

The AMI concept

The Active Microwave Instrumentation AMI on board ERS, consists of 2 different radars C-band (5.3 GHz) operating at vertical polarization (VV) which share common electronics. The SAR provides Image and wave mode. The AMI-wind or scatterometer provides the wind mode, with three antennas looking sequentially 45 degrees forward, sideways, and 45 degrees backwards with respect to the satellite flight direction. The illuminated swath is 500 km wide, the nodes are separated 25 km, centered within a resolution cell of 50 x 50 km.

The Seasat scatterometer used Ku-band, so the use of C-Band on ERS-1 was much questioned. The main reasons for using C-band were: that SAR was already decided to be in C-band, there was no microwave radiometer to correct for rain and furthermore, a share of electronics with SAR would reduce the costs.

A number of issues had to be tackled, as there were no datasets at C-Band before the ERS-1 launch. Therefore, intensive airborne campaigns were needed to prepare for the launch in order to prove the adequacy sensitivity of the C-Band and to develop a C-band empirical model CMOD, which is at present in its 4th version.

The reasons for success of the AMI-wind on ERS, were mainly the outstanding calibration approach, based on the use of natural targets and ground based transponders, together with the close co-operation between scientific groups, industry and the ESA project teams involved.

The payload of ERS-2 is the same as for ERS-1, with the addition of a Global Ozone Monitoring Experiment instrument GOME, and a modified ATSR. In particular, the AMI-wind has been kept, thus providing for at least seven years of continuous scatterometer data.

From research to operations

One key element for the continuation of the scatterometer mission beyond the ERS by embarking an advanced scatterometer in the Metop series, has been the interest of Meteorological Institutes in developing specific data assimilation techniques for the scatterometer data. The data provided by the ERS scatterometer is now routinely assimilated into NWP models by operational

meteorological organizations, which have reported improvements in their weather forecast skills.

Front runner is ECMWF, which in a study for ESA in 1986, carried out assimilation of Seasat data on their NWP model, proving both feasibility and potential interest, with a view to ERS. Another key element was the number of new unforeseen applications, mainly over land and ice, which has also raised interest in non-meteorological communities.

The next scatterometer to be flying in an European satellite is ASCAT, an advanced scatterometer adapted for the operational Metop context planned as from 2003. ASCAT on Metop is a new concept, but relies heavily on the ERS heritage, especially for that which concerns the processing of wind products.

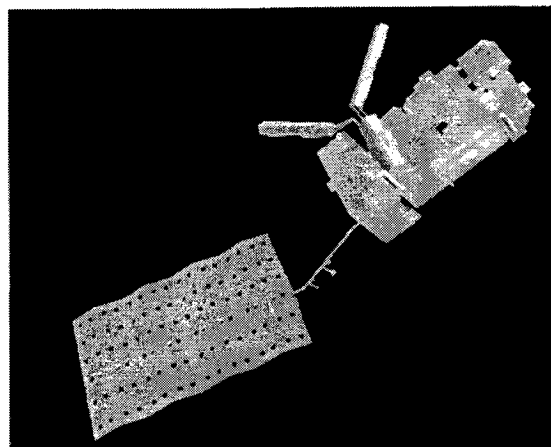
ASCAT is being developed by Dornier in the context of the ESA-EUMETSAT EPS/Metop Program. ASCAT will not only ensure continuity to the successful ERS mission, but provide an even better coverage and resolution thanks to an improved design and operational environment

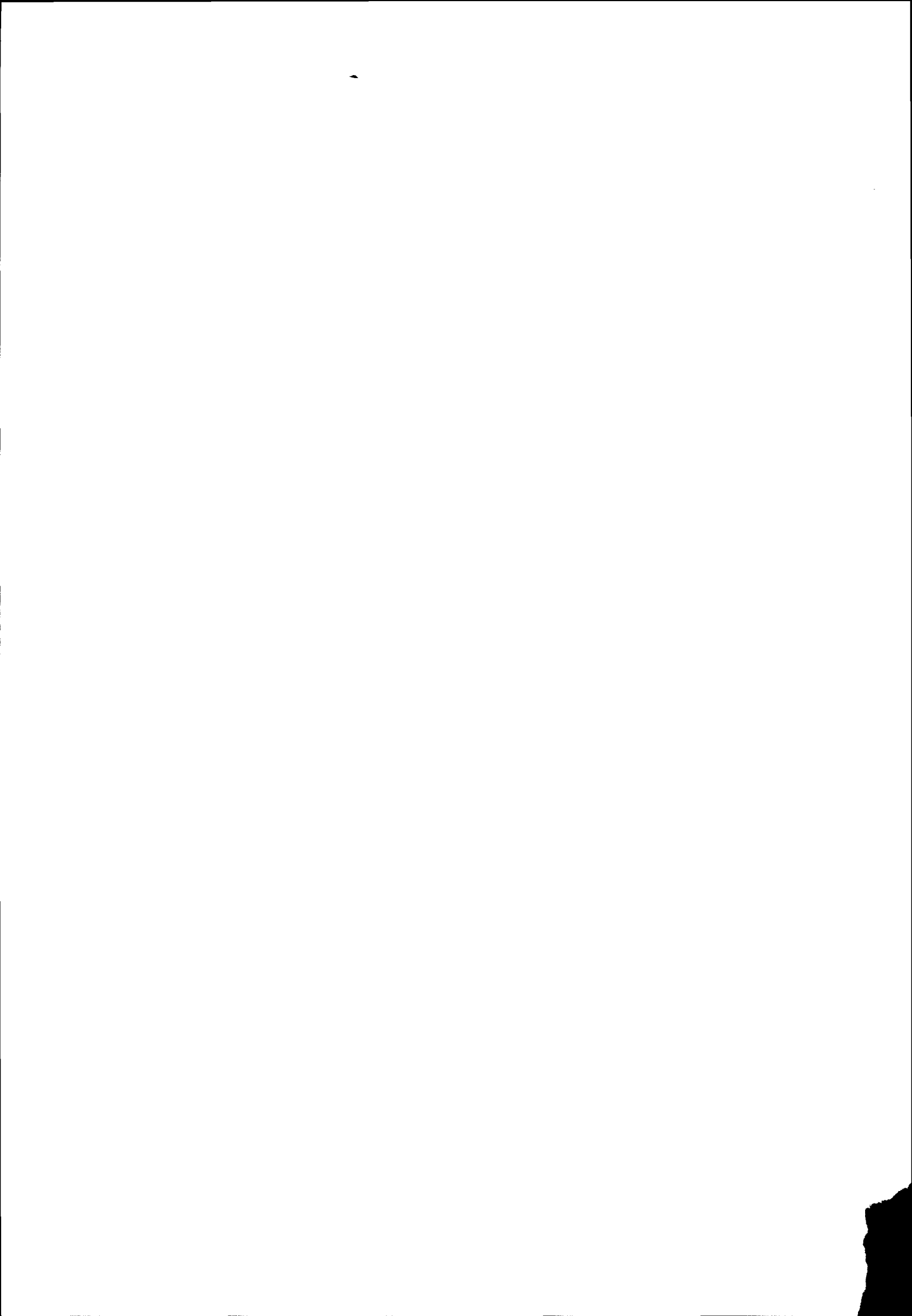
Conclusions

The ERS mission, and in particular the scatterometer mission, has been successfully demonstrated by ESA. ASCAT on Metop will serve the operational needs of European Meteorologists for wind vectors over the oceans. ASCAT on Metop will also enable scientists to continue and to develop research in Earth Sciences, as it was for ERS and will be for Envisat.

Thus, monitoring the Earth's atmosphere and its surface on a global scale has become a reality, leading to a better understanding of its physical processes.

Figure 2: Metop artist's view





PERSPECTIVES FOR THE ADVANCED SCATTEROMETER (ASCAT) ON METOP

J. Kerkmann and D. Klaes

EUMETSAT, Am Kavalleriesand 31, D-64295 Darmstadt

Phone: +49 6151 807514, Fax: ...555, E-mail: kerkmann@eumetsat.de

ABSTRACT

The Advanced Scatterometer (ASCAT) on Metop is a follow-on to the wind mode of the Active Microwave Instruments (AMI) on ERS-1&2. The prime objective of the instrument is to measure the wind field at the ocean surface. Other mission objectives, which are supported by ASCAT, include the measurement of ice boundaries, sea ice concentrations, sea ice type, snow cover over land, soil moisture and snow/ice liquid water content.

ASCAT will be a real aperture C-band radar with high radiometric resolution and stability. The beam directions (45° , 90° and 135° relative to the sub-satellite track), the radar frequency (5.25 GHz) and the vertical polarisation will be the same as for the ERS scatterometer. Spatial sampling (25 km) and horizontal resolution (50 km, i.e. overlapping footprints) will also be identical to the ERS scatterometer, but a research mode will be added with 25 km resolution (12.5 km sampling). Since ASCAT will have a dedicated microwave source plus a double swath of 550 km width, the area coverage will be about three times greater than for the ERS scatterometer. Another important change is the shifting of the swath to higher incidence angles (mid beam 25° to 54.5° ; fore/aft beam 33.7° to 65.3°). This will help to increase the directional skill of the scatterometer wind measurements, in particular at near swath.

It is expected that the high area coverage of ASCAT data will lead to a larger positive impact of scatterometer data on short and medium range weather forecasts. ASCAT measurements will also be important for improving our understanding of the ice drift in the polar regions. The high resolution mode will allow studying mesoscale wind structures over the world oceans, and in particular it will help to improve the tracking of tropical cyclones and polar lows. In combination with other scatterometer instruments (e.g. SeaWinds) and altimeters, it will give the forecaster a wealth of information on the ocean surface and contribute significantly to climate monitoring. Concerning the tropical circulation, ASCAT data will be particularly useful for the prediction of El Niño – Southern Oscillation (ENSO) events and the onset of monsoons.

1. THE INITIAL JOINT POLAR SYSTEM (IJPS)

The EUMETSAT Polar System (EPS) is the European contribution to the Initial Joint Polar System (IJPS), and

later the Joint Polar System (JPS), which will continue the current system of polar orbiting weather satellites, composed of a morning (AM) and an afternoon (PM) satellite, and currently operated by the U.S. (Langevin et al., 1998). From end 2003 on, the European Metop satellites will provide the service in the morning orbit, whereas the U.S. continue to provide the service in the afternoon orbit.

EPS Mission Objectives: OPERATIONAL METEOROLOGY CLIMATE MONITORING

- Temperature and moisture sounding for NWP
 - High accuracy/vertical resolution
 - All weather capability
 - Troposphere/ stratosphere and tropo/strato interaction
- Imagery of clouds and land/ocean surfaces
- Air-sea intercalations
- Ozone mapping and monitoring
- Data collection and location
- Direct broadcast/support to nowcasting

Tab.1: EPS Main Mission Objectives.

The EPS is composed of the Space Segment, comprising three Metop satellites, the launcher service, a Ground Segment and is planned to cover 14 years of operations.

The satellites of the EUMETSAT Polar System (EPS) will be launched into a sun synchronous, near polar orbit with an equator crossing time of 09:30 AM (descending node), i.e. the so-called morning orbit. The main mission objectives for the system are Operational Meteorology and also Climate Monitoring (Klaes et al., 1998). In addition, the Search and Rescue Instruments and also the Space Environment Monitor are embarked. The main missions are summarised in table 1.

EPS capabilities / payload

- Global VIS/IR Imagery: AVHRR
- Atmospheric Sounding (temperature, moisture, species):
 - IR/MW imaging sounders: HIRS/IASI, AMSU/MHS
 - UV/VIS imaging sounder : GOME-2
 - limb viewing radio-occultation sounder: GRAS
- 2-D wind field at ocean surface: ASCAT
- Data Location and Collection: ARGOS terminal
- Global and Local Data Access: HRPT / LRPT

Tab.2: EPS payload and capabilities.

To achieve these objectives the appropriate payload will be embarked on Metop, with a number of sounding instruments. Table 2 summarises the EPS payload, related to the mission objectives.

In summary, the scientific payload on the Metop space craft, which is developed jointly with the European Space Agency (ESA), comprise the:

- Infrared Atmospheric Sounding Interferometer (IASI)
- Advanced Very High Resolution Radiometer (AVHRR/3)
- High Resolution Infrared Radiation Sounder (HIRS/4)
- Advanced Microwave Sounding Unit -A (AMSU-A)
- Microwave Humidity Sounder (MHS)
- GNSS Radio Occultation Sounder (GRAS)
- Advanced Scatterometer (ASCAT)
- Global Ozone Monitoring Experiment (GOME-2)

Data are exchanged via a transatlantic link between the EPS and the NOAA Ground Segments, so that each Ground Segment disposes of the full data set of the Joint System. This includes blind orbit support.

The EPS Ground Segment comprises a central facility, which provides space craft control, and data processing, distribution and archiving up. Full level 1b data are planned to be distributed to the User Community as well as selected level 2 products. The Satellite Application Facilities (SAF) form the decentralised part of the Ground Segment and are considered as Centres of Expertise on several meteorological application areas. They provide data and products as well as algorithm development.

Data and products are archived in the EUMETSAT Unified Archive (U-MARF), so that the User has one defined interface to EUMETSAT data.

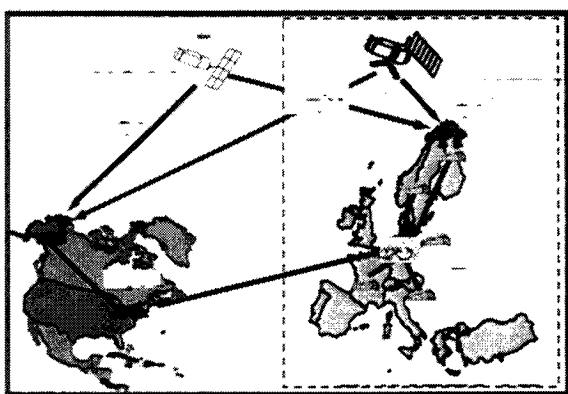


Fig. 1: The Initial Joint Polar System (IJPS).

2. THE ADVANCED SCATTEROMETER (ASCAT)

The first scatterometer instrument in space was the SEASAT-A Scatterometer System (SASS), on board of the experimental oceanographic satellite SEASAT-A that operated between July and October 1978.

SEASAT-A measurements were ended by an abrupt power system failure less than 4 months after launch.

Thirteen years later, on 17 July 1991, ESA launched the European Remote Sensing satellite, ERS-1, which includes as part of its payload a C-band scatterometer to measure wind vectors over the sea surface under all weather conditions. The ERS-1 scatterometer differs from the SEASAT scatterometer in that the radar antennae are mounted only on one side of the satellite illuminating a 500 km wide swath to the right side of sub-satellite track. But instead of two, it has three independent antennae pointing in 45° (fore beam), 90° (mid beam) and 135° (aft beam) direction with respect to satellite propagation. ERS-2, launched in 1995, also carries a scatterometer resulting in a contiguous dataset of sea surface winds from 1991 to the present. With a resolution of 50 km and a sampling distance of 25 km, the ERS scatterometer produce about 160000 valid 3-beam measurements per day.

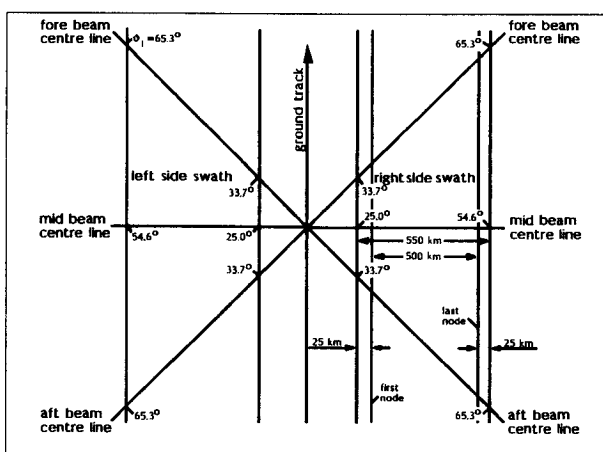


Fig. 2: ASCAT system geometry: ground projection showing dimensions and local incidence angles.

The Advanced Scatterometer (ASCAT) on Metop is intended as a follow-on to the ERS scatterometer on-board ERS-1 and ERS-2. ASCAT is a real aperture C-band radar (5.255 GHz frequency) with high radiometric resolution and stability. The beam directions (see fig.2), the radar frequency and the polarisation (VV) are the same as for the ERS scatterometer. Spatial sampling (25 km) and horizontal resolution (50 km, i.e. overlapping footprints) will also be identical to the ERS scatterometer, but a research mode will be added with 25 km resolution (12.5 km sampling). Since ASCAT will have a dedicated microwave source (i.e. there will be no shared use with a SAR) and a double swath of 550 km width, the area coverage will be about three times greater than for the ERS scatterometer (see fig.3). The double swath coverage is provided by 6 antennae arranged in 3 pairs of V-shaped assemblies. In order to improve the skill in the retrieval of the wind direction, the swath has been moved to higher incidence angles (mid beam 25° to 54.5° ; fore/aft beam 33.7° to 65.3°). This implies an increase in the stand-off distance between each wind

swath and the sub-satellite track as compared to the ERS scatterometer.

The prime objective of the ASCAT mission is to measure the wind field at the ocean surface in the range of 4 to 24 m/s with an accuracy of 3 m/s vector rms. Other objectives that are supported by the ASCAT mission are:

A. Measurements over the oceans:

- Sea ice boundaries
- Sea ice concentration and type

B. Measurements over land:

- Soil moisture
- Snow cover
- Snow/ice liquid water content

The hardware for ASCAT will not be identical to the one of the ERS scatterometer. A part of the processing of the data will already be performed onboard (e.g. some spatial filtering is done by averaging the spectra derived from successive echoes) resulting in a low data rate load on the telemetry link. It will not require onboard knowledge of satellite position/pointing and will be controllable by parameter setting from the ground station.

The following table summarises the characteristics of ASCAT.

Characteristics	Value	Unit
Scan rate	3.763	s
Sampling interval	continuous	-
Grid cells/scan	44	-
Swath	25.0-54.5 (mid) 33.7-65.3 (side)	deg
Swath width	2 times 550	km
Cell resolution	50/25	km
Along track grid spacing	25.0/12.5	km
Across track grid spacing	25.0/12.5	km

Tab.3. Scanning characteristics of ASCAT.

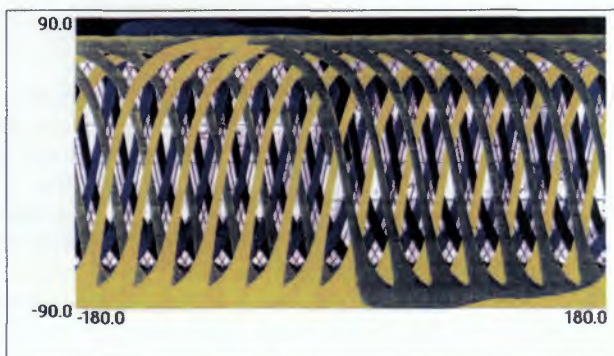


Fig.3: ASCAT coverage for one day.

3. CHANGES WITH RESPECT TO THE ERS SCATTEROMETER

The most obvious change of the ASCAT instrument with respect to the ERS scatterometer is the increased coverage due to the double swath, the slightly increased swath width and the dedicated microwave source. This will significantly improve the monitoring of tropical cyclones as the cyclones will be more frequently "hit" by the scatterometer. In addition, the gaps in the coastal zones caused by switching the Active Microwave Instrument (AMI) on ERS from one mode to another will disappear. This will be an advantage for the monitoring of tropical cyclones in the Eastern Pacific, close to the coast of Mexico and the U.S., where a large number of tropical cyclones are borne.

The impact of a greater area coverage of scatterometer measurements on numerical weather forecasts has been studied, among others, by Undén et al. (1997). The tandem operations of ERS-1 and ERS-2 scatterometers in April-May 1996 provided an ideal opportunity to investigate this impact. Four parallel assimilation experiments in 3D-Var were performed: using no scatterometer data (NOSCAT), using ERS-1 or ERS-2 data only and using both ERS-1 and ERS-2 data (ERS1+2). Table 4 summarises the results of the impact on the surface wind analysis. The departures between first guess and scatterometer observations are given for each experiment. The vector rms difference is reduced by 0.1 and 0.08 m/s when using ERS-1 and ERS-2 data respectively, and by 0.15 m/s when using both ERS-1 and ERS-2 data, demonstrating a good complement between both scatterometers, their separate benefits being juxtaposed without particular overlap when using them together.

Experiment	Vector rms (m/s)	Difference w.r.t. NOSCAT
NOSCAT	3.40	/
ERS-1	3.30	-0.10
ERS-2	3.32	-0.08
ERS1+2	3.25	-0.15

Tab.4: RMS departures between the first guess and scatterometer observations obtained using no scatterometer data (NOSCAT), ERS-1 or ERS-2 data only and both ERS-1 and ERS-2 data (ERS1+2) (from Undén et al., 1997).

As already mentioned, the shifting of the swath towards higher incidence angles will help to improve the retrieval of the wind direction from the σ^0 triplets. Table 5 shows some statistics of ERS scatterometer minus ECMWF analysis winds. It can be seen that the departure standard deviation for the wind direction decreases with increasing node number. Also the vector rms decreases with increasing node number, indicating that the overall errors of scatterometer winds are smaller at high incidence angles.

Node	Wind direction			
	Nbr.	Bias	Sd	Vrms
1	9168	0.88	23.81	3.73
3	9511	0.92	21.13	3.37
5	9717	1.26	19.89	3.21
7	9783	1.46	19.17	3.16
9	9794	1.10	19.07	3.17
11	9762	1.42	18.86	3.15
13	9700	1.48	18.69	3.15
15	9656	1.29	18.71	3.15
17	9638	1.11	18.31	3.14
19	9677	0.98	18.36	3.11

Tab.5: Departure statistics of ERS-1 scatterometer winds minus ECMWF analysis wind directions for all odd nodes. Direction statistics are only made when the average wind speed exceeds 4 m/s. Nodes are numbered from inside swath. Nbr = number of observations used in the collocation experiment, Sd = standard deviation, Vrms = vector rms (from Stoffelen and Anderson., 1993).

The high resolution mode (research mode) of the ASCAT measurements will be particularly beneficial for studying the mesoscale wind structure in tropical cyclones and polar lows and for the estimation of the surface wind in closed or semi-enclosed seas. Quilfen et al. (1997, 1998) experimentally produced a few sets of ERS scatterometer measurements at 25x25 km² resolution (12.5 km sampling). They illustrated that the high resolution will provide more consistent wind fields in coastal areas allowing to use the measurements up to a few tens of kilometres from the coast. They also showed that enhancing the resolution by a factor of two allows a more precise location of the wind maxima and minima and of the position of tropical cyclones (see fig.4).

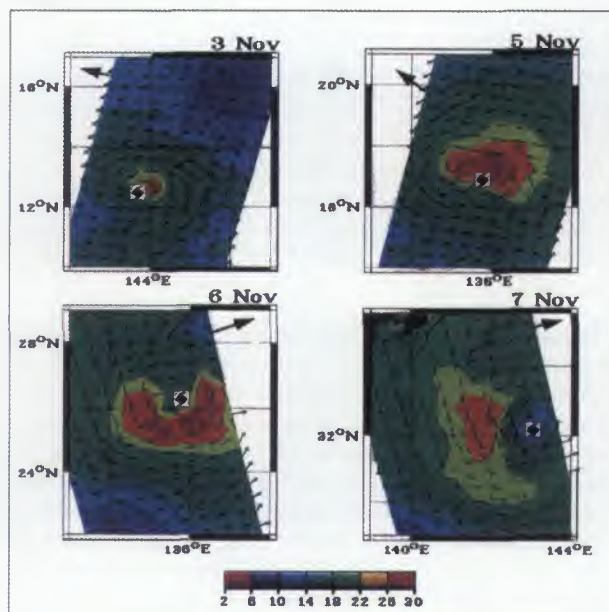


Fig.4: High resolution surface wind field from the ERS-1 scatterometer of tropical cyclone Elsie for 3, 5, 6 and 7 November 1992 (from Quilfen et al., 1998).

As regards NWP applications, the current resolution of global models is lower than the resolution of scatterometer data. Therefore, the data are thinned to about 100 km before handling them to the assimilation system. However, the upper limit for the horizontal resolution set by the hydrostatic approximation, i.e. 10 km, is by far not reached. It can be expected that the resolution of global NWP models will improve during the next decade. In addition, scatterometer data are also assimilated into regional NWP models, which would benefit from high resolution scatterometer data.

4. OPERATIONAL APPLICATIONS

There are a number of operational applications of scatterometer data that have developed as a result of ERS research and demonstration. Scatterometer winds are routinely used for the monitoring of tropical cyclones over the worldwide oceans as well as for climate monitoring. For Oceanography, scatterometer data are one of the driving input data, whereby the data are used in two ways: by assimilation in the ocean models or by direct use of the wind product. More recently, IFREMER in France is operationally producing sea ice maps from scatterometer data on a weekly basis. Fig.5 depicts a comparison if the sea ice edge product for the Antarctic derived from ERS scatterometer data with the same product derived from SSM/I data. The best fit of the scatterometer ice edge with the coincident SSM/I ice edge is found for the 50% isopleth.

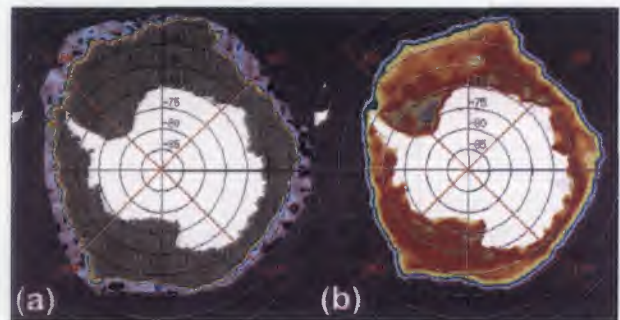


Fig.5: Comparison of the ice edge mask for the Antarctic derived from: (a) ERS-1 scatterometer data; (b) SSM/I passive microwave data (from Cavanié et al., 1997).

The assimilation of scatterometer data in NWP models remains so far the main operational application of scatterometer data. The impact of scatterometer winds on the analysis is generally very large in the S. Hemisphere where conventional observations are sparse (e.g. Ingleby and Bromley, 1991). In the N. Hemisphere the impact on the analysis is much smaller. As regards the impact on the forecast, a positive impact was found whenever strong cyclones were observed in the area of investigation (e.g. Anderson et al., 1991, Ingleby and Bromley, 1991, Undén et al., 1997).

The recent switch from the 3D-Var to the 4D-Var assimilation system at ECMWF has led to a significant increase of the impact of scatterometer data on the

forecast. First tests with the high resolution ECMWF model (T639) also show an improvement in the use of scatterometer data as compared to the current model (T319). However, the assimilation of scatterometer data into NWP models needs still to be improved (sharper structure functions, situation dependent structure functions) and the underestimation of the wind speed in the vicinity of tropical cyclones needs to be resolved.

A rather dramatic example of the impact of scatterometer winds on a five-day forecast is given in fig.6. Fig.7 shows the verifying analysis corresponding to the forecasts in fig.6. The CON forecast (top panel) completely fails to detect the hurricane Luis. The 4D-Var forecast shows a clear improvement with the storm nearly in the right position, but it underestimates its intensity. Finally, the 4D-Var forecast with scatterometer winds reflects the real intensity of the storm, although it predicts the cyclone to be further to the east than its actual position.

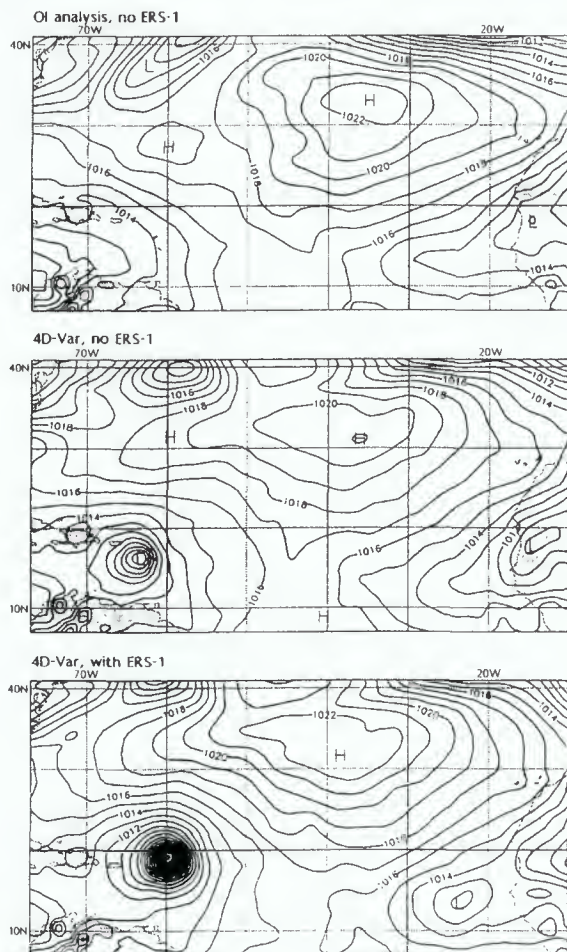


Fig.6: Mean sea level pressure five-day forecast with the ECMWF model valid at 6-9-95, 12 UTC. Upper panel: forecast from the Optimum Interpolation (OI) assimilation system without scatterometer data. Middle panel: forecast using the 4D-Var assimilation system without scatterometer data. Bottom panel: forecast using the 4D-Var assimilation system with scatterometer data from ERS (from Le Meur et al., 1998).

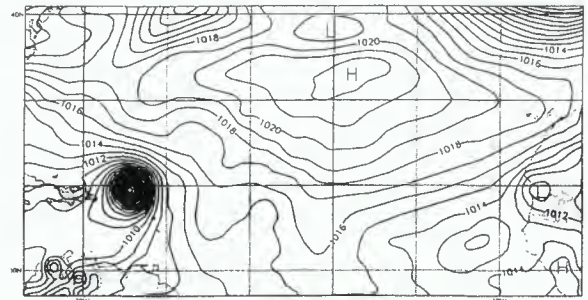


Fig.7: Analysed mean sea level pressure field for 6 September 1995, 12 UTC, corresponding to the five day forecasts shown in fig.6 (from Le Meur et al., 1998).

5. EMERGING APPLICATIONS

Beyond the original mission of the ERS scatterometers, intended to provide measurements of the wind vector over the oceans, a large number of new unforeseen applications have emerged. These applications cover not only the ocean, but also land surfaces and continental or sea ice with frequent global coverage.

As regards land applications, new methods for the retrieval of soil moisture and vegetation type/coverage have been developed. Comparison of soil moisture retrieved from scatterometer data with in-situ measurements reveal a good agreement for both, the 0-20 cm layer and the 0-100 cm layer (Wagner, 1998). Concerning vegetation types, most information comes from higher incidence angles, i.e. "vegetation types start to emerge at 30 degrees incidence angle" (Habermeyer et al., 1998). Vegetation types have so far been successfully retrieved for the Sahel area and for Siberia. An example for fractional vegetation cover for the Sahel area is given in fig.8. The seasonal variability can clearly be seen, with the September retrievals showing significantly more Sahelian vegetation coverage than in December.

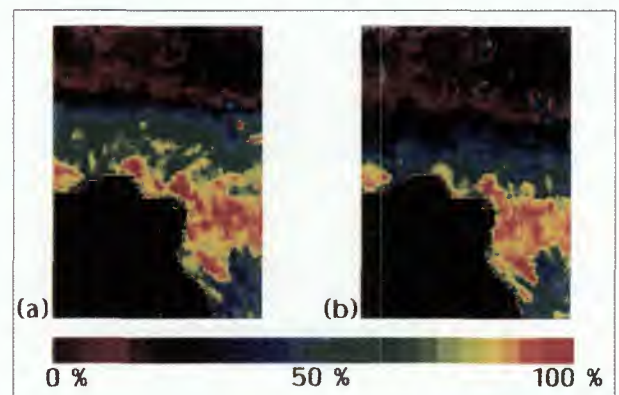


Fig.8: Equivalent fractional vegetation cover over Africa (Hapex Sahel) for September 1992 (a) and December 1992 (b) retrieved from ERS-1 scatterometer data (from Woodhouse and Hoekman, 1997).

As regards snow and ice applications, several years of backscatter time series from Greenland and Antarctica

ice sheets have shown that there is a clear impact of the dry snow on the scatterometer measurements, suggesting that it is possible to estimate the snow accumulation rate from scatterometer data (e.g. Wismann, 1998). It has also been demonstrated that it is also possible to identify and locate the percolation zone (and its temporal variation) and the ablation regions. Furthermore, it could be shown that the anisotropy pattern of the scatterometer data over Antarctica correlate well with the location and orientation of sastrugi, as developed in response to katabatic winds. Finally, ice features can be well tracked on a monthly basis with scatterometer data. Even the tracking of large icebergs (larger than 180 km²) is possible on a single pass basis, allowing the determination of ocean currents (e.g. Young, 1998).

6. REAL-TIME AND OFF-LINE SERVICES

The EPS user community will be provided with the EPS/Metop data and products in three different ways:

1. Via communication links with the EPS ground segment in near real time.
2. Via communication links with the Satellite Application Facilities (SAFs).
3. Via communication links with the EUMETSAT multi-mission archive (U-MARF).

As regards the near real-time (NRT) service, there will be two possibilities for receiving the EPS data:

- By local reception based on the direct read-out services of EPS, namely the High Resolution Picture Transmission (HRPT) and Low Resolution Picture Transmission (LRPT) services. The full instruments science data and the satellite bus auxiliary data are continuously broadcasted to the ground in L-band on the HRPT link, whereas a subset of the data is broadcasted to the ground in VHF-band on the LRPT link. The data which can be obtained in this manner are those generated when the satellite is in the visibility of the local receiving station. A possible way of controlling the access to the data is encryption.
- By receiving the data from the central processing facility based on the global read-out service of EPS. All the instruments science data, the satellite bus auxiliary data and the housekeeping telemetry are continuously recorded on board of the Metop satellite and dumped to the EPS ground segment, once per orbit, on the Global Data Stream (GDS). The Metop GDS will be acquired in a European receiving station at high latitudes. The blind orbits not covered by the European station will be received by a NOAA ground station and send the the EPS ground segment.

As regards the archive, after analysing the commonalities among the programmes EUMETSAT has decided to develop a multi-mission, incremental archiving infrastructure, including user access

capability, called the Unified Meteorological Archiving and Retrieval Facility (U-MARF). The objectives are to:

- Offer integrated user access to the whole EUMETSAT data products and services, including the historical archive from Meteosat 1 to 7;
- Rationalise the development and operations costs;
- Exploit and take advantage of new technologies;
- Build in flexibility and scalability to accommodate future new data and archive growth potential.

Ingestion, archiving and making retrievable data and products from the EUMETSAT programmes for at least 20 years of mission lifetime constitutes the primary purpose of the U-MARF. For EPS, approximately 100 Terabytes/year have to be handled. The prime functions of the user services will be the user registration, directory and guide, inventory and browse and the ordering and follow-up. User administration, user help desk and future interoperability with other providers of Earth Observation data will also be supported. It should be noted that, because of the fast evolution of technology, transcription of the data and products must also be an integral function of the U-MARF. An overview of the functions of the U-MARF is given in fig.9.

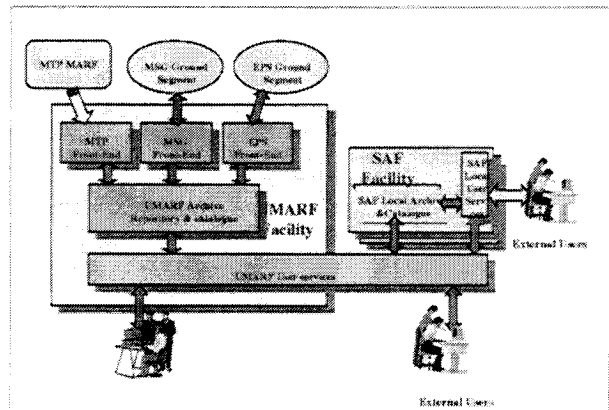


Fig.9: Functions overview of the EUMETSAT multi mission Unified-Meteorological Archiving and Retrieval Facility (U-MARF).

7. SATELLITE APPLICATIONS FACILITIES

EUMETSAT has started the development of a network of Satellite Application Facilities (SAFs) which together with the central facilities will constitute the future EUMETSAT Application Ground Segments for Meteosat Second Generation (MSG) and EPS. Each SAF is planned to be developed over a period of 5 years. The SAFs will be located in a National Meteorological Service (NMS) or other approved institute of an EUMETSAT member state. The scope of the SAF activities shall be to deliver products or software to derive these products, at the level of geophysical parameters, based primarily on the satellite data. This may imply combining data from various satellite sources, and does not exclude incorporation of

other data sources if necessary and compliant with EUMETSAT requirements.

In 1997, three pilot SAFs have started their activities, namely the SAF in support to Nowcasting and Very Short Range Weather Forecasting (host: Instituto Nacional de Meteorologia, Spain), the SAF for Ocean and Sea Ice (host: Météo France) and the SAF dedicated to Ozone Monitoring (host: Finnish Meteorological Service). Four additional SAFs dedicated to Climate Monitoring, Numerical Weather Prediction (NWP), Land Surface Analysis (LSA) and GRAS Meteorology, respectively, are likely to start their activities in 1999. This will make altogether seven SAFs, of which three, namely the Ocean & Sea Ice SAF, the NWP SAF and the Land Surface Analysis SAF plan to make use of data from the ASCAT instrument. The SAF on Ocean & Sea Ice will develop the algorithms for ASCAT-related products listed in table 6. The Land Surface Analysis SAF will explore the use of ASCAT data for retrieving soil moisture, whereas the NWP SAF will develop so-called "observation operators" for ASCAT data for optimal use of ASCAT data in NWP assimilation schemes. The use of ASCAT data for the retrieval of vegetation parameters, ice drift and soil/snow conditions is currently not planned within the SAF activities.

Product Name	Characteristics	Coverage Area (Resolution)	Frequency
Surface Wind Vector	Wind vector at 10 m height above the ocean surface	Regional and Global (50/25 km)	Frequency according to orbit repeat cycle
Atlantic Sea Ice Edge	Location separating areas infested by more than 20% ice from open water	N-E Atlantic Ocean (10 km)	once per day
Atlantic Sea Ice Cover	Sea ice coverage in % occupying the relevant ocean area	N-E Atlantic Ocean (10 km)	once per day
Atlantic Sea Ice Type	Sea ice type to distinguish between multi-year and first-year ice	N-E Atlantic Ocean (10 km)	once per day

Tab.6: Products of the Ocean & Sea Ice SAF related to the ASCAT instrument. The Sea Ice products will be multi-sensor products from AVHRR, SSM/I, ASCAT and AMSU.

REFERENCES

- Anderson, D., Hollingsworth, A., Uppala, S. and P. Woiceshyn, 1991: A study of the use of scatterometer data in the European Centre for Medium-Range Weather Forecasts Operational Analysis-Forecast Model: 1: Quality assurance and validation. *J. Geophys. Res.*, 96, No. C2, 2619-2634.
- Cavanié, A., Ezraty, R. and F. Gohin, 1997: Sea ice monitoring. In: *Land Surface Observations using the ERS Windscatterometers*, Institute for Applied Remote Sensing, Wedel, Germany, 4-6.
- Habermeyer, M., Schullius, C., Alvarez Perez, J. and S. Marshall, 1998: Extracting land cover information from ERS scatterometer data to support backscatter modelling for soil moisture estimation. *Proceedings of the Workshop on Emerging Scatterometer Applications, ESTEC, Noordwijk, NL, 5-7 October 1998.*
- Klaes, K.D., Langevin, M., Marcorelles, B. and E. Oriol-Pibernat, 1998: The Missions of the EUMETSAT Polar System. 9th AMS Conference on Satellite Meteorology and Oceanography, Paris, 25-29 May 1998, 561-564.
- Ingleby, N.B. and R.A. Bromley, 1991: A diagnostic study of the impact of SEASAT scatterometer winds on numerical weather prediction. *Mon. Wea. Rev.*, 119, 84-103.
- Langevin, M., Klaes, D., Marcorelles, B. and J. Perez, 1998: The EUMETSAT Polar System. 9th AMS Conference on Satellite Meteorology and Oceanography, Paris, 25-29 May 1998, 557-560.
- Le Meur, D., Isaksen, L., Hansen, B., Saunders, R. and P. Janssen, 1998: Global validation of ERS wind and wave products. Final report to the European Space Agency, ESA contract No. 8488/95/NL/CN, ECMWF.
- Quilfen, Y., Chapron, B., Elfouhaily, T. and K. Katsaros, 1997: High resolution scatterometry for the ASCAT instrument. Third ERS Symposium, Florence, Italy, 14-21 March 1997, ESA SP-414, Volume III, 1233-1237.
- Quilfen, Y., Chapron, B., Elfouhaily, T., Katsaros, K. and J. Tournadre, 1998: Observations of tropical cyclones by high resolution scatterometry. *J. Geophys. Res.*, 103, No. C4, 7767-7786.
- Stoffelen, A. and D. Anderson, 1993: Characterisation of ERS-1 scatterometer measurements and wind retrieval. *Proceedings of the Second ERS-1 Symposium, ESA SP-361, Volume II, 997-1002.*
- Uden, P., Kelly, G., Le Meur, D. and L. Isaksen, 1997: Observing system experiments with the 3D-Var assimilation system. Technical Memorandum, No. 244, ECMWF Research Department, 32 pp.
- Wagner, W., 1998: A comparison of ERS scatterometer retrieved soil moisture data with field observations in the Ukraine. *Proceedings of the Workshop on Emerging Scatterometer Applications, ESTEC, Noordwijk, NL, 5-7 October 1998.*
- Wismann, V., 1998: Snow accumulation on Greenland derived from NSCAT and ERS scatterometer data. *Proceedings of the Workshop on Emerging Scatterometer Applications, ESTEC, Noordwijk, NL, 5-7 October 1998.*
- Woodhouse, I. and D. Hoekman, 1997: Land surface parameter retrieval. In: *Land Surface Observations using the ERS Windscatterometers*, Institute for Applied Remote Sensing, Wedel, Germany, 15-18.
- Young, N., 1998: Antarctic iceberg drift and ocean currents derived from scatterometer image series. *Proceedings of the Workshop on Emerging Scatterometer Applications, ESTEC, Noordwijk, NL, 5-7 October 1998.*



The SeaWinds Scatterometer for the Quikscat and ADEOS-II Missions

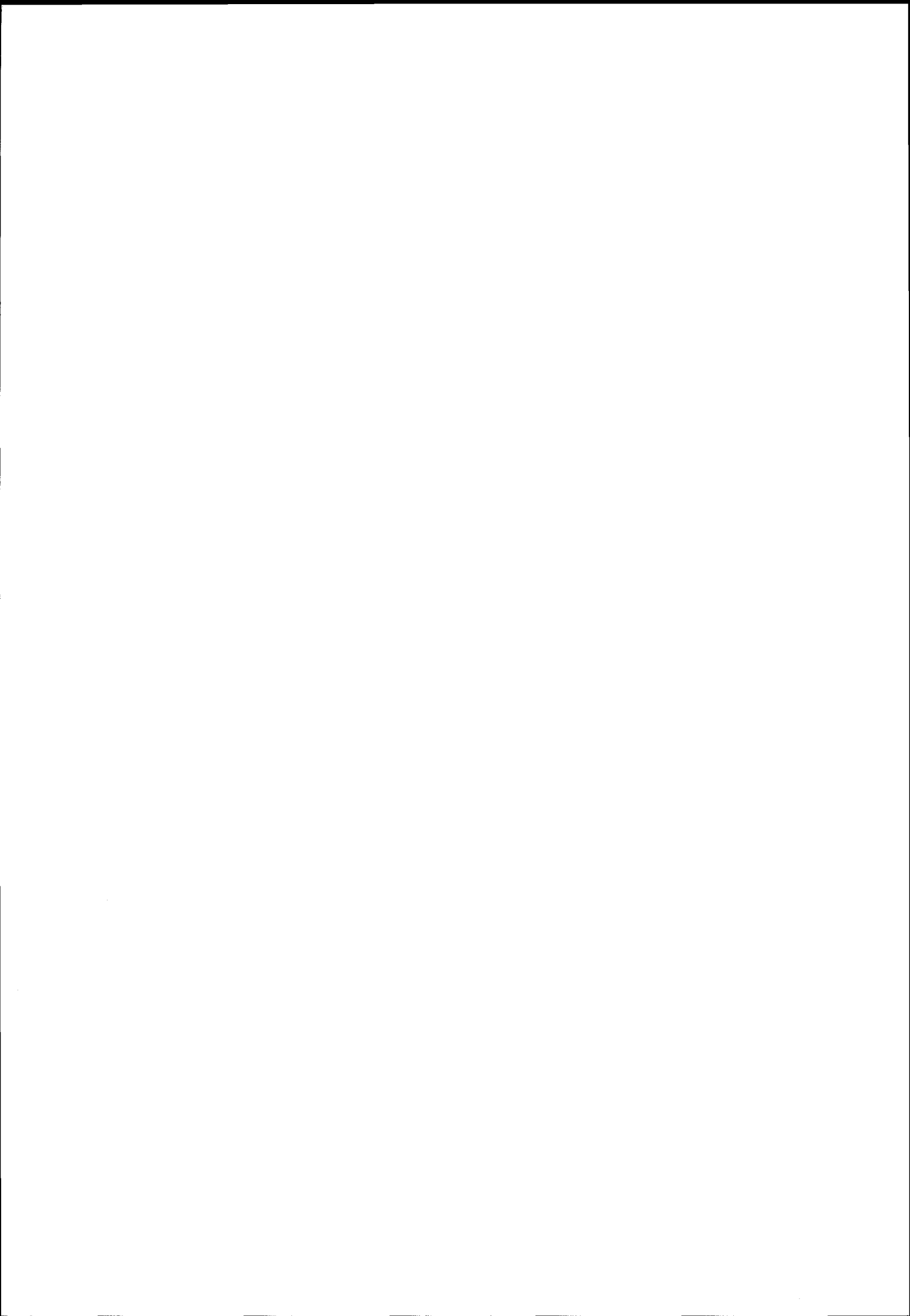
Michael W. Spencer

*California Institute of Technology, Jet Propulsion Laboratory
Pasadena, CA*

Phone: 1-818.354.1175; e-mail: mws@shiokaze.jpl.nasa.gov

The NASA SeaWinds scatterometer is scheduled to fly aboard the Quikscat mission in November 1998, and the Japanese ADEOS-II spacecraft in 2000. In a significant design departure from previous 'fan-beam' scatterometer systems, such as AMI on ERS-1,2 and NSCAT, SeaWinds will be a 'pencil-beam' system. The pencil-beam system has the advantages of 1) being a more compact instrument and thus easier to accommodate on multi-sensor spacecraft and small satellites, 2) constant incidence angle backscatter measurements, 3) no 'nadir gap' where wind can not be retrieved.

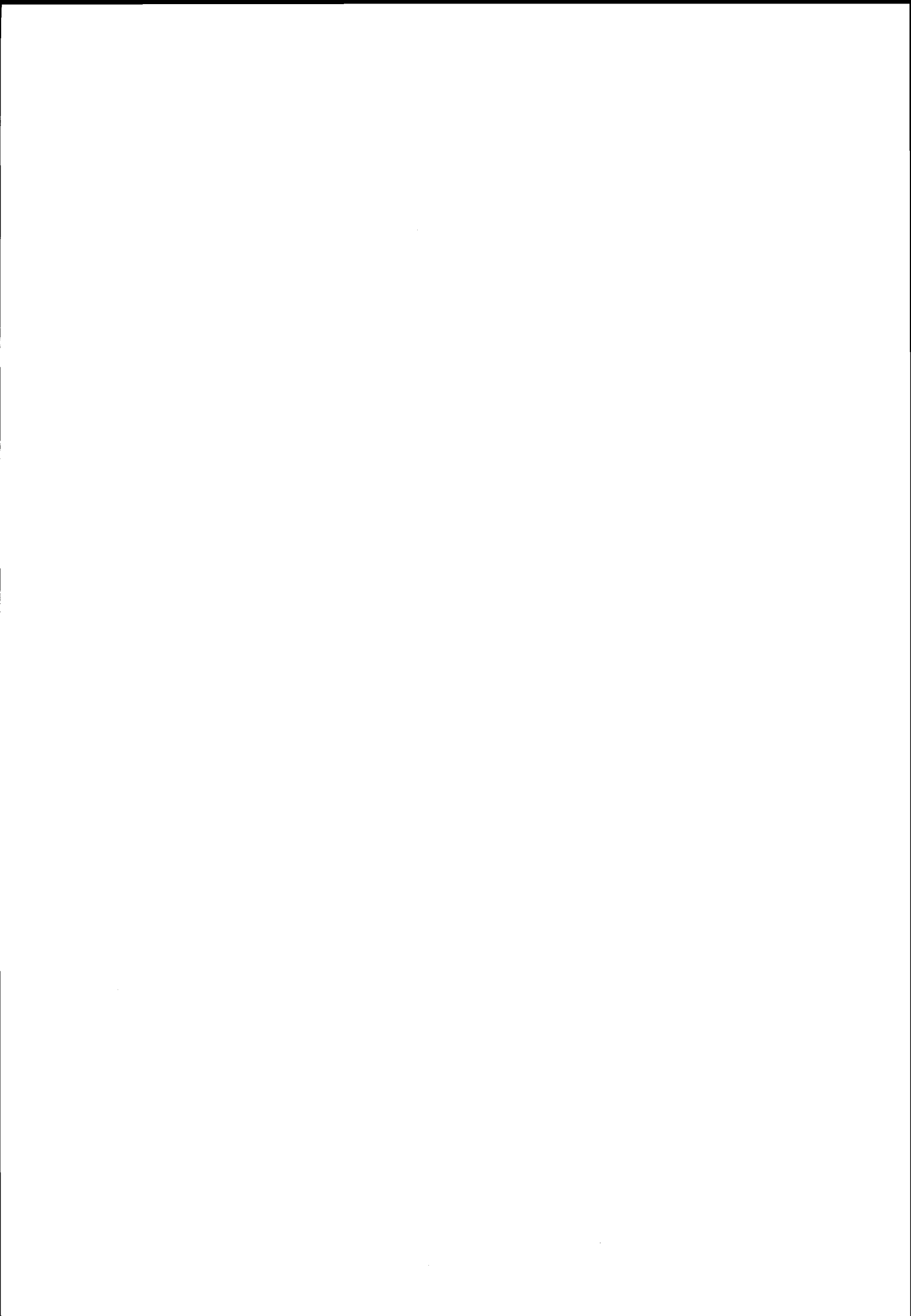
In this presentation, the design of SeaWinds will be described. The geometry, resolution, calibration, and processing of the backscatter measurements will be discussed. A technique to improve the resolution of the backscatter beyond the antenna beam limit by the addition of range filtering will be described. Simulated 'enhanced resolution' land images will then be presented to demonstrate the expected performance of the instrument.



Land Session

Chair: V. Wismann, IFARS

Rapporteur: C.-C. Lin, ESA/ESTEC



LAND SURFACE MONITORING WITH SPACEBORNE SCATTEROMETERS

Volkmar Wismann

Institute for Applied Remote Sensing, Klarastraße 81, 79106 Freiburg, Germany
T: +49-(0)761-2851717; F: +49-(0)761-2851719; E: wismann@ifars.de

ABSTRACT

Spaceborne scatterometers are active microwave instruments for measuring the normalized radar cross section (NRCS) of the Earth surface. These measurements are independent of cloud coverage and illumination by the sun and provide a global coverage within 3 to 4 days. Thus they are well suited for a wide range of operational monitoring tasks. Presently, the scatterometer is exclusively dedicated to the determination of the wind speed and direction over the oceans. It is increasingly acknowledged that, despite the coarse resolution, also a variety of geophysical parameters can be measured and monitored over land surfaces and sea ice. This paper presents an overview of recent developments for obtaining information on, e.g., sea ice, snow properties, thawing of soils, soil moisture, and vegetation from spaceborne scatterometer data.

INTRODUCTION

The first spaceborne scatterometer was operated during the American Skylab mission in 1973 and 1974, demonstrating the feasibility of spaceborne scatterometers. Between June and October 1978, the American SEASAT-A Satellite Scatterometer (SASS) proved that accurate wind field measurements could be made over the oceans from space. Since August 1991 the scatterometers aboard the European ERS satellites (ERS-1 and ERS-2) measure operationally the normalised radar cross section (NRCS) of the Earth's surface at C-Band (5.3 GHz). A global map of the NRCS is depicted in Figure 1.

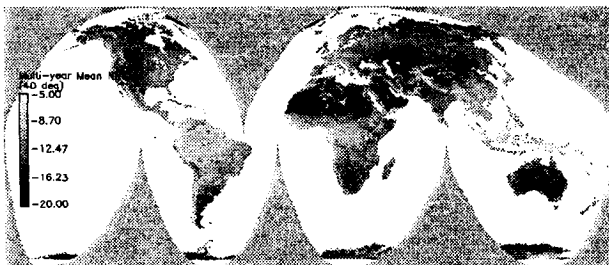


Figure 1 : Map of the mean C-band NRCS at 40° of incidence angle.

During its short lifetime between August 1996 and June 1997 the Japanese ADEOS satellite provided the same type of measurements with the NSCAT system but for K_u-Band (14 GHz) at horizontal and vertical polarisation. In the near future further scatterometers

will be flown mainly for operational wind measurements over the oceans. This is the reason why these systems are often called windscatterometers or even named *SeaWinds*. Table 1 provides an overview over past, present and future systems.

Satellite	Instrument Radar Band	Operation Launch
SEASAT	SASS - K _u -Band	Jun '78 - Oct '78
ERS-1	AMI - C-Band	Since Jul. '91
ERS-2	AMI - C-Band	Since Mar. '96
ADEOS	NSCAT - K _u -Band	Aug. '96 - Jun. '97
QuikScat	SeaWinds - K _u -Band	24. Nov. '98
ADEOS II	SeaWinds - K _u -Band	2000
METOP	ASCAT - C-Band	2003

Table 1 : Overview over past, present, and future spaceborne scatterometer systems.

The scatterometer measurements are independent of cloud coverage and illumination by the sun and provide typically a global coverage within 3 days. Presently, the scatterometer is dedicated only to determining the wind speed and direction over the ocean by measuring the normalised radar cross section of the sea surface. Despite its coarse resolution it was recognised that the spatial and temporal variability of a variety of geophysical parameters can be measured and monitored over sea ice and land surfaces. (Frison and Mougin, 1996a, 1996b, 1998; Kennett and Li, 1989a, 1989b; Kerr and Magagi, 1994; Long and Hardin, 1994; Magagi and Kerr, 1995; Mougin et al., 1994, 1995a, 1995b; Rott and Rack, 1995; Wiesmann and Mätzler, 1994; Wismann and Boehnke, 1994; Wismann et al., 1993, 1994a, 1994b, 1995, 1996a, 1996b).

Most of the data examples presented in this paper originate from the Active Microwave Instrument (AMI) flown on ERS-1 and ERS-2. This instrument operates at C-band (5.3 GHz) and uses three antennae with vertical polarisation (VV) in the scatterometer mode. They are looking 45 degrees forwards (Forebeam), sideways (Midbeam), and 45 degrees backwards (Aftbeam) with respect to the satellite flight direction. The incidence angle of the radar ranges from 18 to 57 degrees, illuminating a 500 km wide swath on the right hand side of the satellite track. The along-track and cross-track spatial resolution is 50 km (ESA, 1992). The measurement geometry is depicted in Figure 2.

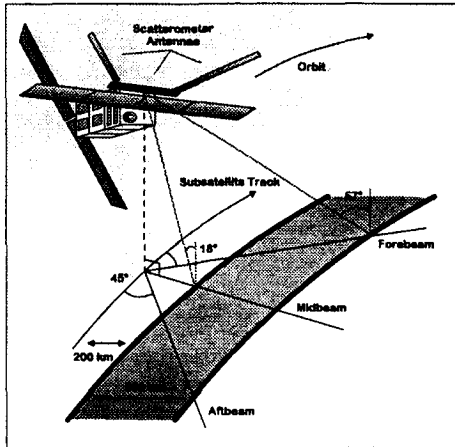


Figure 2 : Schematic of the ERS-1 spacecraft and the scatterometer measurement geometry.

Besides the strength of the radar backscatter the dependence of the NRCS on the incidence angles (slope) provides additional information on surface properties, allowing to discriminate between volume scattering, e.g., within a dense canopy, or surface scattering, e.g., from bare soil. Figure 3 depicts the NRCS as a function of incidence angle for two sites on Greenland and Siberia. Data are plotted for winter and summer to indicate also the seasonal variation. A global map of the slope is shown in Figure 4. Although this map looks similar to the NRCS map in Figure 1 there are obvious differences, which are related to surface characteristics.

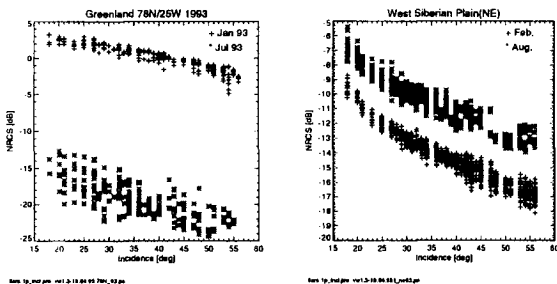


Figure 3 : Incidence dependence of the NRCS for two locations (Greenland and Siberia) and winter and summer, respectively.



Figure 4 : Map of the mean slope (defined as the derivative of the NRCS with respect to incidence angle).

The excellent calibration and maintenance of the ERS instruments guarantee high quality data, which, for the first time, allow a precise evaluation of the spatial and especially the temporal variability of the NRCS of the Earth's surface. Figure 5 depicts a time series of the C-Band NRCS for a location on Greenland. The measured seasonal variability of 0.3 dB indicates the accuracy of the instrument while the overall temporal stability reflects the excellent calibration and maintenance of both scatterometers. It is noteworthy that there was a switchover from ERS-1 to ERS-2 in May 1996, which is not visible in the data.

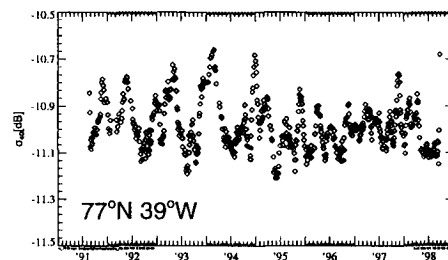


Figure 5: Time series of the C-Band NRCS at 77°N; 39°W on Greenland.

FROZEN SOIL MONITORING

Based on ERS scatterometer data a method was developed to monitor the state (frozen/thawed) of the upper layer of the soils in arctic to temperate climate regions (Boehnke and Wismann, 1996a, 1996b, 1997a, 1997b). When the vegetation cover is sparse or absent, the NRCS at C-band depends mainly on the moisture content of the soil, the dielectric constant, the penetration depth and the surface roughness. The radar backscatter increases with soil moisture and with surface roughness. When liquid water in soil freezes, the dielectric constant of the soil decreases dramatically. This process is reversed in spring when the soil thaws. From NRCS time series it can be seen that in spring, during snow melt, the radar cross section first decreases by up to 5 dB and shortly later, when the soils start thawing, increases dramatically.

Figure 6 shows two typical time series of the NRCS at 40° of incidence angle (σ_{40}) for two grid points in Siberia, their geographical positions are given in the figure. Note the extreme temporal stability of the radar cross section during early spring and the large variations (>5 dB) associated with the onset of thawing. This is delineated for begin of April and June for the grid points located south and, respectively. As can be seen from the σ_{40} time series of the northern grid point, spring snow melting first leads to a strong short-term decrease of 4 dB. This can be explained by the increasing wetness of the snow leading to an enhanced absorption of the microwaves in the wet snow cover and the subsequent low radar return from melt water ponds formed on the frozen grounds when infiltration is still blocked.

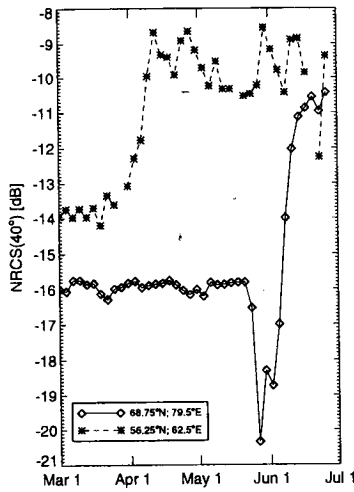


Figure 6 : Time series of σ_{40} for two grid points in spring 1993.

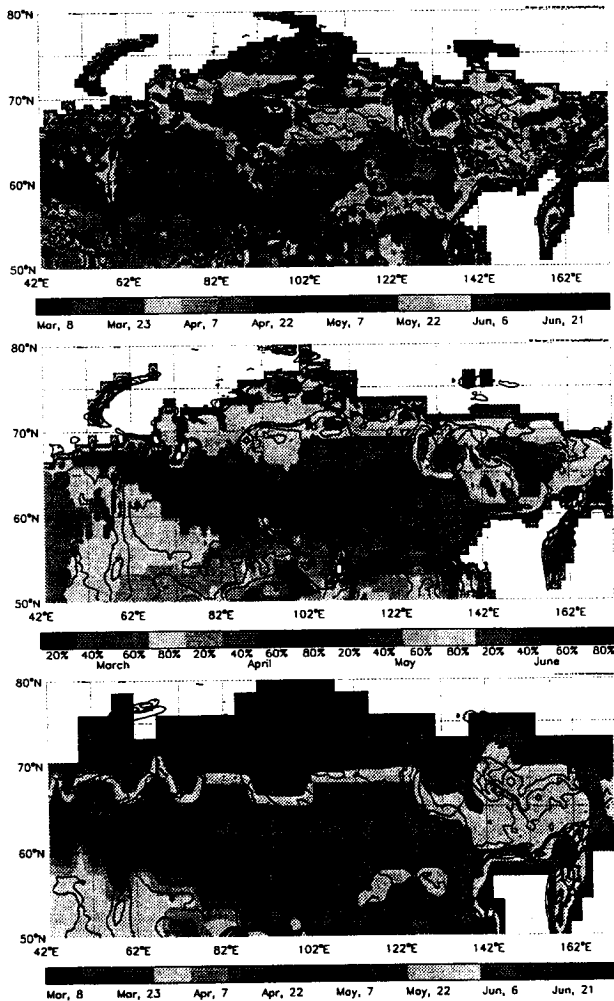


Figure 7 : Maps of Siberia, depicting isochrons of the "onset of spring" derived from scatterometer, SSM/I snow cover, and temperature data for 1992 (from top to bottom).

The application of a change detection algorithm to the scatterometer data over the Siberian test site revealed isochron-maps of thawing for a region extending from 50° N to 80° N and from 42° E to 172° E. The signatures on these maps correlate well with the geographical distribution and the interannual variability of air temperature¹ and snow cover². These isochron-maps are shown in Figure 8 and Figure 8 for 1992 and 1995, respectively. Each colour represents the area thawed before the date marked under the colour scale. Each of the 16 colours corresponds to a period of 8 days between March 1 and June 28. Superimposed are contour lines for elevations of 100, 250, 500 and 1000 m (Lee and Hastings, 1995).

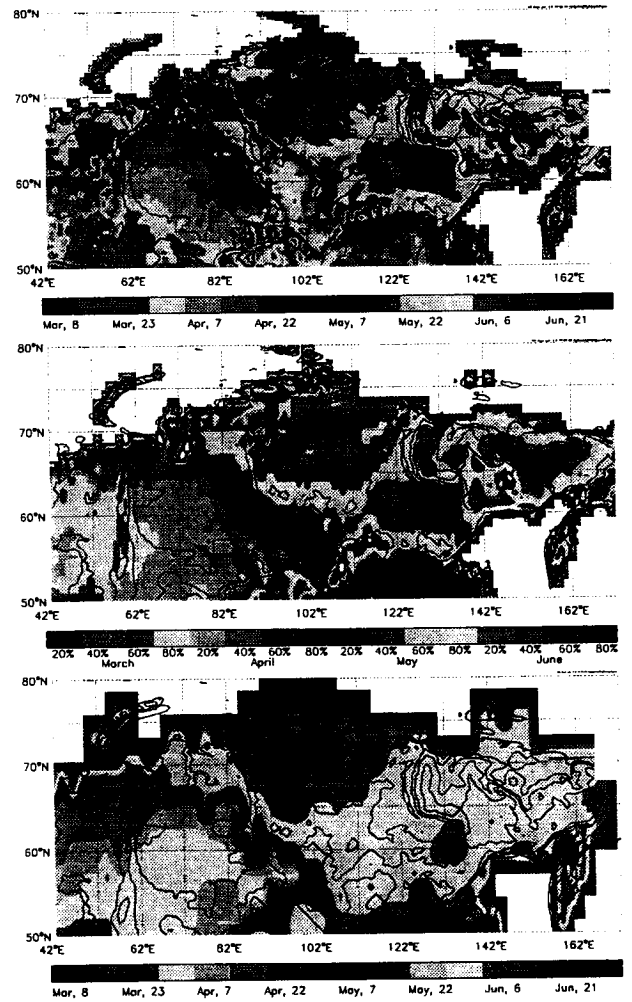


Figure 8 : Same maps of Siberia as in Figure 7 but for 1995.

¹ Global temperature data of the NCAR/NCEP reanalysis were provided by NOAA Climate Diagnostics Center.

² Ralph Ferraro, Microwave Sensing Group, NOAA/Satellite Research Laboratory, provided global snow cover and precipitation data derived from SSM/I radiometer data.

The temporal and spatial evolution of the onset of thawing differs significantly over the years. In 1992, the onset of thawing is late. After the southern part of the test site starts thawing in April, thawing gradually moves towards the north coincident over the complete range of longitudes. By the middle of May, thawing has reached most of Siberia with the exception of the Central Siberian Plateau. For 1995, thawing commences early in the southwest and progresses towards the northeast somewhat slower than in 1992, so that by the middle of May in both years, approximately the same area has thawed (green to grey colours). In both years, the Central Siberian Plateau starts thawing in June. On a regional scale the onset of thawing follows orographic particulars, e.g., mountainous regions like Ural, Werchojansk, and Stanowoi thaw later than regions of lower elevation. It is remarkable how well some isochrons are in accordance with the elevation contour lines, especially in eastern Siberia.

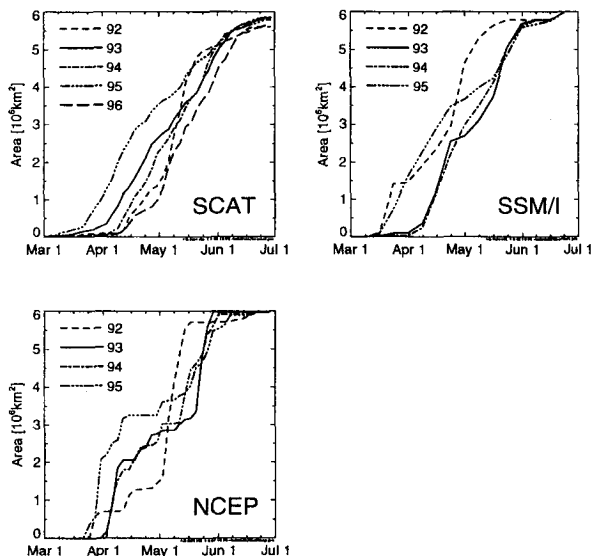


Figure 9 : Time series of the extent of the area detected as thawed (SCAT), depleted of snow cover (SSM/I), and with mean air temperatures above 0°C (NCEP).

For a sub-region of the Siberian test site encompassing the West Siberian Lowland and the Central Siberian Plateau (55° - 70° N; 50° - 120° E), the interannual variability of soil thawing was estimated. The thawed area was derived from the scatterometer data, the SSM/I snow cover information, and the air temperature data for time steps of 3 days. The slope of the area versus time curves is rather constant for all the years except for 1992 (see Figure 9). In the years 1993 to 1996, the thawed area gradually increases throughout spring, whereas in 1992, the onset of thawing is late, but then the majority of the Siberian sub-region thaws much quicker than in the other years. In 1995 thawing begins very early and in

1996 very late. The overall large-scale interannual variability is on the order of one month.

Analogous time series plots are shown for the SSM/I snow cover data and the air temperature data in Figure 9. The characterizations of "spring" from the scatterometer data, the SSM/I data and the air temperature data agree well. The early progress in 1995 and the rapidity of the "onset of spring" in 1992 are consistent. Discrepancies are found for 1992, where the "onset of spring" in the SSM/I data (the area no longer covered with snow) is detected very early. The step-like increases in the NCEP-plot arise from the large grid size of the data being 2.5° by 2.5° .

PREDICTING INUNDATION

The Pantanal in South America is one of the largest tropical wetlands. It is located in the upper Paraguay River basin, covering an area of $137,000\text{ km}^2$, located mainly in Brazil, only in the West, small parts are in Bolivia and Paraguay. Presently, the main river system is still unregulated. The climate of the Pantanal is tropical with a marked wet season between November and March. The annual rainfall across this region is generally 1000 - 1700 mm/a . Maximum inundation occurs in February in the northern regions and due to the delayed drainage of the river system as late as June in the southern part. The total area inundated can vary from $11,000$ to $110,000\text{ km}^2$. Hamilton et al. (1995) demonstrated that microwave radiometer data can be used to monitor the inundation in the Pantanal area.

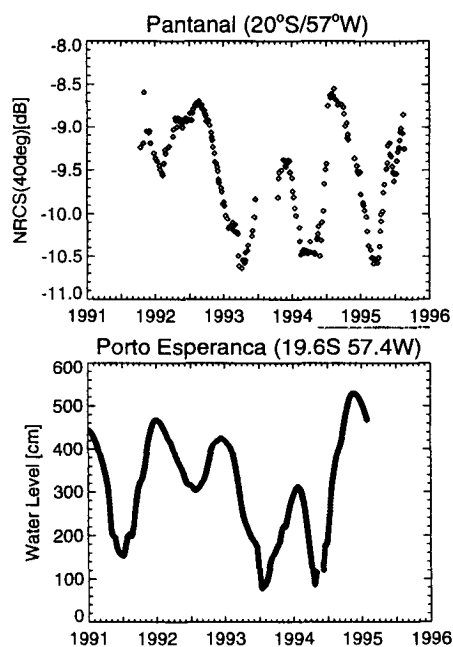


Figure 10 : Time series of the NRCS (top) and of the water level at Porto Esperanca (bottom).

Wismann and Boehnke (1996a) analysed ERS-1 scatterometer over the Pantanal region acquired between

November 1991 and August 1995. During this period the inundation extent varied considerably, the relatively wet year 1992 was followed by dry years 1993 and 1994, while in 1995 a maximum inundation was encountered. The waterlevel at the station Porto Esperance³ is representative for the inundation extent in this area. The time series of the water level and of the NRCS for the respective area is shown in Figure 10.

The high correlation between the water level and the NRCS also reflects the large interannual variability. Furthermore a phase shift between both time series of 1-2 months was found, whereby the radar signal leads the inundation extent. The radar cross section reacts to the onset of vegetation growth in the rainy season which happens timely between the actual precipitation in the north and the flooding in the south. However, there is no satisfactory explanation for this phase between the water level and the NRCS. But, the possibility of predicting the inundation extent by means of scatterometer measurements at least 1 month in advance might have a great impact on various ecological and economic aspects related to the rivers Paraná and Paraguay.

MONITORING VEGETATION

The radar cross section of the Earth's surface decreases typically with incidence angle θ . The slope of the NRCS versus incidence angle curve is indicative for the responsible radar backscatter mechanism and/or for the properties of the backscattering surface. For pure volume scattering, this slope is zero, while for surface scattering this slope decreases with surface roughness. For vegetated areas the radar backscatter is governed by a combination of volume and surface scattering, whereby the amount of volume scattering depends on the canopy coverage and its density. Thus, the slope provides additional information to the NRCS measurement. We define the slope (α) as:

$$\sigma_0 = a\theta^\alpha$$

whereby α is computed by a linear regression between $\log(\sigma_0)$ and the incidence angle θ . Wismann et al. (1996b) introduced the Radar Backscatter Index (RBSI) in order to combine the complementary information of the slope and the NRCS:

$$RBSI = \frac{\sigma_0(40^\circ - 57^\circ)}{|\alpha|}$$

This parameter improved the discrimination between different surfaces by taking into account not only the strength of the radar backscatter, but also information on the backscatter mechanism.

³ Water level data for the Paraguay River were provided by Senhor Vinicius and Senhor Avila of Departamento Nacional de Águas e Energia Elétrica (DNAEE), Brazil.

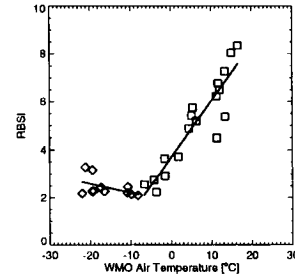


Figure 11 : RBSI as a function of air temperature at the WMO-station Salechard.

Siberia is well-suited to study the effect of air temperature on the development of vegetation covers since the temperature varies from -30°C to $+20^\circ\text{C}$ throughout the year. The growth of vegetation follows the increase of the temperature in spring and summer, giving rise to a gradual increase in vegetation density, with a maximum in late summer. This process is reversed starting in autumn with the decrease of temperature. With decreasing vegetation density, the ratio between the contributions of volume and surface scattering to the NRCS also changes. This phenomenon is well-reflected when looking to the RBSI dependence on temperature as shown in Figure 11. When the canopy is frozen (at least below -10°C) the RBSI stays constant. Although the dielectric properties of moist vegetation change by more than an order of magnitude due to freeze/thaw processes, this transition does not occur typically at 0°C , but at temperatures well below due to the presence of super-coolants such as sucrose solutions in the plant fluids. For temperatures above 0°C , the dielectric constant of vegetation is relatively insensitive to changes in temperature. Therefore, the increase in RBSI with temperature has its origin in the increase of vegetation density. Figure 12 illustrates the correlation between canopy density and RBSI for Siberia (Wismann et al. 1996b).

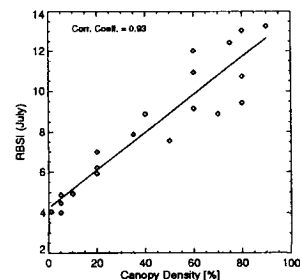


Figure 12 : Correlation between the RBSI and canopy density.

The high correlation between the RBSI and the canopy density was used to produce a map of canopy density for Siberia, which is shown in Figure 13. The boundaries between the forest and the Tundra in the north and between the forest and the wheat belt in the Kazakhstan steppe in the south are well depicted on the map. The latter are classified as areas of negligible canopy density

due to extremely low RBSI values. When comparing this map with a forest map of this area, a lot of details are in good agreement, e.g., the dense forest along the Ural mountains, especially on the western slope, the variability of the vegetation along the river Ob in the West Siberian Lowland, and different forest types and densities in the Central Siberian Plateau. Also the small and isolated forests north of Semipalansk (51°N; 80°E) are detected.

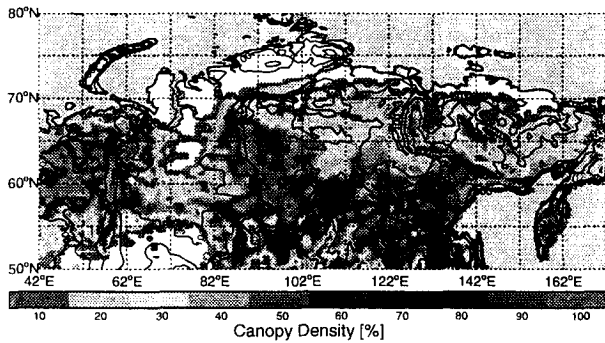


Figure 13 : Canopy density map of Siberia, derived from RBSI data.

The seasonal variability of the NRCS as depicted in Figure 14 accentuates the areas with strong seasonal variations in the vegetation cover, e.g., due to seasonal rainfall like in the Sahel region. Here the scatterometer data allow monitoring the interannual variability as shown in Figure 15. The comparatively high wetness in 1994 can be delineated from the enhanced NRCS as well as from the fact that the seasonal NRCS increase reached far more north than in the other years (Wismann et al., 1995).

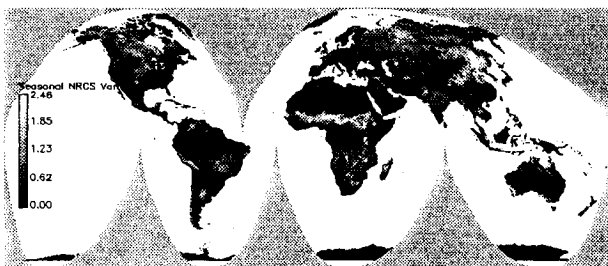


Figure 14: Seasonal NRCS Variability.

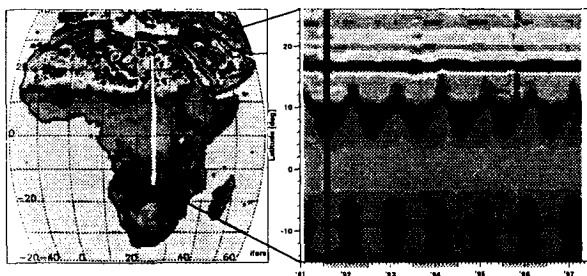


Figure 15 : Hovmoeller diagram of the NRCS along a cross section through Africa.

SOIL MOISTURE MEASUREMENTS

The dielectric properties of soil strongly depend on its moisture content. However, due to the limited penetration depth of microwaves into the soil, scatterometer can only provide moisture estimates in the soil surface layer (0.5 – 5 cm). This layer is the interface between the highly dynamic atmosphere and the deeper soil layers, and hence its moisture content is subject to short-term fluctuations on temporal scales of less than one day, depending on the type of soil. The resulting NRCS fluctuations are shown in Figure 16⁴. Increases in NRCS are well correlated with precipitation events while the seasonal variation due to vegetation effects (dashed curve in the NRCS times series) is much smaller. Wagner et al. (1998) used the ERS scatterometer data in order to estimate the degree of saturation of the soils. As a result maps of the Iberian Peninsula were produced which show the spatial and temporal variability of the soil moisture (see Figure 17) which reveal the seasonal rain variability (winter rain) as well as the interannual variation. A drought was encountered in 1992 and 1993 and flooding in 1995/1996.

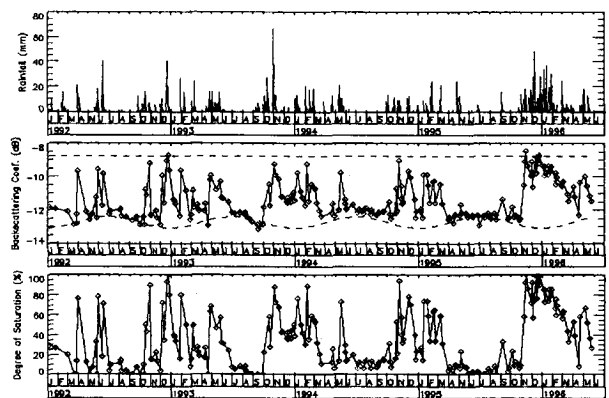


Figure 16 : Time series of rainfall (top), NRCS (middle), and degree of saturation for the station Beja, Portugal.

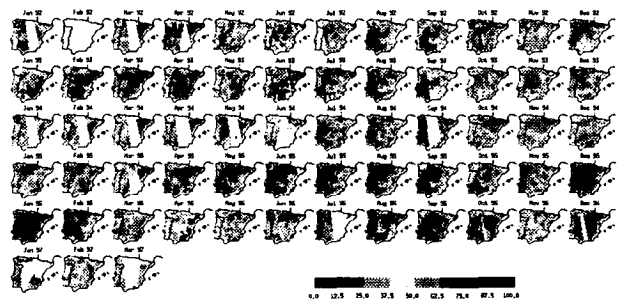


Figure 17 : Time series of maps of the degree of saturation for the Iberian Peninsula.

⁴ Figure 16 and Figure 17 were provided by W. Wagner, Space Application Institute, Joint Research Centre, Ispra, Italy.

CONCLUSIONS

Despite its poor spatial resolution the scatterometer is well suited for global monitoring task due to the good temporal and spatial coverage and the relative small amount of data. Examples were presented demonstrating the sensitivity of radar cross section to changes in ice, snow, soil, and vegetation properties, allowing a wide range of applications of these data in the field of global monitoring.

The ERS data are of excellent quality in terms of calibration and temporal stability, they are provided in near real-time and thus well suited for any kind of operational data assimilation tasks, e.g., into numerical climate and weather models.

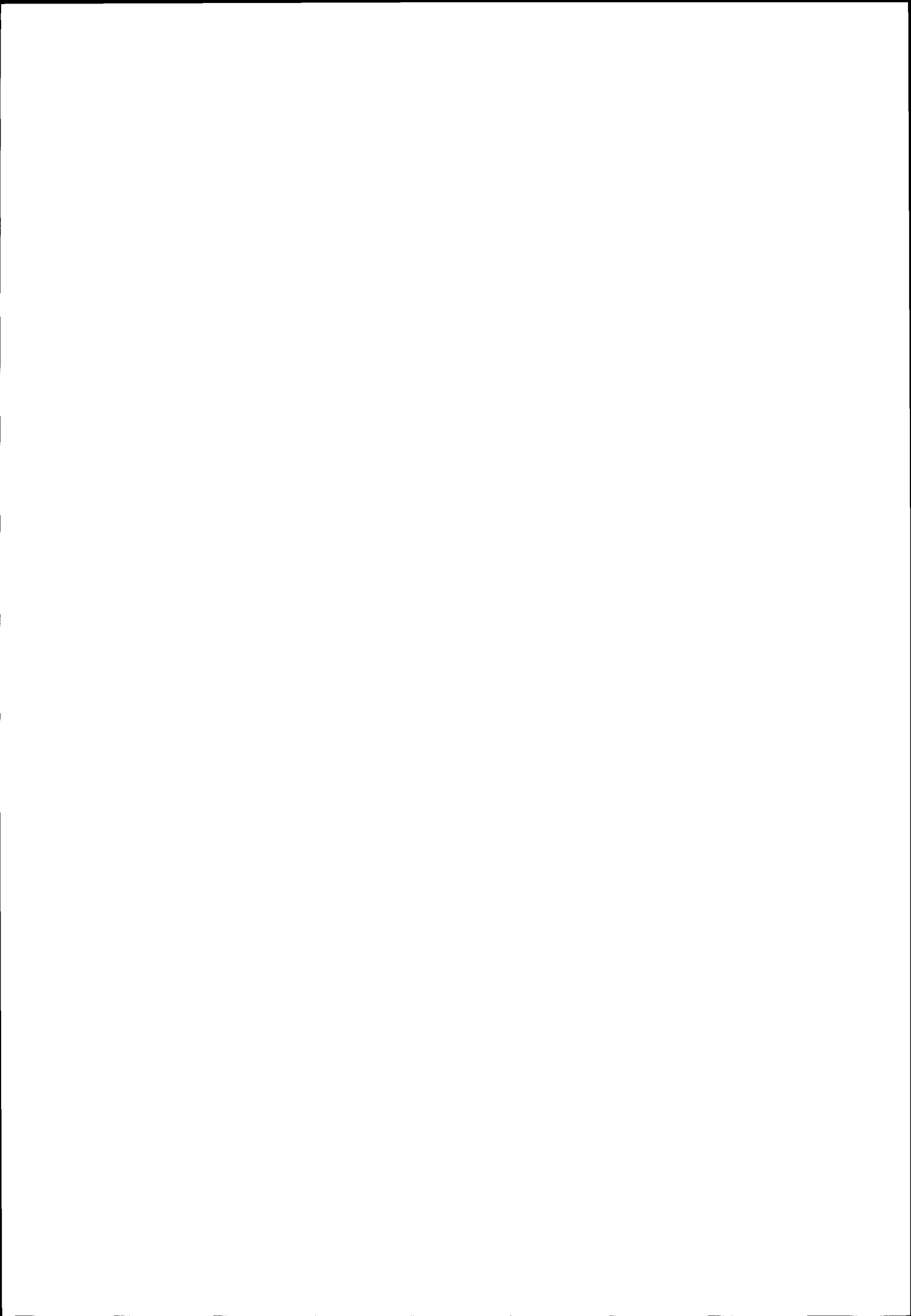
So far the ERS scatterometers have collected a unique data set for climate monitoring which should be continued in the future.

ACKNOWLEDGEMENT

A part of this work was conducted under ESA study contract No. 11103/94/NL/CN. The ERS and NSCAT data were provided by: the Centre ERS d'Archivage et de Traitement (CERSAT), France.

REFERENCES

- Boehnke, K. and V. Wismann, ERS Scatterometer Land Applications: Detecting the Thawing of Soils in Siberia, *Earth Observation Quarterly*, ESA Publication Division, 52, 4-7, 1996a
- Boehnke, K. and V. Wismann, Thawing of Soils in Siberia Observed by the ERS-1 Scatterometer Between 1992 and 1995, *Proceedings of the IGARSS '96*, Lincoln, USA, May 27-31, Volume IV, 2264-2266, 1996b.
- Boehnke, K. and V. Wismann, Detecting soil thawing in Siberia with ERS Scatterometer and SAR, *Proceedings of the 3rd ERS Symposium*, Florence, Italy, March 17-21, ESA SP-414, Vol. I, 35-40, 1997a.
- Boehnke, K. and V. R. Wismann, Thawing processes during Siberian spring observed by ERS Scatterometer and SAR, *Proceedings of the IGARSS '97*, Singapore, August 3-8, Volume IV, 1826-1828, 1997b.
- ESA, ERS-1 System, ESA Publications Division ESTEC Noordwijk, The Netherlands, ESA SP-1146, 87 pages, 1992.
- Frison P.-L., Mougin E., Monitoring global dynamics with ERS-1 wind scatterometer data, *Int. J. of Remote Sensing*, 17, 3201-3218, 1996a.
- Frison P.-L., Mougin E., Use of ERS-1 wind scatterometer data over land surfaces, *IEEE Trans. Geosci. Remote Sensing*, 34, 550-560, 1996b.
- Hamilton, S. K., S.J. Sippel, and J.M. Melack, Inundation patterns in the Pantanal wetland of South America determined from passive microwave remote sensing, submitted to Water Resources Research, 1995.
- Kennett, R. G., and F. K. Li, Seasat over-land scatterometer data, part I: Global overview of the Ku-band backscatter coefficients, *IEEE Trans. Geoscience and Remote Sensing*, 27, 5, 592-605, 1989a
- Kennett, R. G., and F. K. Li, Seasat over-land scatterometer data, part II: Selection of extended area land-target sites for the calibration of spaceborne scatterometers, *IEEE Trans. Geoscience and Remote Sensing*, 27, 6, 779-788, 1989b
- Kerr, Y.H., and R.D. Magagi, Use of ERS-1 windscatterometer data over land surfaces, Space at the Service of our Environment, Proceedings of Second ERS-1 Symposium, Hamburg, 11-14 October 1993, ESA SP-361, 381-388, 1994.
- Lee, W. R. III and D. Hastings, TerrainBase Global DTM Version 1.0 (on CD-ROM), National Geophysical Data Center and World Data Center-A for Solid Earth Geophysics, Boulder, Colorado, USA, 1995.
- Long, D. G., and Hardin, P. J., Vegetation studies of the Amazon Basin using enhanced resolution Seasat scatterometer data, *IEEE Transactions on Geoscience and Remote Sensing*, 32(2), 449-460, 1994.
- Magagi, R.D., and Y.H. Kerr, Temporal and Spatial variabilities of surface roughness response over Hapex-Sahel area: use of ERS-1 windscatterometer. *Proceedings of the IGARSS '95*, Firenze, Italy, 10-14 July, 1287-1289, 1995.
- Mougin, E., A. Lopes, C. Proisy, A. Warich, P. L. Frison, D. Lo Seen, and P. Lecomte, Analysis of ERS-1 scatterometer data over land surfaces - preliminary results, *Proceedings of Second ERS-1 Symposium*, Hamburg, Germany, 11-14 October 1993, ESA SP-361, 393-398, 1994.
- Mougin E., Lo Seen D., Rambal S., Gaston A., Hiernaux P., A regional Sahelian grassland model to be coupled with multispectral satellite data. I. Description and validation. *Remote Sens. Environ.*, 52, 181-193, 1995a.
- Mougin, E., Lopes, A., Frison, P. L., and Proisy, C., Preliminary analysis of ERS-1 wind scatterometer data over land surfaces, *International Journal of Remote Sensing*, 16(2), 391-398, 1995b.
- Wagner, W., G. Lemoine, H. Rott, A method for estimating the profile soil moisture content from ERS scatterometer and soil data, submitted. To *Remote Sens. Environ.*, 1998.
- Wiesmann, A. and C. Mätzler, Monitoring the temporal behaviour of land surfaces with ERS-1 wind scatterometer data, *Proceedings of Second ERS-1 Symposium*, Hamburg, Germany, 11-14 October 1993, ESA SP-361, 399-404, 1994.
- Wismann, V. and K. Boehnke, Land surface monitoring using the ERS-1 scatterometer, *Earth Observation Quarterly*, ESA Publication Division, No. 44, 11-15, 1994.
- Wismann, V. and K. Boehnke, Can the ERS-1 Scatterometer be used to forecast the inundation extent in the Pantanal Wetland?, *Proceedings of the IGARSS '96*, Lincoln, USA, May 27-31, Volume II, 839-841, 1996a.
- Wismann, V., K. Boehnke, and C. Schmullius, Large scale C-band radar signatures of land surfaces measured by the ERS-1 Scatterometer, *Proceedings of the IGARSS '93*, August 16-19, 1993, Tokyo, Japan, 1392-1394, 1993.
- Wismann, V., K. Boehnke and C. Schmullius, Radar signatures of land surfaces measured by the ERS-1 Scatterometer, *Proceedings of The Second ERS-1 Symposium: Space at the Service of Our Environment*, October 11-14, 1993, Hamburg, Germany, ESA SP-361, 405-410, 1994a.
- Wismann, V. R., K. Boehnke, and C. Schmullius, Global land surface monitoring using the ERS-1 scatterometer, *Proceedings of the IGARSS '94*, California Institute of Technology, Pasadena, California, USA 8-12 August, 1488-1490, 1994b.
- Wismann, V. R., K. Boehnke, and C. Schmullius, Monitoring ecological dynamics in Africa with the ERS-1 scatterometer, *Proceedings of the IGARSS '95*, Congress Center Firenze, Italy, 10-14 July, 1532-1525, 1995.
- Wismann, V., A. Cavanie, D. Hoekman, I. Woodhouse, K. Boehnke and C. Schmullius, Land surface observations using the ERS-1 scatterometer, *Final Report Part I*, ESTEC Contract 11103/94/NL/CN, 57 pages, 1996a.
- Wismann, V., K. Boehnke A. Cavanie, R. Ezraty, F. Gohin, D. Hoekman, and I. Woodhouse, Land surface observations using the ERS-1 scatterometer, *Final Report Part II*, ESTEC Contract 11103/94/NL/CN, 65 pages, 1996b.



A COMPARISON OF ERS SCATTEROMETER RETRIEVED SOIL MOISTURE DATA WITH FIELD OBSERVATIONS IN THE UKRAINE

Wolfgang Wagner

Space Applications Institute, Joint Research Centre of the European Commission, TP 262, I-21020 Ispra (VA), Italy
e-mail: wolfgang.wagner@jrc.it, phone: +39-0332-78-6335

&

Institute for Photogrammetry and Remote Sensing, Vienna University of Technology, Gusshausstr. 27-29, A-1040
Vienna, Austria

ABSTRACT

Soil moisture, which is the water held in the soil within reach of plants, constitutes only about 0.005 % of the global water resources. Despite the soil water reservoir is small, it exerts an important control on the interactions of the hydrosphere, biosphere, and atmosphere. In this paper a method to estimate the moisture content in the soil profile from ERS Scatterometer retrieved surface wetness series and soil data is presented. It is found that about five different levels of soil moisture in the 0-20 cm and 0-100 cm layers can be distinguished.

1. INTRODUCTION

The objective of this study was to assess the accuracy of a method for soil moisture retrieval from ERS Scatterometer data using an extensive data set of gravimetric measurements from the Ukraine (Section 2). The ERS Scatterometer is a radar operating at 5.3 GHz with a spatial resolution of 50 km. It has been flown on board of the European Remote Sensing Satellites ERS-1 (from 1991 to 1996) and ERS-2 (from 1995 onwards) and is the first spaceborne scatterometer that has been providing global coverage for several years. First results using the ERS Scatterometer for soil moisture retrieval are reported in Wagner et al. (in press¹), Pulliainen et al. (1998), and Magagi and Kerr (1997).

In Wagner et al. (in press²) an algorithm to retrieve the surface soil moisture content from ERS Scatterometer data is introduced. The method accounts for heterogeneous land cover and the effects of vegetation growth and decay on the signal. The problem is that it appears hardly feasible to validate remotely sensed surface wetness values because of the high spatial and temporal variability of the moisture content in the soil surface layer. The chances for a successful validation are improved if a method for estimating the moisture content in the soil profile is available. This is related to the properties of the soil moisture fields that are discussed in Section 3. An algorithm for estimating the profile soil moisture content from the remotely sensed surface wetness value and soil data is defined and validated with the field measurements from the Ukraine (Section 4).

2. DATA BASE

In the former Soviet Union soil moisture is measured regularly at 3000 agrometeorological stations (Vinnikov and Yeserkepova, 1991). The moisture content is measured by the gravimetric method three times per month during the warm season, specific for each crop. For this study, a five years (1992-1996) soil moisture data set from the Ukraine comprising measurements of the 0-20 cm and 0-100 cm soil layers from 99 stations was available (Groisman, 1998). At these stations measurements are carried out at maize, spring wheat, or winter wheat fields, or any combinations of these crops. Table 1 shows the number of maize, spring wheat, and winter wheat fields and the respective period of observation. The data set contains in total 14293 average field wetness values for the 0-20 cm layer and 12835 for the 0-100 cm layer from 211 fields. For each field auxiliary information including wilting level, field capacity, porosity (also called total water capacity), and bulk density for both layers is available. Throughout the text soil water values are presented as % volumetric soil moisture.

Crop	No Stations	Period of Observation
Maize	70	April - September
Spring wheat	70	April - July
Winter wheat	71	April - July and September - November

Table 1: Period of soil moisture observations and number of stations for maize, spring wheat and winter wheat.

3. SOIL MOISTURE VARIABILITY

Many processes that act on different space and time scales control soil moisture, and the degree of variability of the soil moisture field depends on the scale and the nature of the controlling processes. The variability of the soil moisture content in the remotely sensed surface layer (0.5-2 cm) is particularly high because this is the active layer for evaporation and because of the variable microrelief of the soil surface. The work of Konstantin Vinnikov, Alan Robock and their colleagues (Vinnikov et al., 1996 and submitted)

has contributed significantly to our understanding of the variability of the soil moisture field. They separate the variability into a small-scale land-surface related component and a large-scale atmospheric-forcing related component. The small-scale variability (tens of meters in the spatial and up to a few days in the temporal domain) is related to the complex topography of the landscape, and the variable soils and vegetation cover. This small-scale component may be regarded as noise in comparison with the long-term and large-scale signal related to atmospheric forcing. The spatial or temporal autocorrelation function ρ may be expressed in terms of these two components:

$$\rho(x) = \eta e^{-\frac{x}{L_s}} + (1-\eta)e^{-\frac{x}{L_a}} \quad (1)$$

$$\eta = \frac{\sigma_s^2}{\sigma_s^2 + \sigma_a^2} \quad (2)$$

where x either distance or time
 L_s scale of land-surface related variability
 L_a scale of atmosphere related variability
 σ_s^2 variance of land-surface related variability
 σ_a^2 variance of atmosphere related variability

The parameter η is a measure for the relative magnitude of the small-scale compared to the large-scale variability. With increasing depth of the soil layer η will in general decrease, and the scale of the atmosphere related component L_a will increase. For soil layers larger than about 10-20 cm, $L_a \approx 1-4$ months in the temporal domain and $L_a \approx 400-800$ km in the spatial domain (depending also on the climatic conditions).

These particular properties of the soil moisture field have several implications. Firstly, let us regard the measurement process. In the radar measurement, it is averaged over the resolution cell of the sensor, and the high-frequency components of the soil moisture field are averaged out. Therefore the variance of the *observed* field is reduced compared to the original soil moisture field when the resolution cell of the observing system increases. Fig. 1 shows the variance of the observed soil moisture field, which can be derived directly from the autocorrelation function (Journel and Huijbregts, 1978), versus the size of the resolution cell for assumed parameters of the autocorrelation function. Although the parameters of the autocorrelation function differ from region to region, it can nevertheless be concluded that at the observation scale of 50 km of the ERS Scatterometer the information about the small-scale variability is lost. On the other hand, the large-scale atmospheric related variability is fully preserved.

Since η and L_a will in general increase with the depth of the considered soil layers, the chances of a successful validation of the remotely sensed soil wetness values using field observations increase when the depth of the

considered soil layer increases. In fact, because of the high variability of the moisture content in the surface layer Schmugge and Jackson (1996) think that there is a limit to the accuracy which can be expected when ground samples are used to verify remotely sensed *surface* wetness estimates, a problem particularly felt at the observation scale of the ERS Scatterometer.

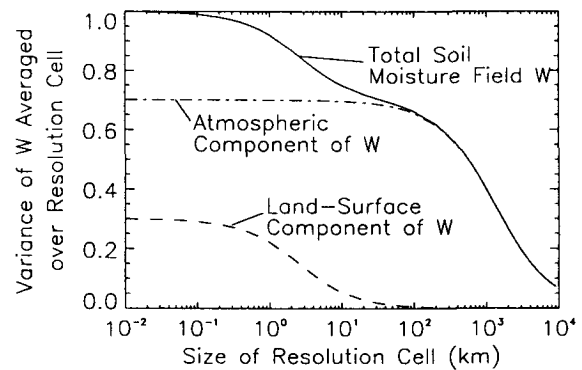


Fig. 1: Reduction of the variance of the soil moisture field W due to the averaging process. Assumed values for the autocorrelation function (1) are $\eta = 0.3$, $L_s = 1$ km, and $L_a = 500$ km.

4. PROFILE SOIL MOISTURE RETRIEVAL

An algorithm for estimating the moisture content in the soil surface from ERS Scatterometer data is presented in Wagner et al. (in press^{1,2}). The method accounts from heterogeneous land cover and seasonal vegetation development, and yields a relative measure of the moisture content, m_s , in the remotely sensed surface layer which is about 0.5-2 cm (Schmugge, 1993). In Fig. 2 ERS Scatterometer retrieved m_s values are compared to rainfall series recorded at the station Poltava, Ukraine, for the period from March to December 1996. In the months from March to May, on the average 4.5 measurements were acquired per week since both ERS-1 and ERS-2 were in orbit. From June on, the average number of measurements per week is 2.2. It can be seen that particularly until May most rainfall events are associated with a peak in the m_s series, with an associated decline in the dry period afterwards. After that, some rainfall events like in the middle of July are missed.

The relatively low m_s values in March and December are caused by freezing or the presence of wet snow. Such "wrong" values can be removed from the series, if auxiliary data are available.

In the middle diagram of Fig. 2 it is shown how the surface moisture series would look like if an observing system with a revisit time of 35 days, such as the Synthetic Aperture Radar (SAR) on the ERS satellites, would be employed. The shape of the resulting temporal profile is more or less arbitrary, given little information

about the moisture conditions. In this example, such an observing system would indicate wet soil conditions in the beginning of August, because the measurement is made by chance during or shortly after some 50 mm of rain, while in reality, the soil is relatively dry in this

period. This example demonstrates the need for an observing system with a high temporal sampling rate if the highly variable surface wetness conditions are to be monitored.

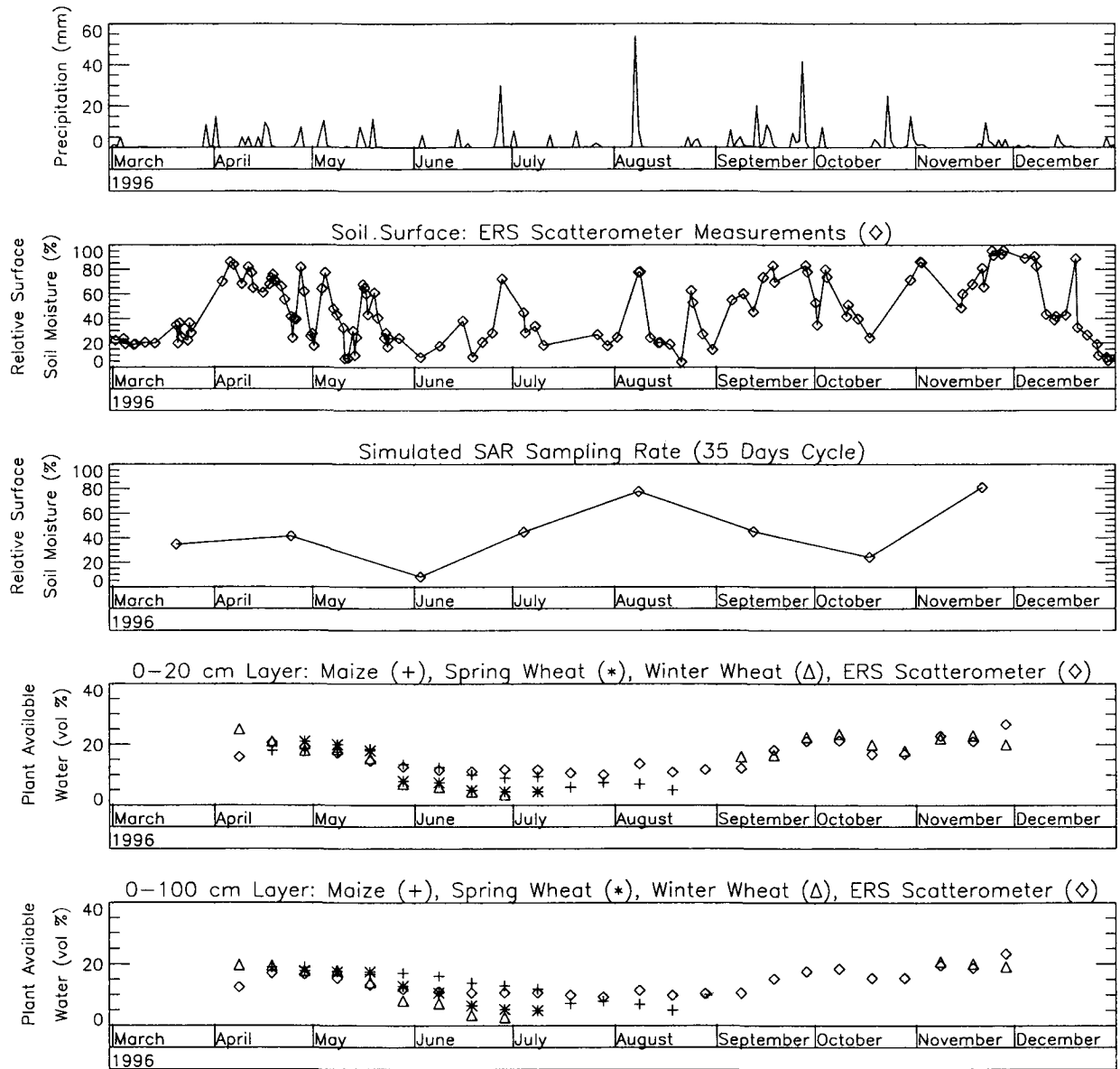


Fig. 2: Comparison of rainfall, ERS Scatterometer retrieved soil moisture, and field measurements of soil moisture for the station Poltava, Ukraine (34.55°E, 49.6°N) for the year 1996. The top diagram shows the rainfall measurements at this station, and the second diagram from the top shows the ERS Scatterometer retrieved relative surface wetness values (%). The third diagram is the same as the second, with the exception that only measurements taken about every 35 days are shown. Thereby the evolution of the moisture conditions as depicted by SAR systems can be seen. In the bottom two diagrams the moisture content in the 0-20 cm and 0-100 cm soil layers estimated from the ERS Scatterometer data and measured on the maize, spring- and winter wheat fields is shown.

The availability of frequent surface observations should give an indication of the wetting and drying trend in deeper soil layers. This is because the moisture content in the soil profile bears a memory of the weather patterns in the last few days to weeks that should be

reflected in the m_s series. The variability of the moisture content in the profile is damped when compared to the variability in the surface layer, and therefore it appears sensible to use a filter which smoothes the m_s series to reproduce the trend in the deeper layers.

In Wagner et al. (submitted) a method is introduced to estimate the profile soil moisture content that is based on an exponential filter function. The exponential filter has the advantages that it accounts for the decreasing influence of measurements with increasing time, and that the response of the profile to changes in the surface soil moisture conditions is retarded. A Soil Water Index (*SWI*) is defined:

$$SWI = \frac{\sum_i m_s(t_i) e^{-\frac{t-t_i}{T}}}{\sum_i e^{-\frac{t-t_i}{T}}} \quad \text{for } t_i \leq t \quad (3)$$

where m_s is the surface soil moisture estimate from the ERS Scatterometer at time point t_i . The parameter T is a characteristic time length that is expected to increase with the depth of the soil layer and to decrease with increasing hydraulic conductivity of the soil. For the Ukraine, setting T equal to 15 days for the 0-20 cm layer and 20 days for the 0-100 cm layer resulted in a good fit.

The *SWI* is a trend indicator ranging between 0 and 1. If calibration points for the dry and wet case can be found then the absolute soil moisture content could be estimated assuming a linear relationship between the *SWI* and the soil moisture content W :

$$W(t) = W_{min} + SWI(t)(W_{max} - W_{min}). \quad (4)$$

W_{min} and W_{max} are the minimum and maximum occurring soil wetness values for a particular layer and soil. The soil parameters commonly used to define critical soil moisture values are the wilting point, the field capacity, and the porosity. The wilting point *WL* is defined as the soil moisture content at which the suction to remove the remaining water from the soil is too great for plants to exert. The field capacity *FC* is the soil moisture content when deep percolation has nearly stopped after the soil was thoroughly wetted by heavy rain or irrigation. The porosity is the relative pore volume of the soil and is equal to the total water capacity of the soil *TWC*, i.e. the soil moisture content at which all the pores are filled with water.

To investigate how W_{min} and W_{max} are related to *WL*, *FC*, and *TWC*, the frequency distribution of the gravimetric measurements from the 211 fields in the Ukraine was analysed. Fig. 3 and Fig. 4 show the histograms of W for the 0-100 cm layer for two fields with very different characteristics. The first field (Fig. 3) has heavy loamy texture and the great majority of the measured soil moisture values is relatively evenly distributed in the range from wilting level (18 %) to field capacity (33 %). On the other hand, the loamy sand field in Fig. 4 has low values for both the wilting level (2 %) and the field capacity (16 %), and the frequency distribution of W resembles a log-normal distribution with the centre

near the field capacity. A considerable percentage of the values are above field capacity, but all are lower than 30 %.

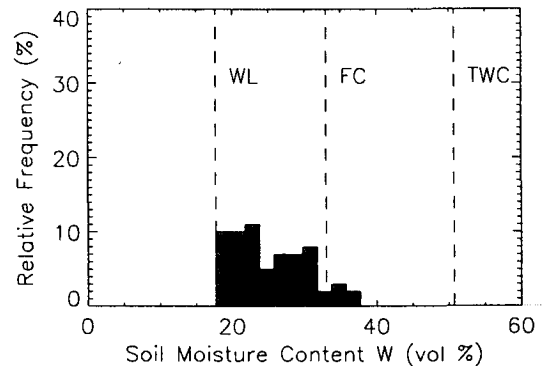


Fig. 3: Histogram of soil moisture content W in % in the 0-100 cm layer at the winter wheat field at the station Belovodsk (39.58°E, 49.21°N). The field has a chernozem soil with a heavy loamy texture. The wilting level *WL*, field capacity *FC*, and total water capacity *TWC* are indicated by the dashed lines.

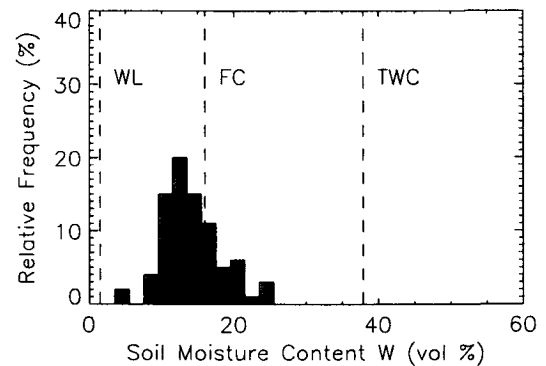


Fig. 4: Histogram of soil moisture content W in % in the 0-100 cm layer at the winter wheat field at the station Sarny (26.65°E, 51.33°N). The field has a dark grey podzolic soil with a loamy sand texture.

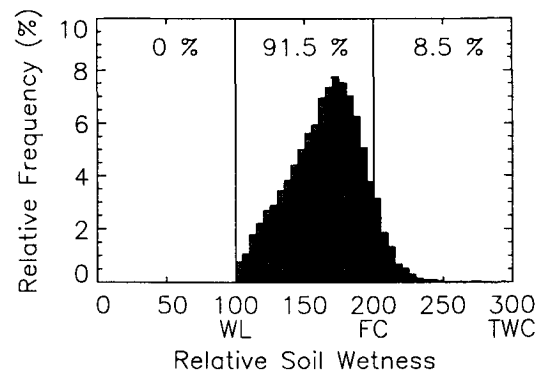


Fig. 5: Summary statistics for the soil moisture content in the 0-100 cm layer based on measurements from 211 fields in the Ukraine.

A summary statistics for all 211 fields is prepared by dividing the range of possible soil moisture values into three departments: from zero wetness to WL , from WL to FC , and from FC to TWC ; and by calculating the frequency distributions within these three departments separately. The resulting summary histograms for the 0-100 cm layer is shown in Fig. 5. It can be seen that the histogram has a bell curved shape with the minimum at WL , and the maximum around half way between FC and TWC . A similar histogram is obtained for the 0-20 cm layer, although it is more evenly distributed and has a peak at wilting point.

The choices of W_{min} and W_{max} for Eq. (4) are based on the results of the summary statistics. This means that it is required that the SWI is capable of accounting for very different frequency distributions of W that reflect variations in soil type and the climatic gradient from the more dry conditions in the south to the more humid conditions in the north of the Ukraine. Let us set W_{min} equal to WL , and W_{max} equal to $(FC+TWC)/2$. Then the water available to plants PAW can be derived from (4):

$$PAW(t) = SWI(t) \left(\frac{TWC + FC}{2} - WL \right) \quad (5)$$

Area extensive PAW values are calculated from ERS Scatterometer using the field constants reported at the fields of the agrometeorological network.

5. ERROR ANALYSIS

Because geostatistical methods cannot be meaningfully applied to estimate areal averages from the field measurement, the remotely estimated PAW values are directly compared to the field observations. Since the ERS Scatterometer only provides information about the atmospheric-forcing related component of the soil moisture fields, the land-surface related variability causes differences in the two data sources. However, it can be observed in Fig. 2 (which shows a typical example how the remotely estimated area-extensive PAW values compare to the measurements on the maize, spring wheat and winter wheat fields) that both the trend and the absolute level are in relatively good agreement. A scatter plot of ERS Scatterometer estimated soil moisture values versus field measurements for the 0-100 cm layer for the station Glukhov can be seen in Fig. 6. The scattering is high, and the correlation coefficient R between the remote sensing and maize field data is 0.41, for spring wheat 0.53, and for winter wheat 0.58. However, the degree of scattering is not surprising given the influence of the land-surface. To get an idea of the small-scale variability of the soil moisture, the PAW measurements of the spring and winter wheat fields versus the maize field are plotted in Fig. 7. The correlation coefficients between the fields are also small: 0.3 for spring wheat versus maize, and 0.51 for winter wheat versus maize.

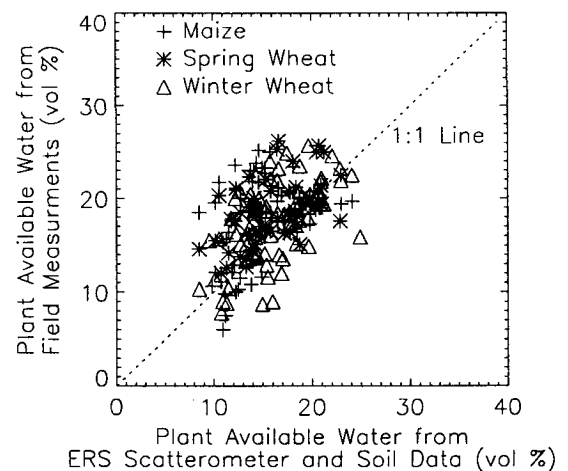


Fig. 6: Scatter plot of plant available water PAW in the 0-100 cm layer measured on maize, spring- and winter wheat fields versus the area-extensive ERS Scatterometer estimates for the station Glukhov, Ukraine (33.9°E, 51.6°N). The data cover the period 1992 to 1996.

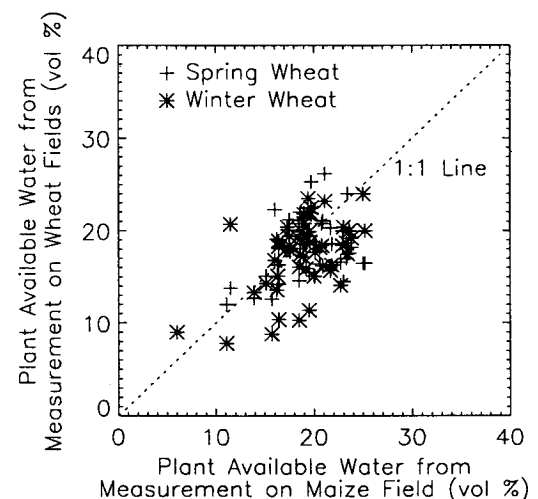


Fig. 7: Scatter plot of plant available water PAW in the 0-100 cm layer measured on the spring and winter wheat fields versus the values measured on the maize field for the station Glukhov, Ukraine (33.9°E, 51.6°N). The data cover the period 1992 to 1996.

More important for evaluating the accuracy of the method is the r.m.s. error. For the example of Fig. 6, the r.m.s. error between the remote sensing and the maize data is 5.2 % (volumetric soil moisture), 4.4 % for the spring wheat, and 3.7 % for winter wheat. In Fig. 8 the histogram of the r.m.s. error for the 0-100 cm layer calculated for each of the 211 fields (i.e. for all maize, spring- and winter wheat fields) is shown. 95 % of the values are below 7 %, and the mean error 4.9 %. For the 0-20 cm layer the corresponding values are 8 % and 6.2 %. There may be two reasons why the results for the 0-20 cm layer is less good than for the 0-100 cm layer. Firstly, the land surface related variability of soil moisture is more important for shallow soil layers, and

secondly, the temporal dynamics of the 0-20 cm layer is higher than of the 0-100 cm layer, putting a more stringent requirement on the sampling rate. Overall, these values are surprisingly low and allow to distinguish about five soil moisture classes: very dry, dry, humid, wet, and very wet. (The total water capacity divided by two times the r.m.s. error gives a number of about five.) The error between the ERS Scatterometer estimates and the true areal soil moisture values should be smaller than that.

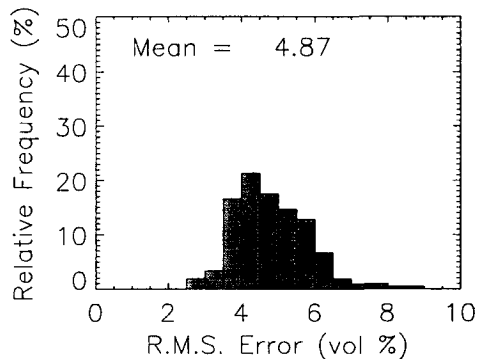


Fig. 8: Histogram of r.m.s. error between soil moisture values estimated by remote sensing and field observations for 211 fields in the Ukraine.

6. CONCLUSIONS

The results show that the ERS Scatterometer is a powerful sensor for monitoring soil moisture. The main reasons are its high temporal sampling rate and its capability to acquire measurements independent of the sun and cloud cover. This allows to follow the temporal evolution of the highly variable surface moisture conditions and provides an indication of the wetting and drying trend of the soil profile. Although the low spatial resolution of 50 km restricts the range of applications, this problem is less felt when it is considered that the correlation length of the observed large-scale atmosphere related component of the soil moisture field is a few hundred kilometres. This means that the trend of the profile soil moisture content related to atmospheric forcing observed at a the observation scale is similar to the trend at much smaller scales, which was confirmed by the results achieved when comparing field measurements and ERS Scatterometer estimated soil wetness values.

ACKNOWLEDGEMENTS

I would like to thank Konstantin Vinnikov, Alan Robock, and Pavel Groisman for their invaluable help with the Ukrainian soil data. CERSAT kindly provided the ERS Scatterometer data.

REFERENCES

- Groisman, P. (1998) Description of soil moisture data and accompanying information for the agricultural regions of Western Russia and The Ukraine, *Report of the Hydrology Science & Service Corporation, JRC Contract N.En. 9701838V*, 10 p.
- Journel, A. G., Ch. J. Huijbregts (1978) Mining Geostatistics, *Academic Press*, London etc., 598 p.
- Magagi, R. D., Y.H. Kerr (1997) Retrieval of soil moisture and vegetation characteristics by use of ERS-1 wind scatterometer over arid and semi arid areas, *J. Hydrology*, No. 188-189, pp. 361-384.
- Pullianen, J. T., T. Manninen, M. T. Hallikainen (1998) Application of ERS-1 Wind Scatterometer Data to Soil Frost and Soil Moisture Monitoring in Boreal Forest Zone, *IEEE Trans. Geosci. Remote Sens.*, Vol. 36, No. 3, pp. 849-863.
- Schmugge, T. J. (1983) Remote Sensing of Soil Moisture: Recent Advances, *IEEE Trans. Geosci. Remote Sensing*, Vol. GE-21, No. 3, pp. 336-344.
- Schmugge, T. J., T. J. Jackson (1996) Soil moisture variability. In *Scaling up in hydrology using remote sensing*, edited by J.B. Steward, E.T. Engman, R.A. Feddes, Y. Kerr, *John Wiley & Sons*, New York etc., pp. 183-192.
- Vinnikov, K. Y., A. Robock, N. A. Speranskaya, C. A. Schlosser (1996) Scales of temporal and spatial variability of midlatitude soil moisture, *J. Geophysical Research*, Vol. 101, No. D3, pp. 7163-7174.
- Vinnikov, K. Y., A. Robock, S. Qui, J. K. Entin, M. Owe, B. Choudhury, S. E. Hollinger, E. G. Njoku, Satellite Remote Sensing of Soil Moisture in Illinois, USA, *Special GCIP Issue of J. Geophysical Research*, submitted.
- Vinnikov, K. Y., I. B. Yeserkepova (1991) Soil Moisture: Empirical data and model results, *J. Climate*, Vol. 4, pp. 66-79.
- Wagner, W., G. Lemoine, H. Rott, A Method for Estimating the Profile Soil Moisture Content from ERS Scatterometer and Soil Data, *Remote Sens. Environ.*, submitted.
- Wagner, W., G. Lemoine, M. Borgeaud, H. Rott, A Study of Vegetation Cover Effects on ERS Scatterometer Data, *IEEE Trans. Geosci. Remote Sensing*, in press².
- Wagner, W., J. Noll, M. Borgeaud, H. Rott, Monitoring Soil Moisture over the Canadian Prairies with the ERS Scatterometer, *IEEE Trans. Geosci. Remote Sensing*, in press¹.

EVALUATION OF SSM/I DATA FOR IMPROVING SURFACE PARAMETER RETRIEVAL WITH ERS WIND SCATTEROMETER DATA OVER SAHEL.

Frison P.-L.¹, Mougïn E.¹, Karam M.², Hiernaux P.³

¹ CESBIO, 18 av. E. Belin, 31401 Toulouse cedex 4, France
Tel : (33) 5 61 55 85 37, Fax : (33) 5 61 55 85 00, E-mail : frison@cesbio.cnrs.fr

² GenCorp Aerojet, Azusa, CA 91702 USA
Tel : (818) 812 1154, Fax : (626) 969 5772, E-mail : Mostafa.Karam@aerojet.com

³ ICRISAT / CIPEA B. P. 12404, Niamey, Niger
Tel : (227) 72 25 29, Fax : (227) 73 43 29, E-mail : P.HIERNAX@cgnet.com

ABSTRACT

SSM/I data at 19 GHz are compared to ERS wind scatterometer data over a sahelian area. Observations show an overall good concordance between 19 GHz polarisation difference and σ^0 acquired at 45° of incidence angle. Observed differences between both data set are mainly attributed to difference in the atmosphere sensitivity of both sensors. A semi-empirical model based on the radiative transfer theory is then used to simulate SSM/I brightness temperatures. Finally, an inversion method is developed to retrieve herbaceous biomass from SSM/I data. Results show that ERS scatterometer is better suited than SSM/I to retrieve surface parameters.

INTRODUCTION

Coarse resolution microwaves spaceborne sensors have demonstrated their potential for arid and semi-arid areas monitoring [1], [2]. Past studies have shown that microwaves data acquired by the wind scatterometer (WSC) on board ERS-1 and -2 (*European Remote Sensing*) satellites, as well as passive radiometer data (acquired either by SSM/I - *Special Sensor Microwave Imager* - or SMMR - *Scanning Multichannel Microwave Radiometer*) are better suited than GVI (*Global Vegetation Index*) derived from AVHRR (*Advanced Very High Resolution Radiometer*) data to monitor areas with low vegetation biomass [3], [4].

Radiometers measure the brightness temperature of the scene, $T_B = e \cdot T_s$, where e is the scene emissivity depending on surface parameters (soil roughness, soil moisture content, and vegetation parameters) and T_s is the physical surface temperature. Due to the high frequencies used by spaceborne radiometers (higher

than 19 GHz), measurements are also sensitive to atmospheric parameters like the integrated cloud, vapour water content, and physical air temperature. On the other hand, the ERS wind scatterometer measures the backscattering coefficient, σ^0 , which depends on surface parameters of the scene observed, and is independent of atmospheric constituents (the instrument operates at 5.3 GHz).

In a previous study [5], we developed an inversion procedure based on a signal modelisation study, to retrieve surface parameters from ERS-1 wind scatterometer data over a Sahelian area. The study period extended from 1992 to 1995. This method allowed to retrieve herbaceous biomass with 33% of relative error with respect to ground measurements. The purpose of the present study is to investigate whether additional information could be extracted from the passive microwave radiometer SSM/I. To this end, SSM/I data are analysed over the same Sahelian area and compared to ERS-1 scatterometer data for the period August 1991 - October 1993. The combination of a regional grassland ecosystem model to a radiative transfer model allows the temporal evolution of the 19 GHz SSM/I response to simulated and compared to observations.

DESCRIPTION OF THE STUDY REGION

The study area and ground measurements

The study area is located in the northern part of Gourma, Mali, in Africa. This 50 x 50 km² area lies between 17° N and 16.5° N and from 1.5°W to 2°W. This region is characterised by a long dry season, with no vegetation, followed by a rainy season extending from July to September. This later mainly determines vegetation development, which starts after the first rainfall while senescence occurs at the end of the rainy

season. The landscape is homogeneous and characterised by gently undulating sandy soils, covered with a sparse annual herbaceous layer. This later and bare soil spread over 5-30% and 70-95% respectively of total cover, depending of annual rainfalls.

Ground data consist of measurements of the total herbaceous above-ground biomass, expressed in kg dry matter per ha (kg DM ha^{-1}) performed at the end of the rainy season. A detailed description of measurements procedure can be found in Hiernaux and Justice, 1986. From these measurements, carried out in 4 sample sites of 1 km square each, an average above-ground biomass is calculated, that we consider to be representative of the whole region under study. In 1992 and 1993, the maximum biomass at the end of the rainy season reaches $400 \text{ kg DM ha}^{-1}$ and $620 \text{ kg DM ha}^{-1}$ respectively, while annual rainfall obtained from the meteorological station of Gourma-Rharous (16.9° N , 1.9° W) are 154 mm and 160 mm respectively.

Simulations of vegetation parameters

The daily evolution of surface parameters is simulated using the Sahelian grassland STEP model [6]. STEP is an ecosystem model which describes the relevant processes of the soil-vegetation-atmosphere system to simulate herbaceous growth and soil water dynamics. Moreover, structural parameters such as vegetation cover fraction v_c , canopy height h_c , which are essential parameters for coupling with physical models of reflectivity are also simulated. In this study, the STEP model is used to simulate, at a daily time step, the vegetation parameters (biomass, vegetation cover, canopy height, and vegetation volume fraction) and volumetric water content in the upper soil profile.

DESCRIPTION OF SATELLITE AND METEOROLOGICAL DATA

ERS-1 wind scatterometer data

Only data acquired by wind scatterometer on board ERS-1 satellite in 40° to 45° range of incidence angle are shown here. The time-period concerned extends from August 91 to December 93. The spatial resolution is about $50 \times 50 \text{ km}^2$.

SSM/I data

SSM/I data used in this paper were acquired by sensors onboard DMSP (*Defense Meteorological Satellite Program*) F8 (from Aug. 1991. to Dec. 1992) and F11 satellites (from Dec. 1992 to Oct. 1993). The ascending equator crossing time is about 6:15 a.m.

local time for F8 while it is around 6:30 p.m. for F11 satellite. For multi-temporal comparison and for minimising cloud cover, only data acquired during early morning are retained.

From the four frequencies at which SSM/I operates, only 19.3 and 37 GHz data at both vertical and horizontal polarisation are retained in this study. Measurements are acquired across a 1400 km swath width, at 53.1° of incidence angle with respect to the local earth normal. Their spatial resolution, of $43 \times 69 \text{ km}^2$ and $28 \times 37 \text{ km}^2$ at 19 and 37GHz respectively, justify the comparison with ERS wind scatterometer data. Absolute brightness temperature calibration is $\pm 3\text{K}$. A more detailed description of the sensor can be found in [7].

Meteorological data

Meteorological data having an influence on SSM/I brightness temperatures are surface (T_s) and air temperature (T_a) and integrated water vapour content (IWC). They are obtained from Re-analysis level III-B global atmospheric archive processed and delivered by ECMWF (*European Centre for Medium-Range Weather Forecasts*) services. These data are available for the period extending from August 1991 to October 1993 at a spatial resolution of $2.5 \times 2.5^\circ$.

EXPERIMENTAL OBSERVATIONS

Only data at 19 GHz are shown because of the strong correlation between 37 GHz and 19 GHz channels: the correlation coefficient between the two frequencies is 0.98 and 0.89 for V and H polarisation respectively.

Figure 1 represents the temporal evolution of SSM/I data acquired at 19 GHz over the study area for the period extending from January 1992 to October 1993. Vertical and horizontal brightness temperatures, T_V and T_H , are shown in Figure 1a. Circles represent a 10 day-compositing process in order to minimise cloud effects [8]. Also are plotted the weekly average surface temperature derived from ECMWF data, the green biomass simulated by STEP, and rainfall measured at the Gourma-Rharous meteorological station. As expected, brightness temperatures, for both polarisation, exhibit the same general trend than surface temperature, except during the rainy season where surface parameters are subject to large variations. Brightness temperatures display a sharp decrease (up to 10 K) at the beginning of the rainy season. Then, they increase (except for V polarisation in 1993) and recover the surface temperature evolution with a time delay of around one month earlier for H with respect to V polarisation.

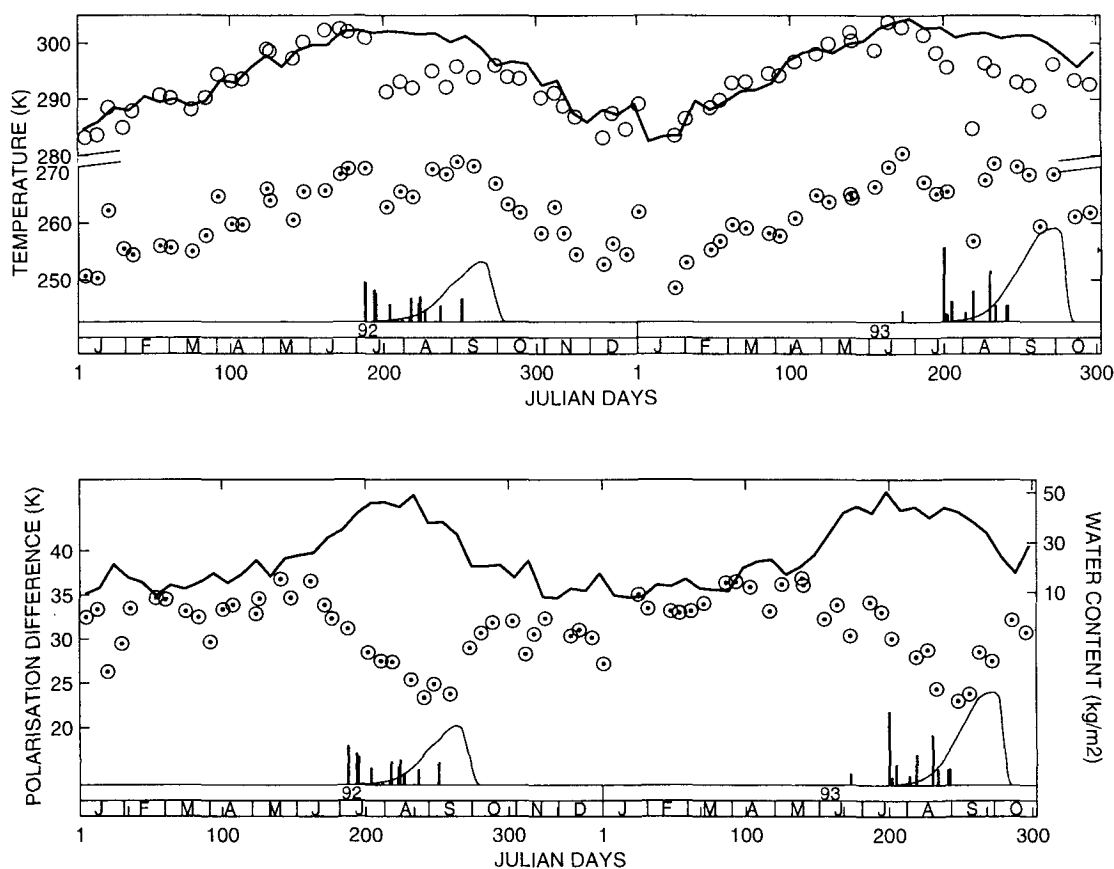


Figure 1: a) Temporal evolution of SSM/I 19 GHz brightness temperature - (o : vertical polarisation, \odot : horizontal polarisation) and surface temperature (—). b) Temporal evolution of SSM/I 19 GHz brightness temperature polarisation difference (\odot) and integrated water content (—). Also are plotted on bottom, vegetation (—) temporal evolution and rainfall (|) - (January 92 - October 93)

Figure 1b represents the temporal evolution of SSM/I brightness temperatures polarisation difference, $\Delta T = T_V - T_H$, and weekly-averaged IWC, in $\text{kg}\cdot\text{m}^{-2}$, derived from ECMWF archives. These two plots display an opposite trend. ΔT begins to decrease when IWC increases and this decrease continues even when IWC remains high and constant, while vegetation grows. Then, the polarisation difference increases at the end of the rainy season when the IWC decreases. During the dry season, where IWC remains low and constant, ΔT increases slowly with surface and air temperature until the next rainy season.

The temporal evolution of SSM/I ΔT and ERS scatterometer σ^0 at 45° incidence angle over the period extending from August 1991 to October 1992 is plotted in Figure 2. Both plots are roughly the mirror reflection each from the other. Particularly, the σ^0 peak is time coincident with the annual minimum of ΔT values. This peak was found to be not coincident

either with the peak of green biomass or with the peak of the vegetation volumetric water content, [5]. However, a delay can be observed between the fall of ΔT which arises about one and two months earlier than the increase of the scatterometer response for 1992 and 1993 respectively. At the end of the rainy season, the increase of ΔT occurs at the same time than the increase of σ^0 . Moreover, on the contrary of ΔT , the radar response remains constant during the dry season. Minimum ΔT values differ from less than 0.5 K between 1992 and 1993 (which has higher productivity than 92), while maximum of σ^0 values differ from about 1 dB for the two years.

It is interesting to note the respective high and low values for σ^0 and ΔT in January 1991. This is due to a strong precipitation occurred in this month leading to vegetation development during the dry season.

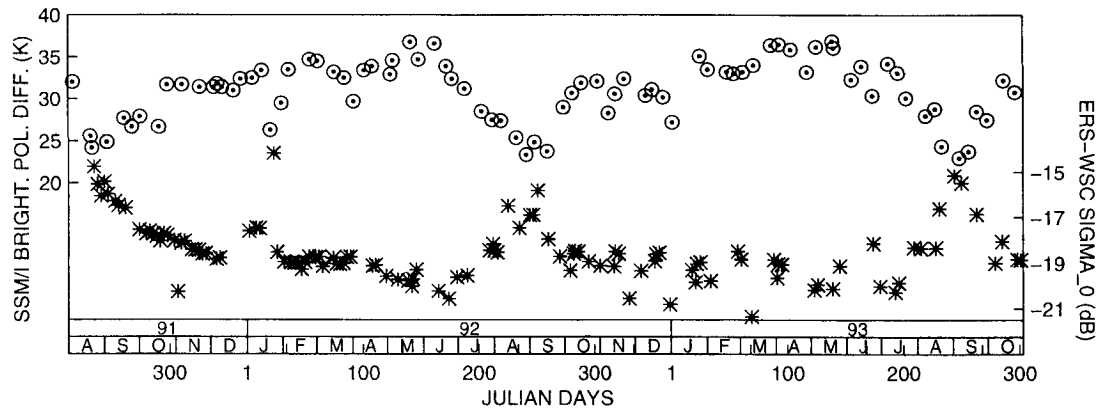


Figure 2 : Temporal evolution of σ^0 acquired by the ERS-1 wind-scatterometer at 45° of incidence angle (*) and SSM/I polarisation difference 19 GHz(\circ).

MODELISATION STUDY

In order to have a better understanding of SSM/I data sensitivity to the various surface parameters, a modelisation study is performed to simulate brightness temperatures as seen by SSM/I for the period extending from May to November 1992. As vegetation is sparse, the scene brightness temperature $T_{B \text{ scene}}$ (as seen from a ground mounted radiometer) is considered to be the sum of the contribution of bare soil and vegetation canopy, each term being weighted by its respective cover fraction:

$$T_{B \text{ scene}} = (1-v_c) T_{B \text{ bare soil}} + v_c T_{B \text{ canopy}}$$

where v_c represents the vegetation cover fraction and $T_{B \text{ bare soil}}$ and $T_{B \text{ canopy}}$ represent bare soil and vegetation canopy brightness temperatures, respectively. The soil emission $e = 1-R$, where R is the soil reflectivity is derived from either the geometrical optics model [9], or from Fresnel reflectivity, depending on the surface roughness (see below). The dielectric constant of the soil surface is estimated from the soil texture and the soil moisture with a semi-empirical model [10]. The vegetation brightness temperature is computed using a model based on an iterative solution of the radiative transfer equations [11]. Only the herbaceous layer is considered, with regard to vegetation canopy, as trees and shrubs fraction cover does not exceed 1% of the surface. The vegetation canopy is represented as a collection of elliptic disc randomly oriented within one layer. The dielectric constant for leaves is computed with the dispersion Ulaby and El-Rayes' model [12]. The brightness temperature measured from a spaceborne sensor, $T_{B \text{ sp}}$, is derived from $T_{B \text{ scene}}$ as follows :

$$T_{B \text{ sp}} = \tau_a T_{B \text{ scene}} + T_{\text{SKY}}$$

where τ_a and T_{SKY} represent the atmospheric transmissivity and the atmospheric radiation derived from the Liebe model using IWC and air temperature [13], [14]. Atmospheric parameters are obtained from ECMWF data while all the vegetation parameters (as v_c , vegetation height, vegetation volume fraction) are simulated by the STEP model. Simulation results compared to SSM/I polarisation difference are shown on Figure 3.

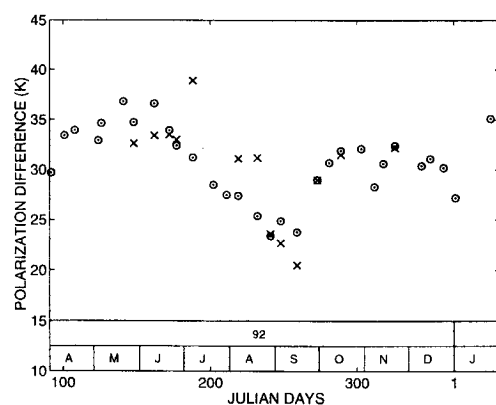


Figure 3 : Polarisation difference simulations (x) compared to SSM/I observations (\circ).

The overall trend is well described by simulations even if discrepancies with experimental data can be observed. For example, the simulated value at the beginning of July, after the first rains when soil begins to be wet, is higher than SSM/I observation. This discrepancy is due to the high sensitivity of the model to soil moisture content which significantly increases ΔT . For this reason, soil roughness cannot be taken as constant during the whole period of study, but is taken as a rough surface (with standard deviation of the surface height and surface correlation of 0.02 m and 0.1 m respectively) during all the rainy season, *i.e.*

between August and September. For the other period, soil surface is assumed to be a planar interface. These choices are made due to the absence of appropriate ground measurements at this scale.

Furthermore, the analysis of the different contributions between bare soil and vegetation canopy shows that this latter has no significant contribution to ΔT of the whole scene. The vegetation contribution is negligible due to the small vegetation cover encountered in these semi-arid areas.

From these considerations, the brightness temperature polarisation difference of the whole scene is simplified as follows :

$$\Delta T_{B_{sp}} = \tau_a \Delta T_{B_{scene}} = \tau_a (1-v_c) \Delta T_{B_{bare\ soil}}$$

It turns out from this expression that the polarisation difference depends on vegetation only through the vegetation fraction cover v_c .

INVERSION METHOD

In order to test the suitability of SSM/I data for surface parameter retrieval, an inversion method is performed. Atmospheric parameters (IWC, T_a) are supposed to be known. Emphasis is put on vegetation biomass retrieval since this is the only parameter that can be used for validation. The inversion method is similar to the one realised for wind-scatterometer data [5]. It is restricted to the vegetation growth time period during which the smooth temporal evolution of vegetation is simulated with a 2-parameter logistic function. On the other hand, the vegetation fraction cover v_c , can be directly derived from vegetation biomass during this period. The method selects the best logistic function which minimises the sum of the distance between simulated ΔT and observed by SSM/I over the whole considered period.

Table 1 presents the peak of biomass retrieved with this inversion method. They have to be compared with values simulated by the STEP model for validation purposes. Also are shown peaks of biomass retrieved from WSC data, [5]. Results are less good than those obtained with WSC data. In particular, the difference in biomass production between 1992 and 1993 is not detected by SSM/I data. This might be explained by the small inter-annual variation between the minimum ΔT values.

	1992	1993
STEP (ground truth)	400	620
SSM/I	550	500
ERS - WSC	500	650

Table 1 : Maximum biomass ($kg\ DM .ha^{-1}$) retrieved from SSM/I data and compared to STEP simulations (considered as ground truth) and values retrieved with ERS-1 wind scatterometer data [5].

CONCLUSION

SSM/I and wind scatterometer data are compared over a sahelian site located in Gourma, Mali for a period extending from August 1991 to December 1993. The temporal evolution of SSM/I brightness temperature polarisation difference at 19 GHz shows an overall similarity with the one of ERS-1 wind scatterometer σ^0 acquired at 45° of incidence angle. However, the sensitivity of SSM/I brightness temperatures to temperature and atmospheric water content induces discrepancies between ΔT and σ^0 temporal evolution. A semi-empirical model based on the radiative transfer theory is used to simulate SSM/I brightness temperatures over the time period extending from April to November 1992. The general trend of SSM/I data is well simulated. However, the high sensitivity of the model to soil moisture leads to discrepancies with observations. Results show that ΔT is sensitive to vegetation development through the vegetation cover fraction as this latter is directly linked to the one of bare soil. Finally, an inversion procedure similar to one realised in a previous study with ERS WSC data is performed on the SSM/I data. Results are less good than those obtained from WSC data. In the future, SSM/I data should be examined over a longer time period. Particularly more contrasted years in term of annual rainfall (and hence primary productivity) should be included in the analysis.

ACKNOWLEDGMENT

The authors would like to thank the EOS Distributed Active Archive Centre (DAAC) at the National Snow and Ice Data Centre, University of Colorado, Boulder, CO which have provided SSM/I data.

REFERENCES

1. Kerr Y.H., Magagi R.D., 1993: Use of ERS-1 wind-scatterometer data over land surfaces: arid and semi-arid lands. *Proc. of the 2nd ERS-1 Symposium*, Hamburg, 11-14 Oct., 383-388.
2. Justice C.O., Townshend J.R.G., Choudhury B.J., 1989: Comparison of AVHRR and SSMR data for monitoring vegetation phenology on a continental scale. *Int. Journal of Remote Sensing*, vol.10, n° 10, 1607-1632.
3. Townshend J.R.G., Choudhury B.J., Giddings L., Justice C.O., Prince S.D., Tucker C.J., IJRS, 1989, Comparison of data from the SSMR with data from AVHRR for terrestrial environment monitoring: an overview. *Int. Journal of Remote Sensing*, vol. 10, n° 10, 1687-1690.
4. Frison P.-L., Mougin E., 1996, Monitoring global vegetation dynamics with ERS-1 wind-scatterometer data. *Int. Journal of Remote Sensing*, vol.17, n° 16, 3201-3218.
5. Frison P.-L., Mougin E., Hiemaux P., 1998, Observations and Interpretations of Seasonal ERS-1 wind-scatterometer data over Northern Sahel (Mali). *IEEE Trans. Geosci. and Remote Sensing*, vol. 28, n°5, 781-780.
6. Mougin E., Lo Seen D., Rambal S., Gaston A., Hiemaux P., 1995, A regional Sahelian grassland model to be coupled with multispectral satellite data. I. Description and validation. *Remote Sensing of Environment*, vol. 52, 181-193.
7. Hollinger J. P., Peirce J. L., Poe G. A., 1990, SSM/I Instrument Evaluation. *IEEE Trans. Geosci. and Remote Sensing*, vol. 28, n°5, 781-780.
8. Choudhury B. J., 1989, Monitoring Global Land Surface Using Nimbus-7 37 GHz data. Theory and Examples. *Int. Journal of Remote Sensing*, vol. 10, n° 10, 1579-1605.
9. Tsang L., Kong J. A., Shin R. T., 1985, Theory of microwave remote sensing, *John Wiley & Sons, New-York*.
10. Dobson M. C., Ulaby F. T., Hallikainen M. T., El-Rayes M. A., 1985, Microwave dielectric behavior of wet soil, Part II: Dielectric mixing models. *IEEE Trans. Geosci. and Remote Sensing*, vol. GRS 23, 25-34.
11. Karam M. A., 1997, A physical model for microwave radiometry of vegetation. *IEEE Trans. Geosci. and Remote Sensing*, vol. 35, n°4, 1045-1058.
12. Ulaby F. T., El-Rayes M. A., 1987, Microwave dielectric spectrum of vegetation. Part II: Dual-dispersion model. *IEEE Trans. Geosci. and Remote Sensing*, vol. 25, 550-557.
13. Liebe H.J., 1985, An updated model for millimeter wave propagation in moist air. *Radio Science*, vol. 20, n°2, 1069-1089
14. Liebe H. J., 1989, *MPM - an atmospheric millimeter-wave propagation model*, *Int. Journal of infrared and millimeter waves*, vol. 10, n° 6, 631-650.

Feasibility study in using scatterometer data for wetland rice mapping yielding methane emission indicators for global applications.

Hans van Leeuwen¹, Rob Verhoeven¹, Hugo Denier van der Gon²,

Hans van der Woerd³, Leon Janssen⁴, Jan Tjalling⁴

¹SYNOPTICS, Costerweg 1-k 6702 AA Wageningen, Tel: 31 317 421221, Fax: 31 317 416146, Email: main@synoptics.nl

²WAU, Dept. Soil Science & Geology, Duivendaal 10, 6700 AC Wageningen Tel: 0317 485234 Fax: 0317 482419

³IVM, De Boelelaan 1115, 1081 HV Amsterdam, Tel: 020 4449506; Fax: 020 4449506

⁴RIVM/LLO, Postbus 1, 3720 BH Bilthoven, Tel: 030 2742771, Fax: 030 2285731

ABSTRACT

Methane is one of the principal greenhouse gases. Its estimated contribution to the radiative forcing of climate in 1990 was about 18% [6], making it the second most important greenhouse gas. Although the individual sources contributing to the global methane budget are identified, there are large uncertainties in their source strength estimates. Rice paddies appear to account for between 5 and 30 % of the total global methane emissions. The bottom-up analysis of methane emission lacks monitoring of rice growth area and inundation status.

In this study the feasibility of upscaling information on rice from field level to regional level using high resolution SAR and scatterometer data is evaluated. The objective is to verify whether the scatterometer sensor is suitable to monitor and map wetland rice paddies in order to define indicators of methane emission on national level. Clear indications are found that the specific time-signature of rice in central Philippines in 1995 when studying the SAR and scatterometer observations remained visible.

Once proven that the scatterometer can be a useful tool for mapping and monitoring rice, the study will be extended to the South Chinese rice region to test the suitability on large scale.

Keywords: ERS, scatterometer, SAR, methane, rice, upscaling.

I. INTRODUCTION

Within the context of the National Remote Sensing Programme NRSP-2 of the Netherlands Remote Sensing Board (BCRS) a project has been formulated called UPRICE. The project aims at producing accurate regional estimates of methane emission from rice fields, based on ERS SAR images and provides therefore a potential tool for upscaling methane emission information from field to regional level. SAR images provide synoptic maps of rice paddies and their flooding status throughout the growing seasons, which is used as input for a model predicting methane emission. Rice paddies are an important source of methane because rice is grown under flooded conditions [7]. As a result oxygen supply from atmosphere to soil is severely limited causing anaerobic conditions. In these conditions methanogenic bacteria produce methane as the end product of anaerobic decomposition of organic matter. Methane may be emitted

from soil to atmosphere by rice plant-mediated gas transport (hollow roots and stems) and ebullition.

Further upscaling of methane emission to continental scale is foreseen by innovative use of wind scatterometer data. If successful, this upscaling of methane emission from local statistics and emission process studies to sub-continental scale in a coherent and systematic manner will serve to support the work in IPCC (Intergovernmental Panel on Climate Change) and FCCC (Framework Convention on Climate Change of the United Nations).

Methane emissions are currently inventoried on a world-wide one-degree grid by RIVM in the EDGAR database. EDGAR was originally a database for atmospheric modellers but is also used to analyse national emission estimates [6]. To match field-level methane emissions and the global figures, it is intended to use radar data from the ERS satellite together with other available geographical data to scale up rice information using high and low spatial resolutions.

The intermediate spatial levels covered by the ERS sensors are 100 x 100 km (25 m resolution, 12.5 m pixel spacing) for the synthetic aperture radar (SAR) and 500 x 500 km (50 km resolution, 25 km pixel spacing) for the windscatterometer (WSC). Figure 1 shows the spatial coverage of the ERS SAR and WSC sensors.

II. METHODS AND MATERIAL

The following steps are considered to set-up the study:

1. Selection of the test site and available geographical information to validate the results
2. Inventory of existing data sets high and low resolution radar data suitable for upscaling, mapping and monitoring of rice information
3. Co-registration of the imagery and available geographical information in the Philippines
4. Evaluation on information on the rice crop with the high resolution data in the Philippines
5. Conclusions and recommendations on the upscaling of this information using low resolution scatterometer data

The ERS satellite covers the whole earth in 35 days. Windscatterometer data are distributed on a monthly basis and consist of a full world-wide coverage. First step is a pre-selection of windscatterometer data by geographic region and

date. A refinement on this selection is made considering date and location of the ERS SAR coverages, using the following rules:

1. In order to avoid incidence angle differences [8], WSC mid beam data from only one single track were selected, yielding WSC time series with an interval of 35 days.
2. Time difference between WSC and SAR acquisitions on so-called 'upscale moments', i.e. moments that WSC and SAR values are to be compared, is as small as possible.

ERS SAR data were selected on basis of their availability during the rice growing season in the test area, yielding five images in the year 1995. Four moments were defined as 'upscale moments', having three days difference between SAR and WSC acquisitions. An overview of the ERS acquisitions over the provinces of Tarlac and Nueva Ecija, Luzon, Philippines, is given in table 1.

Table 1. Acquired ERS SAR and windscatterometer data over Luzon, Philippines.

ERS Sensor	Date	Days between acquisitions
WSC	01-13-1995	-
WSC	02-19-1995	37
WSC	04-01-1995	41
SAR	04-04-1995	3
WSC	05-06-1995	32
SAR	06-13-1995	38
WSC	07-15-1995	32
SAR	07-18-1995	3
WSC	08-19-1995	32
WSC	10-28-1995	70
SAR	10-31-1995	3
WSC	12-02-1995	32
SAR	12-05-1995	3

The project focuses on the central rice plain of the Philippines. In this area field measurements on methane emission from rice paddies are available through the International Rice Research Institute (IRRI) and the Philippine Rice Research Institute [3]. WAU is currently working on a field-scale methane emission [2].

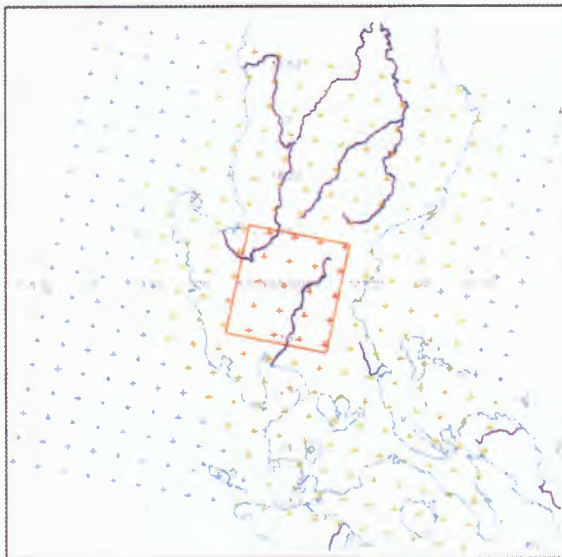


Figure 1. Location of ERS windscatterometer pixels (+ signs) and ERS SAR coverage (red rectangle) over Luzon, Philippines.

For comparison of WSC and SAR data the latter has to be resampled to the coarser geometric level of the windscatterometer. Each SAR image is covered by approximately 4 x 4 windscatterometer pixels which means that each WSC location covers about 2000 x 2000 SAR values. Integration of SAR pixels can be done by either coherent (phase preserved) or incoherent (magnitude) adding. For coherent adding, both amplitude and phase information of the SAR pixel is needed, as provided by the single look complex (SLC) products of ERS. The processing line of SAR imagery consists then of the following steps:

1. Multi-looking, i.e. along-track integration of data.
2. Slant range to ground range conversion
3. Geo-referencing (definition of transformation matrix)

For each WSC pixel, position within the SAR coverage will be searched and the selected subset will be integrated into one value. In this way a time-series of and WSC scatterometer data had been made.

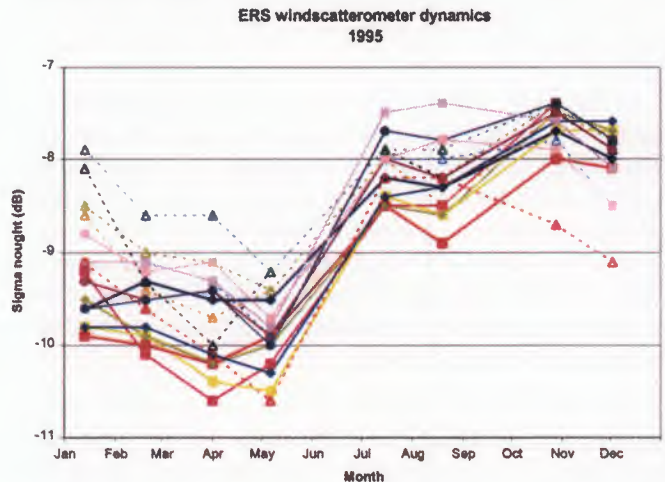


Figure 2. Time series of windscatterometer values. Dotted lines with triangular markers indicate mountainous areas, other represent rice areas.

III. RESULTS

In this section the results of studying high resolution and low resolution radar data from the ERS SAR and the scatterometer are presented. With local information of the Nueva Ecija region some validation of the high resolution ERS SAR time-series is performed.

Figure 2 shows changes of windscatterometer values in rice areas as a function of time. The strong increase of values around June corresponds to rainfall and the biomass increase of especially the valley rice crop in the second half of May and in June, having its effect on both 'mountain' and 'valley'-pixels.

In the study region validation material is available for 1994 [3], The rice cropping practises are not expected to change dramatically in one year. In figure 3 the rice cropping pattern in the region of Nueva Ecija (Luzon) in 1994 is presented. A double-cropping rice system characterizes the area, with a high-input dry season crop and a somewhat

input-reduced wet season crop. This year-round crop growing is possible because of the temperature range and the irrigation water provided by the Upper Pamapnaga River Irrigation System. Most of the study area has received full supply of irrigation water for more than 20 years [3]. In the diagonal of the figure is the Talavera river. The somewhat lighter texture soils along the river are intensively grown to vegetables and cash crops. (see table 2).

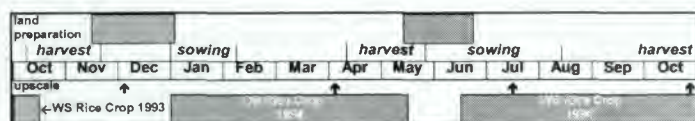


Figure 3. Rice cropping patterns in Nueva Ecija, Tarlac, Philippines, during 1993 and 1994.

The rice cropping pattern in figure 4 shows the transplanted and the direct seeded rice in the region. The transplanted rice exhibit an inundation period of about 6 weeks, which is started in the beginning of the wet season. The high biomass of the rice transplanted in May/June can be seen as green colours in July in figure 5. The strong purple colors indicate that biomass is present in the dry season (rice or other crops: intercropping activities) and at the end of the wet season. The cycle of an average high yielding variety rice crop is about 120 days, which coincides with the scheme in figure 3.

The crop calendar is generally followed by the results of the high resolution SAR data and confirms the assumption that the rice cycles and crop stages using radar data can be

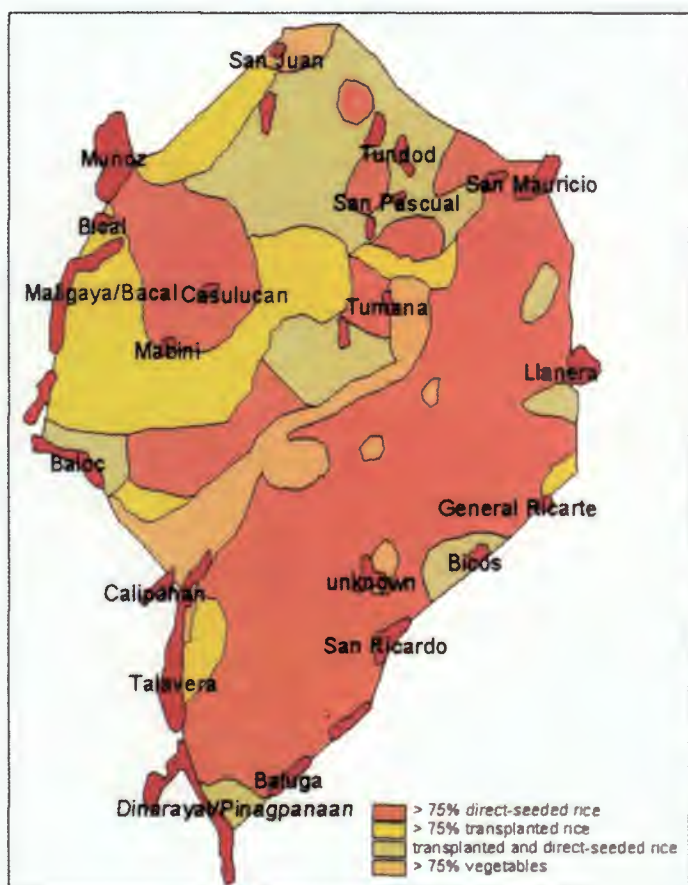


Figure 4. Map of Nueva Ecija, Luzon, Philippines with different rice cropping systems and vegetables in 1994.

seen ([1],[4] & [5]). The mapping of rice compared to other crops is generally possible when having enough observations in time. In figure 5 the vegetable crop can be distinguished with the blue colours (right under or at diagonal). For monitoring of growth in terms of biomass requires a local validation of semi-empirical backscatter models, which is not done in the course of this study [5]. The monitoring of rice cycle evolution is done by studying time-series and RGB figures as mentioned before, which give clear indication of the presence of rice in the region. The rice-cropping culture in terms of cycles can be followed using high resolution SAR data, although more data is needed during the season at the right moments: data take during the transplanting period is therefore essential

With these results using ERS SAR data and the results of the scatterometer (WSC) time-series of figure 2 upscaling from field to regional level using scatterometer data is expected to be possible. It should be noted that this area is a major rice growing area and pixels of the WSC are relatively little contaminated by other land use or objects (infrastructure / cities).

In figure 2 it is shown that the backscatter behaviour of the WSC rice pixels can be distinguished from the WSC mountain pixels. In figure 6 the dynamic behaviour of the WSC rice pixels and the 'upscaled' ERS SAR values

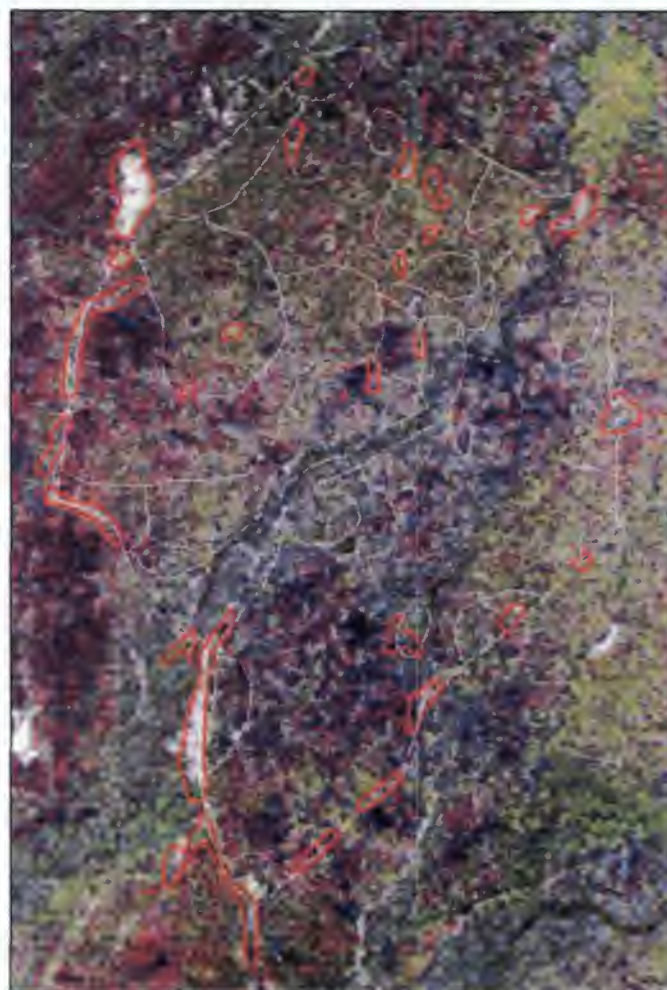


Figure 5. Acquisition dates June 13th (red), July 18th (green) and October 31 (blue), 1995. Vector overlay of figure 4 shows also the cities (red) and rice types (white).

(averaged to the size of one WSC pixel) at the moments of upscaling is similar and amounts 3 to 4 dB, which is expected [5]. Furthermore, the standard deviation in the WSC signatures gives indication on the amount of non rice-information included in one pixel. In general the rice-signature of the scatterometer complies with the expected timing of the crop calendar in figure 3, which is promising for application in China in the second phase of this project in 1999.

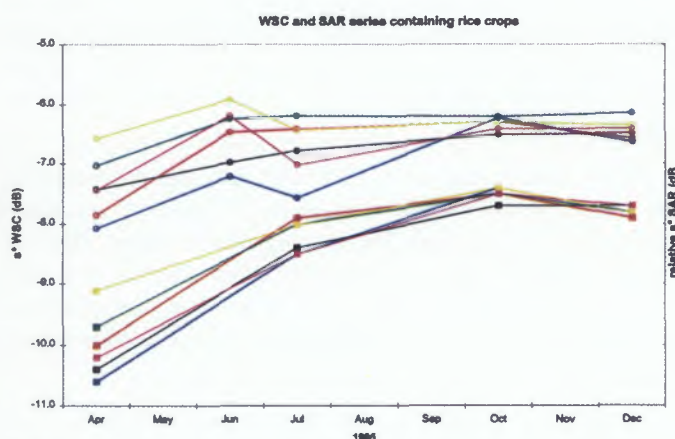


Figure 6. ERS windscatterometer (lower set) and upscaled SAR values (higher set) as function of time.

IV. CONCLUSIONS

- The temporal signature of scatterometer data of rice in the case of the Philippines seems to be consistent with expected behaviour seen with the high resolution ERS SAR.
- The flooding period of the rice growing seasons in the beginning of the wet season has its clear effect on the scatterometer rice signature.
- Thematic distinction between mountain and rice area is possible using the scatterometer (even without correction for local incidence angle effects).
- The rice crop and other vegetation can not be distinguished on windscatterometer resolution due to large variety of surface/crops within a pixel. On large scale it is expected that the clearly dominant presence of the rice crop will have its effect on the periodicity of the scatterometer signature.
- ERS SAR can distinguish rice cycles in high resolution mode. The rice cycle information seen by the scatterometer is generally in correspondence with the ERS SAR (high res mode) and crop calendar and therefore expected to be useful on large scale.
- In this study it seems feasible to upscale actual rice 'surface information' towards a regional scale using scatterometer data.
- This confirms the ability of the scatterometer sensor to map and monitor inundated rice fields. Therefore scatterometer data might be used in the future to make regional methane emission estimates.

REFERENCES

- [1] Aschbacher J., 1995, Rice mapping and crop growth monitoring, An ERS/SAR demonstration project, Earth Observation Quarterly, 49: 1-3.
- [2] Denier van der Gon H.A.C. 1996, Methane Emission from Wetland Rice Fields, PhD Thesis, Wageningen Agricultural University, 182 p.
- [3] IRRI, Field variabilities of soil and plant. Their impact on rice productivity and their use in modeling of soil kinetics and rice yield, Terminal report 1992-1995, The International Rice Research Institute (IRRI) & Universitat Leipzig, Los Banos, Philippines, 1995.
- [4] Kurosu T., M. Fujita and K. Chiba, 1995, Monitoring of rice crop growth from space with ERS-1 C-band SAR, IEEE Trans. Geosci. Rem. Sens. 33, 4: 1092-1096
- [5] Le Toan T., F. Ribbes, N. Floury, L.F. Wang, K.H. Ding, J.A. Kong, M. Fujita and T. Kurosu, 1996, Rice crop mapping and monitoring using ERS-1 data based on experiment and modelling results, Submitted to IEEE Trans. Geosci. Rem. Sens.
- [6] Olivier, J.G.J et al, 1996. Description of EDGAR Version 2.0: A set of global emission inventories of greenhouse gases and ozone-depleting substances for all anthropogenic and most natural sources on a per country basis on $1^\circ \times 1^\circ$ grid. RIVM report nr 771060 002/ TNO-MEP report nr R96/119.
- [7] Van Leeuwen, H.J.C., 1997, 'On a methodology of Radarsat image processing for flood mapping and monitoring in Bangladesh'. Internal technical paper as part of a SYNOPTICS subcontract to the EGIS I project, febr. 1997, Dhaka, Bangladesh.
- [8] Wagner, W., 1998, Vegetation as observed with the AVHRR and the ERS scatterometer: A case study over the Iberian Peninsula. This Workshop at ESTEC, Noordwijk.

Extracting Landcover Information from ERS Scatterometer Data to Support Backscatter Modelling for Soil Moisture Estimation

49

Martin Habermeyer¹, Christiane Schmullius¹, Jose Alvarez Perez² & Stewart Marshall²

¹ German Aerospace Centre (DLR), Institute of Radio Frequency Technology

P.O. Box 1116, D-82230 Wessling, Germany

Tel : +49-8153-28.2337, fax : +49-8153-28.1449, e-mail : chris.schmullius@dlr.de

² Environmental Science Division, University of Nottingham

Sutton Bonington Campus, Loughborough, LE12 5RD

Temporal information about soil moisture and flooding extent is an important parameter for global scale methane models. Methane is a 'greenhouse gas' of major importance, but the amount of terrestrial sinks and sources are not well known. A model for CH₄ emissions from wetlands and rice paddies has been developed at Nottingham University. One of the main input parameters to the model is the soil moisture content and areal extension of flooded conditions.

This project aims to i) extract duration and geographical extent of flooding/standing water during thawing in Siberia and ii) to define validity ranges/thresholds for large scale soil moisture estimations from ERS scatterometer data. Siberia has been chosen as project area because of its importance for the global methane budget, vast natural landsurface types, and proven possibility to monitor seasonal land surface changes with the scatterometer.

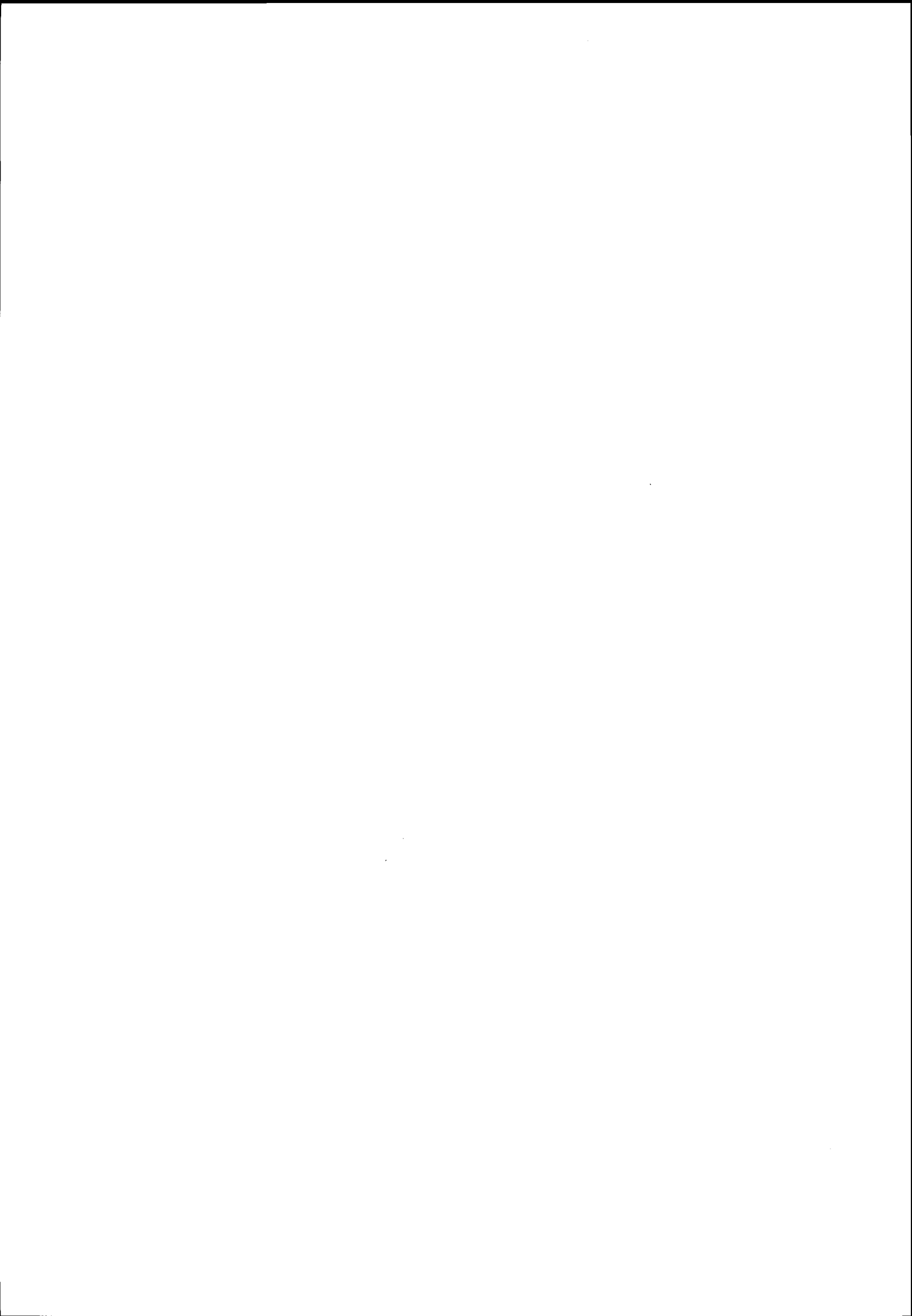
Two methodologies are being developed to retrieve soil moisture information:

- image processing techniques are applied to extract significant time frames and incidence angle ranges and to determine areas of statistical similarities as input to the backscatter model;
- a model is being developed of the physical backscatter mechanisms for various surface types to enable moisture retrieval and flooding status.

This paper presents the state of the image processing part of the joint project. The questions arising from an image processing point of view: which channels (dates, incidence angle ranges) are important to determine the soil moisture adequately as input to the methane model? How much information (intrinsic dimensionality) is contained in the huge data set provided by the scatterometer? Which surface classes can be derived from the scatterometer data?

Two different image processing techniques are pursued to extract the relevant information: a 'classical' approach in form of principal components analysis and a newer one in form of a feature selection method with a k-nearest neighbour algorithm incorporating a genetic algorithm. The principal components analysis (PCA) identifies the landsurface dependent backscatter variation depending on time and incidence angle and therefore leads to a quantification of the importance of each channel. Whereas the PCA approach only shows the evidence that can be given by an image of a certain incidence angle taken at a certain time, the genetic algorithm goes one step further: it combines feature selection (in this case the channels of interest) and optimisation of classification, which can be understood as a fusion of the data and methods applied to the data. The Genetic Algorithm is combined with a k-nearest neighbour algorithm. Both algorithms are applied on the Siberian test area and interpreted using a landscape map elaborated by the International Institute for Applied Systems Analysis, Laxenburg, Austria.

Keywords: principal components analysis, genetic algorithms, feature selection, spatial-temporal analysis



VEGETATION AS OBSERVED WITH THE AVHRR AND THE ERS SCATTEROMETER: A CASE STUDY OVER THE IBERIAN PENINSULA

Wolfgang Wagner

Space Applications Institute, Joint Research Centre of the European Commission, TP 262, I-21020 Ispra (VA), Italy
e-mail: wolfgang.wagner@jrc.it, phone: +39-0332-78-6335

&

Institute for Photogrammetry and Remote Sensing, Vienna University of Technology, Gusshausstr. 27-29, A-1040
Vienna, Austria

ABSTRACT

The AVHRR is a spaceborne sensor working in the visible and infrared part of the electromagnetic spectrum and the ERS Scatterometer is a radar operating in the microwave range (C-band). Both sensors have acquired long-term global data sets that allow to study vegetation from a regional to global scale. In this paper, the spatial and temporal patterns of a number of parameters derived from these two sensors are compared. While in many studies the usefulness of the AVHRR to monitor vegetation development has been confirmed, the present study suggests that this is not case for the ERS Scatterometer. On the other hand, future research may show that the ERS Scatterometer is valuable for the study of general vegetation phenology. Both the ERS Scatterometer and the AVHRR provide information about land cover patterns. More research is needed to determine if the ERS Scatterometer can provide value-added information about vegetation patterns compared to the AVHRR.

1. INTRODUCTION

The Advanced Very High Resolution Radiometer (AVHRR), which has been flown on a series of NOAA (National Oceanographic and Atmospheric Administration) polar orbiting satellites, has extensively been used for monitoring and mapping vegetation from a regional (e.g. Sannier et al., 1998) to global scale (e.g. Loveland and Belward, 1997). The big advantages of the AVHRR are its global coverage and the continuity of data provision since 1978. The first radar to provide global coverage for several years (since 1991) is the ERS Scatterometer flown on board of the European Remote Sensing Satellites ERS-1 and ERS-2. In a number of studies the potential of the ERS Scatterometer for vegetation applications was investigated, and it was found that the ERS Scatterometer may be useful for global vegetation monitoring and discrimination (Wismann et al., 1996; Frison and Mougin, 1996; Schmullius, 1997).

In this paper the results of a comparison of ERS Scatterometer and AVHRR data over the Iberian Peninsula are presented. One obvious limitation of the ERS Scatterometer is its much coarser resolution (~50

km) compared to that of the AVHRR (~1 km). For the comparison, the spatial resolution of the AVHRR had to be degraded to match the resolution of the ERS Scatterometer.

The comparison is done in two steps. Firstly, the temporal evolution of backscattering parameters is compared to Normalised Difference Vegetation Index (NDVI) time series (Section 3). Secondly, the spatial patterns of backscattering parameters are compared to a vegetation abundance map derived from AVHRR imagery (Section 4). The results have partly been published in Wagner (1998) and Wagner et al. (in press²).

2. DATA BASE

Pre-processing of the AVHRR data was done at the Space Applications Institute of the Joint Research Centre, and included standard calibration procedures, atmospheric correction, cloud detection, geometric registration by matching vector coastline segments, and resampling to build a European mosaic (Millot, 1994). The Normalised Difference Vegetation Index (NDVI) was calculated for the period September 1991 to September 1994 and averaged to a resolution of about 50 km employing the impulse response function of the ERS Scatterometer.

The vegetation abundance map based on AVHRR data used in this study is shown in Fig. 1. It was produced by Hirscheider and Sommer (1997) using a linear spectral unmixing algorithm. In this method the fractional cover of the endmember classes "bare soil", "vegetation", and "water" is estimated from monthly composite images of NDVI and surface temperature. The map in Fig. 1 is based on NDVI and surface temperature imagery from September 1993. It was chosen amongst NDVI images and vegetation abundance maps because it showed the best visual agreement with the backscatter maps.

ERS Scatterometer data from the period from September 1991 to May 1996 were processed using the method described in Wagner et al. (in press¹). The three antennas of the ERS Scatterometer measure the backscattering coefficient σ^0 from different incidence angles θ .

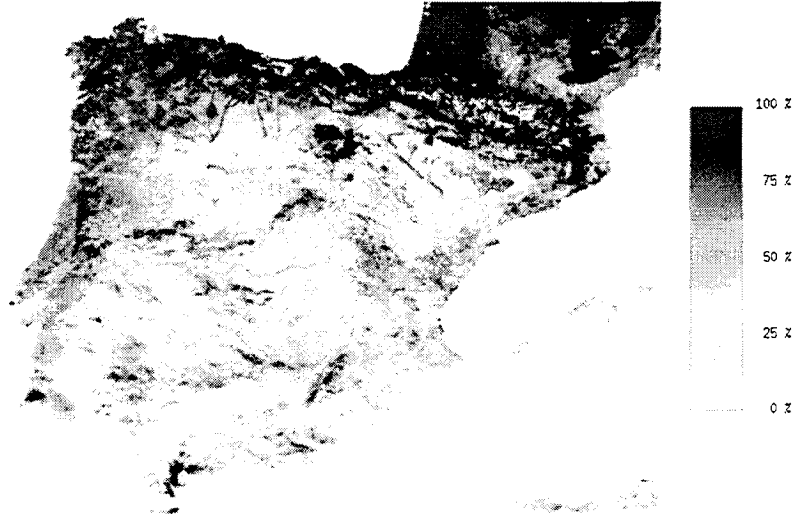


Fig. 1: Vegetation abundance map derived from AVHRR imagery. With the kind permission of Andreas Hirscheider and Stephan Sommer, Space Applications Institute.

This allows to calculate the slope σ' that is defined as the first derivative of σ^0 with respect to θ . The dependency of σ' on the incidence angle can be modelled using a linear relationship:

$$\sigma'(\theta) = \sigma'(40) + \sigma''(40)(\theta - 40). \quad (1)$$

Fitting a regression line to data acquired during a particular period of the year allows to calculate the slope and curvature at the reference angle at 40° , $\sigma'(40)$ and $\sigma''(40)$. Because the noise of σ' derived from the backscatter triplet is large, and to make sure that the σ' values are evenly distributed over the entire incidence angle range from 18° to 59° , data from several years must be used in the regression. Therefore $\sigma'(40)$ and $\sigma''(40)$ represent mean values for a particular period of the year averaged over a long period of records. Averaging of σ' is possible without losing substantial information, because the slope depends on vegetation and surface roughness, but it is not or only little correlated to the rapidly varying soil moisture content. While the curvature is generally stable over the year, the slope $\sigma'(40)$ varies seasonally (see next section). The seasonal variation is modelled with:

$$\sigma'(40, t) = C' + D' \cdot \Psi(t) \quad (2)$$

where C' is a constant, D' is the dynamic range of the slope, and $\Psi(t)$ is some empirical periodic function. Knowing the incidence angle behaviour of the slope, the backscattering coefficient at the reference angle can be calculated from each individual ERS Scatterometer measurement:

$$\sigma^0(40) = \sigma^0(\theta) - \sigma'(40)(\theta - 40) - \frac{1}{2}\sigma''(40)(\theta - 40)^2 \quad (3)$$

3. VEGETATION DYNAMICS

In a first step the temporal behaviour of the slope $\sigma'(40)$ is investigated. The slope is a measure for the relative contributions to total backscatter from the soil surface and the vegetation volume. Since for bare soil surfaces σ^0 decreases in general strongly with the incidence angle, $\sigma'(40)$ should be lowest (high gradient) in winter, and highest in summer when vegetation has reached its maximum wet biomass (low gradient). This is confirmed by Fig. 2a to 2c where the seasonal variation of $\sigma'(40)$ for three sites located in different climatic regions is shown: Iberian Peninsula (Mediterranean climate), Canadian Prairies (dry continental), and Mali (wet-dry tropical). In general, vegetation tends to reach its maximum height during the high-sun season, but water availability and temperatures are also important (Strahler and Strahler, 1996). Therefore climographs showing mean monthly temperatures and mean monthly rainfall are also displayed in Fig. 2.

It can be observed that over the Iberian Peninsula and Canada the highest slope values are around July/August. There are some differences in the shape of the temporal profiles that may be related to differences in the temperature regimes. The early vegetation development in Spain may also be a consequence of winter rainfall and summer drought. In Mali plants cannot grow during the dry period from November to May. Only in the beginning of July - some weeks after the first rainfalls - enough vegetation biomass has developed to prompt an increase of $\sigma'(40)$. The maximum $\sigma'(40)$ values coincide with the end of the rainfall season in September.

For the Iberian Peninsula, a spatial picture of the seasonal cycle of the slope is given in Fig. 3 which shows monthly $\sigma'(40)$ images over the Iberian

Peninsula. Over the entire region the slope is steepest around December/January, and highest around July.

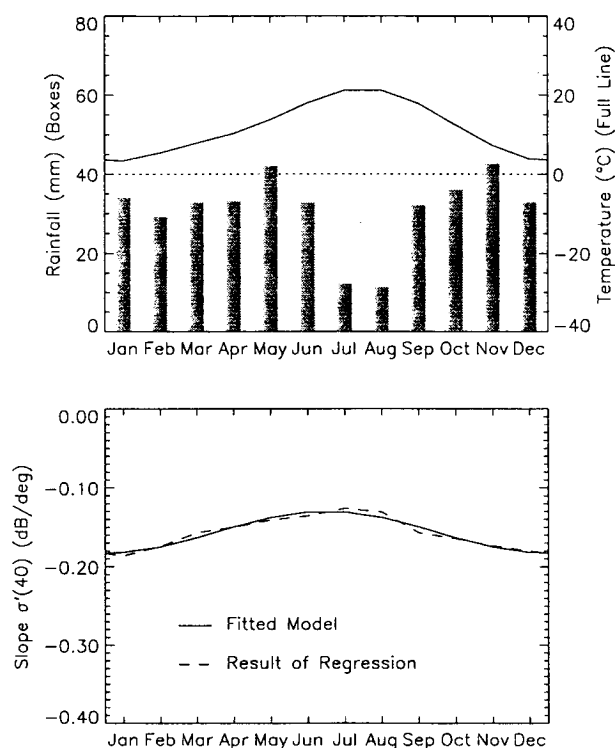


Fig. 2a: Climograph and seasonal variation of the slope $\sigma^0(40)$ for Valladolid, Spain (4.77°W , 41.63°N).

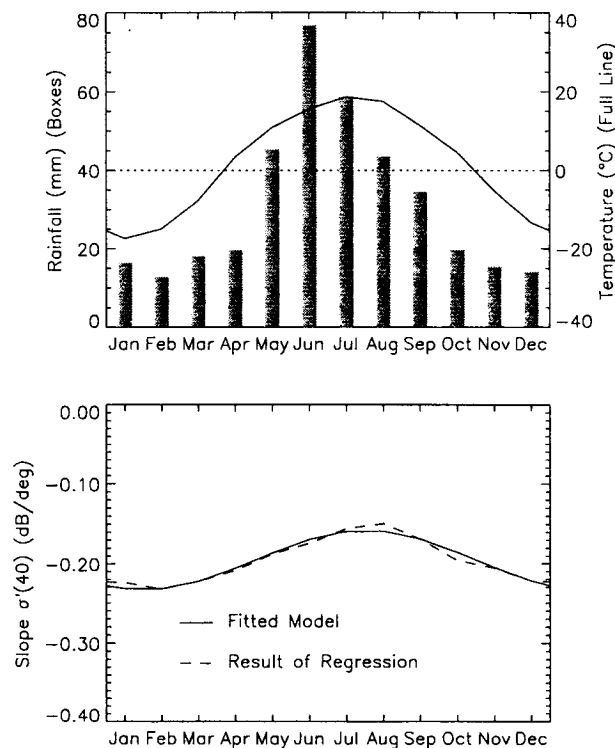


Fig. 2b: Regina, Canada (104.7°W , 50.5°N).

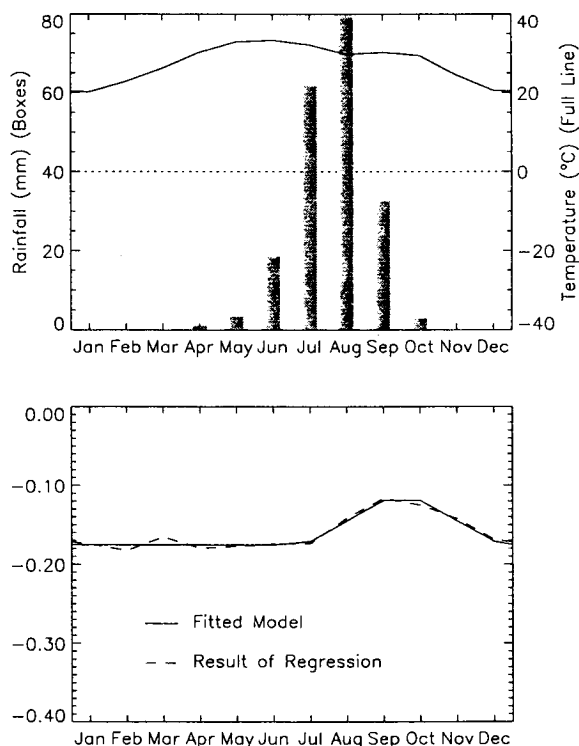


Fig. 2c: Tombouctou, Mali (16.44°W , 3.0°N).

When Fig. 3 is compared to mean monthly NDVI images in Fig. 4 it can be recognised that the peak of $\sigma^0(40)$ occurs with a certain time delay after the peak of the NDVI. In the south of the Iberian Peninsula the time delay is about three months and in the north about one month. The explanation is that while the vegetation is photosynthetically most active in spring (as indicated by the NDVI) it reaches its maximum wet biomass only in summer (as indicated by the slope).

These examples suggest that the slope may be useful for monitoring vegetation biomass. However, it is not possible to monitor vegetation biomass over one season because σ^0 derived from one backscatter triplet is noisy. Only if σ^0 values are averaged over several years then the measurement noise is suppressed, and the resulting mean values may be useful for the study of vegetation phenology.

After the analysis of the seasonal variation of the slope the impact of vegetation growth and senescence on the temporal variability of the backscatter intensity $\sigma^0(40)$ is investigated by comparing $\sigma^0(40)$ time series to daily NDVI values and rainfall observations. In Fig. 5 the evolution of these parameters is shown for an agricultural region around Beja in the south of Portugal. When comparing the NDVI and the backscatter series it can be observed that $\sigma^0(40)$ varies on much shorter time scales than NDVI. For example, in the winter 1992/93 $\sigma^0(40)$ varies several times between its maximum and minimum values while the NDVI profile is relatively smooth.

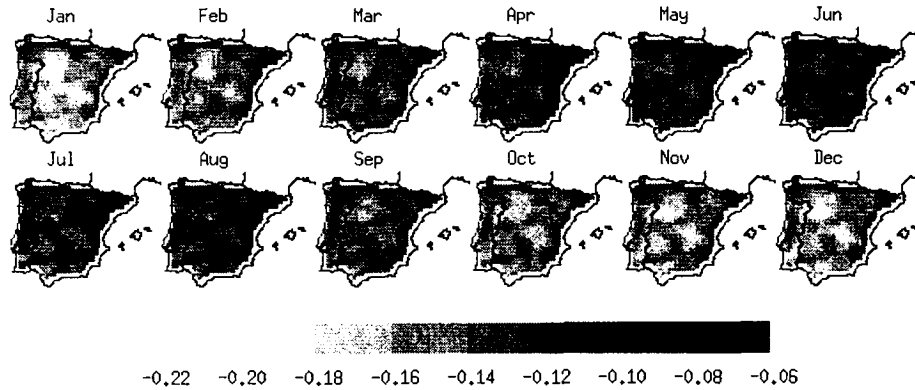


Fig. 3: Seasonal variability of the slope $\sigma'(40)$ in dB/deg over the Iberian Peninsula derived from ERS Scatterometer data acquired during the period September 1991 to May 1996.

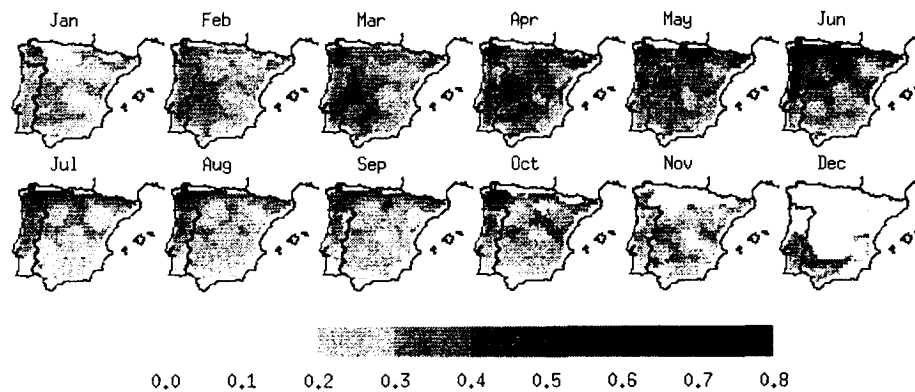


Fig. 4: Mean monthly NDVI values over the Iberian Peninsula derived from AVHRR imagery acquired during the period September 1991 to September 1994. If less than 6 NDVI values per month are available then the mean value is not calculated (white areas).

The day to day changes in the NDVI are mainly due to "noise" caused by the viewing geometry, partial cloud cover, etc.. On the other hand, the comparison of the backscattering with the rainfall series shows that the evolution of $\sigma^0(40)$ can to a large extent be explained if the changes are interpreted as changes in the surface soil moisture conditions. However, also seasonal vegetation cover effects should be important to explain the temporal evolution of the backscattering coefficient, because the slope σ' changes and this change must necessarily be reflected in σ^0 . In Wagner et al. (in press²) the concept of the crossover angles is introduced that states that at some incidence angle the $\sigma^0(\theta)$ curves of winter and summer vegetation should cross over, which means that at this "crossover angle" σ^0 is relatively stable over the year. To illustrate this let us regard the cloud model, which has widely been used to describe backscattering from various vegetation types (Attema and Ulaby, 1978; Ulaby et al., 1986):

$$\sigma^0(\theta) = \frac{3\omega \cos\theta}{4}(1-\gamma^2) + \sigma_s^0(\theta)\gamma^2 \quad (4)$$

σ_s^0 σ^0 of the bare soil surface (m^2m^{-2})

ω Single-scattering albedo

γ^2 Two-way transmissivity

The first term on the right hand side describes the contribution to the canopy backscattering coefficient σ^0 from the vegetation layer, and the second term the contribution from the soil surface reduced by the vegetation attenuation. When vegetation grows the transmissivity γ^2 changes. Therefore, mathematically, our "crossover angle" could be found where:

$$\frac{\partial \sigma^0(\theta)}{\partial \gamma^2} = 0. \quad (5)$$

Differentiation of Equation (4) results in the condition:

$$\frac{3\omega \cos\theta}{4} = \sigma_s^0(\theta) \quad (6)$$

The incidence angle, where the condition (6) is satisfied is the crossover angle. At lower incidence angles, the backscattering coefficient decreases with increasing vegetation biomass, and at higher incidence angles it increases. Since the bare soil backscattering coefficient increases with soil moisture, the crossover angle for dry soil conditions must be smaller than the crossover angle for wet conditions: $\theta_{dry} < \theta_{wet}$.

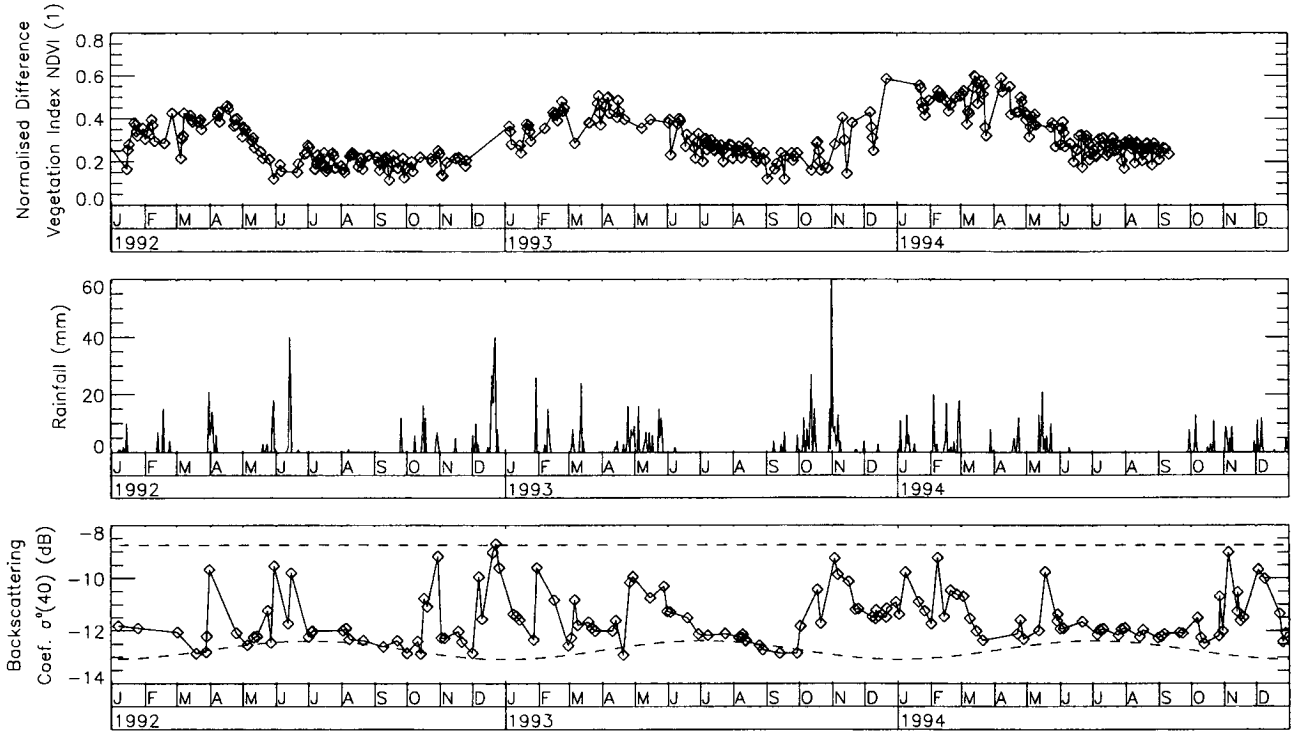


Fig. 5: Temporal evolution of the NDVI (top), rainfall observations (middle), and backscattering coefficient $\sigma^0(40)$ (bottom) over an agricultural region around Beja, southern Portugal (7.9°W , 38.0°N). The dotted lines in the bottom diagram show the backscattering coefficients for dry and wet soil conditions, σ_{dry}^0 and σ_{wet}^0 .

Assuming that these crossover angles exist, the temporal evolution of the canopy backscattering coefficient for dry soil conditions σ_{dry}^0 at the reference angle of 40° is given by:

$$\sigma_{dry}^0(40, t) = C_{dry}^0 - D\Psi(t)(\theta_{dry} - 40) \quad (7)$$

where C_{dry}^0 is a constant, and where $D\Psi(t)$ represents the seasonal variation of the slope. For wet soil conditions, the backscattering coefficient σ_{wet}^0 is given by:

$$\sigma_{wet}^0(40, t) = C_{wet}^0 - D\Psi(t)(\theta_{wet} - 40) \quad (8)$$

Empirical observation shows that θ_{dry} is approximately 25° and θ_{wet} about 40° . Having estimates for θ_{dry} and θ_{wet} the constant terms C_{dry}^0 and C_{wet}^0 can be extracted for each grid point automatically.

The sensitivity $S(t)$ of σ^0 to changes in the surface moisture content can then be calculated:

$$\begin{aligned} S(t) &= \sigma_{wet}^0(40) - \sigma_{dry}^0(40, t) = \\ &= C^S - D\Psi(t)(\theta_{wet} - \theta_{dry}) \end{aligned} \quad (9)$$

where C^S is a constant value. It is now possible to quantify the relative magnitude of soil moisture and seasonal vegetation cover effects on σ^0 . The magnitude

of soil moisture effects is represented by C^S , and the magnitude of seasonal vegetation cover effects by $D(\theta_{wet} - \theta_{dry})$. Fig. 6 shows these two terms based on the entire data set from the Iberian Peninsula. It can be seen that independent of land cover, soil moisture effects are more important than vegetation cover effects.

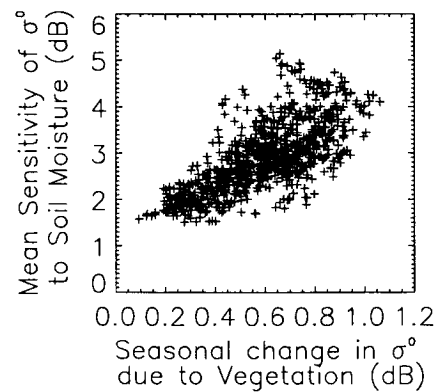


Fig. 6: Soil moisture versus seasonal vegetation cover effects on backscattering coefficient σ^0 .

4. SPATIAL VEGETATION PATTERNS

A number of parameters are now available that fully describe the backscattering behaviour at each point. These can now be compared to the vegetation abundance map derived from the AVHRR imagery

(Section 2). Table 1 shows the correlation between the vegetation abundance and the backscattering parameters. The correlations R are calculated based on the data from the entire Iberian Peninsula (842 points).

C'	D'	C_{dry}^0	C_{wet}^0	C^S
70	-55	42	-9	-54

Table 1: Correlation coefficient R in % between AVHRR derived vegetation abundance and backscattering parameters.

The results show that with increasing vegetation abundance C' and C_{dry}^0 increase while D' and C^S decrease. The correlations are not particularly high, but still high enough, to conclude that both the AVHRR and the ERS Scatterometer convey similar information about spatial vegetation patterns. If smaller regions would have been considered then the correlations may be as high as 90%. The reason for the observed similarity may be that most of the spatial variability of the backscattering parameters is related to the percentage of translucent vegetation like grassland and agricultural areas, and non-transparent vegetation like forest, bushes, and shrubs within the resolution cell (Wagner et al., in press²). Using advanced methods such as the linear spectral unmixing algorithm used to generate the abundance map, such information can also be obtained from AVHRR data.

5. CONCLUSIONS

It has been shown that the ERS Scatterometer has only limited capabilities for monitoring vegetation over one year because individual slope σ' values are noisy and because σ^0 is more sensitive to changes in soil moisture than to changes in biomass. Therefore the ERS Scatterometer poses no alternative to AVHRR for monitoring purposes. However, for the study of general vegetation phenology, σ' values averaged over several years may give a better impression about biomass development than vegetation indices from AVHRR. With respect to spatial vegetation patterns, the ERS Scatterometer gives an indication about the distribution of non-transparent (forests, bushes) and translucent (grassland, agricultural) vegetation and may therefore be useful for global vegetation mapping. However, such information can also be derived from AVHRR imagery at a much better resolution, and further research is required to see if the ERS Scatterometer can provide value-added information or not.

ACKNOWLEDGEMENTS

I want to thank Andreas Hirscheider and Stefan Sommer for useful discussions and the provision of the vegetation abundance map. CERSAT kindly provided the ERS Scatterometer data.

REFERENCES

- Attema, E. P. W., F. T. Ulaby (1978) Vegetation modeled as water cloud, *Radio Science*, Vol. 13, No. 2., pp. 357-364.
- Frison, P. L., E. Mougin (1996) Monitoring global vegetation dynamics with ERS-1 wind scatterometer data, *Int. J. Remote Sensing*, Vol. 17, No. 16, pp. 3201-3218.
- Hirscheider, A., S. Sommer (1997) Regional Desertification Indicators and Remote Sensing Models, In "MEDALUS III Project: Regional Indicators", Third Interim Report, J. Brandt & N. Geeson (Eds.), pp. 11-18.
- Loveland, T. R., A. S. Belward (1997) The IGBP-DIS 1 km land cover data set, DISCover: first results, *Int. J. Remote Sensing*, Vol. 18, No. 15, pp. 3289-3295.
- Millot, M. (1995) NOAA AVHRR Pre-Processing, Workshop on Agrometeorological Models: Theory and Applications in the MARS Project, *Publication EUR N°16008 EN of the Office for Official Publications of the European Communities*, pp. 173-179.
- Sannier, C. A. D., J. C. Taylor, W. D. Plessis, K. Campbell (1998) Real-time vegetation monitoring with NOAA-AVHRR in Southern Africa for wildlife management and food security assessment, *Int. J. Remote Sensing*, Vol. 19, No. 4, pp. 621-639.
- Schmullius, C. (1997) Monitoring Siberian Forests and Agriculture with the ERS-1 Windscatterometer, *IEEE Trans. Geosc. Remote Sensing*, Vol. 35, No. 5, pp. 1363-1366.
- Strahler, A., A. Strahler (1996) Physical Geography, Science and Systems of the Human Environment, *John Wiley & Sons Inc.*, New York etc., 637 p.
- Ulaby, F. T., R. K. Moore, A. K. Fung (1986) Microwave Remote Sensing, Active and Passive, Volume III: From Theory to Applications, *Artech House*, Norwood.
- Wagner, W. (1998) Vegetation Cover Effects on ERS Scatterometer Data, Technical Note No. I.98.05, *EC Joint Research Centre*, Ispra, Italy, January 1998, 193 p.
- Wagner, W., G. Lemoine, M. Borgeaud, H. Rott, A Study of Vegetation Cover Effects on ERS Scatterometer Data, *IEEE Trans. Geosci. Remote Sensing*, in press².
- Wagner, W., J. Noll, M. Borgeaud, H. Rott, Monitoring Soil Moisture over the Canadian Prairies with the ERS Scatterometer, *IEEE Trans. Geosci. Remote Sensing*, in press¹.
- Wismann, V., A. Cavanie, D. Hoekman, I. Woodhouse, K. Boehnke, C. Schmullius (1996a) Land Surface Observations using the ERS-1 Windscatterometer, Part I, *ESA ESTEC, Contract No. 11103/94/NL/CN*, 57 p.

RESOLUTION ENHANCEMENT OF ERS SCATTEROMETER DATA

J. L. Álvarez Pérez *, S.J. Marshall *, C. Schmullius **, M. Habermeyer ** & K. Gregson

* Environmental Science Division, University of Nottingham, Sutton Bonington Campus,
Loughborough LE12 5RD, UK

** Institut für Hochfrequenztechnik, DLR, Postfach 11 16, 82230 Wessling, Germany

ABSTRACT

The enhancement of ERS scatterometer data is an issue of remarkable importance as far as land applications are concerned. The coarse resolution of the instrument is determined by diffraction phenomena and it is variable with the incidence angle and the antenna from which the echo is detected. This heterogeneity is overcome by normalising the resolving power of each measurement at ground stations. This proceeding is necessary for the use of the data in the wind vector computation for which the scatterometer was launched. However, it is possible to build land images only with data whose resolution performance is better than the normalised value of the product. It is shown in this paper that resolution enhancement of these images, nominally with 46 km square resolution, can be improved to reach a value of 25 km square.

1. INTRODUCTION

One of the major problems restricting the applicability of ERS scatterometer data to land studies is their poor resolution. Scatterometers have been proved useful for monitoring the wind and wave conditions on the ocean surface, where the resolution drawback is not of such a great significance. The capacity of scatterometer measurements to purvey a high degree of information on terrestrial scenes could be exploited further if some improvement is made to the resolution of the instrument.

There has been some controversy about the enhancement of resolution in radar images of the earth's surface obtained from spaceborne scatterometry. Much of the work has been done by Long *et al.* (Ref. 1), who developed a method, scatterometer image reconstruction (SIR), to enhance the resolution of Seasat-A scatterometer (SASS) data (Ref. 2-4). This algorithm is based on the overlap of the nominal resolution cells during the successive passes of the satellite over the study area. This technique has also been used for ERS scatterometer data (Ref. 5-7) and more recently to the Special Sensor Microwave/Imager (SSM/I) passive imagery by the same authors (Ref. 8). A critical remark on this work was made by Walker (Ref. 9-10), who suggested that SIR is more a segmentation technique than an actual super-resolution technique. According to Walker, only the resolution of inadequately sampled data could be improved with such a method, which was the case for the SASS data but not for the ERS scatterometer. Walker (Ref. 10) also proposed a limit of 25 km to the achievable, improved resolution, as imposed by ground processing of the data. He recommended the application of Wiener filtering to improve the spatial resolution of the ERS scatterometer.

The objective of the methods described in this paper is to analyse the factors defining the resolution of ERS

scatterometer data and to improve it whenever possible. It is not proposed to increase the bandwidth of the signal in the frequency-domain and, therefore, no super-resolution technique is intended. Within this context, the finest resolution limit will be shown to be 25 km square under certain circumstances, but not for all the measurements. Wiener filtering has been applied as reported in the following sections.

2. ERS SCATTEROMETER IMPULSE RESPONSE FUNCTION

2.1 Preliminary Assumptions

The following approximations will be made in discussing the impulse response function and data acquisition model for the scatterometer:

1. Both sensor and ground are assumed to remain stationary from the time of transmission of a pulse to the reception of the corresponding echo.
2. The scene on the ground does not change during the period of time over which the image is constructed.
3. The ground swath illuminated by the satellite beam is assumed to be flat, and the curvature of the Earth is not considered.
4. At C-band atmospheric perturbations can be regarded as unimportant (Ref. 11) and ideal wave propagation is assumed. Therefore, neither refraction nor attenuation of the radar pulses by the atmosphere are considered.
5. Any image produced from the recorded scatterometer coefficient values is considered to be the result of perfect non-coherent illumination of the land surface.

It is of prime importance that the measurements from which an image is formed are taken within a narrow band of incident angles and either from the mid-antenna or from any of the other two. This is so because the mid-antenna has different dimensions from the fore- or aft- antennas and because, as shown below, antenna performances is variable with the incidence angle.

2.2 Angle and Range Discrimination from the Antennas. Resolution Cell

The resolution of a device is defined to be its half-power response width. From a physical point of view, it is the radius of the area with which each measurement is associated. The scatterometer's spatial resolution is defined by two factors. The first is the diffraction effect due to the finite size of the antenna. The second is range discrimination, brought about by the short pulse length of the transmitted signal. The received echo signal, $r(t)$, will be proportional to the transmitted amplitude, $s(t)$, delayed by the return-trip time, and the antenna pattern, assumed separable into elevation, $a_e(\theta)$, and azimuth, $a_a(\varphi)$, components:

$$r(t) \propto a_{\theta}(\theta) \cdot a_{\phi}(\phi) \cdot s\left(t - \frac{2R}{c}\right) \quad [1]$$

where c is the speed of light. Discrimination in angle is determined by the angular half-power width of these two antenna pattern functions. Results from the pre-launch testing of the satellite showed that the antenna beam widths were 26° in elevation and 0.9° in azimuth for the fore- and aft- beams and 24° in elevation and 1.4° in azimuth for the mid-beam (Ref. 12). A resolution cell is determined by the intersection of the area illuminated by these beams and the ring bounded by two concentric circles representing constant distances from the satellite and differing of one another by $c \cdot \tau / 2$, where τ is the length of the pulse (figure 1). Therefore, the along-track resolution is defined by $a_{\phi}(\phi)$ and the very short length of the transmitted pulse determines the across-track resolution.

As shown in figure 2, across-track resolution ranges from 15 km to 35 km for the mid-antenna and from 25 km to 46 km for the fore- and aft- antennas. Along-track resolution will be within the range 14-25 km for the fore and aft- antennas and within 20-27 km for the mid-antenna.

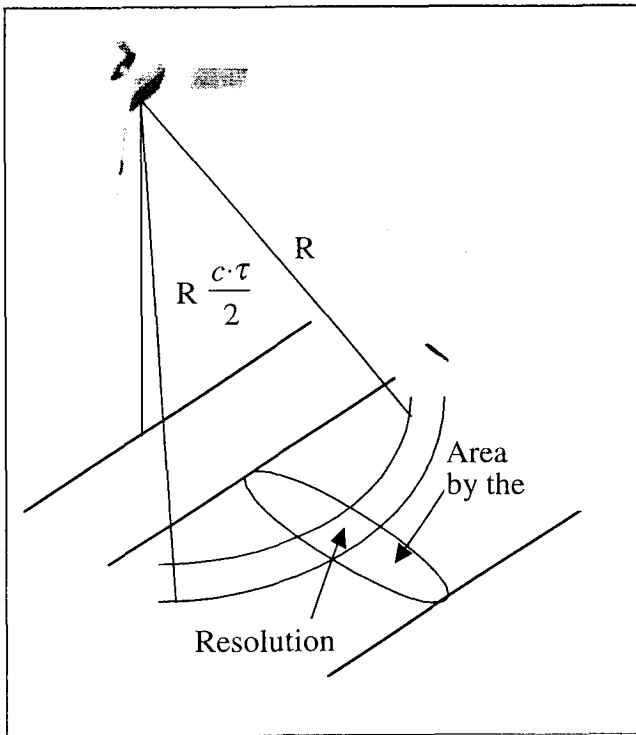


Figure 1. Resolution cell for the mid-beam

2.3 Ground Processing

The function of the ground processors is to convert the digital radar echo samples into final products consisting in grids of 19 x 19 pixels representing an area of 500 km square. Each node holds three values of the backscattering coefficient, corresponding to each antenna. Echoes are integrated for regular periods corresponding to 25-km movements of the spacecraft along the satellite subtrack. Therefore, the Nyquist frequency is 0.02 km^{-1} .

As the spatial resolution of the echo samples is heterogeneous, a normalising operation is carried out in the integration of the

returned signals. This is performed by using a Hamming window with rectangular symmetry and results in the convolution of the impulse response function of the signal with that window. Thus, the spatial resolution of the ERS scatterometer data is normalised to the worst performance at the antennas, namely, 46 km square. This necessary process of normalisation degrades some of the data.

The frequency spectrum of the Hamming window is shown in figure 3. It is a rapidly decreasing function with very small sidelobes, the biggest of which is 22 dB below the central peak value. The figure shows that the processed signal maintains any significant component with a spatial frequency equal to or smaller than the Nyquist frequency, provided that the noise-to-signal ratio is less than the unity within these frequencies.

2.4 Total Impulse Response Function of a Scatterometer Image

The formation of each 500 km x 500 km product is a time-invariant, spatially linear and isoplanatic process. According to the assumptions made above, the resulting two-dimensional function, g , can be described by

$$g(\vec{x}) = h(\vec{x}) \otimes (d(\vec{x}) \otimes f(\vec{x})) + n(\vec{x}) \quad [2]$$

where f is the backscattering response of the target, n includes all that we consider as noise, h is the Hamming window and d represents the diffraction effect 'tapered' by range discrimination. It is assumed in [2] that h has cylindrical symmetry for the sake of simplicity, as no major differences are expected from its actual rectangular symmetry.

Unlike oceans, land can be considered to have relatively long periods of change and it is possible to construct scatterometer images by integrating data acquired during different passes of the satellite over a study area, but either from the mid-antenna only or from any of the other two. In the work reported here, the weight function in the integration was again a Hamming window. The space-domain radius drawn for this second Hamming window was 25 km instead of 46 km. Then, the following is obtained:

$$\begin{aligned} g(\vec{x}) &= h'(\vec{x}) \otimes h(\vec{x}) \otimes (d(\vec{x}) \otimes f(\vec{x}) + n(\vec{x})) \\ &= h(\vec{x}) \otimes \tilde{f}(\vec{x}) + \tilde{n}(\vec{x}) \end{aligned} \quad [3]$$

where h' is the second Hamming window, and \tilde{f} and \tilde{n} contain the effects of h' and d . The effect of convolving h and h' with n is to reduce its variance.

In Fourier-space, equation [3] is more conveniently expressed as

$$G(\vec{k}) = H(\vec{k}) \cdot \tilde{F}(\vec{k}) + N(\vec{k}) \quad [4]$$

where the upper case letters are the Fourier-transforms of the functions given by the names in lower case.

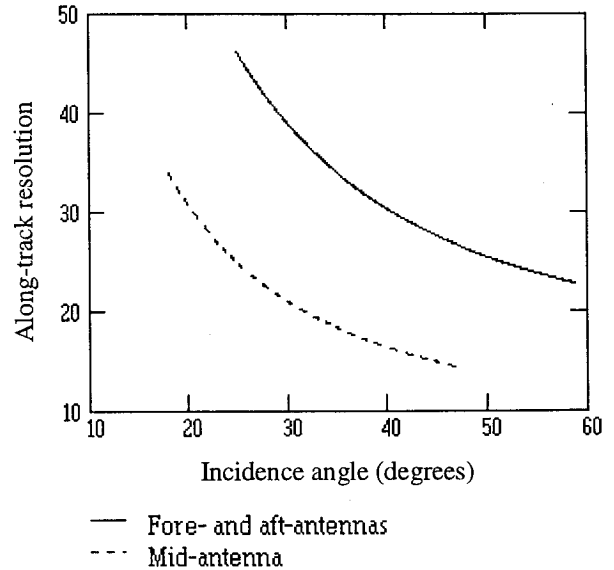
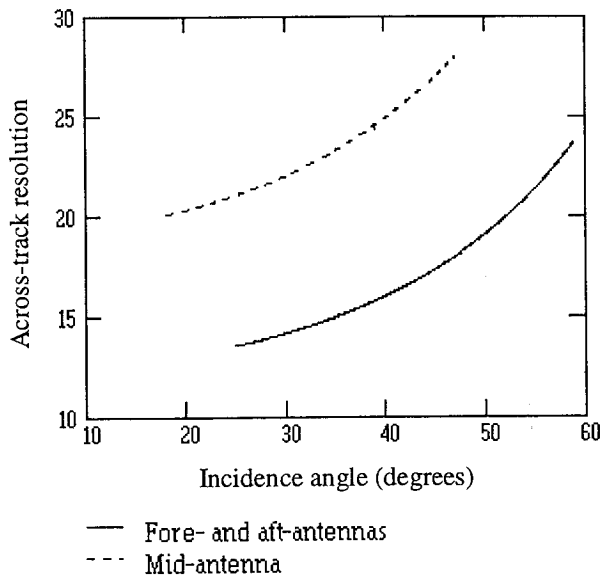


Figure 2. Along-track and across-track resolution of the scatterometer before ground processing

As the backscattering signal is a sampled quantity and all the processing is discrete, equations [3] and [4] are transformed into their matrix representations:

$$\mathbf{g} = \mathbf{h} \otimes \tilde{\mathbf{f}} + \tilde{\mathbf{n}} \quad [5]$$

Overlap between different periods in the convolution is avoided by padding the vector $\tilde{\mathbf{f}}$ with zeros. The matrix \mathbf{h} is assumed to be block-circulant, and therefore the complete set of eigenvectors is obtained from the unitary transform matrix given by the discrete Fourier-transform (Ref. 13). Thus, it is possible to write [5] in the Fourier-space as

$$\mathbf{G} = \mathbf{H} \cdot \tilde{\mathbf{F}} + \tilde{\mathbf{N}} \quad [6]$$

If $\tilde{\mathbf{f}}$, which can be seen as the image prior to Hamming windowing, has been formed with measurements such that their resolution according to figure 2 is better than 46 km square, it is possible to improve that spatial resolution. Equations [5] and [6] represent the degradation phenomenon to which $\tilde{\mathbf{f}}$ is subject.

3. WIENER FILTERING OF ERS SCATTEROMETER DATA

3.1 Preliminary Concepts in Image Restoration

The problem of image restoration is the determination of an original object function, or matrix in a discrete formulation, given the recorded image and knowledge about the kind of degrading process that have occurred. This process is expressed in the situation described in equation [5] by the convolution of the 46-km wide Hamming window with our object function $\tilde{\mathbf{f}}$.

The mathematical difficulties of restoration stem from the existence and uniqueness of an inverse transformation, called deconvolution, that allows the retrieval of $\tilde{\mathbf{f}}$ from $\tilde{\mathbf{g}}$ and, due to the presence of noise $\tilde{\mathbf{n}}$, also from its possible instability.

From an algebraic point of view, the first two problems correspond to the inversion of the matrix \mathbf{H} and the question of its rank. If the rank is smaller than the number of elements in $\tilde{\mathbf{f}}$, there is no unique solution for $\tilde{\mathbf{f}}$. The point then is to add some constraint to the problem. One useful constraint is set in the formulation known as Wiener filtering or minimum mean-square-error restoration.

The power spectrum of the image G is 0.02 km^{-1} for images built with mid-beam echoes for incidence angles between 25° and 40° and with fore- and aft- beam echoes beyond 50° , as shown above, and can provide a maximum resolution of approximately 25 km square.

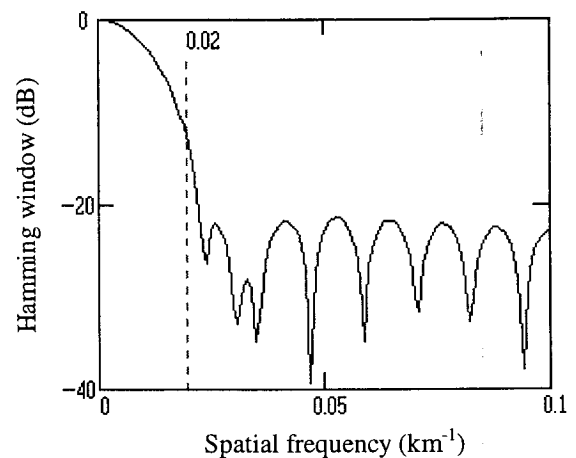


Figure 3. Fourier-transform of the Hamming window function. The dashed line indicates the Nyquist frequency (0.02 km^{-1}).

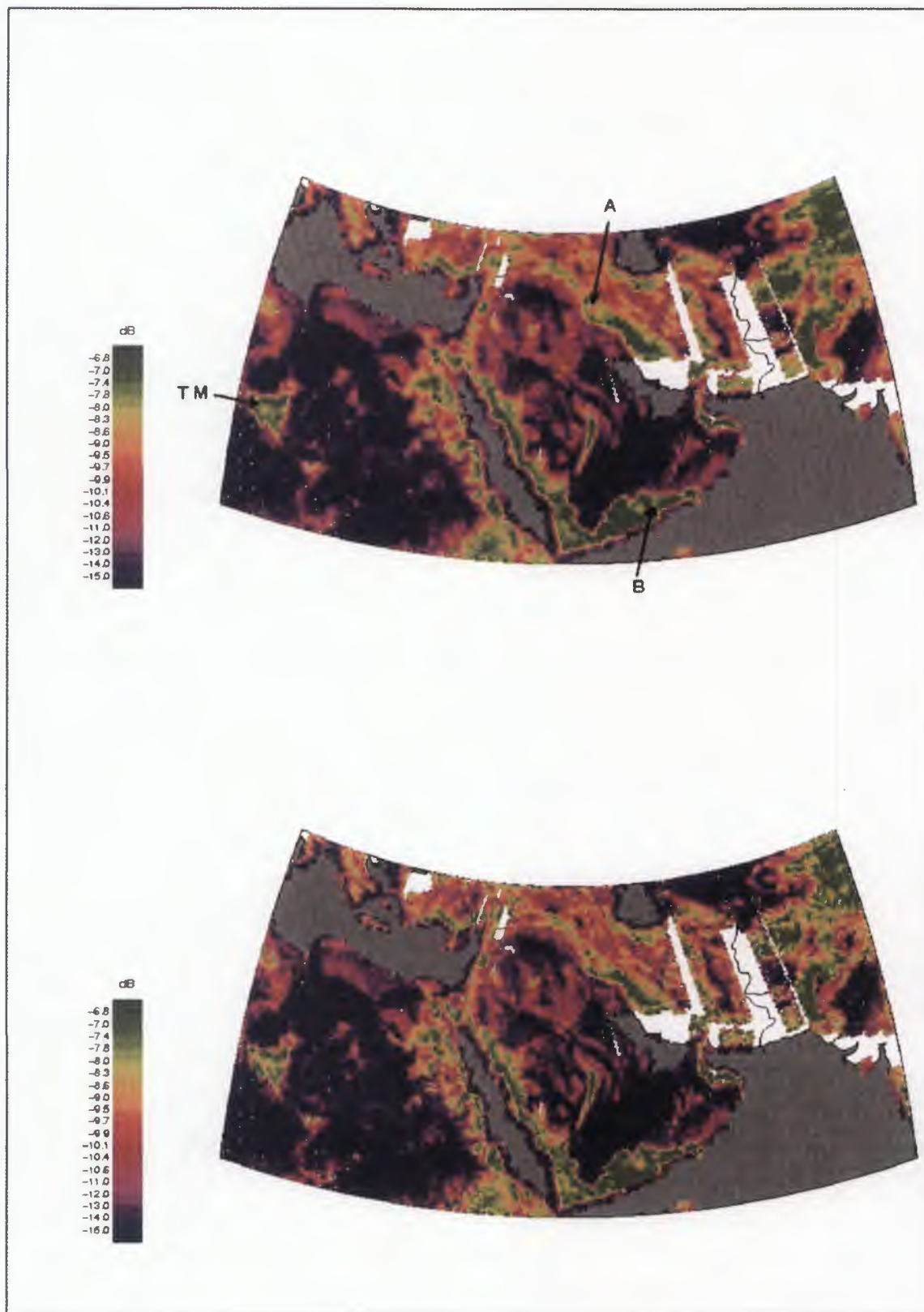


Figure 4. Scatterometer images of the Middle East created with data acquired with the mid-antenna at incidence angles between 25° and 35° during the month of June 1997. The upper image has been built with 46-km square resolution data and the lower image is the result of applying the resolution enhancement algorithm described here, and its resolution is approximately 25 km square

3.2 Wiener Filtering

To solve the practical deconvolution in our case, a stochastic framework can be adopted. The criterion, or constraint, is to impose the condition for the solution to be an estimate such that the expected value of the difference between that estimate and the original \tilde{f} is minimised over the ensemble of possible original vectors \tilde{f}_s . Deconvolution is then performed by the filter (Ref. 14):

$$K_w(k_x, k_y) = \frac{H^*(k_x, k_y)}{|H(k_x, k_y)|^2 + \Phi(k_x, k_y)} \quad [7]$$

$$\Phi(k_x, k_y) = \frac{S_{\tilde{n}\tilde{n}}(k_x, k_y)}{S_{\tilde{f}\tilde{f}}(k_x, k_y)}$$

where k_x and k_y are the spatial frequencies, and $S_{\tilde{n}\tilde{n}}$ and $S_{\tilde{f}\tilde{f}}$ are the Fourier-transforms of the covariance functions of the noise and the original and unknown object \tilde{f} , respectively. Noise is assumed to be signal-independent and all the underlying random processes determining \tilde{f} and \tilde{n} to be stationary.

The covariance function of \tilde{f} is unknown and, therefore, Φ cannot be predicted *a priori*. It is common in the literature to take a constant value, Φ_0 , for Φ , where this constant is chosen experimentally: different values are tried until a value providing the most "apparently satisfactory" result is taken to be the correct (Ref. 15). A different approach has been used here. The filter K_w gets its maximum, $\frac{1}{2\sqrt{\Phi_0}}$, for

$H(k_x, k_y) = \sqrt{\Phi_0}$. If this value is too high, noise will be amplified for the corresponding spatial frequencies by a factor of $\frac{1}{2\sqrt{\Phi_0}}$. On the other hand, the smaller the maximum

is, the broader the correlation length of the ensemble of \tilde{f}_s becomes. As high correlations are not expected between distant points, a tolerance threshold for the amplification of the noise is to be fixed in compromise with the correlation length (Ref. 13). Once this is fixed, the covariance of the ensemble of possible original objects \tilde{f} is assumed to be exponential with a central value approximated by the variance of the values in the image to be restored.

Resolution enhancement is performed in the next section following the methods explained here for a testing area.

4. APPLICATION OF THE WIENER FILTER RESTORATION TO A LAND IMAGE

As an example of the application of the algorithm, a comparison between two images, one with the original 46-km square resolution and the other with an enhanced 25-km square resolution, is shown here (figure 4). The area employed is a part of the Middle East and the images have been built with data acquired during the month of June of 1997 at angles within the range of 25° and 35° and from the mid-antenna.

It is possible to see some increase in the definition of the limits of the landscape features. This happens, for instance, in the area of the Tibesti mountains (labelled as point TM). It is also to be noted that some small features are highlighted in figure 4b, such as the points labelled as A and B.

Border effects are expected to occur at the boundary of the images and near the empty areas where the scatterometer was not working during the period of time under consideration.

5. CONCLUSIONS

In this paper we have analysed the main factors defining the resolving power of the ERS scatterometer and it has been shown that it is possible to build images for which the original performance at the spacecraft can be recovered, and therefore a better resolution obtained.

The method depends on the collection of data during different passes of the satellite over an area, that makes it appropriate for relatively perdurable scenes such as land or sea-ice. This precludes its use for oceanic monitoring. There is also a limitation upon the variety of angles for which improvement in resolution is obtained. The theoretical optimum of 25 km square is possible for images formed with measurements acquired from the mid-antenna between incidence angles of 25° and 40°, whereas an improvement to 30 km square is possible between 18° and 25°.

6. REFERENCES

1. Long D G Hardin P J & Whiting P T 1993, Resolution enhancement of spaceborn scatterometer data, *IEEE Trans. Geosci. Remote Sensing*, **31**, 700-715
2. Hardin P J & Long D G 1994, Discrimination between tropical formations using reconstructed high-resolution Seasat-A scatterometer data, *Photogram. Eng. Remote Sensing*, **60**, 1453-1462
3. Long D G Whiting P T & Hardin P J 1992, High-resolution land/ice imaging using Seasat scatterometer measurements, *Proc. Int. Geosci. Remote Sensing Symp.*, Houston, TX, May 92, 440-442.
4. Long D G & Hardin P J 1994, Vegetation studies of the Amazon Basin using enhanced resolution Seasat scatterometer data, *IEEE Trans. Geosci. Remote Sensing*, **32**, 449-460
5. Early D S Long D G & Drinkwater M R 1993, Enhanced-resolution ERS-1 scatterometer imaging of Southern-ocean Sea-Ice, *ESA Journa-European Space Agency*, **17**, 4, 307-322
6. Early D S Long D G & Drinkwater M R 1994, Comparison of enhanced resolution images of Greenland from ERS-1 and Seasat scatterometers, *Proc. Int. Geosci. Remote Sensing Symp*, Pasadena, CA, Aug. 8-12, 1994, 2382-2384
7. Long D G Early D S & Drinkwater M R 1994, Enhanced resolution ERS-1 scatterometer imaging of Southern Hemisphere Polar Ice, Pasadena, CA, Aug. 8-12, 1994, 156-158

8. Long D G & Daum D L 1998, Spatial resolution enhancement of SSM/I data, *IEEE Trans. Geosci. Remote Sensing*, **36**, **2**, 407-417
9. Pulliainen J Grandell J Hallikainen M. Virtanen M Walker N Metsaemaeki S Ikonen J P Sucksdorff K & Manninen T 1996, Scatterometer and Radiometer Land Applications, *ESRIN Contract: 11122/94/I-HGE (SC)*
10. Walker N P 1997, Limitations of the possible resolution enhancement of ERS-1 scatterometer images, *IEEE Trans. Geosci. Remote Sensing*, **35**, **1**, 196-198
11. Ulaby F T Moore R K & Fung A K 1986, *Microwave Remote Sensing: Active and Passive*, vol II, III. Reading, MA: Addison-Wesley
12. Attema E P W 1991, The Active Microwave Instrument On-Board the ERS-1 scatterometer, *Proceedings of the IEEE*, **79**, **6**, 791-799
13. Andrews H C & Hunt B R 1997, *Digital image restoration*. Englewood Cliffs : Prentice-Hall
14. Rosenfeld A 1982, *Digital picture processing*. Vol.1. 2nd ed. San Diego : Academic Press
15. Bates R H T 1986, *Image restoration and reconstruction*. Oxford: Clarendon

GLOBAL VEGETATION MONITORING USING THE ERS-1 SCATTEROMETER: IMAGE GENERATION AND PROPERTIES.

M. Abdel Messeh and S. Quegan

Sheffield Centre for Earth Observation Science, University of Sheffield, Sheffield S3 7RH, UK
Tel: +44 (114) 2223705, Fax: +44 (114) 2223739, Email: m.messeh@sheffield.ac.uk

ABSTRACT

Global backscatter images generated from the ERS-1 Wind Scatterometer (WSC) data are of potential value in large scale studies of vegetation dynamics. Methods of generating global backscatter images from the scatterometer raw data are presented. This involves averaging in time, space and across incidence angles; a method for estimating the relative errors in these three averaging procedures is introduced. The relevance and effects of adopting a model for the incidence angle dependence of the backscatter is evaluated. Patterns arising in the backscattering coefficient for different azimuth angles are shown. Images of variability are used to detect disturbance and/or data artefacts. The seasonal backscatter changes of a range of vegetation types are examined and related to the vegetation biophysical properties.

1. INTRODUCTION

Monitoring the dynamics of vegetation is increasingly important as deforestation, climate change and desertification become major issues. At the global scale, monitoring vegetation dynamics can be critical for studying long term climate changes such as global warming and its subsequent effect on vegetation activity. Regionally, we require information on biophysical drivers, such as the freeze/thaw cycle at high latitudes and rainfall and soil moisture in semi-arid areas.

Low resolution satellite sensors provide an efficient and economic (versus high resolution sensors) means of obtaining global and/or regional coverage on a regular (monthly or less) basis. For example, the Normalized Difference Vegetation Index (NDVI) derived from the red and near-infrared channels of the AVHRR sensor is commonly used to monitor vegetation vigour.

Microwave sensors represent an attractive complement to optical sensors because they are weather independent and can operate both day and night. The relevance of low resolution microwave data for vegetation monitoring has been realized only fairly recently, due

to analysis of the data from the WSC carried on the ERS satellites. This paper extends this analysis and deals with four subjects: generation of global backscatter (σ^0) images, images of variability, azimuth angle effects, and the behaviour of σ^0 for different vegetation types.

2. GENERATING GLOBAL σ^0 IMAGES

The scatterometer nodes are positioned with respect to the position of the satellite, forming a set of coordinate systems with different orientations. For comparisons with other data types (e.g. weather, soil, GVI, etc.), we would like to map the WSC measurements onto a regular grid. In our study, this was chosen to be $0.5^\circ \times 0.5^\circ$, to match the output from a global vegetation model. In creating such backscatter images, three issues have to be addressed: temporal averaging, methods of spatial interpolation with their implications for spatial resolution, and incidence angle modelling. These three issues are interrelated because creating a global backscatter image requires many measurements which are spread over time, distance (from each grid point) and a range of incidence angles.

2.1 Temporal Averaging

Using the CIA world map database as a reference, it was found that the WSC covers about 95.7% of the Earth's total land area after 15 days of data acquisition and 96.2% after 30 days. These figures suggest generating half monthly WSC images, as they give near global coverage with less variability due to target changes during the averaging time (Section 4.2).

2.2 Spatial Interpolation

Spatial interpolation is concerned with determining how the value of σ^0 at a certain grid point is calculated from the original measurements. This value is derived from all the overlapping WSC measurements that lie within a certain area around that point (the influence zone). If we assume that the value of σ^0 at a certain

grid point can be derived by the same process as was used to derive the WSC original measurements from the instantaneous power, then the influence zone will be circular with the same 85 km width as the Hamming filter used to generate the original WSC measurements.

The σ^0 value can be calculated in various ways from the measurements affecting a given grid point. An ideal method would be to use deconvolution to restore the original measurements at the antenna pattern scale, then resample them onto the new grid. This method is not feasible, as it needs an accurate knowledge of the antenna pattern (which is not available), and would require long execution times. A simpler alternative is to use a weighted average of the WSC measurements, expressed as a spatial convolution operation. For a rectangular weighting this degrades the spatial resolution to about 87 km. A Hamming weighting which matches the original filter used to generate the scatterometer data, leads to resolutions varying from about 62 to 65 km. The results generated in this paper use a rectangular window for simplicity.

2.3 Incidence Angle Effect

Each original measurement is acquired at a different incidence angle, which affects the measured σ^0 . The averaging procedure must account for this by normalizing the data to a single incidence angle θ_{ref} , or allowing only a limited range of incidence angles. The latter is normally not attractive as the number of available measurements might be very small for some grid points.

When generating σ^0 images without any prior information about the nature of the land cover, we need to use a simple model. Six empirical models were tested by fitting them to the original WSC data for a given area and month. The goodness of fit was estimated using the coefficient of determination, R^2 , which is the ratio of the variances of the predicted and observed values of σ^0 . For a perfect fit, $R^2 = 100\%$. Table 1 shows the different models and their corresponding R^2 values, averaged over 14 different land cover types and for the whole of 1995.

It can be seen that no model is clearly to be preferred for global σ^0 image production, and that overall, the models did not perform too well. However, some of the models performed much better for certain land cover types; for example, the constant γ model had $R^2 \cong 79\%$ for tropical evergreen forest. This is expected because the dominant volume scattering is best described by constant γ . Model 6 was the best for 6 cover types, especially temperate and boreal forest types. The two exponential models, 4 and 5, came second, being the

Table 1. The performance of incidence angle models.

Model name	Formula	R^2 %
Constant γ	$\sigma^0 = \gamma \cos \theta$	48.26
Lambert law	$\sigma^0 = k \cos^2 \theta$	49.50
Generalized Lambert	$\sigma^0 = k(\cos \theta)^{2n}$	48.83
Model 4	$\sigma^0 = k e^{-\theta/\theta_0}$	50.80
Model 5	$\sigma^0 = k_1 e^{-k_2 \sin \theta}$	50.94
Model 6	$\sigma^0 = k \frac{\sin 2\theta}{\sin \theta} (1 + \cot \theta)$	52.61

best for most of the other cover types. Note that the performance of any of the models depends on both the month and the cover type. It is also inversely related to the heterogeneity of the area under observation (hence it is generally inversely related to its size).

3. VARIABILITY IN SCATTEROMETER IMAGES

Many measurements are averaged at each grid point. Their variability is important both to indicate how representative the mean image is, and whether there is underlying geophysical variation.

For radar data, where the standard deviation (SD) in a uniform region is proportional to the mean value, an appropriate measure of variability is the normalized standard deviation, k_p (SD/mean). The variability can be attributed to four components as follows:

$$k_p^2 = k_{pi}^2 + k_{pt}^2 + k_{ps}^2 + k_{pg}^2 \quad (1)$$

where: k_{pi} is the interference variability component

k_{pt} is the temporal variability component.

k_{ps} is the spatial variability component.

k_{pg} is the incidence angle variability component.

In the following, we analyse the relative sizes of these sources of variability and how to minimize them.

3.1 Interference Variability

This component describes the pure noise-like effects in the measurements. It is given by (Ref. 5):

$$k_{pi}^2 = \frac{1}{N_s} \left[\frac{1}{N_r} \left(1 + \frac{1}{\text{SNR}} \right)^2 + \frac{1}{N_n} \left(\frac{1}{\text{SNR}} \right)^2 \right] \quad (2)$$

where N_s is the equivalent number of independent samples integrated to get one grid point value. It is 14.31 for the Fore/Aft beams and 16.04 for the Mid beam.

$N_r = 32$, is the number of received signal + noise samples.

$N_n = 28$, is the number of noise only samples.

SNR = 282 dB Hz, is the signal-to-noise ratio.

Using (2), k_{pi} was found to be ~4.7% for the Fore/Aft beams, and ~4.4% for the Mid beam.

3.2 Temporal Variability

This component arises from target changes during the time interval covering the data used in the averaging. In order to assess time effects we limited the range of incidence angles to 35° - 45° and distances of measurements from the grid points to less than 25 km.

The relative importance of temporal variability depends on the vegetation type, but on average comprises about 8% of the total variability for the Fore/Aft beams, and about 18% for the Mid beam for March 1996. This may differ for other months when the vegetation has a different rate of change. A current difficulty in extending this analysis is that it involves manual selection of data satisfying the incidence angle and distance conditions to ensure enough measurements are available to estimate k_{pt} .

3.3 Spatial Variability

This component arises from the fact that measurements have different distances from the grid point and it is clearly affected by the homogeneity of the area under study. It is estimated by choosing a time range of 0 - 15 days and an incidence angle range of 35° - 45°. For measurements located within a distance of 42.5 km from the grid point, the spatial variability component constitutes about 22% of the total variability for all three beams.

3.4 Incidence Angle Variability

In order to quantify the effect of averaging σ^0 values with different incidence angles, we limit the averaged measurements to a time range of 0 - 15 days and a distance of 25 km from the measurement to the grid point. Unlike the previous two components, we can partially correct this component using incidence angle models (Section 2.3). For example, using the constant γ model, the average improvement from the

uncorrected to the corrected k_{pg} values for tundra and arid shrubland is about 19% for the Mid beam and 39% for the Fore/Aft beams; for tropical evergreen forest it is much higher because of the good fit of the constant γ model to the data.

The incidence angle variability (after correction) constitutes about 43% of the total variability for the Fore/Aft beams, and about 60% for the Mid beam. All values are calculated over the full incidence angle range (25° - 59° for the Fore/Aft beams and 18° - 47° for the Mid beam).

3.5 The Total Variability

Since k_{pt} , k_{ps} , and k_{pg} are interrelated and the method used to isolate each component does not provide a full separation, we would expect the estimated total (calculated using (1)) to be larger than the total variability observed in the measurements. In fact it is about 11.5% larger. This inaccuracy can be used to correct the individual components, assuming equal proportions of inaccuracies.

In order to improve the representativity of the σ^0 images, it is desirable to minimize the image variability, i.e., minimize all four components. The interference component, k_{pi} , is small and can be neglected. The temporal component can be minimized by using 15 day images. (This component can be relatively large for some cover types, such as arid shrubland.) The spatial variability component can be reduced by limiting the spatial averaging extent to a radius of 25 km instead of 42.5 km. The highest component is k_{pg} (about 68.4% with no correction) and therefore it is essential to minimize it using incidence angle models (Section 3.3). The residual effects are still significant as their contributions to total variability are on average: interference component (4.59% \equiv 0.2 dB), temporal variability (14% \equiv 0.6 dB), spatial variability (18.8% \equiv 0.8 dB), and incidence angle variability (37.7% \equiv 1.4 dB).

It is particularly desirable to minimize k_{pg} in order to emphasise target dependent terms, k_{pt} and k_{ps} , to indicate physical changes in the target.

3.6 Images of Variability

Figure 1 shows an image of k_p values derived from the Aft beam data for March 1996. Very high k_p values (reaching 150%) occur throughout the year in deserts in North Africa, Saudi Arabia, Turkmenistan, west China and Australia. These can be attributed to changes in small-scale surface roughness produced by

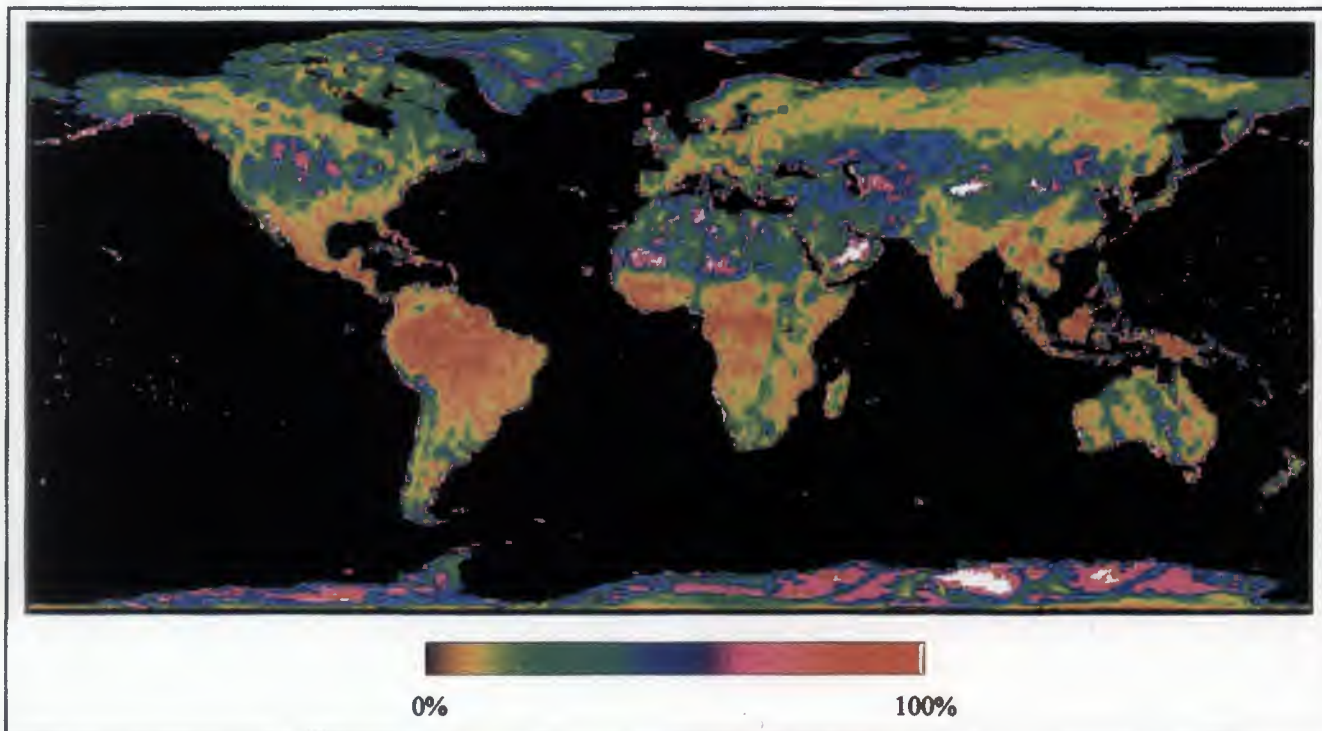


Figure 1: The normalized standard deviation (k_p) image derived from the Aft beam scatterometer data for March 1996.

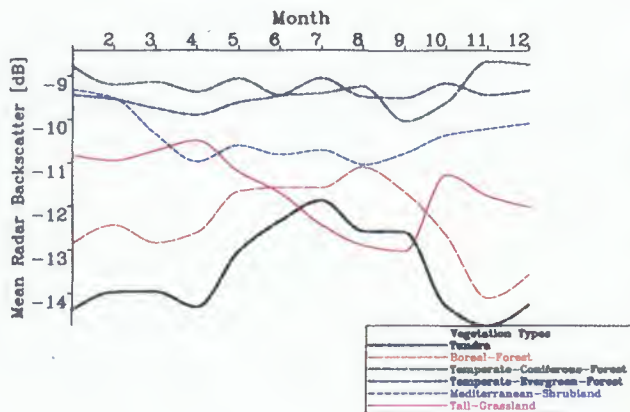


Figure 2: The seasonal behaviour of σ^0 during 1995 (Mid beam).

wind-blown sand (Ref. 4), but may also result from azimuth angles effects caused by the existence of sand dunes (see Section 5). In the Great Plains of North America, where the major vegetation cover is essentially long and short grassland, containing vast areas cultivated for cereals, k_p is again large throughout the year with a slight decrease in July and August. This may be connected with agricultural practices and spring snowmelt. The tropical regions in South America,

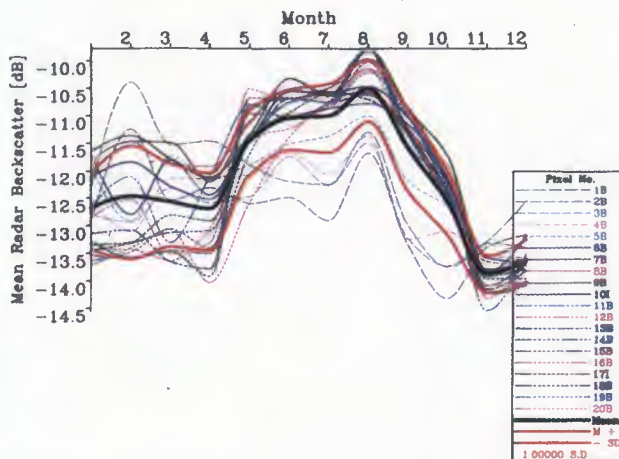


Figure 3: The seasonal behaviour at individual grid points in the boreal forest region during 1995 (Mid beam).

Africa and Indonesia show little change ($k_p < 10\%$), as expected in rain forest areas.

In other cases, variability is restricted only to certain times. High k_p values at higher latitudes in the early part of the year can be attributed to changes in snow cover. These high values occur later as latitude increases, starting around April for the boreal forest area ($\sim 58.5^\circ$ N), May for the tundra ($\sim 70.0^\circ$ N), and

June for regions in the very north of Canada (71° - 84° N), such as Baffin Island.

Figure 1 also shows linear artefacts in Africa coinciding with descending satellite paths and western Australia coinciding with ascending paths. It seems likely that these indicate malfunctioning of the sensor or data processing chain, despite the data quality flags indicating normal functioning of the sensor.

4. THE BEHAVIOUR OF SPECIFIC VEGETATION TYPES

The temporal behaviour of σ^0 in 1995 was examined for 14 selected vegetation types. Six of these types are shown in Figure 2. These temporal sequences suggest that σ^0 is related to weather and/or vegetation activity with a clear increase in σ^0 from winter to summer for most vegetation types. Examples of vegetation types showing different behaviours and the reasons for this are described below:

Temperate Coniferous Forest:

This is stable evergreen coniferous forest with a relatively small total change of σ^0 (~1.4 dB). The small decreasing trend in σ^0 from January to August can be attributed to the drier summer conditions. The stronger decrease in September may indicate exceptionally dry conditions during this month.

Temperate Evergreen Forest:

The seasonal variations in this forest are determined more by temperature than by precipitation (Ref. 1). The water content does not change much, σ^0 is fairly stable, with a maximum change of 0.84 dB. The summer increase in σ^0 corresponds to the growing season of this northern hemisphere forest.

Mediterranean Shrubland:

This vegetation type belongs to the mediterranean ecosystem which is characterized by a very hot and dry summer. The shrublands of the Mediterranean Basin can vary from very low shrubs (< 0.6 m) to high shrubs (> 2 m) which are essentially small trees (Ref. 1). The chosen area comprises almost 50% shrubs and 50% grass. This mixture, along with the dry summer conditions, explains the seasonal pattern of σ^0 : low σ^0 values begin as the grass starts dying around April, and continue throughout the summer up to October.

It should be noted that within the general trends observed for given vegetation types (Figure 2) subclasses of behaviour occur. For example, Figure 3

shows the seasonal behaviour at individual grid points for the boreal forest. The labels next to the grid points numbers indicate if a certain grid point lies (I)nside the standard deviation limits (± 1.0 SD) for each month, (O)utside for every month, or (B)etween (some months inside, some outside). On average, any grid point is within one standard deviation limit for approximately 7.85 months. This is a percentage of 65.4%, which is very close to the probability of any measurement falling within the one standard deviation limit for a normal distribution (68.2%). These figures suggest that we can use the mean σ^0 value within this region as representative of the behaviour of the whole region.

Figure 3 shows that some subclasses appear to exist within the main class. For example, several grid points show an increase in σ^0 in February followed by a decrease in March. These grid points show no evidence of being spatially related. Topographic effects do not provide an explanation for these sub-patterns as they do not occur throughout the whole year. Similar sub-patterns were found for all tested ground cover types, but further investigation is required to establish the reasons for such behaviour.

5. AZIMUTH ANGLE EFFECTS

The azimuth angle (viewing direction) for a given node is defined as the angle between the line connecting the satellite vertical projection to the node and the north direction at the node. The backscattering coefficient for 5 grid points from 5 different cover types (tropical forest, tundra, arid shrubland, boreal forest and mediterranean shrubland) is plotted against azimuth angle in Figure 4.

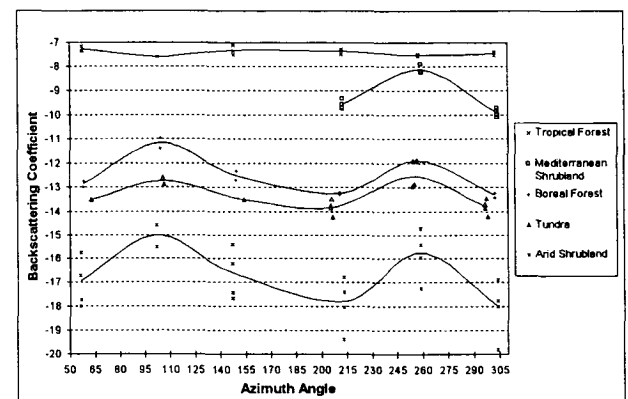


Figure 4: σ^0 against the azimuth angle for five ground cover types during March 1996.

Note that σ^0 has maxima around 101.7° and 258.5° and minima around 56.2°, 213° and 303.8° for all types except the tropical forest. The occurrence of these

maxima and minima might be related to the orientation of anisotropic features that exist in the tested areas. Some of the above angular values support the suggestion in Ref. 4 that they are caused by sand dunes oriented at about 40° from the North in arid regions.

This is because we get minimum σ^0 parallel to 56.2° and 213° and maximum σ^0 parallel to 101.7°, which is almost perpendicular to the 56.2° - 213° direction.

For the boreal forest, the site studied (south of Lake Athabasca in Canada) exhibits an oriented texture produced by sub-glacial landforms. The glacial lineation patterns to the south of the Lake were observed in Landsat images to have an orientation of ~55.6° (Ref. 2). This could explain the observed azimuth effects at this site. However, the occurrence of maxima and minima at similar angles for all cover types suggests a systematic bias.

6. CONCLUSIONS

A spatial interpolation algorithm was developed to construct images of radar backscatter by averaging WSC data over time. For a rectangular filter the spatial resolution degrades to about 87 – 88 km; this could be improved by using a different spatial filter. The different models used to normalize the effect of the incidence angle proved to be sensitive to the land cover type. Although some of models performed very well for certain land cover types, the overall average performance was not too good ($R^2 < 52\%$). This is due to the complicated nature of the backscattering problem, which involves many different scattering processes.

The total variability in the backscatter images was attributed to four components: noise-like effects, temporal change, spatial variation and incidence angle variability. Their contributions to total variability were on average: interference component (4.59% \equiv 0.2 dB), temporal variability (14% \equiv 0.6 dB), spatial variability (18.8% \equiv 0.8 dB), and incidence angle variability (37.7% \equiv 1.4 dB). It is recommended to use 15 day images to reduce temporal variability, and to limit the spatial averaging extent to a radius of 25 km to reduce the spatial variability. Most important is to use incidence angle models to reduce k_{pg} , as this constitutes the highest contribution.

Variability images, generated as a by-product of the global backscatter images, were used to identify regions of dynamic activity and system defects. The highest variability was found in deserts and attributed to the existence of sand dunes. High variability was also

found in the Great Plains of North America probably caused by agricultural practices, but further investigation is required to establish this. Changes in snow cover are likely to be the cause of high variabilities over other northern areas in North America during the early part of the year (April to June). Linear artefacts over Africa and Australia indicate malfunctioning of the WSC instrument and/or processing chain.

The backscatter from 14 vegetation types for 1995 shows behaviour which can be explained in terms of biophysical activity and weather patterns. Individual grid points indicate the existence of subclasses of behaviour within a given cover type. Further investigation is required to establish the reasons for such behaviour.

Azimuth angle effects were found to exist in almost all the tested ground cover types. Geophysical reasons for these azimuth patterns could include sand dunes in semi-arid regions and glacial lineation in the boreal forest in Canada and tundra in Alaska. However, the azimuth patterns have maximum and minimum backscatter at the same angles for four out of the five examined cover types, suggesting an origin in properties of the WSC system.

REFERENCES

1. Archibold, O. W., 1995, *Ecology of World Vegetation*, (London, UK: Chapman & Hall).
2. Clark, C. D., 1990, Remote Sensing Scales Related to the Frequency of Natural Variation: An Example From Paleo-Ice-Flow in Canada, *IEEE Trans. Geosci. and R. Sens.*, vol. 28 (4), pp. 503-508.
3. Frison, P.-L., and Mougin, E., 1996, Use of ERS-1 Wind Scatterometer Data Over Land Surfaces, *IEEE Trans. Geosci. and R. Sens.*, vol. 34 (2), pp. 550-560.
4. Frison, P.-L., and Mougin, E., 1996, Monitoring Global Vegetation Dynamics with ERS-1 Scatterometer Data. *Int. J. R. Sens.*, vol. 17 (16), pp. 3201-3218.
5. Ulaby, F. T., Moore, R. K., and Fung, A. K., 1982, *Microwave Remote Sensing: Active and Passive, Vol. II: Radar Remote Sensing and Surface Scattering and Emission Theory*, (Reading, Massachusetts: Addison-Wesley Publishing Company).

THE RETRIEVAL OF REGIONAL SCALE GEOPHYSICAL PARAMETERS IN SEMI-ARID AREAS USING DATA FROM THE ERS- WINDSCATTEROMETER

Iain H. Woodhouse* and Dirk H. Hoekman**

* Remote Sensing Group, University of Dundee, Dundee DD1 4HN, Scotland, UK.
Tel: +44-(0)1382 344933, Fax: +44-(0)1382 345415, i.h.woodhouse@dundee.ac.uk

** Department of Water Resources, Wageningen Agricultural University,
Nieuwe Kanaal 11, 6709 PA Wageningen, The Netherlands

ABSTRACT

The method presented applies a mixed target modelling approach to estimate sub-pixel fractional vegetation cover, and bare surface reflectivity (related to soil moisture) at a regional scale. The model represents the footprint area as a combination of part dense, homogeneous vegetation and part bare soil (with homogeneous roughness and dielectric properties). Inversion of this model is then carried out using a retrieval procedure that incorporates a priori information in a quantitative manner. The method is applied to the estimation of fractional cover and surface reflectivity over semi-arid areas in Africa (Niger, Nigeria). Through a comparison of retrieved values with in situ measurements and ancillary data some possible explanations are presented for the results observed.

The results illustrate the applicability of spaceborne scatterometer data for measuring geophysical parameters over land, and offers a physically based alternative to empirical indices for estimating regionally variable parameters.

Keywords: Scatterometer, ERS Windscatterometer, modelling, soil moisture, vegetation cover.

1. INTRODUCTION

An increasing number of studies have shown the applicability of low resolution space borne scatterometers for monitoring surface parameters over land and ice, in addition to their design function of measuring ocean wind fields (Refs. 1, 2) several studies have highlighted the relationship between the low resolution scatterometer data and surface geophysical parameters such as vegetation cover, surface roughness and surface soil moisture content (Refs. 3-6). While the nominal ground resolution of the data is coarse (≈ 50 km) the ability to provide global coverage within 4 days, regardless of local weather conditions or solar illumination, makes the WSC instrument ideally suited for meso-scale monitoring of global land surface characteristics.

In addition to qualitative observations of land cover processes is the ever-present need for suitable algorithms to retrieve quantitative estimates of geophysical parameters from remote sensing measurements suitable for inclusion into global climate models. Pixel and sub-pixel level inversion is possible using scatterometer data due to their high radiometric accuracy and range of measurement incidence angles. The purpose of this paper therefore is to describe the results of a simple mixed-target model that has been developed for investigating the potential of extracting geophysical products from scatterometer data. Through a comparison of retrieved values with ancillary data from the Hapex-Sahel project in Niger (e.g. in situ measurements and spaceborne remotely sensed data) and early results from sites in Spain, some possible explanations are presented for the results observed. The final results demonstrate the utility of meso-scale scatterometer data for monitoring and quantifying regional-scale surface characteristics.

2. THE ERS-1 WINDSCATTEROMETER

The ERS Wind Scatterometers are mounted on the ESA ERS-1 and 2 platforms, and were designed to obtain information on wind speed and direction over the sea surface. The instrument consists of 3 antennas producing 3 beams looking 45° forward, sideways and 45° backwards with respect to the satellite's orbit direction. These beams continuously illuminate a 500km wide swath as the satellite moves along its orbit.

Across the swath local incidence angles range from $18-47^\circ$ for the mid-beam and $25-59^\circ$ for the forward and aft beams, and 19 measurements are made across the swath. Thus three backscatter measurements at each grid point are obtained at three different viewing angles, and two different incidence angles.

The Wind Scatterometer has a spatial resolution of the order of 50km along and across track with a radiometric stability of <0.22 dB, and a localisation accuracy of better than 5km. The operating frequency is 5.3GHz (C-Band) with vertical transmit and receive (VV) polarisation. WSC measurements have been made nearly continuously since July 1991, although variations in the coverage do occur due to alterations in the orbital repeat cycle and operation of the SAR instrument.

3. BACKSCATTER MODEL

The backscattered signal from a scatterometer measurement cell may consist of contributions from a number of surface features. These include volume scattering from various types of vegetation of changing density and surface scattering from a variety of bare soil types and rock surfaces. Features such as open water and man-made structures, when present, will also contribute. For the present study, the resolution cell is represented by an equivalent surface consisting of a combination of only two surface types: dense, homogeneous vegetation (pure volume scattering) with a fractional surface area denoted by C , and bare soil with effective (homogeneous) roughness and dielectric properties (surface scattering). The total backscatter is therefore considered to be an incoherent sum of three backscattering mechanisms: these are (vegetation) volume scattering, surface scattering from the bare soil layer, and specular (double-bounce) reflection between the trunk and ground. In addition, a fourth term may be added which accounts for all other contributions not included in the first three. Since this term may include contributions from such features as highly specular surfaces, its overall effect may be considered to be a random term on the forward model.

Mathematically, the total backscattering cross-section σ^0 consists of a linear sum of those four contributions:

$$\sigma^0(\theta) = C\sigma_c^0(\theta) + (1-C)\sigma_{bare}^0(\theta) + \sigma_{double}^0(\theta) + \sigma_{others}^0(\theta) \quad (1)$$

where

θ : local incidence angle,

C : equivalent fractional vegetation cover,

σ_c^0 : contribution from equivalent vegetation

cover (volume scattering with $\sigma_c^0 / \cos^4\theta = const$),

and

$$\sigma_{bare}^0(\theta) = \frac{|R_g|^2}{2s^2 \cos^4\theta} \exp(-\tan^2\theta/2s^2) \quad (2),$$

where

R_g : Fresnel reflection coefficient at normal incidence,

s : RMS slope of the surface roughness,

$$\sigma_{double}^0 = TR_1R_2 \sin^2(\theta + 45^\circ) \quad (3),$$

where

T : scaling factor,

R_1 : Fresnel reflection coefficient of the local ground,

R_2 : Fresnel reflection coefficient of the trunk.

This model contains a maximum of 8 unknowns. With the assumption of mixed targets, no dependence on the azimuth look-angle has been foreseen, *i.e.*, no predominant terrain slope within a resolution cell is included in the model. Simplifying assumptions are made in the present study to reduce the number of unknowns:

a) σ_c^0 has been tuned to the respective geographical locations under investigation based on existing data;

b) both R_1 and R_2 have been estimated assuming a complex dielectric constant of $\epsilon = 10-j$;

c) σ_{others}^0 represents a random term (noise), hence not subject to inversion.

The remaining 4 unknowns are constrained during the inversion process as follows:

$0 \leq C \leq 1$, where $C = 1$ corresponds to a 100 % vegetation cover;

$0 \leq |R_g| \leq 1$, where a high value of $|R_g|$ corresponds to a high soil moisture content;

$0 \leq s$, where a higher value represents a high surface roughness;

$0 \leq T$, the double bounce term which allows for the existence of a local maximum of NRCS around 45° incidence angle.

4. PARAMETER INVERSIONS IN THE SAHEL

4.1 Spatial Variation of Retrieved Parameters

Figure 2 shows the results of applying the retrieval algorithm to the WSC data over the African test site for 4 months: May, July, September and December 1992. These months are representative of the range of conditions; *i.e.* dry May and December, and wet July and September with increased vegetation growth.

The figure shows sets of retrievals over the African test area, for percentage vegetation cover, reflectivity (scaled from 0.0 to 0.17), double bounce contribution (scaled from 0 to 43), and RMS slope (scaled from 0.0 to 0.6) for 4 months.

Retrieved reflectivity values are consistently lower than one would expect from a uniform target area. This is thought to be primarily a consequence of assuming that the measured signal originates entirely from the

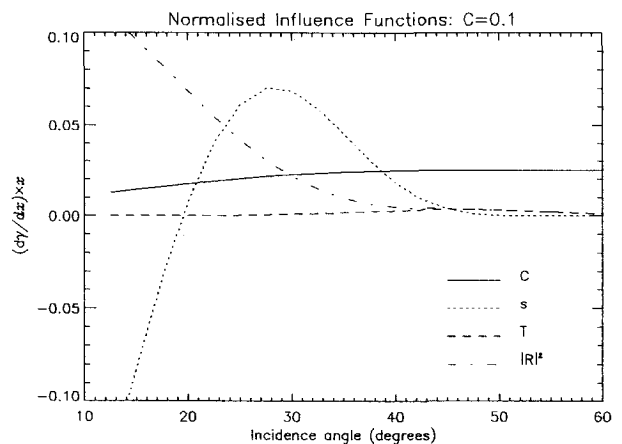


Figure 1: Influence functions showing the sensitivity of the modelled signal to relative changes in the magnitudes of the model parameters.

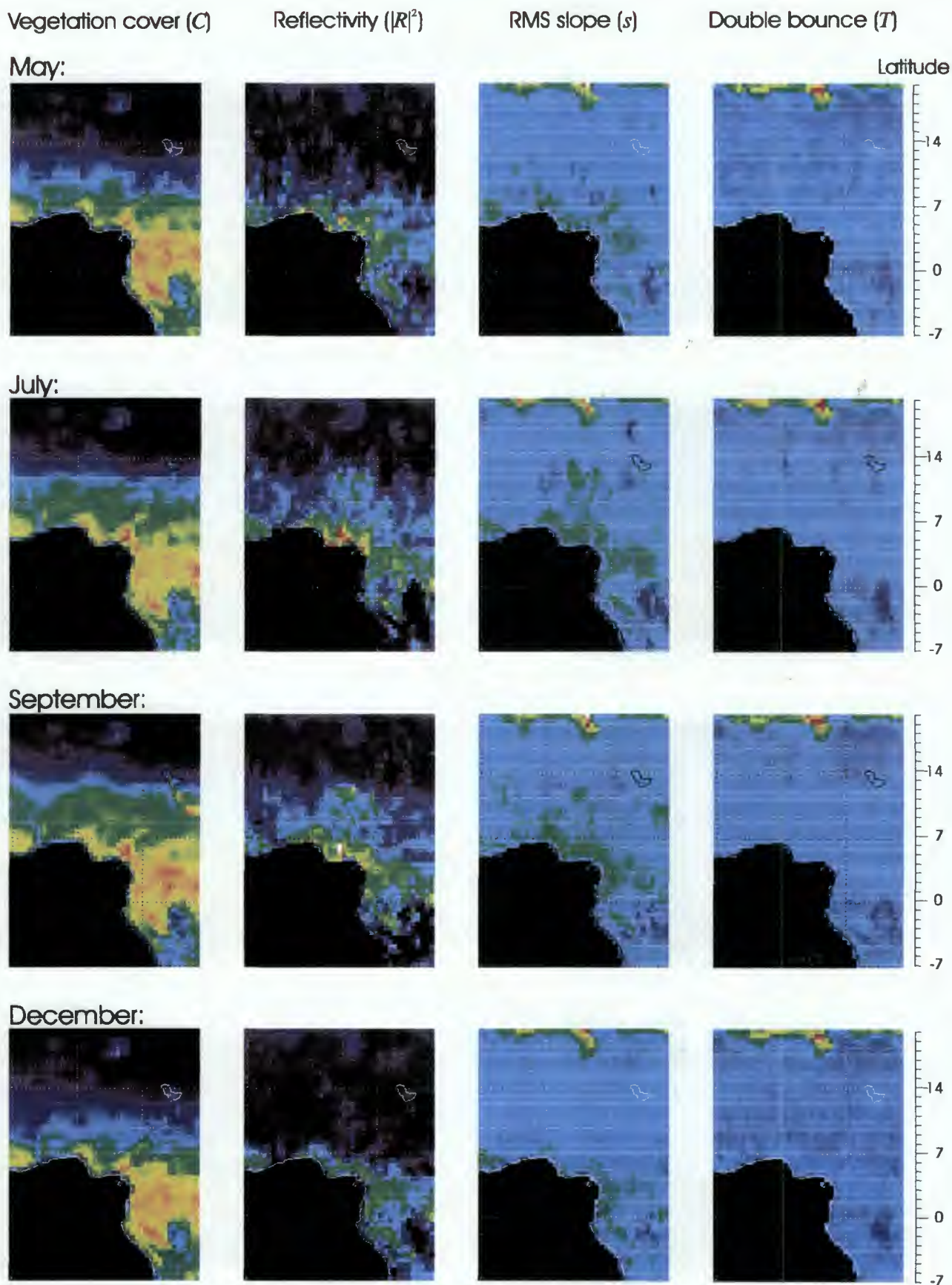


Figure 2: Retrieved parameters for four months in 1992 (half-degree gridding). May and December are representative of the dry season, with less vegetation cover in the Sahel. The wetter months of July and September show higher vegetation coverage and reflectivity.

fractional area (1-C) while in general the surface scattering will be dominated by scattering from smaller patches within this area. The final reflectivity estimate is therefore averaged over a larger area than the dominant signal source.

In general the retrievals follow the expected pattern with vegetation cover and reflectivity highest around the equator and in areas of known tropical forest, and drop to near zero in the desert regions. The seasonal variability also follows the expected pattern, with the September retrievals showing significantly more Sahelian vegetation coverage and reflectivity (related to

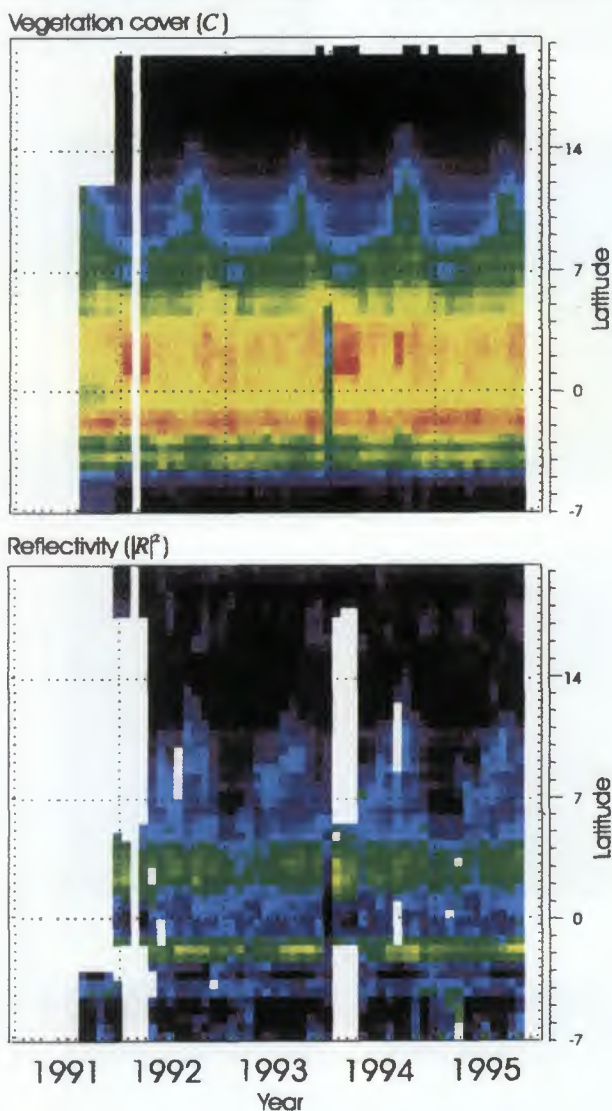


Figure 3: A Hovmoeller diagram of monthly retrieved vegetation cover (top) and reflectivity for a line of latitude through 12°E for the period 8/91 to 10/95. Note that the onset of the regrowth is preceded by an increase in the reflectivity, a consequence of the increased rainfall. (The sharp edge at 4.5°S is the coastline, below which is open water.)

soil moisture) than in the dry December month.

A further encouraging feature of the results is that there are many geographical features which are identifiable that were not present in the *a priori* data. The location of Lake Volta and the Niger Delta are very clear for instance, as are the Air Mountains in Niger. Perhaps the most striking feature is the appearance of high reflectivity retrievals during the wet months in the vicinity of Kano, situated in Nigeria to the west of Lake Chad, and close to the border with Niger. The exact cause of these high levels of reflectivity has yet to be identified, but this area does contain numerous wetlands and seasonally flooding rivers.

4.2 Vegetation Dynamics Over the Sahel

Backscatter characteristics in the semi-arid savannahs of the Sahel show a significant seasonal variation with annual differences of up to 4dB (Refs. 2, 4). During the dry season the soils exhibit very low backscatter characteristics, and vegetation cover is sparse, while in the wet season vegetation re-growth is widespread resulting in a significant increase in the backscatter characteristics. Such vegetation dynamics are apparent in Figure 2, and are further examined over a longer period of time in Figure 3 which shows a Hovmoeller diagram for a line of latitude through 12° East for the period 8/91 to 10/95, where each column represents retrieved parameters from one month of data. In this diagram the annual regrowth of the savannah vegetation is very clear, as is the inter-annual variation of the onset and extent of the summer growth. It is also apparent from this figure that the onset of the vegetation regrowth is preceded by an increase in the reflectivity, a consequence of the increased rainfall. This time delay of

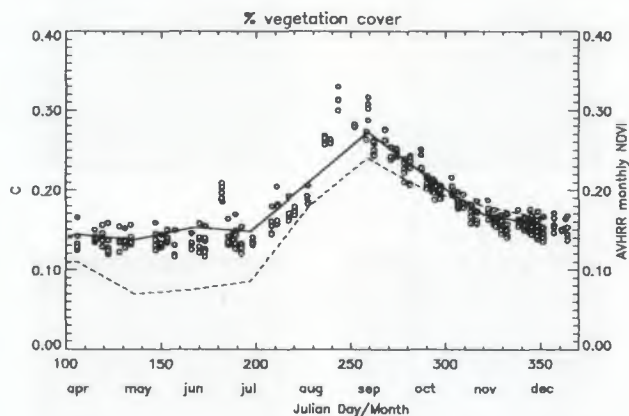


Figure 4: Correlation of NDVI (---) and retrieved vegetation cover (—) for Hapex-Sahel area. The retrieved vegetation cover for single passes are shown as circles with a tone proportional to the measurement latitude, with lighter points indicating a higher latitude. The retrieved values indicated that even within the test area there is a measurable variation in the vegetation coverage retrieved.

about 1–2 months between the start of the rainfall in the wet season and the subsequent regrowth is a common feature of semi-arid areas and is a consequence of the delay between the start of the seasonal rainfall and the vegetation re-growth (Refs. 7, 8).

A more detailed investigation of the seasonal trends within the Sahel, were made using monthly retrievals for the period April to December 1992. Figures 4 and 5 show the results of retrieving vegetation cover and reflectivity, and are compared against the monthly averaged NDVI for the West Central Supersite (Ref. 9) and total monthly precipitation for the area (Ref.10). The trends of both the retrieved parameters are clearly well correlated with the additional data.

5. RETRIEVAL OF PARAMETERS OVER SPAIN

Initial investigations have shown that the retrieval algorithm when applied to the Mediterranean region exhibits general trends in the vegetation cover that one would expect for the area. The seasonal variations were also qualitatively as expected. Testing of the algorithm for individual sites in Spain are currently under investigation.

6. SUMMARY

While the model described is simple and makes many assumptions about the surface characteristics under observation, it never-the-less retrieves realistic values of vegetation cover that compare favourably with other measurements, and exhibits temporal and spatial patterns compatible with data from other sources. Retrieved parameters of reflectivity, while having magnitudes much less than might be expected, do indicate relative temporal and spatial variations that are most likely related to surface soil moisture content.

Although the algorithm presented illustrates the applicability of WSC data for measuring geophysical parameters over land, and offers a physically based alternative to empirical indices for estimating regionally variable parameters with little or no ground truth, there are a number of systematic enhancements that can be made to the method. These include the inclusion of more precise *a priori* information that is location and season dependant, including site specific estimate of vegetation backscatter properties. This may include the analysis of ground data or high resolution SAR data, or through the synergistic use of optical/IR low-resolution data such as AVHRR. The forward model may also be enhanced through the inclusion of more target types (e.g. surface water, urban features), or through more rigorous modelling of the existing target types (e.g. inclusion of local relief effects).

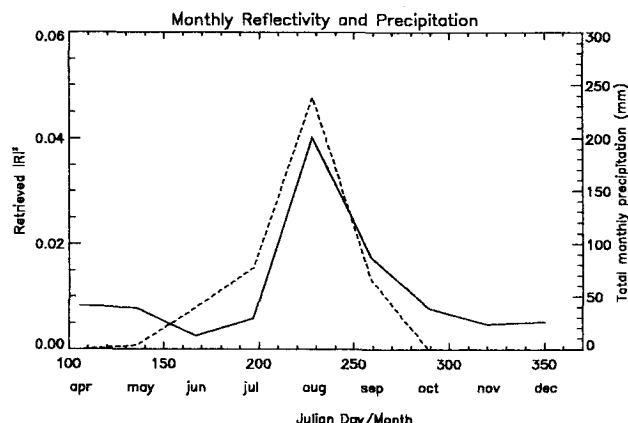
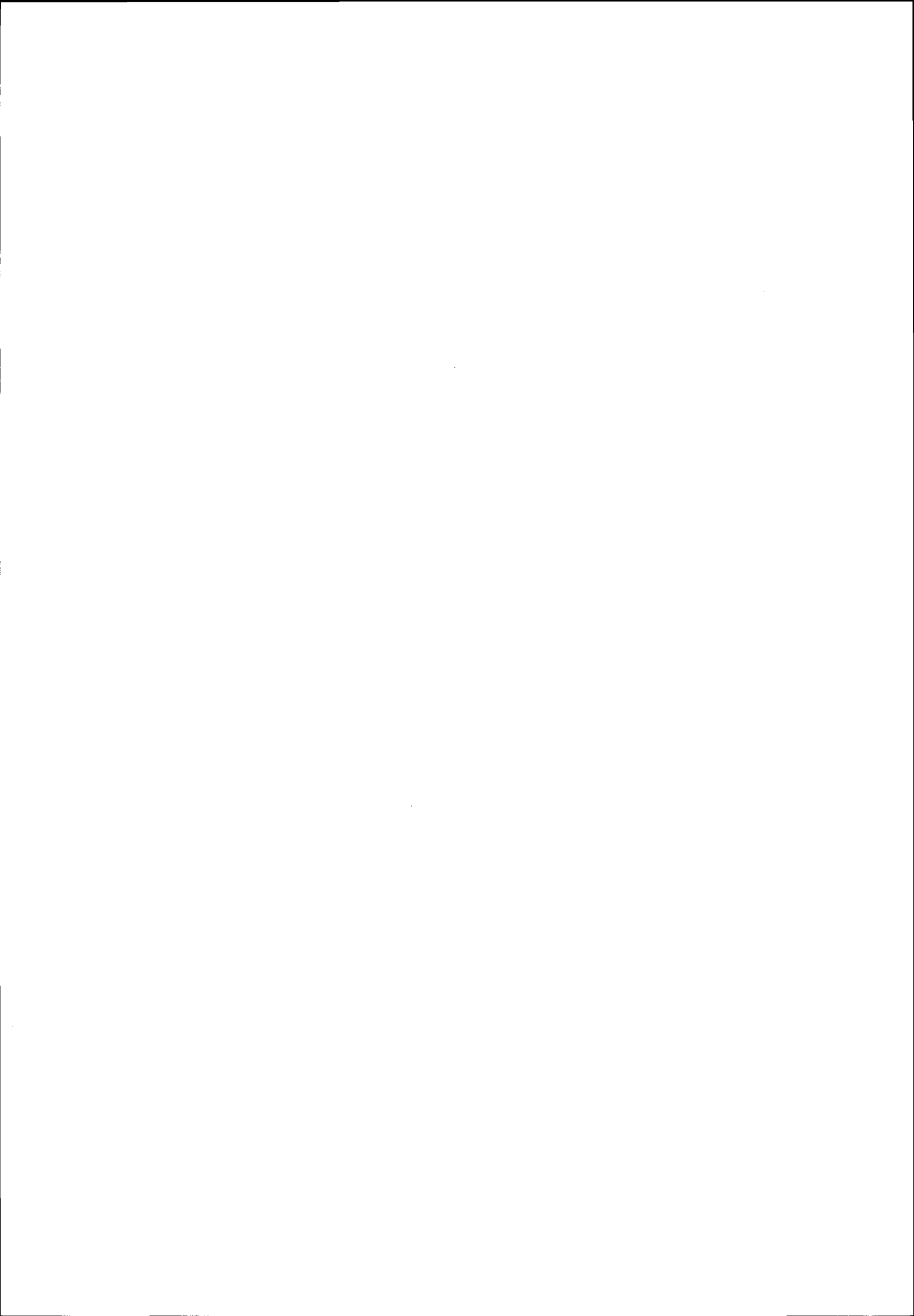


Figure 5: Monthly retrieved reflectivity (—) and total monthly rainfall (- - -) for 1992 in the Hapex-Sahel test area.

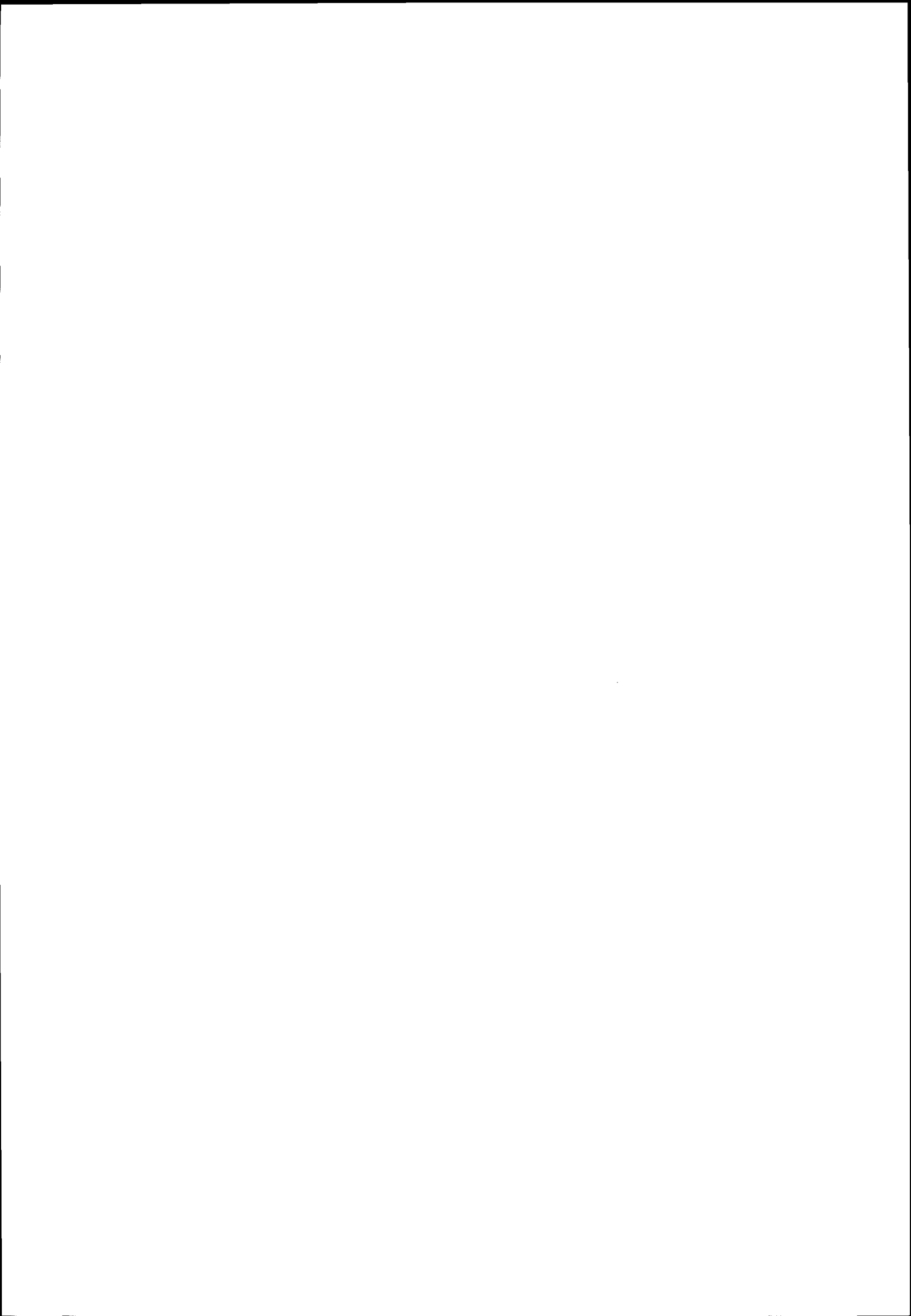
1. P.L. Frison & E. Mougin 1996. Use of ERS-1 wind scatterometer data over land surfaces. *IEEE Trans. on Geosci. Remote Sensing*, 34(2):550-560.
2. V. Wismann et al. *Land surface observations using the ERS-1 Windscatterometer*. Technical report, European Space Agency, 1996. Final report for ESA Contract No. 11103/94/NL/CN.
3. Y.H. Kerr & R.D. Magagi 1993. Use of ERS-1 Wind-Scatterometer data over land surfaces: arid and semi-arid lands. In *Proceedings of the Second ERS-1 Symposium - Space at the Service of Our Environment*, pp. 383-388, Hamburg, Germany. ESA.
4. V. Wismann, et al. 1995. Monitoring ecological dynamics in Africa with the ERS-1 Scatterometer. In *Proceedings of the International Geoscience and Remote Sensing Symposium: IGARSS'95*, pp.1523-1525, Firenze, Italy.
5. J. Pullianinen et al 1996. Land applications of ERS-1 Wind Scatterometer in Boreal forest zone. In *Proceedings of the International Geoscience and Remote Sensing Symposium: IGARSS'96*, pp. 583-585, Lincoln, Nebraska, USA. IEEE.
6. P.L. Frison et al 1998. Observations and interpretation of seasonal ERS-1 Wind Scatterometer data over Northern Sahel (Mali). *R. S. Env.*, 63:233-242.
7. S. Ringrose & W. Matheson 1991. A Landsat analysis of range conditions in the Botswana Kalahari drought. *Int. J. Remote Sensing*, 12(5):1023-1052.
8. V. Wismann et al 1996. *Land surface observations using the ERS-1 Windscatterometer: Part II*. Technical report, European Space Agency. Final report for ESA Contract No. 11103/94/NL/CN.
9. S.D. Prince et al. 1995. Geographical, biological and remote sensing aspects of the Hydrologic Atmospheric Pilot Experiment in the Sahel (HAPEX-Sahel). *R. S. Env.*, 51:215-234.
10. Y.H. Kerr et al 1995. *HAPEX Sahel Information System: CD-ROM 3 (Ground Data v3 08/95)*. Technical report, CESBIO, Medias-France, Orstom, CNES.



Snow & Ice Session

Chair: R. O. Ramseier, Microwave Group, Canada

Rapporteur: J. Johannessen, ESA/ESTEC



SNOW & ICE SESSION SUMMARY

Rapporteur: J.A. Johannessen

Highlight of results

Several years of NRCS time series (SASS, ERS Scat, Nscat) from Greenland and Antarctic ice sheets show:

- possibility to estimate snow accumulation rate from the reduction in NRCS imposed by dry snow accumulation;
- possibility to locate the percolation zone and its temporal variation;
- possibility to identify and locate ablation regions and their temporal variations.

Sigma-0 characteristics over Antarctica show large azimuthal dependence: anisotropy patterns correlate well with location and orientation of sastrugi (as developed in response to catabatic winds).

Simple snow layer model (for Greenland) which accounts for volume scattering and penetration depth effects show qualitative (and perhaps quantitative) agreement with observations.

Ice features can very well be tracked with scatterometer on a monthly time scale (outside the summer period). Motion estimates and trajectory paths compare well to similar estimates from passive microwave observations as well as to direct estimates from satellite tracked buoys.

An empirical C-band backscatter model for the Arctic Ocean works well when the amount of open water is small.

Relatively strong interannual variability in NRCS in Weddell Sea is possibly associated with flooding of the sea ice and meltwater ponds during summer.

Fundamental differences are encountered in the seasonal variability and characteristics of the radar backscatter for Arctic and Antarctic (flooding of sea ice by snow loading is common in Antarctic but not in the Arctic).

Tracking of icebergs larger than 180 km² reflect the impact of the Antarctic coastal current with a speed up to 20-25 cm/s. Area of retroreflection are also found in agreement with in situ observations.

Preparation to use scatterometer (plus optical and PMR) for operational sea ice monitoring and forecasting in the Norwegian-Greenland-Barents Seas and the Arctic Ocean is underway in regards to the ASCAT launch/ operation.

The best fit of scatterometer ice edge with the coincident SSM/I ice edge is found for the 50% isopleth.

Summary of Emerging Applications

The table below summarise the emerging applications into the following three categories: operational; pre-operational; and new but not mature enough.

	<i>SNOW AND ICE SHEET</i>	<i>SEA ICE</i>
OPERATIONAL		Sea ice flag indicator Sea ice extent and concentration monitoring
PRE-OPERATIONAL	Snow accumulation rate Location and temporal changes of the percolation zones Location and temporal changes of ablation zones	Sea ice feature motion estimation and drift trajectory determination Iceberg motion estimation and drift trajectory determination
NEW BUT NOT YET MATURE	Location and orientation of sastrugis	Iceberg calving rate Polynia monitoring Sea ice dynamics

Future Plans & Work

- With improved sampling rate and number of polarization and frequencies anticipated in the near future the analysis and interpretation for snow and ice application will improve further.
- With the availability of better DEM (from INSAR and/or radar altimeter) the utilization of NRCS for monitoring seasonal and interannual ice sheet changes can advance further. There is also a need to further investigate the altimeter waveform characteristics.
- Synergism between passive and active microwave sensors is highly promising and should be used systematically.
- Difference between NSCAT and ERS SCAT observations are mostly explained by the frequency shift (Ku-band versus C-band). However, due to antenna geometry differences there is also an impact of the shift on the retrieved NRCS which needs to be kept in mind (and eventually corrected for) in comparison analyses.
- Snow behavior on ice needs further studies. Onset of melt both for snow covered sea ice and ice sheet regions can be monitored on a regular basis.
- Old ice fraction estimates need to be improved.
- Influence of incidence angle will not be possible to examine from Quikscat.

Recommendations

- Long time series are needed. (50-year programme should emerge!!!)
- After Envisat commissioning a one-year tandem operation with ERS would allow for excellent intercomparison of ASAR and ERS SCAT. What would be ideal time separation?
- 25-km resolution product should be made available on regular basis.
- Data exchange/availability must be flexible and user friendly.
- SHEBA experiment and/or other should be used for provision of high quality in-situ data products.

The following new operational application and monitoring aspects need to be encouraged and implemented.

- Sea ice flag of the scatterometer data
- Ice sheet changes such as associated with snow accumulation and onset of melt
- Iceberg calving and drift estimates
- Sea ice feature tracking and motion estimates
- Polynia evolution
- Sea ice dynamics.

FROM RESEARCH WITH SYNERGISM TO OPERATIONS: SCATTEROMETER-PASSIVE MICROWAVE RADIOMETER APPLICATIONS TO SEA-ICE AND SNOW

René O. Ramseier and Caren Garrity

Microwave Group-Ottawa River, Inc., 3954 Armitage Ave., RR#1

Dunrobin, Ontario, K0A 1T0, Canada

Tel.: 613-832-0411; Fax.: 613-832-4166; E-mail: icedoctors@igs.net

ABSTRACT

We provide a review of passive microwave radiometry and scatterometry sensors flown on different space missions, as well as some important references relating surface measurements with scatterometry. The paper continues with three central themes; ice signatures, snow signatures and feature tracking, which are the basic elements of the papers submitted for this workshop on scatterometry applications. Suggestions are being made on future aspects involving multi-frequency as well as sensor synergism to optimize scatterometry and radiometry. We also compare the advantages of using passive microwave radiometers and scatterometers.

1. INTRODUCTION

Recent dramatic changes in weather conditions have made both the public and the media very sensitive to potential dangers facing future generations aboard our spaceship earth. The specific nature of the cryosphere, which is often perceived as the "weather kitchen" of our globe, remained very elusive until the advent of all-weather remote sensors. When the Russian satellite Cosmos 243 was launched in 1968, and four years later, when NASA's NIMBUS 5 Electrically Scanning Microwave Radiometer (ESMR) was put into orbit, the first 24-hour, all-weather, all-season global ice signatures became available. ESMR operated from 1972 to 1976 (Parkinson et al., 1987). Since December 1972, when the imaging sensor ESMR was launched, a number of satellites have continued with the passive microwave tradition (SMMR, SSM/I's) over the last 26 years. The SMMR (Scanning Multichannel Microwave Radiometer) operated from late 1978 until 1987 and provided a slight overlap with the first SSM/I (Special Sensor Microwave/Imager) (Gloersen et al., 1992). A succession of SSM/I's have operated since then and will continue into the foreseeable future (Kwok et al., 1998).

A combined space-borne radiometer/scatterometer flown on the Skylab missions between May, 1973 and February, 1974, did not yield any data when combined with ice-related surface experiments (Campbell et al., 1977; Pierson et al., 1978). It was the advent of the short-lived Seasat mission (June, 1978-October, 1978) that provided the first ice-related quantitative results

from active and passive microwave sensors (Carsey, 1985). Carsey (1985) studied the behavior of summer Arctic sea ice based on the microwave data obtained by the Seasat scatterometer system (SASS), radiometer the scanning multichannel microwave radiometer, and the synthetic aperture radar (SAR). The scatterometer provides essential information on the ice surface conditions, while the passive microwave radiometers give information on the ice concentration. Due to the wetness of the ice surface (snow) during the melt period the 37 GHz signal is virtually independent of the ice types present. The backscatter coefficient and brightness temperature of old ice become similar to first year ice and is controlled primarily by snow wetness and surface morphology. Depending on frequency, this event is delayed due to the longer wavelength of the scatterometer sensors. At some point during the summer the first year ice may have a higher backscatter coefficient reversing the effect during the cold period of the year. The overall time series behavior shows an increase in the backscatter transiting from a wet surface to a cold surface, while the 37 GHz radiometer shows the opposite trend in brightness temperature.

In July 1991 the European Space Agency (ESA) launched the first European remote-sensing satellite (ERS-1) that included a scatterometer in its suite of sensors. This effort, and the follow-up with ERS-2 in June, 1996, has provided further insight into the use of scatterometer data for cryogenic applications and prompted ESA's interest in the future for potential scatterometer applications.

It is not by accident that I have started with space-borne passive microwave radiometry. There are a number of reasons for this: First, we can learn much from 20 years of passive microwave experience. Secondly, the multi-frequency polarization approach has resulted in significant improvements to algorithms, e.g. ice concentration and ice type determination. Finally, sea-ice models have been generated which couple atmosphere, floating ice and the ocean (Harder, 1996) which today can be initiated with real time data generated by space-borne sensors. What we have learned is that no single sensor solves all the ice problems. It is encouraging to see that many authors look at the passive microwave radiometer and the scat-

terometer as complementary sensors. Unfortunately, the realities of life have so far prevented the incorporation of a passive microwave radiometer into a single space platform. Seasat in 1978 gave us a very successful short-lived window into the future, which has not yet been repeated, although the METOP program came very close!

2. OVERVIEW

2.1 Past Work

The introduction has already dealt with some of the historical aspects. It would be a mistake not to mention some of the early, ground-breaking scatterometer work done with surface-based and airborne sensors that provided the *raison d'être* for space-borne sensors. Rouse (1969), using a sensor developed by the Kansas group (Moore, 1966), was able to identify different sea-ice types. With the use of dual-polarized, and scatterometers operating at different frequencies. Parashar et al. (1974) were able to classify ice accurately in 85% of the cases tried, including old ice, first year ice, young ice and open water. An early airborne experiment with a 13.5 GHz dual-polarized scatterometer by Gray et al. (1977) was able to discriminate between old ice, thick first year and young ice, as well as the variation in backscatter at different incidence angles over sea-ice. Since the mid-seventies much more work has been done in scatterometry, primarily in support of future space sensors.

Since the launch of ERS-1, a limited number of papers have appeared in the open literature discussing scatterometry in combination with sea-ice and sea ice processes. The first group to explore the possibilities of mapping ice extent was IFREMER (*Institut Français de Recherche pour l'Exploitation de la Mer*). To retrieve wind fields in the vicinity of the ice edge, it became necessary to develop algorithms using the ERS-1 scatterometer, known as the active microwave instrument in wind mode (AMI-wind), rather than to use results from the SSM/I (Cavanie et al., 1993). (This is understandable since the real time access to SSM/I is still a problem today.) They make use of the fact that backscattering over the open ocean, by comparing the forward beam with the aft beam, is strongly anisotropic due to the surface winds, whereas over ice it is isotropic. Over consolidated sea ice, Drinkwater and Carsey (1991) have shown that the backscatter coefficient is a linear function of the incidence angle using results from SASS. Gohin and Cavanie (1994) and Ramseier et al. (1994) demonstrated that the slope of the backscatter coefficient and incidence angle depend on ice type. Gohin and Cavanie (1994), Ezraty et al. (1994), as well as Gohin (1995), use this property to map the backscatter coefficient σ^0 for a constant incidence angle of 40 degrees. In summary, the IFREMER Group has developed the definitive tools to map sea ice using the ERS-1 and 2 scatterometer data.

Navigation in ice-frequented waters has always been a challenge. Numerous obituaries have been written for early explorers who tried to reach destinations which were "blocked" by ice. Today the challenge is still there, but we now have several excellent tools at our disposal to reduce the risks of traveling through, under and over the ice. An initial attempt was made by Ramseier et al. (1994) to examine, along with the SSM/I ice data, the potential of using ERS-1 scatterometer data, in support of ice navigation. This attempt made use of surface measurements obtained with the German RV "Polarstern" during its winter cruise in the Weddell Sea, June-July 1992. Total ice concentration based on SSM/I data, the ice thickness as estimated visually from the ship's bridge, and the backscatter coefficient from the ERS-1 were compared with the ship's speed along a track from 61°S to 70°S. The correlation coefficients of ship speed with the individual parameters gave -0.94 for ice concentration, -0.92 for ice thickness and 0.29 for the backscatter. The poor correlation with the backscatter coefficient is because of the lack of ERS-1 scatterometer data due to the sharing of the sensor with the SAR mode. (This is a common problem, also experienced by the IFREMER Group.) It is certainly a subject worth pursuing since roughness of ice is directly related to ship performance, together with ice concentration for any given ice type. A combination of daily passive microwave data and scatterometer data could provide some indices that might prove useful for navigation.

Drinkwater et al. (1993) describe a novel approach to enhance the nominal 50-km resolution of the AMI-wind to approximately 14-km by using a new method of image reconstruction. This new technique effectively maps the Southern Ocean sea-ice cover on a weekly basis. The result is that it provides information on sea-ice features which might not be detected by the SSM/I. Assumptions, such as that the surface characteristics of sea-ice during the sampling interval of one week do not change, may limit the usefulness of the product depending upon its intended application. The technique complements the availability of SAR due to the lack of coverage and possible costs.

Scatterometry for mapping snow properties shows potential in the field of remote sensing of snow and ice. A retrieval algorithm for snow depth, developed by Chang et al. (1987) based on passive microwave data from snow over land, was applied to homogeneous snow covers on sea-ice in the Weddell Sea (Garrity, 1991). This resulted in an underestimation of snow depth due to free water in the snow cover. Passive microwave data uses the natural microwave emission from a medium that is dependent on the dielectric properties, and absorption losses. A snow cover increases absorption losses based on the amount of free water content, thus reducing the penetration depth of the medium. Calculating the penetration depth for the SSM/I frequency of 37 GHz

and a snow wetness of 4%, the penetration depth would be 0.4 cm at an incidence angle of 40 degrees. The penetration depth is dependent upon the wavelength of the sensor, so applying this example to 5 GHz increases the depth to 12 cm. This fact alone has great implications for mapping snow depth, melt, and surface features such as snow dunes and sastrugi.

Rott et al. (1993), using the AMI-wind, demonstrated that they could identify three parameters which characterize the firm of the Antarctic ice sheet. The mean intensity, the incidence angle gradient, and the azimuthal asymmetry of backscattering were related to spatial variations in the snow's metamorphic state of accumulation rate, temperature, and wind. Earlier measurements by Remy et al. (1992), using the Seasat SASS, are in accordance with the above findings. Based on the surface roughness caused by prevailing winds, that cause the formation of sastrugies, the backscatter coefficient is higher when perpendicular to the prevailing wind direction rather than parallel. In areas where the snow pack is strongly layered due to temperature gradient metamorphism, the backscatter coefficient is higher than in areas where a homogenous snow pack exists. Regions with high snow accumulation rates and void of inhomogeneities show a low backscatter coefficient.

2.2 Current Work and Workshop Overview

We would like to introduce three papers that appeared in 1998 in the literature to illustrate the combined approach of using different data sets as well as different satellite sensors. Gohin et al. (1998), in their paper "Evolution of the passive and active microwave signatures of a large sea-ice feature during its 2.5 year drift through the Arctic Ocean" were able to track a large sea-ice feature as it aged from second year to multi-year ice (fourth year). Besides tracking the feature with the AMI wind-derived backscatter coefficient and the SSM/I 37 GHz brightness temperature, they also tracked three points (P1-P3) associated with the feature shown in Figure 1. As the feature approaches the North Pole area it starts to become elongated, progressing in elongation as it reaches the Fram Strait. The points of interest are the ice signatures and the tracking algorithm used.

The second paper by Kwok et al. (1998) derived sea-ice motion from satellite passive microwave imagery and corroborated the results with SAR and buoy motion. They tracked the ice in the Arctic Ocean and Weddell Sea every three days, and daily in the Fram Strait and Baffin Bay. The surprising results showed that error for tracking ice using 25 km grid-sized 37 GHz brightness temperature was only 1 km larger than the 12.5 km grid-sized 85.5 GHz data. It is interesting to note that these measurements were only made during the nearly dry phase of the snow, that is, between October, 1992 and May, 1993. They found that the passive microwave motion gave a better agreement

with the SAR than the buoy motion. The particular point of interest here is the tracking algorithm.

The third paper Liu et al. (1998) used the NASA scatterometer (NSCAT), scatterometer and passive microwave data (SSM/I) to track sea-ice motion and compared the results with buoy data. They found that the NSCAT motion data coincided with the SSM/I and buoy data.

Workshop papers. The eight workshop papers fall into three categories: ice signature (4), snow signatures (3), and ice tracking (1), where one of the ice signature papers also includes tracking.

2.3 Microwave Sea-ice Signatures

Gohin et al. (1998) make a general observation that the evolution of the backscatter coefficient is in the opposite direction from the one for the brightness temperature since the emissivity $\epsilon=1-\Gamma$ (reflectivity) for a given wavelength and polarization. An area extending from the north side of the island Novosibirskiye Ostrova to the tracked feature at the point P3 in Figure 1 gave the highest backscatter coefficient. The explanation given by the IFREMER group is that the topography of the ice surface is rather rough, as the pack has likely been pushed and compressed due to the proximity of the coast. Figure 1 shows that the area is composed predominantly of first-year ice. In other words, deformed first-year ice can give a higher backscatter coefficient than multi-year ice. The tracked feature, embedded between P3 and P1, has a brightness temperature of a two-year old ice type as explained by the IFREMER group. Figure 5 in Gohin et al. (1998) shows the signature regime for the three periods. Given are the parameters σ^0 and 37V (K) with the standard deviations, as well as the spectral gradient ratio ($GR[37V/19V]=(Tb[37V]-Tb[19V])/(Tb[37V] + Tb[19V])$), which is being used to solve for the multi-year ice concentration in % (Steffen et al., 1992). Comparing the σ^0 with the 37 GHz data for the first two periods, 1992-93 and 1993-94 shows that the σ^0 is nearly constant, varying little with time, and decreasing only in the spring for the same reason as given below. This fact is not surprising since the AWI-wind operates at 5.3 GHz which means that the snow is transparent, while at 37 GHz the signal varies with time reflecting changes taking place within the snow cover. These changes are primarily associated with the amount of moisture in the snow, decreasing in late fall and increasing during the spring (Garrity, 1992). In a similar way the old ice fraction varies in the opposite direction when compared with the brightness temperature or the GR. The third period (1994-95) behaves in a different manner. As the authors point out the tracked feature is in the vicinity of the Fram Strait, where it is being elongated due to the higher velocity of the currents. During the cold period, as the old ice

diverges, new ice is being formed causing an increase in brightness temperature and a gradual decrease in σ^0 .

The overall result is that the old ice fraction derived from the NASA algorithm generates questionable fractions. This conclusion is also reached by Gohin et al. (1998), who showed that the tracked feature initially did not diverge based on shape and backscatter values, consequently the overlying snow is responsible for the changes in brightness temperature.

2.4 Ice Tracking

By recognizing common ice features in sequential satellite imagery it is possible to track them for displacement measurements. The observed motion depends on the resolution of the imagery. Kwok et al. (1998) applied this technique to passive microwave radiometry which originally was developed for SAR imagery (Fily and Rothrock, 1987; Kwok et al., 1990). The method requires the determination of spatial offsets from two passive microwave images separated in time to determine a maximized cross-correlation coefficient of the brightness temperature field. In the first step, the peak of the sampled surface is derived from the nominal resolution, while the second step uses the oversampling to refine the location of the feature. This is then repeated for all other features in the imagery. To further refine the results, filters are applied to remove outliers as well as conditions on the difference (<10%) in the mean brightness temperature of both features. The difference assists in the removal of features contaminated by atmospheric effects. The sampling intervals are performed over one to three days depending on the expected motion of the ice. This technique is not applicable during the summer from the time of onset of melt in the spring to the freeze in the fall, typically June-September. The sharp increase in brightness temperature is primarily a result of the increased moisture in the snow (e.g. 0-3%, Garrity, 1992). Atmospheric effects on the 85 GHz channels are often concentrated within the marginal ice zone, and often can be neglected within the high ice concentration areas (Lubin et al. 1997).

The advantage of the 37 GHz channels over the 85 GHz channels is that they are much less influenced by the atmosphere. Three-day ice motion pictures of the Arctic Ocean using the 85-GHz passive microwave data on a grid spacing of 80 km provided motion vectors in all areas, including slow moving first-year ice in coastal areas. In areas where the motion vectors are higher, such as in the Greenland and Weddell Seas, vectors can be generated on a daily basis. A comparison of the passive microwave motion vectors with the SAR motion vectors showed a better agreement with the SAR motion than with the buoy motion vectors. A buoy measurement is associated with a particular ice floe in contrast to the SAR and SSM/I derived ice-feature motion that is an average of a large area.

Liu et al. (1998) have employed a similar tracking method as Kwok et al. (1998) to the NSCAT 13.9-GHz backscatter data. They derived daily sea-ice drift information using wavelet analysis for features at a scale of 50-100 km. Comparison of NSCAT with SSM/I 85 GHz derived motion vectors provide good quantitative agreement as well when compared with buoy motion data. There are areas where the NSCAT data produced no motion vectors when compared with the SSM/I. These areas are primarily located in the coastal areas where first-year ice is predominant and where ice motion shows small displacements when compared with the sensor resolution.

Gohin et al. (1998) used a similar approach as Fily and Rothrock (1987) to obtain a first-guess ice displacement field. The second step takes into account the stability of the σ^0 in time. The procedure is much more involved and is well described by the IFREMER group. Using this method they tracked a multi-year ice feature over an eight-week interval. The ice displacements were merged with the corresponding buoy displacements for three years during the "winter" months from October to May.

2.5 Snow cover

The mapping of snow cover accumulation over continental ice shows some promise with the use of AMI-wind. If the snow is wet, only a portion of the depth is seen, depending on the distribution of the free water within the snow cover. Due to the lower frequency of the ERS-1/2, compared with the SSM/I, the snow can be monitored further into the melt-season. There are three papers using scatterometer satellite data to monitor snow over land: 1) snow accumulation on Greenland, and 2) the directional anisotropy backscatter over the East Antarctic snow cover as well as 3) observed changes on the Greenland and Antarctic ice sheets. There are no papers presented that discuss snow accumulation over sea-ice related to scatterometer data. This may be due to the sea-ice roughness causing an isotropic background. However, since the snow cover depth on sea-ice ranges from zero to generally one meter, the scatterometer potentially would sense the snow cover and sea-ice interface during the melt-season.

The first paper by Wismann (proceeding) illustrates the use of NSCAT and ERS-1/2 scatterometer data to map the radar backscatter from dry-snow accumulated on firn. The contrast between dry snow and the percolation zone provides a medium with two layers that is modeled. It would be interesting if the 2-layer radar backscatter model using 5.3 and 14 GHz could be compared with the SMMR brightness temperatures at 6 and 19 GHz for mapping snow accumulation. The higher frequencies of the SSM/I have shown a decrease in brightness temperature as the snow depth increases on sea-ice using 90 GHz (Comiso et al.,

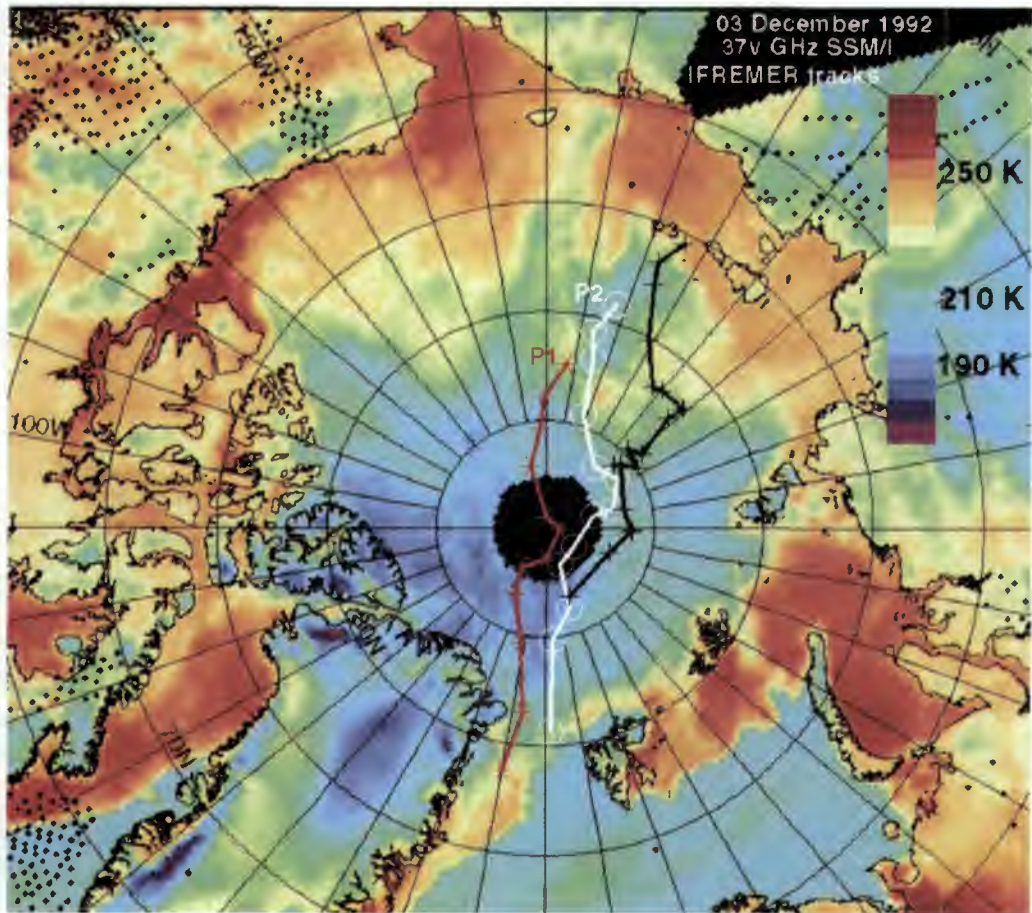


Figure 1. SSM/I passive microwave brightness temperature image at 37 GHz, vertical polarization, of 3 December 1992 showing the Arctic Ocean and adjacent waters. The points P1, P2, and P3 denote the starting position of the tracks across the Arctic Ocean as determined by (Gohin et al., 1998). P3 is located the edge of the transition between first year ice and old ice (second year). The area between P1 and P3 denotes the tracked second year ice feature. The numbers next to the brightness temperature scale from the top down denote in general first-year ice, second year ice and multi-year ice respectively.

1989), and a stronger relationship at 19 and 37 GHz (Garrity, 1991). These higher frequencies are strongly influenced by the amount of free water in the snow cover (Garrity, 1992), causing an error in the empirical relationship with the on-set snow depth.

Drinkwater and Long's (proceeding) paper shows an 18-year span in location and extent of a dry-snow zone using the NASA Seasat, ERS-1/2 and NSCAT scatterometers. Reductions in dry snow extend since 1978 from Greenland indicates an increase in summer melting. The onset of melt may also be earlier, resulting in a longer melt season. Using the changes in backscatter, surface properties of the snow cover provide information on wind fields for the East Antarctic. In the third paper, Young and Hyland (proceeding) present differences in ERS-1/2 C-band and ku-band NSCAT as they related to snow properties.

3. Discussion and Conclusions

Examining the ice signatures derived from the scatterometer data (Gohin et al., 1998) leave a number of questions open. It is not at all clear what kind of errors are introduced by neglecting the backscatter slope dependence on ice types. The backscatter alone can not be used to classify old ice, since backscatter coefficients of rough first-year ice also give high σ^0 . In tracking ice the time interval chosen is critical since a weekly average might miss important dynamic events (Liu et al., 1998). Variation in the methods used for tracking ice also provide different results. The method used by Liu et al. (1998) for NSCAT provides motion vectors for both old ice and first-year ice regions. On the other hand, the motion vectors derived from either 85 or 37-GHz channels (Kwok et al. 1998) provided good coverage for all ice types -- even better than the data originating from buoys. Some advantage could perhaps be gained by the use of the AWI-wind scatterometer. Its lower frequency would provide information on features extending somewhat into the melt period and perhaps earlier in the freeze period. In other words, the summer window (melt phase) could potentially be shortened when compared with the passive microwave channels which are much more sensitive to the moisture content of surface snow on sea-ice (Garrity, 1991).

When comparing products generated from the passive microwave data with those of the AMI-wind results one is struck by their remarkable similarities. This, however, should not come as a surprise since the emissivity is equal to one minus the reflectivity, reflectivity being a function of the backscatter. Differences noted above are primarily due to the larger wavelength of the AMI-wind. Tracking the ice edge poses greater difficulties with the scatterometer than with the passive microwave radiometer, particularly if the ice edge is diffuse. Tracking of features on both old ice and first-year ice seem to provide slightly better results with the SSM/I than the AMI-wind. This can be explained in

part by the better resolution of the 85-GHz channel on the SSM/I. At present, neither sensor provide tracking capabilities during the melt period, although some windows of opportunity do occur (Garrity, 1991).

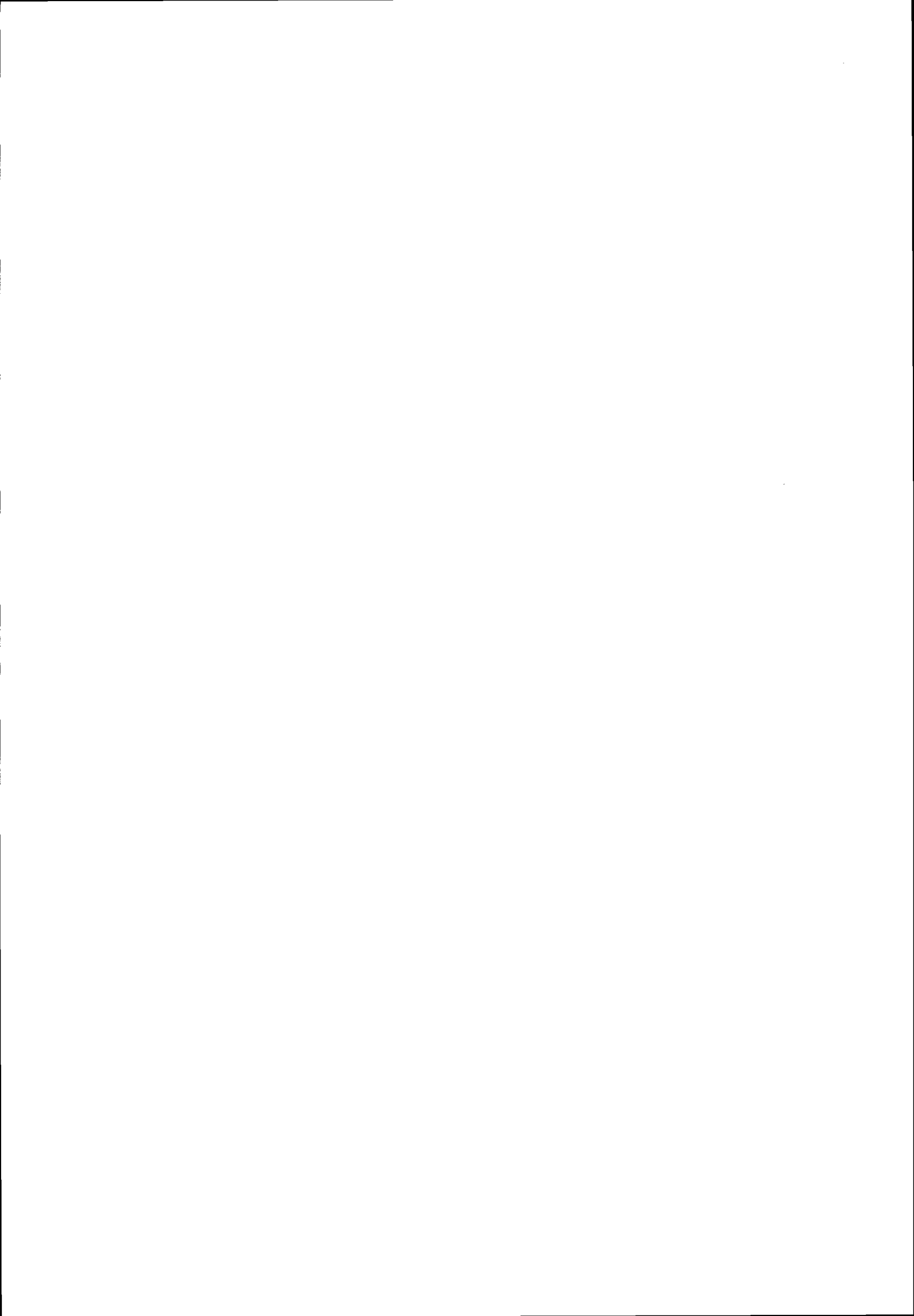
The identification of rough ice might be by itself independent of ice type, and could provide a parameter for ship transiting (Ramseier et al., 1994). Similarly, slush at the snow-ice interface, covered by dry snow, could also be mapped and incorporated as a parameter in support of navigation. The snow work on the continental ice sheets, as well as the shelf ice as related to the overlying snow, seem to provide more tangible results at the present time.

Finally, all this leads us to several future considerations, such as the compatibility of the two sensors, the potential synergistic benefits, and the possibility of having both types of sensors operating from the same platform.

References

- Carsey, F.D., Summer Arctic sea ice character from satellite microwave data, *J. Geophys. Res.*, 90(C3), 5015-5034, 1985.
- Cavanié, A., F. Gohin, Y. Quilfen, and P. Lecomte, Identification of sea ice zones using the AMI-wind: Physical bases and applications to the FDP and CER-SAT processing chains, Proc. Second ERS-1 Symp. ESA Spec. Pub. SP-361, 1994.
- Chang, A.T.C., J.L. Foster, and D.K. Hall, Microwave snow signatures (1.5mm to 3 cm) over Alaska, *Cold Regions Science and Technology*, 13, 153-160, 1987.
- Campbell, W.C., R.O. Ramseier, R.J. Weaver, and W.F. Weeks, Skylab floating ice experiment, Miscellaneous Spec. Pub. No. 34, Dept. Fisheries and Environment, Ottawa, 1-37, 1977.
- Comiso, J.C., T.C. Grenfell, D.L. Bell, M.A. Lange, and S.F. Ackley, Passive microwave in situ observations of winter Weddell sea ice, *J. Geophys. Res.*, 94(8), 10891-10905, 1989.
- Drinkwater, M.R., D.G. Long, and D.S. Early, Enhanced-resolution ERS-1 scatterometer imaging of Southern Ocean sea ice, *ESA J.*, 17, 307-322, 1993.
- Drinkwater, M.R., and F. Carsey, Observation of the late summer to fall sea ice transition with the 14.6 GHz Seasat scatterometer, Proc. IGARSS'91, vol. 3, 1597-1600, 1991.
- Ezraty, R., F. Gohin, and A. Cavanié, Arctic sea ice during the winter to summer transition as seen by the AMI-Wind and ATSR/M of ERS-1, *EARSel Adv. Remote Sens.*, GE-25(5), 570-580, 1994.

- Fily, M., and D.A. Rothrock, Sea ice tracking by nested correlations, *IEEE Trans. Geosci. Sens.*, GE-25(5), 570-580, 1987.
- Garrity, C., Characterization of snow on floating ice and case studies of brightness temperature changes during the onset of melt, in *Microwave Remote Sensing of Sea Ice*, *Geophys. Monogr. Ser.*, vol. 68, edited by F.D. Carsey, pp.313-328, AGU, Washington, D.C., 1992.
- Garrity, C., Passive microwave remote sensing of snow covered floating ice during spring conditions in the Arctic and Antarctic, PhD dissertation, Graduate Program in Earth and Space Science, York University, North York, Canada, pp.348, September 1991.
- Gloersen, P., W.J. Campbell, D.J. Cavalieri, J.C. Comiso, C.L. Parkinson and H.J. Zwally, Arctic and Antarctic sea ice, 1978-1987: Satellite passive microwave observations and analysis, *NASA Spec. SP-511*, 1992.
- Gohin, F., Some active and passive microwave signatures of Antarctica sea ice from mid-winter to spring 1991, *Int. J. Remote Sens.*, 16, 2031-2054, 1995.
- Gohin, F. and A. Cavanié, A first try at identification of sea ice using the three beam scatterometer of ERS-1, *Int. J. Remote Sens.*, 15, 1221-1228, 1994.
- Gohin, F., A. Cavanié, and R. Ezraty, Evolution of the passive and active microwave signatures of a large sea ice feature during its 2½-year drift through the Arctic Ocean, *J. Geophys. Res.*, 103(C4), 8177-8189, 1998.
- Gray, A.L., R.O. Ramseier, and W.J. Campbell, Scatterometer and SLAR results obtained over Arctic sea ice and their relevance to the problems of Arctic ice reconnaissance, *Proc. Fourth Canadian Symp. on Remote Sensing*, 424-443, 1977.
- Harder, M., Dynamics, roughness, and age of Arctic sea ice - Numerical investigations with a large-scale model, *Reports on Polar Research*, Alfred Wegener Institute for Polar and Marine Research, 203, 1996.
- Kwok, R., J.C. Curlander, R. McConnell, and S. Pang, An ice motion tracking system at the Alaska SAR facility, *IEEE J. Oceanic Engineering*, 15(1), 44-54, 1990.
- Kwok, R., A. Schweiger, D.A. Rothrock, S. Pang, and C. Kottmeier, Sea ice motion from satellite passive microwave imagery assessed with ERS SAR and buoy motions, *J. Geophys. Res.*, 103(C4), 8191-8214, 1998.
- Liu, A.K., Zhao, Y., and T. Liu, Sea-ice motion derived from satellite agrees with buoy observations, *EOS*, 79, (30), 353, 1998.
- Lubin, D., C. Garrity, R.O. Ramseier, and B. Whritner, Total sea ice concentration retrieval from the SSM/I 85.5 GHz channels during the Arctic summer, *Remote Sens. Environ.*, 62, 63-76, 1997.
- Moore, R.K., Radar scatterometry-An active remote sensing tool, *Proc. Fourth Symp. on Remote Sensing of Environment*, Univ. of Michigan, Ann Arbor, 339-373, 1966.
- Parashar, S.K., A.W. Biggs, A.K. Fung, and R.K. Moore, Investigation of radar discrimination of sea ice, *Proc. Ninth Int. Symp. on Remote Sensing of Environment*, Univ. of Michigan, Ann Arbor, 323-332, 1974.
- Parkinson, C.L., J.C. Comiso, H.J. Zwally, D.J. Cavalieri, P. Gloersen and W.J. Campbell, Arctic sea ice, 1973-1976: Satellite passive-microwave observations, *NASA Spec. Pub. SP-489*, 1987.
- Pierson, W.J., W.E. Marlatt, Z.H. Byrns, and W.R. Johnson, Oceans and atmosphere in: *NASA Lyndon B. Johnson Space Center, Skylab EREP investigation summary*, *NASA Spec. Pub. SP-399*, 189-256, 1978.
- Ramseier, R.O., I. Arnon, R. Ezraty, C. Garrity, F. Gohin, and K. Strübing, The potential role of ERS-1 scatterometer data in support of ice navigation, *Proc. First ERS-1 Pilot Project Workshop*, *ESA Spec. Pub. SP-365*, 169-174, 1994.
- Remy, F., M. Ledroit and J.F. Minster, Katabatic wind intensity over Antarctica derived from scatterometer data, *Geophys. Res. Letters*, 19(10), 1021-1024, 1992.
- Rott, H., H. Miller, K. Sturm, and w. Rack, Application of ERS-1 SAR and scatterometer data for studies of the Antarctic ice sheet, *Proc. Second ERS-1 Symposium*, *ESA SP-361*, 1994.
- Rouse, J.W., jr, Arctic ice type identification by radar, *Proc. IEEE*, 57, 605-614, 1969.
- Steffen, K., J. Key, J. Cavalieri, J. Comiso, P. Gloersen, K. St. Germain, and I. Rubenstein, The estimation of geophysical parameters using passive microwave algorithms, in *Microwave Remote Sensing of Sea Ice*, *Geophys. Monogr. Ser.*, vol. 68, edited by F.D. Carsey, pp.201-231, AGU, Washington, D.C., 1992.



SNOW ACCUMULATION ON GREENLAND DERIVED FROM NSCAT AND ERS SCATTEROMETER DATA

Volkmar Wismann

Institute for Applied Remote Sensing, Klarastraße 81, 79106 Freiburg, Germany
T: +49-(0)761-2851717; F: +49-(0)761-2851719; E: wismann@ifars.de

ABSTRACT

Radar cross section measurements over Greenland by the scatterometers of the European ERS-1 and ERS-2 as well as by the Japanese ADEOS satellite have been analysed. For large areas of Greenland, especially in the transition region between the percolation and dry-snow zone, an almost linear decrease in normalized radar cross section was observed being up to 0.75 dB/year and 1.7 dB/year for C-band and K_u -band, respectively. This reduction can be attributed to increasing attenuation of the radar backscatter due to dry-snow accumulation on the firm of the percolation zone. A 2-layer radar backscatter model accounting for the measurement parameters of the ERS and NSCAT scatterometers and considering a firn layer buried by dry-snow was used to estimate the thickness of the dry-snow layer and to derive a snow accumulation rate. The spatial pattern and absolute values of accumulation rates so inferred agree well with recent synthesis of ground-based observations.

INTRODUCTION

Spaceborne scatterometers are active microwave instruments for measuring the normalized radar cross section (NRCS) of the Earth surface. These measurements are independent of cloud coverage and illumination by the sun and provide a global coverage within 3 to 4 days. Thus they are well suited for a wide range of operational monitoring tasks.

The first spaceborne scatterometer was operated during the American Skylab mission in 1973 and 1974, demonstrating the feasibility of spaceborne scatterometers. Between June and October 1978, the American SEASAT-A Satellite Scatterometer (SASS) proved that accurate wind field measurements could be made over the oceans from space. Since August 1991 the scatterometers aboard the European ERS satellites (ERS-1 and ERS-2) measure operationally the normalised radar cross section (NRCS) of the Earth's surface at C-Band (5.3 GHz) and VV-polarisation ESA, 1992). During its short lifetime between August 1996 and June 1997 the Japanese ADEOS satellite provided the same type of measurements with the NSCAT system but for K_u -Band (14 GHz) at horizontal (HH) and vertical (VV) polarisation.

Presently, the scatterometer is exclusively dedicated to the determination of the wind speed and direction over

the oceans. It is increasingly acknowledged that, despite the coarse resolution, also a variety of geophysical parameters can be measured and monitored over land surfaces and sea ice, for details it is referred to the overview paper by Wismann (this issue).

The excellent calibration and maintenance of the ERS instruments guarantee high quality data, which, for the first time, allow a precise evaluation of the spatial and especially the temporal variability of the NRCS of the Earth's surface. Figure 1 depicts a time series of the C-Band NRCS for a location on Greenland. The measured *seasonal variability* of 0.3 dB indicates the accuracy of the instrument while the overall temporal stability reflects the excellent calibration and maintenance of both scatterometers. It is noteworthy that there was a switchover from ERS-1 to ERS-2 in May 1996, which is not visible in the data.

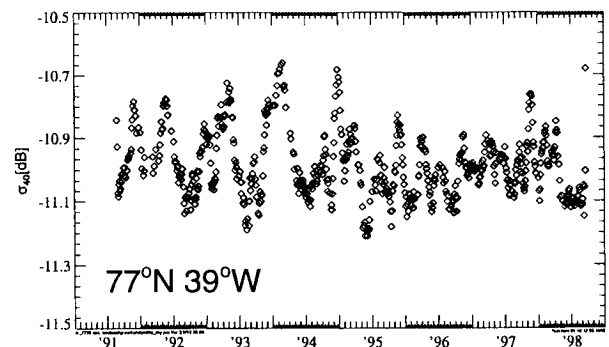


Figure 1: Time series of the C-Band NRCS at 77°N; 39°W on Greenland.

MONITORING SNOW PROPERTIES ON GREENLAND

Greenland's snow and ice surface can be divided into four shell-like zones: the central dry snow zone at high altitudes is surrounded by the percolation zone, the wet-snow zone, and the ablation zone. These facies result from different diagenesis of the snow and ice cover which is determined by the amount of snow-accumulation and melt and, therefore, on the local climate at the respective elevation (Benson, 1962). A large lateral shift of the borderlines between the different snow and ice facies will result even from a

slight climate change due to the very gentle slope of the ice shield. Therefore, monitoring these borders can provide information on climate change. The capability of discriminating different snow and ice facies by radar remote sensing was shown for the C-band SAR of ERS by Fahnstock et al. (1993) and for the SEASAT K_u -band and the ERS C-band scatterometers by Long and Drinkwater (1994a, 1994b).

RADAR BACKSCATTER DATA

In this analysis ERS and ADEOS radar backscatter measurements over Greenland were used which have been obtained from August 1991 to September 1998 and from September 1996 to June 1997, respectively. These data were re-sampled to a grid with a resolution of 0.5° in latitude and 1° in longitude which approximately corresponds to the spatial resolution of the ERS scatterometer. For 3-day intervals average radar cross sections (σ_{40}) were computed for each grid point by linear regression between the measured NRCS and their respective incidence angles. σ_{40} is the value of the regression line at 40° incidence angle.

Two typical time series plots of σ_{40} are depicted in Figure 2 and Figure 3 for locations in the percolation zone and further towards the dry-snow zone, respectively. The dominating signal is an almost linear decrease in radar cross section. In July 1995 and July 1997 this decline in radar cross section was interrupted when the summer melting of snow reached far uphill and the dry-snow pack was transformed into firn by a melt-related metamorphism (Wismann et al., 1996b; Wismann and Boehnke, 1997). These episodes lasted less than two weeks before σ_{40} again, tends to decrease similarly.

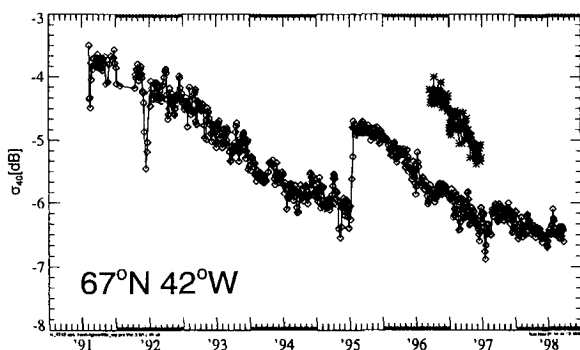


Figure 2 : Time series of σ_{40} at 67°N ; 42°W , diamonds and stars represent ERS C-Band (AMI) and ADEOS K_u -Band (NSCAT) data, respectively.

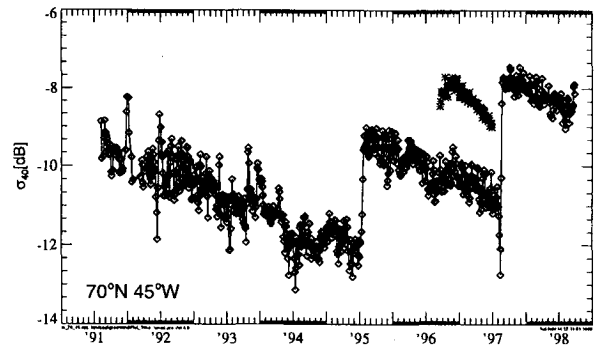


Figure 3 : Same as Figure 2 but for σ_{40} at 70°N ; 45°W .

NRCS MODELING

The model describing the decreasing radar backscatter at the dry-snow/percolation zone boundary is based on the following physical picture: During 1991-1995, the boundary of the dry-snow zone evidently moved downslope from its previous location. Thus ice layers and pipes in the percolation zone (which cause strong backscattering) were progressively buried under several years accumulation of dry-snow.

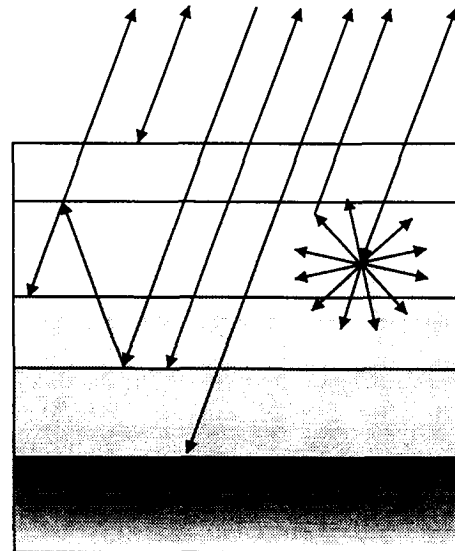


Figure 4 : Schematic of the 2-layer model, showing the layered dry snow on top of firn snow.

Dry-snow overlying the percolation zone structure diminishes backscattering by means of at least two mechanisms. First, scattering depends on the dielectric contrast between ice structures and the surrounding snow. The ice structures are incompressible but the snow densifies as being buried, reducing this contrast. Quantitative modeling shows, however, that this effect is likely to be small. Second, propagation through the dry-snow layer to and from ice structures of the firn layer is effectively attenuated by absorption in the snow, by scattering within the dry-snow layer, and by reflection

away from the ice structures of the firm as well as from the radar at internal density layer interfaces (West, et al., 1996). Interface reflection, in particular, leads to significantly greater effective attenuation than would otherwise be expected. A schematic of the model is depicted in Figure 4, while Figure 5 shows results from the respective radar backscattering fading model that accounts for effective attenuation due to absorption, scattering and layering. The model parameters include radar frequency, polarisation, and incidence angle (5.3 GHz, VV-polarisation, and 40 degrees for ERS and 14 GHz, VV and HH polarisation for ADEOS), together with parameters in an idealized physical model of layered dry-snow overlying the percolation zone ice structure. The overlying snow is modeled as a stack of discrete, planar layers of randomly varying thickness and density. The average density of the overlying snow is set, for this calculation, to 400 kg/m^3 , independent of depth. The effective permittivity of each layer is governed by its density and a size distribution of snow particles (i.e. ice, idealized as spherical). The size-distribution is log-normal with a 1 mm mean particle diameter and a logarithmic variance of 1.4. Layer density is assumed to follow a Gaussian distribution (with independence of distinct layers) and layer thickness is assumed to be exponentially distributed. The density variance is set by reference to ground-based Antarctic observations (West et al., 1996); typical layer densities vary from approximately 250 to 500 kg/m^3 . The mean layer thickness varies depending on the snow accumulation rate; typical values include 3 and 6 cm.

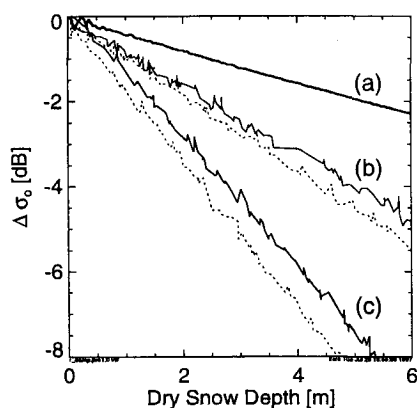


Figure 5 : Reduction of σ_{40} of firm as a function of the thickness of a covering dry-snow layer. For C-band and 1 mm grain size (a), and K_u -Band with grain sizes of 0.5 (b) and 1 mm (c). The solid and dotted lines are for VV and HH polarisation, respectively.

Monte-Carlo simulations over an ensemble of randomly layered stacks were performed in order to obtain theoretical estimates of backscatter fading as a function of snow depth overlying the percolation zone ice structure, as shown in Figure 5. Computed fading is

comparable to that observed, assuming either 3 cm or 6 cm mean layer thickness.

ESTIMATING SNOW ACCUMULATION

For a thin dry-snow layer the radar cross section is dominated by the scattering from the firm, but with increasing thickness of the dry-snow layer the backscatter from the buried firm is reduced significantly. Maps of the NRCS decrease at C-band (ERS) and K_u -band (NSCAT) are depicted in Figure 6 for the period September 1996 to June 1997 when ERS and ADEOS provided simultaneously data. Both data sets show similar spatial patterns, although, at K_u -band the sensitivity to snow accumulation is approximately twice as high as at C-band. This is in accordance with the NRCS trends depicted in Figure 2 and the results of the modeling shown in Figure 5.

These model curves can be used to transform the NRCS decrease to snow accumulation rates. The spatial pattern of these snow accumulation rates as well as their absolute values agree well with observations reported by Ohmura and Reeh (1991). There is a zone of high accumulation stretching along the westward slope having one maximum around 69°N and a second maximum far in the north around 76°N 60°W . Ohmura and Reeh gave precipitation rates of 500-600 mm/year for the maxima which corresponds approximately to 2 metres of dry-snow when assuming values for snow density of 0.35 g/cm^3 to 0.4 g/cm^3 .

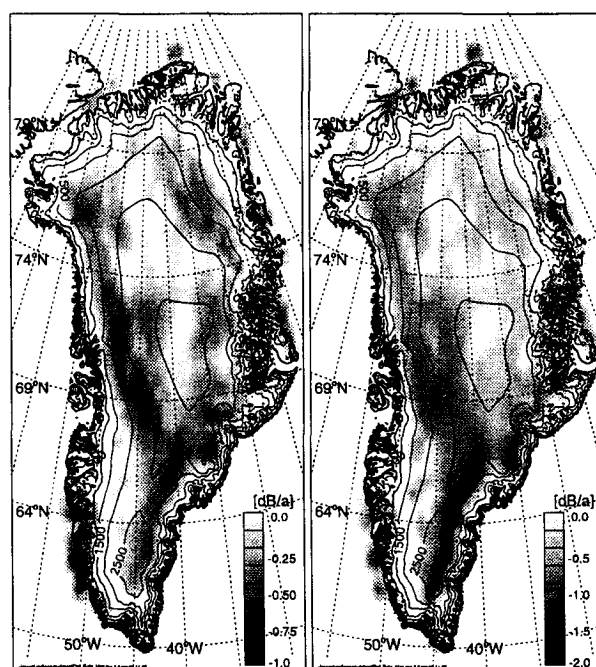


Figure 6 : Maps of NRCS decrease for C-band (left) and K_u -band (right) for the period Sep. '96 to June '97. The scales differ by a factor of 2.

CONCLUSIONS

Despite its poor spatial resolution the scatterometer is well suited for global monitoring task due to the good temporal and spatial coverage and the relative small amount of data. This application of the scatterometer data demonstrates the sensitivity of radar cross section to changes in snow properties allowing to estimate the spatial variability of snow accumulation for large areas of Greenland.

The ERS data are of excellent quality in terms of calibration and temporal stability, they are provided in near real-time and thus well suited for any kind of operational data assimilation tasks, e.g., into numerical climate and weather models.

So far the ERS scatterometers have collected a unique data set for climate monitoring which should be continued in the future.

ACKNOWLEDGEMENT

A part of this work was conducted under ESA study contract No. 11103/94/NL/CN. The ERS and NSCAT data were provided by: the Centre ERS d'Archivage et de Traitement (CERSAT), France.

REFERENCES

- Benson, C. S., Stratigraphic studies in the snow and firn of the Greenland ice sheet, SIPRE Res. Rep. 70, 1962.
- Echelmeyer, K., W. D. Harrison, T. S. Clarke and C. Benson, Surficial glaciology of Jakobshaven Isbræ, West Greenland: Part II. Ablation, accumulation and temperature, *Journal of Glaciology*, Vol. 38, No. 128, 169-181, 1992.
- ESA, ERS-1 System, ESA Publications Division ESTEC Noordwijk, The Netherlands, ESA SP-1146, 87 pages, 1992.
- Fahnstock, M. R., Bindschadler, R. Kwok, and K. Jezek, Greenland ice sheet surface properties and ice dynamics from ERS-1 SAR imagery, *Science*, Vol. 262, 1530-1534, 1993.
- Long, D. G., and M. R. Drinkwater, Comparison of enhanced resolution images of Greenland from ERS-1 and Seasat scatterometer, *Proceedings of the International Geoscience and Remote Sensing Symposium, IGARSS '94*, Pasadena, California, USA, 8-12 August, 2382-2384, 1994a.
- Long, D. G., and M. R. Drinkwater, Greenland ice-sheet surface properties observed by the Seasat-A scatterometer at enhanced resolution, *J. of Glaciology*, Vol. 40, No. 135, 213-230, 1994b.
- Ohmura, A. and N. Reeh, New precipitation and accumulation distribution maps for Greenland, *J. of Glaciology*, Vol. 37, No. 125, 140-148, 1991.
- Rott, H. and W. Rack, Characterisation of Antarctic Firn by means of ERS-1 scatterometer measurements, *Proceedings of the International Geoscience and Remote Sensing Symposium, IGARSS '95*, Congress Centre Firenze, Italy, 10-14 July, 2041-2043, 1995.
- West, R. D., D. P. Winebrenner, L. Tsang, and H. Rott, Microwave emission from density-stratified Antarctic firn at 6 cm wavelength, *J. of Glaciology*, 42(140), 63-76, 1996.
- Wiesmann, A. and C. Mätzler, Monitoring the temporal behaviour of land surfaces with ERS-1 wind scatterometer data, *Proceedings of Second ERS-1 Symposium*, Hamburg, Germany, 11-14 October 1993, ESA SP-361 (European Space Agency), 399-404, 1994.
- Winebrenner, D. P., E. D. Nelson, R. Colony, and R. D. West, Observation of melt onset on multiyear Arctic sea ice using the ERS-1 synthetic aperture radar. *Journal of Geophys. Res.*, 99, 22425-22441, 1994.
- Wismann, V. and K. Boehnke, Monitoring snow Properties on Greenland with ERS Scatterometer and SAR, *Proceedings of the 3rd ERS Symposium*, Florence, Italy, March 17-21, ESA SP-414, Vol. II, 857-862, 1997.
- Wismann, V., A. Cavanie, D. Hoekman, I. Woodhouse, K. Boehnke and C. Schmullius, Land surface observations using the ERS-1 scatterometer, *Final Report Part I*, ESTEC Contract 11103/94/NL/CN, 57 pages, 1996a.
- Wismann, V., K. Boehnke A. Cavanie, R. Ezraty, F. Gohin, D. Hoekman, and I. Woodhouse, Land surface observations using the ERS-1 scatterometer, *Final Report Part II*, ESTEC Contract 11103/94/NL/CN, 65 pages, 1996b.
- Wismann, V., D. P. Winebrenner, and K. Boehnke, Snow accumulation on Greenland estimated from ERS scatterometer data, *Proceedings of the International Geoscience and Remote Sensing Symposium - IGARSS '97*, Singapore, August 3-8, Volume IV, 1823-1825, 1997.

SEASAT, ERS-1/2 AND NSCAT SCATTEROMETER-OBSERVED CHANGES ON THE LARGE ICE SHEETS

Mark R. Drinkwater* and David G. Long**

*Jet Propulsion Laboratory, California Institute of Technology
4800 Oak Grove Drive, CA 91109, USA

**Electrical and Computer Engineering Dept., Brigham Young University
Provo, UT 84602, USA

ABSTRACT

Satellite-borne wind scatterometers are effective tools for monitoring ice sheets, and microwave imaging techniques enable comparison of historic and contemporary scatterometer data in climate change studies. We document scattering characteristics of the Greenland and Antarctic ice sheets using data from the NSCAT, ERS-1/2 and Seasat SASS instruments. C- and Ku-band data enable characterization of frequency- and incidence-angle dependent scattering characteristics, together with regional and seasonal melting delineation. NSCAT-SASS data differences indicate 18 year changes in microwave backscattering coefficient in response to decadal time-scale changes in the spatial patterns of ice sheet accumulation and ablation.

1. INTRODUCTION

Controversy over the relationship between global warming and changes in the Greenland ice sheet [Refs. 1, 2] make it imperative to accurately quantify mass balance and the time and space scales of variability in snow accumulation and ablation. Briefly in 1978, and since 1991, microwave radar has been used to study relationships between backscatter characteristics and snow and ice surface structures on temperate glaciers and polar ice-sheets [Refs. 3, 4]. On this basis, satellite microwave radar

data have been used on large ice sheets to map the relative size and locations of ice sheet physical zones or 'facies' [Refs. 5, 6].

Microwave backscattering depends on both the roughness and physical characteristics of the snow and ice [Refs. 7, 8]. For example, liquid water in snow dramatically changes the permittivity and thus its scattering signature. This provides an efficient means of monitoring backscatter changes which accompany diagenetic changes forced by seasonal ablation and/or metamorphic processes. Synthetic aperture radar (SAR) provides high resolution images of ice sheets, but the spatio-temporal coverage of 100×100 km SAR images is limited. Scatterometers provide comparatively lower resolution but more frequent coverage, and also measure the backscatter coefficient over a broad range of incidence angles [Ref. 9]. Here we study changes in the Greenland and Antarctic ice sheets using data from the C-band (5.3 GHz) European Space Agency ERS-1 and 2 (EScat) wind scatterometers, NASA's Ku-band (13.6 GHz) scatterometer (NSCAT), and the NASA Seasat scatterometer (SASS).

2. SCATTEROMETER IMAGING OF ICE SHEETS

The EScat wind scatterometer instrument (launched on ERS-1 in July 1991 and ERS-2 in April 1995) measures the vv-polarized normalized radar cross-section σ_{vv}^0 at various azimuth and incidence angles along a single 500 km-wide swath. EScat acquires these 50 km resolution data on a 25 km grid and has successfully compiled a continuous measurement dataset from 1991 until the present day. The only measurement conflict occurring in the polar regions is that the Scatterometer subsystem of the Active Microwave Instrument (AMI) is periodically switched off during competing high-data-rate SAR-mode operation. This results in some data black-outs in the vicinity of operable Antarctic SAR receiving stations.

The complementary NSCAT sensor was launched in August 1996 aboard the Japanese ADEOS-I satellite. Unfortunately, an untimely failure of the ADEOS platform in June 30, 1997 resulted in a curtailed NSCAT dataset lasting a period of only 10 months - and the loss of a valuable tool for ice studies. NSCAT nonetheless recorded the normalized radar cross-section, σ^0 (hh- and vv-polarized) while crossing the polar regions several times daily. Measurements at various azimuth and incidence angles were made in hexagonal 25 km resolution cells on a 25 km grid, along two 600 km wide swaths separated by a 400 km wide gap. The Ku-band SASS, from which NSCAT originated,

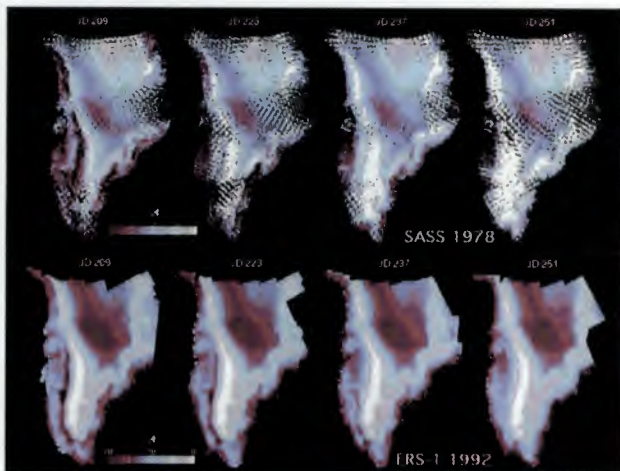


Figure 1. Greenland time series images generated from 1978 SASS and 1992 ERS-1 scatterometer data for selected days of the year. Colors indicate $\sigma_{vv}^0(40^\circ)$ at Ku- and C-band, respectively.

also operated for only 100 days between June 28 and October 10, 1978 before Seasat failed. It made 50 km resolution measurements along two 500 km swaths on an irregular sampling grid.

Over glacial ice, σ° (dB) is approximately a linear function of θ in the range $20^{\circ} \leq \theta \leq 55^{\circ}$ [Ref. 5];

$$\sigma^{\circ}(\theta) = A + B(\theta - 40^{\circ}) \quad (1)$$

where the coefficients A and B depend on surface characteristics and polarization. The term A is the 'incidence-angle-normalized' backscatter coefficient σ° , at 40° , and B describes its dependence on θ . A and B are both sensitive to snow and ice physical characteristics and surface roughness. The scatterometer image reconstruction algorithm with filtering (SIRF) is used to generate enhanced resolution images of A and B from scatterometer data from Greenland and Antarctica [Refs. 5, 9-11]. Resulting 6-day average images at 3-day intervals are derived as a trade-off between resolution enhancement and temporal averaging. The EScat images have a resolution of approximately 20-25 km and NSCAT images a resolution of around 8-10 km. The resulting ice sheet dataset, comprising 3-daily data, is sampled to the same pixel spacing (8.8 km) and then compared and described in this paper.

3. ICE SHEET BACKSCATTER VARIABILITY

3.1 Greenland

The surface of the Greenland ice sheet is subdivided into 'facies', the boundaries of which are established with respect to extent of melt or ablation influence [Ref. 6]. Within each facies, near-surface snow and ice properties have unique characteristics. At the lowest elevations, summer melting removes the entire annual accumulation of snow to reveal bare glacier ice. The *firn line* delimits the upper margin of this zone, separating it from the 'soaked' facies where saturation of the

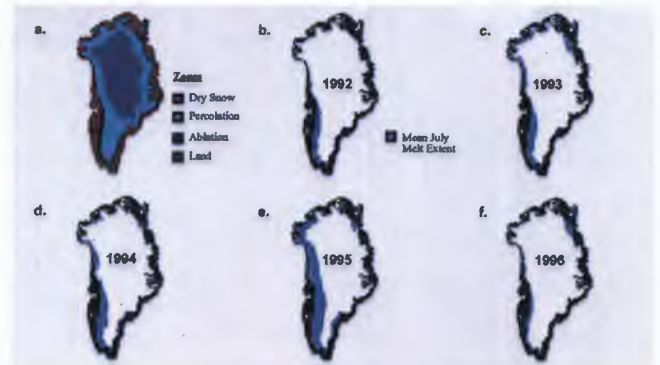


Figure 2. (a) Greenland snow and ice facies determined from coincident EScat and NSCAT data; and (b)-(f) mean monthly July ice-sheet melt extent from EScat data.

annual snow layer occurs. The upper limit of soaking is called the *saturation line*. Localized melt-water percolation occurs between this and the upper limit of surface melting, the *dry snow line*. In the 'percolation' facies annual increments of snow are neither completely wetted nor raised to the melting point. Percolation decreases with elevation diminishing to a negligible amount at the lower boundary of the dry snow zone. As glacier facies are not always expressed as strong gradients in surface properties, they are best discerned with microwave measurements which penetrate up to several meters into the surface of the snow and ice [Refs. 5, 8].

Seasonal modulations of σ° in Fig. 1 indicate changes in surface-layer properties in summer. Meltwater alters the surface reflectivity and transmissivity, limiting sub-surface volume scattering effects by increasing absorption and extinction. In addition, σ° is influenced by layering which results from seasonal snow accumulation and melt patterns [Ref. 5]. The spatial extent of summer melt appears as low σ° values around the lower elevation fringe of the ice sheet, particularly on day 209. The surface-melt signature is similar at both frequencies.

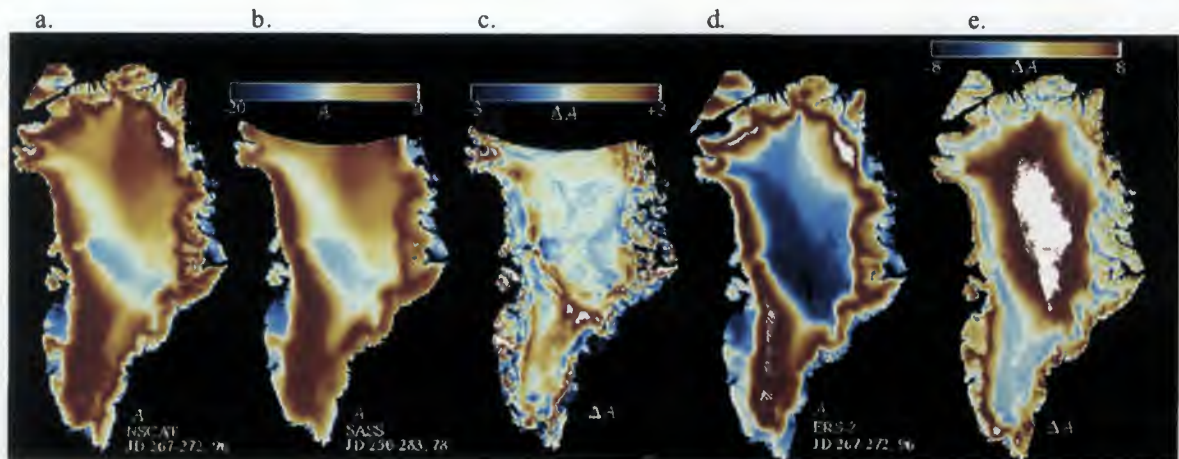


Figure 3. (a) NSCAT A image for the period 267-272, 1996; (b) SASS A image for days 250-283, 1978; (c) NSCAT-SASS A difference map of Greenland. (d) ERS-2 A image for days 267-272, 1996; and (e) NSCAT - ERS (Ku - C band) A difference image for days 267-272.

Differences in melt extent between the upper and lower panels are accounted for by interannual variability in the length and spatial extent of the melt seasons. Typically, melting ceases by day 237, with refreezing then increasing σ° at both frequencies. Monthly mean July melt extent is shown together with the facies in Fig. 2. The 1990's saw two of the smallest (1992: $8.1 \times 10^4 \text{ km}^2$; and 1996: $10.4 \times 10^4 \text{ km}^2$), and perhaps the largest (1995: $25 \times 10^4 \text{ km}^2$) melt extent in the last two decades. Melting in July 1995 is more extensive than at any other time during the satellite data record [2], encroaching upslope upon the dry snow zone along the entire north-western ice-sheet flank. Percolation zone stratigraphic discontinuities and a horizon comprising a high proportion of solid ice in layers, lenses and ice pipes is created as meltwater percolates downwards and refreezes at depth ($\sim 1\text{m}$) [6]. The lower elevation boundary of this zone is clearly indicated in Fig. 1 by a sharp transition between low and extremely high backscatter values. As the surface cools during autumn, the penetration depth increases beyond the depth at which ice lenses form and volume scattering from buried scatterers increases σ° in both Ku- and C-band images to some of the highest known values on earth [7, 8]. Low σ° values in central Greenland are well separated from percolation zone values exceeding -5 dB. Additionally C-band microwaves penetrate dry snow more effectively than Ku-band. Shorter wavelengths are scattered more effectively by snow grains, and thus the Ku-band σ° exceeds C-band values. The frequency difference A image (*i.e.* NSCAT-EScat) in Fig. 3(e), and a contour value of 1.8 dB is used to define the lower boundary of the dry-snow zone shown in Fig. 2(a).

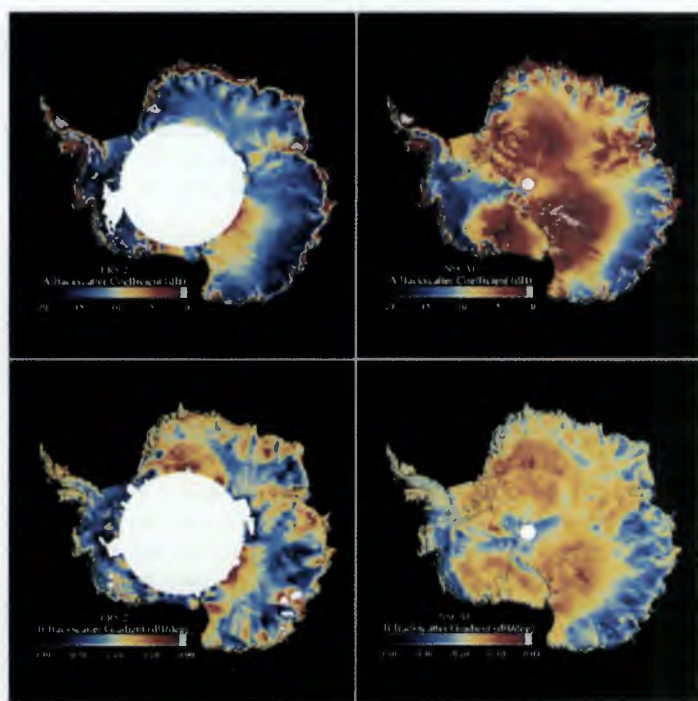


Figure 4. Mean Antarctic scatterometer ice sheet images for 20-30 September, 1996, for: (a) ERS-2 A values; NSCAT A values; (c) ERS-2 B values; and (d) NSCAT B values.

Downslope of the firm line, in the saturated facies, horizons are obliterated by the effects of summer melting, reducing winter contrast between the ablation and saturated zones. As a result the two are indistinguishable, and the radar senses only a broad 'ablation zone' [5]. Near the ice sheet margins, the surface autocorrelation function determines A and B by surface scattering, and the roughness scale causes greater backscattering at Ku-band than C-band of up to 8 dB in Fig. 3(e). Together with the seasonal variations in σ° this is used to define the 1996 extent of the ablation zone in Fig. 2A.

3.2 Antarctica

Overlapping ERS-2 and NSCAT data are shown for the second half of September in Fig. 4, to illustrate the corresponding C- and Ku-band austral spring ice sheet responses. This period is prior to the summer melt and illustrates the typical winter ice-sheet signature of Antarctica. Notably, there are a much broader range of backscatter variations than in Greenland. The simple pattern of relatively lower C-band backscatter in the central region of the ice sheet is clearly not reproduced as in Fig. 3, and the ice sheet facies are limited to simply dry snow and percolation zone. High snow accumulation regions ($> 200 \text{ kg m}^{-2} \text{ a}^{-1}$) around the peripheral slopes of the ice sheet, particularly in Wilkes Land in East Antarctica, and Ellsworth Land and Marie Byrd Land, have typically low EScat and NSCAT A values, together with relatively lower NSCAT B values (Fig. 4). For instance, accumulation values in the vicinity of Siple Station ($75^{\circ} 54'S 83^{\circ} 54'W$) are of the order of $550 \text{ kg m}^{-2} \text{ a}^{-1}$ [Ref. 12]. Further low A values are associated with high orographic precipitation along the western flank of the Antarctic peninsula [Ref. 13]. Despite low A values and high accumulation in some regions, EScat B values, appear locally sensitive to surface roughness and internal scattering effects, particularly around a number of volcanic peaks in Marie Byrd Land. Such interesting signatures are observed around Mount Takahē ($76^{\circ}15'S 112^{\circ}W$), Crary Mountains ($76^{\circ}45'S 118^{\circ}W$), Mount Hampton ($76^{\circ}29'S 125^{\circ}48'W$) in the Executive Committee Range, and the Ames Range ($75^{\circ}45'S 132^{\circ}W$), and are evident as saturated EScat B in Fig. 4c. The fact that NSCAT A values remain depressed around these volcanic peaks, despite high EScat B values, suggests that the effect is confined, however, to below the surface and is related to internal layering or buried crevasses only visible in more deeply penetrating, longer-wavelength, C-band data.

In Fig. 4, A images attain their highest values at both frequencies at high elevations in the central Antarctic ice sheet, in relatively low accumulation regions ($< 100 \text{ kg m}^{-2} \text{ a}^{-1}$). Strong layering in these regions promotes high B values (in Fig. 4c and d) and depth hoar development is thought to add a significant contribution to volume scattering totals in regions having NSCAT A values exceeding -2 dB. Depth hoar development is known to generate grain radii exceeding 0.5 cm in diameter in these regions through temperature-gradient metamorphism under strong vertical vapour fluxes. Large grains cause strong, wavelength-dependent Mie scattering at both Ku-band, and C-band rather than Rayleigh scattering. The

result is an order of magnitude difference in A values, despite similar B values.

High A values are also observed in a number of lineaments and elongated features in the central part of the Antarctic ice sheet in the higher resolution NSCAT images. Several large ice streams flowing into the Ronne and Filchner ice shelves are identified in Fig. 4b, inland extensions of the Slessor Glacier (79°30'S 24°W) and southward trending tributaries of the Recovery Glacier (81°S 33°W) can be traced in the NSCAT data poleward of the of the EScat swath limit (with values exceeding -3 dB). Catchment areas are also visible for several large ice streams (Reedy, Scott and Amundsen Glaciers) flowing into the Ross ice shelf. These penetrate the Queen Maud Mountains into Ice Stream A, ultimately leading into the Ross Ice shelf. Blue

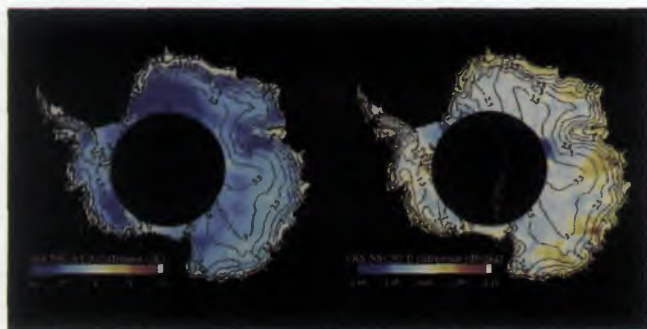


Figure 5. Frequency difference images illustrating (a) ERS-2 - NSCAT A difference; and (b) ERS-2 - NSCAT B difference, for the time period shown in Fig. 4.

ice regions, having a hard wind-swept, sublimating bare-ice surface also display high Ku-band values (10 dB higher than C-band), as for instance in the Queen Fabiola Mountains (72°S 36°E) in Queen Maud Land.

In contrast to Greenland, the Antarctic ice sheet experiences summer melting only at the lowest elevations around the coast. The percolation zone is limited to this geographic area in Antarctica. Melt events, although short-lived, are recorded in both NSCAT and EScat backscatter records as a dramatic summer depression in backscatter values due to snow wetting. The recent envelope of melt extent is clearly reflected in Fig. 4a as the halo of high coastal and ice shelf A values exceeding -5 dB, and in Fig. 6 as ΔA values close to 0 dB. As in Greenland the reason for the extremely high values is the formation of percolation features such as ice layers, lenses and glands in the firm. The resulting backscatter contrast between summer and winter months can exceed 20 dB, as in the case of the Larsen Ice Shelf (63°S 62°W).

Although limited in latitudinal extent by the EScat swath limit, the differences in Fig. 6 illustrate regions of frequency-dependent ice-sheet backscattering. Notable features which bear similarity to Greenland are the fringe of ΔA values where melting has its greatest impact. Recent intense melting on the Amery, Fimbul and Larsen ice shelves, leads to slightly positive differences, due to the greater penetration

depth at C-band, and resulting higher volume scattering from buried ice lenses. Interestingly, the Ross ice shelf shows a large east-west gradient in ΔA . The eastern side of the ice shelf is known, for instance, to preferentially experience more cumulative melt days [Ref. 14] each year throughout the last decade, thereby building more ice lenses and layers.

The regions of the largest ΔA differences (< -5 dB) in West Antarctica (Fig. 5a) occur in Marie Byrd Land, and are confined to the region poleward of the Executive Committee Range. In East Antarctica a large portion of Queen Maud Land (with an extension into the Lambert Glacier drainage basin) and Antarctic Plateau regions poleward of 75°S have absolute A differences exceeding 5 dB. Since these areas correspond with regions of low azimuthal anisotropy [Ref. 15] and low accumulation rates (< 100 kg m⁻² a⁻¹), it is suggested that wavelength-dependent differences result largely from the frequency of occurrence of depth hoar in the firm, and the effects of snow grain volume scatter.

Frequency difference B image values in Fig. 5b show relatively uniform near-zero values throughout central Antarctica, indicating the negligible contribution of surface roughness effects in these dry snow regions. The largest positive differences are confined close to the coast in the percolation zone, and further inland in regions of intense, persistent katabatic winds. Examples may be found in Enderby Land near Mizuho Station (71°20'S 46°30'E), and in other regions where the erosion environment prevents high accumulation such as Princess Elizabeth Land (70°S 90°E), Wilkes Land (70°S 123°E), and George V Land (70°S 140°E). Not coincidentally, these regions display the highest azimuthal anisotropy [Ref. 15], and estimates of A and B , using equation (1), are susceptible to a high degree of variance. Nevertheless, the positive ΔB values suggest a significant influence from wind-induced, erosional surface-roughness features such as sastrugi, and cross-bedding caused by seasonal erosion and uneven accumulation.

4. DECADAL CHANGE

Acquisition of NSCAT data during the same September season as Seasat, enabled long-term, 1996-1978 change maps to be derived over both ice sheets in late September. In Greenland, this period corresponds with late autumnal cooling over the ice sheet, while in Antarctica it corresponds with the austral spring. Since melting may influence a large portion of the Greenland ice sheet, change is primarily influenced by diagenetic changes resulting from snow-surface melt. However, since most of Antarctica may be regarded as a 'dry-snow' zone, changes result not from the effects of positive summertime air temperatures. Rather these changes express the effects of net, long-term variations in snow accumulation and thus layering in the snowpack, or significant dynamic adjustments of the ice sheet, expressed as large-scale surface roughness changes. The results shown in Fig. 3c and Fig. 6, illustrate the decadal time-scale changes on the Greenland and Antarctic ice sheets, respectively.

4.1 Greenland

Subtle differences in σ_{v} (i.e. NSCAT-SASS) between Fig. 3a and b are shown in Fig. 3c, (where Fig. 3b is the result of combining and median filtering the relatively sparse SASS measurements). Surfaces experiencing large changes over the intervening 18 year period are in Fig. 3c noted as dark tones with values > -3 dB. Patterns appear highly correlated with the snow and ice facies boundaries in Fig. 2a. and the zones of largest interannual variability. The upslope melt extent has a large interannual variability and the mean July melt area in Fig. 2 clearly does not capture the maximum extent of melting often experienced within a narrow range of dates. Fig. 3c therefore contains microwave radar archaeological evidence for previous melting within the dry snow zone, through the influence of buried scatterers beneath recent years of snow accumulation. Patterns suggest a recent upslope migration of the upper boundary of the percolation zone, particularly in response to the extreme summer of 1995 (in Fig. 2e). NSCAT probably penetrates deep enough to 'see' percolation inhomogeneities formed along the lower elevation fringes of the dry snow zone, and the frequency difference image in Fig. 3e corroborates these changes. Fig. 3e highlights zones of wavelength-dependent volume scattering. As dry snow has a lower σ_{v} at C-band, due to the primary backscattering occurring from Rayleigh scattering from snow grains (in the absence of strong stratigraphy), this zone has large positive values > 8 dB in Fig. 3e. A contrast reversal occurs in the zone influenced by percolation, due to EScat penetrating deeper and responding more to buried ice lenses than NSCAT. This results in slightly negative percolation zone values.

Lower accumulation rates result in more pronounced stratification, and greater backscattering from subsurface layers at high incidence angles. This is particularly true for instance in the north-east Greenland dry-snow zone, and is seen in SASS data [Ref. 5]. Thus, we suggest that time series of multiple frequency, enhanced resolution *A* images and their associated *B* values, together offer greater potential for retrieving snow accumulation than single channel, fixed incidence angle instrument data.

4.2 Antarctica

Decadal differences of the kind illustrated in Fig. 3b and Fig. 7

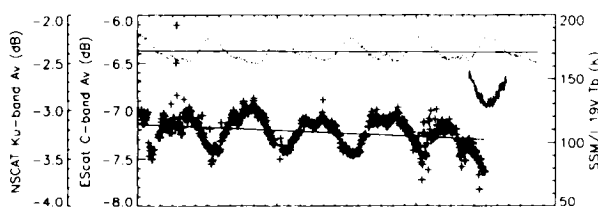


Figure 6. Interannual time series indicating Antarctic plateau ($78^{\circ}\text{S } 122^{\circ}30'\text{E}$) mean v-pol EScat and NSCAT *A* values, and corresponding 19GHz v-pol SSM/I brightness temperatures, for the period 1992 – 1997.



Figure 7. NSCAT-SASS *A* and *B* difference images for the same 23-28 September 6-day period in 1996 and 1978, respectively.

arguably suffer from the effects of interannual variability, particularly if seasonal variations in backscatter are large. Fig. 6 shows the recent past in the form of an interannual time-series spanning 1992-1997 in a region experiencing no melting, and expected constant forcing. The upper dotted line indicates a neutral long-term trend in passive microwave 19 GHz v-pol brightness temperatures which is suggestive of constant mean air temperatures. Nonetheless, a distinctive seasonal cycle is observed, with maximum temperatures in summer and minimum temperatures in winter and a dynamic range of ~ 20 K. Scatterometer measurements from both ERS-2 (crosses) and NSCAT (solid line) are anticorrelated with SSM/I, exhibiting ~ 0.5 dB amplitude in the seasonal cycle with peak backscatter values attained in August. The main conclusion from Fig. 6 is that the maximum error in decadal time-scale difference images, occurring as a result of interannual variations in the seasonal cycle is of the order of 0.5 dB for ice-sheet surfaces experiencing no melt.

Fig. 7 shows the 18-year *A* and *B* differences (v-pol), computed after late September images acquired during the SASS and NSCAT missions. Excluding ice shelf regions, in some cases of which the changes have been dramatic, there are a number of regions with 18-year reductions in Ku-band *A* values exceeding 2 dB and *B* values exceeding -0.5 dB/deg. In West Antarctica, the largest declines are observed in Ellsworth Land in the location of the Evans Ice Stream and the US "Eights" base ($75^{\circ} 20'\text{S } 77^{\circ}\text{W}$), and slightly north of the Pine Island Glacier ($75^{\circ}\text{S } 102^{\circ}\text{W}$). In this high accumulation region, an 18 year overall increase in annual accumulation is expected to have had a significant impact on the snow density and layer thickness, together with the mean grain radius. It is speculated at present that the resulting increases in layer spacing and fraction of lower density snow, have caused a decrease in *A* and *B* values at these elevations. This area of corresponding *A* and *B* decreases may be tracked westwards around Ellsworth Land between the 1000 and 1500m elevation contours. Both below and upslope of this broad region, *A* differences become positive, suggesting large spatial gradients in changes over the last 20 years, and that the West Antarctic increase in accumulation occurred at a distinctive elevation. This suggests a combination of orographic and adiabatic influences upon changes precipitation patterns.

In East Antarctica a further significant-sized region of negative

ΔA and ΔB values occurs in Princess Elizabeth Land at 70°S 85°E. This correspondence between reductions in A and B values similarly implies a snow accumulation increase, albeit within a broader range of elevations between 1000 to 3000m. Other centers of positive ΔA values of 1-2dB are dispersed throughout East Antarctica. Further analysis is required to examine whether these changes are a response to accumulation changes or long-term variations in the katabatic wind regime.

5. CONCLUSIONS

Scatterometers clearly provide important information about the large ice sheets. This precisely calibrated spatial and temporal record is complementary to passive microwave images from SSM/I and snap-shot images produced by higher resolution radar sensors such as SAR. Time series of images with large-area coverage, such as that shown here, are suitable for monitoring changes in the characteristic zones of ice sheets in response to changes in accumulation, metamorphism and melting. Significant 18 year differences between early NSCAT and Seasat SASS images indicate large-scale changes in radar backscatter in response to changing snow and ice surface conditions.

Frequency combinations and the addition of passive microwave emission data from SSM/I help compensate for the wavelength-dependent scattering albedo of the snow and the high incidence angle component of volume backscatter caused by snow grains, as opposed to the stratification induced scattering. This allows dependencies of the backscattering on snow density, temperature, ice particle radius and layer depth to be better parameterized. In this manner, algorithms are presently being developed to monitor the seasonal progression of snow accumulation and firnification using combined frequency scatterometer and passive microwave datasets. Future multi-channel, active-passive empirical algorithms developed along these lines will be invaluable for extending and testing current theoretical electromagnetic scattering models, and in validating our understanding of the physical basis for the observed microwave signatures.

Decadal variability in Greenland and Antarctica is forced primarily by the North Atlantic and El Niño Southern Oscillations, respectively. Regional impacts are greater than normal ablation and/or higher than normal snow accumulation. Greenland results indicate an upslope increase in the extent of the percolation zone and reduction in dry-snow extent since 1978, with the largest changes occurring in the south western flank of the ice sheet. This implies that the region of melting on the ice sheet has risen to its highest altitude in the recent past. Observations of the interannual variability show July 1995 was an extremely large melt season, probably the most significant over the 18 year interval since Seasat in 1978. Changes are consistent with the decadal warming trend and increase of more than 1.0°C between 1979 and the present day in Greenland. In contrast, West Antarctic changes appear to suggest increases in snow accumulation have taken place. Such changes imply an increased poleward moisture flux in these regions.

6. ACKNOWLEDGEMENT

MRD completed this work at Jet Propulsion Laboratory, California Institute of Technology under contract to the National Aeronautics and Space Administration and supported by NASA Code YS and the NSCAT Project Office.

7. REFERENCES

1. Zwally H.J., A.C. Brenner, Growth of the Greenland Ice Sheet, *Science*, 246, 1587-1591, 1989.
2. Abdelati W., K. Steffen, Snowmelt on the Greenland Ice Sheet as Derived from Passive Microwave Satellite Data, *J. Climate*, 10(2), 165-175, 1997.
3. Rott H., Synthetic Aperture Radar Capabilities for Glacier Monitoring Demonstrated with Seasat SAR Data, *Z. fuer Gletscherkunde u. Glazialgeol.*, 16, 255-266, 1980.
4. Jezek, K.C., M.R. Drinkwater, J.P. Crawford, R. Bindschadler, R. Kwok, Analysis of synthetic aperture radar data collected over the southwestern Greenland ice sheet, *J. Glaciology*, 39, 131, 119-132, 1993.
5. Long D.G., M.R. Drinkwater, Greenland Observed at High Resolution by the Seasat-A Scatterometer, *J. Glaciology*, 32, 2, 213-230, 1994.
6. Benson C.S., Stratigraphic Studies in the Snow and Firn of the Greenland Ice Sheet, *CRREL Res Rep.*, 70, Cold Regions Res. Eng. Lab., Hanover, NH, 120pp., 1962.
7. Rignot, E., Backscatter Model for the Unusual Radar Properties of the Greenland Ice Sheet, *J. Geophys. Res.*, 100, E5, 9389-9400, 1995.
8. Jezek, K.C., P. Gogineni, M. Shanableh, *Geophys. Res. Lett.*, 21, 1, 33-36, 1994.
9. Drinkwater M.R., D.G. Long, D.S. Early, *ESA Journal*, 17, 307-322, 1994.
10. Long, D.G., and M.R. Drinkwater, Cryosphere Applications of NSCAT Data, *IEEE Trans. Geosci. and Remote Sens.*, In Press.
11. Early D.S., D.G. Long, Resolution Enhancement of Scatterometer Data, *IEEE Trans. Geosci. Rem. Sens.*, In Press.
12. Mosley-Thompson, E., J. Dai, L.G. Thompson, P.M. Grootes, J.K. Arbogast, and J.F. Paskievitch, Glaciological Studies at Siple Station (Antarctica): Potential Ice-Core Paleoclimatic Record, *J. Glaciol.*, 37, 125, 11-22, 1991.
13. Giovinetto, M.B., and N.M. Waters, Dependence of Antarctic Surface Mass Balance on Temperature, Elevation, and Distance to Open Ocean, *J. Geophys. Res.*, 95, D4, 3517-3531, 1990.
14. Zwally, H.J., and S. Fiegles, Extent and Duration of Antarctic Surface Melt, *J. Glaciol.*, 40, 463-476, 1994.
15. Early, D.S., and Long, D.G., Azimuthal Modulation of C-band Scatterometer σ^0 over Southern Ocean Sea Ice, *IEEE Trans. Geosci. Rem. Sens.*, 35,5, 1997.

Directional Anisotropy of C- and ku-band Microwave Backscatter from the East Antarctic Snow Cover: Differences and Similarities

Neal W. Young & Glenn Hyland

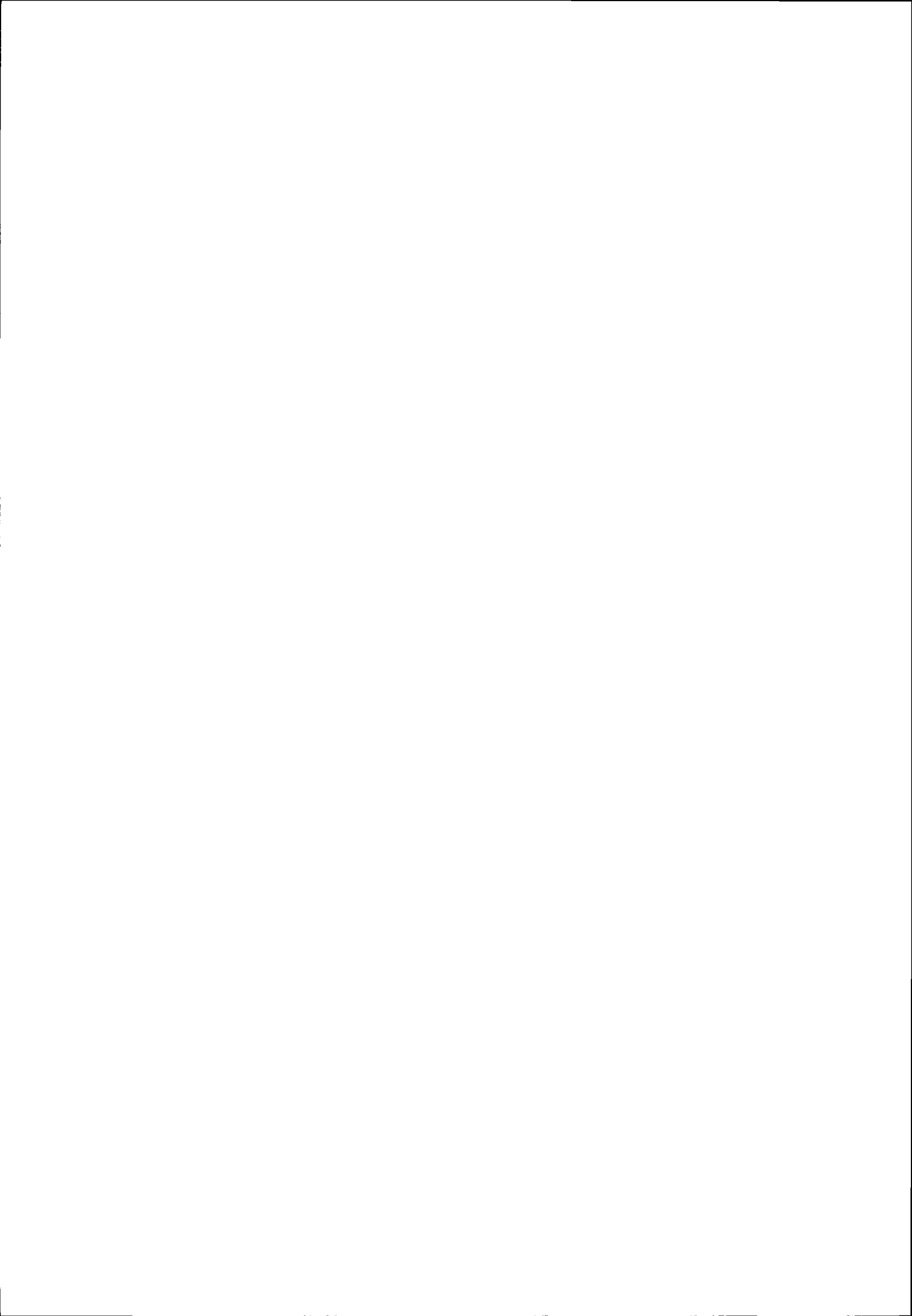
Antarctic CRC & Australian Antarctic Division
GPO Box 252-80, Hobart, Tasmania 7001, Australia
e-mail: Neal.Young@utas.edu.au

Measurements of the microwave backscatter from the Antarctic ice sheet have been obtained by the single-sided, right-looking, C-band wind scatterometer carried by the ERS-1 and 2 satellites and by the dual-sided, ku-band NSCAT instrument on ADEOS. The different operating wavelengths and antenna geometry of the two types of instrument facilitates an investigation of the influence of the observing system on the backscatter measurements, system performance, and the nature of observed anisotropy.

The backscatter exhibits a character which varies with the near surface properties of the snow cover and systematically with location on the ice sheet. There is a distinct directional asymmetry in the intensity of the backscatter which can be detected and measured over the whole ice sheet and related to the persistent wind field. Analysis of long time series of backscatter measurements shows that the asymmetry effect appears to be stable, even in areas where the signal is weak. Its orientation and amplitude are compared to ground observations of the orientation of surface roughness elements.

The axis of the minimum in the directional asymmetry coincides with the longitudinal axis of surface micro-relief, mainly in the form of snow dunes and sastrugi, and with the mean wind observed at automatic weather stations. In addition to the surface features, the scatterometers actually detect structures related to the surface roughness which have been preserved within the snow cover through burial by progressive snow accumulation and thus provide a time-integrated result. This detection of the local mean orientation of the micro-relief allows information to be derived about the direction and strength of the persistent surface (katabatic) wind field. Regions exhibiting the largest amplitude in the asymmetry are associated with areas of greatest roughness and strongest or most stable/persistent winds.

Similar orientations are obtained from the two different scatterometers but with a smaller amplitude in the directional anisotropy from the ku-band system, $\pm 3\text{dB}$ compared to $\pm 5\text{dB}$. Systematic biases are observed in several large regions between the satellite-derived orientations and those of the field observations and between results from the two different scatterometers. The instrument related biases are stable with time and appear to represent real effects derived from differences between the two scatterometer systems. We use the stability of the observations and snow properties to explore these differences and their impact on interpretation of scatterometer data.



AN EMPIRICAL C-BAND BACKSCATTER MODEL OVER ARCTIC SEA ICE FROM ERS-1 AMI-WIND DATA

Alain Cavanié IFREMER/DRO/OS
Centre IFREMER de Brest, B.P. 70, 29280 PLOUZANE, FRANCE
Phone: (33)0298224410, FAX:(33)0298224533
cavanie@ifremer.fr

ABSTRACT

Using ERS-1 AMI in Wind mode backscatter data, an empirical C-band backscatter model for Arctic ocean sea ice is developed. One or three parameter models are tested, and shown to be overly simplified when compared to the six parameter model proposed. The parameters are determined by minimization of a cost function, using 30000 backscatter triplets. Thus, the model's quality can be evaluated. To discriminate the few outliers corresponding to open water areas undetected by the CERSAT's open water screening algorithm, the minimization is applied twice, using the first estimation of the sea ice backscatter model to reject a few hundred backscatter triplets too distant from the model. The procedure is repeated every two months from September 1992 to July 1993, setting in evidence important seasonal variations. This model can serve to produce maps of backscatter at an incidence angle of 40° from a single swath of AMI Wind data.

INTRODUCTION AND FORMULATION

Backscatter measurements made with space-borne scatterometers correspond to large footprint sizes, several hundred or even thousands of square kilometers. It has been shown previously that, over sea ice, backscatter averaged over such large footprints is isotropic in azimuth [1], so that an empirical model needs only consider the incidence angle dependence.

The AMI-Wind is a three-beam, C-band VV polarized instrument designed to measure winds over the ocean surface. An interesting aspect of the measurements of its antennas is that they are regrouped over the same geographical surfaces along 19 lines off-track, and extend from 18 to 56 degrees in incidence angle. This data source is well adapted to study a model of sea ice backscatter applicable to large footprint sizes.

The empirical model takes the general form :

$$\sigma^\circ = A_1 T + A_2 T^2 + A_3 T^3 + \sigma_{40}^\circ (1 + A_4 T + A_5 T^2 + A_6 T^3) \quad (1)$$

where $T = (\theta - 40)/40$

in which θ is the incidence angle expressed in degrees ; σ° is the backscatter coefficient expressed in dB. Equation (1) describes a family of curves which vary as a function of the value of the backscatter coefficient at an incidence angle of 40°, σ_{40}° . The development could of course be extended further, but as a first try, will be limited to third order terms,

plots of σ° as a function of incidence angle showing little curvature. The equation can be solved to obtain σ_{40}° :

$$\sigma_{40}^\circ = (\sigma^\circ - (A_1 T + A_2 T^2 + A_3 T^3)) / (1 + A_4 T + A_5 T^2 + A_6 T^3) \quad (2)$$

The value of σ_{40}° would be the same for measurements of the forward and central antennas taken over the same footprint, if the expression was perfectly correct and noise of different sources absent. It is therefore natural to seek estimations of the parameters A_i by minimizing the function S , defined as :

$$S = \sum [(\sigma_{40}^\circ)_2 - (\sigma_{40}^\circ)_1]^2 / N \quad (3)$$

where $(\sigma_{40}^\circ)_1$ corresponds to the expression on the right of equation (2) for the backscatter and incidence angle measurements of the central antenna and $(\sigma_{40}^\circ)_2$ to the same expression, but for the average of the forward and rear antenna backscatter and incidence angle measurements. The sum is to be taken over a large number, N , of measurements, extending over the whole incidence angle range.

Knowing that the standard error of the backscatter measurements is around 5% which corresponds to 0.211 in dB, and neglecting incidence angle errors which are very small, a minimum value of S , due to instrument and speckle noise, can be estimated to be :

$$\text{Min}(S) = [1 + 0.5](0.21189)^2 = 0.06735 \quad (4)$$

This evaluation takes into account that backscatter over sea ice is isotropic in azimuth, so that the fore and aft beam measurements, made at the same incidence angles, can be averaged, reducing the variance of their average to half that of a single measurement, and that speckle and instrument noise for all three measurements are independent. Only if the backscatter model was perfect could this minimum value of M be reached when the expression given by equation (3) is minimized, but approaching it should indicate a good model fit to actual backscatter over sea ice.

DATA SETS OVER THE ARCTIC OCEAN

The data used are extracted from the CD-ROMs produced by the CERSAT [2], which contain the entire ERS-1 AMI-Wind backscatter data set. Only a small subset of this data is used, corresponding to sea ice covered regions of the Arctic ocean, north of 70° N, for which all three antennas gave backscatter measurements and which were detected as being over sea ice by the CERSAT ice detection algorithm [3].

The C-band backscatter maps at 40° incidence angle, produced by the CERSAT, were studied to choose six different time periods in 1992 and 1993 during which SAR mode operation of the AMI (Active Microwave Instrument) did not exclude too large a part of the Beaufort sea. These periods are the following : 7-13.09.1992, 2-8.11.1992, 25-31.01.1993, 1-7.03.1993, 10-16.05.1993, 5-11.07.1993.

Initially, the first thirty thousand points of these data sets were used in the minimization of S, imposing only as selection criteria that all three antennas had returned backscatter values and that the CERSAT ice detection algorithm indicated the point of measurement to be over sea ice. This, as shown in the next paragraph, led to include points tainted by the presence of open water, since the CERSAT ice detection algorithm is intended to screen out all regions with even very small concentrations of ice present. In a second selection, a further criterion imposed on measurement points was that the value of $[(\sigma_{40}^{\circ})_2 - (\sigma_{40}^{\circ})_1]^2$, computed using the first approximation of the parameters A_i , be less than 2.

EVALUATION OF MODEL PARAMETERS USING THE DATA

Not only were six parameter solutions sought, but also one parameter (A_2 to A_6 set to zero) and three parameter solutions (A_4 to A_6 set to zero), in order to evaluate the importance of different terms. For the first selection of data points, the minimization of S was carried out simply, starting with initial values of all the A_i set to zero, then incrementing or decrementing each A_i individually and testing to see whether S had decreased in so doing. Increments started at a value of 0.1, and were decreased by a factor of ten when S decreased by less than 0.02 after one pass through all the parameters investigated; the processing was stopped when the increments reached a value of 10^{-5} . For the second selection of points, a similar procedure was adopted, but seeking first the one parameter minimization with A_1 set to a value of -6.0, the three parameter minimization starting from the value of A_1 thus found, and the six parameter solution taking as a starting point the values of the three parameter minimization, all other parameters being set to zero initially. This procedure proved fairly rapid when searching for the one and three parameter solutions, the minimum being reached within about one hundred iterations, but much slower when seeking the six parameter solutions, around ten thousand iterations being then necessary. Streamlining of the procedure was not studied further, as being more time consuming than the computer effort required for this study.

TABLE 1

MONTH	Min(S)	A_1	A_2	A_3	A_4	A_5	A_6
SEPTEMBER	0.36987	-6.75985	17.331	-9.52855	0.0423	1.49311	-0.400799
SEPTEMBER	0.43626	-6.85489	1.0568	-0.9211			
SEPTEMBER	0.47621	-7.02399					
NOVEMBER	0.221437	-4.93677	6.93333	-2.73416	0.0825	0.510199	0.0984998
NOVEMBER	0.249202	-6.4449	1.046	-0.63211			
NOVEMBER	0.267843	-6.54890					
JANUARY	0.216739	-4.96596	5.77345	-0.444099	0.07861	0.387198	0.295501
JANUARY	0.240888	-6.50090	1.29700	-0.732100			
JANUARY	0.267982	-6.64700					
MARCH	0.248825	-4.90468	5.25337	-1.41131	0.07751	0.333199	0.2176
MARCH	0.271736	-6.43960	1.37810	-0.82110			
MARCH	0.302924	-6.60800					
MAY	0.184716	-4.28072	3.73349	-1.09041	0.1275	0.20330	0.30339
MAY	0.21512	-6.67100	1.62200	-1.03111			
MAY	0.259075	-6.68590					
JULY	0.303489	-22.2236	61.2833	-31.40300	-0.837494	3.38115	-1.5225
JULY	0.63588	-8.3619	4.4511	-2.24111			
JULY	0.92144	-8.8200					

Table 1 summarizes results obtained using the first selection of points, Table 2 those of the second selection. As expected, the comparison of results between the two tables shows an important reduction in the minimized values of S, when the outliers are screened out. However, values of the parameters A_i are not modified very much, which suggests that the method is stable with respect to outliers which are in fairly small number, respectively 1030, 435, 340, 463, 286, and 533 data points were screened out when selecting the 30000 data points for the six periods chosen. That the number of points rejected is higher in September and July is due to the fact that open water areas are greater in these months than in the others.

Important variations in the parameters A_1 to A_3 generally occur when passing from the three parameter to the six parameter model. These variations are due in part to the fact that the mean value of σ_{40}° , $M(\sigma_{40}^{\circ})$, is initially unknown, but on the order of -10 dB, which causes a redistribution of values between the first and last three parameters. The values of S after minimization, Min(S), given in Table 2, are reasonable for the six parameter models, being only about twice the estimated value due to total measurement noise, estimated by Eq. 4, July being an exception, probably due to surface melt and puddles. Clearly, introducing a first order non-linearity improves the model behaviour in all cases, in fact much more significantly than passing from the one parameter to the three parameter model. This was predictable from plots of backscatter in dB as a function of

incidence angle over the Arctic ocean, which show fairly linear trends but with different slopes for their upper and

lower limits.

TABLE 2

MONTH	Min(S)	A ₁	A ₂	A ₃	A ₄	A ₅	A ₆
SEPTEMBER	0.139985	-5.57284	10.0011	-0.169204	0.05941	0.894196	0.365602
SEPTEMBER	0.170954	-6.72179	0.81910	-0.63110			
SEPTEMBER	0.184722	-6.81999					
NOVEMBER	0.106407	-3.66532	1.61002	0.422984	0.17960	0.1043	0.33769
NOVEMBER	0.133100	-6.40379	0.81900	-0.521110			
NOVEMBER	0.145115	-6.48589					
JANUARY	0.110803	-3.33744	0.238092	0.533883	0.19960	-0.0176	0.343489
JANUARY	0.141330	-6.44800	1.0610	-0.621110			
JANUARY	0.159813	-6.5668					
MARCH	0.114889	-2.81919	-1.50111	0.75203	0.22960	-0.14770	0.3557
MARCH	0.159520	-6.4257	1.15900	-0.632100			
MARCH	0.181021	-6.54980					
MAY	0.117461	-3.30356	0.462904	1.13200	0.1986	0.02769	0.439589
MAY	0.158772	-6.68599	1.57900	0.00000			
MAY	0.197349	-6.83699					
JULY	0.230866	-22.2732	59.0242	-30.4406	-0.846593	3.26425	-1.46032
JULY	0.533843	-8.2801	4.28800	-2.32111			
JULY	0.805607	-8.75					

Families of curves of the backscatter model (Figures 1.a to 1.d), as determined from the individual data sets selected every two months, show that, although the coefficients of the model vary from month to month, the general trend of the curves is very similar, from November to May. In these months, curvatures of the σ_{40}° isolines appear quite negligible. However, in September and even more in July, when surface melting and ponding modify the behaviour of backscatter, σ_{40}° isolines show an important curvature. In these months, assuming a straight line relationship between backscatter in decibels and incidence angle locally, in order to transform σ° measurements to σ_{40}° estimates, will lead to reduce the high σ_{40}° estimates, and increase the low σ_{40}° estimates. Extrapolation of the σ_{40}° isolines beyond the cloud of data points should, as always, be considered with caution. This is particularly true in the low incidence angle range, below the 18° incidence angle limit of the AMI Wind, where specular reflection will play an increasing role and augment backscatter as incidence angle decreases.

BACKSCATTER MAPS AT 40° INCIDENCE ANGLE

The backscatter model can be usefully applied to the construction of backscatter maps at any given incidence angle, and in particular at 40°, which is a reference angle used by the CERSAT. Having established the backscatter model, single backscatter measurement of the AMI in Wind mode, σ° , can be used to provide an estimate of the backscatter at 40°, using equation (2). Considering the noise level to be similar for all three antennas, the noise level of the estimation was reduced, simply by taking the mean value of the three σ_{40}° estimates obtained from the triplet of backscatter measurements. Plate 1 shows the results of projecting these estimates on the NSIDC (National Snow and Ice Data Center) 25 km polar stereographic projection. Of each data set, the first 50000 points such that $[(\sigma_{40}^{\circ})_2 -$

$(\sigma_{40}^{\circ})_1]^2$ is less than 2.0 were used in this construction, the value of σ_{40}° assigned to a given pixel being the last available.

In order to evaluate the quality of such maps, two maps were produced from successive backscatter triplet sets of size 25000, for each period considered. Here, as in the backscatter maps of Plate 1, only measurement point such that $[(\sigma_{40}^{\circ})_2 - (\sigma_{40}^{\circ})_1]^2$ is less than 2.0 were used in this construction. The mean and standard deviation of the difference between individual pixel linear backscatter values were then computed, eliminating pixels whose backscatter values had not been evaluated in both cases, as well as land points. Table 3 summarizes results which are very consistent from one month to the other.

Knowing that the maximum backscatter values are around 0.165, the mean and standard deviations appear rather small in all months. Comparison of the two successive maps in September indicates that there was a regional evolution in backscatter during this period, which can explain why the standard deviation is higher in that month.

Comparison of such maps with those produced by the CERSAT show that their values are quite comparable to those of the present CERSAT product. The construction using an empirical backscatter model has the advantage that data of a single swath can be interpreted and mapped at a reference incidence angle. Of course the technique could be modified to average over a given time period all measurements falling within a given pixel, but for real time applications or the study of ice dynamics, using only the latest information available appears a better choice.

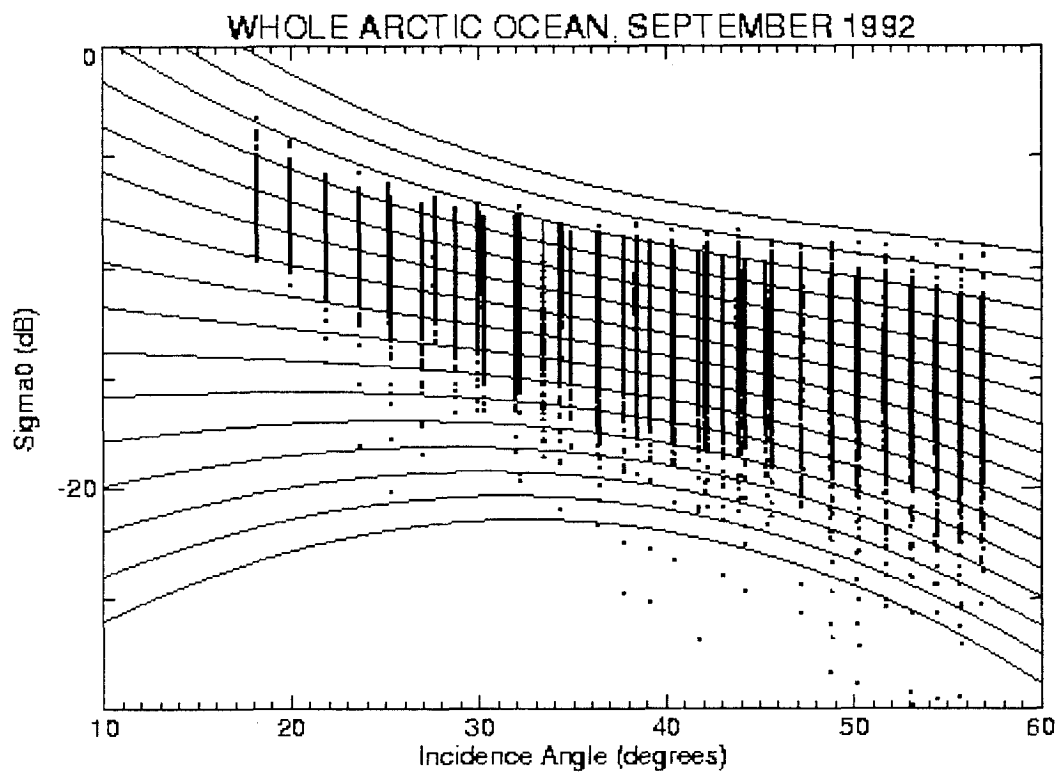


Fig. 1.a

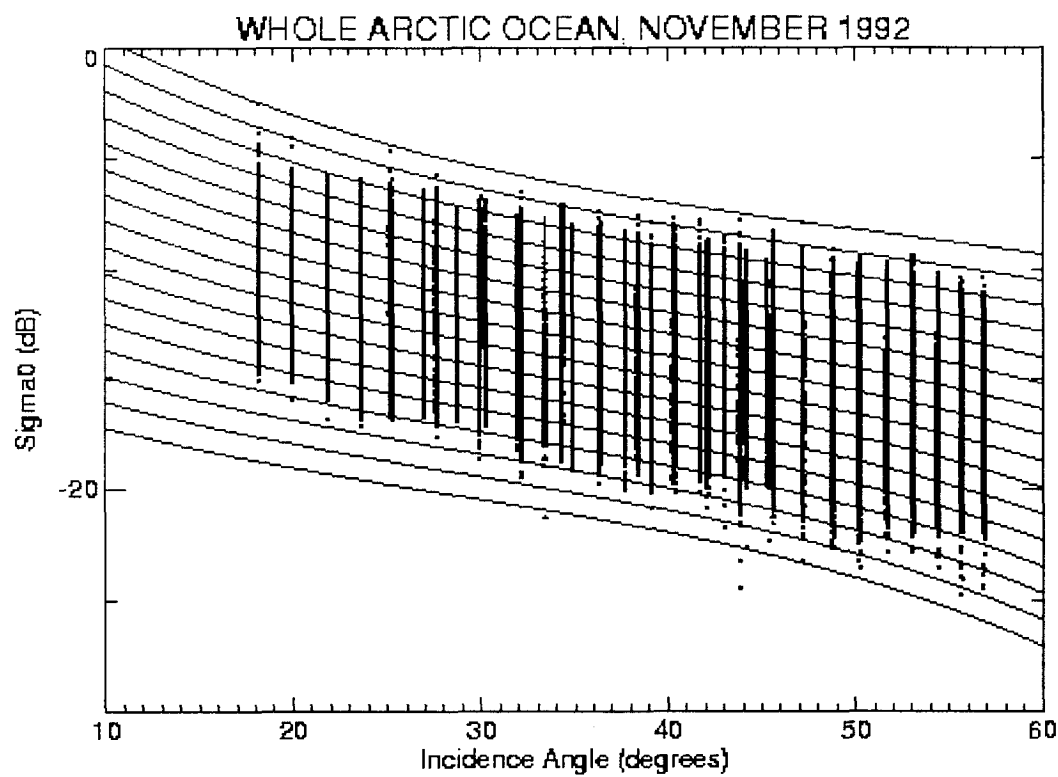


Fig. 1.b

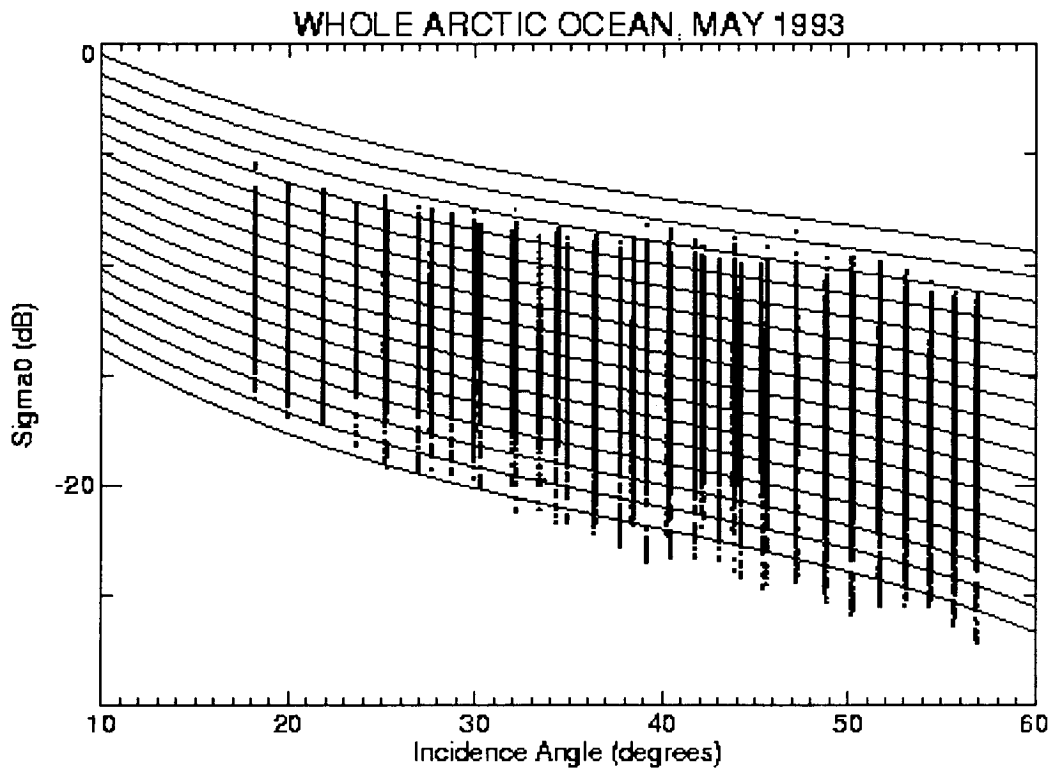


Fig. 1.c

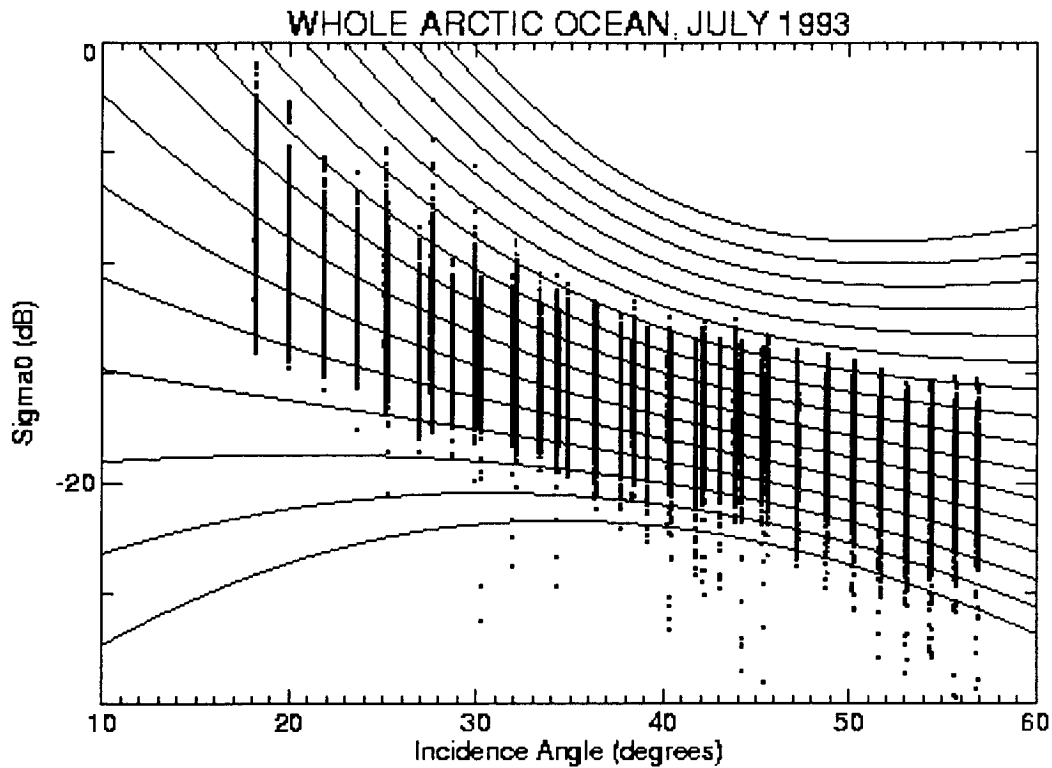


Fig. 1.d

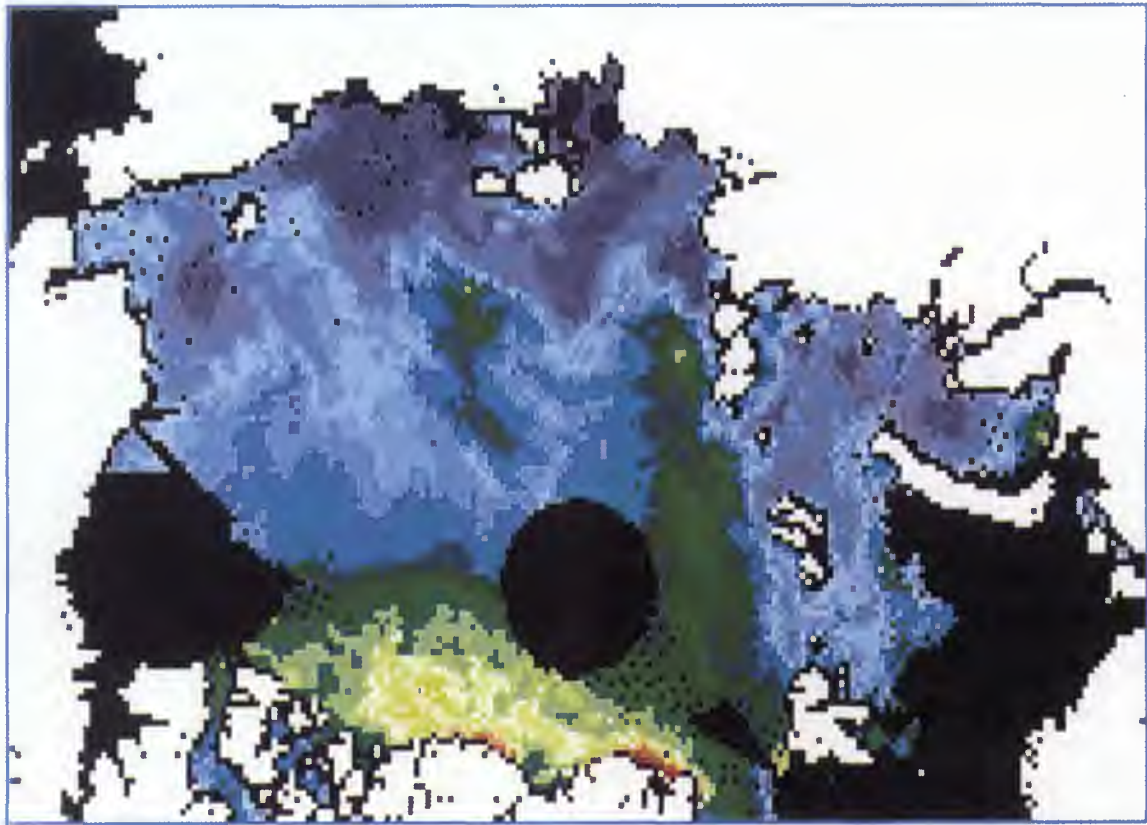


Plate 1.a Backscatter at 40° in March 1993

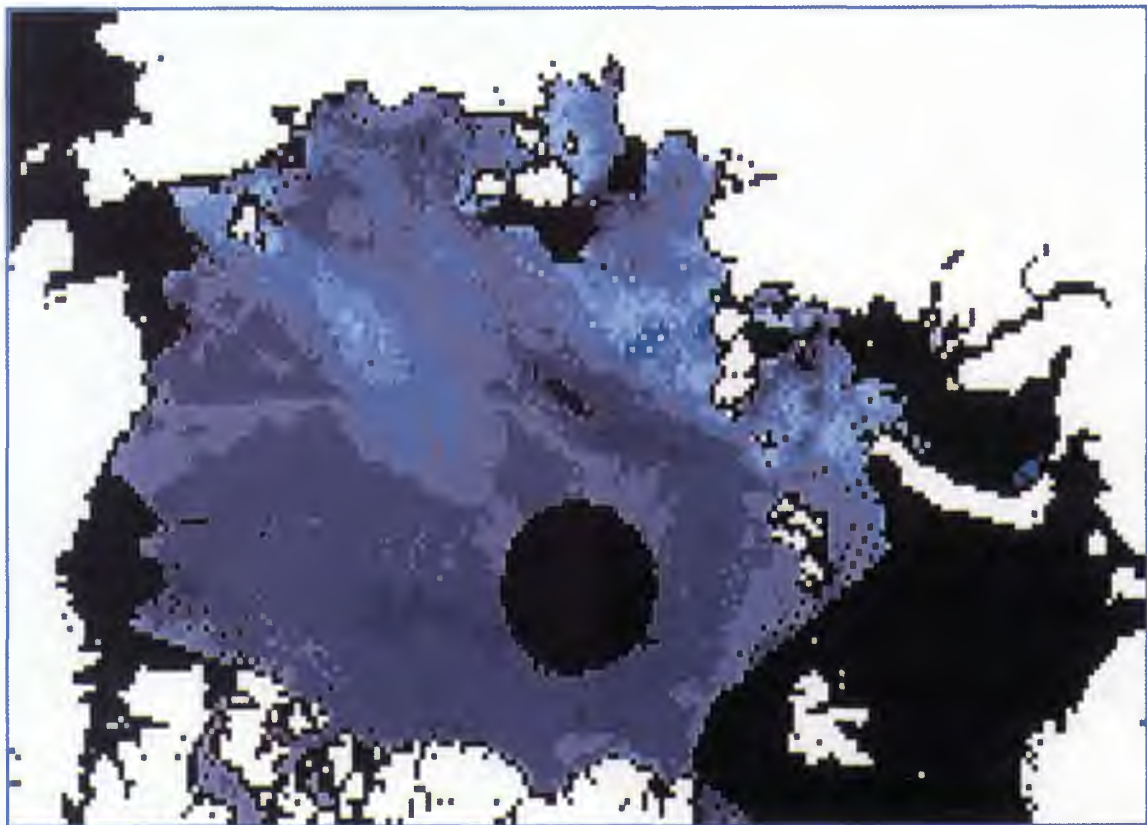


Plate 1.b Backscatter at 40° in July 1993

TABLE 3

Month	Number of Pixels	(Mean Value)*10 ³	(Std Deviation)* 10 ³
September	5800	2.937	8.8887
November	8347	0.7732	6.4854
January	7760	0.4368	4.2614
March	7852	-0.08539	4.937
May	7982	0.03032	4.391
July	7891	-0.3938	4.994

However, the empirical backscatter model explicitly assumes that to a given σ_{40}° value corresponds only one type of ice. This is not always the case; as seen on the maps, first year ice near the ice edge, modified by wave action, has σ_{40}° values quite similar to those of the ice of the transition zone between first and second year ice, deep within the pack. The same phenomenon was already observed in the Antarctic ocean in another context [4], using the maps of backscatter at 40° produced by the CERSAT. By chance, these different ice types can be distinguished by their different geographical positions and the presence of inner pack first year ice.

ESTIMATION OF THE STANDARD DEVIATION OF ESTIMATED σ_{40}°

From the triplet of backscatter and incidence angle measurements made by the AMI Wind for a given node, three independent estimations of σ_{40}° can be made using Equation (2). The standard error of these individual estimated, $s(\sigma_{40}^{\circ})$, can be experimentally evaluated using the following equation :

$$s(\sigma_{40}^{\circ}) = \sqrt{\sum_1^3 [\sigma_{40}^{\circ}(i) - \sigma^{\circ}]^2 / 2}$$

where $\sigma_{40}^{\circ}(i)$ are the three individual estimations of σ_{40}° obtained from a given measurement triplet, and σ° the average value of the $\sigma_{40}^{\circ}(i)$. The division by 2, instead of 3, is made to compensate for the fact that the average value, and not the expectancy, of the $\sigma_{40}^{\circ}(i)$ is used in the equation. For Equation (5) to furnish a reasonable estimate of $S(\sigma_{40}^{\circ})$, the bias and standard error of the three $\sigma_{40}^{\circ}(i)$ must be similar.

Table 4 gives the experimental mean and standard deviation of $S(\sigma_{40}^{\circ})$, for the six periods of measurement, estimated from 60000 backscatter triplets. From this table, taking the mean value plus twice the standard error as a reasonable upper value, it can be estimated that the individual estimations of σ_{40}° will in general have a standard error less than one decibel. Since three independent estimations are made at each geographical position, their average will have a standard error around one half decibel.

TABLE 4

MONTH	SEPT.	NOV.	JAN.	MARCH	MAY	JULY
Mean $s(\sigma_{40}^{\circ})$	0.3007	0.2503	0.2440	0.2571	0.2390	0.4093
Std.Error $s(\sigma_{40}^{\circ})$	0.3384	0.3103	0.2523	0.2854	0.2569	0.3170

The highest values of the geographical distribution of $s(\sigma_{40}^{\circ})$ occur at the ice edge. High values, say beyond 1.5, which are regrouped in small clusters, are probably areas of low ice concentration, undetected by the CERSAT open water mask. As expected from results presented in Table 4, the July map shows the highest values of $s(\sigma_{40}^{\circ})$. This period is one of rapid change, to which the method applied to define the backscatter model is probably less well adapted.

CONCLUSIONS

Because the AMI Wind offers backscatter measurements over the same geographical areas but at notably different incidence angles, and because sea ice backscatter for large footprint sizes is isotropic in azimuth, it was possible to derive an empirical relationship between backscatter and incidence angle to a good approximation. It is clear that, because of a seasonal evolution of the ice behaviour, the coefficients of the model must be refreshed regularly, perhaps on a weekly basis outside of the period of thaw,

during which the model parameters certainly change very rapidly. Except during the summer period, backscatter in decibels at C band appears as having an almost linear relationship to incidence angle for a given ice type, but the slope of the relationship varies with ice type, described in the model only by its value of backscatter at 40° incidence angle.

The present work is directed especially towards ASCAT, whose two swaths and 25 km resolution mode will make near-real time use of scatterometer data to monitor sea ice a real possibility. Unlike other methods presently employed, the use of an empirical ice backscatter model allows the data of a previously uncovered zone to be immediately transcribed into σ° values at 40°, or any other incidence angle chosen within a reasonable range. Moreover, the possibility of employing the standard error of the σ_{40}° , $s(\sigma_{40}^{\circ})$, to furnish an ice mask, or more modestly, to contribute in part to it, appears promising from results

already obtained; however, this question should be investigated further, since ASCAT's range of incidence angles will be somewhat different from that of the AMI-Wind.

The general technique is of course applicable to scatterometers in other frequency bands, and might therefore be of some interest for NSCAT data at Ku band. This could prove useful for a better interpretation of Quikscat or SeaWinds data over sea ice, since these instruments make their measurements at only two incidence angles.

Moreover, the approach taken to construct an empirical backscatter model could be extended to land ice applications, in such regions where the hypothesis of isotropy in azimuth of backscatter can be justified or anisotropy corrected for, in the case of gently sloping terrain.

BIBLIOGRAPHY

- [1] Cavanié A., F. Gohin, Y. Quilfen and P. Lecomte, Identification of sea ice zones using the AMI-Wind : Physical bases and applications to the FDP and CERSAT processing chains, in *Procs. Second ERS-1 Symposium, Space at the Service of our Environment*, Hamburg, Germany, 11-14 October 1993. ESA. SP 361, Vol. II, 1009-1012, 1994
- [2] CERSAT, Off-line Wind Scatterometer ERS Products, CERSAT C2-MUT-W-01-IF, Version 2.0, 1996
- [3] CERSAT, Scatterometer Polar Ice Grids User Manual, CERSAT C2-MUT-W-03-IF, 1996
- [4] F. Gohin, Some Active and Passive Microwave Signatures of Antarctic Sea ice from mid-winter to spring 1991, *Int. J. Remote Sensing*, Vol. 16, N0.11, 2031-254, 1995

POSSIBILITIES FOR A SYNERGETIC USE OF COARSE RESOLUTION ACTIVE AND PASSIVE MICROWAVES FOR SEA ICE RETRIEVALS

J. Grandell

Finnish Geodetic Institute, Geodeetinrinne 2, FIN-02430 Masala, Finland
tel: +358-40-548 3858 fax: +358-9-295 55 200 email: Jochen.Grandell@fgi.fi

ABSTRACT

The complementary use of ERS-1 Wind Scatterometer and SSM/I radiometer data for sea ice retrievals is investigated, due to the apparent deficiencies while employing these data separately. The widely used SSM/I NASA Team algorithm was selected to complement a more recently developed scatterometer algorithm. One of the main differences of the two data sources comes from their sensitivity to atmospheric effects. The relatively high-frequency SSM/I (19-85 GHz) is more sensitive to seasonal changes in atmospheric transmissivities, while the scatterometer, operating at 5.3 GHz is more capable to filter these effects. Therefore, especially mixed pixel estimates, e.g. around ice edges or polynyas, could be enhanced by the use of both active (ERS-1 AMI Wind Scatterometer) and passive (SSM/I) microwaves. Based on the results obtained, a synergetic algorithm for the ERS-1 AMI Wind Scatterometer and the SSM/I is introduced. This synergetic algorithm is then applied over the whole Northern Hemisphere for a global perspective.

Keywords: Scatterometry, radiometry, sea ice, synergy

1. INTRODUCTION

The most usual methodology currently in active and passive microwave remote sensing for sea ice retrievals is to treat the various data sources separately. In addition, there is generally no (or only limited) ground truth data available to assist in evaluating the achieved retrieval results. This is especially true for the wide Arctic and Antarctic study areas. Therefore, it is generally considered acceptable to use another spaceborne data source for reference in sea ice studies. The use of these data sources in a synergetic way has, however, only been briefly investigated so far. Synergy has been successfully attempted by e.g. Beaven et al. (Ref. 1). By fusion of ERS-1 Synthetic Aperture Radar (SAR) and SSM/I microwave radiometer data they managed to improve the ice type concentration estimates, as multiyear ice is generally misclassified as first-year ice during melt and freeze-up periods by the SSM/I NASA Team algorithm.

2. DATA AND STUDY AREA

2.1 Data

Data from the Special Sensor Microwave Imager (SSM/I), a microwave radiometer operating between 19 and 85 GHz, was employed mainly as reference data, due to the relatively well known characteristics of the instrument. The first continuous source of spaceborne scatterometer data became available with the launch of ERS-1, which its three-beam AMI wind scatterometer. Based on this, a study period from 1992 to 1996 was established.

2.2 Study area

Two smaller study areas were selected in the Greenland Sea and the East Siberian Sea for the initial scatterometer algorithm development (see Figure 1). However, for the synergetic method demonstration, a global perspective was sought, and the full circumpolar (North and South Pole) areas were selected for this purpose.

Northern Hemisphere with the test sites

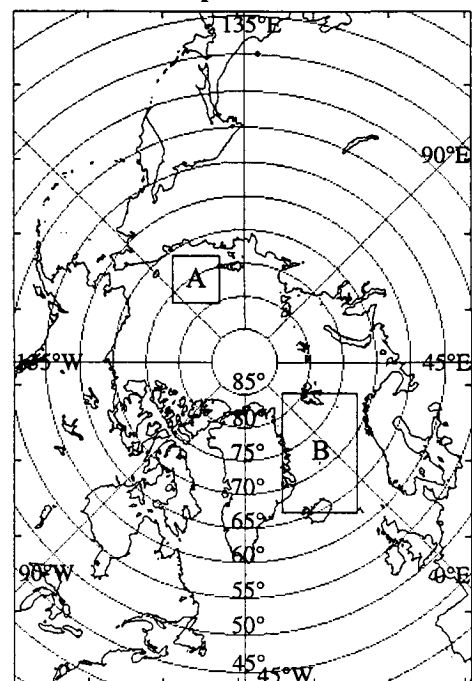


Figure 1. Study areas in the Greenland Sea and East Siberian Sea.

3. ALGORITHMS

3.1 Reference SSM/I NASA Team algorithm

The NASA Team algorithm was originally introduced for the Scanning Multi-Channel Microwave Radiometer (SMMR) which operated on Nimbus-7 from 1978 to 1987 [2]. Since the launch of the first SSM/I radiometer in 1987, it has been applied for use with this instrument, and currently daily sea ice maps are produced by employing the NASA Team algorithm. The algorithm is based on the use of two independent variables, the polarization ratio PR and gradient ratio GR . These variables are defined as [2]:

$$PR = \frac{T_B(19V) - T_B(19H)}{T_B(19V) + T_B(19H)}, \quad (1)$$

$$GR = \frac{T_B(37V) - T_B(19V)}{T_B(37V) + T_B(19V)}. \quad (2)$$

By using these two variables and empirical coefficients derived from algorithm tie points, defined separately for the Northern and Southern Hemispheres, we get the equations for first-year C_F and multiyear C_M sea ice concentrations. A clear disadvantage of the algorithm is the rigidity of these tie points, as they do not adapt to seasonal (annual or diurnal) changes in ice or snow surface conditions.

3.2 Scatterometer algorithm

For distinguishing open water from sea ice, two parameters are used. The first one is the anisotropy index [3], which accounts for the azimuthal behavior of the scatterometer data for a 25 km pixel. The second one is the slope index [4], which uses the incidence angle behavior (for an incidence angle range of 16 to 60 degrees off-nadir) as an indicator of the nature of the target pixel. These parameters are defined as

Anisotropy index:

$$\phi(x, y) = \frac{\sigma^0(\theta)_{\text{fore}} - \sigma^0(\theta)_{\text{aft}}}{\sigma^0(\theta)_{\text{fore}} + \sigma^0(\theta)_{\text{aft}}}, \quad (3)$$

Slope index:

$$SL(\theta) = -\frac{\left\{ \sigma^0(\theta)_{\text{mid}} - \frac{1}{2} [\sigma^0(\theta)_{\text{fore}} + \sigma^0(\theta)_{\text{aft}}] \right\}}{\theta_{\text{mid}} - \frac{1}{2} (\theta_{\text{fore}} + \theta_{\text{aft}})}, \quad (4)$$

where the indexes mid, fore and aft refer to the corresponding beams of the ERS AMI Wind Scatterometer.

Due to the strong ambiguous behavior of these parameters, their use must be combined for a meaningful sea ice retrieval. This ambiguous behavior is more significant in far-range (large incidence angles). Therefore, near-range measurements should be emphasized during analysis, although this may reduce the amount of data significantly [5]. The basic structure of the scatterometer algorithm is shown in Figure 2.

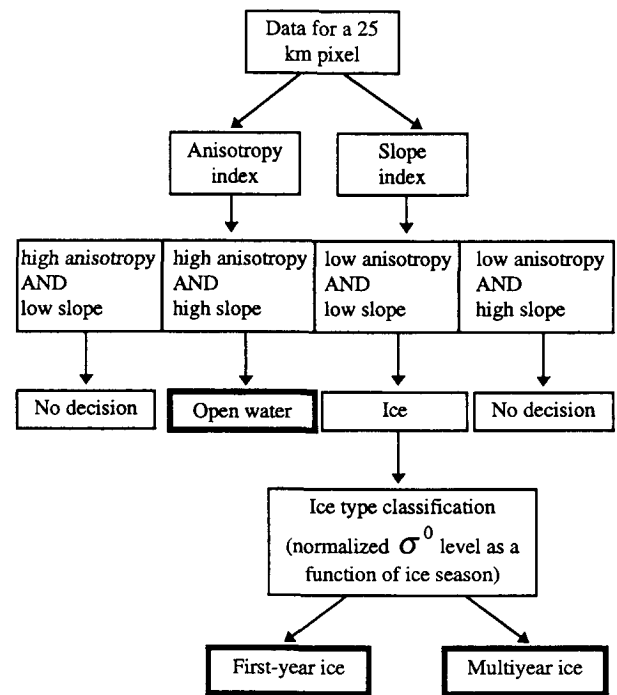


Figure 2. Structure of the ERS-1 Wind Scatterometer algorithm for sea ice detection and classification.

In Figure 3 and Figure 4 histograms of the anisotropy and slope index values in the area surrounding the Antarctic, in May and August, 1995. Two different ice situations are considered, i.e. a case where the SSM/I NASA Team algorithm estimates open water (0% sea ice concentration) and a case of full ice cover (85% or higher sea ice concentration by NASA Team). Only near-range measurements are included (fore-beam incidence angles from 18 to 35 degrees). The histograms clearly demonstrate the ambiguous behavior of the anisotropy index in the selected incidence angle range. However, only a very slight ambiguous behavior can be noticed in the slope index results. It must be noted, though, that even if the anisotropy values show a rather wide spectrum in the open water results in Figure 3, the values are clearly more concentrated in the ice covered results. This justifies the use of the anisotropy index for a classification algorithm, although not as a stand-alone parameter.

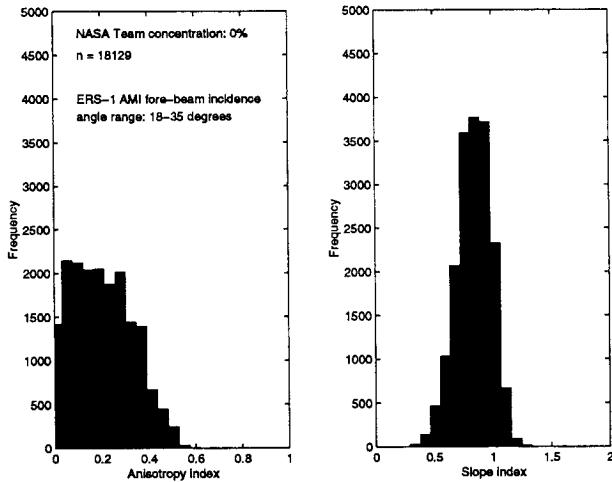


Figure 3. Histogram of the near-range anisotropy and slope index values obtained from ERS-1 AMI wind scatterometer data, when the SSM/I NASA Team algorithm estimates open water (0% sea ice concentration).

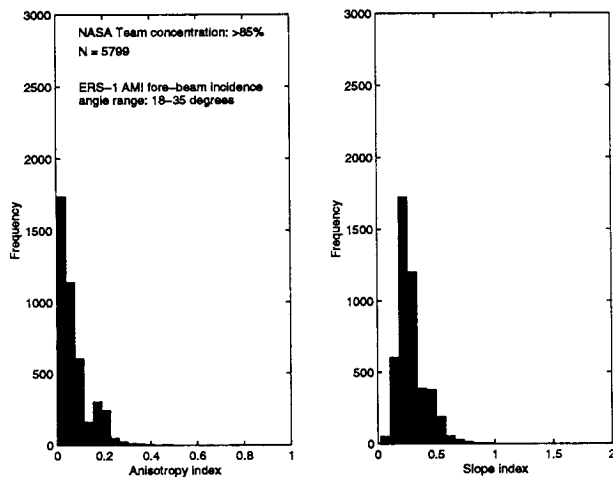


Figure 4. Histogram of the near-range anisotropy and slope index values obtained from ERS-1 AMI wind scatterometer data, when the SSM/I NASA Team algorithm estimates ice (sea ice concentration of 85% or higher).

3.3 Example retrievals

As an example, a comparison is shown Figure 8 of the Scatterometer algorithm and SSM/I NASA Team retrievals in the East Siberian Sea. For this areal coverage study, any pixel with a sea ice concentration of 15% (by the NASA Team algorithm) or higher was classified as being ice covered. This concentration isopleth is obviously not the only choice available, and in addition, a 50% isopleth is used for all comparisons. The use of a higher concentration isopleth reduces the obtained ice coverage, indicating a presence of a large number of mixed pixels in the data set.

All of the five study years (from 1992 to 1996) are shown as individual plots. The results show that in general, the scatterometer and SSM/I algorithm give similar results. However, there are some obvious differences. The scatterometer data points appear to follow the 50% SSM/I isopleth line closer than the 15% isopleth. This is, however, expected due to the classification principle of the scatterometer algorithm with two main classes to distinguish (ice and open water). For example, a pixel with a 49% ice coverage would, in the optimum case, be classified as open water. Another clear difference in the results is evident during spring melt, when the scatterometer seems to detect this behavior sooner than the SSM/I. The data points are too sparse to explore this further, however, but the behavior would suggest that the two instruments differ in observing changes in ice (and snow) structure during melt periods.

A scatter plot is shown in Figure 5 of the ERS-1 AMI Wind Scatterometer ice extent retrievals as a function of corresponding SSM/I NASA Team retrievals. For the SSM/I results, the 50% isopleth has been used to define the ice edge, as the time series comparisons showed it to be a better choice when compared to the 15% isopleth. A clear linear behavior is obvious, and the correlation coefficient (r) is 0.937. The distribution of data values is rather wide, and ranges from approximately 200 000 km² to the maximum value of 640 000 km² (for the 800 km x 800 km test site).

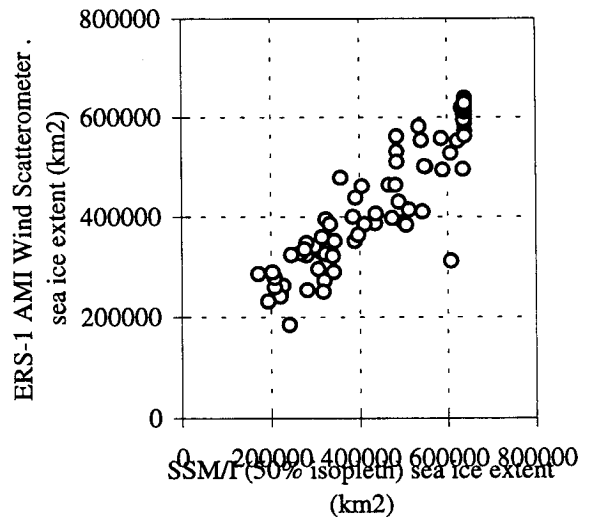


Figure 5. Scattergram showing the retrieved ERS-1 AMI Wind Scatterometer sea ice extent values in the East Siberian Sea test site as a function of corresponding SSM/I sea ice extents obtained by employing the 50% isopleth. The data are from the whole study period from 1992 to 1996.

4. NEED FOR SYNERGY

Both of the individual instruments discussed, i.e. the SSM/I and the ERS-1 AMI wind scatterometer, are suitable for sea ice monitoring. However, there are various advantages and disadvantages in their basic characteristics, for example:

1. The atmospheric effects between the SSM/I and the ERS-1 scatterometer are clearly different, as the former operates in a frequency range from 19 to 85 GHz and the latter in a single frequency of 5.3 GHz. These atmospheric effects are demonstrated by presenting the atmospheric transmissivity profiles in a variety of conditions in Figure 6. The NASA Team algorithm does include a simple weather filter. This filter, however, is only applicable over ice-free ocean surfaces. Over mixed pixels, such as in the marginal ice zone or polynyas, the sea ice retrievals could be enhanced by the use of additional scatterometer data.
2. The scatterometer algorithm employs data from a single-frequency and polarization instrument (ERS-1/2 AMI), although with various incidence angles. If compared to a seven-channel instrument, such as the SSM/I, less retrievable information is thus included in the data. However, a binary classification (ice or water) is an oversimplification of the real ice situation with plenty of mixed pixels present (water and ice) on 25 km scales. Therefore, after eliminating some of the weather related effects in the SSM/I data, as suggested above, the concentration information provided by the SSM/I should be included in the final retrieval product.

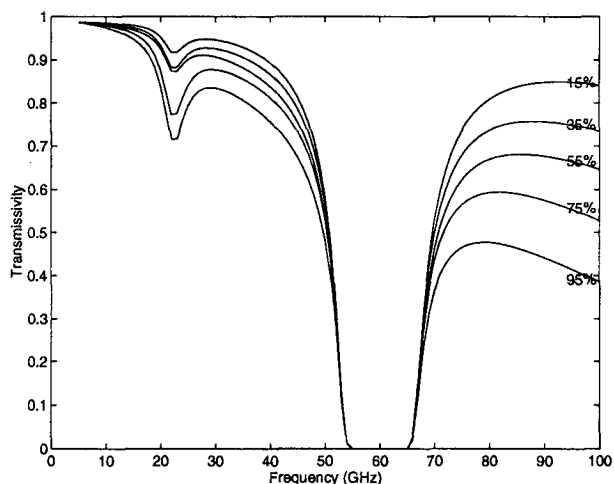


Figure 6. Statistical behavior of the atmospheric transmissivity at 50° angle of incidence. The curves show the percentages of time when the transmissivity exceed a certain value (example data from Finland) [6].

The basic structure of the synergetic algorithm is shown in Figure 7. The algorithm uses both the NASA Team and the scatterometer algorithms in its first stage, which is to determine whether a pixel can be classified as open water. The NASA Team open water classification can be considered to be reliable, if the concentration estimate is 0% due to the evidently successfully filtered weather effects. This will assist the scatterometer open water detection, if the scatterometer algorithm fails due to a poor data coverage, when near-range measurements cannot be emphasized. In special circumstances the synergetic algorithm may employ only SSM/I data for its retrieval: (a) if no scatterometer data is available for a study pixel or (b) if the scatterometer algorithm determines a pixel to be open water, while the NASA Team algorithm shows a sea ice concentration of the pixel to be higher than 85%. This situation is regarded as a failure of the scatterometer algorithm. The mixed pixel atmospheric effects would rarely be severe enough to cause a weather filtered sea ice concentration this high, conflicting with a scatterometer open water retrieval result.

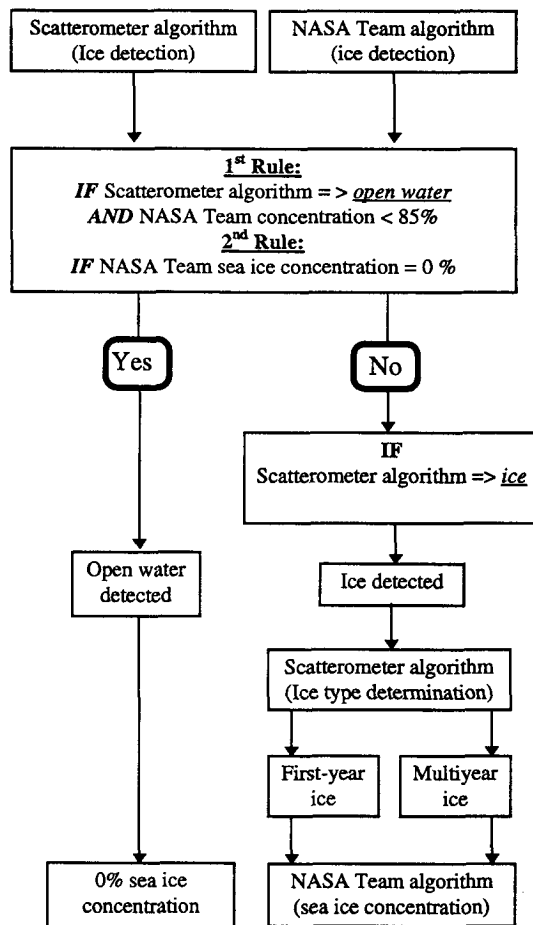


Figure 7. Structure of the synergetic sea ice algorithm for the SSM/I radiometer and the ERS Wind Scatterometer.

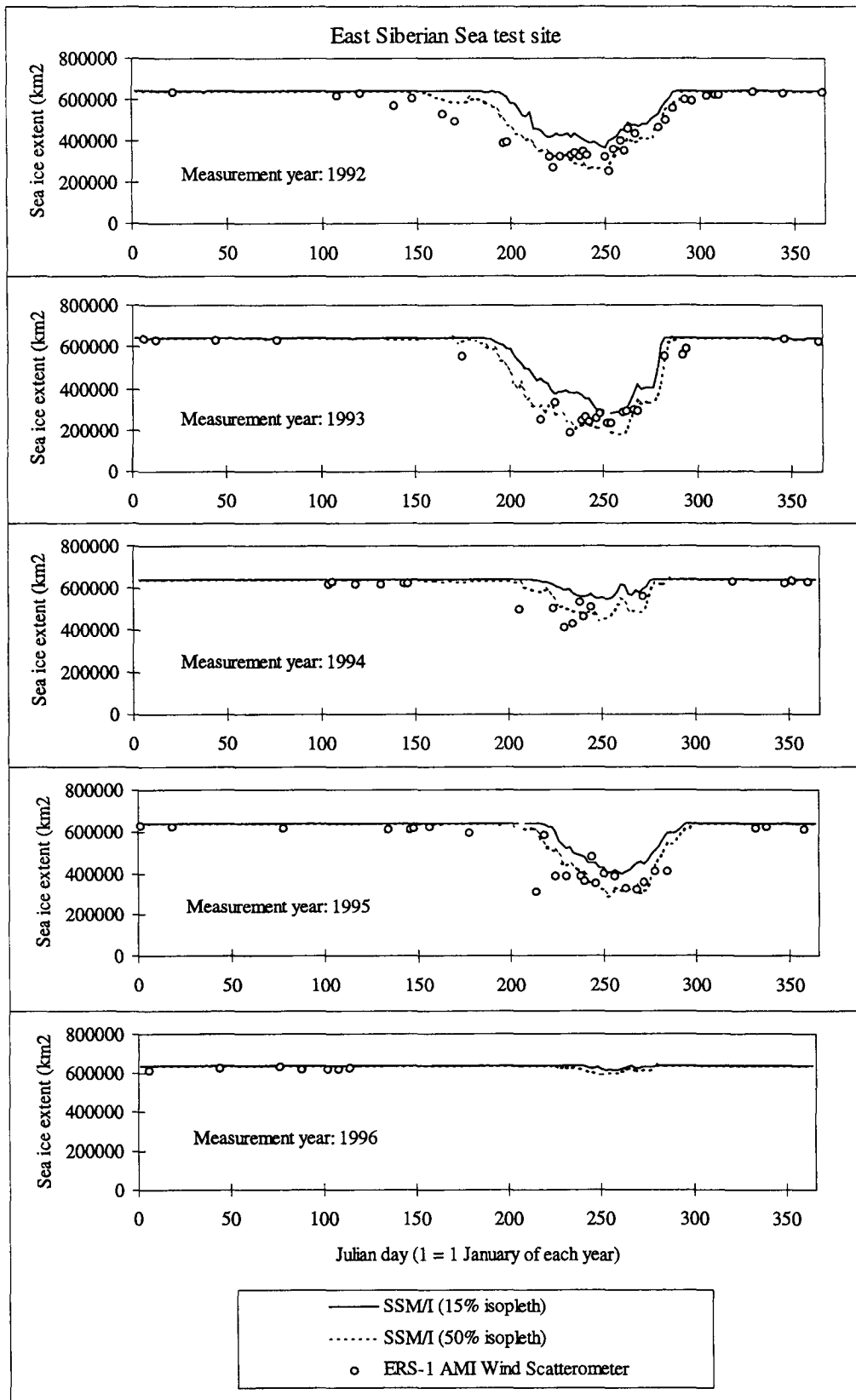


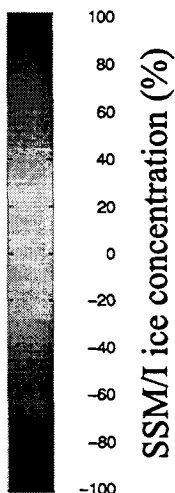
Figure 8. Time series sea ice extent results from 1992 to 1996 for the East Siberian Sea test site. For each measurement year, two SSM/I results are shown (15% and 50% isopleth used to define the ice edge). Due to the relatively poor ERS-1 AMI Wind Scatterometer data coverage, only discrete sea ice extent values are shown for the scatterometer results.

Example of a Synergetic SSM/I and ERS-1 AMI Sea Ice Retrieval (Northern Hemisphere, March 1995)

NASA Team (SSM/I)
sea ice concentration



Scatterometer algorithm
(ERS-1 AMI) sea ice retrieval



Synergetic algorithm sea
ice concentration result



Synergetic algorithm
classification result



Ice concentration = 0...100%
Land = -50
Missing data = -100%

dark brown = first-year ice
light brown = multiyear ice
green = water
blue = land or missing data

Figure 9. Example of a retrieval result in the Northern Hemisphere in March 1995 by employing the synergetic sea ice retrieval algorithm (ERS-1 Wind Scatterometer and SSM/I NASA Team algorithms).

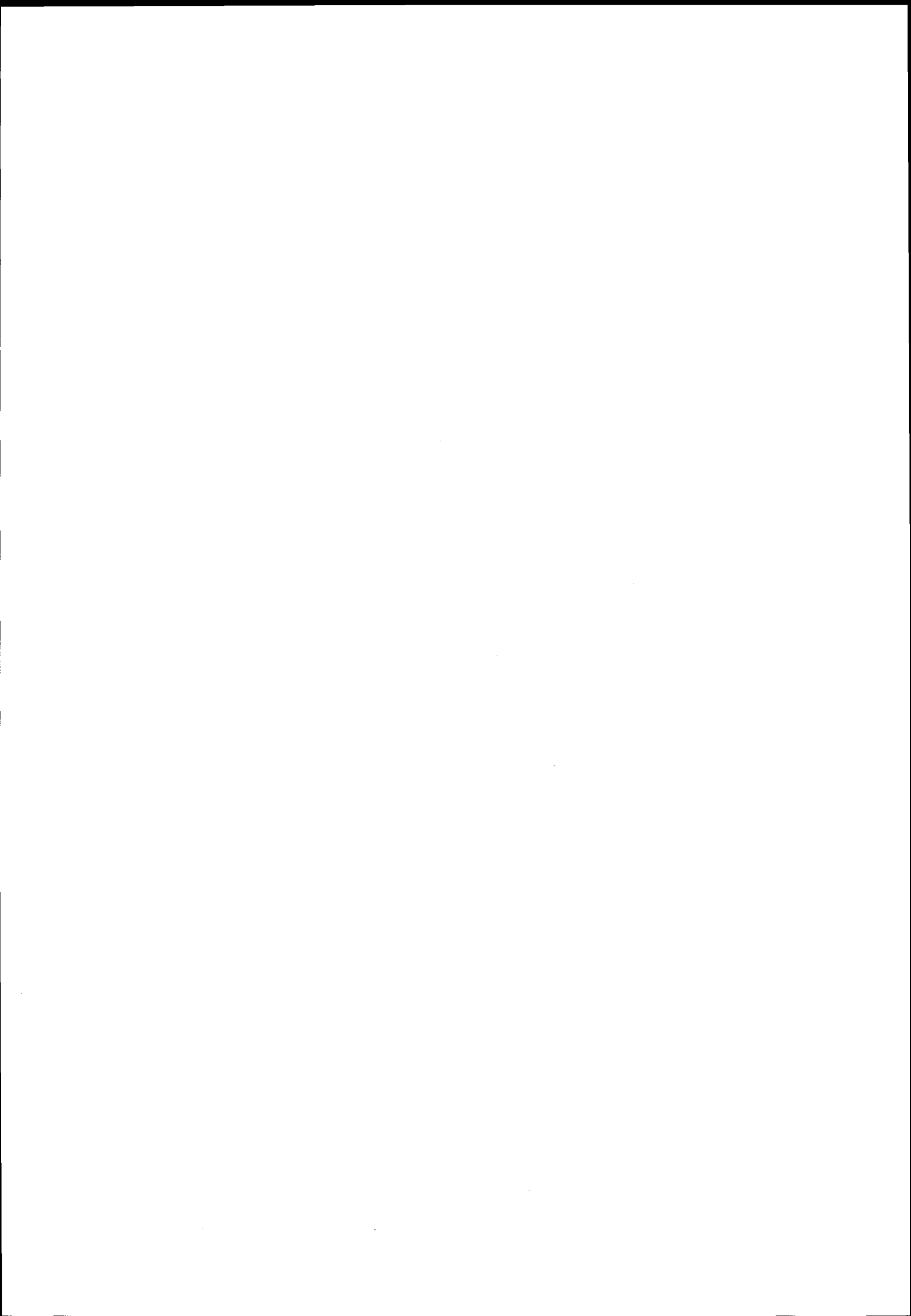
5. RESULTS AND DISCUSSION

In Figure 9 we show an example of the retrieval results of the synergetic algorithm. The example is for Northern Hemisphere measurements in March, 1995. The following advantages of the synergetic algorithm can be summarized, based on experiences from their individual use the synergetic example [5]:

- Complementary data sources, mainly beneficial for the scatterometer with more missing data (due to ERS-1/2 operational characteristics).
- Obvious atmospheric disturbances of the SSM/I filtered out by the scatterometer.
- Ice concentration data provided by the SSM/I NASA Team, not available from the scatterometer algorithm.
- Ice type classification provided by the scatterometer algorithm, as NASA Team classification is known to be inaccurate for certain ice conditions.
- Better detection of polynyas within the ice area, due to less influence to atmospheric effects. This is balanced by the NASA Team algorithm, not allowing open water pixels if the NASA Team ice concentration is higher than 85%.

6. REFERENCES

- [1] Beaven, S., Gogineni, S., Carsey, F., Fusion of satellite active and passive microwave data for sea ice type concentration estimates, *IEEE Trans. Geosci. Remote Sensing*, Vol. 34, No. 5, pp. 1172-1183, 1996.
- [2] Cavalieri, D., Gloersen, P., Campbell, W., Determination of sea ice parameters with the Nimbus-7 SMMR, *J. Geophys. Res.*, vol. 89, no. D4, pp. 5355-5369, 1984.
- [3] Wismann, V., Cavanie, A., Hoekman, D., Boehnke K., and Schmillius, C., Land Surface Observations using the ERS-1 Wind Scatterometer, Final report for ESTEC Contract: 11103/94/NL/CN, 54 pages, 1996.
- [4] Gohin, F., Some active and passive microwave signatures of Antarctic sea ice from midwinter to spring 1991, *Int. J. Remote Sensing*, Vol. 16, No. 11, pp. 2031-2054, 1995.
- [5] Grandell, J., Johannessen, J., Hallikainen, M., Development of a synergetic sea ice retrieval method for the ERS-1 AMI wind scatterometer and SSM/I radiometer, *IEEE Trans. Geosci. Remote Sensing*, in press, 1998.
- [6] Pulliainen, J., Kärnä, J-P., Hallikainen M., Development of geophysical retrieval algorithms for the MIMR, *IEEE Trans. Geosci. Remote Sensing*, Vol. 31, No. 1, pp. 268-277, 1993.



Scatterometer Data for SAF Sea Ice Products

Lars-Anders Breivik and Harald Schyberg

Norwegian Meteorological Institute, Oslo

P.O.Box 43 Blindern

N-0313 Oslo, Norway

l.a.breivik@dnmi.no

ABSTRACT

The *EUMETSAT Ocean and Sea Ice SAF* Sea Ice product will be based on information from available satellite measurements: the radiometer instruments AVHRR and SSM/I and the wind scatterometer. To combine information from the different sensors an inverse method based on a Bayesian approach will be used. Beside the satellite measurements pre-information on the uncertainty involved are needed. Based on this an ice probability will be calculated daily for each grid point in a 10 km resolution grid. The actual resolution will be dependent on the available observations. The method is demonstrated by use of parameters from ERS-2 scatterometer data.

1. INTRODUCTION

Parts of the EUMETSAT (European Meteorological Satellite organization) satellite ground segments will within year 2002 be distributed to several Satellite Application Facilities, SAFs located and co-sponsored by national meteorological centres. A SAF dedicated to satellite derived Ocean and Sea Ice products is under development coordinated by Meteo France. As a part of this the Norwegian Meteorological Institute, DNMI, the Danish and the Swedish Meteorological Institutes are responsible for development of the High Latitude Products. This work is coordinated by DNMI. The input data will be from polar orbiting satellites received locally or through international meteorological networks. The aim is to produce gridded products with 10 km horizontal resolution daily or twice daily. The products will be Sea Surface Temperature, Radiative Fluxes and Sea Ice. The users targeted by the SAF are mainly meteorological and oceanographical centres needing comprehensive information on the ocean/atmosphere interface for modelling purposes. This means National Meteorological / Numerical Weather Prediction Centres, Ocean Modelling centres, Polar Research centres and other users as offshore industry, navigation, research, etc.

This paper describe the method designed for the SAF multi-sensor sea ice product with emphasis on use of scatterometer data. The product will contain: ice edge, estimations of ice cover and ice type that distinguish between multi year and first year ice. The objective of horizontal resolution is 10 km, and the product will be provided once per day. AVHRR, Advanced Very High Resolution Radiometer, today onboard the NOAA satellites and planned for next generation European

satellites METOP, is the only instrument that is able to provide information on such resolution. SSM/I, Special Sensor Microwave Imager and scatterometer will provide cloud and precipitation independent ice information of from 15 to 50 km resolution, however overlapping observations will make enhancement of the resolution possible.

2. THE MULTI-SENSOR APPROACH

The scientific challenge in making a combined product from the available sensors, AVHRR, SSM/I and scatterometer, is to obtain a single reliable ice product from the various observations involving different, and possibly contradicting, information. For doing this, it is necessary to use an algorithm which takes into account the uncertainties in the ice estimates of the various instruments. It is therefore essential not only with an ice estimate, but also with knowledge of the uncertainty or degree of accuracy involved. For example, there are uncertainties in AVHRR caused by possible cloud contamination, and there are instrumental noise affecting all instruments.

A good general tool for combining various data sources containing uncertain information is given by the Bayesian (inverse method) approach. Using this approach, several measured parameters can be combined to yield an optimal estimate. Combining independent information in this way will enable production of ice maps with much improved temporal and spatial resolution.

The approach is based on knowledge of the averaged relationship between ice properties and the measured quantity together with knowledge of the scatter of the expected measurement value for a given ice type. This knowledge can be expressed as a probability distribution for the measurement variable given the ice type. Assume e.g. that the satellite has measured a parameter A . From calibration data sets we can find the response of this parameter on an ice type I_k in terms of the probability distribution $p(A|I_k)$, the probability of doing an observation near A given that the ice type is I_k . This can be used to obtain an estimate of the probability of the ice type being I_k given the measurement, $p(I_k|A)$. Using Bayes theorem, we have

$$p(I_k|A) = \frac{p(A|I_k)}{\sum_j p(A|I_j) p(I_j)} p(I_k). \quad (1)$$

The summation is performed over all possible, mutually exclusive ice types I_j . Thus, knowing the probability distribution for a measured parameter $p(A|I_j)$ for all possible ice types I_j we have a powerful tool for estimating the probability of each ice type. An estimate of the prior probability for the ice type, $p(I_j)$, is also needed. A simple algorithm for ice edge detection can be made by allowing I to have two values, "ice" and "water". The equation then gives a probability estimate for ice given the measurements. Setting both the prior probabilities for ice and water, $p(\text{ice})$ and $p(\text{water})$ equal to 50%, we get

$$p(\text{ice}|A) = \frac{p(A|\text{ice})}{p(A|\text{ice}) + p(A|\text{water})} \quad (2)$$

This framework can be generalized to a method for combining several satellite measured parameters to an optimal ice property estimate. It must be stressed that the method requires more than just thresholds on the measured parameter indicating an ice class. Such thresholds just give information on the relation between I and the most probable value of A . Here we use the full probability distribution of the measurement given the ice property. The method works in such a way that the measured parameters which the statistics shows to be most secure in distinguishing between ice properties, are the ones that alter the probability. Another advantage is that we not only obtain estimates of the most probable value of the ice parameters, but also the certainty of the estimate.

3. SEA ICE RETRIEVAL FROM WIND SCATTEROMETER DATA

Currently scatterometer data from the European Remote Sensing satellite, ERS-2 is available. As a part of the METOP program data from the Advanced SCATerometer, ASCAT, will be available for ice analysis from 2002. This scatterometer is quite similar to the ERS scatterometer in specifications. Between ERS and ASCAT data from american scatterometers, QuickScatt and Seawinds, are likely to be available. However the instrument configuration is basically different, and the results from ERS can not be directly applied.

The ERS scatterometer is a microwave radar sequentially illuminating the sea surface measuring the backscattered signal. The power of the reflected signal is dependent on the sea surface roughness. Following Cavanie et al. 1994, two properties of the backscattering over ice can be used to derive sea ice information. Firstly, backscattering is relatively isotropic over sea ice compared to the strong anisotropic behaviour, which is the basic for wind direction retrieval, over water. Secondly, the change of backscatter with incidence angle shows larger variation over water than over sea ice. In addition the difference between expected backscatter over water and the measured one can be used. Furthermore, the change of backscatter with incidence angle over sea ice can be linked to ice types and used for sea ice classification.

To distinguish between sea ice and open water an

algorithm, following the multi sensor approach, has been developed combining the three ice detection parameters suggested by IFREMER:

- Backscatter isotropy / anisotropy, A
- Distance of observation from scatterometer wind model result, C
- Derivative of backscatter with respect to incidence angle, D

From collocation with data from DNMI's operational ice service, which is based on manual interpretation on AVHRR data, SSM/I data and previous analysis, we have obtained datasets of A , D and C over different areas known to be ice and known to be water. The datasets were sorted according to incidence angle, and it turned out that the 3 parameters are complementary as regards swath coverage. This gave the probability distributions (PDFs): $p(A|\text{ice})$, $p(D|\text{ice})$, $p(C|\text{ice})$ and $p(A|\text{water})$, $p(D|\text{water})$, $p(C|\text{water})$ for 19 incidence angles corresponding to the 19 nodes across the ERS-2 scatterometer ground track.

If we assume that these events are independent we have, $p(A, D, C|\text{ice}) = p(A|\text{ice})p(D|\text{ice})p(C|\text{ice})$, and similarly for water.

An estimate of ice probability given the scatt measurement is then found by using *Bayes theorem*:

$$p(\text{ice}|A, D, C) = \frac{p(A, D, C|\text{ice})}{p(A, D, C|\text{ice})p(\text{ice}) + p(A, D, C|\text{water})p(\text{water})} p(\text{ice}) \quad (3)$$

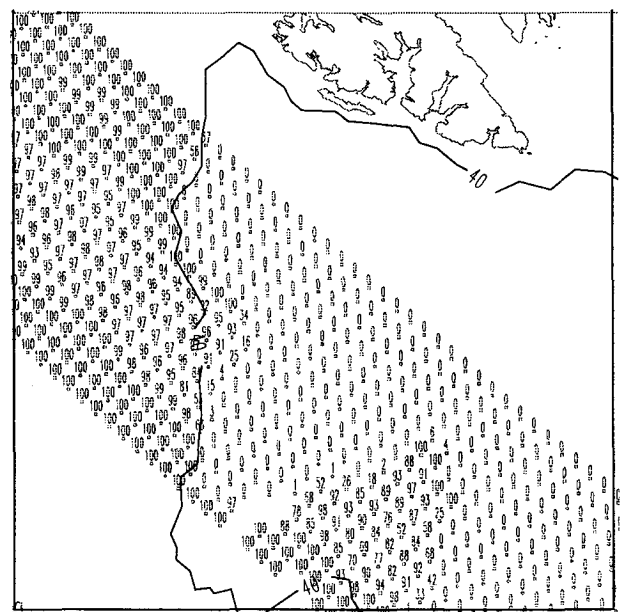


Figure 1: Scatterometer ice probability estimates south of Svalbard 17 February 1998. Solid line: Ice edge from DNMI operational sea ice service.

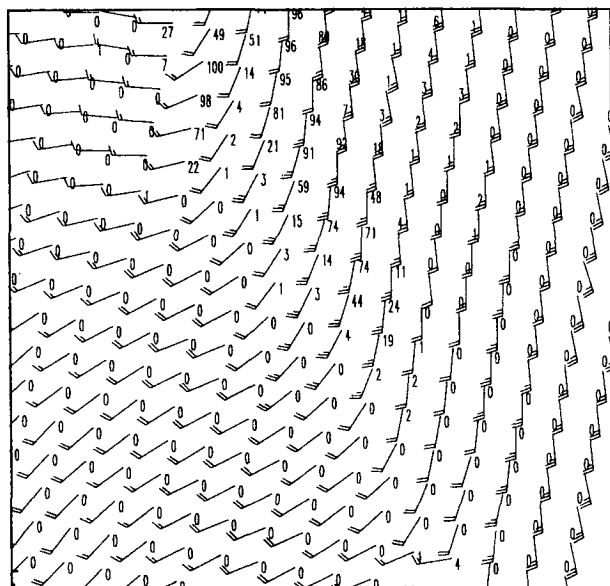


Figure 2: Scatterometer wind vectors and ice probabilities in a non-ice area with wind parallel to the satellite ground track.

In the shown example in Fig. 1 prior probabilities $p(\text{ice})$ and $p(\text{water})$ are both assumed to be 50%. The probability distribution functions are assumed to be Gaussian. Generally there is a good agreement between the ice edge from DNMI's operational ice service and the scatterometer observations.

In cases where the wind blows along the satellite ground track the sea surface will seem isotropic also over open water. The use of the anisotropic coefficient might then lead to wrong conclusions as shown in the example on Fig. 2. This is a case from the sea west of Ireland where there obviously are no sea ice. Scatterometer based ice probabilities are plotted together with scatterometer wind vectors. It is seen that in an area with strong wind, and wind direction along the satellite ground track, the ice probabilities reach up to 100%. Wind information from a background NWP model can be used to derive wind direction dependent PDFs over water. This might help in solving the along track wind problem.

4. SEA ICE ANALYSIS

An analysis algorithm to produce a grided multi-sensor product has been developed. The ice probabilities for each grid point are calculated on basis of all single observations covering that grid point within a time period using the above described approach. To avoid smoothing of the information no spatial interpolation between observation points and grid points are performed. The example in Fig. 3 shows iso-lines of ice probability from a 10 km resolution analysis of three days of ERS-2 scatterometer observations. Before the analysis probabilities in all grid points are equal 50% which explain the isolines along the coast and in areas with no observations. Detailed structures are seen indicating resolution enhancement achieved by using several overlapping passages of satellite data. The inclusion of

SSM/I and AVHRR data, as well as increased number of scatterometer data provided by ASCAT (METOP), is expected to give enough information for a 10 km product on a daily basis.

One month of scatterometer data from the winter 1998 have also been collocated with ice-type analysis from DNMI's operational sea ice service to obtain datasets of A , D and C over different areas known to be first year ice, FY, and known to be multi year ice, MY. This gives us the probability distributions (PDFs): $P(A,D,C | \text{FY})$ and $P(A,D,C | \text{MY})$. Using this in the framework described above, an ice-type analysis has been performed in two steps.

- 1) ice/water analysis as in the previous example
- 2) ice-type analysis on ice covered areas

The results presented on Fig. 4 are, as in the previous example, based on three days of scatterometer data, 15-17 February 1998. Multi year ice is plotted black, while first year is plotted light grey. The results are in good agreement with the operational ice analysis.

5. CONCLUSIONS

The aim of the SAF Sea Ice product development is an operational production chain for a daily sea ice analyse on a 10 km resolution grid. The scientific challenge lies in making this on basis of information from very different sensors, the passive and the active microwave sensors and the optical sensors with variations in resolution as well as in geophysical and instrumental uncertainties. In the SAF this analysis will be done by using the Bayesian approach. Pre-knowledge of probability distributions of measured quantities given ice properties are used to design weights for the analysis. The final Sea Ice analysis will be the optimal result with the given information. Beside the ice parameters the analysis shall include estimates of the uncertainty involved. The method has been tested, and work well for scatterometer data from ERS-2. Work is ongoing to integrate SSM/I and AVHRR observations in the analysis. For scatterometer data possible better parameters that include the wind speed dependence over open water and the incidence angle dependency direct into the PDFs may also be investigated.

REFERENCES

- Cavanie, A., F. Gohin, Y. Quilfen and P. Lecomte, 1994, Identification of Sea Ice Zones using the AMI Wind: Physical Bases and Applications to the FDP and CERSAT Processing Chains. In: Proceedings Second ERS-1 Symposium, Hamburg 11 - 14 October 1993.

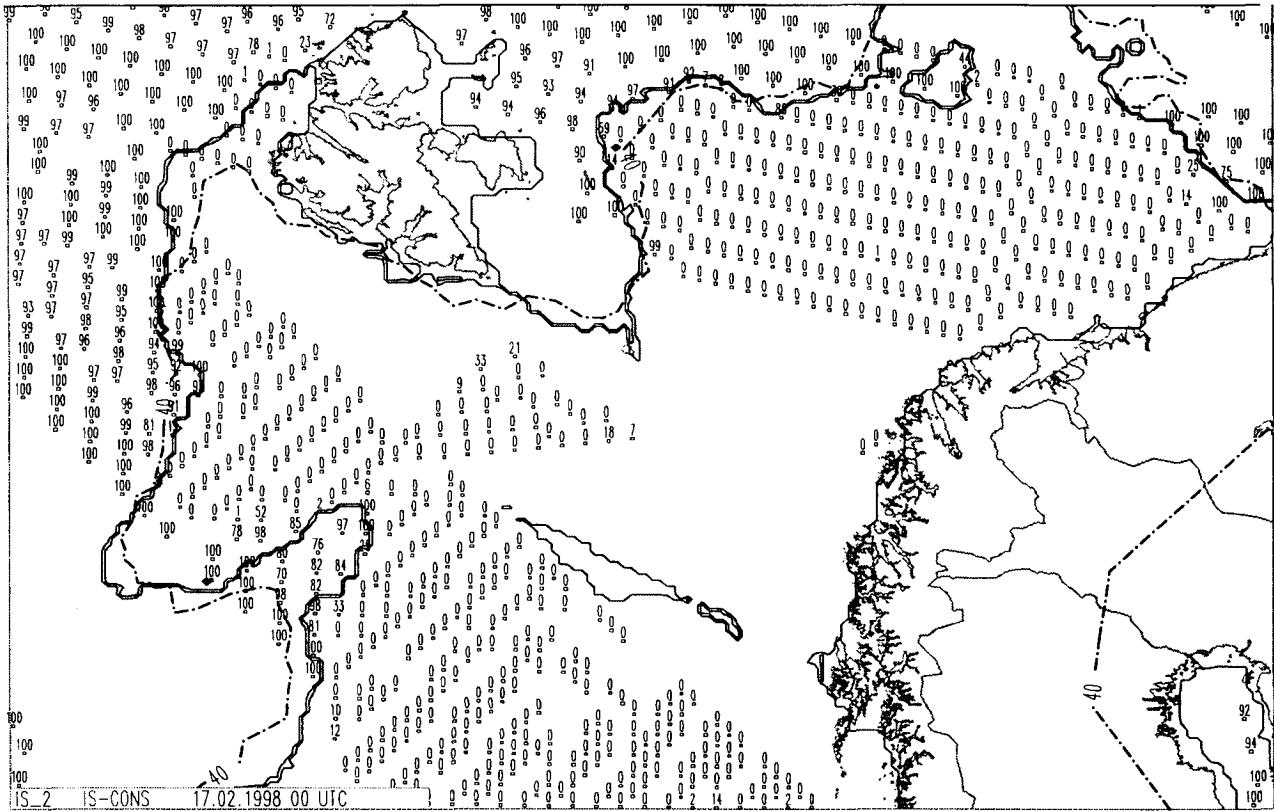


Figure 3: Solid lines: Iso-lines for ice probability based on 3 days of ERS-2 scatterometer data, 15-17 February 1998. Broken line: Ice edge from the operational sea ice analysis valid 17 February. Plotted numbers are ice probabilities in scatterometer observation points from 17 February.

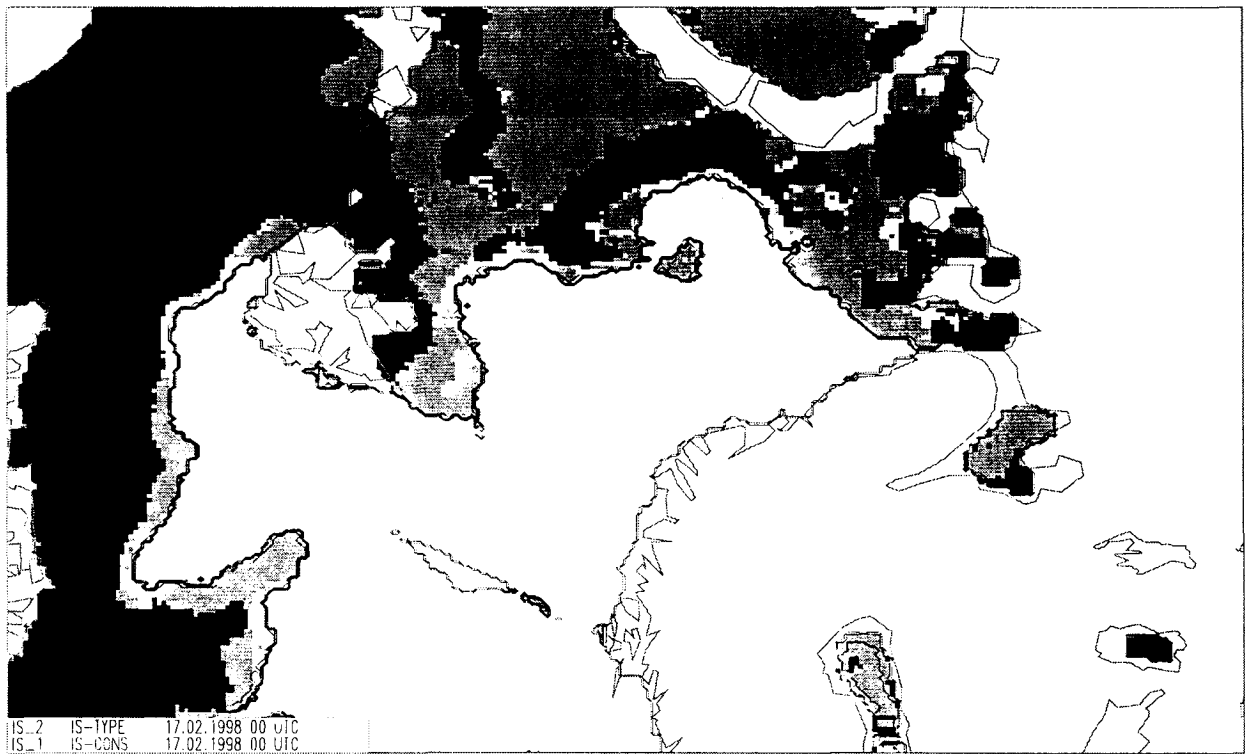


Figure 4: Areas with first year, gray, and multi year, black, ice cover. The analysis are based on 3 days of ERS-2 scatterometer data, 15-17 February 1998. Solid lines are iso-lines for ice probabilities as in Fig. 3.

INTERANNUAL VARIABILITY IN WEDDELL SEA ICE FROM ERS WIND SCATTEROMETER

Mark R. Drinkwater*, Peter Wadhams**, Doug Low** and Xiang Liu*

*Jet Propulsion Laboratory, California Institute of Technology
4800 Oak Grove Drive, CA 91109, USA

**Scott Polar Research Institute, University of Cambridge
Lensfield Rd, Cambridge, CB2 1ER, UK

ABSTRACT

ERS-1/2 SAR and Wind Scatterometer data are analyzed together with DMSP SSM/I microwave radiometer data to investigate interannual variability in Weddell Sea ice and summer melt signatures during the period 1992-1997. Simultaneous SAR and Scatterometer images were obtained during a February 1995 cruise of the H.M.S. *Endurance* and aerial photographs collected for validation of the satellite observations. Accompanying field data are used to illustrate the observed interannual variability, and to validate the first ever field observations of extensive summer melt ponding in the Weddell Sea, Antarctica. A preliminary algorithm is designed to detect the occurrence of melting in the Weddell Sea, and the date upon which the surface begins to melt. In contrast to melt, conspicuous, anomalous summer increases in sea-ice backscatter reveal a process unique to Antarctic sea ice, involving surface flooding of perennial ice floes and upward meteoric ice growth. Time series data indicate that flooding is particularly widespread, and that subsequent freeze-up in these regions potentially contributes a significant volume of sea ice to the total mass budget of the Weddell Sea.

1. INTRODUCTION

Fundamental differences exist between the Antarctic and Arctic when it comes to spatial and temporal variability in sea-ice conditions in response to seasonal atmospheric and oceanographic forcing. In summer, the Arctic remains largely covered by multiyear ice, surviving each summer melt period by way of its thickness, to accrue incrementally more thickness in winter. Antarctica has no perennial ice counterpart, and for the most part non-landfast sea ice reaches an age of only second-year ice before drifting into high oceanic heat flux regimes and rapidly melting. Sea-ice dynamics regulate the maximum age of the ice cover, particularly in the Weddell and Ross Seas, where the Gyre circulation sweeps sea ice northwards. The relative age and thickness of the residual autumn ice cover is a critical variable to the stability of the upper ocean in these regions, as summer melting helps to freshen and stabilize the mixed layer and together with the residual perennial ice cover prevents complete removal of the summer ice cover.

In the Antarctic, melting largely takes place from beneath the ice, as summer air temperatures rarely rise above 0°C. Consequently, the expression of classical surface melt-ponding has never been observed and the surface retains a snow cover year-round. Conversely, Arctic summer melting results in the expression of melt ponds over up to 60% of the surface as the

snow cover disappears completely. Meltwater infiltrates the warm, porous sea ice, flushing out its salt content to leave it relatively brine-free. The fact that the Antarctic snow cover is retained throughout summer helps to insulate the ice and protect it from temporarily warm air temperatures [Ref. 1]. In perennial sea-ice regions, surface flooding can occur with resulting upward meteoric ice growth occurring during autumnal freeze-up [Ref. 2].

In this paper, we study the combined seasonal effects of sea-ice advection and summer melting upon time-varying microwave signatures extracted from a number of fixed regions in the north-western Weddell Sea. The resulting data set extends from 1992-1997, enabling the long-term mean annual signal to be extracted. The residual interannual anomaly time-series illustrates extreme variations in regional melting and/or sea-ice dynamics.

2. DATA SETS

Several active and passive satellite microwave data sets were combined with field data from the north-western Weddell Sea. Synthetic Aperture Radar (SAR) images (100 × 100 km) and wind scatterometer data were collected by the ERS-1 and 2 spacecraft (hereafter EScat). The latter were processed into images at 3 day intervals [Refs. 3, 4] for the period 1992-97. EScat measured the vv-polarized normalized backscatter coefficient σ_{vv}^0 (dB) along a 500 km-wide swath and the backscatter at a mid-swath incidence-angle of 40° is expressed as A. A number of EScat sample boxes are defined and numbered in the North-western Weddell Sea, in Fig. 1. Additional coincident daily SSM/I data were extracted from these regions and used to confirm melting. Passive microwave brightness temperature (T_b) values approach a blackbody response (*i.e.* close to 273 K) at the melt-point of sea ice.

Pairs of overlapping ERS-1 SAR swath data were acquired on 11 and 14 February (orbits 18704 and 18747), and 12 and 15 February, 1995 and mosaicked. In Fig 1 the descending and ascending strips (dashed) span several hundred kilometer long transects. These crossed the open ocean limit of the marginal ice zone (MIZ) at around 65° S into high concentration (> 95 %) perennial ice south of 67° S.

Coincident field data were acquired between 10-15 February, 1995 from H.M.S. *Endurance* [Ref. 5]. The British Royal Navy icebreaker positioned herself to collect simultaneous *in-situ* data during ERS-1 overpasses. One helicopter facilitated surface data collection while another was equipped for aerial

Weddell Sea/Larsen Ice Shelf ESCAT Data, ERS-1 SAR images overlain

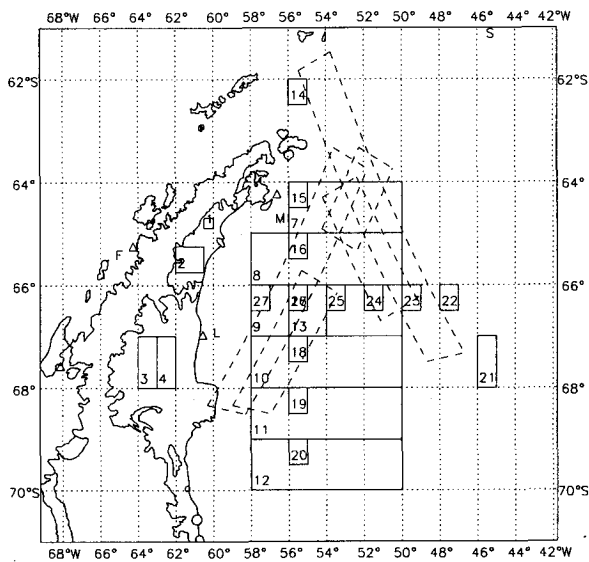


Figure 1. Weddell Sea map indicating numbered sample boxes for ESCAT and SSM/I data, overlapping ERS-1 SAR mosaics (dashed) on 11 and 14 February, 1995, and meteorological stations (triangles) situated at Faraday (F), Marambio (M), and the Larsen Ice Shelf (L).

photography. The 11 and 14th February descending pair of SAR swaths were acquired during local daylight (09:25hrs), thereby enabling detailed air-photo comparisons.

3. SEASONAL TO INTERANNUAL VARIABILITY

Time series microwave signatures extracted from the sea-ice boxes in Fig. 1 show variability indicative of seasonal and annual changes in the characteristics of the snow and ice floe surfaces together with the proportions of ice types advected through each region. To rule out dynamic effects, four control regions (1-4) were investigated on the Larsen Ice Shelf (LIS) in conjunction with meteorological station data. Results from box 3 are shown in Fig. 2. The upper panel indicates a large dynamic range in A values as a result of austral summer melt as far as 68° S. Decreases of -20 dB or more occur during active surface melting, and melting is confirmed by concurrent SSM/I 19 GHz v -polarized T_b values tending to 273 K. The middle panel indicates the 5-year mean annual and filtered cycles, and the lower anomaly cycle is the result of removing the $\%$ -year mean from the record. Clearly, the summers of 1992/93 and 1994/95 were anomalous, each with earlier and more extended melt seasons. These years coincide with events marking rapid disintegration of the northern section of the LIS together with the landfast ice between James Ross Island and the peninsula [Ref. 7]. Also the calving of a spectacular iceberg occurred close to box 2 in early 1995 [Ref. 7].

Variability in ESCAT A values is also investigated in two other regions in Fig. 3. The advection of varying fractions of

seasonal or perennial ice through each box is responsible for the large seasonal amplitude in Fig. 3a and b. Oscillations in A during minimum ice extent in box 15 indicate that wind-roughened open water is not responsible for any values exceeding -15 dB in this box. This is typical in stable summer atmospheric boundary layers in the MIZ. Notably, Fig. 3a shows minima in the summer months. April and May peaks in A are typical of high perennial ice concentrations, and show a gradual decline until October. 1992 and 1995 ice seasons suggest large fluxes of old ice (> -10 dB) through this box [Ref. 3], marking the disintegration of fast ice along local parts of the peninsula. To corroborate this, swarms of large floes of perennial ice with > 1 m deep snow were observed during WWGS '92 [Ref. 6]. Figure 3a also shows abrupt melt onsets in late 1992 and '95, consisting of sudden drops of 5 to 7 dB.

Fig. 3b shows an extremely different signal in southern box 20. Peak A values now occur in austral summer in contrast to box 15 minima. A seasonal decline in A values during winter marks diffusion of residual perennial sea ice and advection of an increasing fraction of seasonal sea ice through this region in response to northwards drift of ice away from the Ronne-Filchner ice shelf polynya [Ref. 3].

The distinctive seasonal cycle and maxima in Fig. 3b characterize 1992 surface-flooding signatures documented during Ice Station Weddell (ISW) [Ref. 2]. Snow-covered perennial ice floes surrounding ISW increased their σ_w values in austral summer as a result of ice-surface flooding beneath the snow. Since air temperatures at this latitude are typically too cold for melting, the snow must insulate the ice sufficiently to become isothermal, by heat supplied from beneath. If the snow cover is deep enough for an isostatic imbalance [Ref. 1] then it may flood with seawater through open brine drainage channels,

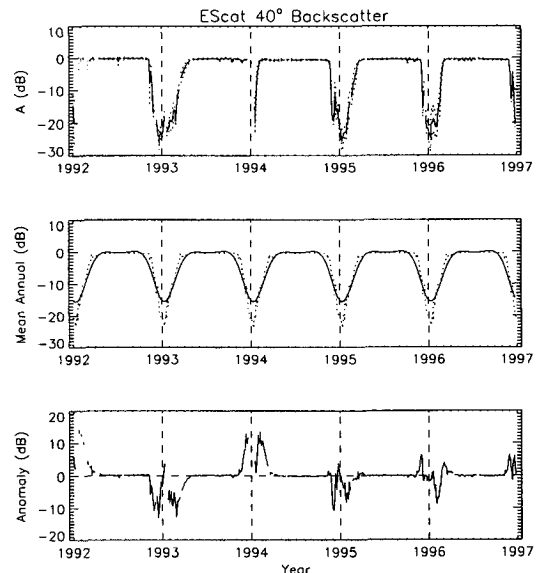


Figure 2. (a) Interannual; (b) mean seasonal cycle; and (c) anomaly time series from the Larsen Ice Shelf (box 3).

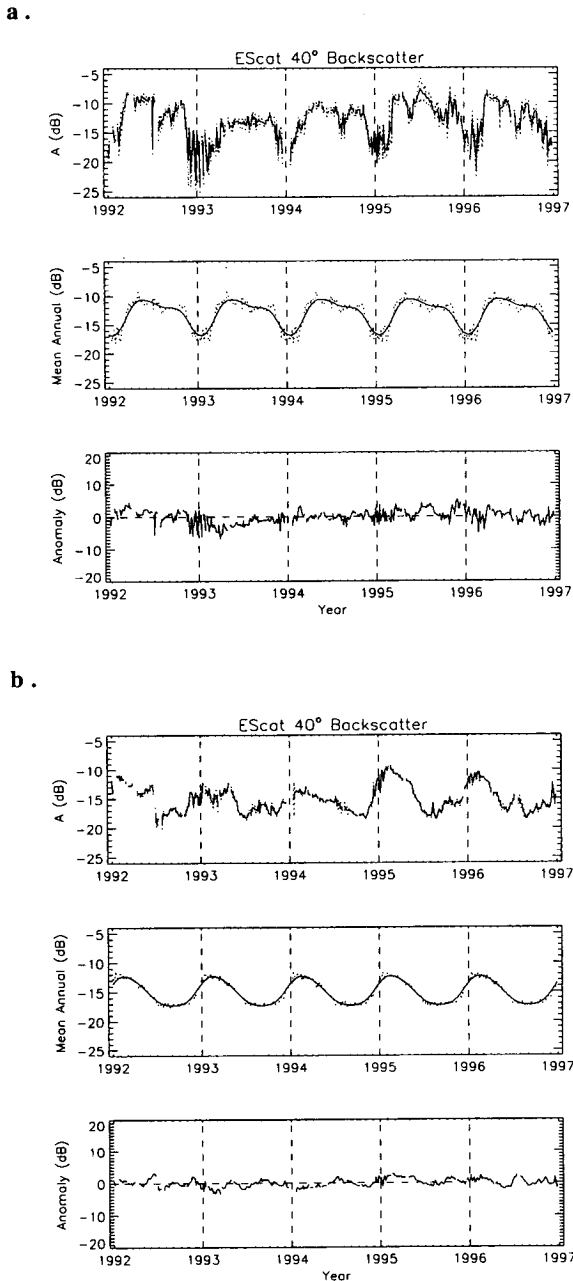


Figure 3. Interannual time series from (a) box 15; and (b) box 20, in the geographic locations of the H.M.S. Endurance Experiment and Ice Station Weddell, respectively.

causing a widespread increase in σ_w^0 [Ref. 2].

4. SUMMER SCATTERING SIGNATURES

In the southernmost boxes, austral summer results in a signal with opposite sense to boxes experiencing direct surface melting. Dramatic reductions in the summer backscatter in

seasonal ice regions can only be associated with the onset of snow-surface melting, particularly in boxes near to the meteorological station Marambio, where air temperatures are well known. SSM/I observations concur by exhibiting blackbody temperatures during periods of warm air temperatures and surface melting.

4.1 Snow Surface Melt and Melt Ponding

Surface melt is demonstrated to have a significant effect upon regional signatures in the north-western Weddell Sea. *In-situ* observations of melting made in February 1995 explain the widespread reduction in A values in box 7, 8, 15, and 16. Fig. 4 shows a 10 km vignette of an ERS-1 SAR scene obtained coincident to aerial photographs made from Endurance (centered on white spots). The photograph from the highlighted box indicates the lower left edge of the large floe, approximately 6 x 7.5 km in size, situated 100 km inside the ice edge at 65.85°S 55.75°W. The anomalous appearance of large melt ponds up to 50m across is evident on the large floe. Similar ponding is also observed on smaller ice floes (15-200m in diameter) seawards to within 2-3 km of the ice edge before floes were too small to support surface ponds. Measurements also indicated that such perennial floes were typically 2.5-4m thick with a 2-15 cm deep snow cover.

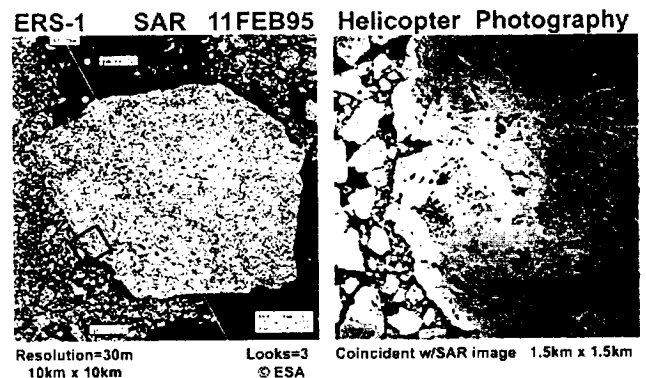


Figure 4. ERS-1 SAR image (left panel) and coincident aerial photograph (right panel) from black box indicating surface melt ponding.

Thus, perennial ice in northern Weddell Sea experiences classical melt-ponding during particularly warm summers. Ponds are expressed in topographic low points on the surfaces of conglomerate ice floes with significant relief. However, the areal extent of melt ponding does not appear to have a significant enough impact at 23° incidence, such that melt ponds are clearly expressed in the high-resolution, filtered 16-bit SAR data. As previously explained in [Ref. 8], this may be due to the fact that rough-surface scattering from high-relief portions of ponded surfaces dominate backscatter signatures.

A preliminary algorithm has been designed to detect the occurrence of melting in the Weddell Sea. A blow up of the 1994-95 melt transition is shown for box 15 in Fig. 5. The

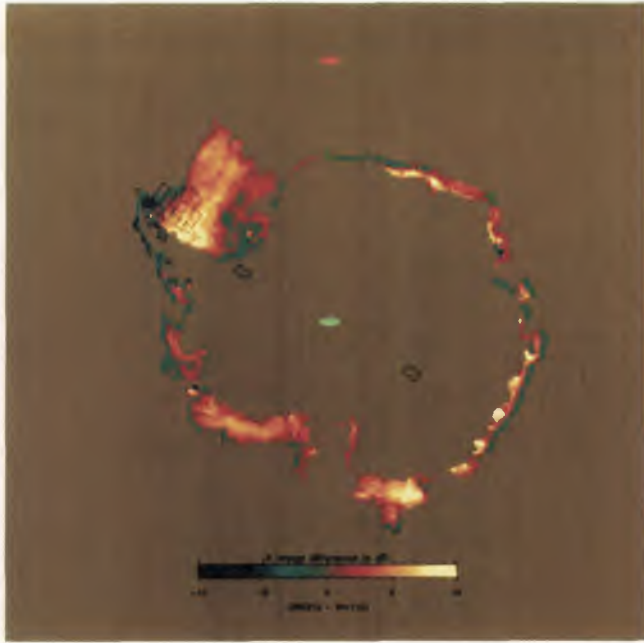


Figure 5. Difference image expressing the pre-summer and mid-summer melt backscatter contrast.

melt detection algorithm is presently configured to detect an

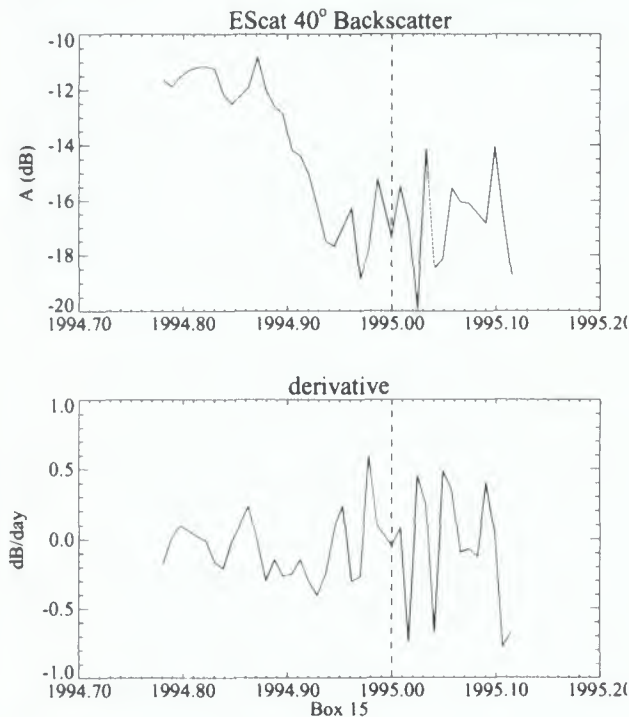


Figure 6. Box 15 melt transition, expressed as: (a) A values; and (b) its time derivative. The vertical dashed line indicates the end of the 1994 calendar year.

onset of surface melt characterized by an abrupt decline in backscatter of more than -5 dB, over a contiguous time period exceeding 9 days. The top panel in Fig. 5 indicates a reduction in backscatter of 7 dB over a period of 21 days (or seven images spaced at intervals of 3 days) in the region observed to be melting in 1995. The accompanying plot of $\delta A/\delta t$ in the lower panel of Fig. 15 indicates that the time derivative also remains negative for a period of 8 consecutive images, or 24 days. The combination of these two criteria has the advantage of filtering out small rapid fluctuations occurring as a result of mid-winter storms or oscillating spring air temperatures.

To spatially characterize the expression of surface melting, a simple snapshot difference image is generated in Fig. 6 to indicate the backscatter contrast between typical winter, 12 November 1994 (*i.e.* pre-melt), conditions and 12 February, 1995, summer conditions (*i.e.* active melting). Blue and green colors indicate negative differences ranging between -10 and 0 dB, while red or orange tones indicate locations where summer backscatter increased. Negative values indicate the widespread occurrence of melting, particularly around the outer ice margin where air temperatures reach their maximum values in summer.

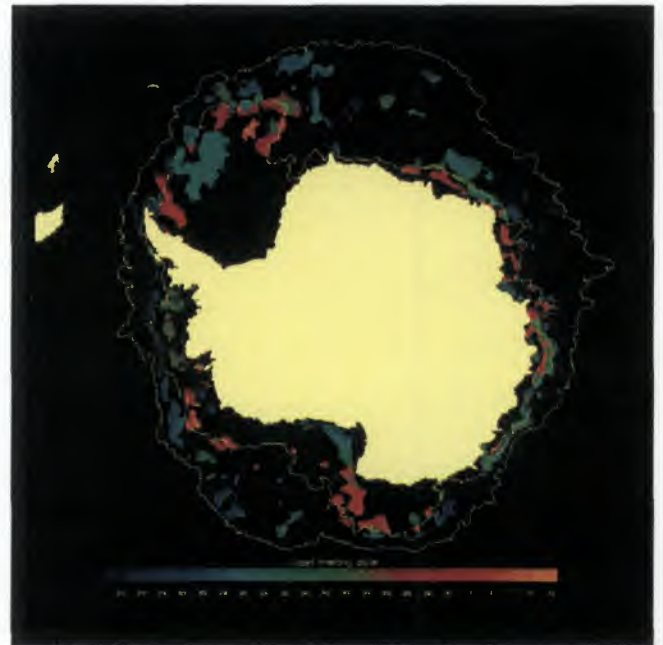


Figure 7. Estimated dates of Antarctic-wide melt onset, with ice-margin contours spanning the maximum and minimum ice extent during the period shown. The land-masked region is shown in yellow.

A preliminary example of the final automated melt-detection algorithm result is shown in Fig. 7 for the 1994-95 melt transition. When the onset of melting occurs the algorithm records the date of the onset of melting in the pixel where the

threshold, described above, was exceeded. The pre-melt ice margin location and the ice margin corresponding with the end of the melt transition period are shown to indicate the extent of sea-ice margin recession during the early melt season. Colorized regions indicate the date of first occurrence of melting. Surface melting is clearly not widespread nor spatially contiguous at any given instant of time during the onset of summer. The result indicates that melting occurs in patches, the location of which is likely dominated by the location of storm tracks supplying warm air masses. Perhaps more importantly, results similar to that in Fig. 7 confirm that atmospheric induced surface melting, and resulting albedo feedback is not the dominant sea-ice removal mechanism in summer; but instead, that the oceanic heat flux and short-wave radiation absorbed by the ocean surface in small lead fractions is more effective in removing the summer sea ice cover.

4.2 Flooding

South of the seasonal melt front, the snowcover rarely experiences surface melting, and the snow-ice interface appears to have the more dominant effect on seasonally varying backscatter signatures. As previously explained, high snow loading and basal melting can cause isostatic imbalance, flooding, and upward meteoric ice growth [Ref. 2]. In 1992, at ISW, resulting slushy, saline and high permittivity basal snow enhanced summer σ_w^0 values. Presently, there is no evidence to suggest that flooding does not also occur on perennial ice floes further to the north, but at some point snow surface melting masks any ice surface scattering signal. The effects of surface melting are clearly seen in the south-western Weddell Sea, where summer increases in backscatter often exceed 5 dB. This feature of the Antarctic sea-ice cover is extremely unique and the widespread nature of summertime increase suggest that summer flooding is commonplace. Another location where extremely large summer backscatter contrast is observed is Lutzow-Holm Bay near the Japanese Syowa base (68°S 37°E). Japanese surface measurements [Ref. 9] confirm the localized occurrence of upward meteoric ice growth in association with surface flooding effects in this region.

5. CONCLUSIONS

EScat σ^0 trends are explained primarily by changes in air temperature and secondly advection of different ice types into/out of the study regions. Results indicate significant interannual variability in the duration and intensity of the melt season, particularly in the north-western region off the east coast of the Antarctic peninsula. The austral summer warming in 1992/93 and 1994/95 was relatively intense, with the anomalous appearance of Antarctic melt ponds, observed for the first time in February 1995. Summer surface melting is expressed in different ways in the microwave data depending on whether north or south of the seasonal isotherm corresponding with snow melting. It would appear from the interannual record that expression of surface melt ponding may more widespread in this region than originally thought, judging from the occurrence of such a melt signature in other years. Similarly the

observation of summer increases in backscatter indicates the widespread nature of processes leading to upward meteoric ice growth, more commonly known as snow-ice. Since most thermodynamic models do not adequately represent this process, these results are expected to shed new light on the seasonality and regionality of this unique Antarctic ice-growth process.

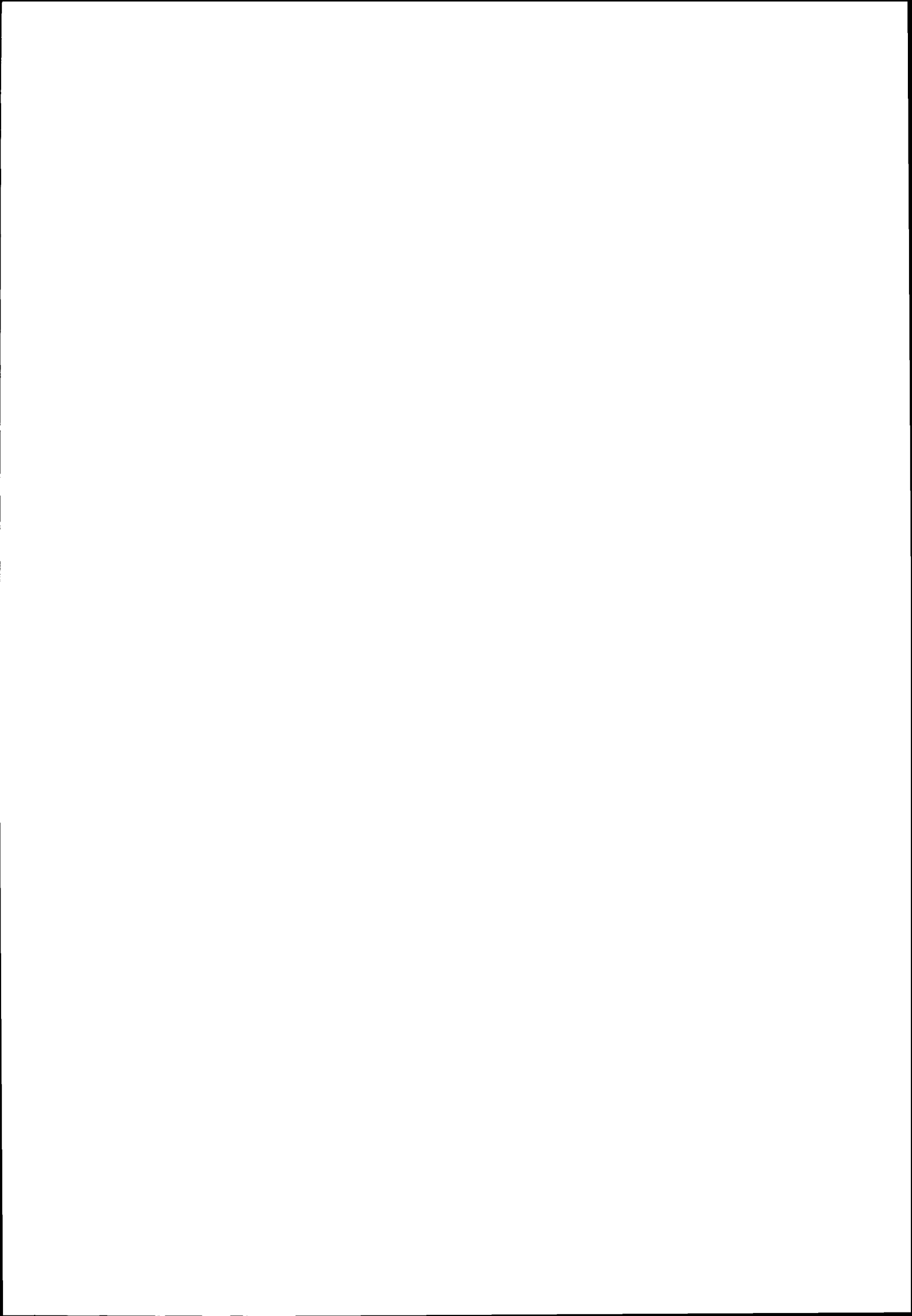
Ongoing work involves further development of the capability to use large-scale tracked ice kinematics products from scatterometer and SSM/I images in conjunction with these interannual time series. Dynamical information such as opening/closing will facilitate correction of the time series, such that advective and dynamic influences upon the backscatter variability may be removed. On this basis, smart algorithms may be developed to extract thermodynamically-driven features from the corrected regional melt signatures such as the fraction of ponded or flooded area.

6. ACKNOWLEDGEMENTS

Thanks are expressed to Peter Wadhams for instigating the H.M.S. *Endurance* field measurement campaign and to BAS for supplying meteorological station and AWS data. MRD and XL completed this work at Jet Propulsion Laboratory, California Institute of Technology under contract to the National Aeronautics and Space Administration and funded by Prasad Gogineni of NASA Code YS.

7. REFERENCES

1. Massom, R., M.R. Drinkwater and C. Haas, Winter Snowcover on Sea Ice in the Weddell Sea, *J. Geophys. Res.*, 102, C1, 1101-1117, 1997.
2. Drinkwater, M.R., and V.I. Lytle, ERS-1 SAR and field-observed characteristics of austral fall freeze-up in the Weddell Sea, Antarctica, *J. Geophys. Res.*, 102, C6, 12593-12608, 1997.
3. Drinkwater M.R., D.G. Long, and D.S. Early, *ESA Journal* 17, 307-322, 1994.
4. Early D.S., and D.G. Long, Resolution Enhancement of Scatterometer Data, *IEEE Trans. Geosci. Rem. Sens.*, In Press.
5. Low, D.G., The Validation of ERS-1 SAR Data For Antarctic Summer Sea Ice, Unpublished M.Sc. Thesis, University of Dundee, 143pp., 1995.
6. Drinkwater, M.R., and C. Haas, Snow, Sea-Ice and Radar Observations during ANTX/4: Summary Data Report, *Berichte aus dem Fachbereich Physik*, 53, Alfred Wegener Institut für Polar- und Meeresforschung, Bremerhaven, Germany, 58 pp., 1994.
7. Rott, H., P. Skvarca, and T. Nagler, Rapid Collapse of Northern Larsen Ice Shelf, Antarctica, *Science*, 271, 788-792, 1996.
8. Drinkwater, M.R., and F.D. Carsey, Observations of the late-summer to fall transition with the 14.6 GHz SEASAT scatterometer, *Proc. IGARSS '91*, 3, 1597-1600, 1991.
9. Kawamura, T., K.I. Oshima, T. Takizawa, and S. Ushio, Physical, Structural and Isotopic Characteristics and Growth Processes of Fast Ice in Lützow-Holm Bay, Antarctica, *J. Geophys. Res.*, 102, C2, 3345-3355, 1997.



ANTARCTIC ICEBERG DRIFT AND OCEAN CURRENTS DERIVED FROM
SCATTEROMETER IMAGE SERIES

Neal W Young

Antarctic CRC and Australian Antarctic Division
GPO Box 252-80, Hobart, Tasmania, 7001, Australia
Phone: +61-3-62262955, fax: +61-3-62262902
Email: Neal.Young@antarc.utas.edu.au
<http://www.antarc.utas.edu.au>, <http://www.antdiv.gov.au>

ABSTRACT

The ERS Wind scatterometer provides frequent measurements of the microwave backscatter of the Antarctic region. From these data a time series of coarse resolution radar images are generated using normalised values of the backscatter. The drift tracks and speed of very large icebergs with horizontal dimensions of tens of kilometres are derived from these images. The area of the largest iceberg detected is about 8000 km² and smallest 185 km². A combination of drift tracks of several icebergs demonstrates the continuity of the East Wind Drift round the East Antarctic coast. Typical values of drift speed averaged over 20 day intervals for these icebergs in the Antarctic continental slope current are up to 11 cm s⁻¹, with maximum values of 23 cm s⁻¹ found between 45°E and 25°W. Drift speeds tend to be greater over the upper break of the continental slope than over the continental shelf or in deeper water. Several icebergs exhibit a retroflexion in their tracks indicating a northwards connection between the westward flowing East Wind Drift and the eastward flowing Antarctic Circumpolar Current.

1. INTRODUCTION

Icebergs found in the Southern Ocean are formed from sections of ice which originally calved from the margins of the Antarctic ice cover, principally from the floating ice shelves and glacier tongues. These icebergs, in time, progressively fracture into smaller icebergs. They are dispersed by the ocean currents. Their size ranges from tens of metres up to tens of kilometres and very occasionally in excess of 100 km.

Very large icebergs, those with linear dimensions of tens of kilometres, can be detected and their motion tracked in a time series of coarse resolution radar images of the Antarctic region derived from ERS wind scatterometer data (Ref. 1). The measurements of backscatter coefficient were first normalised by subtracting the anisotropic components of the backscatter, which are calculated from a simple model of the angular dependencies of the backscatter from snow and ice, in order to derive the isotropic component. Each image in the series was generated from those normalised values by integrating over a time interval of five days. Many features were visible in the images, such as the coastline and surface structure of the Antarctic ice sheet, as well as sea ice, and icebergs. The icebergs usually appeared as brighter objects against a darker background of the surrounding sea ice or ocean.

In this paper the same technique (Ref. 1) is utilised to generate a time series of images using available ERS scatterometer data. The motion of the icebergs is determined by extracting the coordinates of the bright features in each image in the series to give a time series of positions and hence the drift track. Variation in mean drift speed and localities where icebergs became grounded are identified from the drift tracks. The time variation of the backscatter of the central pixel of each individual iceberg is also extracted from the image series. Modelling of the forces acting on icebergs of this scale suggests that they move predominantly with the ocean currents and their motion is little affected by wind (Ref. 2). Hence observing the drift of icebergs provides information on the pattern of the mean ocean current averaged over the upper few hundred metres corresponding to their draft, which is typically in the range from 200 to 350 m for icebergs of this size. The drift tracks of the icebergs and the variation in drift velocity are compared to the bathymetry.

2. ERS-1 WIND SCATTEROMETER DATA

The active microwave instrument [AMI] on the ERS satellites operates at 5.3 GHz in the C-band with VV polarisation (Ref. 3). In the wind scatterometer mode, backscatter measurements of the surface are obtained with three antennas pointing to the right of the space-craft in three directions: abeam, 45° forward, and 45° aft. The incidence angle varies across the swath from a minimum of about 18° to a maximum of about 56°. On each pass, the three antennas of the instrument provide three independent observations of the surface for three different look directions at 19 regularly spaced points across the swath. This pattern of measurements is repeated at regular intervals along the satellite's track. Each measurement is the spatial integral of the backscatter from within the footprint of the antenna beam. The data distributed in the scatterometer data products represent the backscatter coefficient for a circular area with a diameter of 50 km.

Operation of the AMI in wind scatterometer mode has produced an almost continuous sequence of observations of microwave backscatter of the earth's surface over both land and water. Data were acquired by ERS-1 from August 1991 with a changeover to ERS-2 in June 1996. In the polar regions, the geometry and repeat period of the satellite orbit provides frequent observations. South of latitude 55°S total coverage is achieved every three days, and daily at 65°S. The inclination of the satellite orbit and the geometry of the right-looking scatterometer

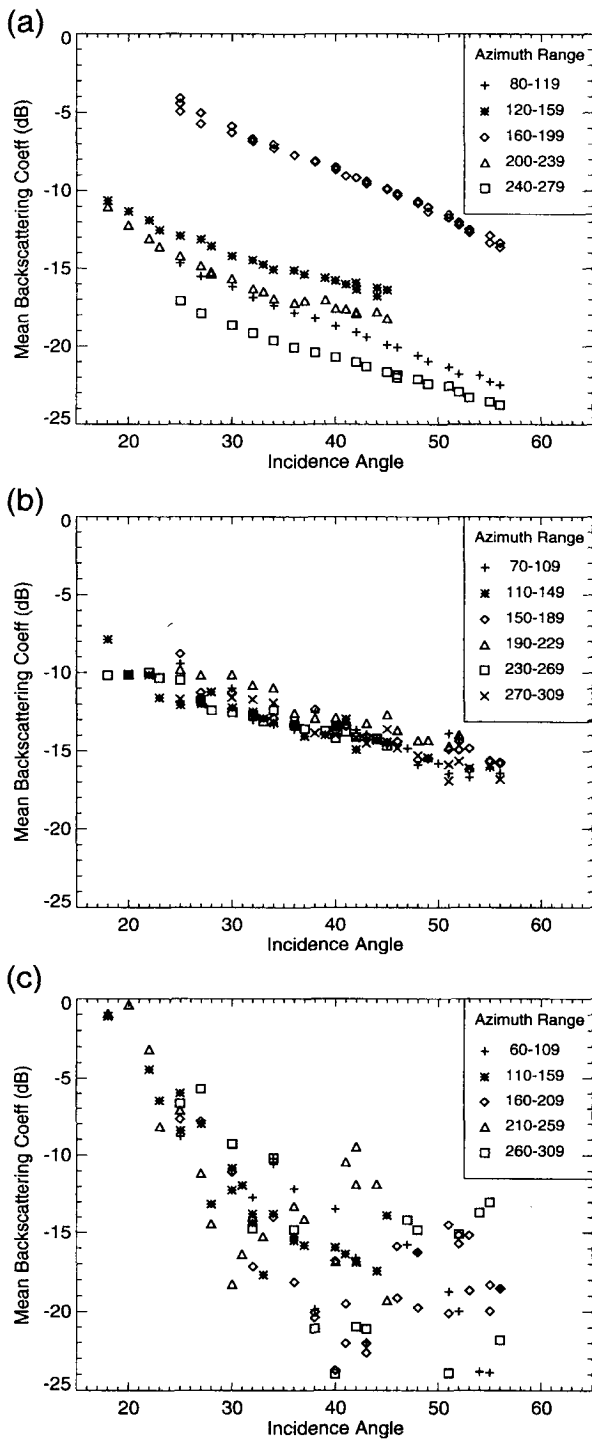


Figure 1. Examples of mean backscatter coefficient (in dB) in a 25 km cell as a function of incidence angle and antenna look-direction for points with three different surface types with data accumulated over July 1995: (a) Antarctic ice sheet in which the backscatter exhibits a strong dependence on azimuth; (b) sea ice for which the dependence on azimuth is very weak; (c) ocean where the backscatter has a quite different character to that in a or b. Each data point represents the average backscatter coefficient for a range of incidence angle of 1° and range of antenna look direction of 10° . The mean values are presented using symbols indicating a range of azimuth of 40° .

antenna system limits the backscatter observations to areas north of latitude 79°S . In the Arctic, on the other hand where the antennas point towards the North Pole, there is complete coverage except for a small circular region in the immediate vicinity of the pole. Thus virtually all of the polar oceans can be monitored at coarse resolution by such a time series of radar images. There are gaps in the scatterometer data series corresponding to periods when the AMI was operated in Synthetic Aperture Radar [SAR] mode and to periods when the AMI did not acquire data for operational reasons, such as orbit adjustment.

The ERS-1 satellite has been operated in three different orbit repeat cycles: 3-day (43 orbits), 35-day (501 orbits), and 168-day (2411 orbits). The maximum spacing between neighbouring ground tracks over Antarctica at latitude 65°S is about 27 km for the 35-day cycle, and about 5 km for the 168-day cycle. The ERS-2 satellite has been operated only in the 35-day (501 orbits) repeat cycle. By combining data from both ascending and descending passes multiple observations are obtained with different incidence angle and antenna look direction for any particular location within the instrument's swath. The 500 km wide swath of the scatterometer together with the spacing between neighbouring tracks provides considerable overlap of swaths for all the mission except the 3-day repeat cycles, and hence multiple observations of any point with a range of incidence angles.

3. MICROWAVE BACKSCATTER FROM ANTARCTIC SNOW AND ICE

Three distinctly different surface types are observed by the scatterometer in the Antarctic region: the snow cover of the continental ice sheet and of icebergs which have calved from it; sea ice in the Seasonal Sea Ice Zone [SSIZ]; and the open ocean. Microwave backscatter from the snow and ice cover over large parts of the Antarctic continent can be stable with time (Ref. 4). This reported stability in the microwave properties was used to investigate the anisotropic character of the backscatter from the snow surface by combining data from many passes to provide measurements for a given point at multiple values of incidence angle and look direction (Ref. 5). Figure 1 shows examples of the variation of the backscatter coefficient as a function of incidence angle for the measurements accumulated over July 1995 in a 25 km cell for the three different surface types. The variation with antenna beam look direction is represented by different symbols corresponding to a range of look direction. In Figure 1a the data exhibit a wide range of values for a given incidence angle, but there is a consistent pattern of largest values for look directions in the range 160° to 199° , and smallest values for 240° to 279° , with intermediate values for other look directions. For each range of look direction, the variation with incidence angle is approximately linear.

From this pattern, the backscatter coefficient for a surface composed of snow and ice with stationary scattering properties can be described by (Ref. 5):

$$\sigma = \sigma_{\theta_0} + \alpha \cdot (\theta - \theta_0) + \beta \cdot \sin(2(\phi + \lambda)) + \epsilon \quad (1)$$

where

σ_{θ_0} is the mean backscatter coefficient normalised to a reference incidence angle θ_0 ,

θ is the incidence angle of the observation,

ϕ is the azimuth, or look direction, of the observation,

λ is the azimuth for minimum backscatter coefficient,

α and β give the amplitude of the anisotropies, and

ϵ is the residual term.

The calculations are made for a regular array of cells 25 km square. A data value is assigned to a cell if the centre of the measurement footprint, as given in the scatterometer data product, falls within the boundaries of the cell. The normalised backscatter σ_{θ_0} , coefficients α and β , and the orientation term λ , are determined for each cell through the least squares solution of Equation 1 which minimises the variance of ϵ for all observations assigned to that cell for a given time interval. The values of the parameters β (amplitude) and λ (orientation with respect to north) describe the directional anisotropy in the backscatter. The values of all parameters vary systematically across the continental and sea ice cover and, over the continent, exhibit little variation with time.

The amplitude of the directional anisotropy over the coastal regions of the ice sheet is very small, particularly over the ice shelves (Ref. 5). Similarly the amplitude of the directional anisotropy over sea ice is almost everywhere small and for many purposes could be neglected (Figure 1b, Refs 5, 6). This low directional anisotropy in the backscatter from sea ice is used in setting a flag in the data product to indicate, for measurements over ocean, the presence of sea ice. By contrast, Figure 1c does not

show a similar systematic pattern with antenna look direction in the backscatter from the ocean surface, apart from a greater dependence on incidence angle because the roughness of the ocean surface is directly related to the prevailing wind which changes in strength and direction. The solution of Equation 1 almost always gives a high variance for the residual term over the ocean. The variance of the residual is typically very small for the snow and ice regions, which is consistent with longer-term stability of the snow and ice microwave scattering properties.

4. GENERATION OF COMPOSITE IMAGES

The normalised backscatter term, σ_{θ_0} , is an average for the integration time interval and represents the isotropic component of the backscatter coefficient which is related to the intrinsic material properties such as the bulk dielectric constant. For each individual observation of the backscatter coefficient obtained from the satellite data stream, a normalised value, adjusted to a reference incidence angle (in this case a nominal value of 30° was chosen), is calculated from (Ref. 1):

$$\sigma_{30} = \sigma - \alpha \cdot (\theta - 30) - \beta \cdot \sin(2(\phi + \lambda)) \quad (2)$$

using values of α , β , and λ calculated for each cell with data accumulated over a suitable interval.

The individual normalised values are used to generate the composite images of mean backscatter for the Antarctic region at regular time intervals. Figure 2 shows the coverage achieved for integration intervals of 1 and 5 days. Although a complete cover of the region can be achieved every three days, data gaps do occur, for instance when

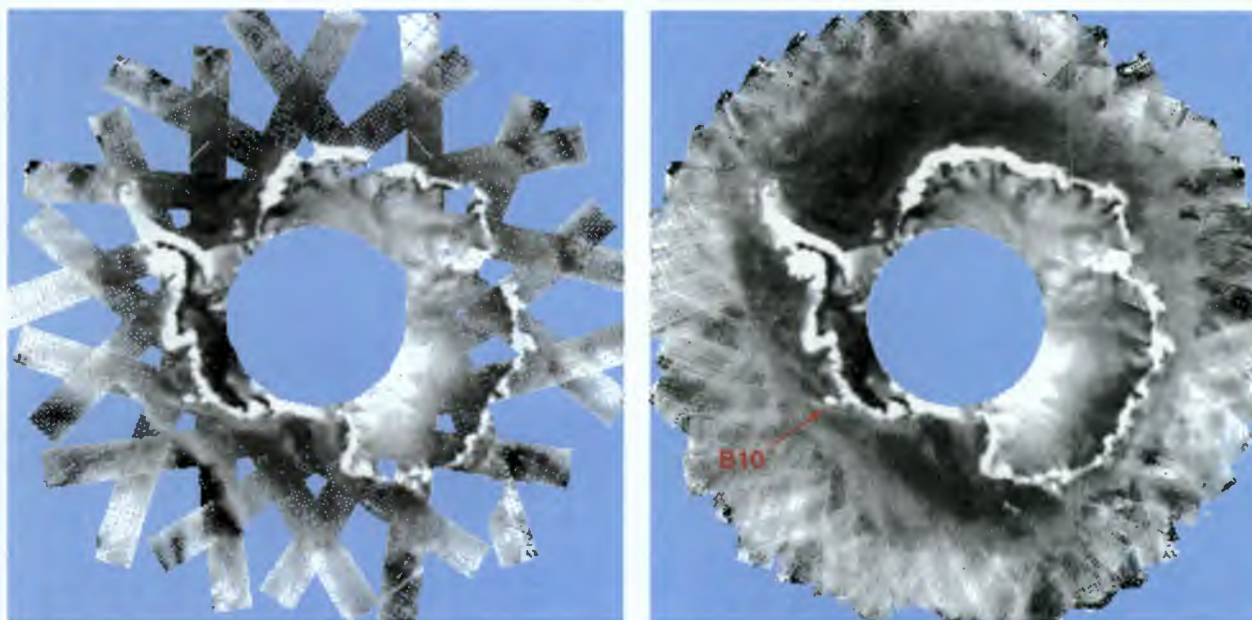


Figure 2. Two images showing the coverage of the Antarctic region south of latitude 55°S for 1-day and 5-day integration intervals. The one-day image shows the pattern of individual swaths of scatterometer data used to build each composite image. The bright feature close to the coast in the lower left quadrant is iceberg B10 (area: $\sim 8,000 \text{ km}^2$)

SAR data are acquired, so a nominal interval of five days is used for the data integration. This process produces a series of images at five day intervals of the mean normalised backscatter over that five days for each 25 km square cell.

The resulting series of images provide an almost continuous record over the duration of the ERS missions. There are a few 5-day intervals for which there was little or no data provided in the data products, such as during orbital adjustment manoeuvres.

5. ICEBERG DETECTION AND DRIFT TRACKS

The largest of the icebergs will be represented by only a few pixels so that brightness rather than texture needs to be used for their detection. An indication of the character of backscatter from icebergs can be gained from a study of the distribution of icebergs around the coast of East Antarctica using the SAR mode of the ERS AMI (Ref. 7). In SAR images icebergs generally exhibit a stronger backscatter compared to the background comprised of a mix of various concentrations of sea ice and open water. Provided the iceberg has a surface cover of snow that was cold and dry then values of mean backscatter coefficient for icebergs are typically -6 dB or greater and usually 5 dB to 10 dB greater than the backscatter coefficient of the surrounding surface. Ice shelves in East Antarctica have values around 0 dB. Thus the icebergs and the continental snow cover were usually the brightest objects in an image.

The scatterometer measurement of the backscatter coefficient represents the integral over all features within its very large footprint so that an object needs to be large compared to the size of the footprint in order to make a significant contribution to the backscatter value. Thus very large icebergs with linear dimensions of tens of kilometres can be expected to have corresponding bright features in the composite images when their surface snow cover satisfies the above conditions. For objects much larger than the footprint actual backscatter values in the composite images will be slightly less than those found in SAR images because of different incidence angles. SAR data is acquired with a nominal incidence angle of 23° and the data used in the generation of the image series is normalised to an incidence angle of 30° . Continental snow cover and sea ice do not exhibit a greatly dissimilar dependence on incidence angle (Figures 1a and 1b), so that the measurements from those two surfaces will be affected to a comparable extent. Hence the contrast in backscatter will be similar to that found in SAR images.

There are conditions that cause the detection of icebergs in the images to be difficult. When surrounded by open ocean, the typically high backscatter from the ocean reduces the backscatter contrast. In addition an increase of moisture content of the snow cover can reduce the backscatter from the iceberg surface to a point where it matches that from the surrounding sea ice and water, or to an even lower value. A temporary decrease in normalised backscatter coefficient of 10 dB and more was observed to be associated with melting of the snow cover on iceberg

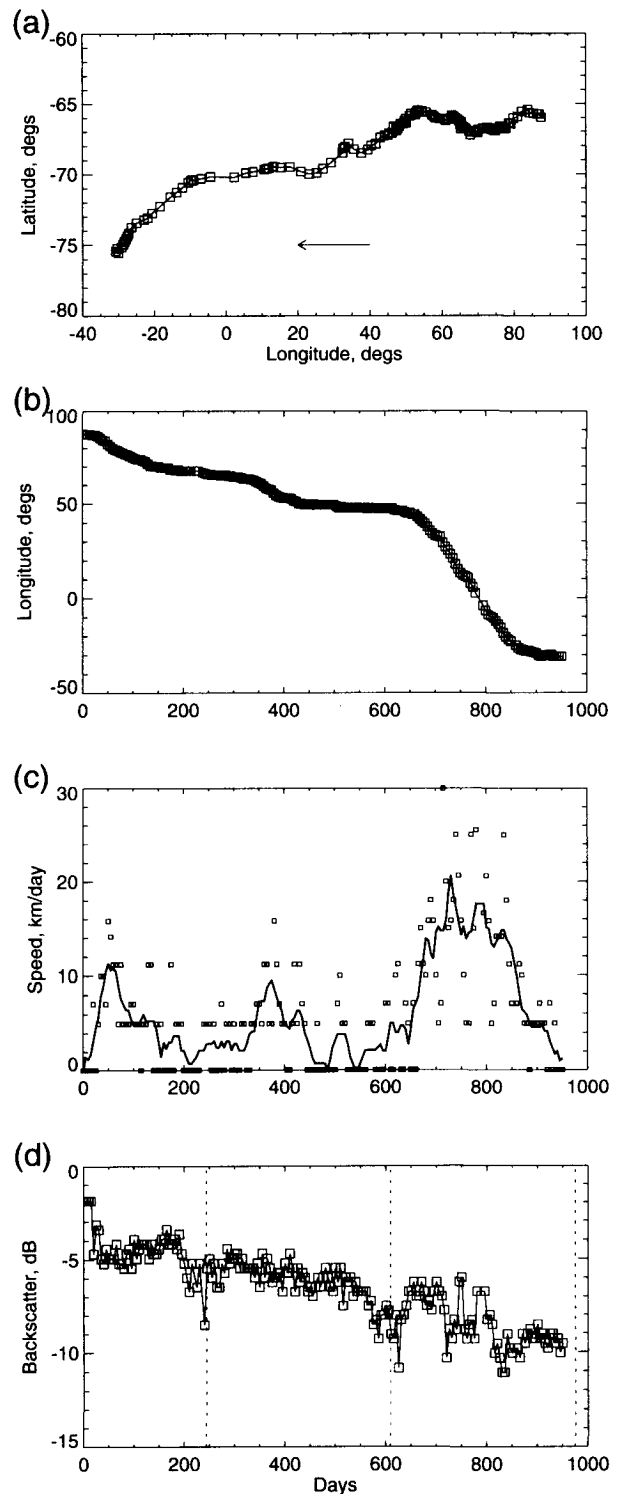


Figure 3. Characteristics of the drift of iceberg W1 from time of calving in May 1994 to end of December 1996. Measurements refer to the central pixel, usually the brightest in the feature. (a) Drift track. (b) Longitude versus time. (c) Estimate of drift speed calculated from displacement of the iceberg between consecutive 5-day composite images. The continuous curve shows the running mean of values over a 20-day interval. (d) Normalised backscatter of feature showing general reduction with time corresponding to reduction in area over lifetime of iceberg.

B10 during the summer months (Ref. 1). Multi-year sea ice can also exhibit strong backscatter so that large expanses of it can be confused for an iceberg. First year and younger forms of sea ice can exhibit a quite variable backscatter value depending on concentration, roughness, floe size, etc (Ref. 8). The essential character associated with backscatter from icebergs is that it is usually consistently strong and generally stable over long periods of time, whereas the backscatter from the surrounding surface can be quite variable and usually smaller.

The motion of an iceberg will tend to smear the feature in the image because of the finite integration time used in building each composite image. In addition, the simple process of binning individual observations into 25 km cells tends to add to the blurring of features. Thus the effective value of the backscatter coefficient is likely to be less than that expected from observed mean values for the backscatter coefficient of individual icebergs.

The drift track of an iceberg is given by the series of coordinates derived for the central pixel of the corresponding bright feature in a set of the images. The velocity is then the rate of change of position between images. In this work the position of each iceberg has been measured at the resolution of a single image cell so that the smallest observable increment of displacement and therefore velocity is 25 km over 5 days. As well as the central coordinates, the normalised backscatter value is also extracted for the central point.

Figure 3 shows various characteristics of the drift of an iceberg from the West Ice Shelf to the Weddell Sea over a period of two and a half years (Ref. 1). The iceberg became grounded for short periods of up to several weeks duration at a number of locations around the coast. This can be

seen in the plot of the drift speed versus time in Figure 3c. Also shown is the average speed calculated as the running mean over 20-day intervals.

Figure 3d shows a generally decreasing trend of normalised backscatter coefficient with time. The decrease in backscatter was proposed to be related to a decrease in area of the iceberg which occurred through progressive calving of smaller icebergs from its margins (Ref. 1). An initial size of 1740 km² determined from an AVHRR image, and backscatter and size measurements of another smaller iceberg were used to provide an approximate calibration for a backscatter versus area relation. From this the resultant area corresponding to the final backscatter value in Figure 3d was estimated at 550 km². Since then the area of this iceberg has been measured in a Radarsat SAR image at 825 km², i.e. 45% of the original area. Given the rough approximations that were needed in the first estimation, the measured area provides an encouraging confirmation of the use of the backscatter record for monitoring the size of large icebergs. Further work is needed to provide a calibration of the backscatter versus area relation and improved methods for extracting the backscatter values corresponding to the background and iceberg features.

6. OCEAN CURRENTS

The motion of very large icebergs is influenced primarily by the ocean currents and is little affected by wind (Ref. 2). Tracking their motion in the image sequence is expected to give an indication of mean current speed and direction averaged over the draft of the iceberg, typically 200-350 m for the icebergs in this study.

Figure 4 shows the drift tracks of eight individual icebergs

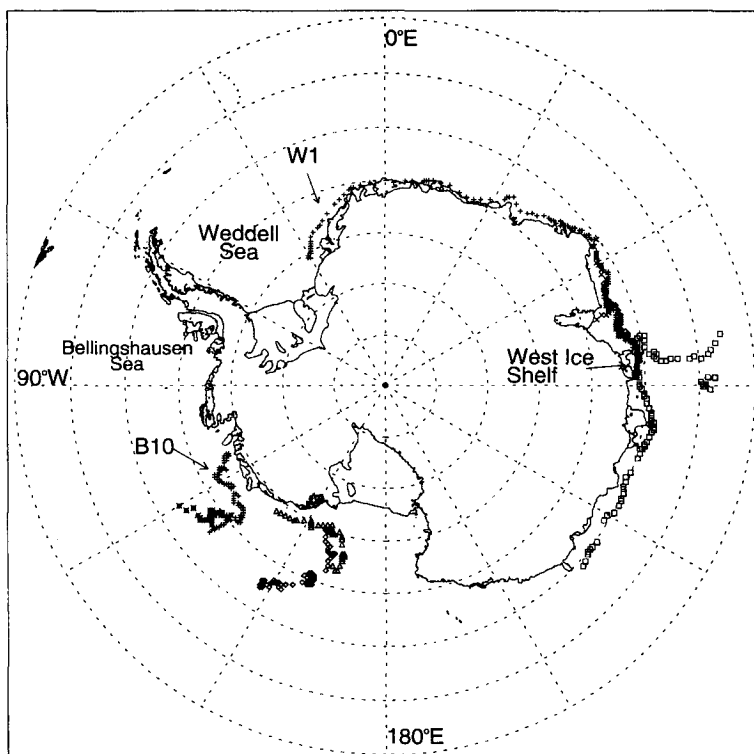


Figure 4. Drift tracks of eight icebergs tracked in the time series of 5-day composite images of normalised backscatter. Close to the coast the sense of the drift is anti-clockwise around the continent with the Antarctic continental slope current. Several tracks exhibit a retroflexion, a stage with northward drift, then a drift to the east with the ACC [Antarctic Circumpolar Current].

that were observed using this series of composite images (Ref 1). Close to the coast their drift is to the west with the Antarctic continental slope current. The tracks of several of the icebergs exhibit a retroflexion so that they are carried northward and eventually join the eastward motion of the southern part of the Antarctic Circumpolar Current. This pattern of iceberg drift is consistent with the pattern of drift of 21 smaller icebergs investigated in earlier work (Ref. 9). The drift track and speed of these icebergs, with horizontal dimensions of the order of 1 km, were observed for periods of up to 2.5 years using satellite transponders. Figure 4 shows tracks around the East Antarctic coast of the first icebergs that have been observed to continue drifting to the west past a retroflexion between about 80°E and 90°E described by the transponder experiment (Refs 9, 10) indicating the continuity of the slope current through this area. It is notable that all icebergs carrying transponders that drifted round the coast of East Antarctica to the west of 100°E were carried north to join the ACC before reaching longitude 75°E (Ref. 9). Similarly in the Weddell Sea none of those icebergs drifted down to the front of the Filchner Ice Shelf but turned away from the coast earlier along their path. It is unknown at this stage whether the difference in behaviour of the very large icebergs discussed in this work from that of much smaller icebergs (Ref. 9) is a result of different horizontal dimensions or of different draught.

Figure 5 shows the relationship of the tracks and drift speed of several icebergs with the bathymetry around the coast of East Antarctica between the Ross Sea and the Weddell Sea. There are two major ocean basins, the Weddell-Enderby Basin in the west, and the Australian Antarctic Basin in the east, connected by the Princess Elizabeth Trough south of the Kerguelen Plateau at about longitude 80°E–85°E. The sense of the drift near the coast is from the east to the west. Along the Australian Antarctic sector of the coastline the icebergs apparently follow the outer edge of the continental shelf close to the upper break of the continental slope, approximately along the 1000 m bathymetric contour (between red/brown and yellow colours in Figure 5). In the Weddell-Enderby sector the tracks follow a similar line but perhaps a little inside the upper break of the slope and over the shelf. The tracks cross and do not skirt around several sub-marine ridges, e.g. at longitudes 100°E, 38°E, and 12°E. This is consistent with the behaviour of iceberg B9 during its drift out of the Ross Sea. When it reached the outer edge of the shelf, B9 approximately followed the upper slope break and crossed Pennell Bank in a water depth less than 500 m without any apparent deviation in its track (Ref. 11). At longitude 17°W the track of one iceberg follows the coast-line into the southern Weddell Sea, well onto the continental shelf. At 80°E another iceberg follows the retroflexion in the current at this longitude and eventually drifts north along the eastern flank of the Kerguelen Plateau on a track similar to some of the icebergs with transponders (Ref. 9). The initial turn to the north and east through the Princess Elizabeth Trough may be related to a southern branch of the ACC passing to the south of the Kerguelen Plateau.

Drift speeds are presented as averages over twenty-day

intervals in Figure 5. Values are typically between 0 and 10 km d⁻¹ in the sector between longitudes 130°E and 45°E. Some of the icebergs became grounded temporarily at several distinct locations around the coast: at longitudes 77°E, between 67°E and 71°E, and between 46°E and 49°E. Further west in the Weddell-Enderby sector between longitudes 45°E and 25°W the greatest drift speeds are found with average values up to 20 km d⁻¹ and extremes up to 30 km d⁻¹ over 5-day intervals. At the far end of one track in the Weddell Sea (30°W) the iceberg is drifting only slowly and there is no evidence of it having become grounded. These drift speeds are consistent with those measured in the same sectors using transponders on icebergs with a linear dimension of the order of 1 km (Ref. 9). The distribution of sea ice can also be seen in the composite images. There was no indication of an association between the observed drift speed and the presence or absence of pack ice about these very large icebergs. Comparison of the drift speeds with measured drift rates for sea ice in the same sectors indicates that the icebergs move much slower than sea ice (Refs 11, 12). Comparison of drift tracks suggests that the very large icebergs moving with the continental slope current tend to keep moving around the continent, whereas sea ice and smaller icebergs with a linear dimension of the order of 1 km showed a tendency for a net northwards motion eventually moving out of the East Wind Drift and into the ACC (Refs 9, 10, 12).

Where the tracks cross the submarine ridges there are marked reductions in drift speed, e.g. at 38°E and 12°E, and to a lesser extent at about 95°E and 105°E. The drift of B9 also showed some decrease in drift speed when it crossed Pennell Bank (Ref. 11). This behaviour across the submarine ridges is consistent with a tendency of the continental slope current to flow at an approximately constant depth in order to conserve vorticity and thus follow the bathymetric contours around the ridges rather than flowing across the obstruction at a greater speed (N. Bindoff personal communication). In the sector between 60°E and 85°E where there are several different tracks, there is some evidence to suggest that the icebergs exhibit greater drift speeds when they are located close to the shelf break, generally in water depths of about 1000 m, and smaller speeds when over the shelf or in deeper water further away from the coast. This is consistent with the location of the core of the Antarctic continental slope current being associated with the upper break of the continental slope. In general the very large icebergs appear to behave as though they are integrating the effect of the various forces acting on them with a long time constant and respond to the long term and broad scale average effect of wind and currents.

7. CONCLUSION

Very large icebergs with linear dimensions of tens of kilometres are detectable in coarse resolution radar images of the Antarctic region derived from ERS wind scatterometer data. The motion is tracked by extracting the coordinates of the central pixel of the bright feature in each image corresponding to an iceberg. The sense of

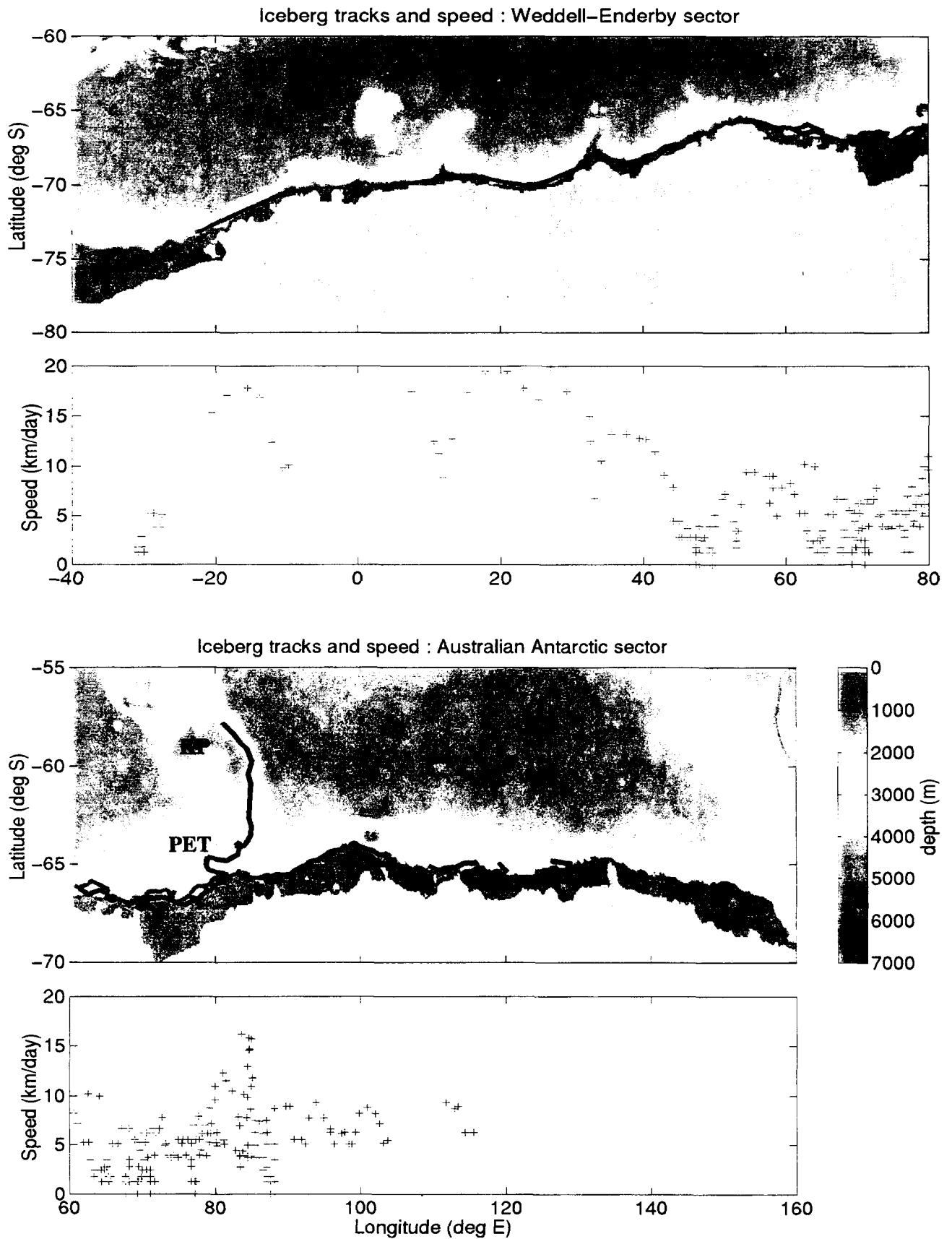


Figure 5. Drift tracks and drift speed of icebergs and bathymetry from ETOP05. The grounded ice sheet is depicted by gray, but ice shelves are not depicted in these maps. KP: Kerguelen Plateau; PET: Princess Elizabeth Trough. Different tracks are distinguished by different colours.

iceberg drift close to the Antarctic continent is from east to west. Drift speeds tend to be greater over or close to the upper break of the continental slope in water depths of about 1000 m than over the continental shelf or in deeper water further offshore. This is consistent with the location of the core of the Antarctic continental slope current being associated with the upper break of the continental slope. Largest values of drift speed are found in the Weddell-Enderby sector between longitudes 45°E and 25°W, with mean values up to 20 km d⁻¹ (23 cm s⁻¹) averaged over 20-day intervals and peak values of 30 km d⁻¹ (35 cm s⁻¹) over 5-day increments. Further east in the Australian Antarctic sector speeds are generally less than 10 km d⁻¹ (11 cm s⁻¹). The drift speed of these very large icebergs is significantly slower than the drift of sea ice. In several locations tracks cross major submarine ridges rather than follow the line of the shelf break. Where the tracks cross the ridges there is a marked decrease in drift speed. The drift tracks of several icebergs exhibited retroreflections with a stage of northward drift, then eastwards, indicating a connection between the westward flowing continental slope current and the southern margin of the eastward flowing ACC.

The results presented here suggest that the motion of these very large icebergs represents the broad scale long-term average flow of the ocean integrated over their draught and that they show little response to shorter term variability in the forcing of the wind field and ocean currents.

Finally, the effective backscatter value derived from a composite image for an iceberg is the area weighted sum of the contribution from the actual iceberg and from the surrounding surface. A time series of these backscatter measurements of icebergs for which the area is comparable to or smaller than the footprint size can provide a record of reduction in area in response to erosion or calving from the margins of the iceberg.

ACKNOWLEDGEMENTS

The ERS (AMI) wind scatterometer data are copyright to ESA, 1991-1998, and were provided through AO project ERS.AO2.AUS103. I also wish to acknowledge the efforts and support of the CERSAT team of the French PAF in the production and dissemination of the data products, as well as J. Anderson, G. Hyland and A. Woolf, of the Antarctic CRC, for their contributions to the preparation of diagrams and the manuscript.

REFERENCES

1. Young NW & Hyland G 1997, Applications of time series of microwave backscatter over the Antarctic region. In *Proceedings of the Third ERS Symposium, Florence, Italy, 14-21 March 1997*. ESA Publication SP-414, 1007-1014.
2. Crepon M, Houssais MN & Saint Guily B 1988, The drift of icebergs under wind action. *Journal of Geophysical Research*, 93, C4, 3608-3612.
3. Vass P & Battrick B 1992, *ERS-1 System*. ESA Publication SP-1146. Pp. 87.
4. Rott H, Miller H, Sturm K & Rack W 1994, Application of ERS-1 SAR and scatterometer data for studies of the Antarctic ice sheet. In: *Proceedings of the Second ERS-1 symposium, 11-14 October 1993, Hamburg, Germany*, ESA Publication ESA SP-361 Vol. 1, pp. 133-139.
5. Young NW, Hall D & Hyland G 1996, Directional anisotropy of C-band backscatter and orientation of surface microrelief in East Antarctica. In: Kingwell, J. (Ed.) *Proceedings of the First Australian ERS Symposium. University of Tasmania, Hobart, 6 February 1996*. COSSA Publication 037, 117-126.
6. Early DS & Long DG 1997, Azimuthal modulation of C-band scatterometer σ^0 over Southern Ocean sea ice. *IEEE Transactions on Geoscience and Remote Sensing*, 35, 5, 1201-1209.
7. Young NW, Turner D, Hyland G & Williams RN in press, Near coastal iceberg distributions in East Antarctica 50°E - 145°E. *Annals of Glaciology* 27.
8. Lytle V, Massom R, Worby AP & Allison I 1997, Floe sizes in the East Antarctic sea ice zone estimated using combined SAR and field data. In *Proceedings of the Third ERS Symposium, Florence, Italy, 14-21 March 1997*. ESA Publication SP-414, 931-936.
9. Tchernia P & Jeannin PF 1984, Circulation in Antarctic waters as revealed by iceberg tracks 1972-1983. *Polar Record*, 22, 138, 263-269.
10. Tchernia, P & Jeannin PF 1980, Observations on the Antarctic East Wind Drift using tabular icebergs tracked by satellite Nimbus F (1975-1977). *Deep-Sea Research*, 27A, 467-474.
11. Keys JR, Jacobs SS & Barnett D 1990, The calving and drift of iceberg B-9 in the Ross Sea, Antarctica. *Antarctic Science*, 2, 3, 243-257.
12. Heil P & Allison I in press, The pattern and variability of Antarctic sea ice drift in the Indian Ocean and Western Pacific sectors. *Journal of Geophysical Research - Oceans*.

Ocean Session

Chair: P. Courtier, LODYC

Rapporteur: P. Lecomte, ESA/ESRIN



Summary of the Ocean Session

Chairman: Philippe Courtier

Laboratoire d'Océanographie Dynamique et de Climatologie (LODYC)
 Université Pierre et Marie Curie
 boîte 100, 4 place Jussieu, 75 252 Paris Cedex
 tel: ++33 1 44 27 70 73, fax: ++33 1 44 27 38 05
 Email: courtier@lodyc.jussieu.fr

Rapporteur: Pascal Lecomte

Directorate of Application Programmes - Remote Sensing Exploitation Division
 ESA / ESRIN, Via Galileo Galilei, 00044 Frascati, Italy
 tel: ++39-6-941 80 670, fax: ++39-6-941 80 612
 Email: pascal.lecomte@esrin.esa.it

Introduction

During the Ocean session of the Workshop on Emerging Scatterometer Application five papers were presented, including the chairman introductory paper, and three others were presented as posters.

Various aspects were covered from Global oceanography (e.g. General circulation modelling) to small and meso scale phenomena (e.g. Mediterranean sea).

The main result of the ocean session is the strong requirement for the continuation of a C-Band scatterometer mission through the end of the century, and in particular to avoid any gap between the end of ERS operations and the beginning of the Ascat era.

In fact scatterometer data became an important tool for many studies (climatology and phenomena analysis) but a potential gap in the data time serie prevent scientific and industrial applications to be developed.

Generalities

Applications for ocean data, gathered and analysed by a variety of means and methods, have grown steadily and apace over the last few decades. This growth has in turn generated an increased demand for data and improved understanding of the oceans, and for more efficient techniques for utilising and exploiting this information. Programs such as TOGA and WOCE have been successful at advancing the scientific and technical knowledge, but we have been less successful at attracting the continuing, long-term investment that is needed to maintain regional and global observing systems.

Oceanographic applications using scatterometer data are responding to this demand for data and are brought into a larger ensemble which includes parameters measured by other spaceborne instruments (e.g. temperature and ocean topography) and by other techniques (e.g. surface and deep water in-situ measurements). Ocean and Atmosphere modelisation is also a major technique for

the derivation of important physical variables describing the ocean - atmosphere interface.

Three points were highlighted during the workshop.

If the traditional operational oceanography is well developed in many countries, space oceanography is only implemented in few of those. The complementarity between these two groups can only be enhanced if they can share and exchange data information and results in an efficient way. This is the scope of Godae (Global Ocean Data Assimilation Experiment) of which the aims to demonstrate the practicality of routine, real-time global ocean data assimilation and prediction. Many agree that such a demonstration is vital if we are to ever realise a permanent, global ocean observing network and prediction system, with all components functional and operating on a global domain. It is also accepted that such a goal requires significant integration across the components. Without this, there is unlikely to be sufficient justification for the individual components to be maintained in their own right beyond the lifetime of research experiments.

Data assimilation in numerical models and data interpretation are two aspects of the oceanography which are complementary and both essential to interpret the phenomena which are observed. These two communities, climatology and phenomena analysis are co-existing, requiring the same geophysical parameters but often in different forms or with different characteristics. New algorithms and techniques have to be developed to answers both requirements.

Maintain a C-Band Scatterometer Mission

It is unanimously recommended to ESA to avoid any gap in C-Band scatterometry between the end of ERS scatterometer operations and the launch of Metop with the advance scatterometer Ascat.

It is underlined that Ku-Band and C-Band scatterometer are not equivalent and in competition, but are complementary as the phenomena observed are not identical. As a result, both data sets are not interchangeable and it is of great importance to continue the unique temporal series of C-Band acquisition for climatology and model forcing. In order to provide sensible results a model spin up is typically of 10 years.

It is recalled that the nominal mission for an ERS satellite is of three years. ERS-1 already double its expected life time and ERS-2 flies already for more than three years. Today, the launch of Metop-1 is foreseen in May 2003, in more than 4 years not considering any delays always possible for such a complex satellite. Even taking into account the strong expertise of ESA engineers, it would be a miracle to have ERS scatterometer operational for such a long period.

Maintaining C-Band acquisition is also important to limit the risk of being without resources in case of instrument, satellite or launch failure (e.g. Adeos-1).

ERS Data Reprocessing

Two aspects have to be distinguished when referring to reprocessing.

On one side it is important to operationally maintain a uniform quality of the data throughout the mission and, in case of anomaly to reprocess as quickly as possible the dataset acquired during this anomaly, with the operational processor.

On the other side a reprocessing of the overall data set is necessary to take into account the evolution of the instrument knowledge and of the algorithms and models which naturally occurred during the few years of the mission. Generally a new processor has to be developed to take this evolution into account.

In the context of ERS, it is noted that ECMWF started the generation of 40 years of daily analysis from 1959 to 1999. As this data set will include ERS data during the period 1991 - 1999, it is recommended to handle the ERS data reprocessing in close cooperation with ECMWF.

Wind - σ^0 modelisation

The limitation in the interpretation of the scatterometer data over the ocean is linked to the understanding of the physics of the interaction of the micro waves with the sea surface.

What is the main factor measured, wind or wind stress, neutral wind or real wind?

Which are the effects of rain, air temperature, sea temperature, fetch, salinity, sea state and wind stability on the measurements?

Today only empirical models are used to derive the wind and very few studies have been started on this subject.

A better quality of the wind derived from scatterometer data will only be possible through an improvement of the algorithms and the models used today.

Algorithms

New algorithmic tools have to be developed in order to combine and assimilate the various new data types made available by spaceborne instruments.

It took few years for the meteorological offices to develop the new algorithmic tools necessary to assimilate adequately the wind products derived from scatterometer measurements. This effort has to be prolonged to all new parameters and to the various interactions between these new parameters and the one already existing.

Oceanography and ice caps

The analysis and the understanding of the interactions between the ice caps, the ocean and the atmosphere is important for oceanography in particular the ice coverage and the ice drifts. The necessity of both C-band and Ku-Band is strongly underlined for ice classification. The need of fan beam, in order to have the same target imaged at various incidence angle, is noted for Antarctic sea/ice analysis and for ice edge monitoring.

Sampling

The basic assumption is that the nominal scatterometer sampling shall be double swath (Ascat type) or equivalent (for example like QuickScat). ERS by far doesn't provide the coverage required because it is single swath and because it is continuously interrupted for SAR acquisitions or by gaps introduced by the switching between Wind and Wind/Wave modes because of the ATSR High rate operations over land.

For climatological applications it is not important to have a better temporal sampling than the one given by a single instrument as soon as important structures (e.g. cyclones) are not systematically missed. In fact it appears that the westward displacement of a cyclone is more or less in phase with the scatterometer swath displacement. The tropical cyclone "Luis", in 1995, was systematically missed by ERS (only two hits) while "Georges" in 1998 was imaged eleven times.

For other application like risk management and phenomena analysis, it is important to double the sampling by having two instruments at 12 hours interval. Combining C-Band and Ku-Band acquisition on two satellites is an asset.

The spatial resolution for future scatterometer mission shall be set to 25 x 25 km. This is a very strong requirement for phenomena analysis (cyclone, mistral) and coastal studies. It is also foreseeable that the requirements for weather forecasting, which are around 100 x 100 km today, will evolve toward a finer resolution probably within the next decade and anyway before the end of the Ascat mission.

Metop and Ascot

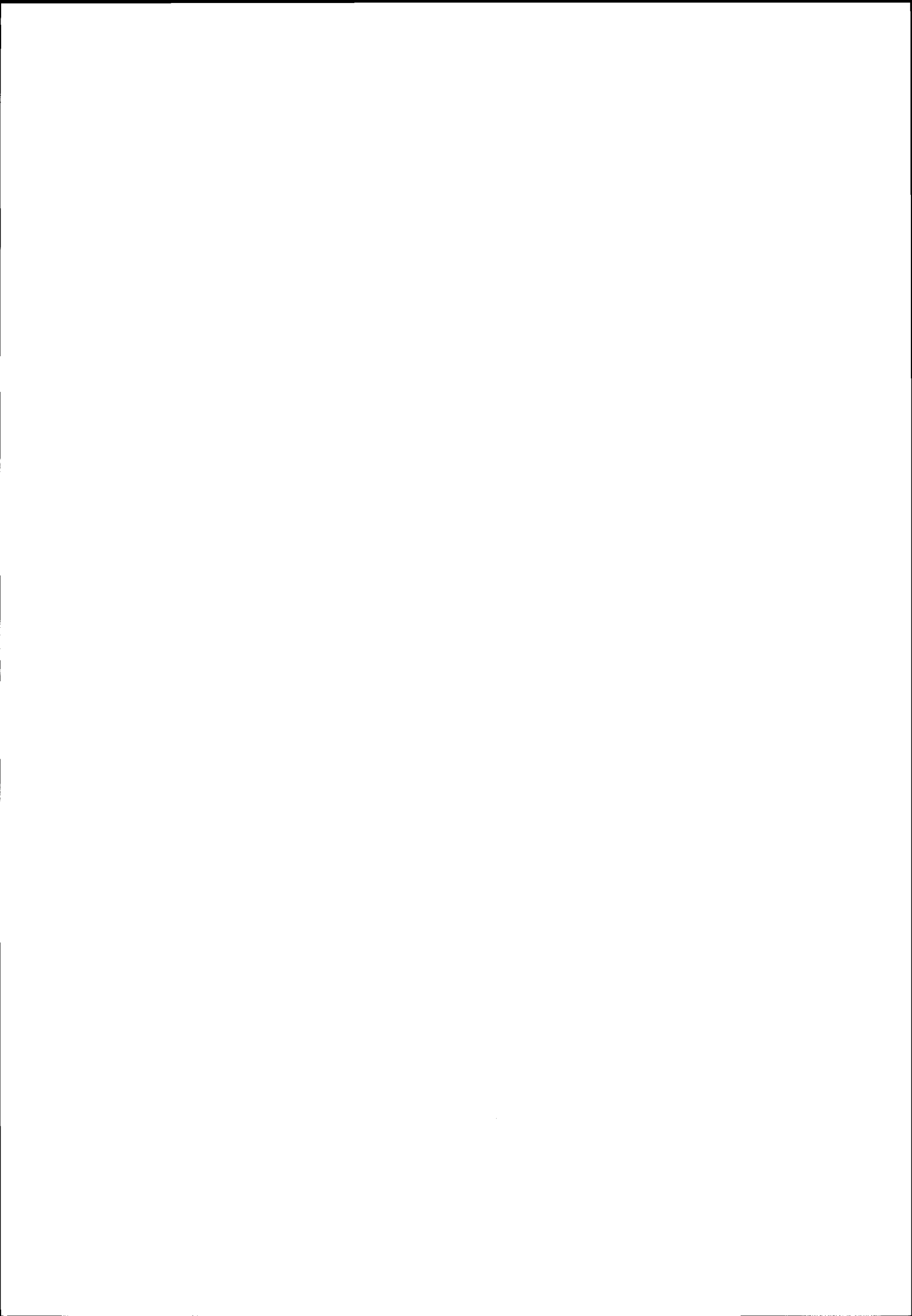
Metop is an operational satellite by opposition for example to Jason 1 which is still presented as an experiment. This is an important fact for the oceanographic community.

25 x 25 km resolution is a must (cf Sampling).

It is very important to consider the archiving and the reprocessing of Metop scatterometer data (cf ERS data reprocessing above) in the context of a long time serie which could start in 1991 for 30 years or more. In this context, the Eumetsat climate monitoring mission is of major importance.

Conclusion

There is unanimity to recognise the importance of scatterometer data in oceanography today, both for climatology and for phenomena analysis. The critical step now is to ensure the continuity of the scatterometer data set through the start of the new millenium.



MERCATOR, the mission.

Prepared by the Mercator project, presented by Philippe Courtier.

Abstract - Mercator, a project initiated by the oceanographic community in France, is described. The objective is to develop an eddy resolving data assimilation system for the ocean. It illustrates the Global Ocean Data Assimilation Experiment (GODAE).

users of Mercator have been clearly identified during the set-up of the project:

I. INTRODUCTION

The Mercator project whose aim is the development of an eddy resolving global data assimilation system is a proposal elaborated by the scientific oceanographic community and endorsed by the French institutes interested in operational oceanography, Centre National d'Etudes Spatiales (CNES), Centre National de la Recherche Scientifique / Institut National des Sciences de l'Univers (CNRS/INSU), Institut Français de Recherche pour l'Exploitation de la MER (IFREMER), Météo-France, Office de la Recherche Scientifique et Technique Outre-Mer (ORSTOM) and Service Hydrographique et Océanographique de la Marine (SHOM).

Seasonal prediction. The meteorological community is considering the operational implementation of seasonal prediction systems. The prediction rely on the integration of a coupled ocean atmosphere model. Initial conditions are required both for the atmosphere and the ocean over the whole globe. Mercator will provide the initial conditions for the ocean whereas the atmospheric data assimilation systems used for numerical weather forecasts will provide the initial conditions for the atmosphere.

Two workshops took place in 1995 in order to draw the general lines of the project while CLS-Argos (Collecte, Localisation par Satellite) was in charge of the synthesis and as such of the phase 0. 1996 was the year where the project was set-up by Jean-François Minster (CNRS / INSU) and the phase A of feasibility was decided (and funded) by the above institutes February, 3rd, 1997, while the phase B was decided September, 17th, 1998. CERFACS (Centre Européen de Recherche et Formation Avancées en Calcul Scientifique) is the focal point for Mercator and Jean-Claude André has been appointed as executive secretary in order, among other things, to ensure an efficient feedback between the project and the institutes.

At this stage, it is not envisaged to operate coupled ocean atmosphere data assimilation systems. A fundamental difficulty would be the difference of time scale of the two fluids, which for the ocean goes beyond the deterministic predictability limit of the atmosphere. This issue will be reconsidered in the future if unstable coupled modes are identified which would then need to be properly controlled during the assimilation process.

Mercator is a contribution to the Global Ocean Data Assimilation Experiment (GODAE) planned for the years 2003-2005.

The European Centre for Medium-Range Weather Forecasts (ECMWF) is presently operating a seasonal prediction system in experimental mode. It is foreseen the Mercator will be developed in collaboration with ECMWF. The main short term priority is the availability of a global system with the emphasis being put on the tropical oceans.

II. MERCATOR PROJECT RATIONALE AND MISSION OBJECTIVES.

The goal of Mercator is the implementation within five to seven years of a system which simulates the global ocean with a primitive equation high resolution model, which assimilates satellite and in situ data, and which is operated in pre-operational mode. In the longer term, the system has to become fully operational and has to contribute to the development of a climatic prediction system relying on a coupled ocean atmosphere model. In addition the system has to be useful for the military and commercial applications of oceanography. Three

Marine applications. The French Navy is presently operating an experimental data assimilation system for the Eastern Atlantic. High spatial resolution, better than a tenth of a degree, is deemed necessary. The primary area of interest is the Eastern Atlantic with also a high priority for the Mediterranean sea.

Coastal applications are not part stricto sensu of the Mercator project. Nevertheless Mercator has to be able to provide lateral boundary conditions for coastal models.

Scientific applications. Besides the operational implementation which produces oceanic fields made available to the scientific community, Mercator will be used as a research tool for producing level 3 (gridded) fields at the occasion of measurement campaigns. Consequently flexibility has to be part of the overall design in order to be able to accommodate specific requirements like being able to concentrate on a given area.

A. Mercator main components

The Mercator system consists of three main components : firstly, an ocean general circulation model, secondly a data assimilation algorithm and lastly a data stream (observations, forcing fields, initialisation fields, validation data ...).

(i) The ocean general circulation model.

The ocean general circulation model of Mercator is a primitive equation model based on OPA which has been developed at Laboratoire d'Océanographie Dynamique et de Climatologie (LODYC). It is recognised that the OGCM will be in constant evolution. At the time of GODAE the model will have been validated at the global scale and with a typical horizontal resolution of $1/12^\circ$. In order to achieve this goal, two lines of development will be followed in parallel :

Global, low resolution. The main priority here is to concentrate on the global aspect of the problem, and in particular on the validation in coupled ocean-atmosphere mode. Mercator will benefit from and rely on the effort made by the French research community in the field of climate simulations and coordinated under the " groupe GASTON ". Two atmospheric models are being used, the code developed by Laboratoire de Météorologie Dynamique (LMD) and the code whose kernel has been jointly developed by Météo-France and ECMWF under the framework of the Arpege-IFS collaboration. The coupling module is OASIS developed by CERFACS.

Furthermore, OPA has been implemented at ECMWF and the sensitivity of seasonal predictions to the OGCM used will be assessed by comparisons with the present experimental seasonal prediction system of ECMWF which makes use of the OGCM HOPE developed by the Max Planck Institute, Hamburg.

Basin, high resolution.

The CLIPPER project which involves scientists from LPO (Brest), LEGI (Grenoble), GRGS (Toulouse) and LODYC (Paris) aims at simulating the Atlantic ocean circulation at a resolution of a sixth of a degree. Several scientific issues particularly relevant for Mercator are being addressed.

The following step is to build on the experience acquired during CLIPPER and to operate in 1999 a prototype system based on OPA which will simulate the North Atlantic and Mediterranean circulation at a resolution of a twelfth of a degree and with TBD vertical levels. Temperature, salinity and horizontal velocity are prognostic variables. The rigid lid hypothesis is made. A mixing layer based on a TKE closure is used

(ii) Data assimilation.

Data assimilation methods are currently in quick evolution, particularly under the impulse of the oceanographic community. It is therefore necessary to allow for flexibility in the algorithms which can be accommodated as well as to offer various possibilities for future evolution. On the other hand, (pre-)operational requirements imply to be rather conservative in the choice for initial implementation. ECMWF has implemented for the seasonal prediction project an existing bidimensional Optimal Interpolation scheme which is not in the position, at the present stage of development, to use altimeter data. The basin, high resolution, initial implementation of Mercator will rely on the already validated code SOFA which uses empirical orthogonal functions of the vertical covariance matrix to decouple the vertical and horizontal directions. SOFA does not assimilate yet in-situ observations, this is a short term development scheduled for 1998.

Data assimilation attempts at combining various information sources (observations, dynamic's of evolution, ...) and as such is a statistical estimation problem. The methods which may be used within Mercator will rely on a specification of the statistics of error (either static or adaptive) in order to be able to improve the system by a careful study of the innovation vector. Besides the theoretical motivation, this choice is motivated by the lesson drawn from the meteorological operational experience that the only Centres still at the cutting edge of weather forecasts have followed this path.

Mercator has to offer the possibility to accommodate the main "modern" data assimilation methods, Optimal Interpolation since it is the initial implementation, variational approach (3D and 4D) in the direct and dual formulation (representers), simplified Kalman filters and adaptive filtering. In order to save computational time, space reduction techniques have to be accounted for in the design. A plausible implementation for the GODAE era would be an adaptive filtering which evaluates key aspects of the statistics of estimation error while the analysis is solved on a limited time window with a variational approach formulated in a reduced space.

It can be shown that all the above methods use more or less the same operators (observation operator, model, projector on the reduced space, covariance matrices of the various errors, gain, ...) or solver (minimization, eigen values), which are in limited number, but with a very different calling sequence. In order to accommodate the above flexibility requirement, the algebraic component of the data assimilation methods and the scientific content of the operators will be made independent.

A generalised coupler, PALM, will solve the algebraic part; it builds on the technical experience acquired with OASIS. The scientific content of the operators will depend on the experience acquired during the experimental phases of the basin, high resolution and global, low resolution implementations, and on the results obtained by the research community.

While the initial experimental implementation may rely on a univariate formulation, a multivariate formulation in order to be able to accommodate several different data types will be implemented quickly afterward.

In the initial experimental phase, the computer resources used for a week of assimilation should be less than twice the cost of a week of the assimilating model integration. At the time of GODAE, the cost of a week of assimilation should not exceed five times the cost of the assimilating model integration.

(iii) Data stream.

Ocean observations, space segment. The requirement of Mercator for oceanic space based data consists of sea surface temperature and altimetry. In the longer term, ocean colour information may be used in coupled physical biological assimilation system, but this is not foreseen as an operational requirement for Mercator at the time of GODAE. Nevertheless this will most likely become soon a research requirement, and as such be thought of within Mercator. There is a requirement of Mercator for global salinity observations, therefore the space agencies are invited to develop, if feasible, the required technologies.

Sea surface temperature fields may be produced using observations from various instruments. The main operational source is the visible/infrared imager AVHRR (Advanced Very High Resolution Radiometer) on board the National Oceanic and Atmospheric Administration (NOAA) operational satellites. AVHRR is also part of the METOP/EPS payload as approved by the Eumetsat Council in June 1996.

Altimetric data are necessary for Mercator. Beyond Topex-Poseidon, the Jason collaborative NASA/CNES programme will provide high precision observations. In parallel, observations of lower precision like onboard the ERS-1 and ERS-2 satellites (and ENVISAT for the near future) of the European Space Agency provide a significant complement. It has to be pointed out that no altimetric operational programmes have been decided yet, it is one of the goal of Mercator to demonstrate the operational need. A fast delivery

product (a very few days) is necessary for some of the Mercator operational applications, but high quality products remain necessary for scientific applications.

Oceanic in-situ observations. Electromagnetic waves do not penetrate beyond a few meters in the ocean it is therefore necessary for Mercator to assimilate in-situ observations which provide access to the vertical structure of the ocean. Temperature, currents and salinity are the parameters to be assimilated. Eulerian observations are useful in that under some sort of stationarity hypothesis, they allow to identify model biases. Nevertheless there is no difficulty for assimilating Lagrangian observations.

Tomography may provide access to the mean thermal structure of the ocean with access to a few degrees of freedom in the vertical. In a project like Mercator, the meteorological experience shows that once the physical interpretation of remote-sensed data is mature enough at the research level, it is still necessary to have one or two persons dedicated to the implementation in the assimilation suite. Therefore assimilation of tomographic data is not considered as a first short term priority for Mercator. The issue will have to be reconsidered a couple of years before GODAE, resources permitting.

Forcings. Reanalysis as performed at the ECMWF are essential for providing consistent thermodynamical and momentum forcings for Mercator. It only covers the period 1979 to 1993 and has not used as surface wind speed observations the passive microwave radiometer SSM/I from the DMSP satellite, neither the scatterometer wind observations (with their 180° directional ambiguity) from the satellites ERS-1 and ERS-2. A reanalysis of the "Scatt years" at higher resolution (T213) would be extremely useful, a bonus would be to cover the whole of the "Topex years", such an effort is taking place at ECMWF within the ERA-40 reanalysis project, nominally at a T106 resolution, possibly at T213, resources permitting. At T213, the smallest half wave length resolved is 95 km and the shortest scales are heavily dissipated, a significant variability of the wind field is then not resolved. Mercator will benefit from the effort to produce as representative as possible wind forcings, conducted in the research community.

The latent heat fluxes at the surface of the ocean can be estimated from satellite data with some accuracy, at least under the Semaphore conditions. This is not the case for the sensible heat flux, which is significantly smaller. Precipitations are largely unknown. Radiation fluxes are heavily dependent

upon clouds whose representation is not the strongest feature of the atmospheric models. It is not a priori obvious that an improvement of the latent heat fluxes of the reanalysis by using satellite data but without the possibility of improving the other fluxes will result in an improved oceanic circulation since the overall consistency will have been lost. Mercator will have to assess its requirements in view of the results obtained during the experimental phases.

Real time. Real time is a key aspect of the various data streams for the operational applications of oceanography. The requirement is of the order of 3 days, and in that respect Jason will be a significant improvement upon Topex-Poseidon.

B Mercator technical requirements.

Considering the computer resources involved in running in a high resolution global oceanic model, the assimilation suite will have to run on the most powerful computers available on the market. In the coming few years, it can be expected that such platforms will rely on moderately high (O100) to high (O1000) parallelism and on distributed memory.

The observational data flow as well as the oceanic fields data flow require a significant amount of Input/Output and of archiving capabilities, while the bandwidth remain limited. Mercator will build on the experience acquired by the ECMWF reanalysis team for the development of the assimilation suite.

A secured data flow has to be designed for sensitive data.

III. SOME STEPS TOWARD OPERATIONAL OCEANOGRAPHY.

France has significantly contributed to the emergence of operational oceanography through an investment in the international observing research programmes. As an illustration, France has been the main contributor to the ERS-1/2 programmes, and beyond the ERS altimetric mission is the partner of NASA in Topex/Poseidon and in the forthcoming Jason. France will also be the main contributor of the space segment of Metop. Concerning in situ data, the involvement in the observing phase of WOCE has also been significant.

In order to valorise this already significant investment, France has to be present in the three aspects of operational oceanography as foreseen in GODAE.

Space segment. Assuming the Metop programme decided, a long term commitment of Europe for the measurement of sea surface temperature and the surface momentum fluxes will have been achieved.

Operational oceanography further requires a long term commitment for high precision altimetry and therefore a follow-on of Jason. As of today, altimetry has been funded by development agencies like CNES, NASA or ESA. Following the example of scatterometry and the transfer of the mission responsibility from the development agency ESA to the user agency Eumetsat, the emergence of operational oceanography will probably imply a similar transfer.

In situ observations. The contribution of France to the in situ part of GODAE is currently being discussed in the Coriolis working group chaired by Ifremer. It could be along 4 actions which build on already existing or planned systems. First an effort similar as during WOCE, typically 5000 per year, should be performed for maintaining the XBT measurements. Second, Lagrangian profilers of the class of the US Palace or the French Provor has to be deployed on a large scale basis, research and development is necessary for the measurement of salinity. Third, Eulerian profilers need to be developed and deployed, with a typical number similar to the Lagrangian profilers. The cost of a profile has to be less than 1000FF for providing a viable long term observing system. Lastly moored and drifting buoys have to be maintained and/or systematically instrumented for oceanographic measurements.

Modelling and Assimilation. The Mercator project is conducting the research and development effort in this area. In order to implement operationally the data assimilation suite to be developed by Mercator, two additional elements are required besides the Mercator team. First, high performance computing facilities and the corresponding archiving system are mandatory. This corresponds to resources comparable to a significant fraction of operational numerical weather prediction requirements. Second a team needs to be in place whose responsibility is to manage and scientifically monitor the incoming data flow (observations, forcings...) and the outgoing data flow (products).

DETERMINATION OF SATELLITE WIND AND WIND-STRESS FIELDS: EVALUATION OF THESE FIELDS IN AN OCEAN GCM

N. Grima *

IFREMER/Brest, Département de Recherche Océanographique
Océanographie Spatiale B.P. 70, 29280 Plouzané, France.

ABSTRACT

This paper aims to evaluate gridded wind and wind stress fields using the asymptotic scatterometer measurements from the European Remote Sensing-1 satellite (ERS-1). The geophysical content of these fields has been tested in the tropical ocean by analyzing their impact when employed as forcing term of an oceanic general circulation model.

Key words: space oceanography, ERS satellite, scatterometer, wind and wind-stress, air-sea interactions, ocean general circulation model, tropical oceans.

1. INTRODUCTION

To increase our knowledge of Oceanic General Circulation Model (OGCM) mechanisms it is essential, at first, to study OGCM forced with prescribed atmospheric forcings. The most important of them is the wind stress at the sea surface.

The contribution of data from operational sensors aboard satellite platforms appears to be one of the solutions to obtain wind stress fields with sufficient quality, regarding the data accuracy as well as their coverage. Sensors from research satellites such as the European Remote Sensing satellites 1 and 2 (ERS-1 and 2) which supply indirect measurements of wind speed and direction, provide very useful information. However, the computation of the wind stress from the observed wind is limited by uncertainties in the value of the drag coefficient.

The tropical Pacific ocean has been chosen as the region for comparing the responses of the ocean circulation model when forced by the ERS scatterometer and numerical wind fields. It is characterized by weak to moderate winds (0-15 m/s) and by the ElNiño/Southern Oscillation (ENSO). The Pacific is the best instrumented of all the oceans, especially in the equatorial part with the presence of the Tropical Atmosphere and Ocean (TAO) buoy array. Our study covers a 3-year period from July 1992 to July 1995, during which weak warm events were observed

*now at: Laboratoire d'Océanographie Dynamique et de Climatologie (LODYC), 4, place Jussieu, 75252 Paris Cedex 05, France. e-mail: nglod@ipsl.jussieu.fr

[Liu *et al.*, 1995; Goddard and Graham, 1997]. The period was selected because of the common availability of ERS scatterometer wind fields and the data from the Arpege-Climat experiment.

2. DATA SETS

In this paper, two data sets are used to force an OGCM. The first data set consists of the sea surface fields from the Arpege-Climat Atmospheric General Circulation Model (AGCM) (BF5 experiment). They are available from 1979 to mid-1995. This climate model, developed by Météo-France and jointly by the European Centre for Medium-Range Weather Forecasts (ECMWF), is a climate version of the operational model whose particularities are described by Déqué and Piedelièvre [1995]. Daily Arpege-Climat fields are available on a reduced T42 gaussian grid with 30 vertical levels. This data set contains the main atmospheric and surface parameters required to force the LODYC-OGCM "OPA" namely: 10 meter wind and wind-stress vectors, net heat flux, net short-wave radiation flux and water flux at the sea surface.

The second data set is mainly based on the sea surface wind vectors which are observed by the scatterometer aboard the polar orbiting European Remote Sensing satellite 1 (ERS-1). The estimation of the sea surface wind vectors is performed at the scatterometer cells (50 km) using the backscattering coefficients measurements [Bentamy *et al.*, 1994; Quilfen, 1995]. These products are archived during the ERS-1 mission and distributed by the "Centre ERS d'Archivage et de Traitement" (CERSAT) located at "Institut Français de Recherche pour l'Exploitation de la Mer" (IFREMER). From these wind vectors, the calculation of wind stress modulus $|\tau|$ and its components τ_x and τ_y , is determined by means of the quadratic bulk aerodynamic formulations.

Wind vector, SST and current measurements from the Tropical Atmosphere-Ocean (TAO) buoys array [Hayes *et al.*, 1991; McPhaden and Hayes, 1991] are used in order to validate the forcing fields and the ocean variables estimated by the OGCM. To make wind comparisons possible, daily buoy wind vectors are referred to 10-m height and neutral stability conditions using a boundary layer procedure [Ezraty, 1985].

3. COMPARISONS BETWEEN ERS AND TAO WINDS

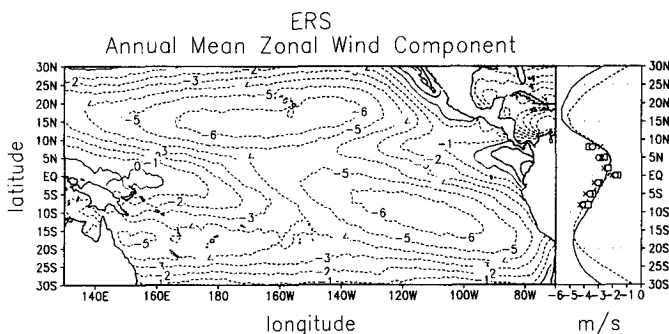


Figure 1. Representation of the annual means (m/s) calculated from July 1992 to July 1995, of the gridded ($1^\circ \times 1^\circ$) zonal component of the wind fields deduced from the ERS scatterometer. On the right hand side of the spatial distribution the zonal averages are represented, in dashed line for the ERS scatterometer fields and in solid line for the Arpege-Climat fields. Crosses, open circles and open squares indicate the zonal averages of the TAO buoy, ERS and Arpege-Climat collocated data, respectively.

Differences between the ERS and Arpege-Climat zonal wind fields appear as regards the magnitude and variability of the principal geophysical structure (on the right hand side of Figure 1). Poleward 15° , the ERS annual mean zonal wind field is smaller than that of Arpege-Climat. This overestimation of the wind by the atmospheric model is due to a very weak meridional displacement of the Hadley circulation, and may be related to poor parametrization of the convective regions in the model [Slango *et al.*, 1995]. In the equatorial belt, comparisons between the mean ERS scatterometer zonal winds and the TAO buoy observations do not show large differences.

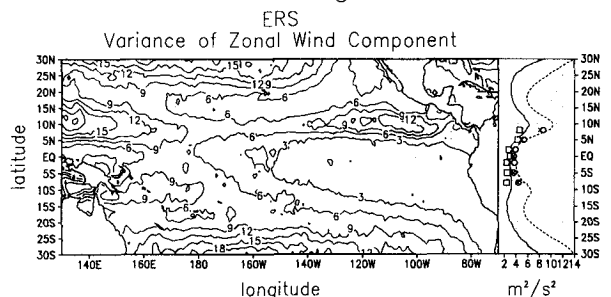


Figure 2. As the Figure 1 but for the variance (m^2/s^2).

As is shown on the right hand side of Figure 2, Arpege-Climat variances are smaller than those of ERS. The difference which is small around the equator, increases dramatically under the ITCZ. The meridional variation of the ITCZ described by Mitchum [1987] and by Waliser and Somerville [1994], is more clearly depicted by the satellite winds than by the climate model analysis. It is clear from the comparison with the TAO buoy observations that zonal wind variations described by the scatterometer data are more realistic than those of Arpege-Climat. The analysis on the meridional component will reinforce this point.

ERS and Arpege-Climat zonal and meridional wind components have been compared with the 61 TAO

buoy wind vectors from July 1992 to July 1995, and over the equatorial Pacific ocean.

Correlation coefficients between ERS and TAO (CCET) are computed. ERS wind components, with a mean value of the significant CCET of 0.82 and 0.72 for the zonal and meridional components, respectively, depict with accuracy wind variability over the equatorial Pacific ocean. These CCET are always higher than the coefficient of correlations computed between atmospheric simulations and buoy measurements (CCAT) which average 0.57 and 0.62 for the zonal and meridional components, respectively (not shown). However, we note that the CCET are lower for small absolute values of the zonal wind components. In the western Pacific ocean (ex: $156^\circ E$ and $165^\circ E$), comparisons between ERS and TAO winds are more difficult than in the eastern part because the winds are weak and have a high variability [Bentamy *et al.*, 1996].

4. DESCRIPTION OF THE OCEANIC MODEL AND THE FORCING EXPERIMENTS

4.1. Ocean General Circulation Model (OGCM) description

This study was performed with the OGCM "OPA" version 7 developed by modelers from "Laboratoire d'Océanographie DYnamique et de Climatologie" (LODYC) [Delecluse *et al.*, 1993]. The OGCM "OPA" solves the primitive equations: i.e. Navier-Stokes equations simplified by the classic hydrostatic and Boussinesq approximations with a rigid lid and incompressibility. The "TOTEM" version of "OPA" was used in this study [Dandin, 1993; Maes, 1996]. Its horizontal domain covers the belt between $50^\circ N$ and $50^\circ S$ in latitude and its spatial resolution is irregular. Distances between two latitudes are equal to 1.5° to the north and south sides and reach $1/3$ degree (≈ 37 km) at the equator. Zonal resolution in the middle of oceanic basins is equal to 0.75° and rises to $1/3$ degree near coastal regions. The model is defined on 30 vertical levels from 0-m to a 5000-m limit. In the first 200 meters the vertical resolution is 10 meter, it decreases progressively to 600 meters between the last two levels. The time step required is set at one hour for stability. The surface boundary conditions are defined by wind-stress, net heat flux, penetrative solar radiation and freshwater budget at the sea surface. A feedback term is required in a forced simulation to prevent excessive surface warming by positive biases in the heat fluxes.

4.2. Forcing experiments

The two experiments discussed hereafter extend from April 1992 to July 1995. The first one, called ERS-O, has been forced with weekly ERS scatterometer wind data (used to compute wind-stress, heat flux and freshwater flux). The second one, called ARP-O, has been forced with weekly Arpege-Climat fluxes. Both experiments start from the same initial conditions which are derived from "TOTEM" forced by Arpege-Climat over a 7-year period (1984-1991)

[Maes, 1996]. These runs have permitted the model to reach a quasi-equilibrium state. In order to reduce the influence of this first guess on the ERS experiment, only oceanic responses from July-1992 to July-1995 have been studied.

First, "TOTEM" was forced from 1985 to mid-1995 by daily surface fluxes from the Arpege-Climat atmospheric model version BF5.

On the other hand, weekly wind-stress fields from ERS complemented with weekly fluxes computed through the bulk aerodynamic formulae and Arpege-Climat solar heat flux, infrared radiation and precipitation were prepared to define surface fluxes for "TOTEM". As mentioned above, SST used to compute complementary fluxes for ERS experiment, comes from the gridded ($1^\circ \times 1^\circ$) weekly SST fields calculated by Reynolds and Smith [1994].

5. OGCM SIMULATION RESULTS

The 5-day average from ERS-O and ARP-O simulations are compared and also with TAO buoy measurements. In the first section, the mean structures in temperature and current are described and in the second section their variabilities.

5.1. Averaged fields

5.1.1. Thermal response along the equator

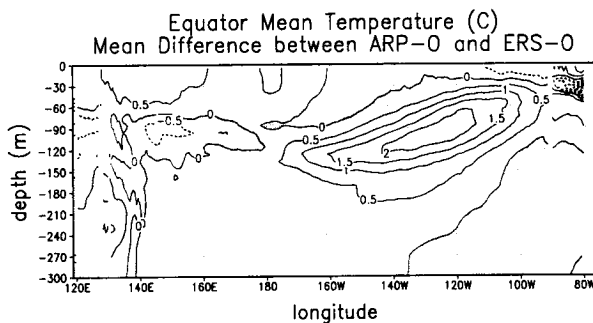


Figure 3. Vertical distribution of the annual mean temperature ($^\circ\text{C}$) differences between ARP-O and ERS-O along the Equator in the Pacific ocean. Positive values indicate that ARP-O simulations give warmer results than ERS-O.

The annual mean differences of temperature between the vertical distributions (0 to 300 m depth) along the equator regarding ERS-O and ARP-O are represented in Figure 3. Major differences appear in the subsurface with negative values in the western upper thermocline and positive values in the eastern thermocline. These results tend to indicate that the thermocline in ERS-O is slightly closer to the sea surface than in ARP-O. The temperature from the ARP-O is higher than that from ERS-O in the area of the eastern Pacific ocean between 60 and 150 m depth where the thermocline reaches to the sea surface. At this location, the difference is greater than 2°C . The "warm pool" from ERS-O, in the western part of the Pacific ocean between the sea surface

and 60 m depth, is slightly colder (0.5°C) than the Arpege-Climat thermal response.

5.1.2. Zonal currents along the equator

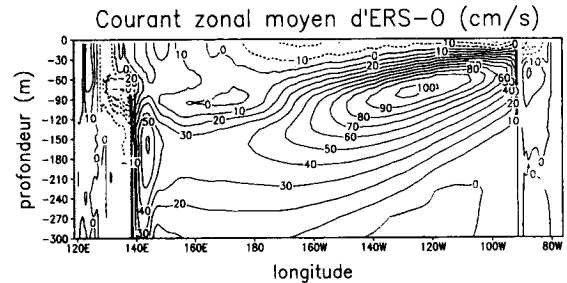


Figure 4. Vertical distribution of the annual mean zonal current (10^{-1} m/s) along the equator in the Pacific ocean, in A) the ERS-O experiment and in B) the ARP-O experiment. They are represented on the vertical OGCM grid. Positive values and not dashed regions indicate eastward current.

The equatorial currents (South Equatorial Current (SEC) and Equatorial Under-Current (EUC)) are mainly wind driven [e.g.; McPhaden, 1993a, 1993b; Halpern et al., 1995; Blanke and Raynaud, 1997]. The annual mean values of the ERS-O zonal current is represented in Figures 4. As shown in these figures, temperature differences in the eastern Pacific are probably due to the presence of stronger ERS equatorial under-currents and weaker ERS-O SEC than in ARP-O. On average, the velocities of the ERS-O EUC reach 1.0 m/s around 90 meters at 125°W , whereas the ARP-O simulated EUC maximum is around 0.8 m/s .

In the eastern Pacific, the SEC simulated by Arpege-Climat winds through the OGCM (-0.3 m/s) is higher than in ERS-O (-0.1 m/s). Furthermore, the extension of the South Equatorial Current (SEC) stops before the dateline in ARP-O, while it persists almost up to 160°E in ERS-O. As is shown in Figure 1, on the equatorial section, this corresponds to the stronger Arpege-Climat trades in the eastern and western Pacific. Conversely, the vertical structure of currents exhibits stronger reversals with Arpege-Climat, suggesting a more extensive penetration of the Australian monsoon over the western Pacific.

To determine which of the two simulations is in best agreement with observations, mean current profiles are computed from TAO buoy current meter and Acoustic Doppler Current Profiler (ADCP) data at locations 110°W , 140°W and 165°E (Figure 5), where time series are available and consistent.

At 110°W , the current profile from ERS-O appears to agree well with TAO current meter measurements, at the sea surface. It is slightly stronger between 20 and 90 meters and weaker below. The ARP-O underestimates the current between the sea surface and 50 meters and below 90 meters by about 0.1 m/s ; between 50 and 90 meters it is in good agreement with the buoy observations.

At 140°W , the profile current from ERS-O, between the sea surface and 60 meters, is in very good agreement with the TAO buoy observations. The EUC

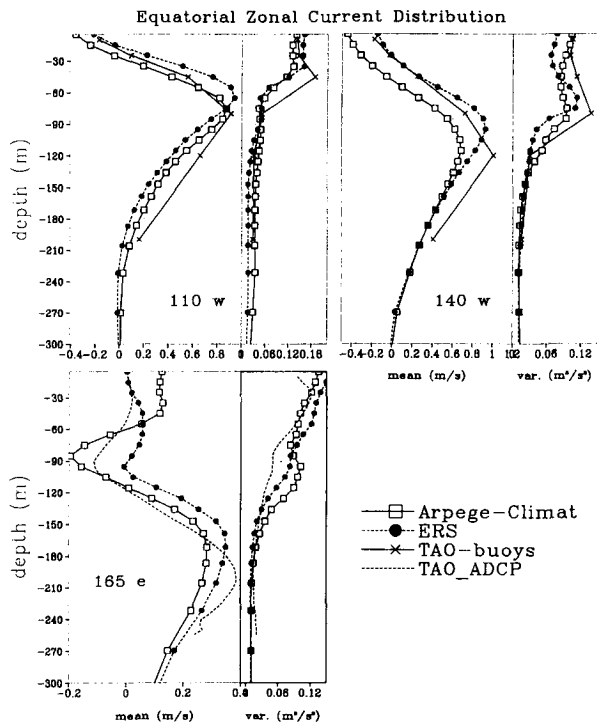


Figure 5. Comparisons along the equator of the annual mean zonal current (m/s) profiles (on the left side) and of their variability (m^2/s^2) (on the right side) are represented at three TAO moorings, in a) at $110^\circ W$, in b) at $140^\circ W$ and in d) at $165^\circ E$, for ERS in dashed line with closed circles, for Arpege-Climat in solid line with open squares and for TAO buoys in solid line with crosses.

maximum is around 90 m depth, while it is around 120 m in the TAO data, however, on average, its intensity (0.9 m/s) is very close to the observations (1.0 m/s). Below 100 meters, the current from ERS-O is weaker than the buoy measurements. At $110^\circ W$ and $140^\circ W$, both ERS-O and ARP-O currents show slight variability in the upper thermocline compared to TAO data.

At $165^\circ E$, the equatorial zonal currents derived from ERS-O are in good agreement with the TAO ADCP observations at 20 meters depth. The zonal currents simulated in ERS-O are in the opposite direction to TAO buoy measurements, at around 100-m depth, whereas the Arpege-Climat results are stronger than the observations. These differences are probably due to the inconsistency between the ERS scatterometer wind-stress fields and the precipitation fluxes derived from the Arpege-Climat model which are used to complete the ERS surface fluxes to force "TOTEM".

5.2. Equatorial variability

Comparisons between the TAO buoy data and the two simulations show good agreement. In the context of their contribution to the ocean circulation, we compare, in terms of correlation, the thermal and current time series from the ERS-O and ARP-O with in-situ measurements along the equator.

5.2.1. Sub-surface variability in temperature derived from ERS-O and ARP-O

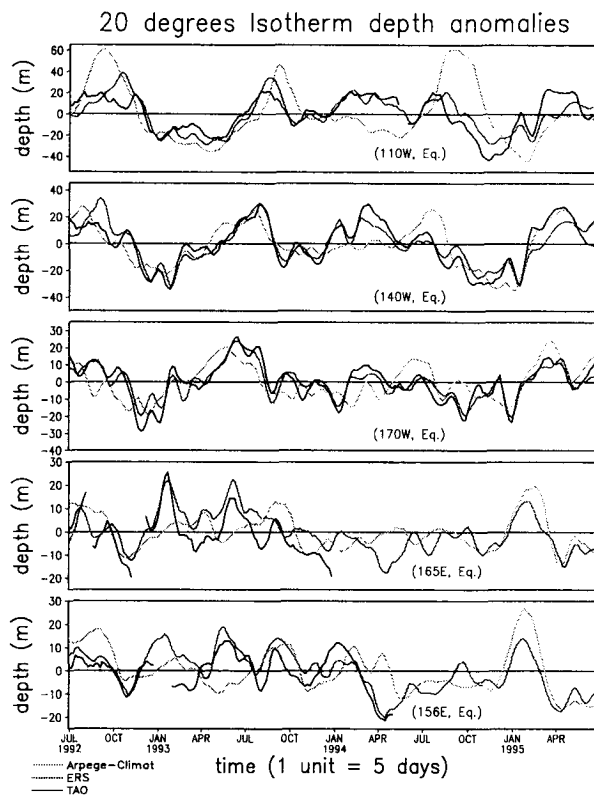


Figure 6. Comparison of the depth anomalies of the $20^\circ C$ isotherm, in meters, derived from ERS-O and ARP-O, with buoy measurements along the equator at locations $110^\circ W$, $140^\circ W$, $170^\circ W$, $165^\circ E$ and $156^\circ E$. A 25-day running mean filter has been applied for graphic clarity. Positive values indicate a rise of the thermocline.

Five buoy locations have been chosen along the equator ($110^\circ W$, $140^\circ W$, $170^\circ W$, $165^\circ E$ and $156^\circ E$) to describe the variability of the $20^\circ C$ isotherm depth during the study period (Figure 6, positive values indicate a rise in the thermocline).

East of the dateline ($110^\circ W$, $140^\circ W$ and $170^\circ W$), after a poor rise in the thermocline at the beginning of the second half of 1992, a deepening of the thermocline between 30 and 40 meters occurs in November 1992 and January 1993 at $170^\circ W$. These signals seem to precede the eastern Pacific events where we observe the deepening of the thermocline at $140^\circ W$ in December and February and less clearly at $110^\circ W$ between January and July 1993. It is followed by a rise in the thermocline with peaks of 30 meters between July and October 1993. After weak rises and periods of deepening of the thermocline over one year (October 1993 - October 1994), the depth anomaly of the $20^\circ C$ thermocline decreases twice to a depth of around 35 meters between the end of November 1994 and February 1995 at $170^\circ W$ and is propagated to the east where it reaches a depth of 50 meters in November 1994 at $110^\circ W$. This warming event which according to Liu *et al.* [1995] could be an El Niño event, is well depicted by the ERS-O outputs, which have sufficient quality, regarding data accuracy as well as coverage, to characterize the high fre-

quency variability (period of a few weeks) of the surface winds. While a strong seasonal cycle dominates the variability in the eastern Pacific, the high frequency variability (period of a few weeks) depicted by Arpege-Climat is smaller than that observed by the TAO data or captured by ERS in the eastern Pacific. It can even be out of phase around the dateline.

In the western Pacific, at 165°E and 156°E , the strong rise of the thermocline during January 1993, with a depth anomaly of around 25 meters, is depicted accurately in ERS-O (22 meters), while generally speaking, between October 1992 and October 1993, ARP-O presents weak variability. This event is the ocean response to a succession of westerly wind bursts observed in the warm pool from December 1992 to January 1993 [Smith *et al.*, 1996a, 1996b]. The succession of thermocline rises during 1993 is well simulated by the ERS forcing such as the one between June and July 1993, while the Arpege-Climat winds underestimate them. The beginning of the deepening of the thermocline, in April 1994, from ERS-O is perfectly correlated with observations, whereas from ARP-O it is in the opposite phase at the time of this event. Unfortunately, there are no TAO buoy data from January 1995 to April 1995 to validate the cooling simulated by the ERS and Arpege forcing experiments.

- surface current

Time series of the zonal current components from July 1992 to July 1995 using the two simulations and TAO buoy measurements are computed (shown only at sea surface). They are located at 110°W , 140°W and 165°E at three depths, 10 m depth for the three buoys, 100 m depth for the buoy located at 165°E and 80 m depth for the other two, where TAO buoy current measurements are available. The hourly TAO buoy data are averaged every 5 days in accordance with the OGCM outputs which are linearly interpolated with depth at the TAO current-meter depth when it is necessary. Since the buoy data include strong high-frequency variations, a 15-day running mean filter has been applied for graphic clarity.

The strong correlation between surface wind variations and the near surface current variations are also well represented by the two experiments. We observe that the seasonal cycle of the zonal current component is better characterized in the eastern Pacific (140°W and 110°W) than in the western part of the ocean. Moreover, the important shifts of current flowing from East to West or inversely are generated with success in ERS-O, while the Arpege-Climat wind variations are less successful in reproducing shifts of current direction, especially at 140°W .

Current variability at the sea surface (5 m) simulated in ERS-O is depicted more accurately than the ocean response in ARP-O, as is shown in Figures 7. Correlation coefficients between the observations and the ERS-O currents are 0.80, 0.74 and 0.67 from east to west, while they are 0.37, 0.29 and 0.37 between the observations and the ARP-O currents (the underlined numbers have correlation coefficients in a 95% confidence interval). However, strong high-frequency variations depicted by the buoy data in the western Pacific appear to be smoothed out by both responses from ERS-O and ARP-O. ERS-O results are in better

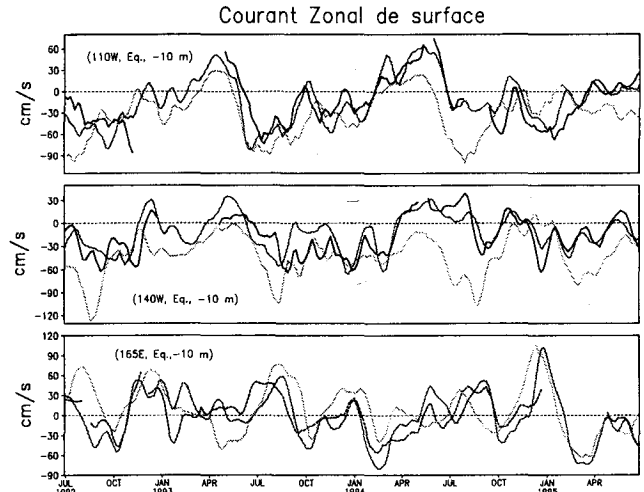


Figure 7. Comparison of the zonal component of the current (10^{-1} m/s), along the equator at three locations (110°W , 140°W and 165°E) and at 10-m, between the ERS-O, ARP-O and with the buoy measurements. A 25-day running mean filter has been applied for graphic clarity. Scales on the y-axis are different and positive values indicate an eastward current.

agreement with the TAO observations in the eastern part of the Pacific ocean.

At 80 and 100 meter depths in the three locations (not shown), the ERS-O current variations are still in good agreement with observations, the correlation coefficients are 0.29, 0.70 and 0.69 from east to west, while they are 0.02, 0.64 and 0.39 between ARP-O current and TAO buoys. At 165°E , the buoy time series are short, but ADCP at this location provides a long time series which shows that the variability of the ERS-O current is well depicted with a slight westward bias (0.10 to 0.20 m/s). This bias is due to the difference between the position of the current core observed by the TAO buoy observations and simulated by the ERS winds and may be related to a model bias. The zonal current response in ARP-O is not in phase with observations.

In the eastern part of the Pacific ocean, at 140°W and 80-m depth, the zonal current core is nearly at its maximum, the intensity of the current tops 1 m/s between April and September. We clearly observe the seasonal signal which is well simulated by the scatterometer and the atmospheric model winds through the OGCM, but the accuracy of the ERS winds in depicting the higher variability (at periods of a few weeks) improves significantly the correlation between ERS simulations and TAO buoy observations. Arpege-Climat winds generate weaker zonal currents than those observed in the sub-surface.

At 110°W and 80-m depth, the correlation coefficients computed between the two experiments and the buoy observations are not significant. However we observe some current variations which are better simulated by the ERS winds than with Arpege-Climat, for example those between December 1992 and January 1993.

We have clearly shown that uncertainties concerning surface and subsurface current variations can be greatly reduced by using the ERS winds through the

OGCM. These good results also underline the accuracy of the OGCM "OPA" physics in generating realistic current variations.

6. CONCLUSION

The "OPA" Ocean General Circulation Model has been used to test the ability of the ERS-1 scatterometer gridded wind and wind-stress fields to force an OGCM (experiment called ERS-O in this paper). Through the oceanic responses, the ERS-1 scatterometer surface wind fields are compared with those from the Arpege-Climat model (experiment called ARP-O in this paper). This study has also been instrumental in demonstrating the robustness of the OGCM "OPA" physics.

The impact of the ERS surface winds is more significant in the description of the principal oceanic parameter variations. The oceanic fields emphasize that the ERS wind fields generate more realistic thermal and current anomalies than the Arpege-Climat, in agreement with observations. We clearly show that through the OGCM, the accuracy of the ERS scatterometer surface wind fields, in terms of variability, is instrumental in depicting the high frequency (at periods of a few weeks), as well as the seasonal variations of the thermocline and currents.

Because surface winds are recognized to be the main parameter to driving the ocean circulation, we have not investigated in detail the impact of the other forcing terms, such as net heat fluxes and the water budget. However we have reinforced the consistency between ERS wind stress fields and the other forcing terms by using the ERS wind fields in the bulk aerodynamic calculations. The heat fluxes, as well as the water budget can have a deciding role, especially in the western Pacific ocean where the oceanic forcing is principally thermohaline. The ITCZ is characterized by cumulo-nimbus activities and high precipitation can also have a significant impact on surface density and on salinity concentration. The results of the OGCM forced by the ERS winds could be improved by the contribution of other satellite sensors to generate more realistic global net heat fluxes and global water budget. However the homogeneity and coherence between the different fields must be studied. The improvement in time and space resolution of satellite wind fields using scatterometer (ERS-2, NSCAT and QSCAT missions), altimeter (ERS-2, TOPEX/POSEIDON) and radiometer (SSM/I) will also have a positive impact on OGCM simulations.

REFERENCES

- Bentamy, A., Y. Quilfen, P. Queffeuilou, and A. Cavanié, Calibration of the ERS-1 Scatterometer C-band Model, *IFREMER Tech. Rep. DRO/OS-94-01*, 72 pp, IFREMER/Brest, B.P. 70, 29280 Plouzané, France, 1994.
- Bentamy, A., Y. Quilfen, F. Gohin, N. Grima, M. Lenaour, J. Servain, Determination and validation of average wind field from ERS-1 scatterometer measurements, *The Global Atm. and Ocean Syst.* 4, 1-29, 1996.
- Blanke, B., and S. Raynaud, Kinematics of the Pacific Equatorial Undercurrent: An Eulerian and Lagrangian Approach from GCM Results, *J. Geophys. Res.* 27, 1038-1053, 1997.
- Dandin, P., Variabilité basse fréquence simulée dans l'océan Pacifique tropical, Thèse de doctorat de l'université Paris VI, 1993.
- Delecluse, P., G. Madec, M. Imbard, and C. Levy, OPA version 7 ocean general circulation model reference manual, *Rapport interne LODYC 93/05*, 111 pp, 1993.
- Déqué, M., and J. Ph. Piedelièvre, High resolution climate simulation over Europe, *Clim. Dyn.* 11, 321-339, 1995.
- Ezraty, R., Etude de l'algorithme d'estimation de la vitesse de frottement à la surface de la mer, *Contrat IFREMER n 85-2-42-5000. Contrat ESTEC n 6155/85/NL/BI*, IFREMER/Brest, B.P. 70, 29280 Plouzané, France, 1985.
- Goddard L., and N. E. Graham, El Niño in the 1990s, *J. Geophys. Res.* 102, 10,423-10,436, 1997.
- Halpern, D., Y. Chao, C.-C. Ma, and C. R. Mechoso, Comparison of tropical Pacific temperature and current simulations with two vertical mixing schemes embedded in an ocean general circulation model and reference to observations, *J. Geophys. Res.* 100, 2515-2522, 1995.
- Hayes, S. P., L.J. Mangum, J. Picaut, A. Sumi, K. Takeuchi, TOGA-TAO: a moored array for real-time measurements in the tropical Pacific, *Ocean. Bull. Am. Meteorol. Soc.* 72, 339-347, 1991.
- Liu, W. T., W. Tang, and L.-L. Fu, Recent warming in the Pacific may be an El-Niño, *Eos, Transaction, American Geophysical Union* 76, 429-437, 1995.
- Maes, C., Equilibre du Reservoir Chaud de l'Océan Pacifique Tropical Ouest, Thèse de doctorat de l'Université Paris-VI, 1996.
- McPhaden, M. J., and S. P. Hayes, On the Variability of Winds, Sea Surface Temperature, and Surface Layer Heat Content in the western Equatorial Pacific, *J. Geophys. Res.* 96 supplement, 3331-3342, 1991.
- McPhaden, M. J., TOGA-TAO and the 1991-1993 El-niño Oscillation Event, *J. Oceanogr.* 6, 36-44, 1993a.
- McPhaden, M. J., Trade Wind Fetch Related Variations in Equatorial Undercurrent Depth, Speed, and Transport, *J. Geophys. Res.* 98, 2555-2559, 1993b.
- Mitchum, G.T., trade winds fluctuations associated with El-Niño Southern Oscillation events *J. Geophys. Res.* 92, 9464-9468, 1987.
- Quilfen, Y., ERS-1 Off-line Wind Scatterometer Products, *Technical Report IFREMER/CERSAT*, 58 pp, 1995.
- Reynolds, R. W., and T. M. Smith, Improved global sea surface temperature analyses using optimum interpolation, *J. Climate* 7, 929-948, 1994.
- Slingo, J.M., K. R. Sperber, J. S. Boyle, J.-P. Ceron, M. Dix, B. Dugas, W. Ebisuzaki, J. Fyfe, D. Gregory, J.-F. Gueremy, J. Hack, A. Harzallah, P. Inness, A. Kitoh, W. K.- M. Lau, B. McAvaney, R. Madden, A. Matthewa, T. N. Palmer, C.-K. Park, D. Randall, and N. Renno, Intraseasonal oscillations in 15 atmospheric general circulation models: Results from an AMIP diagnostic subproject, *Clim. Dyn.* 12, 325-357, 1995.
- Smith, W. D., D. Herbert, and J. N. Moum, Local ocean response to a multiphase westerly wind burst, 2: Thermal and freshwater responses *J. Geophys. Res.* 101, 495-22,512, 1996a.
- Smith, W. D., D. Herbert, and J. N. Moum, Local ocean response to a multiphase westerly wind burst, 1: Dynamic response, *J. Geophys. Res.* 101, 22,495-22,512, 1996b.
- Waliser, D. E., and R. C. J. Somerville, Preferred latitudes of the intertropical convergence zone, *Journal of Atmospheric Sciences* 51, 1619-1639, 1994.

NSCAT BACKSCATTER COEFFICIENT VARIABILITY

N. Tran¹, C. Mejia¹, S. Thiria¹, M. Crepon¹ and F. Badran²

¹ Laboratoire d'Océanographie Dynamique et de Climatologie (LODYC)
BP 100, Université P. et M. Curie, PARIS 6
4 Place Jussieu - 75005 PARIS (FRANCE)

² CEDRIC, Conservatoire National des Arts et Métiers
292 rue Saint Martin - 75003 PARIS (FRANCE)

Abstract

We present a preliminary analysis of the global variability of the residual errors of NSCAT's Ku-band VV- and HH-polarized ocean backscatter radar cross section. Our objectives are to consider the sensitivity of the normalized radar cross section to geophysical parameters.

1 Introduction

The NASA scatterometer (NSCAT) is a microwave radar measuring the backscatter coefficient (σ^o) which is sensitive to the surface ocean waves of wave length of the order of some centimeters. The small scale ocean surface roughness increase with increasing local winds, and this increased roughness enhances the backscatter coefficients of the ocean. This indirect relationship forms the basis of using radar scatterometry for ocean wind measurements. The NSCAT measurements are related to the surface wind and the incidence angle by empirical Geophysical Model Functions (GMF). Any process which modulates this small scale roughness may also affect the scatterometer measurements. The variability in the backscatter coefficients residual errors between measurements and model results at given wind vector and incidence angle is due to the effects of unmodeled geophysical parameters (as rain, sea state, surface current, atmospheric stability, etc...) on NSCAT data in the Geophysical Model Functions.

2 Residual error analysis

We compared the σ^o measurements with the computed σ^o by two empirical models (one for each polarization) which have been determined by using neural networks (NN) (Ref. 2). These functions are calibrated with collocated data between the European Center wind vectors (ECMWF) and

NSCAT reprocessed backscatter coefficients from CERSAT/IFREMER. This global data set include a large range of situations permitting to extract mean tendencies.

Because the backscatter coefficients residual errors vary in a wide range and are function of the wind vector and the incidence angle, we computed the normalized residual error δ_{pp} (where the subscript pp is used to represent HH or VV for horizontal and vertical polarizations respectively) for each polarization. This residual error is the difference between backscatter coefficients obtained from pp-NN model function using corresponding ECMWF neutral wind speeds at 10 m and backscatter measurements from NSCAT scatterometer over the computed one:

$$\delta_{pp} = \frac{\sigma_{pp}^o(NN - GMF, ECMWF) - \sigma_{pp}^o(NSCAT)}{\sigma_{pp}^o(NN - GMF, ECMWF)}$$

This coefficient is then used to study the sensitivity of the radar cross section to geophysical parameters.

A simple bin-averaging has been used to compute normalized residual error fields on boxes of 2° of latitude by 2° of longitude grid for data from February to May 1997. The wind speeds only range between 7 and 10 m/s in order to avoid problems linked to low and high wind speeds. For low wind speeds, the computed values of backscattering coefficients are less accurate (Ref. 2). Two incidences angles have been investigated: incidence angles of $30 \pm 2^\circ$ and $40 \pm 2^\circ$ for both polarizations.

3 Results

We computed δ_{pp} with backscatter coefficients in linear space. In the Figure 1, the map show the distribution of error structures for the vertical polarization at 30° of incidence angle. We observe a zonal band of negative values in red on this map located along the equator and may coincide with the Intertropical Convergence Zone. This suggest an effect of rain

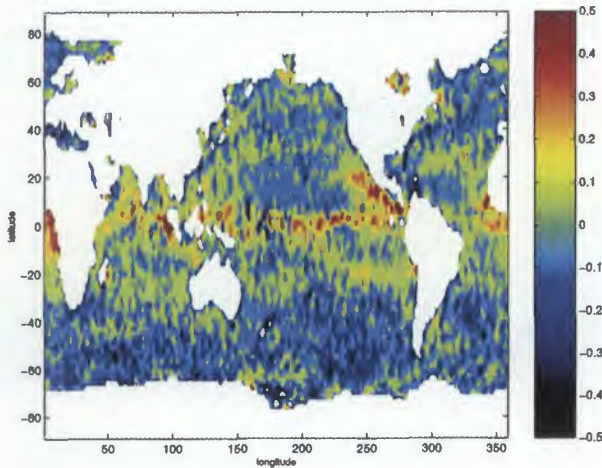


Figure 1: Maps of the normalized residual error field for the vertical polarization and an incidence angle of 30° .

on the backscatter coefficients, because these positive values represent an attenuation of backscatter measurements and it's well known that rain modifies microwave propagation in the atmosphere and their effects are commonly described in terms of reflection and attenuation (Ref. 5). On the other hand the strong error that we observe in the northern Indian Ocean cannot be related to the precipitation due to the Asian monsoon because it is not active during this period of the year. This positive error will be due to another parameter which also decrease the backscatter coefficients like the small significant wave heights measured over there by altimeters. The significant wave height (SWH) are lower in the northern Indian Ocean than in the others oceans as analysed on TOPEX POSEIDON measurements during the same period (not shown here).

Figure 2 shows the variation of the zonal average of δ_{pp} with respect to latitude for the two polarizations and the two incidence angles. These zonal averages present the same trends with this strong attenuation of backscatter coefficients in the tropical region. We also observe for the higher latitudes an increase of the backscatter coefficients which may provide to the large significant wave heights caused by swells and will be consistent with the trends predicted by theoretical models (Refs. 1, 4). But this assessment is opposite to the conclusions of the previous study of Ref. 3 on the effects of long waves with large SWH on the radar backscatter during moderate wind conditions. They found that for moderate wind conditions, there was no obvious difference between the backscatter measurements observed at Ku and C bands for low and high SWH.

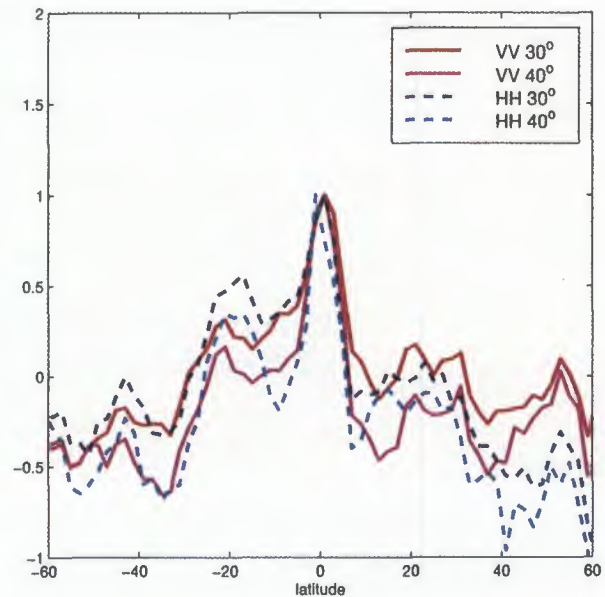


Figure 2: Zonal average of δ_{pp} scaling by the maximum value of the zonal averages with respect to latitude for the two polarizations (VV and HH) and the two incidence angles (30° and 40°).

4 Scaling the residual error by an estimated standard deviation

Because, in fact the standard deviation of the backscatter measurements depends on the same variables as the measurement itself. The knowledge of its variability allow us to mix data on a more large range of incidence angle for each polarization by scaling the residual error by the estimated standard deviation. This leads to have a larger set of data to follow the study of the possible effects of the oceanic and atmospheric parameters on the backscatter measurements.

This estimated standard deviation is computed by a new neural network (VAR-NN) for the vertical polarization (Ref. 2). Here, δ_{VV} is defined by:

$$\delta_{VV} = \frac{\sigma_{VV}^o(NN - GMF, ECMWF) - \sigma_{VV}^o(NSCAT)}{SD_{VV}(VAR - NN, ECMWF)},$$

where σ^o are in linear. The wind speed still range between 7 and 10 m/s. The previous conclusions are enhanced (map not shown) and if we make a zoom on this map (Figure 3), we can note a strong negative value of this new δ_{VV} in the Gulf Stream region which suggest a possible effect of the surface current or of the change on the air-stability across the Gulf Stream boundary. This band is correctly located in

latitude with the Gulf Stream current where there are potential complications in the ocean conditions.

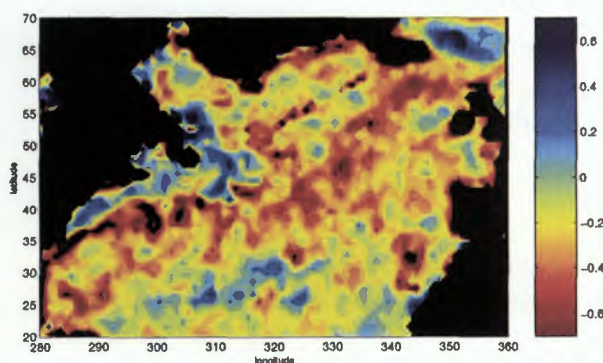


Figure 3: *Zoom in the Gulf Stream region.*

5 Conclusion

The following qualitative assessments can be made: (1) a possible effect of rain in the tropical region, (2) of small significant wave height in the northern Indian Ocean, (3) of large significant wave height caused by swells in the high latitudes and (4) of the sea surface current or of the sharp variation of air-stability in the Gulf Stream region.

But several phenomena may act together on the sea surface roughness and extracting information linked to individual mechanisms is a puzzling task. Such the effects may change the accuracy of radar scatterometry in retrieving the ocean surface winds. So, we suggest for the following to focus interest in specific region where phenomena approximately can be isolated.

A problem is to find an optimal indicator to mix the backscatter coefficients data to investigate these effects of the oceanic and atmospheric parameters on the scatterometer signal.

Acknowledgments We would like to thank the CERSAT/IFREMER who provided the collocations between NSCAT sigma-0 and the analyzed wind vectors of the ECMWF Model. The present study was supported by the EC program NEUROSAT (ENV4-CT96-0314).

References

- [1] Durden S. L. and J. F. Vesecky: A Physical radar cross section model for a wind-driven sea with swell, *IEEE J. Ocean. Eng.*, vol. OE-10, no. 4, pp. 445-451, 1985.
- [2] Mejia C., F. Badran, A. Bentamy, M. Crepon, S. Thiria, N. Tran: Determination of the Geophysical Model Function of NSCAT scatterometer by the use of neural networks, *J. Geophys. Res.* (in revision).
- [3] Nghiem S. V., F. K. Li, S.-H. Lou, G. Neumann, R. E. McIntosh, S. C. Carson, J. R. Carswell, E. J. Walsh, M. A. Donelan and W. M. Drennan: Observations of radar backscatter at Ku and C bands in the presence of Large Waves during the Surface Wave Dynamics Experiment, *IEEE Trans. Geosci. Remote Sens.*, vol. 33, no. 3, pp. 708-721, May 1995.
- [4] Plant W. J.: A two-scale model of short wind-generated waves and scatterometry, *J. Geophys. Res.*, vol. 91, no. C9, pp. 10735-10749.
- [5] Walsh E. J., F. M. Monaldo and J. Goldhirsh: Rain and cloud effects on a satellite dual-frequency radar altimeter system operating at 13.5 and 35 Ghz, *IEEE Trans. Geosci. Remote Sens.*, vol. GE-22, no. 6, pp. 615-622, Nov. 1984.

Scatterometer Winds over the Arabian Sea

David Halpern

Jet Propulsion Laboratory, MS 300-323

California Institute of Technology, Pasadena, CA 91109-8099, USA

Phone: +1-818-354.5327, fax: +1-818-393.6720, e-mail: halpern@pacific.jpl.nasa.gov

The summer south-west monsoon wind produces unique oceanic features in the annual climatology of the Arabian Sea. Sea surface temperature is lower in July than in April. Biological productivity is greatly enhanced throughout the northern half of the Arabian Sea compared to the southern portion. Forecasting the time of monsoon onset, times of subsequent active and lull periods, and associated oceanographic and meteorological conditions remain unsolved and important problems. Features can not be modelled before discovery. The purpose of this paper is to describe the Arabian Sea surface wind field during the monsoon onset in June 1997.

The heretofore absence of suitable wind observations over the Arabian Sea created a mystery about the spatial distribution of surface winds having sub-monthly time scales, especially during the onset of the south-west monsoon. Wind observations from ships are very sparse. During June 1997 only about 15% of the total number of $1^\circ \times 1^\circ$ areas in the Arabian Sea had at least one ship observation every 2 days. Adequate numbers of surface wind recordings to investigate the 1997 southwest monsoon onset were made with the NASA double-swath scatterometer, named NSCAT and launched on the Japanese Advanced Earth Observation Satellite (ADEOS) in August 1996. In 2 days NSCAT recorded 20-40 instantaneous 25×25 km wind velocities, which are referenced to 10-m height, in nearly every 1° -latitude \times 1° -longitude area throughout the Arabian Sea. A 2-day minimum interval was chosen because it is approximately equal to the inertial period for a large portion of the Arabian Sea and 2-3 inertial periods is the time scale associated with the development of Ekman currents. A $1^\circ \times 1^\circ$ region is believed the maximum grid size to adequately capture the intense horizontal gradients associated with the Somali Jet.

The newness of NSCAT data and the recognition that no wind data product is perfect dictate that results be compared with those computed with an independent wind data product. We chose the European Centre for Medium-Range Weather Forecasts (ECMWF) $1.125^\circ \times 1.125^\circ$, 6-hour 10-m height wind velocity data product. Beginning in February 1996, European Remote-Sensing Satellite (ERS-2) wind velocity data was assimilated into the ECMWF forecast-analysis system.

The following topics will be discussed: onset time of monsoon winds, space-time development of Somali Jet; wind divergence; and wind-driven ocean transports. The representativeness of the southward Ekman transport along 8.5°N in June 1997 is addressed with ERS IFR2 monthly mean wind velocity which, unlike numerical weather prediction data products, are created in a uniform fashion with a quasi-uniform quantity of data. In June 1997 the monsoon vortex was absent and southward Ekman transport along 8.5°N was anomalously low since 1992. An empirical relationship is developed between the amount of sea surface temperature decrease and wind speed for 2-day intervals and $1^\circ \times 1^\circ$ areas. In addition, ERS and TOPEX/Poseidon altimeter measurements of significant wave height are used to estimate relative representativeness of 2-day, $1^\circ \times 1^\circ$ NSCAT and ECMWF wind speeds.

Scatterometry for Tropical Cyclones Observation

Yves Quilfen

Ifremer

POBox : BP70, Plouzane, France

Phone : 33-2-9822.4414; fax : 33-2-9822.4533; e-mail : yquilfen@ifremer.fr

Unprecedented views of surface wind fields in tropical cyclones (hereafter TCs) are provided by the European Remote Sensing Satellite (ERS) C band scatterometer. Scatterometer measurements at C band are able to penetrate convective storms clouds, observing the surface wind fields with good accuracy. However the resolution of the measurements ($50 \times 50 \text{ km}^2$) limits the interpretation of the scatterometer signals in such mesoscale events. The strong gradients of the surface wind existing at scales of a few km are smoothed in the measured features such as the intensity and location of the wind maxima, and the position of the centre.

Beyond the ERS systems, the scatterometers on-board the ADEOS and Metop satellites, designed by the Jet Propulsion Laboratory and by the European Space Agency, respectively, will be able to produce measurements of the backscattering coefficient at about $25 \times 25 \text{ km}^2$ resolution. A few sets of ERS-1 orbits sampling TC events were produced with an experimental $25 \times 25 \text{ km}^2$ resolution. Enhancing the resolution by a factor of 2 allows location of the wind maxima and minima in a TC with a much better accuracy than at 50 km resolution. In addition, a better resolution reduces the geophysical noise (variability of wind speed within the cell and effect of rain) that dominates the radiometric noise and hence improves the definition of the backscattering measurements. A comprehensive analysis of the backscattering measurements in the case of high winds and high sea states obtained within TCs is proposed in order to refine the interpretation of the wind vector derived from a backscattering model that is currently only calibrated up to moderate winds ($< 20 \text{ m/s}$) in neutral conditions. Observations of the Topex-Poseidon dual-frequency altimeter are also used for that purpose. Patterns of the surface winds in TCs are described and characteristic features concerning asymmetries in the maximum winds and in the divergence field are discussed.

Study of a Sea-State-Dependent Algorithm for Operational Processing of ERS Scatterometer Data at ECMWF

Didier Le Meur & Lars Isaksen

ECMWF

Shinfield Park, Reading, Berkshire, RG2 9AX England

Phone : +44-118-949.9476, fax : +44-118-986.9450, e-mail : stl@ecmwf.int

ERS scatterometer data have been assimilated operationally at ECMWF since January 1996. The process relies on the use of a variational analysis scheme in which the scatterometer observations are treated as pairs of ambiguous wind vectors. An implicit ambiguity removal is thus performed, consistently with all the information available from the model background and physics as well as the other types of observations. Clear benefits have been obtained from that assimilation in terms of surface wind analysis, with a positive impact on the short-range and medium-range forecasts. Large improvements have also been found in the case of tropical cyclones.

A crucial point was however to properly calibrate the transfer function CMOD4 applied to retrieve wind estimates from the scatterometer backscatter measurements so as to avoid systematically speeding up or slowing down the analysis by using overestimated or underestimated wind observations. A refined sigma nought and wind speed bias correction procedure was introduced for that purpose, deduced from a triple collocation analysis including conventional wind observations from ships, buoys and islands. Those bias corrections allowed to get the best agreement in average between the model and scatterometer data over the whole wind speed range. Nevertheless, systematic errors due to other geophysical parameters than wind not taken into account by CMOD4 were still likely to occur locally.

A statistical study, using collocations with data from the wave model WAM, has shown that the sea state has thus systematic effects on the scatterometer wind retrieval which can be characterised to the first order as a function of the significant wave height. An additional bias correction of CMOD4 in the backscatter space has been developed on that basis to further improve the processing of ERS scatterometer data before assimilation in the ECMWF model.

The presentation will describe the sea-state dependent retrieval algorithm obtained and assess its impact through dedicated assimilation experiments.

CERSAT ACTIVITIES AND SCATTEROMETERS VALUE-ADDED PRODUCTS

Sylvie Pouliquen, Christophe Maroni, Valérie Harscoat, Francine Loubrieu

CERSAT, Département d'Océanographie Spatiale, IFREMER, BP70, 29280 PLOUZANE, FRANCE
Tel (33) 2 98 22 44 92 - Fax (33) 2 98 22 45 33 - Email : fpaf@ifremer.fr

ABSTRACT

CERSAT is the French Processing and Archiving Facility for the satellites ERS-1 and ERS-2, launched by the European Space Agency (ESA) in 1991 and 1995 respectively. CERSAT was designed for ERS-1 low bit rate processing, specializing its activities in two main domains:

- Off-line processing for ERS radar altimeter (OPR) and micro-wave sounder (VLC)
- Off-line processing for AMI-WIND scatterometer (WNF).

Through a close collaboration with the scientific team of the Department of Oceanography from Space, CERSAT started in 1995 the generation of value-added products generated from ERS off-line scatterometer data (WNF): a Mean Wind Fields atlas and a Sea-Ice atlas were generated on CDROMs and distributed to users.

In 1996 Cersat started new activities using NSCAT and ERS data. NSCAT is a double swath scatterometer launched on ADEOS in august 1996 and unfortunately lost in June 1997. To continue after NSCAT, NASA will, in 1998, launch a new scatterometer QuikScat. CERSAT plans to provide the users with the same services as for NSCAT.

Since June 1997 all the products provided by CERSAT are available on our WEB server (<http://www.ifremer.fr/cersat>)

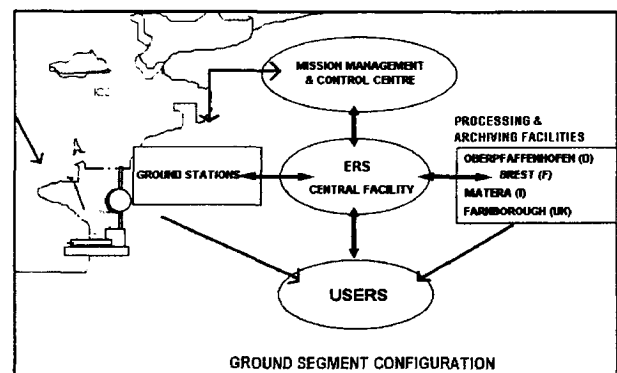
Through our demonstration you will be able to discover these products as well as:

- our WEB server
- ERS/NSCAT atlases generated at CERSAT
-

CERSAT Mission

The ERS1 system has been designed as an end-to-end remote sensing system, performing, from space, microwave measurements of selected earth surface parameters, extracting from these measurements specific environmental and geographical data, and disseminating the results to a large variety of users, both in real time and off-line.

The ERS1 ground segment was designed by ESA to provide services and to satisfy user requirements for products. CERSAT, as a Processing and Archiving Facility, is one component of this complex ground segment.



Within this ground segment CERSAT is in charge of the :

- Off-line processing for ERS Radar Altimeter (OPR) and micro-wave Sounder (VLC)
- Off-line processing for AMI-WIND Scatterometer (WNF)

These data are regularly sent to users on CDROM. OPR data are sent to about 100 users, WNF to more than 140 users.

OPR data are sent to users one month after the availability of the Precise Orbit generated by D.PAF, 4 months after acquisition at the receiving station.

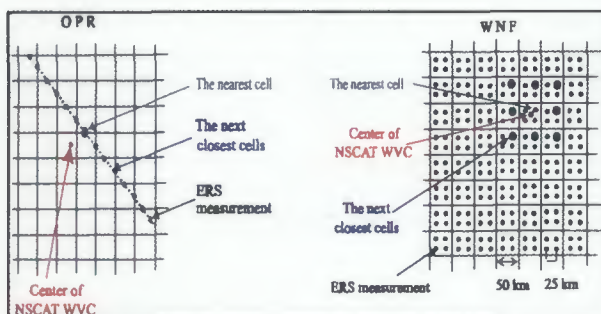
WNF are available one and a half months after the data is acquired at the ground station. We cannot speed up operations because of the late arrival of the data acquired at Prince Albert Station.

Either OPR or WNF products are along-track data that can only be used by scientists who have quite a good experience of satellites sensors.

NSCAT Co-located database

In 1996 CERSAT diversified its activities by handling data from the Nasa SCATterometer (NSCAT) launched on the Japanese satellite ADEOS1 in August 1996.

The collocation of NSCAT data was achieved by selecting, for each point, all ERS-2 Scatterometer or Radar Altimeter observations such that the temporal separation was less than 1 hour and the spatial separation was less than 100 km for the scatterometer or 36 km for the radar altimeter.



How ERS/NSCAT collocated points are chosen

The collocated products delivered to users gave, for each NSCAT collocated point, all NSCAT and ERS-2 nearest cell parameters and statistics on the next closest ERS-2 cells.

The long-term plan is to develop the capability to intercalibrate various satellites, in-situ and modeled wind datasets, to provide the community with homogeneous products for long-term periods. To this effect, pairs of collocated wind measurements from ERS and upcoming Quikscat and Seawinds scatterometers, ERS altimeter and ECMWF wind fields will be generated in the future.

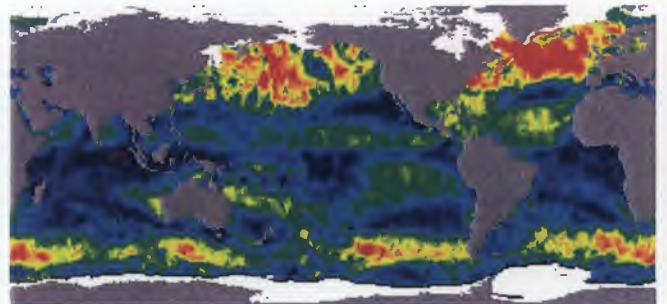
ERS/NSCAT ATLASES

Most oceanographers need more elaborate data than OPR and WNF products. They want, for example, products they can directly use in ocean circulation models.

Therefore, we decided to produce value-added products in collaboration with the scientific team of the Department of Oceanography from Space.

ERS/NSCAT WIND Atlas

The first ERS-1 mean wind field CDROM was issued in June 1995. In May 1998, CERSAT produced a new CDROM containing 7 years of weekly and monthly ERS-1, ERS-2 and NSCAT mean winds.



Weekly Wind Speed derived from ERS2 for the last week of December 1997. You can see big storms in the North Atlantic ocean.

Since winds estimated at a point can vary significantly over periods of a few hours, reconstruction of synoptic fields of surface winds on basin scales from discrete observations is difficult, without using an appropriate method.

We therefore developed a statistical technique for the objective analysis of remote sensor wind data. This statistical interpolation is a minimum variance method related to the Kriging technique widely used in geophysical studies. The analysis scheme is based on the determination of the spatial and temporal structure functions of wind and stress variables (magnitude, zonal and meridional components). The estimators of each variable were then determined and analyzed by the objective method.

These were used to estimate weekly and monthly fields over the global oceans of the wind speed (W), the zonal wind component (u), the meridional wind component (v), the stress magnitude ($|\tau|$), the zonal stress component (τ_x) and of the meridional stress component (τ_y) into 1° latitude by 1° longitude boxes. The standard errors of the above parameters were also computed at each grid point. The wind divergence and the wind stress curl were estimated from the grid scatterometer wind and stress. All these regular wind parameters are

evaluated using a land and sea-ice mask which is derived from ERS scatterometer measurements.



El Niño seen by ERS2 on the ZONAL component of the Wind in August 1997.

These wind fields, which have been distributed to the WOCE scientific community (more than 800 potential users), are already used to force ocean circulation models.

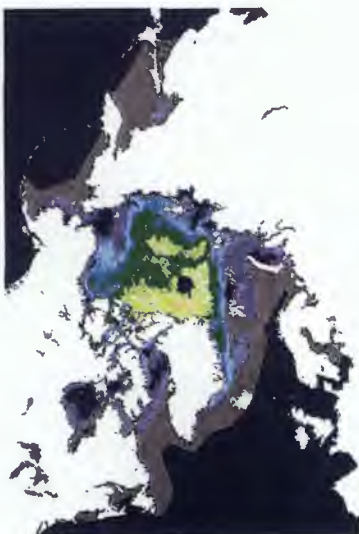
ERS/NSCAT ICE Atlas

Over polar oceans, values of the ERS-2 AMI-WIND/ADEOS NSCAT measurements depend on the dielectric properties of the observed materials, sea water, first-year ice and multi-year ice, on their relative concentrations and on the surface topography. As sea ice ages, its dielectric properties, linked to volume and surface scattering, as well as its surface roughness are altered.

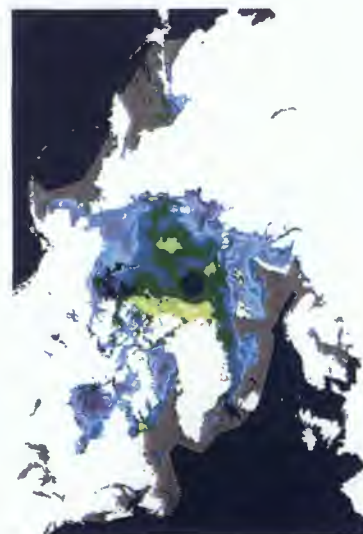
During the summer melt the salinity decreases by drainage of the brine and the bubble content increases. As time passes, the ice surface is also transformed under the action of storms, thaw and freezing; all of these transformations backscattering.

The behaviour of backscatter as a function of the incidence angle is essentially linked to the ice type, including marginal ice (mixture of small broken floes and water), smooth first-year ice of the consolidated pack, or multi-year ice.

Algorithms, specific to ERS C-band scatterometers, were applied to produce in 1996 a sea-ice atlas on CDROM derived from ERS-1 WNF data. This atlas was extended to ERS-2 and NSCAT at the beginning of 1998. It provides maps of the sea-ice coverage as well as a characterization of the sea-ice at 50km resolution, each week for ERS and every 3 days for NSCAT. Distributed on the same grid as SSM/I sea-ice products from the NSIDC, these 7 years of data are a good input for studies on sea-ice climatology.



NSCAT Backscatter coefficient at 40° for 3 days, end of December 1996



ERS-2 Backscatter coefficient at 40° for a week on the same period

CERSAT WWW Server

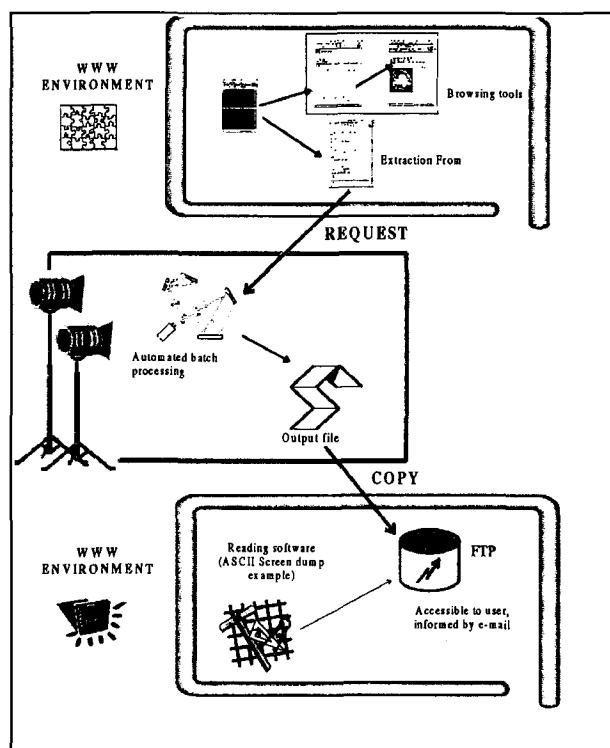
To ease data access to users, data distributed by CERSAT are also available through a WWW server (<http://www.ifremer.fr/cersat>).

One can select period and geographical zone for a specific product. Once the requested product has been extracted from the archive, an email is sent notifying the user that it is available on the ftp site <ftp.ifremer.fr>. Users can also browse through the Wind and Sea Ice atlases directly on the WWW server.

CERSAT strategy in data distribution is to facilitate access to data and user information. As soon as we detect a problem on distributed data, we improve or correct data manipulation tools, provide a new service,.. a NEWS is issued on the server. Regularly we update the Frequently Asked Questions rubric (FAQ) with a compilation of the demand made by email to our hotline: fpaf@ifremer.fr. You should regularly connect to this server. to be well informed.

All the products generated by CERSAT are and will be distributed on the WWW server. Between two issues of a CDROM, new data are also available that way .We plan to improve these services using emerging technologies such as JAVA.

Data browsers and our WWW server will be consultable on a PC during the conference, on request.



Data distribution through CERSAT WWW server

Available data on CERSAT WWW Server

	Radar Altimeter	Scatterometer	Mean Wind Field	Sea Ice	Collocated
ERS1	08/91→06/96	WNF08/91→06/96	08/91→06/96	08/91→06/96	/
ERS2	05/95→on going	WNF03/96→on going	03/96→on going	03/96→on going	
NSCAT	/	Level 1.7 } Level 2.0 } JPL 10/96→06/97	Level 1.7 } Level 2.0 } JPL 10/96→06/97	Level 1.7 } Level 2.0 } JPL 10/96→06/97	WNF } OPR } Level 1.7 ECMWF } Level 2.0 JPL 10/96→06/97

Future with Quikscat

In November 1998, NASA will launch a new KU-band scatterometer. CERSAT will provide the user community with products and services similar to those proposed for NSCAT:

- a collocated database between Quikscat and ERS-2 scatterometer and altimeter
- a collocated database between Quikscat and TOPEX altimeter

A collocated database between Quikscat and SSM/I is foreseen

These data will be available through our WWW server. Once the algorithm are developed we will also generate sea-ice and mean wind field atlases for Quikscat ,in order to provide the user community with an homogeneous dataset for ERS-1/ ERS-2/ NSCAT/ Quikscat. These atlases will then be updated with Seawinds/ADEOSII and Ascat/METOP1 when the satellites are launched.

Applications of Scatterometer Winds to Study El Niño Teleconnection and Asian Monsoons

W. Timothy Liu

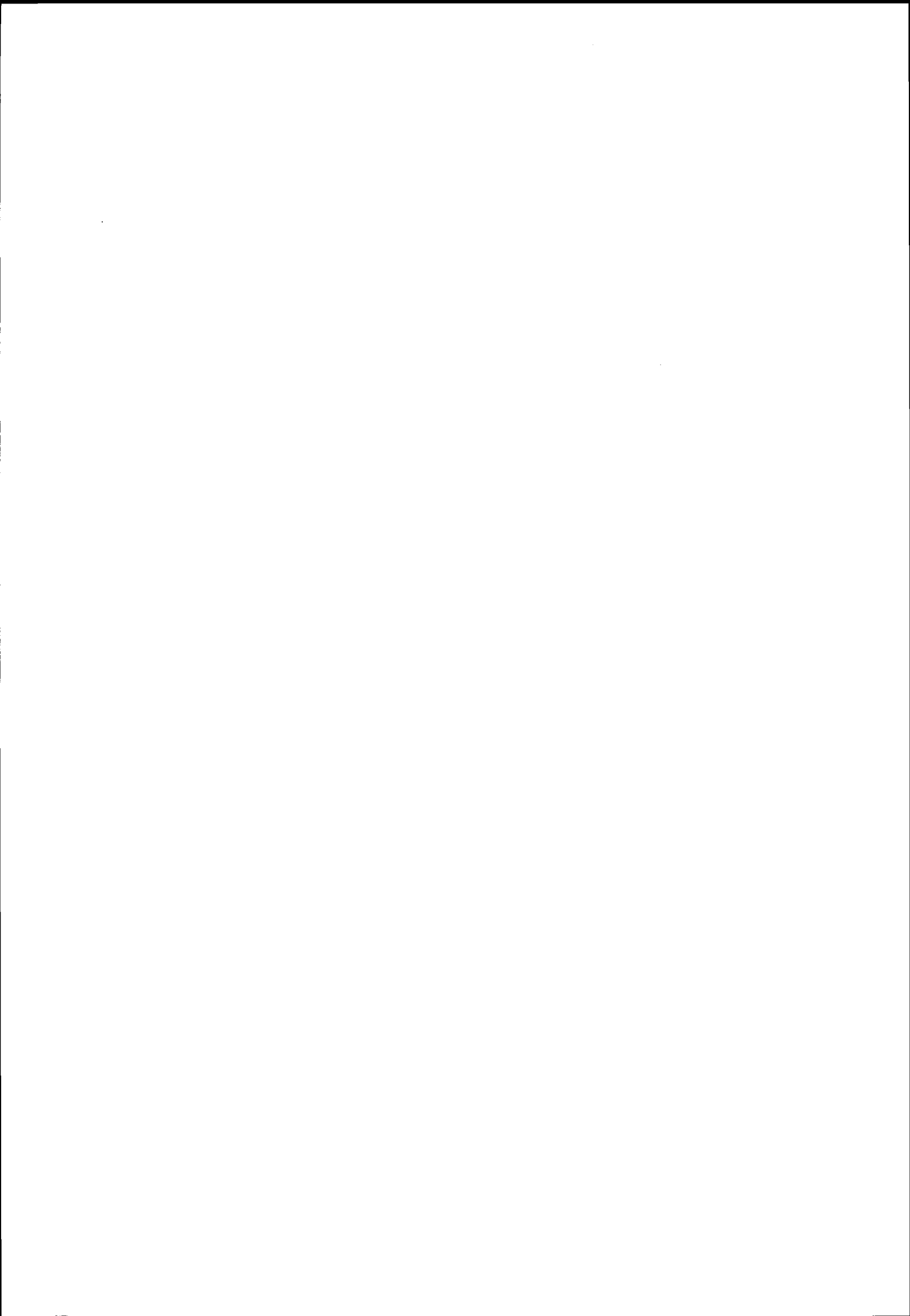
Jet Propulsion Laboratory, 300-323

California Institute of Technology, 4800 Oak Grove Drive, Pasadena, CA 91109, USA

Tel: 1-818-354.2394; fax: 1-818-393.6720; e-mail: liu@pacific.jpl.nasa.gov

Three regions of simultaneous anomalous warming observed in the North Pacific Ocean at the end of May 1997 are related to wind anomalies through different mechanisms, NASA's high-resolution Scatterometer (NSCAT) [Liu et al., 1998] reveals. The anomalous warming along the equator is part of the developing El Niño and is related to the westerly wind anomalies in the central equatorial Pacific and the relaxation of the trade winds. The equatorial westerly wind anomalies are related to the anomalous cyclonic wind pattern in the North-East Pacific. The anomalous warming along the west coast of the United States develops as a pre-existing pool of anomalously warm water and the cyclonic wind anomalies move toward the coast. The warm pool is part of a sea-surface temperature (SST) anomalies dipole that has been present for more than a year in the North Pacific; the warm pole is associated with warm and moist southerly winds and the cool pole with cool and dry northerly winds. The cyclonic circulation also causes anomalous southerly winds along the Mexican coast; the anomalous coastal wind suppresses upwelling and induces anomalous warming.

Monsoons are the seasonal changes of winds forced by continent-ocean temperature contrast. Their annual onset, intensity, and retreat vary greatly, and the variation has strong economic and social impacts to a large portion of the world's population. Over land, the consequences of monsoon are, perhaps, well observed, but the breeding ground over the ocean has been insufficiently monitored. The multi-year space-based observations of wind vectors from ERS-1 and 2, in conjunction with space-based observations of sea surface temperature, precipitable water, and sea level, have helped us to understand the oceanic response to annual wind variations of the two major Asian monsoon systems, the Indian Monsoon over the Arabian Sea and the East Asian Monsoon over the South China Sea.



OCEANOGRAPHIC APPLICATIONS OF SCATTEROMETER DATA IN THE MEDITERRANEAN SEA

S.Zecchetto* and C.Cappa**

*ISDGM-CNR S. Polo 1364, 30125 Venezia, Italy

Tel: 0039 041 5216848, Fax: 0039 041 2602340, e-mail: stefano@ywind.isdgm.ve.cnr.it

**ICG-CNR C. Fiume 4 - 10133 Torino, Italy

Tel: 0039 011 6306807, Fax: 0039 011 6604056, e-mail: claudia@icgaf6.icg.to.infn.it

ABSTRACT

The paper presents an example of oceanographic applications of ADEOS NSCAT scatterometer winds in the central Mediterranean Sea (2-20 E, 35-46 N). Focusing on winter 1996-1997 and spring 1997, the relationships among the oceanic features revealed by the seasonal mean sea surface temperature (SST) field, the scatterometer derived Ekman pumping vertical velocity w_{ek} and total heat flux fields Q_t have been discussed. Despite the approximations in the calculation of the above mean fields, the results show important and permanent correlations between the SST and w_{ek} in the Gulf of Lion, in the Gulf of Genova and in the northern Tyrrhenian Sea, East of the Bonifacio Strait (6-11 E, 40-42 N). The total heat flux and the SST fields appear instead uncorrelated.

While in the northern Tyrrhenian Sea the correlation confirms the wind induced nature of the cyclonic circulation present in this area and the important role played by the funnelling effect induced by the Bonifacio Strait under eastward wind flows, the relationship in the Gulfs of Lion and Genova is of more complicated interpretation, since this area is characterised by a permanent westward circulation and by a cyclonic circulation which is not known if permanent or seasonal. However, the correlation found between SST and w_{ek} in all the seasons analysed included the autumn 1996 (not shown here), indicates a permanent or quasi permanent atmospheric contribution to the water upwelling in this area.

Keywords: Scatterometer, Mediterranean, Ekman pumping, Wind driven ocean circulation.

1. INTRODUCTION

The study of the wind driven sea circulation requires the availability of high quality, high resolution experimental wind data. Respect to the wind fields computed by the atmospheric models, those derived from scatterometer measurements offer a more detailed description of the atmospheric phenomena in the mesoscale (< 100 km). This is particularly important in semi enclosed seas like the Mediter-

anean, almost completely surrounded by mountains, where local or regional phenomena of orographically induced winds and of cyclogenesis play an important role in modifying the general circulation pattern. The use of the scatterometer winds in oceanography implies thus a preliminary detailed analysis of the mesoscale atmospheric phenomena, extensively accomplished starting from the ERS-1 scatterometer data.

To perform a study on mean wind driven circulation, monthly and seasonal mean fields of wind, of atmospheric vertical velocity and of heat fluxes (sensible and latent) are needed. These have been computed using NSCAT wind fields, ECMWF analysis data of air temperature, humidity and atmospheric pressure, and SST mean fields from NOAA satellites.

However, the computation of the mean fields is not without problems, as the spatial and temporal sampling of the area of interest must be adequate to obtain mean field statistically stable. This problem is discussed in the next section. Section 3 deals with the computation of momentum and heat flux fields, while in section 4 the relationships among the winter 1996-97 and spring 1997 mean fields of wind, vertical velocity and total heat flux are discussed.

The paper intends to stress the multi sensor, multi data set approach followed: the more important quantities of the marine boundary layer are, in fact, obtained by means of data coming from different sources, as models and satellite remote sensing, and the ocean driven circulation is investigated using the SST images.

2. THE SAMPLING PROBLEM

The use of scatterometer wind fields in oceanography depends crucially on the spatial and temporal sampling provided by the satellite. There are two oceanographic aspects to take into consideration about sampling: the transient phenomena, for instance the deep water formation in the southern Adriatic Sea and in the Gulf of Lion, due to heavy storm occurrence, and the oceanographic phenomena on monthly or seasonal basis. In the first case frequent measurements of wind vectors over delimited

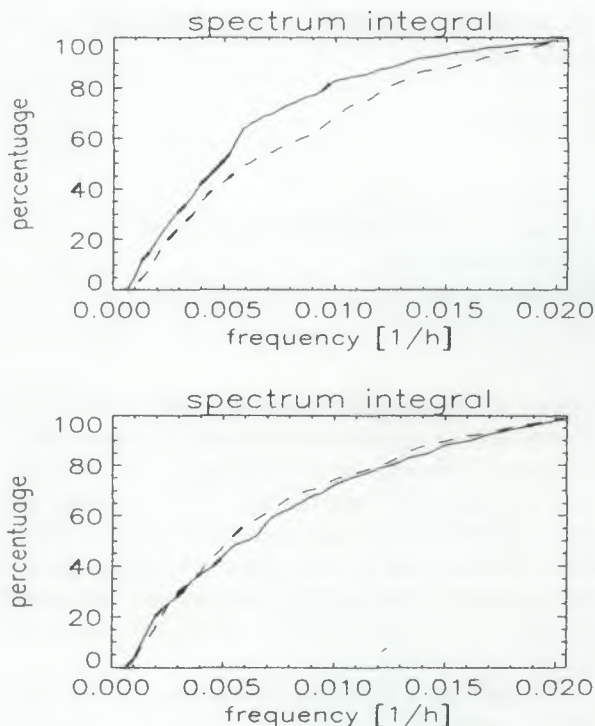


Figure 1. The cumulative function of the zonal wind component u (solid line) and of the meridional component v (dashed line) derived from the respective power spectra. Top: Gulf of Lion. Bottom: Adriatic Sea.

areas and periods are required, whereas in the second case a uniform coverage of the entire basin for long periods is necessary, since short time climatological features of the ocean may involve processes at scales greater than the atmospheric mesoscale. A minimum sampling required in the first case may be estimated in 2 data per day for a four-five days period. For evaluating the minimum sampling rate for seasonal oceanography, we have analysed the frequency spectra of ECMWF analysis wind components in two different sites of the Mediterranean Sea (Gulf of Lion and Adriatic Sea) obtained from three years of data. Figure 1 shows the cumulative function of the zonal wind component u (solid line) and of the meridional component v (dashed line), derived from the respective power spectra. The 90% of wind energy lies in the frequency range $0 \leq f \leq 0.016 \text{ hour}^{-1}$. Therefore, to catch the 90% of the wind energy, a sampling rate of $2f_m$, where $f_m = 0.016 \text{ hour}^{-1}$, is required, corresponding roughly to at least one wind vector every 36 hours, 20 data per month.

This minimum sampling is not reached by ERS scatterometers, which offer a maximum of ~ 12 data

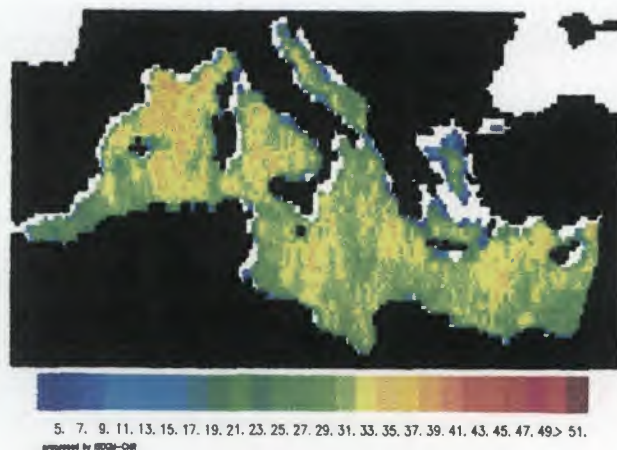


Figure 2. Typical coverage of the Mediterranean Sea provided by NSCAT (December 1996). White areas: less than 5 data per month.

month^{-1} in the Mediterranean. NSCAT, looking both sides and not conflicting with other instruments, overcomes this limitation. Figure 2 shows a typical monthly coverage provided by NSCAT over the Mediterranean Sea. Except close to the coasts, there are about 30 samples per month. With this sampling rate, the 95% of wind energy is measured. The areas better covered result the Gulf of Lion and the Balearic Basin in the western Mediterranean Sea, the South-West and South-East parts of Ionian Sea, and the area South-East of Crete in the Levantine Basin.

3. COMPUTATION OF AIR-SEA FLUXES

Momentum and heat fluxes (the sensible Q_h and the latent Q_e) have been computed through a boundary layer model derived from Kondo theory [7]. The model requires the bulk air and sea temperatures, humidity and atmospheric pressure, in addition to the wind speed. Atmospheric parameters have been obtained from ECMWF analysis fields, and associated to the scatterometer wind fields at the synoptic time closest to the satellite pass time. The sea surface temperature has been derived from the NOAA weekly SST fields, averaged over monthly basis. The ECMWF data (at 0.5 by 0.5 degree of resolution), the SST data (at ~ 0.18 by 0.18 degree of resolution) and the NSCAT winds (at ~ 0.25 by 0.25 degree resolution) have been interpolated into a 0.25 by 0.25 degree regular grid. The choice to associate the to the instantaneous wind fields the monthly SST values represents a rough approximation, however preferable to interpolation of data in the cloudy ar-

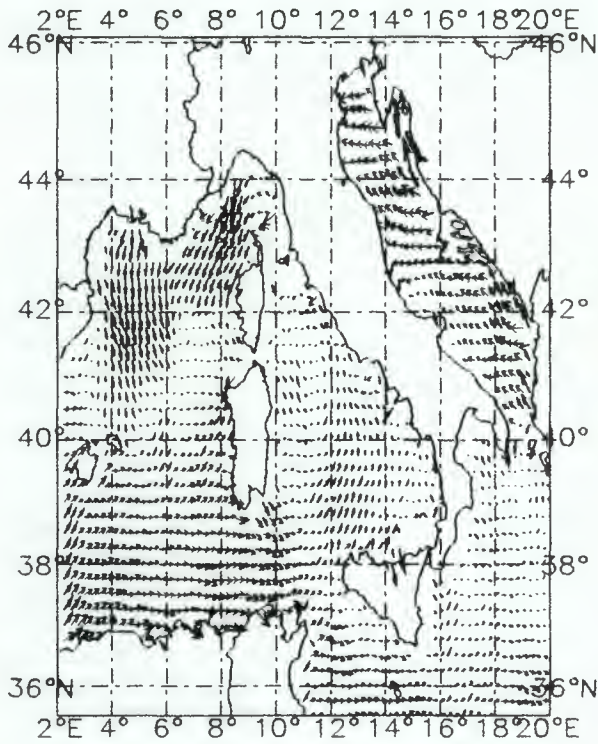


Figure 3. The winter 1996-97 mean wind field in the northern-central Mediterranean Sea. Maximum wind speed: 6.6 m s^{-1} .

eas. Once computed the momentum flux τ , the atmospheric Ekman pumping w_{ek} has been derived as

$$w_{ek} = \frac{1}{\rho f} \text{rot}_z \tau \quad (1)$$

where $f = 2\Omega \sin\phi$ is the Coriolis parameter (Ω is the angular velocity of the rotation of the Earth and ϕ the latitude), ρ is the air density and rot_z is the vertical component of the curl. The Ekman pumping w_{ek} provides an estimate of the vertical velocity at the top of the Ekman layer. Positive w_{ek} indicates upward motion to which it corresponds a cyclonic circulation.

The total heat flux Q_t have been obtained from the absorbed solar radiation Q_s , the infrared backscattered radiation Q_b , the sensible Q_h and latent heat Q_e fluxes, i.e. $Q_t = Q_s - Q_b - Q_h - Q_e$. The values of Q_s and Q_b have been taken from Ref. [6], plot 7b: despite they are pertinent to the Adriatic Sea, they have been considered representative for the entire area of interest.

4. THE OCEANOGRAPHIC APPLICATIONS

The good coverage provided by NSCAT allows to compute the monthly and the seasonal climatological fields and thus to study the oceanographic features



Figure 4. The winter 1996-97 mean Ekman pumping w_{ek} in the northern-central Mediterranean Sea. The white areas refer to values close to zero.

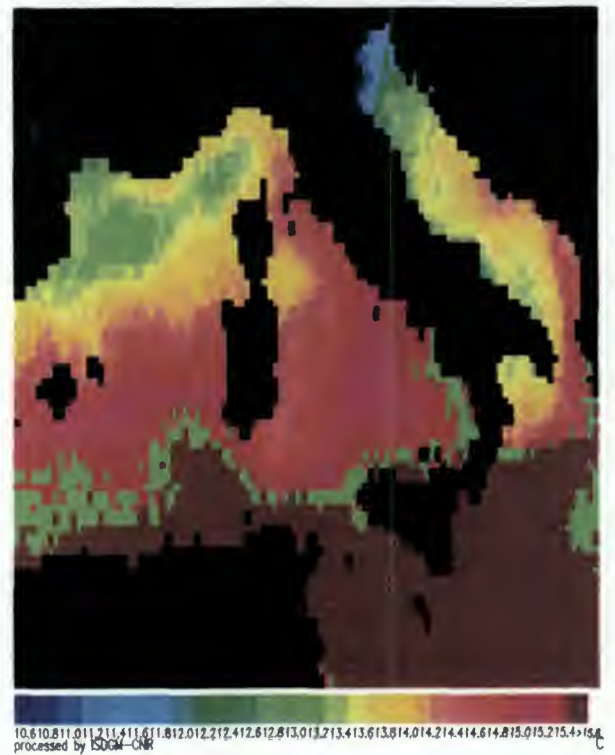


Figure 5. The winter 1996-97 mean SST in the northern-central Mediterranean Sea.

related to the mean momentum and heat fluxes. This kind of study has already been carried out using atmospheric models Refs. [2], [3], [4], [9], [11], [14], but never from experimental data.

Permanent structures of the wind stress vorticity induce corresponding permanent structures in the ocean (Ref. [15], p. 220). Thus, a cyclonic circulation in the atmosphere induces a cyclonic circulation in the sea, which may be detected by the SST signature, since the related water upwelling brings to surface cold water.

To illustrate the possibilities offered by the scatterometer wind fields in oceanography, we have chosen to focus on the northern-central Mediterranean Sea in the winter (December to February) 1996-97 and spring (March to May) 1997. Figure 3 shows the winter mean wind field. The main features are: the mistral type circulation, not particularly developed in this season, in the Gulf of Lion (4-5 E, 41-44 N), the southwestward circulation in the Gulf of Genova (6-10 E, 42-44 N) (producing a wind flow convergence around 6 E, 42 N) and the weak cyclonic circulation centered East of the Bonifacio Strait (11 E, 41 N). It is relevant the wind circulation in the Adriatic Sea, in the northern part from North-East (bora type), progressively rotating clockwise as proceeding southward, where it becomes of scirocco type (from South-East).

The figure 4 shows the winter mean field of w_{ek} . Several features are of interest for further discussion. The first is the large areas of upward atmospheric motion in the Gulf of Genova (9 E, 43 N) and in the Gulf of Lion (6 E, 42 N). Here the w_{ek} field reproduces the characteristic pattern due to the mistral wind system Ref. [16]: the area of upward motion centered at 6 E, 42 N, joining the North of Sardinia to the Gulf of Lion, is associated to the areas of air subsidence centered at 4 E, 42 N, constituting a dipole-like system of w_{ek} . The second relevant feature is represented by the area of positive w_{ek} situated in the Tyrrhenian Sea, East of the Bonifacio Strait separating Corsica from Sardinia, followed southward by an area of air subsidence extending offshore the eastern coasts of Sardinia. According to the analysis of the instantaneous scatterometer wind fields in this area Ref. [16], this pattern is due to the wind funnelling effect produced by the Bonifacio Strait under an atmospheric circulation with a relevant eastward component, such as the mistral or the libeccio. Another small area of positive Ekman pumping lies South-East of Sardinia (10.5 E, 39 N). The third important feature is a large area of atmospheric suction in the central Adriatic Sea (16 E, 43 N). These three winter characteristics have been found in autumn 96-97 (not shown here) and in spring 97 (Fig. 6). Therefore, no matter what the summer pattern of w_{ek} could be, they represent the predominant fea-

tures throughout the year. It must be pointed out that the above results hold for the period considered and consequently they do not describe a seasonal behaviour of w_{ek} in the climatological sense. However, from the experience gained working with ERS-1 and ERS-2 scatterometer data, we believe this may be a real climatological feature.

The near surface circulation in the north-western part of the Mediterranean Sea is characterised by the permanent westward North Mediterranean circulation along the French coast and by a cyclonic mesoscale circulation in the Gulf of Lion. This is referred as a permanent feature by some author Ref. [9] or as a seasonal characteristic induced by the frequent northwesterlies by others Refs. [10], [11].

The winter and spring mean SST fields (Figs. 5 and 7) show a large region of relatively cold water (~ 13 C and ~ 15 C respectively) covering the Gulf of Genova and the Gulf of Lion, where in winter-time a deep water formation occurs Ref. [13]. This cold water area, which persists, with different extension, throughout the year, is partially overlapped by the area of upward vertical motion (Figs. 4 and 6), also of permanent (or quasi permanent) character. Therefore, the cold water appears to result from both the North Mediterranean circulation and the water upwelling induced by the atmospheric Ekman pumping. A closer dependence of the SST pattern from w_{ek} may be inferred in the Gulf of Genova, where the spatial overlapping is more precise.

Another important correlation between winter and spring mean w_{ek} and SST fields is found East of the Bonifacio Strait. Here the SST pattern reveals a presence of a pool of relatively cold water (~ 14 C in winter, ~ 17 C in spring), associated to a cyclonic gyre, close to the position of the positive w_{ek} area. Several studies have been devoted to the understanding of this quasi permanent gyre Refs. [1], [2]. The results of this study indicate that the permanent character of the northern Tyrrhenian gyre is linked to the permanent character of the atmospheric Ekman pumping, supporting the results of Moen Ref. [12], which indicate the vorticity structure of the wind stress field as the main forcing for this cyclonic circulation. The position of the subsiding area South of the cyclonic gyre is consistent with the existence of an anticyclonic gyre reported in Ref. [8], but not visible in the SST map. A further correlation is also found South-East of Sardinia Island (10.5 E, 39 N), whereas the permanent atmospheric Ekman pumping in the central Adriatic Sea do not seem to produce any detectable SST anomaly. Since the SST maps have been obtained from weekly means, some lack of correspondence between SST and w_{ek} may be due to the rather low quality of the SST mean field.

No relevant similarities have been found between the mean Q_t and SST fields at any season. Figure

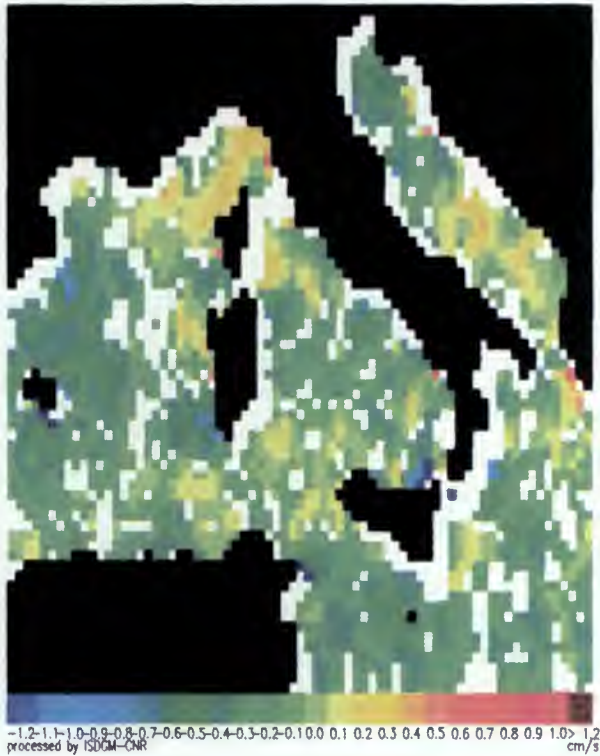


Figure 6. The spring 1997 mean Ekman pumping w_{ek} in the northern-central Mediterranean Sea. The white areas refer to values close to zero.

8 shows, as example, the spring Q_t mean field. This may be interpreted as an indicator of the oceanic upwelling activity, since a continuous renewal of cold water at the sea surface induces a stronger input of heat. For instance, the stronger warming occurring in the Gulf of Lion may be a consequence of the stronger water upwelling in this area respect to the Gulf of Genova.

5. CONCLUSIONS

The example proposed in this paper has shown one of the uses of scatterometer winds in oceanography, consisting of a phenomenological investigation about the similarities in the seasonal patterns of SST, Ekman vertical velocity and total heat flux. Such analysis may be also performed on monthly basis. Unfortunately, despite almost seven years of scatterometer data are actually available, it is not possible to extend this study outside the life period of NSCAT (September 1996 to June 1997), since only this scatterometer has provided a sufficient coverage of the Mediterranean Sea to compute statistically significant mean fields.

The analysis shown in this paper is fairly rough and must be refined in future. A possible improvement may derive from the computation of the mean

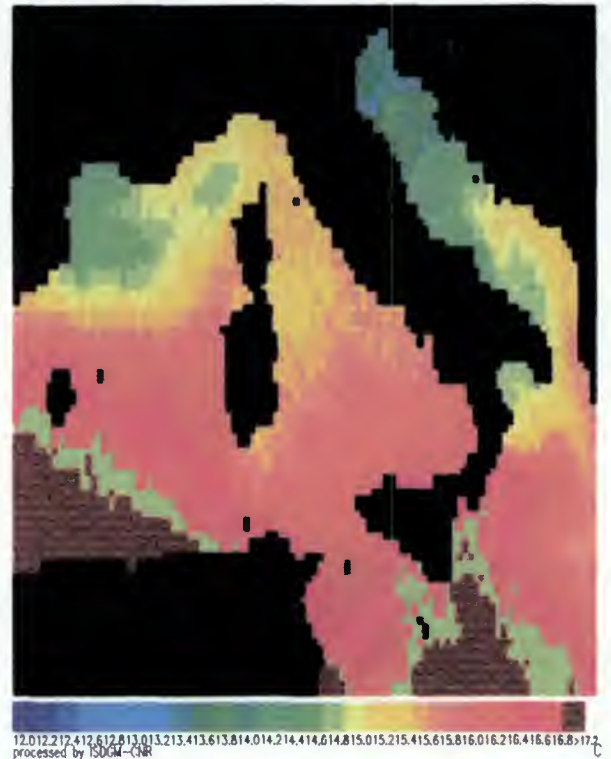


Figure 7. The spring 1997 mean SST in the northern-central Mediterranean Sea.

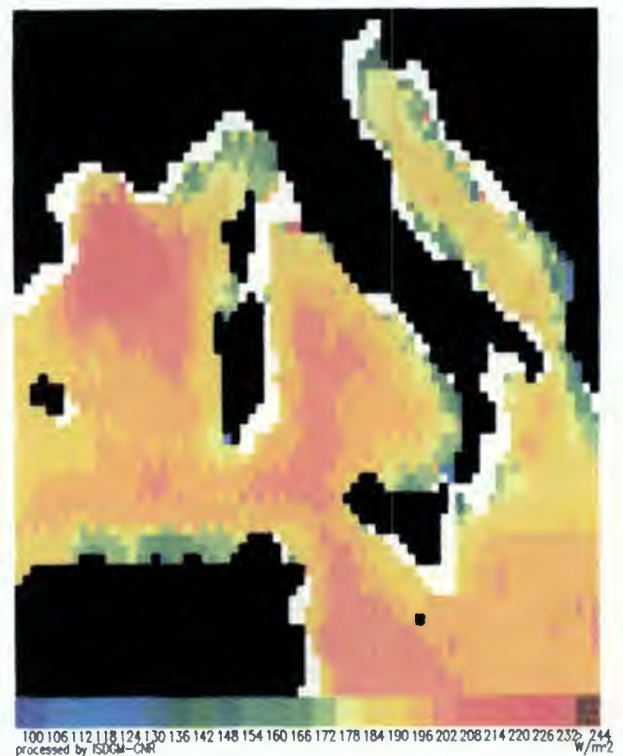


Figure 8. The spring 1997 mean total heat flux Q_t in the northern-central Mediterranean Sea. The white areas refer to values less than 100 W m^{-2} .

SST from original images, instead of from weekly averaged data. This should affect both the computation of τ , through a better estimate of the air-sea temperature difference, and the SST mean fields. A further insight may come also from the analysis of the mean sea level derived from altimeter data.

Also new tools may be envisaged. For instance the vertical velocity w_{Ω} , derived from the Ω equation [5], may help the interpretation of the SST signature. Differently from w_{ek} , which estimates the vertical velocity at the top of the Ekman layer, w_{Ω} describes the vertical motion at the scatterometer wind level, accounting also for the air temperature gradient.

Another relevant use of the scatterometer derived mean fields is as input to the ocean circulation models, but this is different topic.

ACKNOWLEDGEMENTS

This work has been funded by the Italian Space Agency (ASI). The NSCAT data have been provided by the NASA Physical Oceanography Distributed Active Archive Center (PODAAC) at Jet Propulsion Laboratory, California Institute of Technology. We wish to thank Dr. Carol Hsu of JPL for sending us the data and helping in their first interpretation. The NOAA sea surface temperature data have been also obtained from PODAAC.

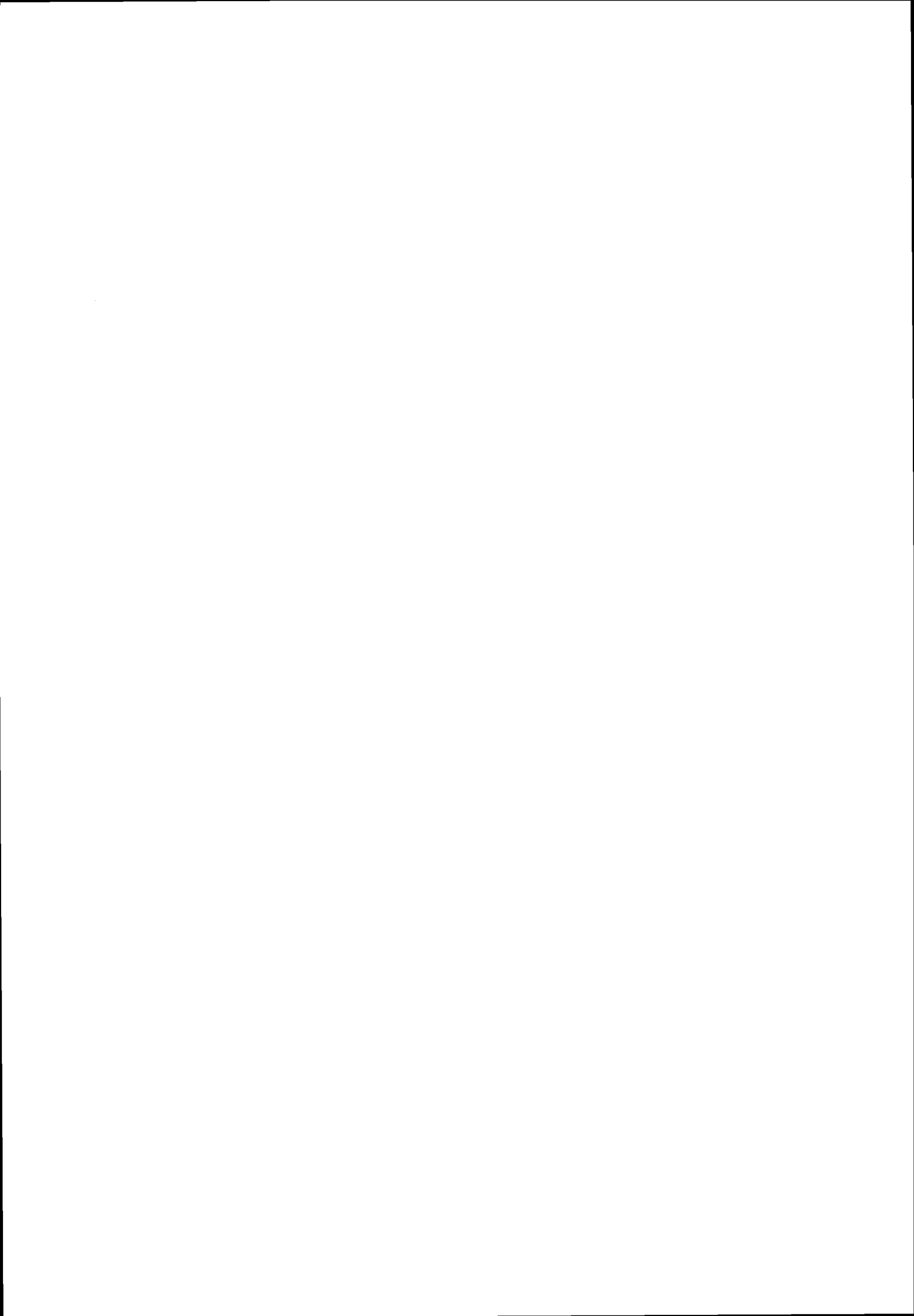
REFERENCES

- [1] Artale, V., M. Astraldi, G. Buffoni and G.P. Gasparini, 1994, Seasonal variability of the gyre-scale circulation in the northern Tyrrhenian Sea, *J. of Geophys. Res.*, **99**, C7, 14127-14137.
- [2] Astraldi, M. and G. P. Gasparini, 1994, The seasonal characteristics of the circulation in the Tyrrhenian Sea, *Coastal and Estuarine Studies*, **46**, 115-134.
- [3] Golnaraghi, M. and A. R. Robinson, 1994, Dynamical studies of Eastern Mediterranean circulation, in *Ocean Processes in Climate Dynamics: Global and Mediterranean Examples*, edited by P. Malanotte-Rizzoli and A.R. Robinson, Kluwer Academic Press, pp. 395-406.
- [4] Heburn, G.W., 1987, The dynamic of the Western Mediterranean Sea: a wind forced case study, *Ann. Geophys.*, **5B**, 61-74.
- [5] Holton, J.R., 1992, An introduction to dynamic meteorology, *Academic Press*, San Diego, California, pp. 511.
- [6] Jayne S. and P. Malanotte-Rizzoli, 1991, The surface thermal forcing of the eastern Mediterranean, Technical Report, Center for Meteorology and Physical Oceanography, Dept. of Earth, Atmosphere and Planetary Sciences, MIT, Cambridge, MA 02139, USA.
- [7] Kondo, J., 1975, Air-Sea Bulk Transfer Coefficient in Diabatic Conditions, *Boundary Layer Meteorol.*, **9**, 91-112.
- [8] Krivosheya, V. G. and I. M. Ovchinnikov, 1973, Peculiarities in the geostrophic circulation of waters of the Tyrrhenian Sea, *Oceanology*, **13**, 822-827.
- [9] Malanotte-Rizzoli, P., 1994, Modeling the general circulation of the Mediterranean, In *Ocean Processes in Climate Dynamics: Global and Mediterranean Examples*, edited by P. Malanotte-Rizzoli and A.R. Robinson, Kluwer Academic Press, 307-321.
- [10] Millot, C., 1987, Circulation in the western Mediterranean Sea, *Oceanologica Acta*, **10**, n. 2, 143-149.
- [11] Millot, C., 1991, Mesoscale and seasonal variabilities of the circulation in the western Mediterranean, *Dynamics of Atmospheres and Oceans*, **15**, 179-214.
- [12] Moen J., 1984, Variability and mixing of the surface layer in the Tyrrhenian Sea: MILEX 80, Final Report, SACLANTCEN Rep. SR-75, SACLANT Res. Cent., La Spezia, Italy.
- [13] Schott, F., M. Visbeck and U. Send, 1994, Open ocean deep convection, Mediterranean and Greenland Seas, In *Ocean Processes in Climate Dynamics: Global and Mediterranean Examples*, edited by P. Malanotte-Rizzoli and A.R. Robinson, Kluwer Academic Press, pp. 203-220.
- [14] Tziperman, E. and P. Malanotte-Rizzoli, 1991, The climatological seasonal circulation of the Mediterranean Sea, *J. of Marine Res.*, **49**, 411-434.
- [15] Wells, N., 1986, The atmosphere and the ocean: a physical introduction, *Taylor & Francis*.
- [16] Zecchetto, S. and C. Cappa, The spatial structure of the Mediterranean Sea winds revealed by ERS-1 scatterometer, submitted to the *Int. J. of Remote Sensing*.

NWP Session

Chair: A. Stoffelen, KNMI

Rapporteur: J. Kerkmann, Eumetsat



METEOROLOGICAL SESSION SUMMARY

Ad Stoffelen

KNMI

Postbus 201, 3730 AE de Bilt, The Netherlands

Tel: 31-30.22.06.585; +31-13.54.36.914 - Fax: 31-30.22.10.407 - e-mail: stoffelen@knmi.nl

1. Overview

Contributions in this session were in the field of scatterometer wind retrieval, quality control, ambiguity removal, and weather prediction impact. Due to a tragic accident, the valuable contribution by J. Nomura from the Japanese Meteorological Agency was cancelled. The workshop organisers express their deepest regrets for his death to his colleagues, family, and friends.

During the lifetime of the ERS scatterometers the NWP user community has played an active role in the interpretation, monitoring, and quality control of ERS scatterometer backscatter measurements over the ocean, and the operational and real-time use of the data is well established. This is not to say that a meteorological session on emerging scatterometer applications is wasted. In fact, the presentations at the workshop showed developments of major importance. Improved ways of data assimilation into Numerical Weather Prediction, NWP, models at ECMWF (4D-var) lead to a better representation of tropical cyclones in the analyses and forecasts, even more so when scatterometer winds are used. The forecasts of tropical cyclones are spectacular. Other papers showed the beneficial impact of the scatterometer on short-range forecasts (in HIRLAM).

Better data coverage would be very beneficial however. In this respect, future scatterometers have great potential. However, challenges remain in the interpretation, monitoring, and quality control of backscatter data from the US scatterometer, SeaWinds on QuikSCAT and ADEOS-II. It was anticipated, however, that the methodologies developed for ERS and NSCAT may be used to arrive at a good quality wind product, suitable for assimilation in NWP. At the workshop it was shown that Ku-band quality control for NSCAT results in an improved wind product. Use of imagery data for quality control also has potential.

A well represented topic in the workshop was variational ambiguity removal, both for NSCAT and ERS winds. As has been reported earlier, the initialisation by NWP wind fields is very beneficial for the ambiguity removal, and in that case both recursive filters and variational methods work well. However, in

variational ambiguity filters there is more flexibility in defining the spatial context of the filter and physical constraints can be formulated. A beneficial variational ambiguity removal on the ERS scatterometer swath was reported, and advancements for an extended swath formulation were shown.

It was suggested that in case of tropical cyclones the ERS scatterometer winds are underpredicting the real wind speed, in particular above 25 m/s. In other words, the sensitivity of the backscatter to wind in the geophysical model function CMOD4 is too strong, and in reality the sensitivity decreases. Continued effort on neural network wind retrieval processing was reported.

2. General Recommendations

After the presentations a splinter working group on meteorology formulated a number of recommendations presented and discussed in the plenary session. The following general recommendations were made:

- The ERS mission should be maintained until the launch of METOP/EPS. The ERS scatterometer wind product is well established and beneficial. Ku-band scatterometers are expected to be beneficial for meteorological use as well, but further development is necessary for operational use. Anyway, scatterometer data coverage was shown to be very important during the workshop. Although the recommendation carries great risk in itself, since the specified ERS mission life time is exhausted, it increases the probability of a continued scatterometer data coverage until METOP/EPS. This leads into the second recommendation.
- Continuity of scatterometer missions. For an optimal and continued exploitation of scatterometer data the operational meteorological community would need to rely on this.
- Improved coverage of scatterometer winds. Experiments with the tandem ERS scatterometers have clearly demonstrated the synergy and added value of an increased data coverage for both short- and medium-range weather forecasting. Moreover, a better temporal coverage will motivate meteorological forecasters to more routinely use scatterometer winds for nowcasting purposes as well.
- The spectacular results for medium-range tropical cyclone forecasting warrant a dedicated tropical

cyclone monitoring mission. It specifically reads mission and not satellite, since it was for instance strongly felt that, in the case of the ERS mission, SAR operations could be much reduced in active cyclone regions and periods.

- High-resolution mode operation should be the baseline for future scatterometers. In particular for enclosed waters, coastal areas, and along the ice edge, a resolution of for instance 25 km, rather than 50 km would be useful. Since effects of fetch, bottom topography, or stability, may become more pronounced in these areas, further research will be needed for an optimal exploitation. For users requiring lower resolution spatial averaging can be adopted before the processing.

- A consistent reprocessing of ERS scatterometer data from 1991 to today is recommended. Scatterometer algorithm developments, orbit manoeuvres, hardware changes, and improved wind processing quality control and monitoring can be taken into account in such exercise. The results will be, a. o., valuable for the ECMWF reanalysis project, ERA40.

- Satellite operators should always provide the best possible real-time product, where a fast feedback loop with the user community should be established. Reprocessing of scatterometer data, following significant improvements in the real-time scatterometer data processing, should be considered regularly in order to obtain proper climate series.

- NWP data assimilation facilities are powerful means for satellite data quality monitoring, validation, and calibration, and these facilities are recommended for consideration in case of diverse satellite instrumentation, such as, e.g., ozone-measuring instruments.

- The use of common quality control indicators amongst the diverse scatterometer wind products and instruments is recommended. This facilitates the use of scatterometer winds in the meteorological user community.

3. Scientific Recommendations

- Non-linear statistical effects in all steps of the scatterometer processing deserve continued attention. In particular, these effects are challenging to cope with in some portions of the SeaWinds swath.

- Cross-validation of C- and Ku-band scatterometer data. This is useful for studying the error properties of both.

- The geophysical model functions, GMFs, can be improved at extreme wind speeds. Dropsonde, buoy, and flight level data has become available to reconsider a recalibration. However, extended efforts to generate good quality validation data in extreme conditions are encouraged.

- Secondary geophysical dependencies of the GMF, i.e., not correlated to the wind vector at 10m height,

can be further investigated for their backscatter sensitivity. In case of a significant sensitivity, the processing should be adopted.

- Quality Control and monitoring are essential issues for use in NWP, and continued developments are encouraged. Specifically, in case of the SeaWinds scatterometer concept, new procedures need to be adopted.

- The development of ice screening methodologies, using actual and historical scatterometer winds is recommended. Accurate ice edge modelling is still difficult. The actual backscatter data contains information on the discrimination of wind sea and ice. This should be exploited to the maximum.

- The wind ambiguities should be provided to the user and improved ambiguity removal methods implemented for all scatterometer wind processors. Continued ambiguity removal algorithm developments are encouraged, in particular variational schemes seem promising.

- Better observation operators. In particular for SeaWinds, much has to be done to arrive at a proper definition of an observation operator for the assimilation of these winds in NWP models.

- Focus on situation-dependent structure functions in scatterometer data assimilation. For the use of surface data, it appears that the structure of the atmospheric flow is important. A better and situation-dependent modelling of the background error structures will probably improve scatterometer impact.

- Exploitation of FASTEX data for the study of the vertical wind and temperature stratification over the oceans. The definition of the vertical error structure may be improved by studying these data collocated with scatterometer winds.

SCATTEROMETRY AND WEATHER PREDICTION

Ad Stoffelen

KNMI, de Bilt, the Netherlands, Email: Stoffelen@knmi.nl

ABSTRACT Over the last years the processing of ERS scatterometer winds has been refined. Scatterometer winds have a clear and beneficial impact in the data assimilation cycle and on the forecasts. Furthermore, ECMWF has shown that ERS scatterometer data improve the prediction of tropical cyclones in 4Dvar, where unprecedented skillful medium-range forecasts result of potential large social-economic value. Nevertheless, scatterometer winds contain much sub-synoptic scale information where the smallest scales resolved are difficult to assimilate into a Numerical Weather Prediction, NWP, model. This is mainly due to the otherwise general sparsity of the observing system over the ocean. In line with this it is found that scatterometer data coverage is very important for obtaining a large impact. In that respect future scatterometer systems such as SeaWinds on QuikSCAT and ADEOS-II, and ASCAT on EPS are promising. Challenging developments are necessary to use these data in an optimal way.

1. INTRODUCTION

After the launch of ERS-1 much improvement has been made in the interpretation of scatterometer backscatter measurements and a good quality wind product has emerged (Stoffelen and Anderson, 1997a, 1997b and 1997c). The consistency of the scatterometer winds over the swath makes them particularly useful for nowcasting purposes and several examples of the usefulness of the direct visual presentation of scatterometer winds to a meteorologist can be given. In this session of the workshop many presentations tackle the problem of ambiguity removal that is needed before presentation of the scatterometer wind product to a meteorologist. Ambiguity removal schemes work well in most cases, but fail in the most dynamic situations, where usually little prior information is available on the direction of the wind. We note that these situations are the most relevant though. Meteorological analysis methodologies as also described in this paper are now applied for ambiguity removal. Other papers deal with Quality Control and studies on improved geophysical interpretation by screening ice contaminated points or investigating the dependency on sea state parameters. The EUMETSAT supported Satellite Application Facilities, SAF, will play an important role in testing the resulting algorithms in an operational environment. In particular the Ocean and Sea Ice SAF wind product, and the scatterometer work in the NWP SAF are relevant in this context.

I will focus in this paper on the scatterometer impact in numerical weather prediction (NWP) as gathered with the ERS-1 and ERS-2 scatterometer winds, and on an outlook into the use of the NASA Ku-band scatterometers.

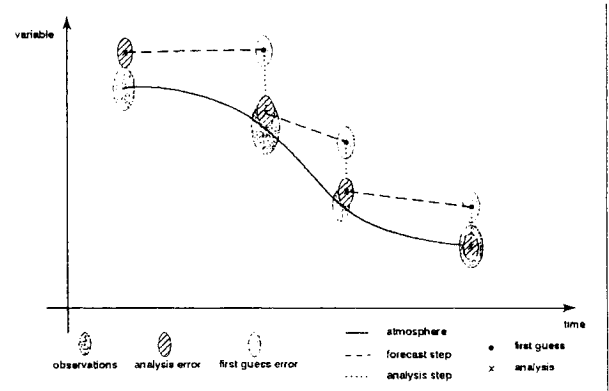


Figure 1 OI or 3Dvar analysis of the atmospheric state (vertical) over time (horizontal). © ESA, 1996.

Experiments at KNMI and ECMWF will first be briefly described in order to introduce the problem. The scatterometer data preprocessing system (PRESCAT) has been developed at KNMI and ECMWF and implemented in the High Resolution Limited Area weather forecasting Model (HIRLAM) and the ECMWF model. Impact experiments were carried out to test the usefulness of the data for the analyses and for short-range forecasts up to two days in HIRLAM. A meteorologically active period where both ERS-1 and ERS-2 scatterometer data are available was selected to test the impact of an increased data coverage. In Stoffelen and Beukering (1997, and this session) these developments are described in detail, and here a brief summary is provided.

At ECMWF, ERS-1 and ERS-2 scatterometer winds were used to carry out similar experiments, but at the global scale and for medium-range forecasting. The scatterometer proves beneficial in dynamical weather conditions, though the static 3D assimilation systems are probably not optimal for surface wind assimilation in such conditions. ECMWF carried out 4Dvar scatterometer impact experiments, where the model tendencies are taken into account in the data assimilation cycle, and a dynamically more consistent analysis results. It is shown that scatterometer winds in 4Dvar lead to unprecedented accurate medium-range forecasts of tropical cyclones.

Accurate weather and wave forecasts are essential to monitor safety at sea for ship routing and tourism, and to issue warnings for coastal land protection in extreme wind and wave conditions, such as tropical cyclones. The prediction of extreme weather events has obviously potentially large social and economic value. The accuracy of short-range weather and wave forecasts over Europe depends to a large extent on the real-time availability of accurate observations over the Atlantic ocean, where conventional measurements are sparse. For the medium range, the coverage over the Pacific and in the tropical hurricane area also becomes critical. ERS-1 scatterometer data have been used to increase the data coverage over the oceans in different Numerical Weather Prediction (NWP) models and showed in general improvement in the short range weather forecasts (e.g., Stoffelen and Anderson, 1997c). In the medium range, beneficial impacts were seen particularly in the Southern Hemisphere (e.g., Bell, 1994). Furthermore, the use of NWP data, with scatterometer winds included, results in improved WAM wave forecasts (Janssen and Hansen, 1996).

In regional weather forecasting the emphasis lies on the short range and on the sub-synoptic spatial scales. Wind observations with a high spatial coverage are essential to resolve these. The scatterometer provides such data, albeit only at the surface. The use of ERS-1 and ERS-2 tandem scatterometer data in HIRLAM may therefore be expected to be more beneficial than the use of only one ERS scatterometer. Also, the ASCAT scatterometer on board the future EUMETSAT METOP satellite and the NASA scatterometer SeaWinds for QuikSCAT or on board of the Japanese ADEOS-II, have such an increased coverage. The HIRLAM data assimilation system at KNMI is started with a cut-off time for observations of 2 hours. Usually only 50% of the ERS scatterometer data are received within two hours. Our experiments confirm the importance for Europe of scatterometer data coverage and suggest that a delivery of data within 2 hours would be very useful.

2. RESULTS

2.1 *Quality Control and Monitoring*

The ERS-2 geophysical validation strategy includes an "ocean" sigma naught calibration procedure as described by Stoffelen (1998a). Moreover, instrument monitoring, see Le Meur et al (1996a), and backscatter QC (Stoffelen and Anderson, 1997a) results in a product with a well characterized quality. Furthermore, the spatial error correlation characteristics have been investigated rigorously (Stoffelen, 1996). It can not be stressed too often that a few low quality observations may destroy the beneficial impact of many good quality observations, and that Quality Control and Monitoring are essential.

2.2 *Wind Tuning*

In order to avoid systematic slowing down or speeding up of the HIRLAM model by scatterometer data assimilation we adopted a careful wind validation. Gaffard and Roquet (1998) show the detrimental effect of systematic wind bias on NWP impact. In fact, the spatial variations in meteorological observations provide the most important information for NWP models. The results of a wind calibration method taking into account the error characteristics of *in situ*, satellite and model winds by Stoffelen (1998b) or Le Meur et al (1997) has been used to estimate the wind biases of the HIRLAM and ECMWF models with respect to the scatterometer. Although scatterometer winds delivered by PRESCAT are found to be approximately 5% low, the HIRLAM first guess has a negligible bias with respect to the ERS scatterometers, and thus is also biased low with respect to the true wind. The ECMWF model is biased high though. These model biases most likely result from the physical parameterizations of the Planetary Boundary Layer and need further attention. We estimate the random ERS scatterometer wind component error to be 1.8 m s^{-1} . The NWP model random error is estimated to be smaller than this, i.e., $1.0 - 1.2 \text{ m s}^{-1}$.

ERS scatterometer backscatter measurements are delivered on a grid of 25 km, but have a spatial resolution of 50 km. The HIRLAM and ECMWF model grid distances are nominally 50 km and 60 km respectively. In order to present the scatterometer data to the HIRLAM model in a spatial representation consistent with the model, we averaged the scatterometer data to a grid of 100 km, whereas ECMWF thins the winds to this same grid. As is argued below, this spatial representation was still too fine to be assimilated by the HIRLAM or ECMWF models in some cases. Anyway, after the ocean calibration and wind tuning, PRESCAT delivers accurate ERS-1 and ERS-2 winds with much sub-synoptic scale information.

2.3 Assimilation

2.3.1 HIRLAM

The tandem scatterometer data assimilation experiment ran from 6-18 February 1996, a period with a disturbed westerly flow over western Europe. Since the North Atlantic is an area with a sparse meteorological observation coverage, scatterometer data are expected to fill in this gap and thus may provide an impact on the weather forecasts over western Europe. The grid used is by approximation equidistant and 5000 by 4000 km with Dublin in the center.

The analysis is a combination of the information provided by a HIRLAM 3-hour forecast, called background, and the observations available in the 3-hour time window centered around the verification time of the forecast (figure 1). The impact of observations in the analysis depends on the ratio of the estimated background over observation error. The scatterometer observation errors are assumed to be spatially uncorrelated (Stoffelen, 1996), and the spatial projection of scatterometer information in the analysis depends solely on the estimated background error structure (figure 2). The typical horizontal projection scale is 250 km. The error structures are multivariate and balanced, indicating that the scatterometer wind observations influence the pressure and temperature fields. Also, the information is projected in the vertical, e.g., a modification of the wind at the surface due to a scatterometer observation results in a fraction 0.25 of that modification at 500 mb. From most scatterometer experiments carried out so far, it can be concluded that forecast impact can only be obtained when the upper air is improved in a consistent way with the modifications at the surface.

For the selected period in February '96 three data assimilation experiments were run

- noERS, control without scatterometer winds,
- ERS1, with only ERS-1 winds assimilated, and
- ERS12, with both ERS-1 and ERS-2 included.

2.3.1.2 Impact over Sea

The background wind fields of all these three experiments were verified against the scatterometer winds. It was found that both the ERS1 and the ERS12 background had a roughly 20% smaller error than the noERS background. We found that the ambiguity removal in experiment ERS12 worked clearly the best, followed by that of experiment ERS1, and the worst performance in experiment noERS. This suggests that phase errors of meteorological systems are smallest for experiment ERS12.

2.3.1.2 Impact over Land

To verify the impact over land we compared the RMS mean sea level pressure (MSLP) modifications,

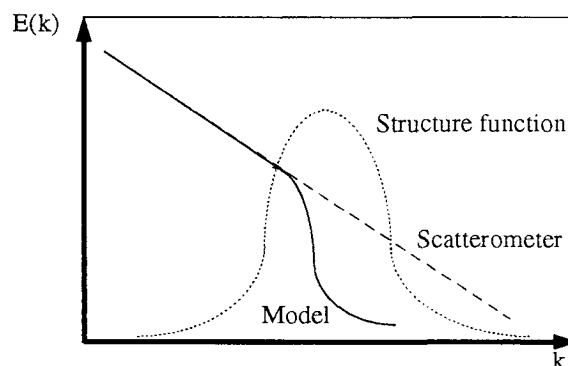


Figure 2 The ERS scatterometer resolves sub-synoptic scale information with large wave number k (dashed) that the NWP model does not resolve (solid). The analysis structure functions (dotted) are designed to incorporate the observed smaller scale structures into the NWP model energy spectrum, $E(k)$.

increments, in the analysis. Since over land the same observations are used in the three experiments, a smaller RMS increment indicates a better background MSLP. The RMS analysis increments over land in the ERS1 and ERS12 experiments were 10-20 % lower than in the noERS experiment, indicating that the background is also improved over land by the assimilation of scatterometer winds.

2.3.1.3 High resolution?

Although we anticipated that the HIRLAM data assimilation system would not be capable of resolving all the sub-synoptic detail in the scatterometer winds, and we had averaged the winds to a 100 km resolution, we still found that the observation consistency check in the analysis rejects scatterometer winds close to sharp troughs and fronts, and substantially smoothes the winds on scales smaller than a few hundred kilometers. In other words, the small-scale information in the scatterometer winds is smoothed out by the analysis. This is due to the estimate of the spatial error correlation scale of the background error. It is determined by what spatial scales the HIRLAM model can realistically describe (figure 2). Over the ocean this is not so much determined by the grid distance used by the model, but by the density of the network of meteorological observations, i.e., a decrease of the grid distance and associated with this an increase of the variability on the smaller scales would only result in a larger error, since no data is available to determine the flow on these small scales.

Scatterometer and other single level wind data will help improve this situation, but probably upper air wind

profile observations will be needed for a substantial improvement over the oceans (Ingmann et al, this issue).

2.3.2 ECMWF 4Dvar

Effects in the global assimilation of scatterometer winds at ECMWF are similar to those observed at KNMI in case of 3Dvar and Optimum Interpolation, OI, methods (Le Meur et al, 1996b). However, ECMWF put a 4Dvar data assimilation scheme into operations in November 1997. In 4Dvar the dynamics of the forecast model over the assimilation window, 6 hours currently, are adapted according to the observations available. As such, the model state can be changed in a dynamically consistent way. This is expected to make a difference in particularly the most dynamical situations. In line with this it is found that tropical cyclones are much better represented and retained in the 4Dvar assimilation cycle than in the 3Dvar assimilation cycle. Scatterometer data are found to often increase the intensity of tropical cyclones, and correct their position. However, if a tropical cyclone is partially captured in the scatterometer swath and not well represented in the ECMWF model, then the analysis of the cyclone may not result in the correct structure (Isaksen et al, 1998). This is due to the influence of the spatial structure functions representing the average error in the ECMWF background, but that does not provide the most ideal analysis increments in all situations. Experiments with situation-dependent structure functions or high resolution analysis are recommended to investigate possible improvements.

2.4 Forecast Impact

2.4.1 HIRLAM

From the 00 UTC and 12 UTC analyses of all the experiments we ran two-day forecasts. The forecasts for forecast leads of 12, 24, 36 and 48 hours were systematically verified with the corresponding analyses for surface wind, pressure and temperature, and 500 mb wind and temperature. Up to a forecast lead of 24 hours, the verifications clearly depend on whether we use the noERS, ERS1, or ERS12 analyses for verification. For the 48 hour forecasts this is not the case, and our conclusions can be firm. It is clear that the ERS12 forecasts are better than the ERS1 and noERS forecasts. On the other hand, the two-day ERS1 forecasts are on average not demonstrably better than the noERS forecasts. This confirms the conclusion of Le Meur (1996) with the ECMWF NWP model that a tandem scatterometer has more than twice the impact of a single scatterometer. Scatterometer data coverage is thus important.

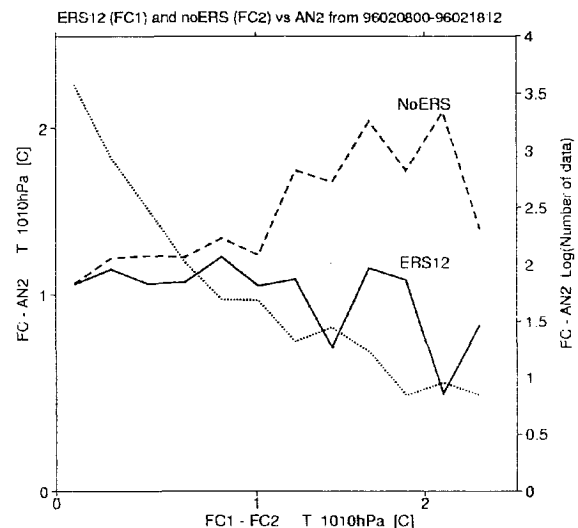


Figure 3 Verification of the ERS12 (solid) and NoERS (dashed) forecasts (left) versus 48-hour forecast impact of ERS1 and ERS2. The right axis represents the number of cases (dotted). The more the ERS12 and NoERS forecasts are different, the better the ERS12 forecast and the worse the NoERS forecast. When scatterometer data has impact, it is thus generally beneficial.

The average forecast impact was different for different parameters and different forecast ranges, but again we find that the forecast impact is generally similar at the surface and in the upper air, indicating that in case of positive impact the scatterometer information at the surface is well propagated in the vertical.

2.4.1 Tropical Cyclones and 4Dvar

The forecasts from 4Dvar analyses in case of tropical cyclones are spectacular. For tropical cyclone George in September 1998, the ECMWF 10-day forecasts over a 13-day period made unprecedented medium-range forecasts of its track. This forecast skill is due to the better representation of tropical cyclones in the 4Dvar assimilation, with respect to their representation in 3Dvar or OI. Parallel experiments with and without the use of scatterometer winds were conducted in order to determine the role of scatterometer data in the forecasts. Isaksen et al (1998) show detailed results, indicating that scatterometer winds play an essential role in 4Dvar for the improved forecasts of tropical cyclones.

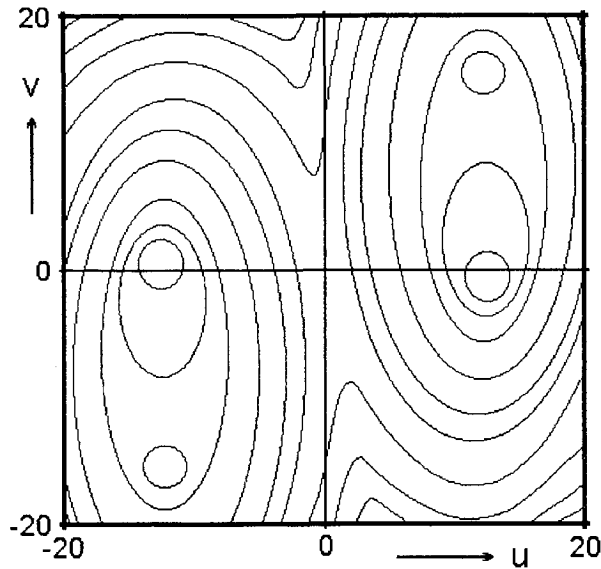


Figure 4 Illustration of wind probability contours as a function of the wind components u and v for a SeaWinds wind vector cell with measurements at four different azimuths including two polarizations. Multiple minima may exist, resulting in a slightly more complex variational assimilation.

3. CHALLENGES

The ERS-1 and ERS-2 scatterometers provide detailed sub-synoptic-scale information that is relevant for nowcasting and longer range forecasting. QC and monitoring routines (in PRESCAT) make the routine use of the winds in NWP models feasible. Further developments to these are carried out in the Ocean and Sea Ice SAF project (Stoffelen et al, this volume).

The HIRLAM analyses are clearly improved by PRESCAT winds, both over land and over sea, and both in case of one and in case of two scatterometers. However, the information provided by the scatterometer on a scale of 100 km is rejected in the NWP data assimilation. An increased density of meteorological observations over the oceans, also in the upper air, is believed to be necessary in order to improve the situation. Experimentation with higher resolution data assimilation and forecast systems is recommended as well however.

In line with the above, from our experiments it is found that scatterometer data coverage is very important to obtain forecast impact. For the HIRLAM experiments, we were not able to demonstrate the forecast impact of one

scatterometer, but found a clear beneficial impact in case we assimilated the ERS-1 and ERS-2 scatterometer wind data in tandem. The synergy of two scatterometers is present also in the ECMWF system.

In fact, it has been realized before that coverage is a weak point of the ERS-1 or ERS-2 scatterometer, and its successor ASCAT on METOP will obtain a threefold coverage. In preparation for METOP KNMI is developing calibration and validation tools and the wind processing chain within the EUMETSAT Ocean and Sea Ice Satellite Application Facility. By the end of 1998 KNMI plans to have a prototype processing chain running in near real-time with ERS data. This prototype is based on PRESCAT. Developments on a.o. ice screening and ambiguity removal are performed in collaboration with IFREMER. Several papers on these topics can be found elsewhere in this session.

We note that for example ambiguity removal works well on average in the sense that it only fails in a few cases, but that when it fails, it is often in extreme weather events like, e.g., hurricanes. These events are of course most relevant and continued effort on improving algorithms is important.

In order to bridge the gap between the ERS scatterometer series and ASCAT on METOP, the meteorological community will have to rely on a new scatterometer concept being developed by NASA, SeaWinds. QuikSCAT will be a dedicated SeaWinds scatterometer mission, scheduled for launch in late 1998. NOAA plans to have a near real-time distribution of the data in place by mid 1999. In 2000, ADEOS-II is planned for launch with a copy of the NASA SeaWinds scatterometer on board.

Fortunately, QuikSCAT will have a large data coverage with its swath of 1800 km wide. That part of the swath that contains a similar amount of information on the full near-surface wind vector as that provided at the nodes of the ERS or NSCAT scatterometers, is of similar width than the total swath width of NSCAT or ASCAT. However, the remaining outer and middle parts of the swath will contain less information than for instance the ERS or NSCAT wind vector cells. The "sweet spots" in the swath will have slightly greater ambiguity in the wind domain (figure 4) than the ERS scatterometers (Stoffelen and Anderson, 1997c), and its effect needs to be tested in order to arrive at a practical implementation. In collaboration with NASA and with EUMETSAT support, KNMI and ECMWF plan to contribute towards an effective interpretation and quality control of the SeaWinds data to the benefit of NWP. Using NSCAT backscatter measurements and collocated winds, a satisfactory geophysical model function for use with SeaWinds has been derived (Wentz and Freilich, 1998). The

sensitivity of the NASA scatterometers to rain is of particular concern. Figa and Stoffelen (1998) propose a QC algorithm rejecting many rain points, that will be tested for use with SeaWinds as well. The rotating pencil beam concept facilitates "ocean calibration", but complicates the interpretation and quality monitoring, since this becomes strongly wind vector cell dependent. We believe, however, that the experience and methodologies developed with the ERS and NSCAT scatterometers can be used successfully over most of the SeaWinds swath.

Given the importance of data coverage and the resolution of the scatterometer wind product, it may be clear that a timely data delivery has a high priority for the monitoring and forecasting of extreme weather events.

REFERENCES

- Bell, R. S., 1994: "Operational use of ERS-1 products in the Meteorological Office", In proceedings of 2nd ERS-1 symposium - Space at the service of our environment. Hamburg 11-14 October 1993, ESA SP-361, pp. 195-200.
- Breivik, L.-A., 1993: "Assimilation of ERS-1 scatterometer wind information in a limited area model", research report from DNMI, Oslo, Norway.
- ESA, The Nine Candidate Earth Explorer Missions - Atmospheric Dynamics Mission, *Special report published by the Eur. Space Agency, ESA SP-1196(4)*, ESTEC, Noordwijk, the Netherlands, 1996.
- Figa, Julia, and Ad Stoffelen, 1998: "NSCAT Scatterometer Quality Control", this volume.
- Gaffard, C. and H. Roquet, 1998: "Impact of the ERS-1 scatterometer wind data on the ECMWF 3D-VAR assimilation system", Submitted to Q.J.R. Meteor. Soc.
- Ingmann, P., A. Stoffelen, L. Isaksen, and G.-J. Marseille, 1998: "On the need for an Atmospheric Dynamics Mission", 4th CGMS winds workshop, Saanenmöser, Switzerland.
- Isaksen, L., D. Le Meur, and A. Stoffelen: "Tropical Cyclone forecasting at ECMWF", this volume.
- Janssen, P. and B. Hansen, 1996: "Analysis of results from 3D-Var E-suites using the WAM model", ECMWF Research Department Memorandum, available from ECMWF.
- Le Meur, D., 1996a: "Monitoring of ERS scatterometer winds", ECMWF Technical Note, available from ECMWF, Reading, UK.
- Le Meur, D., 1996b, personal communication.
- Le Meur, D., L. Isaksen, and A. Stoffelen. 1997: "Wind Calibration by Triple Collocation and Maximum Likelihood Estimation", CEOS Wind and Wave Validation Workshop, June 1997, ESTEC, the Netherlands.
- Stoffelen, Ad, 1996, "Error modeling of scatterometer, *in-situ*, and ECMWF model winds; A calibration refinement", Technical report 193, published by KNMI, Postbus 201, 3730 AE de Bilt, the Netherlands.
- Stoffelen, A., "A simple method for calibration of a scatterometer over the ocean", *J. Atmos. Oceanic Technol.*, in press, 1998a.
- Stoffelen, Ad, "Error modeling and calibration; towards the true surface wind speed", *J. Geophys. Res.* 103 (C4), 7755-7766, 1998b.
- Stoffelen, Ad and David Anderson, "Scatterometer Data Interpretation: Measurement Space and inversion", *J. Atmos. Oceanic Technol.*, 14(6), 1298-1313, 1997a.
- Stoffelen, A. C. M. and D. L. T. Anderson, Scatterometer data interpretation: Estimation and validation of the transfer function CMOD4, *J. Geophys. Res.*, 102(C3), 5767-5780, 1997b.
- Stoffelen, A. C. M. and D. L. T. Anderson, Ambiguity removal and assimilation of scatterometer data, *Q. J. Roy. Meteorol. Soc.*, 123, 491-518, 1997c.
- Stoffelen, Ad, and Paul van Beukering, 1997: "Improved backscatter processing and impact of tandem ERS winds on HIRLAM", *HIRLAM project report nr 31*, IMET, Dublin, Ireland, 1997.
- Wentz, Frank, and Mike Freilich, 1998: "The NSCAT-2 geophysical model function", submitted for publication.

IMPACT OF ERS-SCATTEROMETER WIND DATA ON ECMWF'S ANALYSES AND FORECASTS OF TROPICAL CYCLONES

L. Isaksen¹, D. Le Meur¹, A. Stoffelen²

¹ European Centre for Medium-range Weather Forecasts, Shinfield Park, Reading, RG2 9AX, U.K.

²KNMI Postbus 201, 3730 AE de Bilt, the Netherlands

ABSTRACT

This paper describes the positive impact of ERS scatterometer data on tropical cyclone analyses and forecasts at ECMWF. ERS-scatterometer data is especially valuable because they are available in the data sparse genesis regions of tropical cyclones, and because they are also available in cloudy and rainy conditions. In November 1997 ECMWF introduced the four-dimensional variational assimilation system (4D-Var) in operational use. One of the benefits of this system is the better utilization of ERS-scatterometer wind data because they can be assimilated close to the observation time. This is especially important for near surface winds that can change a lot over a six hour period. The 4D-Var system is also able to propagate scatterometer wind information more properly in the vertical compared to traditional assimilation systems. The 4D-Var system is supplied with both ambiguous winds and performs the selection of one of the winds in a dynamical way using model winds influenced by information from adjacent observations in the decision-making. By default ECMWF is using ERS-2 scatterometer wind data in the daily operational assimilation system. In order to understand and investigate the impact of ERS-scatterometer wind data, assimilations with or without use of scatterometer data has been performed for the most intense part of the 1995 Atlantic hurricane season. A comparison with the then operational ECMWF optimum interpolation (OI) assimilation systems performance has also been done. Both intensity and positional errors of tropical cyclones are investigated for analyses and forecasts. The 4D-Var system shows great improvements compared to the previous OI system, the best results are obtained when ERS-scatterometer data are used.

Key words: hurricane forecasts; variational assimilation of ERS scatterometer winds.

1. INTRODUCTION

Microwave scatterometer winds from the European Space Agency, ESA, Remote Sensing Satellite, ERS, satellites have been used operationally at ECMWF

for several years. Its microwave backscatter measurements are not affected by clouds and precipitation, allowing near surface winds in the vicinity of tropical cyclones (TC) to be inferred. Tomassini, le Meur & Saunders (1998), describe scatterometer impact experiments with the three-dimensional variational data assimilation system at ECMWF, showing beneficial impact. The currently operational four-dimensional variational data assimilation system, 4D-Var (see Rabier et al. (1998)), is able to better interpolate the scatterometer data in space and time. We studied the impact of ERS scatterometer winds on the analyses and forecasts of TCs in August and September 1995, using the ECMWF Optimum Interpolation, OI, and 4D-Var data assimilation methods. OI was operational at ECMWF during the 1995 hurricane season. Improvements are seen for the whole range investigated: analyses and up to five-day forecasts. Unprecedented realistic five-day forecasts of tropical cyclones, and very favourable intercomparisons with other tropical cyclone forecasting centers' predictions were obtained. Due to an improved bias correction of CMOD4 winds it is possible to use scatterometer winds up to 25 m/s (see Le Meur et al. (1997)), this benefits the use of ERS data near hurricanes.

Figure 1 shows how the 1998 hurricane Georges was captured several times by ERS scatterometer data as it moved across the Atlantic.

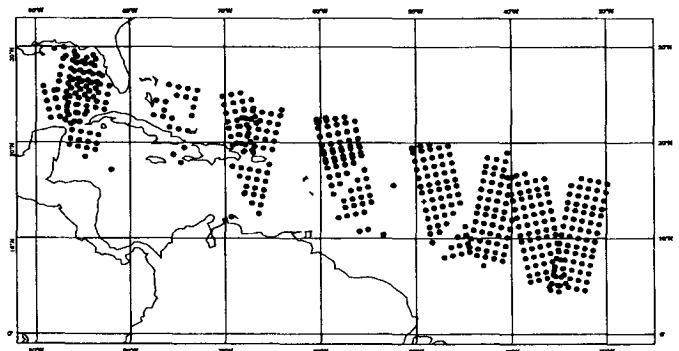


Figure 1. ERS scatterometer data from 16 to 29 Sep 1998 used by the ECMWF 4D-Var assimilation system analyses of hurricane Georges

In section 2, we first outline the data assimilation

methodology used in Numerical Weather Prediction (NWP). Section 3 describes the experiments on the assimilation of scatterometer winds, and in section 4 their results are presented. After discussion of some remaining problems, we present the main conclusions of our paper.

2. DATA ASSIMILATION

The assimilation of ERS scatterometer winds in OI was first performed by Hoffman (1993). In Stoffelen & Anderson (1997a) the procedure applied in the OI-system is well described. In a preprocessing step, two ambiguous winds are retrieved at each node. An ambiguity removal filter subsequently selects a unique wind vector. It is very important that only accurate and representative data enter the data assimilation procedure. To this end, the scatterometer data are quality controlled (QC) by checking for inconsistencies in the messages, checking the magnitude of the inversion residual, eliminating any possible land or ice contamination, rejecting wind speeds above 25 m/s, and by performing a tight monitoring of all scatterometer data in batches of 6 hours (see Stoffelen & Anderson (1997c)). Except for the ambiguity removal filter a similar QC is performed in 4D-Var.

Forecasts and comparisons of observed values with model first guess values are performed at higher resolution, but the resolution of the data assimilation part is only around 250 km, so scatterometer winds are thinned to a resolution of 100 km before assimilation. We show later that the data, despite the thinning, still are valuable in the analyses of TC cases. Stoffelen & van Beukering (1997), have shown that slight improvements of extra-tropical analyses can be obtained by averaging the scatterometer winds at 100 km resolution, similar studies of TCs have not yet been performed.

The obtainable analysis resolution is largely determined by the density of the Global Observing System. In the analysis we benefit from the physical laws that describe e.g. the balance between mass and wind to interpolate the observational and model data. In the assimilation system these relations are described by statistically determined so-called structure functions that represent the typical spatial error structure of the background model field. The background field, in turn, contains all prior information on the state of the atmosphere, and is given by a short-range (6-hour) forecast. The background error structure is almost fully rotational and nearly non-divergent.

2.1. Optimum Interpolation - OI

In the vertical the background error structures do not extend through the entire troposphere, since, in general, they are limited in depth. In operations, ECMWF ran OI during the 1995 hurricane season. In OI the difference between background and analysis is entirely determined by the structure functions. In the case of a TC and near-surface wind data, this means that information on cyclone intensity and position will only enter the analysis in the lower troposphere. The forecast following the analysis may

then reject this information, if inconsistent with the upper troposphere flow, where likely no observations are available to support the surface observations.

2.2. 4D-Var

In January 1996 the three-dimensional variational assimilation system was introduced operationally at ECMWF. A main advantage for ERS scatterometer winds was that both ambiguous winds could be presented to the analysis (see Stoffelen & Anderson (1997a)). The analysis then implicitly performed the ambiguity removal in an adaptive way.

In ECMWF's 4D-Var assimilation system the best possible analysis is sought over a 6-hour period, provided the meteorological observations in this window, the background field at the start of the window time, and the forecast model dynamics over the window period. The advantage of this method is most pronounced when meteorologically active dynamical systems are present. One example being tropical cyclones, where the use of the forecast model dynamics may result in sharper and more deep background update structures in the presence of spatially consistent data. The iterative procedure in the analysis computations will gradually make the forecast fields in the 6-hour period more and more consistent with the available observations, and possibly use some extreme but correct observations that in a static system would be rejected.

Figure 2 features Atlantic hurricane Iris on 24 August 1995. Panel a) shows the background model MSL pressure field, panel b) the MSL analysis and winds at the ERS nodes used, and panel c) the analysis increments, i.e., the impact of the scatterometer data on the analysis. For clarity only unambiguous PreScat winds are shown in panel b), the analysis is supplied both ambiguities. In this case 4D-Var improves the position and intensity of the TC. The ERS scatterometer data has clearly been used properly to intensify Iris.

3. EXPERIMENTS WITH 4D-VAR

In addition to the operational OI assimilation cycle, that did not use ERS scatterometer data, additional 4D-Var experiments were run for the 1995 hurricane season over a 15-day period in August/September. Both experiments using (SCAT) and not using (NoSCAT) ERS-1 scatterometer winds were performed. The only difference between SCAT and NoSCAT assimilation suites were the use of ERS-1 scatterometer data. This allowed a genuine investigation of the impact of scatterometer data in 4D-Var.

During the period three hurricanes (Humberto, Iris, and Luis) and the tropical storm Karen were active in the Atlantic. Humberto and Iris were category 2 storms reaching 95 knots average maximum intensity. Karen did not develop into a hurricane but was 'swallowed' by Iris on 3 September 1995. This gave Iris new energy and helped it to develop into an intense extra-tropical cyclone causing trouble in Europe. Luis was a large category 4 hurricane (maximum average winds of 120 knots) that caused large

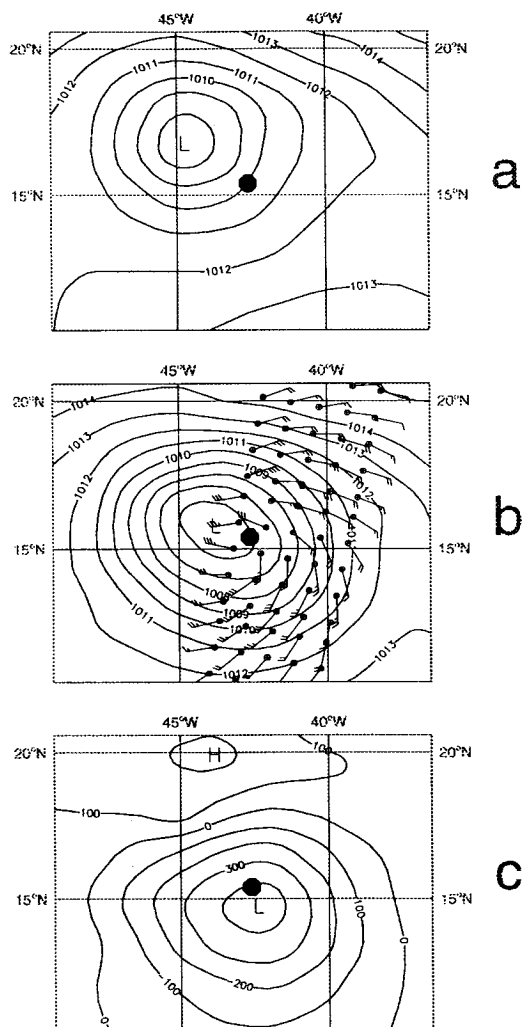


Figure 2. Assimilation of ERS scatterometer data for hurricane Iris on 00 UTC 24 Aug 1995. The observed hurricane position is marked with a filled circle. Panel a): Background model MSL pressure. Panel b): Analysis MSL pressure and ERS winds used (only one wind shown). Panel c): Analysis MSL pressure increment (Analysis-background model).

human and economical damage in the Caribbean. In its extra-tropical life it caused problems on Newfoundland and Greenland. Humberto, Karen and Luis originated from the region near Cape Verde Islands, which is fairly common for Atlantic hurricanes. These types of hurricanes can usually only be identified in their early life by ERS scatterometer observations. This is of vital importance for medium-range TC forecasting for the Caribbean and USA.

4. RESULTS

Figure 3 shows an analysis of hurricane Iris. The figure layout is like in figure 2. From the contour lines one can infer that Iris has been intensified and the hurricane structure has been better identified due to the ERS scatterometer data.

Although ERS winds clearly impact the data assim-

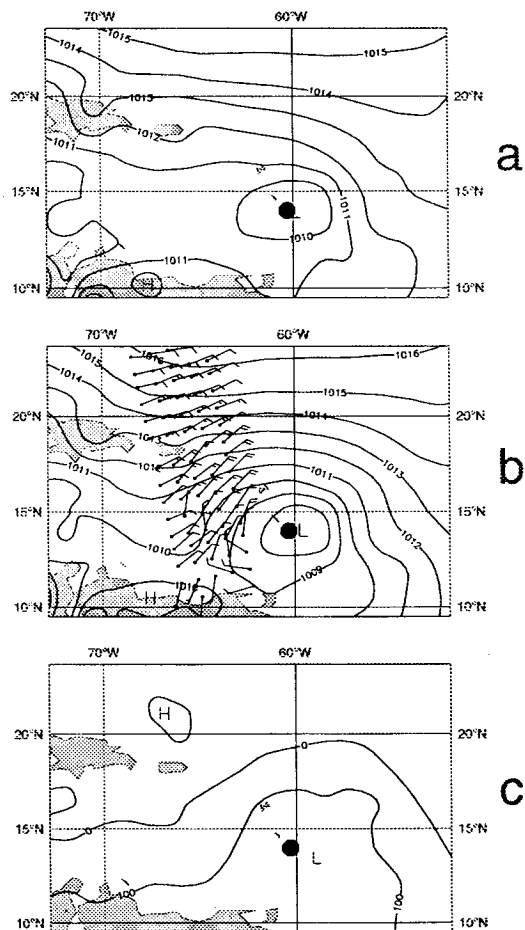


Figure 3. Analysis of hurricane Iris at 00 UTC on 26 August 1995. Layout similar to figure 2.

ilation cycle, it is usually more difficult to demonstrate medium-range forecast impact. Generally it has been seen that 4D-Var analysis increments from ERS survive and help to improve forecasts to a larger extent than OI and 3D-Var. Figure 4 shows in panel c) the 5-day SCAT forecast shortly after the analysis shown in figure 3. Hurricanes Iris and Luis are easy to identify close to their observed position (marked with a filled circle). Karen is also visible in the right position, correctly, much weaker than the other two TCs. From panel b), NoSCAT, it is evident that the intensity and smaller positional error of hurricane Iris in the forecast is triggered by the scatterometer winds. Panel a) shows the inability of the OI system to capture the TCs properly. The 5-day SCAT forecast and the verifying analysis of hurricane Iris are shown in figure 5. The predicted positions of both Luis and Iris are very good. The intensity of Iris is too weak, but it is clearly identifiable, whereas Luis is intensified correctly.

Improvements in the forecasts are generally found even in cases where ERS-scatterometer data only is available on the fringe of the hurricane, i.e., several hundred kilometers away from the center. It supports the general view that the development and track of a hurricane is to a large extent determined by a proper description of the convergent inflow from the surroundings.

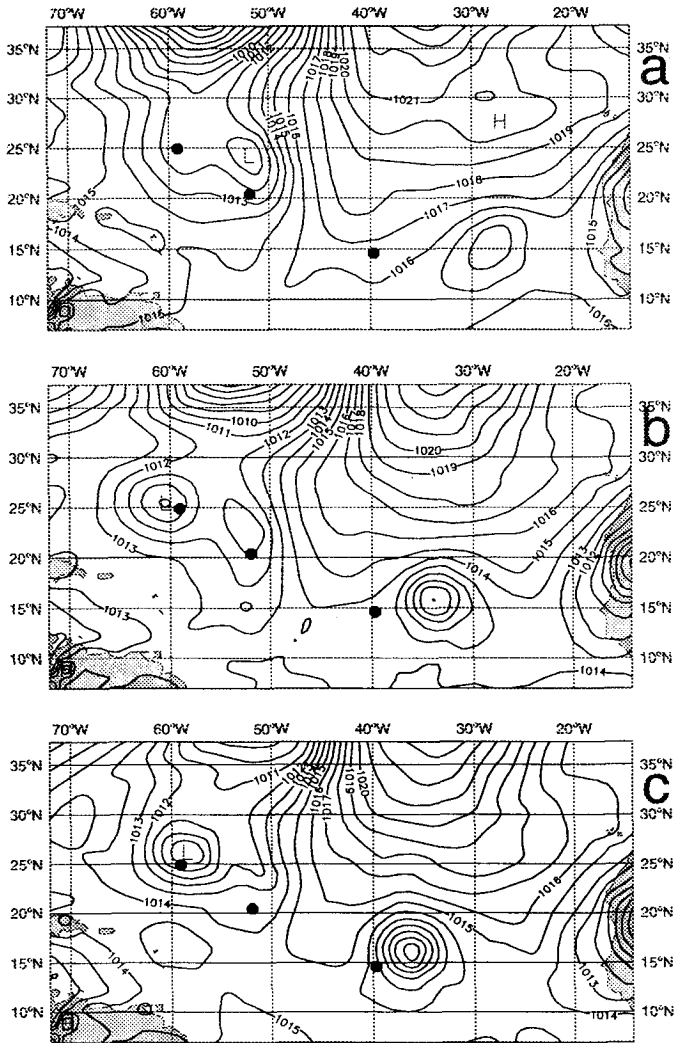


Figure 4. 5 day forecasts of hurricane Iris valid at 12 UTC 31 Aug 1995. Assimilation system used: panel a): OI, panel b): 4D-Var NoSCAT, and panel c): 4D-Var SCAT. The observed hurricane positions are marked with a circle.

To rigorously investigate the skill of OI NoSCAT versus 4D-Var noSCAT/SCAT we classified TC intensity and position forecast skill. For all 15 days the analysis and forecast positions for the TCs were found by calculating relative vorticity maxima (RVM) for 850 hPa fields. Only RVM values above $5 \times 10^{-5} s^{-1}$ were classified as TCs. The RVM disturbances were linked, if possible, to the four TCs in the Atlantic tropical region. Only RVM disturbances within 1200 km from the observed positions were taken into account. During the period of investigation 4D-Var only in very few cases developed spurious TCs. In some other cases the TCs dissolves in the 4-5 day forecasts, this happens most often in OI.

Each day at 12 UTC comparisons were made between OI, 4D-Var NoSCAT, and 4D-Var SCAT of the position and intensity. If the values were within 10 % accuracy the case was classified as neutral, otherwise it was classified as either positive or negative. If an acceptable TC could be found in one assimilation but not the other it was classified as a positive case for the

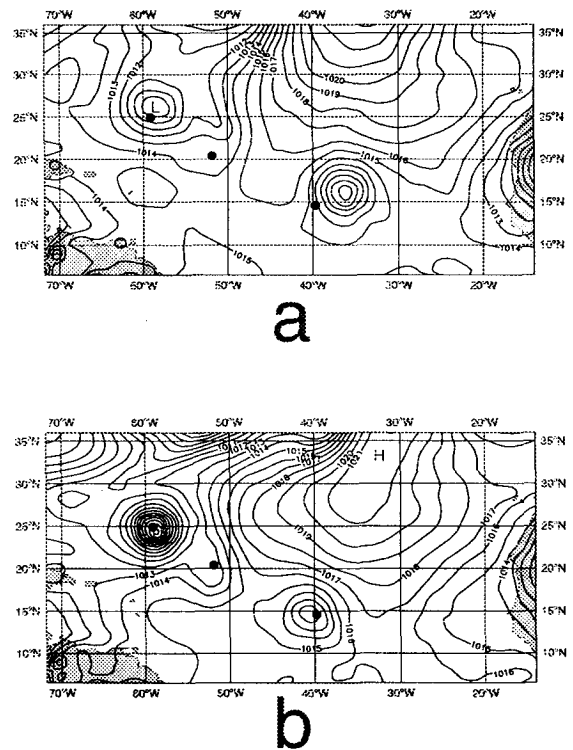


Figure 5. 5 day forecast (a) and verifying analysis (b) of hurricane Iris and Luis valid at 12 UTC 31 Aug 1995

first assimilation. If no acceptable TCs were found in either of the two assimilations compared, the day was not included in the statistics.

From figure 6 it is evident that 4D-Var NoSCAT performs much better than OI NoSCAT. Both intensity in panel a) and position in panel b) are better in more than 50% of cases for the analysis and the 1-, 2-, 3-, 4-, and 5-day forecast. So the analyses and forecasts of TCs are greatly improved when the more dynamical based 4D-Var system is used. It was then investigated if ERS scatterometer winds could improve TC forecasts even more by including the observations in the 4D-Var assimilation. The results are shown in figure 7 where we have plotted the difference in position and intensity forecast skill between the 4D-Var experiments SCAT and NoSCAT.

We can see that scatterometer data generally improve the position and intensity forecast skill of tropical cyclones. It is clear that the change from OI to 4D-Var has been beneficial as well due to 4D-Var's improved dynamical treatment of TCs. It is also clear that 4D-Var manages to assimilate and use ERS scatterometer winds well to the benefit of improved TC forecasts. Previous studies, Isaksen (1997), have shown that ERS-scatterometer data have a beneficial effect on extra-tropical forecasts in the 4D-Var system as well, especially in the more energetic and active winter hemisphere. The main improvements in the extra-tropics happens when cyclones are identified both in the early and in the mature stage. In a way this is very similar to how improvements are obtained in TC cases.

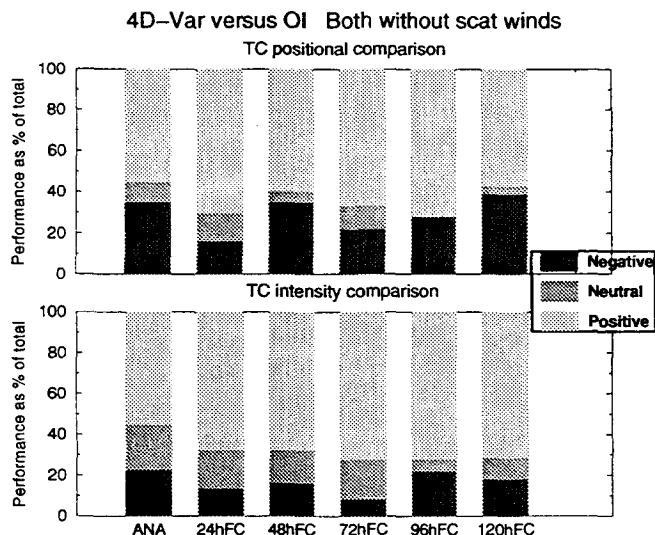


Figure 6. Comparison of 4D-Var NoSCAT and OI analyses and forecasts of intensities and positions of four Atlantic tropical cyclones

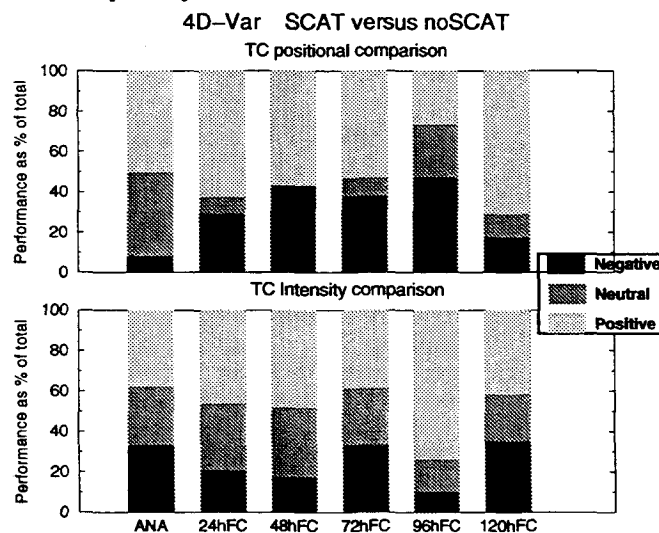


Figure 7. Comparison of 4D-Var SCAT and NoSCAT analyses and forecasts of intensities and positions of four Atlantic tropical cyclones

5. REMAINING ISSUES

Despite the overall beneficial impact of scatterometer winds in 4D-Var, we identified four remaining issues of concern. These are associated with the tropical structure functions, a probable wind speed bias in extreme wind conditions, the insufficient coverage of TCs due to the relatively narrow swaths of ERS scatterometer winds, and occasional errors in the ambiguity removal. Here we will exemplify the two last issues.

5.1. Problems related to narrow swaths

If the TC is only partially captured by scatterometer data, the structure functions are used for extrapolation outside the swath, which can result in a weak-

ening of the TC, because correct winds only 500 km from the TC can be fairly weak.

Figure 8 shows a case where the scatterometer swath partially samples TC Humberto on 26 August 1995 00 UTC. The background field TC position is approximately 200 km too easterly, but well identified and intense (as shown in panel a). An ERS scat track passes on the eastern side of both Humberto and the background field hurricane position. The ERS winds are correctly fairly weak due to the distance from Humberto. Some ERS winds are also affected by hurricane Luis (visible in the south-east corner of figure 8). The assimilation system has clearly got a very difficult task in this situation. The correct wind information from the ERS measurements are propagated by the structure function to surrounding areas, and Humberto background model winds are dampened substantially by the analysis. In reality the analysis should have shifted the system 200 km westerly, but has no observations west of Humberto to justify this. If no ERS observations had been available the background estimate would have been left virtually unmodified, i.e., keeping a stronger TC but in a less correct position.

In other cases (not shown) when say 50% of an intense TC is captured the combined effect of the structure function impact and probable too low ERS wind speeds in extreme conditions can cause the TC to be weakened only on one side. This can cause asymmetries in the analyzed TC geometry, which can result in a poor TC forecast.

A more dense data coverage (like expected from QuikSCAT) would mean that TC's might be captured once or twice every day, with a greater chance to analyse the TC in the correct position. This again will improve the background field forecast which will reduce the amount of difficult cases (like the one shown in figure 8) for the assimilation system to handle.

5.2. Ambiguity removal problems

Figure 9 shows the analysis of TC Humberto at 12 UTC on 29 August 1995. The background field shows a TC approximately 200 km too far south-west of the observed position (marked with a filled circle). The analysis correctly deepens the TC, but not nearly enough considering the high wind speeds measured by ERS. The winds shown are processed at ECMWF and have wind speeds scaled to fit the ECMWF model (see Le Meur et al. (1997)). For this case the maximum speed provided by ESA amounts to 40 knots (CMOD4, see Stoffelen & Anderson (1997b)), whereas the ECMWF-processed winds provide 50 knots (before QC). These winds are representative of the scatterometer footprint with a diameter of 50 km. In this case the assimilation system uses the wrong ambiguous winds on the western side the observed hurricane eye position. The wrong wind directions agree with the background field winds because the background hurricane position is too far westerly. Based on this wrong directional assumption the wind gradients (and implied pressure gradients) are very much reduced compared to the true observed gradients, this partly explains why the hurricane is only intensified slightly.

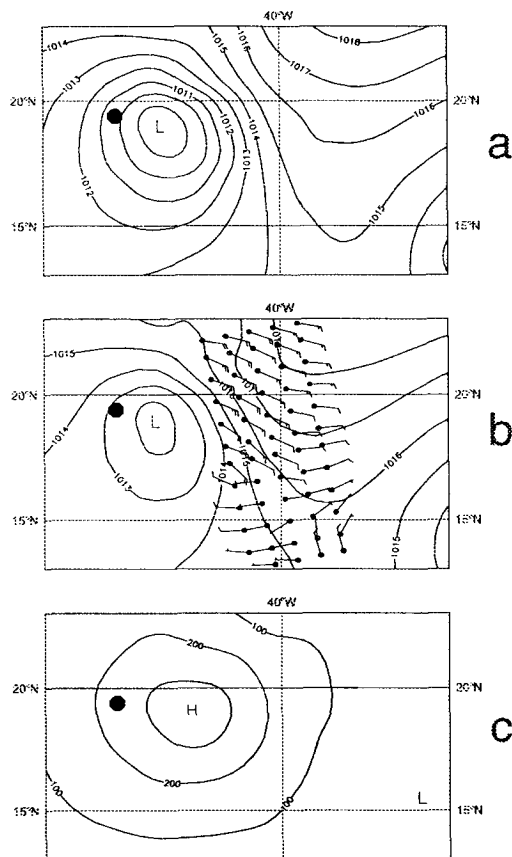


Figure 8. Analysis of hurricane Humberto at 00 UTC on 26 August 1995. Luis is just visible in the south-eastern corner of a) and b). Layout like in figure 2.

Because of the spatial consistency of the scatterometer winds, the spatial extend of a TC can be visually well estimated, even when it is only partially captured. As such, during the assimilation process towards the end of the fitting process, one could apply a scheme where the spatial extend of the structure functions is reduced, in order to achieve a more optimal fit in those locations where the nominal structure function does not provide a close fit of the analysis to the scatterometer observations. This could, potentially, also improve the analysis of fully captured tropical cyclones. On the other hand, there may be a risk of reducing the ambiguity removal skill somewhat, but this should be further investigated. Another issue for further study is the analysis of the vertical structure of a tropical cyclone in 4D-Var.

In this Humberto case the scatterometer winds fully captured the hurricane as can be seen in figure 10. In this case it would have been possible to perform a correct ambiguity removal selection based solely on a maximum vorticity (or minimum divergence) constraint on the observed data. The background field information does in this case more harm to the ambiguity selection. This is not the case in general, it happens occasionally when tropical cyclones, intense extra-tropical cyclones and frontal zones are misplaced in the background field.

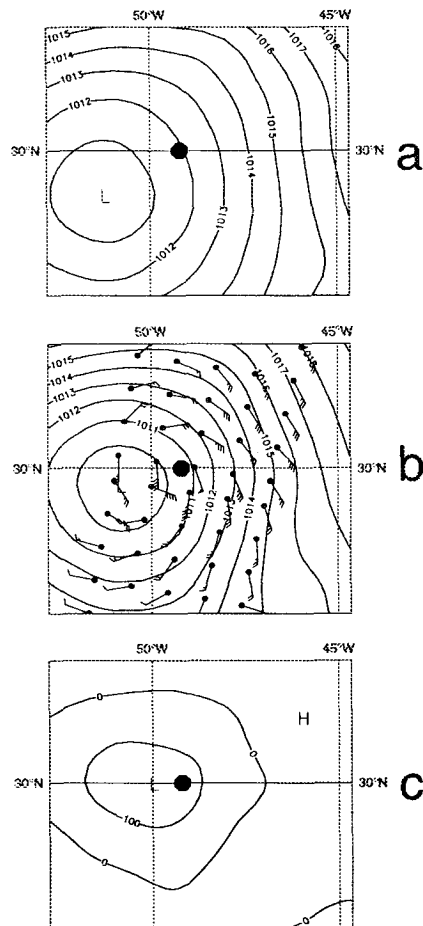


Figure 9. Analysis of hurricane Humberto at 12 UTC on 29 August 1995. Layout like in figure 2.

6. CONCLUSIONS

We have shown that the ECMWF 4D-Var data assimilation system performs better analyses of TCs compared to previous assimilation systems. The use of ERS scatterometer winds further enhances the impact. Unprecedented forecasts of TCs, up to day five, are shown in this paper. More recent experiments with 4D-Var confirm the beneficial effect of ERS scatterometer winds in 4D-Var. The spatial consistency of scatterometer winds may be used to further optimize the analyses and forecasts. In this respect, a larger coverage of winds, such as that from SeaWinds on QuikSCAT, to be launched in November 1998, is expected to be very useful for the further improvement of cyclone analyses and forecasts. This is confirmed by tandem ERS-1 and ERS-2 scatterometer experiments carried out at ECMWF by Le Meur et al. (1997) and at KNMI by Stoffelen & van Beukering (1997).

7. ACKNOWLEDGEMENTS

Lars Isaksen and Didier le Meur acknowledge support from ESA/ESTEC project ref. 111699/95/NL/CN

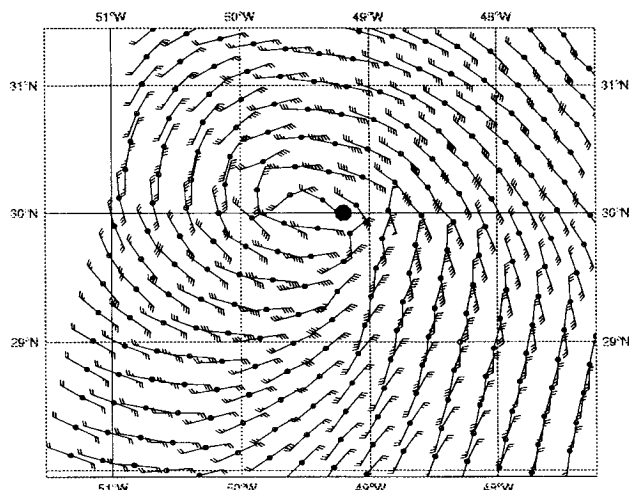
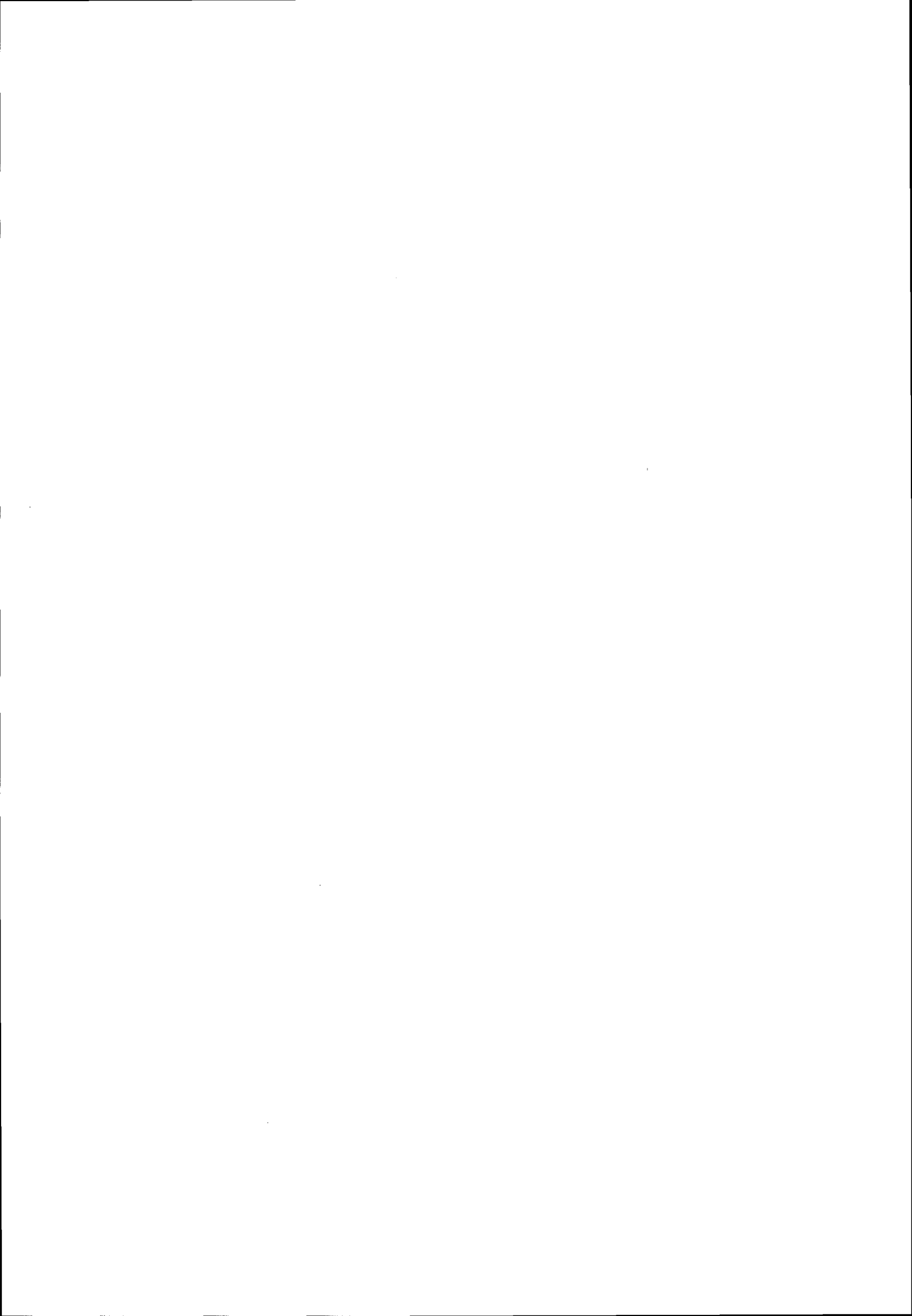


Figure 10. All available ERS winds close to hurricane Humberto at 12 UTC on 29 August 1995. The observed hurricane position is marked with a filled circle

REFERENCES

- Hoffman, R. 1993, A preliminary study of the impact of the ERS-1 C-band scatterometer wind data on the ECMWF global data assimilation system, *J. Geophys. Res.* **98** (C), 10233-10244.
- Isaksen, L. 1997, Impact of ERS scatterometer data in the ECMWF 4D-Var assimilation system. Preliminary studies., in proceedings from Third ERS Symposium on Space at the service of our Environment. ESA publ. SP-414.
- Le Meur, D., Isaksen, L., Hansen, B., Saunders, R. and P. Janssen 1997, Global validation of ERS Wind and Wave Products, Final report to ESA contract no. 8488/95/NL/CN.
- Rabier, F., Järvinen, H., Klinker, E., Mahfouf, J-F. and A. Simmons 1998, The ECMWF operational implementation of four dimensional variational assimilation. Part 1: Experimental results with simplified physics., Submitted to *Q. J. Roy. Meteorol. Soc.*
- Stoffelen, A., and P. van Beukering 1997, Implementation of improved ERS scatterometer data processing and its impact on HIRLAM short range weather forecasts, *HIRLAM TR-31* (Available from the Authors)
- Stoffelen, A., and D. Anderson 1997a, Ambiguity removal and assimilation of scatterometer data, *Q. J. Roy. Meteorol. Soc.* **123**, 491-518.
- Stoffelen, A., and D. Anderson 1997b, Scatterometer data interpretation: Estimation and validation of the transfer function CMOD4, *J. Geophys. Res.* **102** (C3), 5767-5780.
- Stoffelen, A., and D. Anderson 1997c, Scatterometer data interpretation: Measurement space and inversion, *J. Atmosph. Oceanic Technol.* **14** (6), 1298-1313.
- Tomassini, M., D. le Meur and R. Saunders 1998, Near-surface wind observations of hurricanes and their impact on ECMWF model analyses and forecasts, *Mon. Wea. Rev.* Vol. **126**, No. 5, 1274-1286



AMBIGUITY REMOVAL BY VARIATIONAL ANALYSIS OF SURFACE WIND FIELDS

S. Mark Leidner and Ross N. Hoffman

Atmospheric and Environmental Research, Inc.
840 Memorial Drive
Cambridge, Massachusetts 02139 USA
Tel. +1.617.547.6207 • leidner@aer.com

ABSTRACT

In this study, we use a variational analysis method (VAM) to select a wind solution from NASA Scatterometer (NSCAT) ambiguous winds. The main function of the VAM is to determine a "best" gridded surface wind analysis. The analysis is "best" in terms of minimizing a cost function. The ambiguity closest in direction to the minimizing analysis is selected. We processed 3 weeks of NSCAT-1 25 km ambiguous winds, one orbit at a time, on a $1^\circ \times 1^\circ$ global analysis grid. We find that the VAM-selected ambiguities are different from the JPL selection for $\sim 5\%$ of wind vector cells. The differences usually occur in patches in regions of highly curved flow (near the center of cyclones or anticyclones) where wind direction changes over small spatial scales. Differences in ambiguity selection were characterized by comparing the scatterometer winds to GOES-8 imagery over the North Atlantic. In $\sim 30\%$ of the cases examined, the VAM selection corrects evident errors in the JPL winds. In $\sim 10\%$ of the cases, the JPL winds agree with available data better than the VAM selection. For the remaining cases, the selections were equally plausible given the available information.

1. INTRODUCTION

Over the last seven years, satellite-borne radars designed to measure surface wind speed and direction have provided a wealth of wind data over the world ocean. While these instruments measure wind speed accurately (e.g., Freilich and Dunbar [1] report that the NASA scatterometer, NSCAT, measured wind speed to within 1.7 m/s), the wind direction is not uniquely determined.

Wind speed and direction are computed from a number of closely collocated (temporally and spatially) radar measurements from a number of different azimuth angles. The normalized radar cross section (NRCS) of the ocean surface measured by scatterometers, σ^0 , varies with azimuth angle according to the relative directions of antenna and wind speed. An "upwind-crosswind" variation exists because small, wind-generated gravity waves on the ocean surface reflect more of the radar signal when wave crests are perpendicular (i.e., "upwind") to

the radar antenna than when wave crests are parallel (i.e., "crosswind"). To a lesser degree, an "upwind-downwind" variation effects the σ^0 measurement.

The σ^0 measurements are grouped into 50 or 25 km wind vector cells (WVC) for wind retrieval. Modeled σ^0 values are computed from a geophysical model function which requires spacecraft ephemeris (known) and wind speed and direction (unknowns) as inputs. The squared differences between measured and modeled σ^0 values are summed as part of a maximum likelihood estimator (MLE), which estimates how closely the input wind speed and direction explain the observed σ^0 values. Then, wind speed and direction are varied to minimize the difference between measured and modeled σ^0 values. However, over a range of possible wind speeds and directions (i.e., $0 - 30 \text{ m/s}$ and $0 - 360^\circ$), the MLE produces from two to six local maxima, and it is not possible to determine which is closest to the observed wind from MLE values alone. The wind speeds and directions of each of these maxima are called "ambiguities". Choosing a meteorologically consistent set of ambiguities is required to use scatterometer data in operational numerical weather prediction (NWP) models.

Median filter techniques have been used for ambiguity removal, but may fail at swath edges and in regions of strongly curved flow. For NSCAT, the Jet Propulsion Laboratory (JPL) used a median filter initialized by the ambiguity with the highest MLE. This method was completely objective and autonomous. Later, better performance was obtained by initializing the scatterometer wind field with the ambiguity closest to the NCEP gridded surface wind field analysis. This product is referred to as the "nudged" wind product since the median filter is initialized from an outside source. This method is also completely objective but depends on information outside of the scatterometer measurements. The performance of the median filter method has been quite successful (just under 92% agreement between NSCAT-1 data and interpolated ECMWF analyses for speeds from $3 - 30 \text{ m/s}$, Graf [2]) but is not based on any physical model of wind flow. Consequently, the median filter may be satisfied but select physically unrealistic winds, particularly in regions where the flow is strongly curved, sheared or data coverage is incomplete. Patches of unrealistic winds in

the scatterometer data might have a disastrous impact on the quality of analyses and NWP forecasts. Careful quality control (QC) is required, of course, but is made difficult if the model winds were used in the ambiguity removal.

This paper reports on the use of the VAM for ambiguity removal. The VAM relies on *a priori* information (similar to the "nudged" median filter), but makes use of meteorological constraints as part of ambiguity removal. Best results are obtained using "dual ambiguities" in a preliminary analysis.

2. VARIATIONAL ANALYSIS METHOD

We use a variational analysis method (VAM) which produces a gridded surface wind analysis that simultaneously satisfies a number of constraints (Hoffman 1984 [3]). Constraints are defined by a set of functionals, J_i . Each functional is a scalar which measures the departure of the analysis from a given constraint, i . We constrain the analysis to fit the ambiguous wind observations, J_o , the background analysis, J_b , and a number of smoothness criteria which are in the form of penalty functions, J_p . J_b and J_p ensure that the analysis increments are not very different from the background analysis and ensure smoothness in the increments of the velocity components (u, v), divergence, vorticity and vorticity tendency. J_o is a special "obs" functional for measuring the misfit between the analyzed wind field and observed scatterometer wind ambiguities. This function was first developed by Hoffman [3] for SEASAT SASS wind ambiguities, and roughly approximates the surface generated by the MLE to determine ambiguous winds from σ^0 measurements. The weighted sum of all J_i is the total function, J , which is minimized to find a new surface wind analysis. Once the convergence criteria for the minimizer is satisfied, the analysis can be used select an ambiguity. For each WVC, the ambiguous wind closest to the analyzed wind field is designated the "VAM-selected" ambiguity.

3. USE OF DUAL AMBIGUITIES

While more than two winds are often retrieved from a group of collocated σ^0 measurements, one of the two ambiguities with the highest MLE values is very likely (>90%) to be closest to the true wind [4]. This implies that <10% of the third and fourth ranked ambiguities are closest to the true wind. This information can be used to QC the data given to the VAM, and improve ambiguity removal.

We observed that using all available ambiguities in the VAM leads to patches of poor ambiguity selection. This is especially true where there are four ambiguities and the direction of the the third or fourth ambiguity is close to the direction of the background wind field. (Ambi-

guity selection in such cases is often poor because of errors in the background wind field.) Using "dual ambiguities" (i.e., two highest MLE values), however, narrows the choices to one of two possibilities - the two most likely possibilities. This allows for larger wind direction corrections to the background field (> 45°), instead of settling for a third or fourth ranked ambiguity just a few tens of degrees away. Using dual ambiguities, however, limits ambiguity selection to the first or second ranked ambiguity since the analysis will generally be drawn toward one or the other.

To allow for selection from all ambiguities, we have developed a two stage analysis procedure which blends the use of dual and all ambiguities. In the first stage, we use dual ambiguities for 50 iterations of the minimizer to draw the analysis toward the most likely observed winds. In the second stage, we include all ambiguities and continue to minimize until the convergence criteria is met. The second stage allows for readjustment of the analysis in the few cases where the third or fourth ranked ambiguity is closest to the true wind.

During the first stage, we only use dual ambiguities which pass dual ambiguity quality control or "dual QC". Dual QC is based on a conceptual model of dual ambiguities. Nominally, we expect the wind directions of dual ambiguities to be opposed by ~180°. If not, the WVC is suspect and is not included in first stage. Specifically, a WVC fails dual QC and is not used in the first minimization if the directions of the first two ambiguities are within $3\pi/4$ of each other. Dual QC typically eliminates ~20% of WVC's from the first minimization.

4. DATA

Three weeks of 25 km NSCAT-1 data were processed, orbit by orbit, for the period October 15 - November 5, 1996 (234 orbits). The background field is time-interpolated from 12-hourly global ECMWF 10-m wind analyses. The ECMWF analyses are interpolated to the average time of the orbit (defined as the midpoint between orbit begin and end times). To assess the performance of the VAM, we use GOES-8 imagery to locate meteorological features in the North Atlantic. We have previously collocated GOES-8 imagery for orbits which pass over the North Atlantic when the sun elevation angle is sufficient to make use of the visible channel (29 orbits) (Grassotti *et al.*[5]).

5. RESULTS

One measure of the performance of ambiguity removal with the VAM is a direct comparison with another successful ambiguity removal scheme. Here we compare our results with the NWP-initialized median filter used

by JPL for ambiguity removal. The next two sections present statistical and qualitative results, respectively.

5.1 Summary Statistics

Over the three-week period, JPL- and VAM-selected ambiguities differ in a small fraction of all WVC's. Table 1 shows the differences between JPL and VAM ambiguity selection by wind speed. The wind speed of the most likely ambiguity (highest MLE) is used to bin the WVC's.

Table 1: Differences between JPL and VAM ambiguity selection.

Wind Speed (m/s)	# WVC	% Different
0-2	260521	18.379
2-4	836017	11.169
4-16	5867770	3.807
>16	142815	1.438
All	7107123	5.141

JPL and VAM-selected ambiguities disagree most often for low wind speeds. At higher wind speeds, the two methods differ by <4%. Though the percentage difference between the two techniques is small, it is important to examine the selected scatterometer winds to see if there is a difference in the quality of the wind product.

5.2 Case Studies

This section shows an examples of the surface wind field in an areas where the two techniques have chosen different ambiguities. Where possible, we use GOES-8 imagery to independently confirm ambiguity selection from features in the cloud field. We examined 11 North Atlantic scenes where JPL and VAM ambiguity selection differed. From the 11 scenes, 29 subregions were examined in detail. For brevity, we present one of the subregions below and then summarize the results of all 29.

5.2.1 Case of 26 October 1996

Figure 1 shows GOES-8 IR brightness temperature over the North Atlantic, 1315 UTC 26 October 1996. NSCAT data locations are marked by the fine black dots, and WVC's where JPL and VAM-selected ambiguities differ are marked by heavy black dots. The scatterometer crossed 30N on this descending pass at 1314 UTC.

Differences between JPL and VAM-selected ambiguities often occur in small patches. Figure 1 contains four such patches: 1) (35W, 29N), 2) (37W, 41N), 3) (30W, 45N) and 4) (32W, 57N). In region A, satellite imagery shows

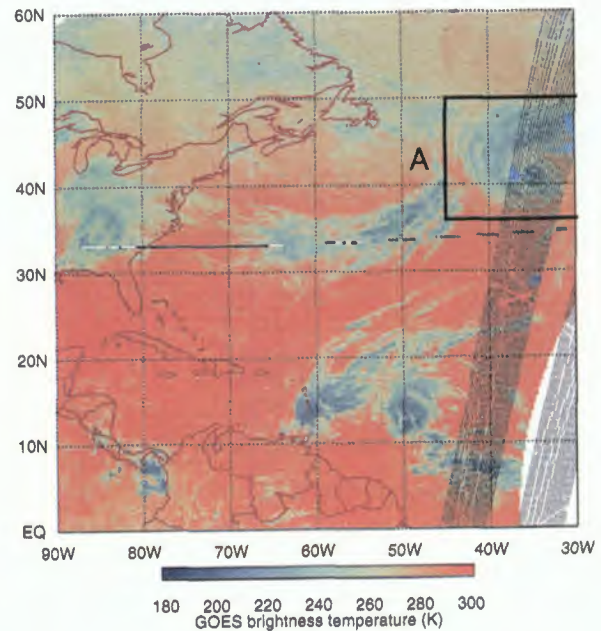


Figure 1: North Atlantic overview 1315 UTC 26 Oct 1996 including GOES-8 IR brightness temperature (K). NSCAT WVC locations are marked by fine black dots. Heavy black dots mark WVC's where JPL and VAM ambiguity selection differ.

that the scatterometer passed over a mature cyclone at (35W, 41N).

Figure 2 shows ECMWF (thin barbs) and VAM (thick barbs) analyses in region A over an image of GOES-8 IR brightness temperature. NSCAT WVC locations are marked by black dots, and points where JPL and VAM ambiguity selection differ are marked by white circles. Since the results presented here are focused on ambiguity removal, it is important to report the background wind field used as a starting point in the variational model (thin barbs). It is also interesting to note several effects of the NSCAT data on the VAM surface wind analysis (thick barbs). The circulation center in the VAM analysis is moved north and east of the center in the ECMWF analysis. The placement in the VAM analysis is in better agreement with the satellite image. Also, the wind speeds around the cyclone are higher (roughly doubled) in the VAM analysis than in the ECMWF analysis.

All JPL ambiguities in subregion A1 of Figure 2 are plotted in Figure 3. The structure of the cyclone can be easily seen in the ambiguous winds. Figure 4 shows JPL and VAM selected ambiguities for subregion A1. An unlikely east-west wind shift exists in the JPL ambiguities in the north west quadrant of the storm (37W, 41.5N). Given the wind field suggested by satellite imagery and the ECMWF analysis, circular wind flow around the cy-

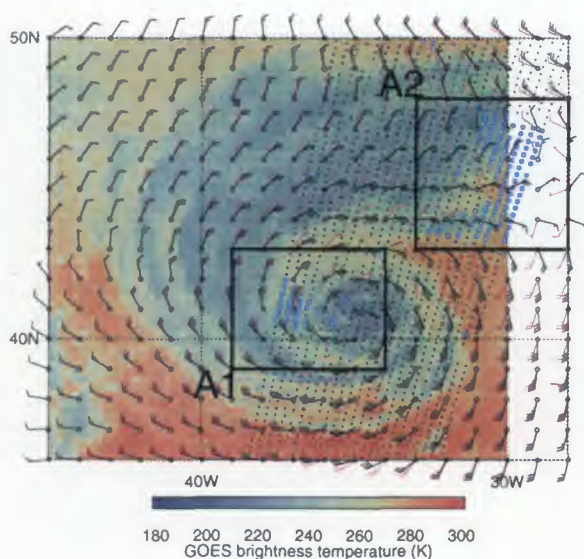


Figure 2: ECMWF (thin barbs) and VAM (thick barbs) analyses in region A with GOES-8 IR brightness temperature. See Figure 1 for the location of region A. NSCAT WVC locations are marked by black dots. White dots mark WVC's where JPL and VAM ambiguity selection differ.

clone center seems more reasonable. Figure 4b shows that the VAM selected ambiguities result in more circular wind flow and move the center of circulation south compared to the JPL selected ambiguities.

5.2.2 Summary of All Cases with Collocated GOES Imagery

The subregion presented in section 5.2.1 is one of 29 that were examined for the three week period. These subregions are a cross-section of regions where VAM and JPL ambiguity selection differ, including cloudy and clear scenes, tropics and mid-latitudes, and coastal and open water regions. The results from each subregion are categorized by the differences between the JPL and VAM selected ambiguities. Using GOES-8 imagery and general knowledge of the local wind field from ECMWF analyses, VAM selected ambiguities are determined to be either 1) clearly improved over JPL selected ambiguities, 2) different from JPL but equally plausible, or 3) clearly worse than JPL selected ambiguities. For reference, VAM selected ambiguities were determined to be a clear improvement over JPL selected ambiguities for the subregion presented in section 5.2.1. For the 29 subregions we examined,

- 10 subregions are clearly improved over JPL selected ambiguities

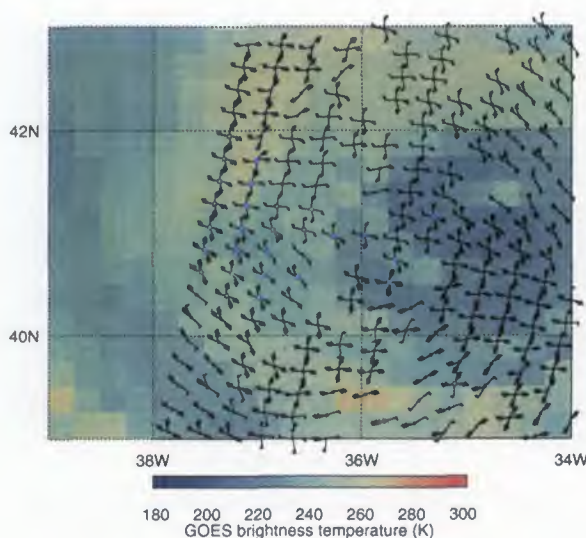


Figure 3: All JPL ambiguities and GOES-8 IR brightness temperature in subregion A1. See Figure 2 for location of subregion A1. White dots mark WVC's where JPL and VAM ambiguity selection differ.

- 16 subregions are different from JPL but equally plausible
- 3 subregions are clearly worse than JPL selected ambiguities

Where the VAM does not clearly improve on JPL selection, it is often not clear if a suitable solution exists in the ambiguous winds. For example, sometimes a front is aligned with a cloud feature in both VAM and JPL selections but displaced one or two WVC's in the perpendicular direction. Analyses from the improved NSCAT-2 model function and JPL processing system may help in some of these cases since four ambiguities are retrieved at more WVC's.

6. CONCLUSIONS/FUTURE WORK

Ambiguity removal using the VAM shows promise and may have advantages over median filter techniques. While JPL and VAM ambiguity selection differ for only ~5% of WVC's, the differences tend to occur in patches. Patches of poorly selected winds can be more harmful to analysis and forecasting systems than scattered errors if not properly QC'd. For ~30% of the subregions examined, VAM selected ambiguities are a clear improvement over JPL selected ambiguities. In more than half of the subregions, the VAM selected ambiguities are not a clear improvement on the JPL choice. In these cases, there was either insufficient information to determine which choice was more likely or a reasonable solution was not present

in the ambiguities. In the remaining cases ($\sim 10\%$), the JPL selected ambiguities are more reasonable than the VAM ambiguities, based on available GOES-8 images and the background wind field.

Further work could be done to investigate the use of the scatterometer backscatter measurements (σ^0) directly for ambiguity removal. This may prove most useful in cases when a suitable solution does not seem to exist in the retrieved winds. Also, we will process the entire 9-month mission using the latest version of the data from JPL (NSCAT-2). Many of the principles learned here will be applicable to NASA's next scatterometer, Seawinds on QuikSCAT.

7. ACKNOWLEDGMENTS

This work was supported under NASA contract 957644. The NSCAT data were obtained from the NASA Physical Oceanography Distributed Active Archive Center at the Jet Propulsion Laboratory/California Institute of Technology. We also thank Joe Ardizzone at NASA Goddard Space Flight Center Data Assimilation Office for providing the ECMWF analyses.

References

- [1] Michael H. Freilich and R. Scott Dunbar. The accuracy of the NSCAT-1 vector winds: Comparisons with NDBC buoys. downloaded from <ftp://nancy.oce.orst.edu:/pub/mhf/validation>, March 1998.
- [2] James E. Graf. Jpl technical notes about nscat-2 data. accompanied NSCAT-2 data release, August 1998.
- [3] Ross N. Hoffman. SASS wind ambiguity removal by direct minimization. Part II: Use of smoothness and dynamical constraints. *Mon. Weather Rev.*, 112(9):1829–1852, September 1984.
- [4] Jet Propulsion Laboratory, Pasadena, CA. *NASA Scatterometer Science Data Product User's Manual*, 1.1 edition, April 1997. JPL doc. D-12985.
- [5] Christopher Grassotti, S. Mark Leidner, Jean-François Louis, and Ross N. Hoffman. Development and application of a visible-infrared rain flag for scatterometer data. *J. Applied Meteorol.*, in press, 1999.

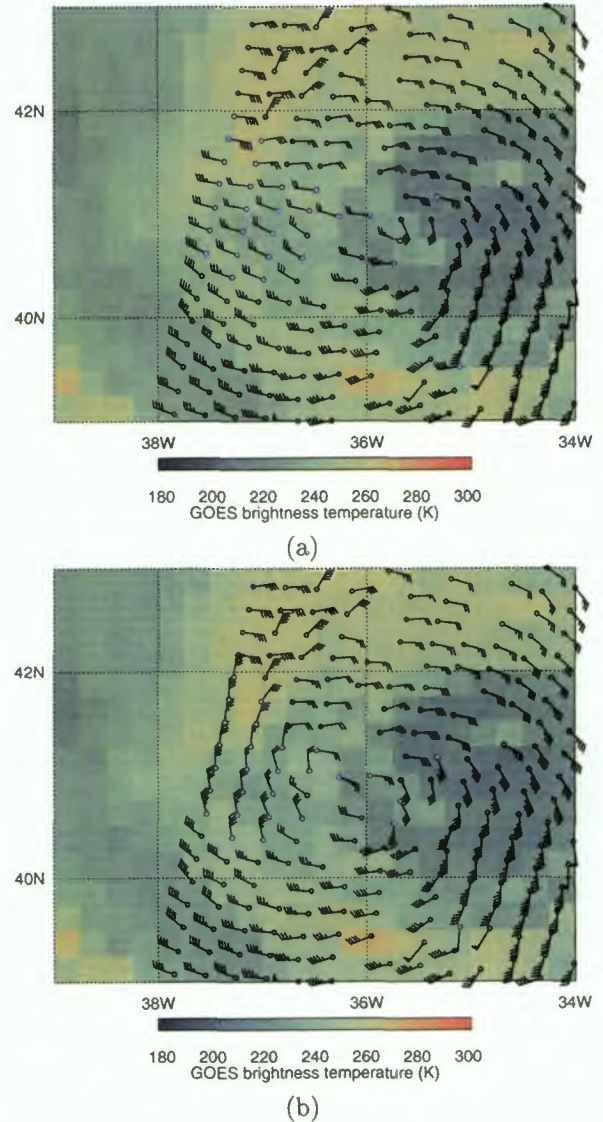
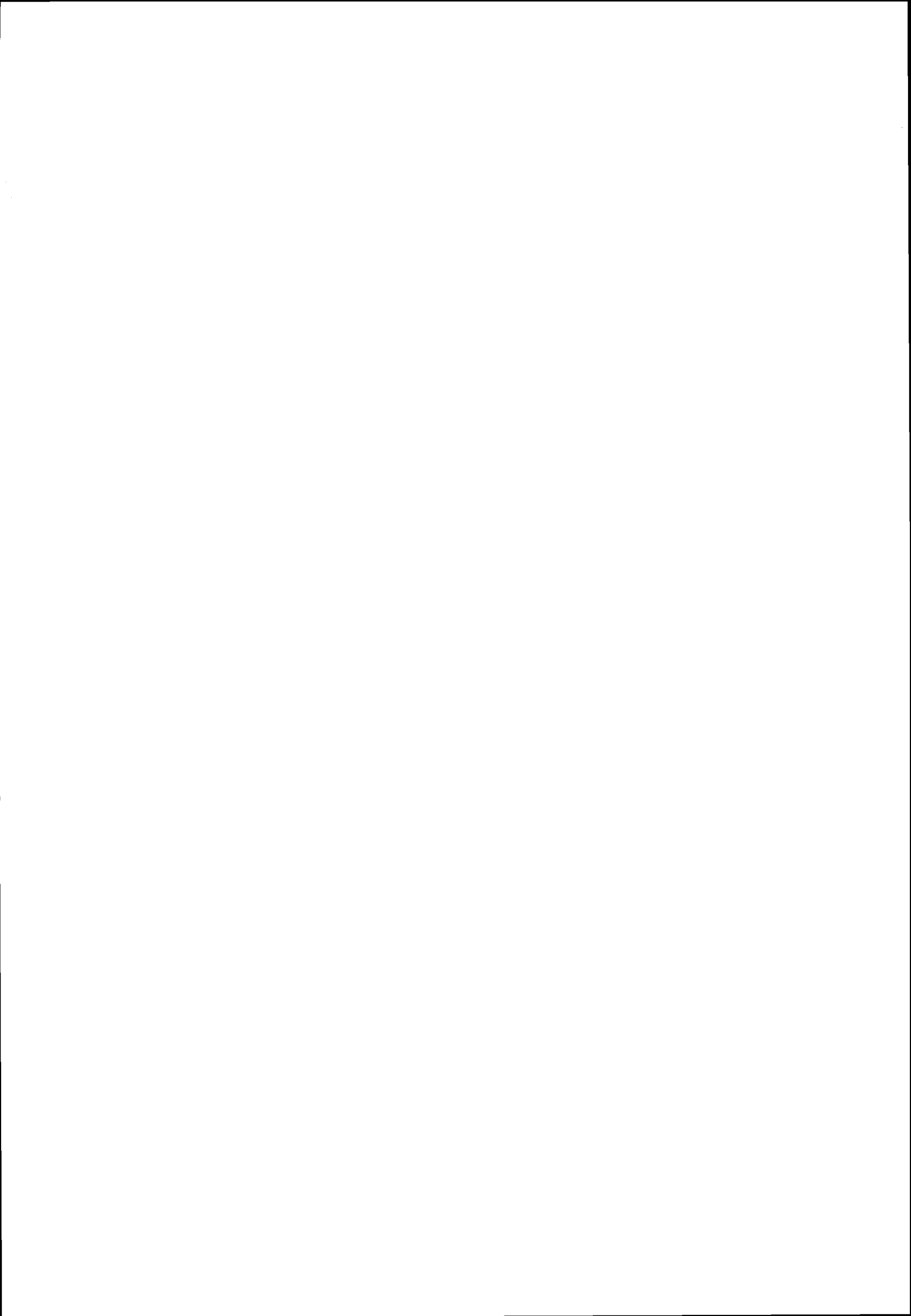


Figure 4: Selected ambiguities from (a) JPL and (b) VAM, and GOES-8 IR brightness temperature in sub-region A1. See Figure 2 for location of subregion A1. White dots mark WVC's where JPL and VAM ambiguity selection differ.



OPTIMAL AMBIGUITY REMOVAL FOR SCATTEROMETER WINDS

Harald Schyberg and Lars-Anders Breivik

Norwegian Meteorological Institute, Oslo
 P.O.Box 43 Blindern
 N-0313 Oslo, Norway
 h.schyberg@dnmi.no

ABSTRACT

For many users of wind scatterometer data it is of interest to have an ambiguity removal system, or dealiasing, resolving the directional ambiguity in the observations. As a part of the ground segment, ESA performs such an ambiguity removal for the UWI wind product.

The ambiguity removal method at meteorological centres such as DNMI, UKMO and KNMI is tuned and evaluated relying on a high quality first guess windfield (6 hrs forecast). The ESA operational scatterometer processing is however constrained to use a lower quality first guess wind field, that is an ECMWF 18 to 36 hrs forecast.

Two algorithms for possible use in the ESA operational environment are evaluated against the currently operational ESA algorithm (CREO)

- "PRESCAT", which is the scheme in operation at several meteorological centers
- A new variational approach based on a Modified Successive Corrections (MSC) numerical method

The operational experience with the PRESCAT scheme is that it generally works well, and only in a few cases it obviously picks the wrong solution. The more recent variational scheme is derived from Bayesian probability theory as finding the one of the wind possibilities giving rise to the windfield with highest probability. This enables us to set up a cost function to be minimized which takes into account the same features as in the PRESCAT scheme. In addition the new scheme is able to take advantage of the fact that the rotational part of the wind dominates over the divergent.

It is concluded that a significant improvement in the operational ESA ambiguity removal can be obtained both by implementing the MSC or the PRESCAT processing, and the MSC scheme performs slightly better.

1. INTRODUCTION

The ESA ground processing of ERS scatterometer winds performs an ambiguity removal with the CREO algorithm described below. The operational constraints for the current ESA processing is such that a +18 to +36 hrs ECMWF forecast is used as a background wind field. This is a background field of lower quality than the background which is used in the ambiguity removal procedure at several meteorological centres. The objective of this study is to investigate whether the ESA

operational ambiguity removal could be improved by implementing a new and upgraded ambiguity removal scheme, still using the same background windfield. A more complete description of the study is given in Schyberg and Breivik, 1998. In section 2 we describe briefly the CREO algorithm run by ESA as well as the PRESCAT scheme and give a detailed account of the variationally based method of successive corrections (MSC). In section 3 we evaluate the performance of the various schemes, before concluding in section 4.

2. METHODS

2.1 The CREO algorithm

The ambiguity removal presently in operation at the ERS ground segment is referred to as the CREO algorithm. The algorithm takes its name from a company called CREO, where Cavanié and Lecomte developed the algorithm under an ESA contract in 1987 (Cavanié and Lecomte, 1987). Possible wind solutions are accumulated over an up to 3000 km part of the swath, and two alternative fields for which the sense of flow is approximately opposite are constructed. The field with the highest number of Rank 1 solutions is chosen as the correct. If the difference of the two alternatives is small, a comparison is made with the meteorological background wind field, and the alternative showing best correlation with the background is chosen. The CREO algorithm was selected after an evaluation together with two other alternatives using simulated data in a study performed by ECMWF in 1989 (Graham et al. 1989). The other two were the SLICE algorithm developed UK Met Office and an algorithm, SUMB, developed by Schwenzfeger, Munich University.

2.2 The PRESCAT scheme

The PRESCAT scheme is a pragmatic iterative scheme based on (1) background information in the form of a windfield from a numerical prognosis which may be of variable quality, (2) spatial coherence of observations and (3) consistency of the backscatter values with the scatterometer model function.

The history of PRESCAT as it is today starts with the CREO algorithm developed by Cavanié and Lecomte as described above. It has further adapted an improved method, SLICE, for imposing the spatial coherence and use of background information as developed by David Offiler at UK Met Office (Offiler, 1987). Ad Stoffelen at ECMWF (see Stoffelen and Anderson, 1995 and 1997) combined and improved the ideas and modified the use of background information resulting in the PRESCAT scheme today run operationally at several centres.

The Norwegian Meteorological Institute (DNMI) is running

operationally a version of this system, which was implemented by Breivik and Haugse (Breivik and Haugse, 1994).

The operational experience with PRESCAT is until now restricted to the use of short range forecast backgrounds, which is of higher quality than what is available in the ESA processing. For such backgrounds PRESCAT generally works well. However, for a small fraction of the observations the scheme seems to pick the wrong wind alternative. In some cases this is evident because the real wind is usually close to be non-divergent, while the scatterometer observations seem to contain an unrealistic divergence.

2.3 The variational method

The non-divergent nature of the wind is not taken explicitly into account by PRESCAT. We therefore found it tempting to use a new ambiguity removal system which takes into account the same three conditions as PRESCAT, but in addition includes the constraint that the scatterometer swath winds should represent a field which is close to non-divergent.

A derivation of the scheme can be done on the basis of variational data assimilation (see Lorenc, 1986). As opposed to PRESCAT, the new scheme, using a variational approach, is optimal in a statistical sense.

Using Bayes' theorem and assumptions on the error statistics, a corresponding cost function J to be minimized with respect to the field x can be found. In our case x is the field of wind vectors at the scatterometer observation points. The cost function consists of a term minimizing the distance to a first guess field, J_b , and a term minimizing the distance to the observations, J_o ,

$$J(x) = J_b(x) + J_o(x). \quad (1)$$

In our application the observations are the ambiguous wind pairs at the scatterometer observation points, which have gone through a processing from a backscatter σ_0 triplet. This pair of wind vectors is what is presented to the scheme, and it is assumed that one of them corresponds to the true wind. The scheme could easily also take into account other surface wind observations within the area, if available, which could give valuable information in the dealiasing.

The background cost term. The scheme is based on having a background or first guess x_b , which is found by interpolating a numerical model wind forecast (in the case of the ESA processing, the ECMWF 10 m wind forecast) to the observation points. The background cost term is given by

$$J_b = \frac{1}{2}(x - x_b)^T B^{-1}(x - x_b) \quad (2)$$

The background covariance matrix B is derived by assuming that all the errors in the background field are in the non-divergent part of the windfield (see Daley, 1991). In this way a constraint of minimizing the divergence over the scatterometer observation points is built in. Here we give a brief description of how the background covariance matrix is found. For more details, see Schyberg and Breivik, 1996.

Observations and theory show that the errors of the wind components u and v are strongly correlated. However, any two-dimensional velocity field, and in particular the deviation of the wind from the first guess field, $v' = (u', v') = v - v_b$, can be decomposed into non-divergent and irrotational components v'_ψ and v'_χ with $v' = v'_\chi + v'_\psi$. Here $e_z \cdot \nabla \times v'_\chi = 0$ and $\nabla \cdot v'_\psi = 0$, where e_z is the vertical unit vector. For those two components the assumption of statistical independence is more realistic than for u and v (see Daley, 1991).

In general the covariance matrix can be derived by specifying the covariance structure for the streamfunction and velocity potential. In the formulation we use here, we assume a Gaussian or a Second Order Auto-Regressive (SOAR) spatial structure for the streamfunction covariance. That is, we assume that windfield can be derived from a streamfunction with error covariance structure represented by either a Gaussian spatial distribution, $\exp[-(1/2)(r/r_0)^2]$, or for the SOAR, $(1 + r/r_0)\exp(-r/r_0)$. r is the distance in space and r_0 is a "decorrelation radius", (see Daley, 1991). From this we can derive the covariance function and covariance matrix for the rotational velocity (see Schyberg and Breivik, 1996). A similar model could be used for the divergent velocity.

Corresponding to the rotational and divergent components of the error, the standard deviation of the background wind error can be split into two parts, $\sigma_v^2 = \sigma_\psi^2 + \sigma_\chi^2$. For the covariance model, we need to specify the value of the total background velocity error variance, σ_v^2 , the ratio $\nu = \sigma_\chi/\sigma_v$ (usually chosen to be a small number) and a "radius of influence", r_0 . In the method used here we have put $\nu = 0$, which means that we only allow deviations from the background field to have a rotational part. Due to the geostrophic nature of the wind outside the tropics, this dynamic constraint is very efficient in enforcing a realistic wind field from the observations. Also in the tropics, e.g. in the case of tropical cyclones, this may be a useful constraint.

The observation cost term. From the model function wind retrieval we can get up to four possible scatterometer wind solutions, which are labelled rank 1 to rank 4. Because of errors and dependencies not taken into account by the model function, the σ^0 triplet will not lie exactly on the wind cone, and the ranking is done in terms of increasing distance from the wind solution on the cone to the observed triplet. Previous statistics shows that one of the two highest rank solutions are correct in almost all cases (Stoffelen and Anderson, 1995). We therefore assume that one of these two solutions is the correct one and base the observation cost function on that, although the extension of the method to more than two solutions is straightforward.

Assuming the observations errors are independent between the various cells, the observation term splits up into contributions from each observation point, represented by a sum over the observation index k . We can derive an expression for each observation cost term using the relation with conditional probabilities derived by Lorenc (1986).

We denote the event of a given scatterometer observation " O_k ", and this observation implies the two wind possibilities v_{Ok1} and v_{Ok2} . Following Lorenc, we have

$$J_{o(\text{scatt})k}(\mathbf{v}) = -\ln[p(O_k|\mathbf{v})] + \text{const.} \quad (3)$$

This probability density can be split up by introducing the mutually exclusive events that "wind \mathbf{v}_{Ok1} is the correct alternative", denoted " R_1 ", and that the other wind is correct, denoted " R_2 ",

$$p(O_k|\mathbf{v}) = p(O_k|\mathbf{v} \cap R_1)P(R_1|\mathbf{v}) + p(O_k|\mathbf{v} \cap R_2)P(R_2|\mathbf{v}) \quad (4)$$

Here " $\mathbf{v} \cap R_1$ " is the event that the wind has the true value \mathbf{v} and the correct wind alternative of the observed pair is \mathbf{v}_{Ok1} .

It is reasonable to model $p(O_k|\mathbf{v} \cap R_1)$ and $p(O_k|\mathbf{v} \cap R_2)$ as two Gaussian distributions in \mathbf{v}_{Ok1} and \mathbf{v}_{Ok2} respectively. Assuming the prior probability of each solution is equal, we find for the cost contribution from each observation

$$J_{o(\text{scatt})k} = -\ln\left(\frac{1}{2}e^{-j_{k1}} + \frac{1}{2}e^{-j_{k2}}\right). \quad (5)$$

Here we have defined, like done by Stoffelen and Anderson (1995),

$$j_{km} = \frac{1}{2} \frac{(u_{Okm} - u_k)^2 + (v_{Okm} - v_k)^2}{\epsilon_s^2}. \quad (6)$$

j_{k1} and j_{k2} measure the distances to the two possible wind observation solutions which are approximately 180 degrees apart. $m = 1, 2$ are the indices on the two winds in the ambiguous wind observation pair. (u_k, v_k) is the windfield at observation point and ϵ_s is the standard deviation of scatterometer wind component observation error. Eq. (5) is usually a function with two minima corresponding to each of the two biased winds.

Solution by successive corrections. It was shown by Schyberg and Breivik (1997) that the above variational problem can be solved by using a successive correction approach which is a generalization of that suggested by Bratseth (1986). The method iterates on an observation estimate vector \mathbf{y} and an analysis vector \mathbf{x} , both containing \mathbf{v} at each observation point. The iteration is initialized by setting \mathbf{x} and \mathbf{y} equal to the first guess field. The iteration value at step $\nu + 1$ is then found from

$$\mathbf{x}_{\nu+1} = \mathbf{x}_{\nu} + \mathbf{B}\mathbf{Q}(\bar{\mathbf{y}}_o(\mathbf{x}_{\nu}) - \mathbf{y}_{\nu}) \quad (7)$$

$$\mathbf{y}_{\nu+1} = \mathbf{y}_{\nu} + (\mathbf{O} + \mathbf{B})\mathbf{Q}(\bar{\mathbf{y}}_o(\mathbf{x}_{\nu}) - \mathbf{y}_{\nu}). \quad (8)$$

Here \mathbf{O} is the diagonal observation error covariance matrix and the matrix \mathbf{Q} is an arbitrary matrix to be chosen so that the scheme converges, and it can be shown that \mathbf{x}_{ν} will then converge towards a value minimizing the cost function defined here. The vector $\bar{\mathbf{y}}_o(\mathbf{x}_{\nu})$ consists of weighted averages $\overline{\mathbf{v}_{Ok}}$ of the two scatterometer observation ambiguous winds at each observation point, where the weight is determined by the value of the analysis variable \mathbf{x} (a set of wind vectors \mathbf{v}_k at each observation point) at the current iteration. The entries of $\bar{\mathbf{y}}_o$ are averaged winds,

$$\overline{\mathbf{v}_{Ok}} = w_1(\mathbf{v}_k) \mathbf{v}_{Ok1} + w_2(\mathbf{v}_k) \mathbf{v}_{Ok2}. \quad (9)$$

The weights are defined by

$$w_1(\mathbf{v}_k) = \frac{e^{-j_{k1}}}{e^{-j_{k1}} + e^{-j_{k2}}} \quad (10)$$

and $w_2 = 1 - w_1$. For a further discussion of this numerical method and the selection of the matrix \mathbf{Q} , see Schyberg and Breivik (1997). The optimal solution defines the most probable set of winds at the observation points.

The weights $w_1(\mathbf{v}_k)$ and $w_2(\mathbf{v}_k)$, with the optimal most probable windfield inserted, can be regarded as posterior probabilities for each of the two wind possibilities. The scheme assumes the ambiguity with the highest posterior probability to be the true one.

This ambiguity removal scheme contains several parameters which must be determined. The accuracy of the scatterometer observations is reflected in the value of ϵ_s , and the quality of the first guess winds enters into a background error variance which scales the background covariance matrix \mathbf{B} , as well as a decorrelation scale which determines the spatial coherence.

Tuning and possible future developments. The MSC method described above contains a set of parameters which should be selected for optimal performance of the scheme. An initial set of experiments was done to tune the parameter set to give a good performance of the method. These initial experiments included intense cyclones where PRESCAT obviously gave erroneous ambiguity removals. For standard deviations of the errors in observation and background, we found it reasonable to rely much on the observation values, and chose 1 m/s for ϵ_s and 8 m/s for the σ_V background wind vector component error.

In the formulation for the elements in the background error covariance matrix \mathbf{B} we used a Gaussian spatial structure. Statistics using a limited dataset (87,000 observations) showed that the results with the SOAR model did not represent any improvement in terms of ambiguity removal skill.

We chose to perform 100 iterations of the MSC scheme, as this seemed to give a sufficient convergence in most cases. The influence radius r_0 is an important parameter determining the spatial coherence of the field. For this parameter we put it to 300 km throughout the first 50 iterations and changed its value to 150 km in the last 50 iterations in order to better capture small scale structures. This reduction seemed necessary in order to get small scale structures in some cyclone centres correct. This is a somewhat pragmatic approach, since we can then no longer explicitly specify a cost function of which MSC converges to the minimum.

No numerical cost function minimization method can guarantee that the minimum reached is the global minimum and not a local one. This is of course also the case for the MSC method, and the ambiguity removal problem is a typical problem where two local minima corresponding to opposite sets of winds may exist. The approach of the method to the convergence limit may therefore change the result of the iterations. The MSC method has the property that the small scales are the ones to converge

most slowly. The Q matrix has here been specified using a new method which make the small scales converge as fast as possible, see Schyberg and Breivik (1997). There seemed however to be cases where this convergence for the small scales was not sufficient, and an increased number of iterations produced a different result.

Although we have done some tuning and experiments with various choices of models for these parameters as discussed above, there may still be some room for further tuning or for new methods for modelling the parameters involved. In particular is the modelling of the first guess error covariance matrix an interesting challenge. We have in the present work based this model on a no divergence assumption and used a matrix independent on location and synoptic situation. This is a problem this method shares with traditional data assimilation methods of assuming a fixed background error covariance structure. This means that the background errors are assumed to have the same spatial distribution in all synoptic situations, which obviously is not an optimal method. A similar problem of course also exists in the way PRESCAT requires spatial coherence.

More recent development in data assimilation could lead to models for flow dependent covariance structures. We also know that there actually is divergence present in the ocean surface wind which has not been accounted for in the model presented here. Another possible development of the MSC method would be to include a model for the divergent part of the wind in the covariance structure functions.

3. EVALUATION

3.1 Experiment setup

To compare the performance of the different ambiguity removal methods, PRESCAT and the MSC variational method as developed at DNMI have been run in parallel in February to April 1998. The results have then been compared to the operational UWI data as processed in near real time by ESA.

As described in Section 2.1, in the operational ESA UWI wind product ambiguity removal is performed by the method CREO. As meteorological background ECMWF 10 m wind forecasts, given on a grid with 1.5 degrees resolution, is used. These forecasts are produced from analysis 00 UTC and are received by ESA only once per day with one day delay. To cover one day of ERS data ESA use the +18, +24, +30 and +36 hours forecasts. When the processing of an ERS orbit starts the closest in time ECMWF forecast is taken as background.

This way of using background information is quite different from the operational wind processing performed at DNMI. Since DNMI is an operational forecast centre a newer background wind field is always available. At DNMI a short forecast 10 m wind field from the operational weather prediction model HIRLAM, available on a 50 km resolution grid, is interpolated in space and time to each scatterometer observation node and used as background. The time interpolation is performed by an FGAT approach (First Guess at Appropriate Time) which means temporal interpolation between +3, +6 and +9 hour forecast (Breivik and Haugse, 1994).

With these differences in the quality of the meteorological background a straightforward comparison between the UWI wind product and the DNMI processed winds is of less interest. To emulate the ESA operational environment in this comparison study, the ECMWF forecasts were used as background for PRESCAT and MSC. The ECMWF forecasts are operationally received at DNMI. The comparison between CREO, PRESCAT and MSC has been organized the following way: The CREO winds are the operationally received UWI wind product as processed by ESA. These are compared with PRESCAT and MSC results obtained with similar wind background as CREO, that is an ECMWF +18, +24, +30, or +36 hours forecast. The ECMWF background is given on approximately 150 km resolution.

Data has been collocated and ambiguity removal has been performed with PRESCAT and MSC in a time period between 12 February and 12 April 1998. The evaluation area is the model area used for the operational weather prediction model HIRLAM, which covers the northern part of the Atlantic ocean down to approximately 20 degrees N. To ensure that areas with sea ice is not allowed to affect the data, only those points where the HIRLAM Sea Surface Temperature analysis was above 2°C was used.

3.2 Statistics

For evaluation of the performance the results from CREO, PRESCAT and MSC have been compared to the operationally DNMI processed scatterometer winds, hereafter called OPR. In OPR, as explained above, ambiguity removal is done by using PRESCAT and a fresh (3 to 9 hrs forecast) meteorological background interpolated in time and space to the scatterometer observation points. The results are also compared with the operational background FGAT and with the ECMWF, +18 - +36 hrs forecast background.

We shall present two different measures of the skill in terms of obtaining results coinciding with the "best reference", OPR. Firstly we present the percentage of winds which are turned relative to the reference, which measures the number of winds which gave a different ambiguity removal. Secondly we present the vector root mean square of the wind vector difference from the reference. While the first measure is interesting from an ambiguity removal point of view, the second measure is probably the most interesting from a user point of view, since it measures the magnitude of the wind error involved in an erroneous ambiguity removal. With this measure ambiguity removal errors at important high-wind-speed situations will count more and calm wind situations less.

Table 1 below shows the numbers of scatterometer observations with wind direction differing more than +/- 90 degrees compared to OPR and FGAT and ECMWF long forecast(+18-+36). When comparing with OPR we are looking at the number of observations where the tested ambiguity removal method, with a poor background, has chosen another, near opposite, wind direction than the operational ambiguity removal with a fresh background.

	CREO	PRESCAT	MSC
OPR	25377, 15.3%	3709, 2.2%	3698, 2.2%
FGAT	25870, 15.6%	5280, 3.2%	4929, 3.0%
ECMWF	26251, 15.9%	3524, 2.1%	4564, 2.8%

Table 1: Number of wind results obtained by CREO, PRESCAT and MSC more than +/- 90 degrees different from OPR (operational) scatterometer data, short forecast FGAT, and long forecast ECMWF. The total number of observations is 165353.

Compared to OPR about 15% of the ESA retrieved wind solutions are different, while only slightly above 2% of the PRESCAT and MSC results are different. Compared to FGAT about 3% of the PRESCAT and MSC are different while still 15% of the CREO results. Compared to the meteorological background used by all three methods, the ECMWF long forecast, 16% of the CREO results are different while results for PRESCAT and MSC is still between 2 and 3%. Looking into details it is seen that MSC performs slightly better than PRESCAT compared to OPR. PRESCAT seems to be slightly more dependent on the background information as the PRESCAT results are closer to the ECMWF.

Looking at vector differences the results are shown in Table 2. In this way of comparing more weight is given to cases with high wind speed. In cases with low wind speed ambiguity removal is particularly difficult, but from a users point of view not as important as cyclones, which are often associated with high winds. The qualitative results are similar as discussed above. However improvement of MSC compared to PRESCAT is more significant. It is also seen that PRESCAT gives slightly more confidence to the background, the ECMWF long forecast. This reflects the fact that the variationally based method relies more on the dynamic constraint and less on the first guess, and is better in getting the wind turned correctly around strong cyclones.

	CREO	PRESCAT	MSC
OPR	6.27	1.96	1.79
FGAT	6.89	3.74	3.61
ECMWF	7.10	4.04	4.07

Table 2: Vector differences between CREO, PRESCAT, MSC and OPR (operational) scatterometer data, short forecast FGAT, and long forecast ECMWF in units of meters per second. Total number of observations is 165353

In the above comparison all available cases have been taken into account. However, as also noted by Stoffelen and Anderson (1995), there is a large number of cases where ambiguity removal is not performed by CREO, and where Rank 1 only is given. In our data-set ambiguity removal has been given up by CREO and Rank 1 provided in 17% of the cases. Excluding these cases in the statistics reduces the fraction of the dataset where CREO fails to about 10%. However, the fraction of cases where PRESCAT or MSC fails, is also reduced, so qualitatively the relative behaviour of the schemes does not change.

4. CONCLUSIONS

This study clearly shows that both MSC and PRESCAT are superior to ESAs operational ambiguity removal. There is a significant fraction of the observations where ESA does not attempt ambiguity removal. Even if these data are excluded from the data-set, the conclusion remains the same.

Skill evaluations in terms of fraction winds turned relative to a reference shows MSC and PRESCAT to be comparable in performance, with MSC slightly superior and less dependent on first guess. The statistics improves in favour of MSC when regarding root mean square vector difference from the reference, which shows that MSC has best skill in the important high-wind cases. This arises from the fact that the variational method relies less on first guess and more on dynamics, particularly in high-vorticity systems. The fact that PRESCAT winds using a 6 hrs first guess is used as reference, could give a certain bias in favour of the PRESCAT method since the same errors related to the method could be present also in the reference data-set. This supports our conclusion that MSC has slightly better skill. It also has a potential for future improvements and the advantage of not very high code complexity.

ACKNOWLEDGEMENTS

The comparison between the various ambiguity removal schemes was done under ESA contract. The ideas behind the MSC scheme were developed in a project supported by the Norwegian Space Centre.

REFERENCES

- Bratseth, A.M., 1986: Statistical interpolation by means of successive corrections. *Tellus* **38A**, pp. 439-447.
- Breivik, L.-A and Haugse, B., 1994: Scatterometer wind retrieval at the Norwegian Meteorological Institute. *DNMI Technical Report no. 124*.
- Cavanié, A and Lecomte, P., 1987: Vol 1 - Study of a method to dealias winds from ERS-1 data. Vol. 2 - Wind retrieval and dealiasing subroutines. Final report of ESA contract No 6874/87/CP-I(sc), Available from ESA Publ. Div. ESTEC, Noordwijk, The Netherlands.
- Daley, R., 1991: Atmospheric Data Analysis. *Cambridge University Press*.
- Graham, R, Anderson, D., Hollingsworth, A. and Bottger, H., 1989: Evaluation of ERS-1 wind extraction and ambiguity removal algorithms: Meteorological and statistical evaluation, ECMWF report to ESA. Available from ESA Publ. Div. ESTEC, Noordwijk, The Netherlands.
- Lorenc, A.C., 1986: Analysis methods for numerical weather prediction. *Quart. J. R. Met. Soc.* **112**, pp. 1177-1194.
- Offiler, D 1987: ERS-1 wind retrieval algorithms. UKMO MET O 19 Branch, Memo. No 86. Available from The National

Meteorological Library, Bracknell, UK.

Schyberg, H. and Breivik, L-A., 1996: Two-dimensional variational analysis of ocean surface wind. *DNMI Research Report no 42*. Available from Norwegian Meteorological Institute, P.O.Box 43 Blindern, N-0313 Oslo, Norway.

Schyberg, H. and Breivik, L-A., 1997: Objective analysis combining observation errors in physical space and observation space. *DNMI research report no 46*. Available from Norwegian Meteorological Institute, P.O.Box 43 Blindern, N-0313 Oslo, Norway.

Schyberg, H. and Breivik, L-A., 1998: Ambiguity Removal Algorithm Evaluation. *DNMI research report no 64*. Available from Norwegian Meteorological Institute, P.O.Box 43 Blindern, N-0313 Oslo, Norway.

Stoffelen, A. and Anderson, D., 1995: The ECMWF Contribution to the Characterisation, Interpretation, Calibration and Validation of ERS-1 Scatterometer Backscatter Measurements and Winds, and their use in Numerical Weather Prediction and Models. European Space Agency Contract report. Issued by European Centre for Medium-Range Weather Forecasts, Reading, 1995. Available from ESA Publ. Div., ESTEC, Noordwijk, The Netherlands.

Stoffelen, A. and Anderson, D., 1997: Ambiguity removal and assimilation of scatterometer data. *Quart. J. R. Met. Soc.* **123**, pp. 491-518.

TOWARDS AN IMPROVED Ku-BAND SCATTEROMETER PRODUCT

J. Figa, A. Stoffelen

KNMI Postbus 201, 3730 De Bilt, The Netherlands

Phone: +31 30 220 6585, Fax: +31 30 221 0843

e-mail: figa@knmi.nl, stoffelen@knmi.nl

ABSTRACT

As a preparation for QuikSCAT, several aspects of the Ku-band geophysical model function and the inversion problem for NSCAT have been looked at. In particular, this study intends to assess the information content of NSCAT winds.

An inversion scheme adapted from PRESCAT has been developed and applied to one week of 50 km cell NSCAT Level 1.7 σ^o 's, and the NSCAT Level 2.0 wind product has been successfully simulated using that scheme. An assessment of the inversion scheme has been carried out using the Maximum Likelihood Estimator (MLE). That quantity indicates how well the backscatter measurements used in the retrieval of a particular vector fit the Geophysical Model Function, and gives therefore a good indication about the quality (interpretability) of that measurement. There exists also some knowledge about the expectation value of the MLE, since the instrument noise is reasonably well modelled, as well as is the variability of the wind speed within a wind vector cell. The MLE can then be normalised by its expected value and this ratio be used as an indicator of the quality of the retrieval.

A threshold of that quantity for the rejection of bad wind retrievals is determined by correlating the inversion residual and the wind vector departure from ECMWF. That threshold ends up rejecting around 2.0% of the NSCAT wind nodes. In order to do a more qualitative assessment of this rejection, collocated SSM/I rain and ECMWF winds are used. Confused sea state and presence of rain seem to be the most likely causes for the rejection of retrieved winds.

We believe the results of our study can be successfully used for the interpretation and retrieval of good quality winds from QuikSCAT.

Keywords: scatterometer, wind, quality control, inversion, cost function, rain, numerical prediction model.

1. INTRODUCTION

QuikSCAT, the next NASA scatterometer, will be launched in November 1998. In order to have an operational product to be assimilated in weather analysis, the information content of QuikSCAT winds has to be assessed. Although featuring a different viewing geometry, QuikSCAT is a Ku-band scatterometer as NSCAT, and should have very similar Quality Control (QC) issues to review, such as the effect of the presence of rain. The general objective of this work is to prepare for QuikSCAT QC challenges, by assessing the information content of the winds retrieved from the NSCAT scatterometer.

This is particularly important in order to assimilate them in weather analysis. Lacking other estimation of the quality of scatterometer wind data, the RMS wind vector difference with the model First Guess winds provides a good QC. However, an important requirement for the effective assimilation of data into weather analysis is to have an assessment of their accuracy independent from the analysis itself.

One possibility to do that in the case of NSCAT winds is to evaluate the wind retrieval performance. The retrieval is an inversion problem for each wind vector cell (WVC) that, given a set of measurements σ_{oi}^o , finds the wind vector (V, ϕ) that according to the Geophysical Model Function (GMF) has the highest probability of representing the true wind. Any inversion problem presented in these probabilistic terms comes down in the end to the minimisation of a cost function J (also called MLE), which in case of the NSCAT wind retrieval has the following expression:

$$J(V, \phi) = \sum_{i=1}^N \left[\frac{\sigma_{oi}^o - \sigma_{si}^o(V, \phi)}{SD(\sigma_{si}^o(V, \phi))} \right]^2$$

$$\sigma_{si}^o = GMF(V, \phi)$$

where σ_{si}^o is the backscatter associated with different trial values of (V, ϕ) through the GMF, $SD(\sigma_{si}^o)$ is its corresponding standard deviation and N is the number of measurements within the WVC. J indicates therefore how well the backscatter measurements used in the retrieval of a particular wind vector fit the GMF, and gives therefore a good indication about the quality (interpretability) of that measurement. The main assumption in the formulation of the problem is related to the GMF, which is empirically determined for fair weather conditions, i.e. average sea state and in the absence of rain. The assumption about the noise of the system through $SD(\sigma_{si}^o)$ is also very important. The noise is assumed to be Gaussian in σ^o and coming from three different sources: the instrument noise, the measurement collocation error due to the variability of the wind within the WVC, and the uncertainty of the GMF for measurements under different geophysical conditions. For this study, we are concerned only with the assumptions made about the noise. Often, when assuming Gaussian errors, an additional term $\sum \{\ln[SD(\sigma_{si}^o)]^2\}$ is added to the previous expression of J . However, we have verified that its contribution is mostly constant and does not affect the wind retrieval significantly. Therefore we will not use it for our study.

The data we will use in this study are the latest and last processed NSCAT Level 1.7 σ^o 's. The GMF will be NSCAT-1 [1]. Collocations with ECMWF First Guess winds and with

SSM/I rain measurements from the NASA Pathfinder data set will be used to assess the QC method.

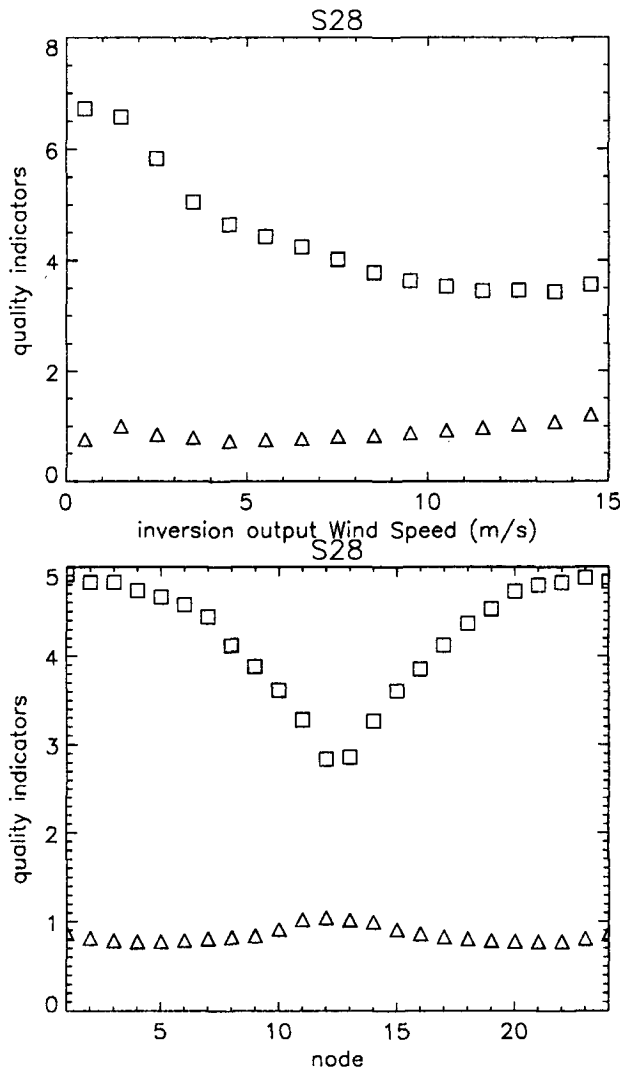


Figure 1. Averaged $SQRT(J)$ (squares) and $R_n = SQRT(J/J^*)$ (triangles) with respect to wind speed (up) and swath position (low). The data used correspond to a week of data (batch S28) in March.

2. METHOD PROPOSED

The best QC indicator would in principle appear to be J itself. However, figure 1 shows that, when using the $SD(\sigma_{si}^o)$ as specified in the NSCAT product, J is strongly dependent on wind speed and swath position. Therefore, it cannot be used for quality assessment of NSCAT wind retrievals in their assimilation in weather analysis, since certain wind speeds and swath positions would be penalised systematically. We have normalised J for any range of wind speed and swath position by its expected value J^* , which we have formulated as follows:

$$J^*(V, \phi) = \sum_{i=1}^N \left[\frac{SD^*(\sigma_{si}^o(V, \phi))}{SD(\sigma_{si}^o(V, \phi))} \right]^2$$

$$SD^*(\sigma_{si}^o) = \left\langle \left| \sigma_{oi}^o - \sigma_{si}^o(V, \phi) \right| \right\rangle = \\ = SD^{instrument}(\sigma_{si}^o) + SD^{\sigma^o collocation}(\sigma_{si}^o)$$

where $SD^*(\sigma_{si}^o)$ represents the expected difference between the observation and the GMF. We have estimated SD^* as measurement noise, considering the different contributions discussed in section 1. As instrument noise we have used Alain Cavanié *et al.* estimations over arctic sea ice [2]. We have calculated the collocation error using the GMF, after estimating from climate spectra a wind speed variability within the WVC of 0.5 m/s. The contribution of the GMF uncertainty has not been included in SD^* , since in case of large GMF error, anomalous geophysical conditions may be present for which the GMF and thus the wind retrieval is invalid. Our purpose is to reject such wind retrievals. Measurements in exceptional geophysical conditions such a confused sea state or rain, should then be detected by our QC indicator, which we formulate as:

$$R_n = SQRT\left(\frac{J}{J^*}\right)$$

Figure 1 shows how J^* successfully normalises J and that R_n is basically independent of the wind speed and swath position, and therefore a good candidate as a QC indicator for NSCAT winds.

3. RESULTS

3.1 Comparisons with the RMS wind vector difference with the ECMWF model First Guess winds (ECMWF-RMS)

For every WVC, four wind solutions have been retrieved using NSCAT-1, and their corresponding R_n values calculated. Because of the symmetry of the problem, in most of the cases we find among them the two main ambiguous solutions with comparable and lowest R_n . However, the ECMWF-RMS of the 180° main ambiguity would be very high and cannot be fairly related to the quality of the solution as estimated from the inversion. Therefore, we have carried out our comparison by taking in account only the solutions within the 180° half plane centred around the ECMWF wind vector. About 50% of the solutions are considered through this selection, which confirms our hypothesis that the problem is indeed symmetric. Figure 2 shows that ECMWF-RMS and R_n are fairly well correlated up to R_n values of 4, which supports the use of R_n as an indicator of the information content of the retrieved solutions. The 'branches' at the right side of the plot appear at certain wind directions relative to the satellite track (plot not shown), and are likely related to the geometry of the measurement system.

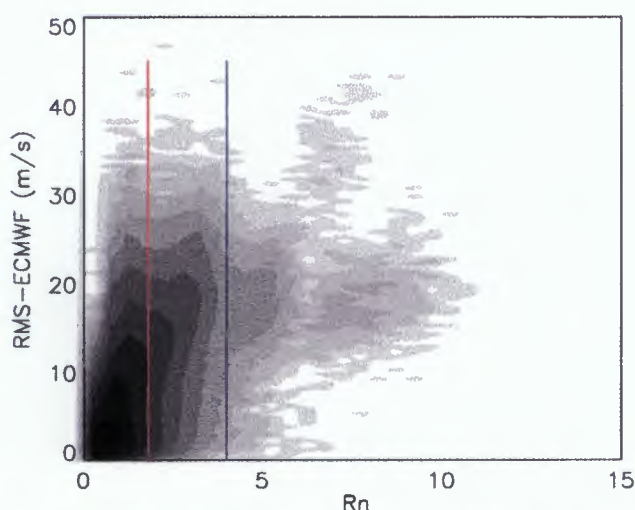


Figure 2. Log-histogram of (R_n .vs. ECMWF-RMS) points corresponding to wind solutions retrieved from batch S28. The two vertical lines correspond to $R_n=1.8$ (red) and $R_n=4.0$ (blue).

WIND SOLUTIONS		avg ECMWF-RMS
accepted	93.9%	4.3 m/s
rejected	6.1%	12.2 m/s

Table 1. QC statistics in percentage of solutions and average RMSM-ECMWF, after applying a threshold of $R_n=1.8$ for rejection to batch S28 data (1744889 solutions).

WIND NODES		
accepted	98.9%	
rejected	1.1%	
post-rejected	0.9%	2.0% total rejected

Table 2. QC statistic in percentage of nodes, after applying a threshold of $R_n=1.8$ for rejection of solutions to batch S28 data).

3.2 The selection of a R_n threshold for rejection of bad retrievals

$R_n=4$ would appear to be the threshold to choose for accepting solutions from the point of view of interpretability. However, when applying that threshold to 1744889 solutions (one week of data approximately), the average ECMWF-RMS of the accepted solutions is 10 m/s, too high to contribute with meaningful information to the weather analysis. A value of $R_n=1.8$ accepts solutions with a more reasonable average ECMWF-RMS of 4.3 m/s. Just as a reference, the operational implementation of roughly the same QC method in the case of ERS-PRESCAT [3], accepts solutions of approximately 5 m/s ECMWF-RMS for $R_n=5$. In

the case of NSCAT, 93.9% of the solutions are accepted, and 6.1% rejected, the latter with a high average ECMWF-RMS of 12.2 m/s, which again supports the effectiveness of the threshold chosen. The percentage of nodes with some solution accepted is 98.9%. Out of these, 1.1% have only one solution left or maybe more than one separated less than 90° . These will most likely not be dealt with properly by the ambiguity removal, so we reject them as well, losing in total only 2.0% of the nodes. The results are summarised in tables 1 and 2.

3.3 The detection of solutions probably affected by rain

Collocations between the retrieved winds and SSM/I rain data from the NASA Pathfinder data set [4] have been found within 0.25 deg. and 30 minutes. In figure 3, it is shown that most of the wind solutions with rain collocations above 12 mm/hr are rejected by $R_n=1.8$ and correspond to high ECMWF-RMS values.

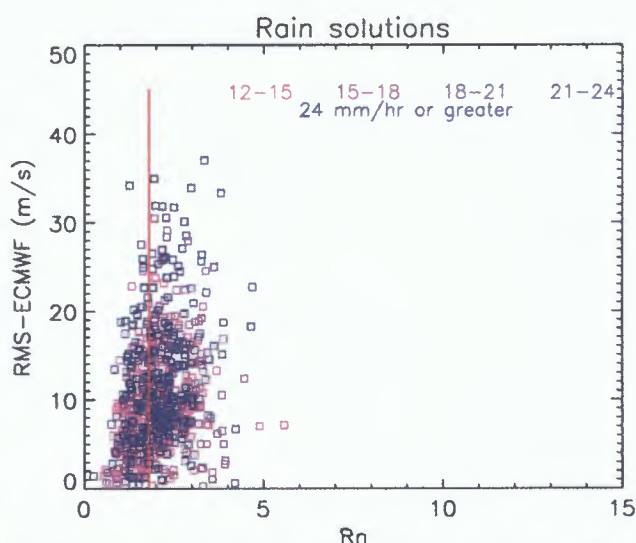


Figure 3. (R_n .vs. ECMWF-RMS) points corresponding to wind solutions retrieved from batch S28 where a SSM/I collocation above 12mm/hr has been found. The red line corresponds to $R_n=1.8$

3.4 Some cases for illustration

We have looked at several particular cases to illustrate how the QC performs. Figures 4a and 4b show two typical NSCAT passes where the QC has been applied successfully. Figure 4a indicates a typical rejection of a clearly aberrant solution. The situation in 4b is a clearly defined north-west wind field as the background ECMWF wind field indicates. The QC rejects the solutions with clearly wrong wind direction and accepts the two main ambiguities..

Figure 4c shows a case of undeveloped sea state in a coastal area, when the wind blows offshore. This is a special sea state that does not correspond to the fair weather conditions for which the GMF has been derived. Many spurious solutions appear in the area, which are rejected by the QC. At a certain distance from the coast, the sea has developed into an equilibrium state according to the present surface wind and the effect disappears

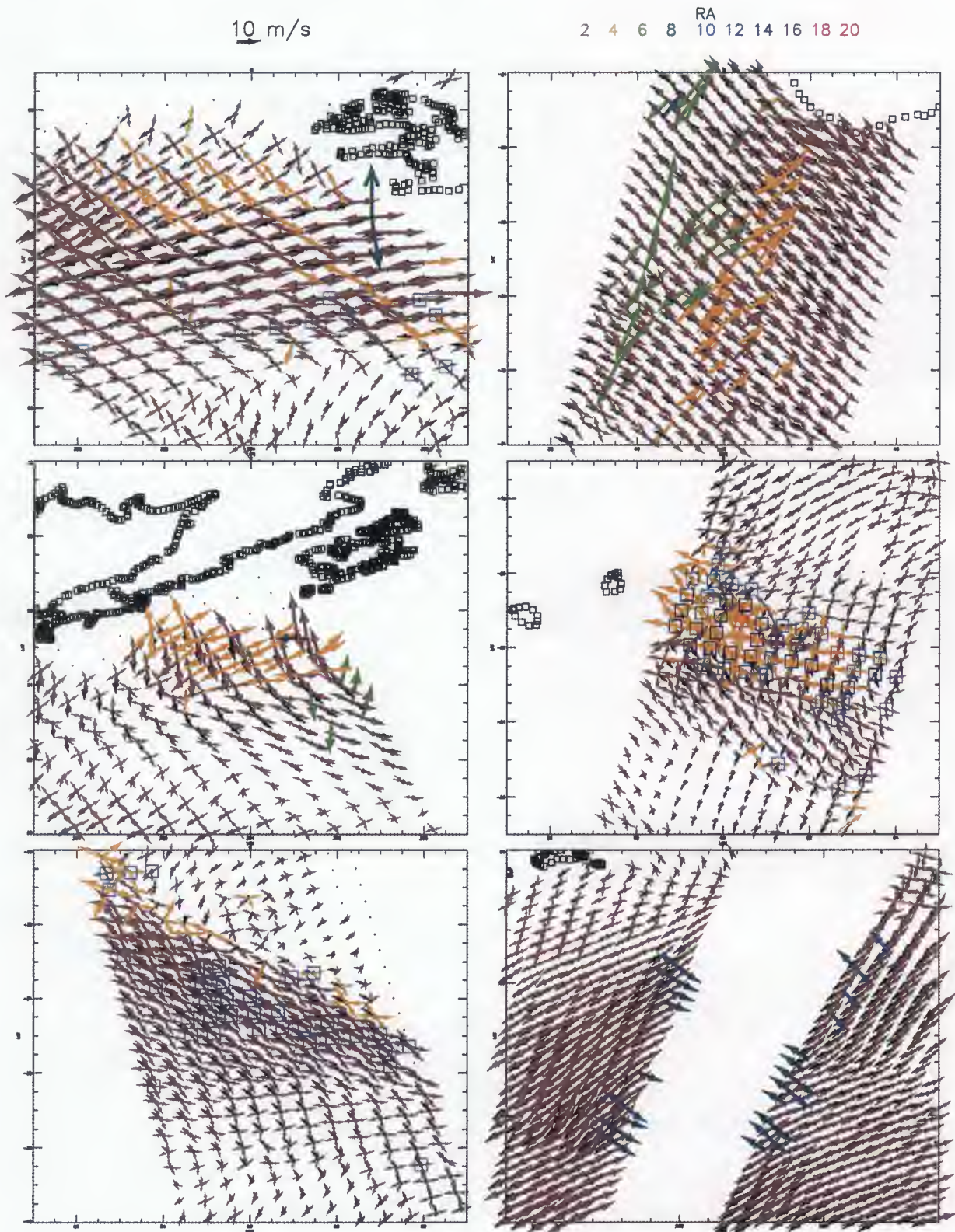


Figure 4. Cases for illustration of how R_n assesses the information content of individual wind solutions. The black arrows are the ECMWF model Fists Guess winds. The NSCAT wind solutions are plotted in different colours according to their values of R_n (see legend above). Therefore, accepted solutions correspond approximately to colour brown, and the rest are rejected. Collocated SSM/I rain measurements are plotted over as squares: light blue, blue and red squares for rain values below 3, between 3 and 12 and above 12 mm/hr, respectively. The points represent locations for which a SSM/I collocation for NSCAT measurements could not be found.

Figure 4d shows a case of tropical rain, therefore not corresponding to the GMF fair weather conditions. This figure suggests that the area where the bad solutions appear matches in general the area where rain has been detected by SSM/I. However, the identification of rain-contaminated solutions from SSM/I collocations only does not seem to correspond always on a node by node basis. This points out the difficulty of developing a rain flag based only on rain observations.

Figure 4e shows a case of rain outside the tropics. As expected, low rain rates do not affect significantly the retrieval. The affected nodes in this case probably correspond to the confused sea state associated to the edge of the rain front, where a few bad retrievals are rejected. We have found that rejections appear systematically in this type of situations.

In figure 4f some situations are shown which illustrate the slight increase in the average R_n value for the inner swath suggested in figure 1 (low). In many cases a few spurious solutions appear systematically in the inner nodes. They normally correspond to high speed winds (above 15 m/s), as is also suggested by the curve trend in figure 1 (up). If we include in figure 1 (low) solutions with wind speed above 15 m/s, the increase of R_n for the inner nodes is accentuated (plot not shown). We think that this problem has to do with the NSCAT-1 GMF, which is known to perform less for inner nodes at high wind speeds. Fortunately, our QC properly rejects these wrong solutions.

3.5 The wind direction dependency of R_n and ECMWF-RMS

Although R_n is basically independent of wind speed or swath position, figure 5 indicates that the inversion performance is wind direction dependent, as is the ECMWF-RMS. That dependency has a symmetry with respect to the satellite track, and is therefore related to the geometry of the measurement system.

4. CONCLUSIONS AND FUTURE WORK

R_n provides a uniform cost for wind speed and swath position. It is a good quality indicator for NSCAT winds and therefore can provide useful additional information for their assimilation.

We find that $R_n=1.8$ is a very reasonable threshold for rejection of bad retrievals, and in many cases it rejects indeed solutions affected by special geophysical conditions non modelled by NSCAT-1, such as confused sea state or rain. In the particular case of rain, we think that a solution flag from a R_n threshold value is probably more appropriate than a node rain flag from SSM/I collocations only. Furthermore, that might be the only viable approach in an operational scenario.

An open issue remains to investigate the wind direction dependency of R_n , which we think related to the definition of J [5] and how it deals with the shape of the NSCAT-1 for the particular geometry of the system and the measurement noise.

After a successful QC over NSCAT winds, we plan an impact study of assimilation of those winds in weather analysis, in co-operation with ECMWF. After that, the objective is to apply this method to QuikSCAT. QuikSCAT is the first of a new generation of Ku-band scatterometers, based on a scanning measuring system, as opposed to the fixed antenna geometry of fan-beam scatterometers such as ERS, NSCAT or ASCAT. In most of the swath, a similar wind retrieval can be applied as for NSCAT, and we can therefore implement the same QC method straightforwardly. In the far swath and nadir areas though, some more development will be necessary, since either the lack of enough backscatter measurements or wind direction information respectively, suggest the use of different inversion approaches.

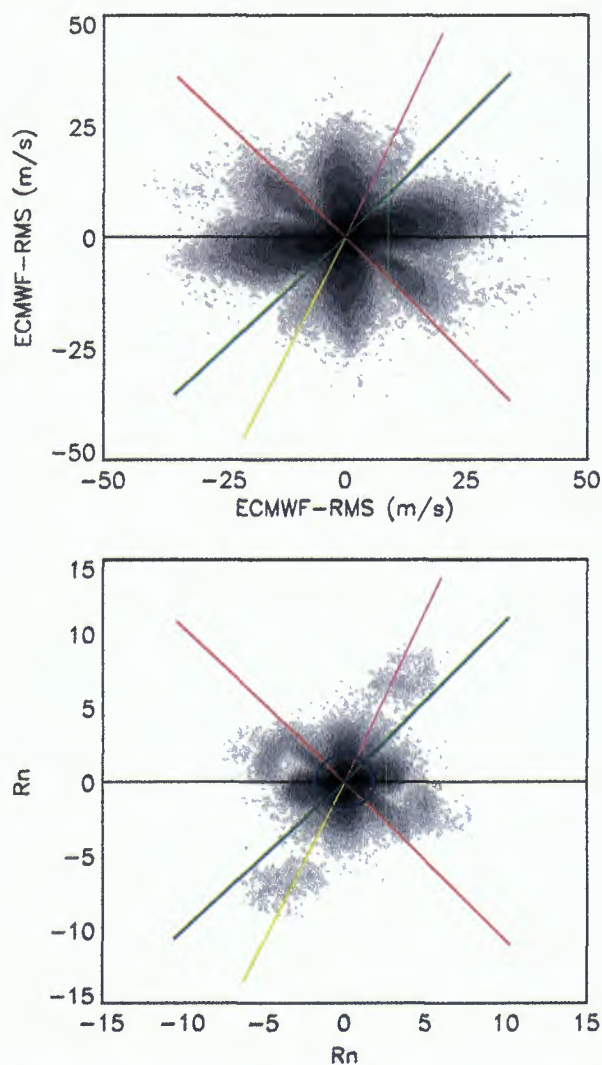


Figure 5. Polar plot representing the log-histograms of R_n and ECMWF-RMS values with respect to retrieved wind direction relative to the satellite track (black line), for batch S28 of data. The coloured lines represent the relative azimuths of the different antennae. The blue circle on the lower plot corresponds to $R_n=1.8$.

REFERENCES

- [1] F.J. Wentz & D.K. Smith. A model function for the ocean normalized cross section at 14 GHz derived from NSCAT observations. Submitted to the *Journal of Geophysical Research*, NSCAT special issue, 1998.
- [2] A.Cavanié & R.Ezraty. Evaluation of Kp on central and lateral antennas of NSCAT over Arctic sea ice. ASCAT SAG, Sept 97 1997.
- [3] A.Stoffelen & D.Anderson. Scatterometer data interpretation: Estimation and validation of the transfer function CMOD4. *Journal of Geophysical Research*, vol102(C3), pp. 5767-5780, 1997.
- [4] F.J. Wentz & R.W. Spencer. SSM/I rain retrievals within a unified all-weather ocean algorithm. Submitted for *Journal of Atmospheric Sciences*, PIP-2 issue, Feb 1996.

- [5] A.Stoffelen & D.Anderson. Scatterometer data interpretation: Measurement space and inversion. *Journal of Atmospheric and Oceanic Technology*, vol.14, pp.1298-1313, 1997.

ACKNOWLEDGEMENTS

This work has been developed under the EUMETSAT NSCAT fellowship in KNMI. The SSM/I data was retrieved from the Remote Sensing Systems web page. The NSCAT data was downloaded from the PODAAC server in JPL.

DEVELOPMENT AND APPLICATION OF A VISIBLE-INFRARED RAIN FLAG FOR SCATTEROMETER DATA

Christopher Grassotti, S. Mark Leidner, Jean-François Louis, and Ross N. Hoffman

Atmospheric and Environmental Research, Inc.
840 Memorial Drive
Cambridge, Massachusetts 02139 USA

ABSTRACT

We report on characteristics of a rain flag derived from collocation of visible and infrared image data with rain rates over the North Atlantic Ocean obtained from microwave imagery (SSM/I) during a 3-week period (15 October 1996 - 2 November 1996). The rain flag has been developed as part of an effort to provide an indication of contamination by heavy rainfall in NASA scatterometer (NSCAT) data sets. The primary results of our analysis indicate: (1) that a simple albedo/infrared brightness temperature threshold is capable of flagging most of the heavy rainfall, though with a fairly high rate of false alarms, and (2) that the small difference in optimal threshold between the tropics and mid-latitudes can probably be ignored. Use of the rain flag in 12 assimilation experiments during this period showed that the number of rain-flagged wind vector cells is generally less than 1% of the number of cells. Overall, the impact from using the rain-flagged data is generally less than 5 *m/s* and localized (less than 5° of longitude and latitude). However, in some cases, the effect of excluding just 1-5 rain-flagged points can change the resulting analysis significantly, because their placement is critical for defining the flow along a front or some other shear-dominated environment.

1. INTRODUCTION

It is known that measurements of Ku-band (13.4 GHz) backscatter from active microwave scatterometers such as NSCAT which operated on board the ADEOS satellite during its 9-month lifetime, can be contaminated by the presence of heavy rainfall in the antenna beam (Refs. [1, 2, 3]). The effect of rainfall on the backscatter signal is complex: both attenuation and amplification are possible, depending on the rain intensity, viewing angle and wind speed. Though it may eventually be possible to correct for these effects, our purpose in this investigation is, more modestly, to develop a rain flag that could

be used to identify measurements with a high probability of rain contamination. One may then simply eliminate those flagged measurements from subsequent wind analyses.

For NSCAT and its interim successor QuikSCAT (QSCAT), devising a rain flag is made difficult by the absence of an onboard passive microwave instrument which could be used effectively to delineate regions with moderate to heavy rainfall. Because of this, we have chosen to make use of visible (VIS) and infrared (IR) imagery which is routinely available from the operational suite of geostationary satellites such as GOES and GMS. Data from these platforms are available generally every half-hour to hour for large regions equatorward of approximately 60N and 60S. The focus of this paper is twofold. First, we report on characteristics of the derived rain flag obtained from a preliminary study using a 3-week data set consisting of collocated GOES-8 imagery and SSM/I-derived rain rates. We examined both temporal and spatial characteristics of the VIS-IR flags and the skill of these flags with respect to instantaneous rain rate categories. Second, we conducted a number of data assimilation experiments during this time period to evaluate the impact of the rain flag on surface wind analyses which used the NSCAT observations.

2. RAIN FLAG DETERMINATION

2.1 Data

The data used for this study covering the time period 15 October 1996 - 2 November 1996 were GOES-8 imagery over the North Atlantic Ocean, and instantaneous rain rates derived from the multichannel Special Sensor Microwave/Imager (SSM/I) onboard the DMSP F10 satellite.

GOES-8 data were remapped to a 0.25 degree latitude-longitude grid, covering the region 270E to 330E longitude, and 0 to 60N latitude. The geostationary imager data used were albedos from visible channel 1 (0.62 mi-

crons) and infrared brightness temperatures from channel 4 (10.7 microns). The albedo data were normalized by the cosine of the solar zenith angle.

SSM/I rain rates produced using the algorithm of Wentz (Ref. [4]) are available globally over the ocean from Remote Sensing Systems already mapped to the same 0.25 degree grid. This algorithm has been developed and tested over several years, and has been validated in a number of algorithm intercomparison campaigns (e.g. the Global Precipitation Climatology Project, and the Precipitation Intercomparison Project). Results from these studies show that it performs comparably to other microwave-based algorithms. Recently, in a detailed review of results from the NASA WetNet Second Precipitation Intercomparison Project (PIP-2), Smith *et al.* (Ref. [5]) showed most microwave algorithms to have root mean square errors on the order of 1 to perhaps 4 *mm/h* and bias uncertainties of ± 30 percent of the true rain rate. A large degree of the uncertainty in microwave accuracy estimates is related to the lack and uncertain quality of ground-based verification data, especially over oceans. Since we are more concerned with using the microwave measurements to flag the degree of attenuation at the NSCAT Ku band, rather than specify a precise rain rate, we believe that the threshold tuning procedure we use here is robust with respect to uncertainties in the SSM/I rain rates.

2.2 Methodology

The approach we use is based on the intuitive notion that cold (or high) and bright clouds are more likely to be heavy rain producers than warmer and less reflective clouds. This idea has been used by a number of researchers in the past (e.g. Refs. [6, 7, 8, 9]); methods based on visible and infrared data perform comparably to microwave retrievals in obtaining rainfall on monthly and longer timescales. This is partly due to the spatial and temporal sampling limitations of the microwave instruments which are situated aboard polar orbiting satellites. However, for short timescales and instantaneous rain rates, the indirect nature of the VIS and IR measurements leads to larger errors, and significant biases and training data dependencies (Ref. [10]). For the NSCAT data the task is somewhat simpler since we seek to flag only moderate to heavy rain areas, rather than to retrieve the rain rate itself. An obvious limitation associated with the use of visible data is the restriction that the technique may only be employed during daytime. Nevertheless, the capability to add an additional level of quality control for up to one-half the scatterometer observations would be extremely useful.

In this study we used the two channels from GOES-8 in conjunction with the rain rates from the DMSP SSM/I. The objective is to find the thresholds in the visible and

infrared data which best correspond to a rain (greater than a critical value)/no rain determination as seen in the SSM/I data. We find the optimum thresholds by maximizing the Heidke Skill Score (Ref. [11]). This metric is based on a binary rain/no rain contingency table and is designed for situations in which the phenomenon of interest occurs rarely. The optimum visible and infrared thresholds will depend on the choice of critical rain rate - in this study we explored both 5 and 10 *mm/h*.

The HSS can vary in the range from -1 to +1 but more generally lies in the range 0 to 1, with 1 representing perfect skill and 0 the skill of a random prediction.

We also calculated the Probability of Detection, POD, and the False Alarm Ratio, FAR. In essence, the POD represents the fraction of all raining points which were correctly identified, while the FAR indicates the percentage of all rain-flagged points which were, in fact, not raining. Ideally, one would like to maximize the POD, while not producing a large FAR.

From the basic contingency sums, all these metrics may be calculated. We computed the sums and corresponding metrics for individual 1-week periods within the entire 19-day period. We also stratified the sums by latitude band into midlatitude (30N - 60N), and tropical (0 - 30N). These are presented in the following section.

2.3 Results

Fig. 1 contains results obtained from data acquired during the first week of the study (15-21 October 1996), which is the training period, in the midlatitudes and tropics. Both panels show the values of albedo and black body temperature of all the rainy points in the sample, plotted as a scatter diagram. Each point is color coded: black if the SSM/I data indicates a rain rate greater than 5 *mm/h*, and white for lighter precipitation. The points with no rain at all are not plotted, for clarity of the diagram, but are included in the HSS computation. The behavior of the Heidke skill score is shown in color in the background of the plots, as a function of the visible and infrared thresholds, which define the predicted rain/no rain boundary. With a sufficiently large number of rain data points in the sample, we expect the skill score to well-behaved. Indeed, both figures show the score to vary smoothly with a maximum value of approximately 0.5. We define the optimum thresholds to be the brightness temperature (TB) and albedo (AL) at which the corresponding HSS is a maximum. For the midlatitude data the optimum TB and AL thresholds which correspond to the critical rain rate of 5 *mm/h* are 240K and 62 percent, and in the tropics the corresponding thresholds are 261K and 64 percent. They are indicated by the dashed lines in the figures; the point of intersection is the optimum VIS-IR threshold.

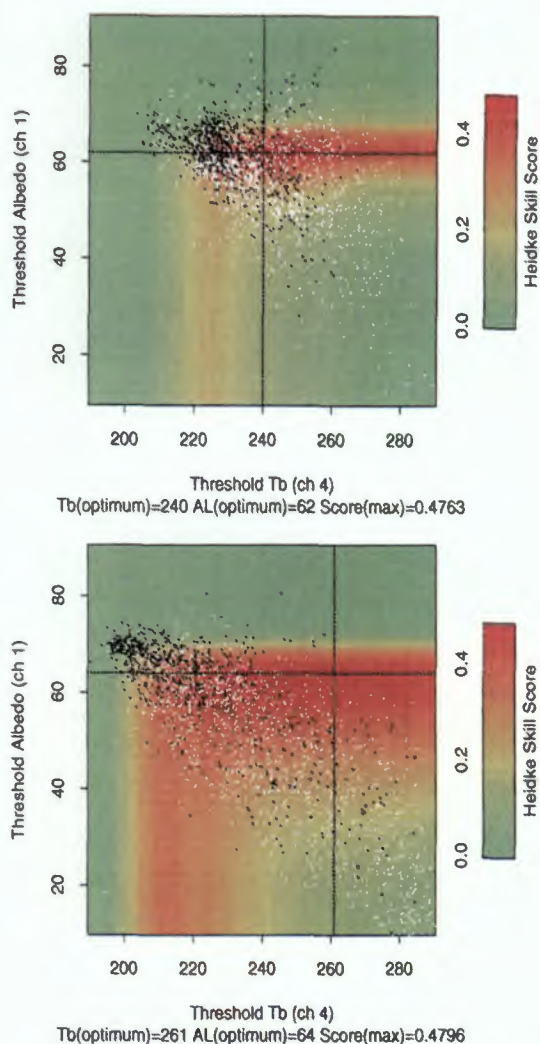


Figure 1: Heidke Skill Score optimization for critical rain rate of 5 mm/h during the period 15 - 21 October 1996. Score is calculated for various thresholds of IR brightness temperature and VIS albedo. Results are shown for midlatitudes (top), and tropics (bottom). Optimum combined thresholds (indicated by dashed lines) are IR temperature of 240 K and albedo of 62 percent in midlatitudes, and 261 K and albedo of 64 percent in tropics. Black data points represent rain rates greater than 5 mm/h, white points represent lighter amounts.

Several important features are evident in these figures. First, we see that visible data adds information (skill) pertaining to rainfall in both regions. This is confirmed by the fact that the scores are consistently higher at AL = 60 percent for most values of TB than at the bottom edge of the figure (which corresponds to an IR-only rain flag). Also, we can see that for this dataset a VIS-only method is more effective in flagging rain cells than an IR-only method. Second, there is a marked difference in the figures, due to a difference in the joint distribution of AL and TB. In the tropics, in scenes containing more reflective pixels (AL \geq 60 percent), there are very few warm pixels. Since most of these bright pixels are also cold, varying the TB threshold from 240K to 300K has almost no effect on the score, when the AL threshold is greater than or equal to 60 percent. The midlatitude distribution of AL and TB differs in that some pixels with AL approximately equal to 60 percent are also those with TB between 240K and 270K. When matched with the SSM/I rain data this means that one sees improved skill for an AL threshold of 62 percent, when the TB threshold is reduced from 270K to 240K. Finally, it is evident from the scatter diagrams that there is no clear separation between light and heavy rain: black and white points overlap to a large extent. That is the reason why the Heidke skill score is not large, even for the optimum threshold. (See additional discussion in following section.)

Table 1: Optimum thresholds as a function of week and critical rain rate. Note that the last week contains 5 days.

Time Period	0-30N			
	RR > 5		RR > 10	
	TB	AL	TB	AL
15Oct-21Oct	261	64	225	66
22Oct-28Oct	248	65	219	66
29Oct-02Nov	233	64	232	68
All Data	276	64	229	66

Time Period	30N-60N			
	RR > 5		RR > 10	
	TB	AL	TB	AL
15Oct-21Oct	240	62	228	63
22Oct-28Oct	249	61	242	62
29Oct-02Nov	227	61	212	61
All Data	240	62	230	63

The optimum VIS-IR thresholds were derived in a similar manner to those above for both critical rain rate categories (5 and 10 mm/h), and for each week. These results for both midlatitudes and tropics are contained in Table 1. In all categories, the optimum albedo thresholds are quite stable from week to week, varying by only 1 or 2 percent within a category. Albedo thresholds in the tropics seem to be marginally higher than those in the midlatitudes, and also exhibit the expected tendency of being generally higher at 10 than at 5 mm/h. Optimum

TB thresholds are more variable in each category. For example, in the tropics the thresholds associated with 5 mm/h decreases by nearly 30 degrees K from the first week to the last. There is no clear trend over the 3-week period, with some categories showing increases, and others showing decreases. Part of the variability may be associated with reduced sample sizes in the last period (see the parameter NR in Tables 2 and 3). Like albedo, the optimum TB thresholds vary with rain rate as expected - in this case, however, decreasing with increasing rain rate.

We then applied the optimum thresholds found for the first week of data (bold face in Table 1) on the data in each of the 3 weeks studied. These results are shown in Tables 2 and 3, which contain the metrics HSS, POD, FAR, and NR (number of raining points). For comparison, the HSS corresponding to the optimum thresholds of that week's data are also included in parentheses, showing the highest score achievable using the threshold approach.

Table 2: Rain Flag verification scores in the region 30N to 60N as a function of week and critical rain rate. See text for variable definitions. Scores are based on using optimum AL and TB thresholds found from dependent data (15 Oct - 21 Oct). The HSS corresponding to the optimum thresholds of that week's (dependent) data are also included in parentheses.

Time Period	30N-60N			
	RR > 5 mm/h			
	NR	HSS	POD	FAR
15 Oct - 21 Oct	651	.48(.48)	.53	.56
22 Oct - 28 Oct	542	.32(.34)	.30	.64
29 Oct - 2 Nov	317	.29(.35)	.47	.78

Time Period	30N-60N			
	RR > 10 mm/h			
	NR	HSS	POD	FAR
15 Oct - 21 Oct	282	.45(.45)	.51	.59
22 Oct - 28 Oct	207	.13(.25)	.12	.85
29 Oct - 2 Nov	113	.25(.36)	.48	.83

In general, the rain flag performs worse at the end of the study period than during the first week as defined by all 3 metrics. However when the rain flag is evaluated relative to its theoretical "optimum", that is comparing the HSS to the value in parentheses, we see that the declining scores are due more to limitations in the 2-channel method, than to a problem of retuning.

In many applications, such as the one presented below, it is important to eliminate the points that are contaminated by heavy rain, but it is less important to retain all the uncontaminated points because the data density is very high. Fig. 2 shows that, despite a relatively low

Table 3: Rain Flag verification scores in the region 0 to 30N as a function of week and critical rain rate. See Table 2 for details.

Time Period	0-30N			
	RR > 5 mm/h			
	NR	HSS	POD	FAR
15 Oct - 21 Oct	700	.48(.48)	.50	.53
22 Oct - 28 Oct	673	.51(.52)	.60	.54
29 Oct - 2 Nov	259	.43(.44)	.49	.61

Time Period	0-30N			
	RR > 10 mm/h			
	NR	HSS	POD	FAR
15 Oct - 21 Oct	266	.41(.41)	.57	.68
22 Oct - 28 Oct	256	.41(.42)	.66	.70
29 Oct - 2 Nov	60	.21(.26)	.47	.86

HSS, the threshold method is able to detect almost 100% of the points with very high precipitation, with a low rate of false alarms for light precipitation.

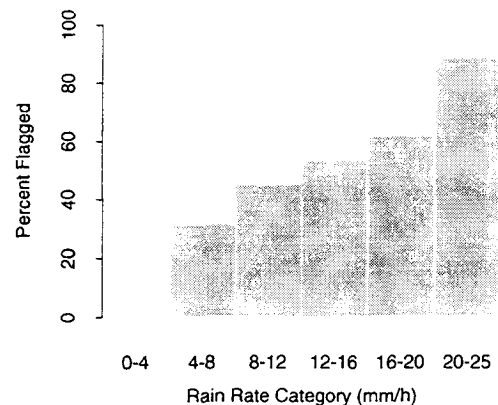


Figure 2: Percentage of points rain-flagged as a function of rain rate category for midlatitudes for period 15 - 21 October 1996. IR temperature and albedo thresholds used corresponded to a critical rain rate of 5 mm/h.

3. RAIN FLAG APPLICATION TO NSCAT DATA

3.1 Approach

To assess the impact of rain on the quality of scatterometer-derived winds, we compare surface wind analyses created with and without rain-flagged data. In this work, a variational approach is used to combine ambiguous scatterometer winds with a background estimate of the wind field. The best fit to the NSCAT data and other constraints determines the optimal analysis. A complete discussion of our variational method is contained in Hoffman (Ref. [12]).

Twelve analysis times were chosen during the three week period of this study. The analyses were created on a 1° resolution grid over the North Atlantic; 270E to 360E (90W to 0W) longitude and 0 to 60N latitude. ECMWF analyses at 1200 UTC are used as the background or first guess fields and all available NSCAT data within 3 h of the analysis time are selected.

To accommodate rain-flagging, GOES-8 IR brightness temperature and albedo were first collocated with NSCAT wind vector cells (WVC). These NSCAT wind vectors were retrieved at 50 km resolution using the NSCAT1 model function. GOES-8 and NSCAT data are collocated to within 30 min and 0.25° latitude and longitude. Most collocations are within 15 min since we generally have GOES data every 30 min. For cases presented here, the optimum mid-latitude threshold values for a critical rain rate of 5 mm/h are used (TB < 240 K, AL > 62%).

The number of NSCAT WVCs flagged for rain in these 12 cases. A small percentage (0.5-2%) of WVCs are flagged in each case. In most cases, flagged WVCs occur in groups and coincide with bright, cold clouds associated with synoptic fronts or tropical convection.

3.2 Results

Two cases are presented here to illustrate the effects of withholding flagged scatterometer winds on surface wind analyses. These cases demonstrate moderate to high impact on the analyzed wind field compared to the other 10 cases.

3.2.1 Synoptic Front

The scatterometer passed over part of a synoptic cold front in the middle North Atlantic (45W, 30N) at 1417 UTC 16 Oct 1996. Fig. 3 (bottom left) shows analyses

using rain flagged data (black barbs) and excluding rain flagged data (red barbs). Away from the front, where no data are flagged, the two analyses are essentially identical. In the vicinity of the front, the analyses differ by up to 4 m/s (vector wind difference). Excluding raining points along the front changes both wind speed and direction. The transition from northwest flow behind the front to southwest flow parallel to the front is smoother, both in speed and direction, in the analysis which excludes flagged data.

Beneath suspected raining points, analyzed wind speeds are reduced by 1 – 2 m/s when flagged data are excluded. Fig. 3 (bottom right) shows a close-up of NSCAT ambiguous winds in the vicinity of the front. The excluded data have higher wind speeds than either surrounding scatterometer winds or the background analysis (not shown). Note that ambiguous wind speeds ahead and behind the front are ≤ 7 m/s, while in suspected raining areas, ambiguous wind speeds are roughly doubled (7 – 15 m/s). The wind directions for a number of the excluded data are also in disagreement with surrounding scatterometer winds and the background analysis. Southerly winds can be seen in the ambiguous winds in Fig. 3 (bottom right) which do not agree with the southwesterly winds elsewhere in the scatterometer data and background analysis. When these data are included, the analyzed winds back to the south and the wind shift is more abrupt.

Similar results were found along synoptic fronts in two other cases: 15 Oct and 31 Oct 1996 (not shown).

3.2.2 Tropical Convection

The scatterometer measured winds at the edge of a convective region in the tropical Atlantic (48W, 9N) at 1424 UTC 27 Oct 1996. As commonly found in this area, the wind field is characterized by fairly uniform easterlies. This simple flow regime helps highlight the effect of the data on the analyzed winds.

As in Fig. 3 (bottom left), Fig. 3 (top left) shows two surface wind analyses, one with (black) and one without (red) rain flagged data. As in the previous case, the analyzed winds are reduced by up to 4 m/s (vector wind difference) in the vicinity of excluded data. Elsewhere, the surface winds are unchanged. The scatterometer winds where rain is suspected stand in contrast to surrounding scatterometer observations and the background wind field (see Fig. 3 (top right)). Observed wind speeds are ~ 5 m/s greater and the wind direction of the ambiguities closest to the presumed easterlies is from the southeast. As expected, when these data are included in the analysis, the analyzed wind speed increases and a southerly component is introduced.

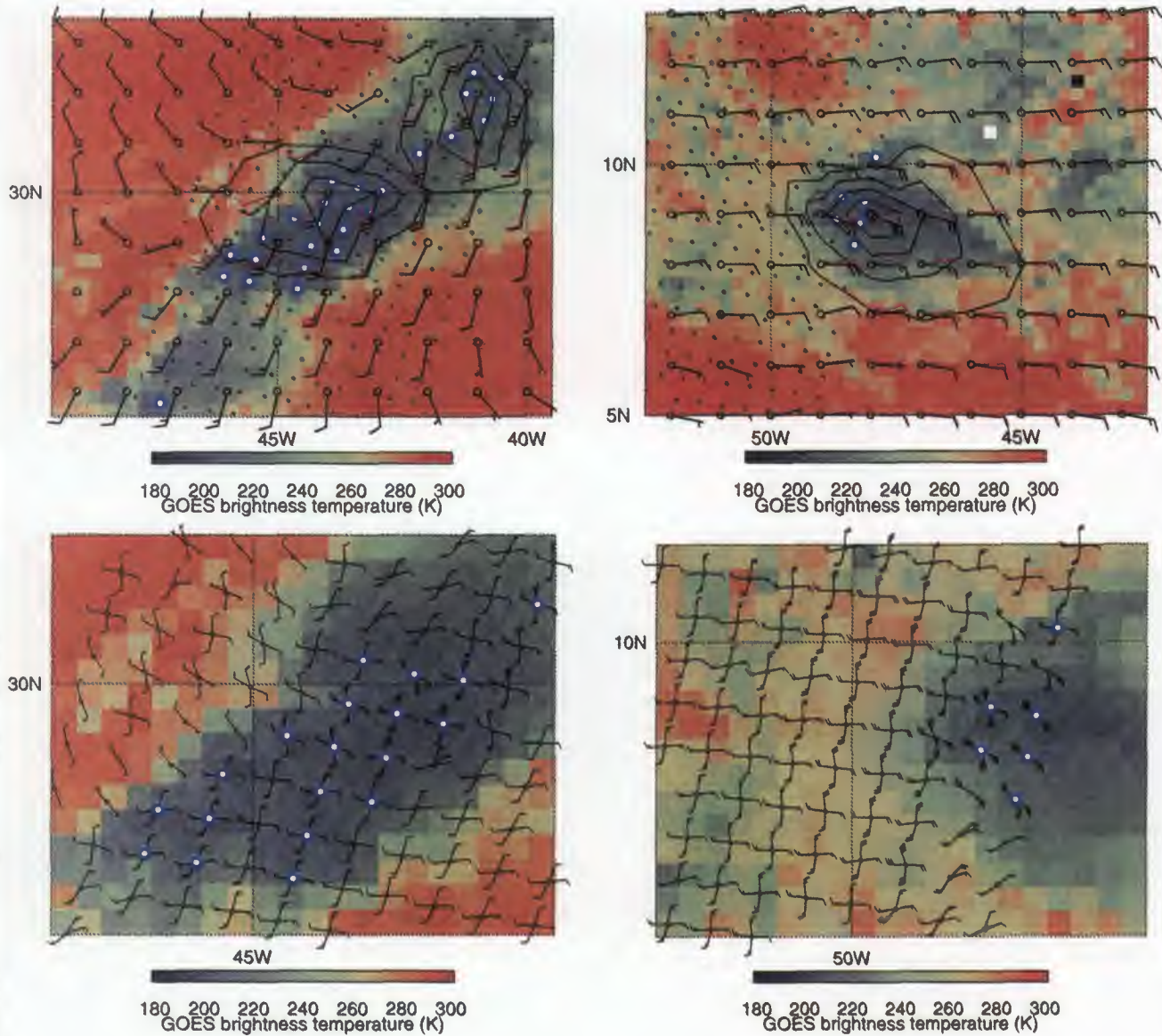


Figure 3: Surface wind analyses with GOES IR brightness temperature (K) for cases of (left column) synoptic front 1415 UTC 16 Oct 1996, and (right column) tropical convection 1415 UTC 27 Oct 1996. Two wind analyses are plotted in each: 1) rain flagged data included in analysis (black) and 2) rain flagged data excluded from analysis (red). Full wind barbs are 10 knots. The vector wind speed difference between black and red analyses is contoured every 1 m/s. NSCAT wind vector cells flagged for rain rate > 5 mm/h are denoted by blue bulls eyes. Bottom row contains close-up of 50-km scatterometer wind ambiguities near rain flagged points in shown in top row.

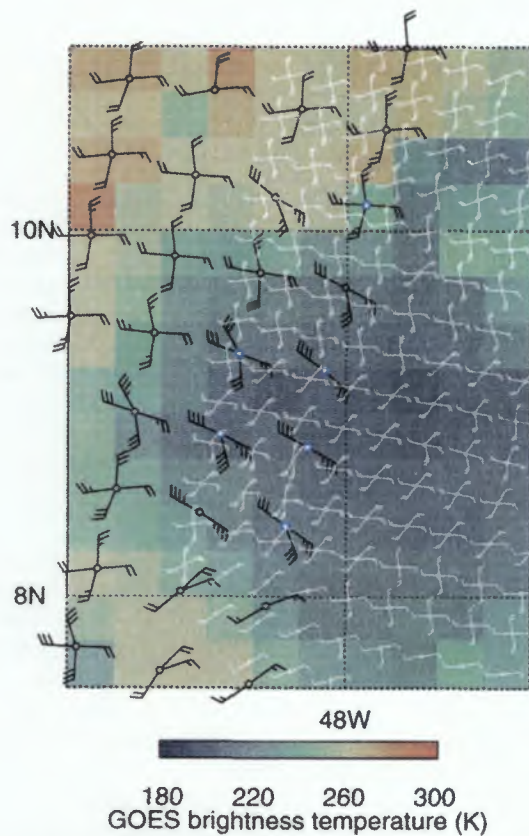


Figure 4: Collocated ERS-2 and NSCAT data for the case of tropical convection shown in Fig. 3 (top right). ERS-2 wind ambiguities (white barbs) valid 1325 UTC 27 Oct 1996, and NSCAT ambiguities (black barbs) valid 1424 UTC are both plotted on collocated GOES-8 IR data valid 1345 UTC. NSCAT wind vector cells flagged for rain rate > 5 mm/h are denoted by blue bulls eyes. Note the large differences in ERS-2 and NSCAT wind speeds for the coldest IR temperatures.

We gain additional insight into these measurements by examining Fig. 4 which contains collocated data from the European Space Agency (ESA) ERS-2 scatterometer, Version 3 processed by Institut Français de Recherche pour l'Exploitation de la Mer (IFREMER/CERSAT), which was available at nearly the same time (valid at 1325 UTC, approximately one hour earlier than NSCAT). The ERS-2 scatterometer operates at the C-band (5.3 GHz), and is therefore only minimally affected by precipitation effects. We see that outside the areas of coldest IR cloud top temperatures the NSCAT ambiguities (black barbs), and the ERS-2 ambiguities (white barbs) are in very good agreement, with the most likely winds coming from the east or northeast at 10 to 20 knots. However, in the area of locally anomalous NSCAT winds, where wind direction changes to the southeast, and speed clearly increases to between 30 and 40 knots, we see no corresponding speed anomalies in the ERS-2 winds, which remain at approximately 15 to 25 knots. This feature is consistent with

the idea that increased direct backscatter from rain drops within the NSCAT scatterometer beam has resulted in spuriously high retrieved wind speeds. Since the incidence angle (and thus the amount of liquid water in the path) varies with antenna, it is also possible that the retrieved wind direction may be affected. Thus in this case, it would be correct to flag these observations as rain-contaminated.

3.3 Discussion

In both cases shown here, when we remove from the analysis the NSCAT data points that are suspected of contamination by heavy rain, the effect is to reduce the analyzed wind speed. Without independent data, the accuracy of one analysis compared to another cannot be determined. But the explanation for the scatterometer wind speeds and directions in potentially raining areas is somewhat uncertain; excluding the flagged data only removes a small fraction of the the available data and still produces a reasonable analysis.

The relatively high scatterometer wind speeds can be viewed as 1) a feature in the true wind field, 2) an artifact of the scatterometer measurements or 3) a combination of effects. From a meteorological perspective, increased surface wind speeds could simply be the result of a downward flux of momentum. Higher wind speeds are often observed in the vicinity of well-developed fronts or convective areas. From this perspective, the observations are a reflection of the true winds and are therefore valuable information. In this instance, one would want to retain these observations since they reflect the true state of the surface wind field. On the other hand, the observation of increased surface wind speeds may result from rainfall contamination. For example, we expect rain to roughen the sea surface when the winds are light, and a roughened sea state increases backscatter at oblique incidence angles, which ultimately increases the retrieved wind speed. At high wind speeds (>15 m/s), rain can dampen the surface capillary and short gravity waves reducing the measured backscatter, which decreases the retrieved wind speed. Additionally, direct backscatter (attenuation) from rain droplets within the scatterometer beam can also increase (decrease) measured backscatter. These are all effects due to rain and have no relation to the actual wind. It is not clear the extent to which each of these effects is present in the cases examined. In at least one case shown here, the fortuitous availability of collocated ERS-2 scatterometer data implies that the NSCAT winds are higher due to increased direct backscatter. Recent work reported by Smith and Wentz (Ref. [3]) supports the notion that some or all of these effects are present depending on the magnitude of the true wind speed.

The analysis method is such that excluding data points

will give more weight to the background field in those areas. Clearly, if the background field is wrong (a distinct possibility over the tropical oceans), removing the data that is suspected of rain contamination may not improve the analysis. More work is needed to determine whether the expected rain contamination error is larger than the expected background error.

4. CONCLUSIONS AND FURTHER WORK

We have used rain rates derived from SSM/I data to estimate the optimal albedo/black body temperature threshold for a given rain rate. Even though this thresholding method is relatively poor at predicting the instantaneous rain rate, with Heidke skill scores no better than about 0.5, it does detect the heaviest rainfall rates successfully. It is therefore useful as a simple way to flag data points that may be contaminated by heavy rain, especially when false alarms are not too important. The difference in the optimal threshold between the tropics and the higher latitudes is not very large. The variation with time appears larger, but is probably the result of a sampling problem due to the small number of points with heavy rain during some of the studied periods. The results of the threshold method that were presented here are somewhat preliminary. We have focused only on one area of the globe and one season. More work is required before it can be stated with confidence that a single set of thresholds is sufficient for all cases.

We have also used the thresholding method to flag and eliminate NSCAT data points that are suspected to be contaminated by heavy rain. The number of rain-flagged wind vector cells is small and localized. The impact of excluding the rain-contaminated winds is generally < 5 m/s and localized ($< 5^\circ$ of longitude and latitude). In some cases, the effect of excluding just 1-5 raining points can change the resulting analysis significantly, because their placement is critical for defining the flow along a front or some other shear-dominated environment.

Because of lack of independent wind data we cannot say, at this stage, whether eliminating flagged data from the NSCAT wind analyses is always beneficial. It depends, at least in part, on the analysis method and the accuracy of the background field used in the analysis. More work is needed in evaluating the magnitude of the expected error due to rain contamination, and comparing it to the expected background field error. Further comparison of the analyses with independent in situ wind data from ships or buoys, or with collocated satellite observations such as the ERS scatterometer would be most valuable. For NWP applications, the impact on forecast skill is the most critical aspect. Impact studies in an NWP setting using the scatterometer data and several

rain-flagging schemes should be conducted.

5. ACKNOWLEDGMENTS

This work was supported under NASA contracts NAS5-918 and NAS7-1260. The NSCAT data were obtained from the NASA Physical Oceanography Distributed Active Archive Center at the Jet Propulsion Laboratory/California Institute of Technology. We also thank Frank Wentz and Remote Sensing Systems, Inc. for providing the gridded SSM/I rain rate data. IFREMER and ESA supplied the ERS-2 data.

References

- [1] T. H. Guymer, J. A. Businger, W. L. Jones, and R. H. Stewart. Anomalous wind estimates from the SEASAT scatterometer. *Nature*, 294:735-737, 1981.
- [2] Michael Spencer and Masanobu Shimada. Effect of rain on Ku-band scatterometer wind measurements. In *Proceedings of the 1990 International Geoscience and Remote Sensing Symposium (IGARSS '90)*. IEEE, New York, 1990.
- [3] D. K. Smith and F. J. Wentz. NSCAT wind retrieval within high rain events. In *American Geophysical Union-1998 Spring Meeting*, Boston, Massachusetts, 25-29 May 1998.
- [4] Frank J. Wentz. Measurement of oceanic wind vector using satellite microwave radiometers. *IEEE Trans. Geosci. Remote Sens.*, 30:960-972, 1992.
- [5] E. Smith and Coauthors. Results of WetNet PIP-2 project. *J. Atmospheric Sciences*, 55:1483-1536, 1998.
- [6] E. C. Barrett and D. W. Martin. *The Use of Satellite Data in Rainfall Monitoring*. Academic, New York, 1981.
- [7] P. A. Arkin. The relationship between fractional coverage of high cloud and rainfall accumulations during GATE over the B-scale array. *Mon. Wea. Rev.*, 107:1382-1387, 1979.
- [8] C. Grassotti and L. Garand. Classification-based rainfall estimation using satellite data and numerical forecast model fields. *J. Applied Meteor.*, 33(2):159-178, 1994.
- [9] A. J. Negri and R. F. Adler. Infrared and visible satellite rain estimation. Part I: Grid cell approach. *J. Climate Appl. Meteor.*, 26:1553-1564, 1987.
- [10] Elizabeth E. Ebert, editor. *Results of the Third Algorithm Intercomparison Project (AIP-3) of the Global Precipitation Climatology Project (GPCP)*, Melbourne, Australia, 27-30 March 1995.
- [11] C. A. Doswell, III, R. Davies-Jones, and D. L. Keller. On summary measures of skill in rare event forecasting based on contingency tables. *Wea. Forecast.*, 5:576-585, 1990.
- [12] R. N. Hoffman. SASS wind ambiguity removal by direct minimization. II: Use of smoothness and dynamical constraints. *Mon. Wea. Rev.*, 112:1829-1852, 1984.

NEURAL NETWORK WIND RETRIEVAL FROM ERS-1 SCATTEROMETER DATA

P. Richaume^{1,*}, F. Badran², M. Crépon¹, C. Mejía¹, H. Roquet³, S. Thiria¹

¹ Laboratoire d'Océanographie Dynamique et Climatologie, Université Paris VI, Paris, France

² Chaire de Recherche Opérationnelle, CNAM, Paris, France

³ Météo-France SCEM/CMS, Lannion, France

ABSTRACT

This paper presents a neural network methodology to retrieve wind vectors from ERS1 scatterometer data. First a neural network (NN-INVERSE) computes the most probable wind vectors. Probabilities for the estimated direction are given. At least 75 % of the most probable wind directions are consistent with ECMWF winds (at $\pm 20^\circ$). Then the remaining ambiguities are solved by an adapted PRESCAT method, which uses the probabilities provided by NN-INVERSE. Several statistical tests are presented to evaluate the skill of the method. Its good performance is mainly due to the use of a spatial context and to the probabilistic approach for estimating the direction. Comparisons with other methods are also presented. The good performance of the neural method suggests that self-consistent wind retrieval is possible.

1. INTRODUCTION

We present a Neural Network method for retrieving wind fields from ERS-1 scatterometer measurements, called σ_0 (sigma naught). A scatterometer is an active microwave radar that measures the ocean roughness for different geometry of observation, incidence angle θ and azimuth χ . Because this roughness is mainly due to the wind stress on the ocean surface, the σ_0 space contains the wind information: speed and direction (see [15] for a full description). The wind retrieval consists in determining the wind parameters given swath of σ_0 cells. This is a difficult inverse problem since the processes are highly non-linear and non-injective. Thus, it is first necessary to model the multiple wind solutions that may occur for the same measurement and then to decide which solution corresponds to the truth. The former refers to the inversion of the process, whereas the latter refers to the removal of ambiguities.

We use a neural network methodology based on the study of Thiria *et al.* [17]. It consists of two separate phases: a first one inverts the ERS-1 measurements with neural networks and provides ambiguous wind vectors (NN-INVERSE), and a second one removes the wind direction ambiguities with an adapted version of an existing algorithm.

The major difference with the usual methods is that NN-INVERSE is a transfer function mapping the wind vector from the σ_0 that models directly the inverse process. The existing methods use a GMF (Geophysical Model Function) [8,14] that models the forward process (e.g. estimates σ_0 given the wind parameters). Thus, they require minimisation between observed and estimated σ_0 at each measurement in order to retrieve the set of possible wind parameters [3,10,13,15,16]. As opposite to this, NN-INVERSE is an explicit model represented by an algebraic function that does not require such minimisation. The NN-INVERSE model estimates directly the set of possible wind parameters given the σ_0 .

2. THE NN-INVERSE MODEL

We use similar architectures as described in [17]. Since the σ_0 measurements strongly depend on the incidence angle θ , the n tracks of the swath are inverted separately. The NN-INVERSE model is made of n modules M_i , ($i = 1 \dots n$) which extract the wind vector from σ_0 . On each track i , the inverse problem is split into two sub-problems leading to the determination of two distinct transfer functions: a transfer function denoted $S\text{-}NN_i$ estimates the wind speed and a second transfer function denoted $A\text{-}NN_i$ estimates azimuth probabilities given the σ_0 triplets and the estimated wind speed. We approximate these $2*n$ transfer functions by using multilayer perceptrons (MLP) [2] since these models are universal approximators [4][5]. The full wind retriever is shown in Fig. 1.

To take advantage of the information embedded in the spatial consistency of the wind field at the scatterometer scale [17], the inputs of the neural networks $S\text{-}NN$ and $A\text{-}NN$ consist of a set of σ_0 cells centred on the analysed one (Fig. 2a) [6]; we denote $G(\sigma_0)$ this input data set. The size and the shape of the neighbourhood we deal with represent an adequate trade-off between the performances and the number of parameters to be estimated during the modelling phase (the so-called learning phase).

Intrinsic errors in the most probable wind directions can remain due to the characteristics of the problem. In most cases they appear as inverted directions at $\pm 180^\circ$. These

* Corresponding author. E-mail: philippe.richaume@cesbio.cnes.fr; prich@lodyc.jussieu.fr

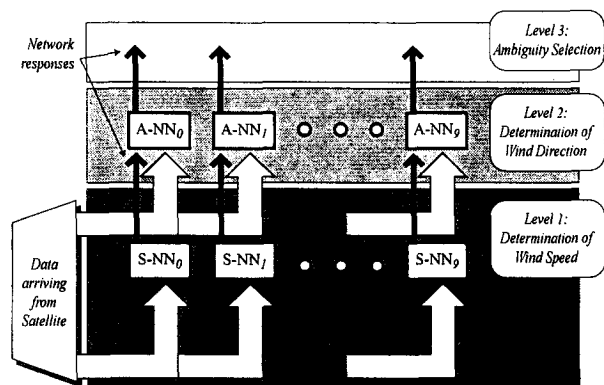


Fig. 1: Architecture of the full NN-INVERSE model showing the connection between $S-NN_i$ and $A-NN_i$.

ambiguities are removed by a third level, which uses the probability of the different aliases provided by $A-NN$.

2.1 Wind speed determination (S-NN)

$S-NN_i$ estimates the wind speed at each cell of the i^{th} track using $G(\sigma_0)$ at the corresponding point. It is a fully connected 4 layered MLP (Fig. 2b). The input layer is composed of 13×3 neurons which represent the 13 different triplets of the spatial window $G(\sigma_0)$. The output layer has a unique linear neuron that estimates the wind speed. The two hidden layers have 26 neurons each with sigmoidal transfer function. Near the edges of the swath adapted non-symmetric spatial windows $G(\sigma_0)$ are defined.

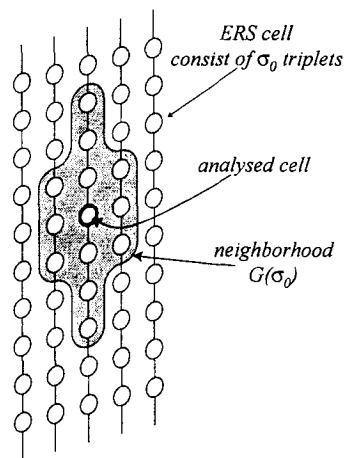
2.2 Wind direction determination (A-NN)

$A-NN_i$ is a fully connected 4 layered MLP (Fig. 2b) which determines the wind direction using $G(\sigma_0)$ and the wind speed \hat{v} estimated by $S-NN_i$. It possesses an input layer of $13 \times 3 + 1$ neurons ($G(\sigma_0)$ and \hat{v}) and two hidden layers of 25 neurons each. According to [17], the $A-NN_i$ has 36 outputs each one providing the posterior probabilities of the associated interval of azimuth, $p(\chi | G(\sigma_0), \hat{v})$. These probabilities are used in order to determine the four most probable azimuths (aliases) with their associated posterior probabilities. Each alias is determined with an accuracy of $\pm 15^\circ$ by computing the expected value of 3 adjacent intervals and combining them.

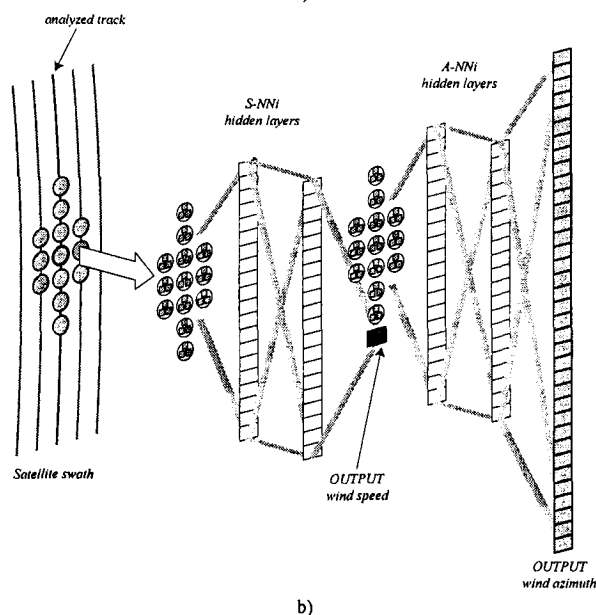
The $S-NN_i$ and $A-NN_i$ models have 1405 and 2616 parameters which are respectively estimated from a learning set. These parameters are determined by minimising a quadratic cost function:

$$C(W) = \sum_k |S_k - Y_k|^2$$

where S_k represents the output computed by the MLP and Y_k the reference output provided by the corresponding data set, the summation being taken on the dedicated learning set. This cost function is simple and sufficient to obtain directly an approximation to the wanted probabilities [12].



a)



b)

Fig. 2: a) Spatial context used for the determination of the wind speed and the wind direction; b) the two stage neural network inversion.

This modelling phase is done once and for all and for each MLP. When using NN-INVERSE, wind parameters are directly computed by applying the associated MLP functions to observations.

3. THE DATA SET

The parameters of the different MLP were computed from ERS-1 scatterometer σ_0 collocated with ECMWF wind vectors interpolated by CERSAT/IFREMER (I-ECMWF hereafter). The data period extends from July 94 to April 96 onto the North Atlantic Ocean, on an area of (100W, 5W) of longitude and of (60N, 20 N) of latitude. The overall data set used consists of approximately 390000 collocated pairs ($G(\sigma_0)$, (v, χ)) for each track; (v, χ) represents the speed and the azimuth of wind at the centre of $G(\sigma_0)$. For each MLP, the learning set (LEARN) is made of about 24000 pairs. The distribution we use is Quasi Uniform for wind vectors

track	0	2	4	6	8	9
bias (m/s)	-0.2	-0.1	-0.1	-0.1	0.0	0.0
RMS (m/s)	1.6	1.5	1.6	1.6	1.6	1.7

Table 1: Performances of NN-INVERSE (S-NN) when approximating the wind speed: the first row gives the error bias with respect to the track and the second gives the RMS error with respect to I-ECMWF speeds.

Track	0	2	4	6	8	9
1 (%)	78.4	79.3	78.1	73.7	71.4	66.3
1+2 (%)	85.1	86.9	87.5	87.6	88.2	86.9
1+2+3 (%)	86.1	87.6	88.4	88.4	88.8	87.6
1+2+3+4 (%)	86.5	88.0	88.7	88.7	89.1	87.9

Table 2: Agreement of the wind direction retrieval with I-ECMWF. Each row displays the performances reached by A-NN_i for each track *i* and for the most probable solution (first alias denoted 1), the first plus the second alias (denoted 1+2), and so on. A given direction is considered correct if the computed direction matches I-ECMWF direction by less than $\pm 20^\circ$.

in the domain $[0^\circ, 360^\circ] \times [3.5 \text{ m/s}, 25 \text{ m/s}]$. In order to test the performances of NN-inverse we built the QU-TEST test set with the remaining data and having the same statistical characteristics. For full wind fields test, we use another set made of 322 contiguous swaths of collocated ERS1 σ_0 and I-ECMWF wind fields observed in May 1996. This test set is denoted S-TEST and does not contain any observations used for learning.

4. PERFORMANCES OF NN-INVERSE BEFORE DISAMBIGUATION

We present now statistical tests to evaluate the accuracy of the NN-INVERSE model against I-ECMWF winds before removing the ambiguities. These tests are independent of errors due to a bad selection of aliases in the ambiguity removal procedure.

Table 1 shows that the error bias and the RMS error on the wind speed are very low and not dependent of the track, which proves the good quality and the homogeneity of NN-inverse methodology since each track is inverted by using a specific NN model.

The results of Table 2 show the good quality of the first rank solution; the first alias (the wind direction having the highest probability and presented in row 1 of Table 2) given by the NN-inverse matches the I-ECMWF direction at $\pm 20^\circ$ in 75% of the collocations; for the first plus the second alias (presented in row 2 of Table 2) in 87% of the collocations. The skill of usual methods is about 60% [13]. These good performances are mainly due to the spatial context used in the input of the S-NN and A-NN and due to the overall neural network ability to model non-linear phenomena.

5. AMBIGUITY REMOVAL

The ambiguity removal is done by using an adapted version of PRESCAT [16] denoted PRESCAT-NN hereafter. In

PRESCAT-NN, we select the different solutions using a trade-off between the closest NN-INVERSE aliases to the direction of NWP first guess and their probabilities. If the probability of the first alias given by NN-INVERSE is high, then priority is given to it.

6. PERFORMANCES AFTER DISAMBIGUATION AND COMPARISONS WITH OTHER METHODS

We check the performances of the NN-Inverse model after the disambiguation phase and compared them to these of ESA and CERSAT/IFREMER wind products on the S-TEST data set. ESA wind retrieval is based on the CMOD4 GMF [16,14] and CERSAT/IFREMER is based on the CMOD-IFR2 GMF [9,10]. In these comparisons we use exactly the same data for the three methods. When one of the methods does not provide a solution for a given signal the associated wind vectors of the two others are also removed from the test.

We also checked the accuracy of the different inversion methods independently of ambiguity removal errors. For this purpose, as suggested by Stoffelen and Anderson [14], we use a subset of S-TEST, denoted S90-TEST. S90-TEST contains only data where the wind direction of the three products are pointing in the same half plane as defined by the I-ECMWF wind. When one product selects an ambiguous direction, the corresponding three products will be thrown out from S90-TEST. We thus reject data with possible ambiguous direction at 180° from S90-TEST.

Table 3 (Table 4) gives the error bias and standard deviation for the wind speed, the wind direction, the wind vector and the percentage of agreement with I-ECMWF wind direction at $\pm 20^\circ$ (denoted Perf@ 20° in the tables) for S-TEST (S90-TEST). The three first columns show the performances computed on the true distribution of S-TEST (S90-TEST). In the three last ones performances are computed as follows: we first consider five bins of wind speed and compute separately the performances in each bin,

Data Set 71436 data inverse model	S-TEST True Distribution			S-TEST Mean Bin Average		
	NN_INV	CERSAT	ESA	NN_INV	CERSAT	ESA
	Speed Bias (m/s)	0.2	-0.1	-0.7	-0.2	-0.9
Speed Stdv (m/s)	1.4	1.4	1.5	1.6	1.5	1.5
Dir Bias (degree)	-0.2	-0.1	-0.5	-0.1	-0.6	0.7
Dir Stdv (degree)	19.9	28.6	46.5	19.6	25.4	48.8
Vector Bias (m/s)	0.2	0.3	0.4	0.7	1.2	1.7
Vector Stdv (m/s)	2.8	3.4	4.9	3.4	3.8	6.7
Perf @ 20° (%)	88.9	82.0	77.4	87.8	82.8	77.4

Table 3: Performances of the different inversion methods on S-TEST; in **bold** the best performances.

Data Set 69133 data inverse model	S90-TEST True Distribution			S90-TEST Mean Bin Average		
	NN_INV	CERSAT	ESA	NN_INV	CERSAT	ESA
	Speed Bias (m/s)	0.2	-0.1	-0.7	-0.3	-1.0
Speed Stdv (m/s)	1.3	1.4	1.4	1.4	1.5	1.4
Dir Bias (degree)	-0.8	-0.9	-0.6	-0.5	-1.1	0.6
Dir Stdv (degree)	14.2	16.3	43.4	14.2	15.6	46.7
Vector Bias (m/s)	0.2	0.3	0.4	0.8	1.1	1.7
Vector Stdv (m/s)	2.3	2.5	4.6	2.9	3.0	6.4
Perf @ 20° (%)	89.2	84.4	78.9	88.3	84.8	78.5

Table 4: Performances of the different inversion methods on S90-TEST; in **bold** the best performances.

later we average these performances in order to give the same weight to each wind speed interval.

In Table 3, the performances are computed after the ambiguity removal and averaged on the 10 tracks. We took the wind vectors given by PRESCAT-NN and the dealiased wind vectors distributed by CERSAT and by ESA. Table 3 displays results in terms of wind vector error statistic estimation (bias and standard deviation) for the three methods and shows that NN-inverse compares nicely with the other methods. We also remark that the standard deviation for the wind speed and wind direction agree with the specifications of ESA, which are ± 2 m/s and $\pm 20^\circ$. NN-inverse is the only method that fulfils these specifications for the wind direction. Moreover, one remarks that the mean bin average performances of NN-inverse are less deteriorated than others, stressing the importance of the quasi-uniform distribution used when learning. We also notice, in this case, that the standard deviation of wind direction and Perf@20° improve showing that at high wind speed the stability of wind direction is strengthened and is measured better by scatterometer.

Comparison between results of Table 3 and Table 4 shows that global performances of NN-INVERSE do not increase very much, but they still appear better than the two others. This is due to the high quality and accuracy of the first rank solution of NN-INVERSE that gives a considerable help to the ambiguity removal. For CERSAT product, the increase of performances is very clear and the good overall score suggests that CMOD-IFR2 is a quite accurate GMF but that the ambiguity removal scheme is weak. Nevertheless, this

could also be explained by the advantage of using spatial context rather than a one cell inversion. Whatever the accuracy of inversion and the skill of the ambiguity removal are, it will not be able to retrieve a good wind field if there are not sufficient well oriented winds (first rank alias).

CONCLUSION

This paper presents a Neural Networks methodology to retrieve the wind vector from ERS1 scatterometer data. The inversion of scatterometer data leads to complex transfer function that may give several values for the direction. The performances of the Neural Network methodology are very good especially for the wind direction since the NN-INVERSE model has a better skill (75%) for the most probable wind direction (rank 1 solution) than the other methods whose skills are about 60% [13]. This clearly shows the improvement of NN-INVERSE with respect to other methods. After disambiguation the correct direction is retrieved with a score of 89%.

Comparison with other methods has been carried out. It appears that the NN have very good skill. The advantages of the neural network method are linked to:

- their ability to model non-linear phenomena without strong assumptions about the forms of the functions and noises involved in the physical processes,
- the possibility to directly estimate the probability of the different wind aliases by using neural networks

working in classifier mode which is of importance for the ambiguity removal phase,

- the possible use, in a simple way, of a spatial context embedding geophysical features which are learned and which improves greatly the performances of the first alias solution and thus the skill of any ambiguity removal algorithm.

In the present study we adapted a version of the PRESCAT algorithm to remove the ambiguities, which uses a meteorological wind field provided by a NWP model as a first guess. The probability estimation of the neural network wind direction is explicitly used as a constraint in this version. Due to the accuracy on the first alias provided by NN-INVERSE method we can envisage a self-consistent Neural Network ambiguity removal method similar to this proposed in [1].

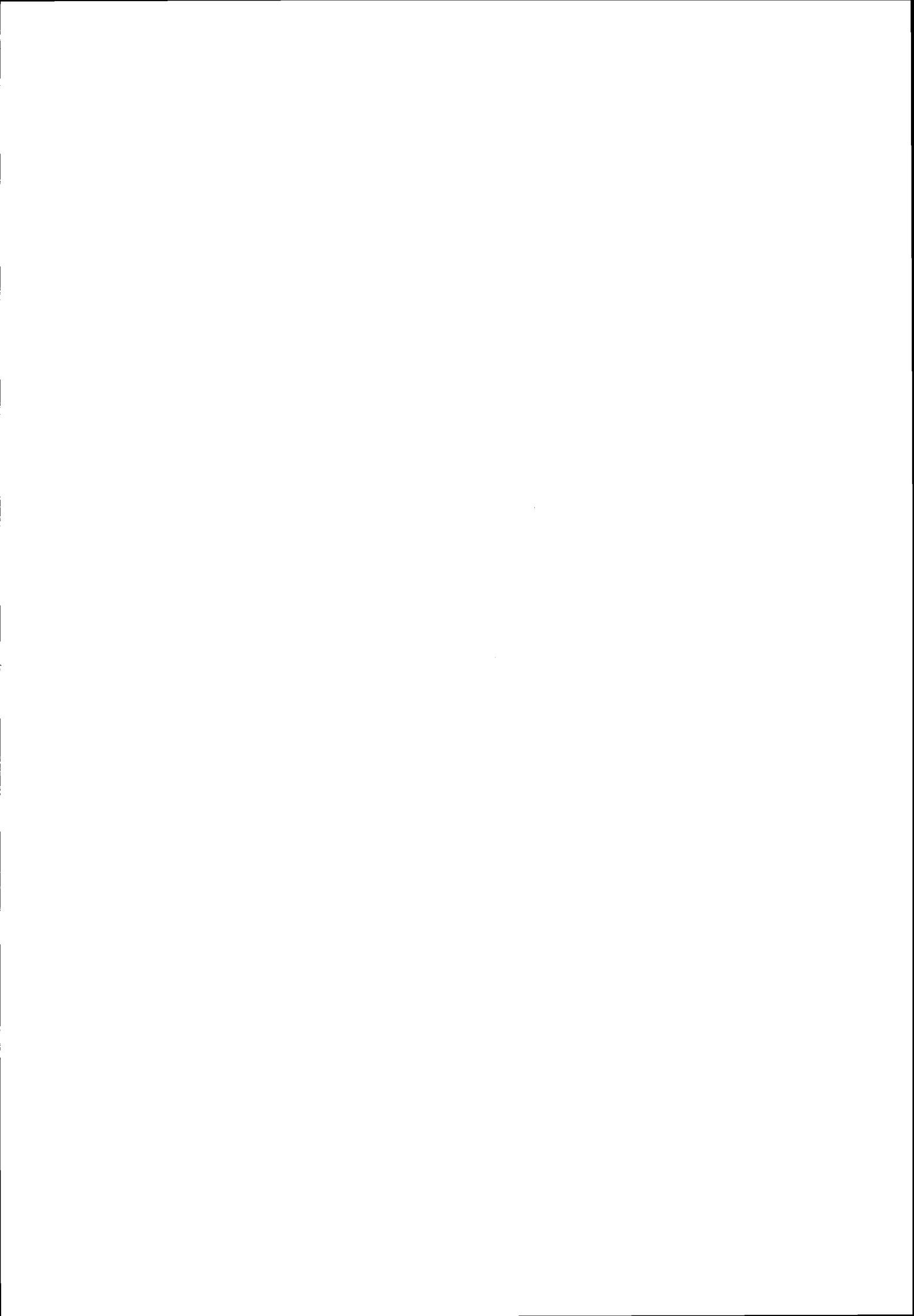
Scatterometer winds are of major interest in geophysics and meteorology [11, 16]. The neural network approach proved to be efficient, accurate, general and re-usable, as for new scatterometers like NSCAT [7] with at most the same performances.

ACKNOWLEDGEMENTS

We would like to thank the CERSAT/IFREMER who provided the collocations between ERS1 σ_0 and the analysed wind vectors of the ECMWF Model. We also thank D. Cornford for stimulating discussions. The present study was supported by the EC program NEUROSAT (ENV4-CT96-0314).

REFERENCES

- [1] Badran, F., S. Thiria, and M. Crépon, Wind Ambiguity Removal by the Use of Neural Network Techniques, *J. Geophys. Res.*, 96, 20521-20529, 1991.
- [2] Bishop, C. M., *Neural Networks for Pattern Recognition*, Oxford University Press, 482 p., 1995.
- [3] Cavanié, A., and D. Offiler; ERS1 Wind Scatterometer: Wind Extraction and Ambiguity Removal, Proc. of IGARSS 86 Symposium, Zurich, (ESA SP-254), 1986.
- [4] H. Hornik, Approximation capabilities of multilayer feed-forward network, *Neural Networks*, Vol. 4, pp 251-257, 1991.
- [5] Leshno, M., V. Ya. Lin, A. Pinkus, S. Schocken, Multilayer Feedforward Networks With a Nonpolynomial Activation Function Can Approximate Any Function, *Neural Networks*, Vol. 6, pp 861-967, 1993.
- [6] Mejia, C., S. Thiria, F. Badran, and M. Crépon, A Neural Network Approach for Wind Retrieval from the ERS-1 Scatterometer Data, in *IEEE Ocean94 Proceedings*, 1, Brest-Sept. 13-16, 1994.
- [7] Mejia, C., S. Thiria, N. Tran, M. CRÉPON, H. Roquet Richaume, F. Badran: The Neural Network GMFs NSCAT scatterometers, Proc. NSCAT SWT meeting, Hawaii, January 1997.
- [8] Mejia, C., S. Thiria, F. Badran, N. Tran and M. Crépon, Determination of the Geophysical Model Function of ERS1 Scatterometer by the use of Neural Networks, In press in *J. Geophys. Res.*, 1997.
- [9] Quilfen, Y. and A. Cavanié, A high precision wind algorithm for ERS-1 scatterometer and its validation, Proc. of IGARSS 91, Espoo, Finland, 873-876, 1991.
- [10] Quilfen, Y. and A. Bentamy, Calibration/Validation of ERS-1 scatterometer precision, Proc. of IGARSS 94, Pasadena, United States, 945-947, 1994.
- [11] Roquet, H. and A. Ratier, Toward direct variational assimilation of scatterometer backscatter measurements into numerical weather prediction model, Proc. of IGARSS 88, Ref ESA SP-284, pp. 257-260, 1988.
- [12] Richard, M. D. and R. P. Lippman, Neural Network Classifiers Estimate Bayesian a posteriori Probabilities, *Neural Computation*, Vol. 3, 461-483, 1991
- [13] Rufenach, C.: Comparison of Four ERS-1 Scatterometer Wind retrieval Algorithms with buoys measurements, *J. Atm. Ocean Tech.*, 304-313, 1998.
- [14] Stoffelen, A and D. Anderson, Scatterometer data interpretation: Estimation and validation of the transfer function CMOD4, *J. Geophys. Res.*, 102, 5767-5780, 1997.
- [15] Stoffelen, A and D. Anderson, Scatterometer data interpretation: Measurement Space and Inversion. *J. Atm. Ocean Tech.*, 1298-1313, 1997.
- [16] Stoffelen, A and D. Anderson, The ECMWF Contribution to the Characterisation, Interpretation, Calibration and Validation of ERS-1 Scatterometer Backscatter Measurements, and Winds, and their use in Numerical Weather Prediction Models, ESA Contract Reports 9097/90/NL/BJ, 1995.
- [17] Thiria, S., F. Badran, C. Mejia and M. Crépon, A Neural Network Approach for Modelling Non Linear Transfer functions: Application for Wind Retrieval From Spaceborne Scatterometer Data, *J. Geophys. Res.*, 98, 22827-22841, 1993.



SATELLITE APPLICATION FACILITIES FOR THE SCATTEROMETER

Ad Stoffelen

KNMI, de Bilt, the Netherlands, Email: Stoffelen@knmi.nl

ABSTRACT EUMETSAT supports the development of Satellite Application Facilities, SAFs, to become an integral part of the satellite ground segment. For scatterometer applications the Ocean and Sea Ice SAF and the Numerical Weather Prediction, NWP, SAF are the most relevant. Although Land and Climate SAFs are under construction, the use of a scatterometer has not yet been considered here. During the life time of ERS-1 and ERS-2 the processing of ERS scatterometer winds has been developed considerably, and many operational centers using scatterometer data followed these developments. In the Ocean and Sea Ice SAF, preparations are made for the wind product of the ASCAT scatterometer on EPS/METOP. A pre-operational product based on the ERS-2 scatterometer is being developed. Quality control and monitoring are essential parts, as well as investigations on ice and sea state sensitivity, ambiguity removal, simulation studies, algorithm development, and documentation. Within the NWP SAF and with support of a EUMETSAT fellowship, future scatterometer systems such as SeaWinds on QuikSCAT and ADEOS-II are being studied. Challenging developments are necessary to use these data in an optimal way.

1. INTRODUCTION

After the launch of ERS-1 much improvement has been made in the interpretation of scatterometer backscatter measurements and a good quality wind product has emerged (Stoffelen and Anderson, 1997a, 1997b and 1997c). The consistency of the scatterometer winds over the swath makes them particularly useful for nowcasting purposes and several examples of the usefulness of the direct visual presentation of scatterometer winds to a meteorologist can be given. In this session of the workshop several presentations demonstrate the added value of scatterometer winds for Numerical Weather Prediction, NWP. Other papers tackle the problems of ambiguity removal or Quality Control, QC, and monitoring that are needed before presentation of the scatterometer wind product to a meteorologist or model.

ASCAT on METOP/EPS uses the same wavelength and measurement geometry as the ERS scatterometer, but is double-sided, resulting in a three-fold coverage. Developments in methodology of interpretation can thus be carried forward from ERS to METOP/EPS. In preparation for METOP/EPS KNMI is developing calibration and validation tools and the wind processing chain within the EUMETSAT Ocean and Sea Ice Satellite Application Facility, OSI SAF. By the end of 1998 KNMI plans to have a prototype processing chain running in near real-time with ERS data. This prototype is based on PRESCAT. Developments on ice screening and ambiguity removal are performed in collaboration with IFREMER. The OSI SAF wind product is further described below.

In order to bridge the gap between the ERS scatterometer series and ASCAT on METOP, the

meteorological community will have to rely on a new scatterometer concept being developed by NASA, SeaWinds. QuikSCAT will be a dedicated SeaWinds scatterometer mission, scheduled for launch in late 1998. NOAA plans to have a near real-time distribution of the data in place by mid 1999. In 2000, ADEOS-II is planned for launch with a copy of the NASA SeaWinds scatterometer on board.

Fortunately, QuikSCAT will have a large data coverage with its swath of 1800 km wide. That part of the swath that contains a similar amount of information on the full near-surface wind vector as that provided at the nodes of the ERS or NSCAT scatterometers, is of similar width than the total swath width of NSCAT or ASCAT. However, the remaining outer and middle parts of the swath will contain less information than for instance the ERS or NSCAT wind vector cells. The "sweet spots" in the swath will have slightly greater ambiguity in the wind domain than the ERS scatterometers (Stoffelen and Anderson, 1997c), and its effect needs to be tested in order to arrive at a practical implementation. Below we describe the developments on SeaWinds planned within the NWP SAF project in more detail.

In collaboration with NASA and with EUMETSAT support, the UK Meteorological Office, KNMI and ECMWF plan to contribute towards an effective interpretation and quality control of the SeaWinds data to the benefit of NWP. Using NSCAT backscatter measurements and collocated winds, a satisfactory geophysical model function for use with SeaWinds has been derived (Wentz and Freilich, 1998). The sensitivity of the NASA scatterometers to rain is of particular concern. Figa and Stoffelen (1998) propose a QC algorithm rejecting many rain points, that will be tested for use with

WP24000: Scatterometer Wind Product Development

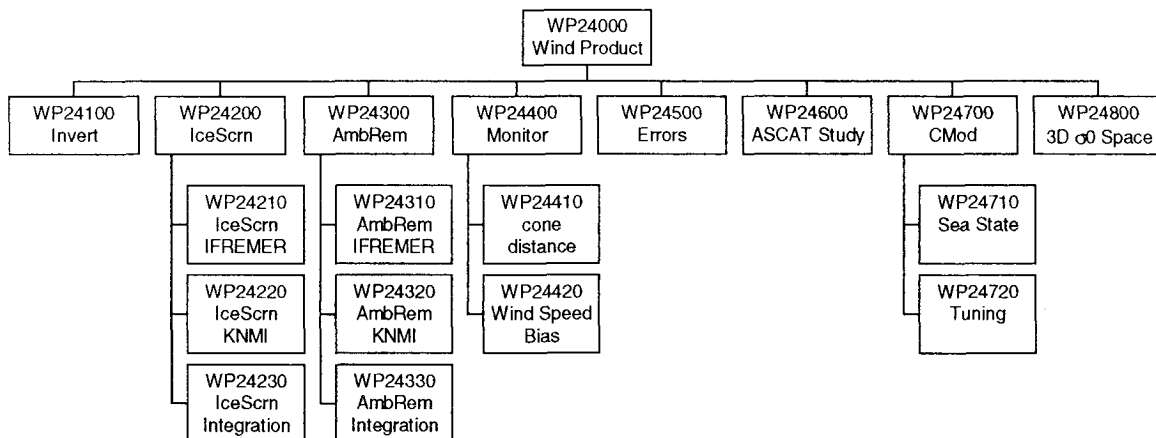


Figure 1 Organization of the Work Packages, WP, of the OSI SAF wind product software developments.

SeaWinds as well. The rotating pencil beam concept facilitates "ocean calibration", but complicates the interpretation and quality monitoring, since this becomes strongly wind vector cell dependent. We believe, however, that the experience and methodologies developed with the ERS and NSCAT scatterometers can be used successfully over most of the SeaWinds swath.

2. OSI SAF Scatterometer Wind Product

The OSI SAF is supported by EUMETSAT and hosted by Météo France. It includes ocean temperature and ice products (Breivik, this volume), developed in co-operation with DNMI, DMI, SMHI, and IFREMER. KNMI is responsible for the OSI SAF wind product and co-operates with IFREMER for its development.

2.1 Scope

The goal of the current project on the OSI SAF wind product is to prepare for ASCAT on METOP/EPS. Processing simulation studies are carried out to support trade-off studies in the design of ASCAT. ASCAT processing, quality control and monitoring tools are developed, based on the methodologies developed for the ERS scatterometers (Stoffelen and Anderson, 1997abc, and Le Meur et al, 1996). New developments on ambiguity removal, ice screening, and sea state sensitivity are initiated. The geophysical model function, GMF, is further refined to include a non-linear wind calibration and a better representation of extreme tropical cyclone conditions. The processing algorithms will be documented. In order to test the operational production of the ASCAT wind product, a near real-time pre-operational ERS scatterometer processing

chain is foreseen from the end of 1998 onwards. A web site at KNMI will visualize the processed winds and their quality monitoring.

2.2 Quality Control and Monitoring

The ERS-2 geophysical validation strategy includes an "ocean" sigma naught calibration procedure as described by Stoffelen (1998a). Moreover, instrument monitoring, see Le Meur et al (1996a), and backscatter QC (Stoffelen and Anderson, 1997a) results in a product with a well characterized quality. Moreover, the spatial error correlation characteristics have been investigated (Stoffelen, 1996). It can not be stressed too often that a few low quality observations may destroy the beneficial impact of many good quality observations, and that Quality Control and Monitoring are essential for NWP. In the OSI SAF the QC will be extended to include a measure of the local ocean surface anisotropy of radar backscattering. By comparing to NWP model winds the QC will be refined. The monitoring scheme implemented at ECMWF will be adopted (Le Meur et al, 1996a).

2.3 Ice Screening

At IFREMER much experience exists on the interpretation of backscatter measurements over ice. Several parameters are known to be correlated to ice parameters, and other combinations of these parameters are unlikely over ice. On the other hand, the distance to the cone is related to the likelihood of a node to be a water surface (Stoffelen and Anderson, 1997a). As such, from the triplet of backscatter measurements at each node some information may be derived on the ice or wind properties. Moreover, when past scatterometer data are used as well, than the combination of

several azimuth and incidence angles in a certain area may reveal sufficient information for the exclusion of ice points, or the acceptance of ocean points in the wind product. IFREMER will use their experience to develop an ice screening subroutine along these lines.

Cross sections in the 3D measurement space reveal a distinction between ice and ocean points (figure 2). In fact, much of the distinction is lost when only an isotropy parameter, and/or a derivative of the backscatter with respect to incidence angle is computed. The distance to the wind cone provides the probability of a water surface. Similarly, a distance to the ice "line" could be computed that provides a measure of the ice probability. Cavanié et al (1998) derived an empirical ice model that may be representative for such an ice "line" in the 3D measurement space. Again, since ice surfaces are generally stationary, an ice parameter history could be kept on a map, in order to constrain the ice likelihood to a very small sub-space of the 3D measurement space. When we succeed, ice screening becomes very effective. Of particular concern for the ice screening routine are melt and freeze processes, including percolation. In the context of the OSI SAF, the effectiveness of the 3D measurement space approach will be investigated, and, if effective, it will be included in the ice screening algorithm.

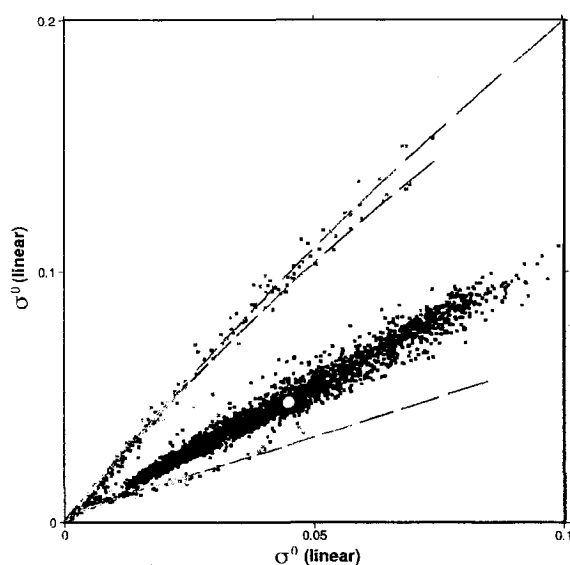


Figure 2 Cross section in 3D measurement space for triplets over ice and open water for node 15 and south of 55S. Only triplets for which the ECMWF sea surface temperature is below 0 °C are black; other triplets are assumed to be over open water and gray-scales according to wind speed. The gray lines indicate the cross-section with the CMOD4 cone surface. The white dot depicts a particular local ice type inferred from recent data. Whereas wind triplets lie along the cone, ice triplets are located closely to a line, and locally, if stationary, close to a point.

2.4 *Wind Tuning*

The results of a wind calibration method taking into account the error characteristics of *in situ*, satellite and model winds by Stoffelen (1998b) has been used to estimate the wind biases of the scatterometer with respect to *in situ* winds. Scatterometer winds delivered by PRESCAT are found to be approximately 5% low, and a small non-linear correction was found as well. The random ERS scatterometer wind component error is estimated to be 1.8 m s⁻¹ and spatially uncorrelated. For extreme winds, such as those found in tropical cyclones, little reliable validation data has been available in the past. Recently, C-band scatterometer aircraft campaigns using dropsonde, flight level, and buoy winds for validation, have provided more clear evidence of reduced sensitivity of the radar backscatter to wind for wind speeds above 25 m s⁻¹ (Carswell et al, 1998). The quantitative results will now be used to improve the C-band wind-to-backscatter relationship.

2.5 *Wind-to-backscatter?*

The scatterometer is generally sensitive to two oceanic parameters (Stoffelen and Anderson, 1997a). In off-shore wind conditions and close to atmospheric fronts the scattering seems more isotropic than in the general case. Wave conditions could be the cause for this. The correlation of the two parameters with the two wind components is very good, resulting in a small scatterometer wind error. Nonetheless, the wind error is much larger than the ERS scatterometer detection error, indicating that there are other geophysical parameters than wind playing a role in the interpretation. This is not surprising, since the atmosphere-ocean interface is of great complexity. In the OSI SAF development plan we have foreseen an investigation of the backscatter sensitivity to sea state. We will take into account the fact that the sea state itself is correlated with the 10m wind.

2.6 *2Dvar Ambiguity Removal*

Although ambiguity removal schemes work well in most cases, they fail in the most dynamic situations, where no good quality prior information is available on the direction of the wind. We note that extreme weather events like, e.g., hurricanes are most relevant and continued effort on improving algorithms is important. The variational meteorological analysis methodology is being applied for ambiguity removal (de Vries and Stoffelen, 1998, Schyberg and Breivik, 1998), thereby relying on prior NWP model information. IFREMER is looking into the possibility of a variational ambiguity removal method that is more independent from such prior information.

2.7 ASCAT simulation

Given the error characteristics of the ASCAT instrument, a model for the interpretation of C-band scatterometer data, and a realistic wind spectrum, one may predict the performance of the ASCAT scatterometer by Monte Carlo simulation. It is useful to do this since the wind retrieval errors are non-linearly related to the ASCAT instrument backscatter errors. Moreover, the sensitivity to instrument errors depends on node position. At this point it is interesting to note that the increased backscatter noise, when going from a 50 km to a 25 km footprint is equivalent to the average wind variability on scales between 25 and 50 km. This means that over the ocean the higher resolution is only relevant in situations with above average wind variability.

2.8 Transfer Function Tuning

ASCAT measures at larger incidence angles than ERS SCAT. The tuning software that was used to derive CMOD4 will be revived for use at these larger incidence angles.

2.9 Measurement Space Visualization

A crucial element in the validation and calibration of the ERS scatterometers is the coherence of the backscatter triplets in the 3D measurement space (Stoffelen and Anderson, 1997a). By making cross-sections through this space, the quality of the data can be subjectively verified. The existing visualization software will be upgraded and extended to be ready to deal with ASCAT.

3. NWP SAF

The aim of the NWP SAF is to improve and support the interface between satellite data and products and the European activities in NWP. The NWP SAF consortium is lead by the UK Meteorological Office (UKMO) and has Météo France, ECMWF, and KNMI as partners. UKMO, ECMWF, and KNMI are involved in developments for the scatterometer processing.

The NWP SAF will:

- co-ordinate user requirements for the interfaces between the data assimilation systems of European NWP centers and satellite data and products, and evaluate priorities for meeting these requirements,
- develop satellite data processing modules, including: pre-processing modules, retrieval modules, assimilation modules (including so-called "observation operators"), modules for monitoring, tuning and quality control, and modules for validation of satellite products and of observation operators, and

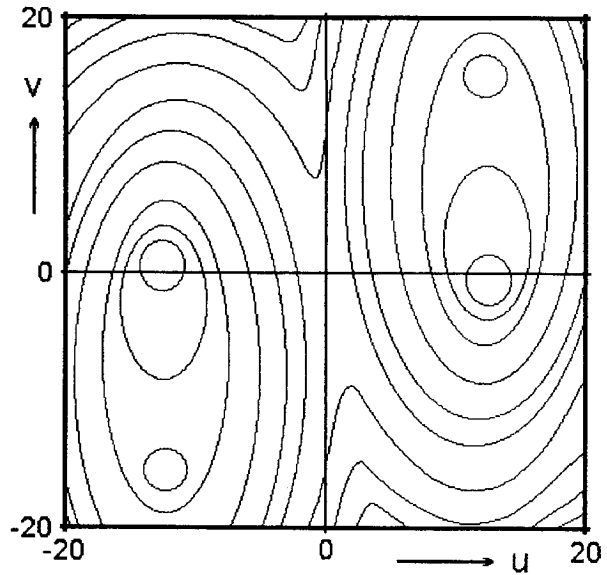


Figure 3 Illustration of wind probability contours as a function of the wind components u and v for a SeaWinds wind vector cell with measurements at four different azimuths including two polarizations. Multiple minima may exist, resulting in a slightly more complex observation operator.

- assist with the implementation of processing modules and to provide user support.

Besides scatterometer data will the NWP SAF be concerned with ATOVS, IASI, MVIRI, SEVIRI, SSM/I, AIRS, AVHRR, GOME, and OMI measurements. The GPS observation operator is dealt with in the GRAS SAF.

2.9 Scatterometers

Observation operators will be developed for ASCAT, NSCAT, and SeaWinds (figure 3). Our baseline is the observation operator in use for the ERS scatterometers at ECMWF (Stoffelen and Anderson, 1997c). Each ambiguous wind solution is associated with a 2D normal-distributed uncertainty. The normal probability distributions of all solutions are added and normalized. The observation operator as defined in variational analysis is the logarithm of this total distribution. In case of a single solution, the observation operator would be quadratic in the difference between observed and analyzed wind component (see figure 3). The solution weights and wind component accuracies need to be further determined; these will determine the ambiguity removal capability implied in the observation operator.

Assessment of scatterometer wind retrieval model by ERS and ADEOS cyclone tracking.

Lidia Saavedra de Miguel

ERS Product Control Service

ERS Mission Coordination and Product Assurance Section

ESA/ESRIN, Via Galileo Galilei, 00044 Frascati, Italy.

tel: +39 6 941 80, fax: +39 6 941 80612

E-mail:

ABSTRACT

In this paper we study the behaviour of scatterometer instrument in extreme wind conditions. Both ERS and ADEOS data are used.

Selected cyclone events are analysed and results are reported in terms of wind retrieval vector and sigma nought behaviour.

On the one hand, it is observed, in the case of ERS, a good agreement between the expected wind direction and the sensed data. This feature suggests that no saturation is present in sigma nought signals. On the other hand, a poor direction pattern from NSCAT winds is noted. This could be related to the sensitivity of the instrument and/or to the ku-band model used.

An underestimation of the wind speed is clear for both satellites. This fact leads to an assessment of the inversion model with a correction applicable in such extreme conditions.

The correction algorithm is applied for some cyclone events during 1997/1998 and the results are available on the web.

1. INTRODUCTION

The wind stress over the ocean is the main mechanism that force the oceanic circulation at small or large scale. Likewise, the wind field modulates air-sea fluxes of heat, moisture, gases and particles, affecting global and regional climate. It is evident that a good knowledge of wind patterns can improve the weather predictions and minimize the damages produced by severe storms.

Satellite scatterometers are active microwave radar that transmit pulses to the ocean surface. The backscatter power received at the instrument is related to the wind field as it generates the waves than roughen the sea surface. The inversion of the Geophysical Model Function (GMF) is the main way used to extract the wind information from the sigma 0 (backscatter) measurements. Primarily, sigma 0 depends not only on the surface roughness, but also on the incidence angle (which is the angle between the incident radiation and the vertical) and the azimuth (angle between the antenna and the wind direction in

the horizontal plane). Parameters as wave height and direction, sea surface temperature, attenuation by rainfall, are normally small and they are neglected when developing a GMF. However, the role of these parameters could become important in events of extreme atmospheric conditions.

The ADEOS Scatterometer (NSCAT) is a ku-band Doppler radar designed to measure backscatter at 25 km resolution, and retrieve wind vectors at 50 km resolution.

The ERS-2 wind scatterometer operates at C band and gets backscatter measurements at about 50 km of resolution sampled on a 25 km grid.

2. DATA SETS

To carry out this study we have used:

- NSCAT Science Products (NSP) Version 4.0. Level 1.7 (Ocean sigma-0's). Level 2.0 (Wind vectors retrieved using NSCAT-1 model function).
- ERS-2 Fast Delivery Products (FDP) with winds retrieved using CMOD-4 model function.
- Collocated NSCAT/ERS products (WNF produced by IFREMER). The criteria for the co-locations are one hour for time separation and 100 km for spatial separation.

3. WIND FIELD

The great underestimation in the measurements of high wind speeds is one of the problems that must be solved in the scatterometry field. One of the main mechanism that yields to such underestimation is the lack of data at high wind range that does not allow to well calibrate the model. The physical parameters mentioned above and the spatial resolution of the scatterometers contribute to this problem.

The first step we follow in order to correct the wind velocity, is to compare the reports from The Ohio State University Atmospheric Sciences Program Homepage with the scatterometer measurements. Basically, the information given in each report is the radius of the winds at 35 and 50 knots (also 100 knots if the cyclone is very big), the maximum sustained wind (not its position) and the centre location. A depict of some reports is given in Fig. 1

To carry out the simplest correction, that is, add to the scat-

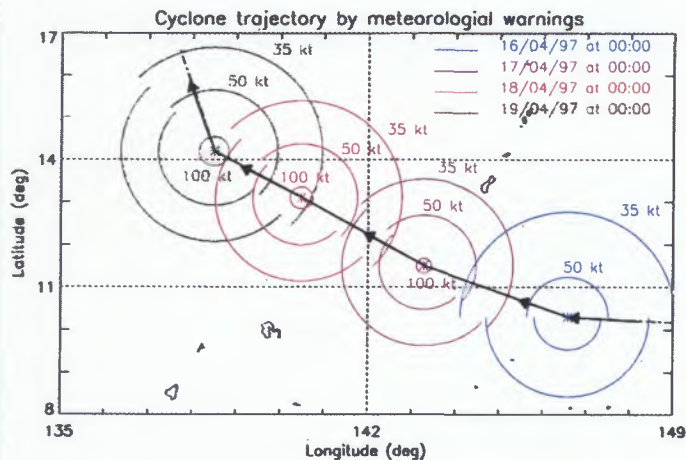


Figure 1: Graphical representation of some reports of The Ohio State University Atmospheric Sciences Program Homepage.

terometer data an amount needed to reach the values given by the reports, we have used 9 cyclones captured with ERS and 30 with NSCAT. The result was a correction very strong for 50 kt and, specially, for 100 kt due to the representativeness error.

3.1 WIND SPEED

3.1.1 REPRESENTATIVENESS ERROR

It is related to the resolution of the scatterometer. It does a 50 km average whereas the report information is taken as a local value. We must see what happens when we have a theoretical model of a cyclone measured with this instrument resolution. The model is a fit of the values of a typical report to a certain function given by:

$$f(r) = a_1 \cdot r \cdot e^{-a_0 \cdot r^{1/2}} + a_2 \tag{1}$$

The parameters a_0 , a_1 and a_2 are chosen computing a non-linear least squares fit whereas the position of the maximum sustained wind is found minimizing the sum of variances.

Now, we construct a filter that averages the model every 50 kms using a 25 kms grid. As it can be seen in fig. 2, depending on the relative position of the filter we will have different scatterometer patterns in the vicinities of the cyclone centre. Moving the filter grid 2.5 kms across the cyclone, allows us to compute the deviation between the model and the scatterometer profile ten times. An average is perform to obtain the representativeness error shown in fig. 3. The error associated to the filter relative position is also drawn. Each wind speed given in the report, previous to the comparison with the wind scatterometer speed, must be changed by its percentage value that depends on its distance to the cyclone centre. An example of this procedure is plotted in green colour (fig.3).

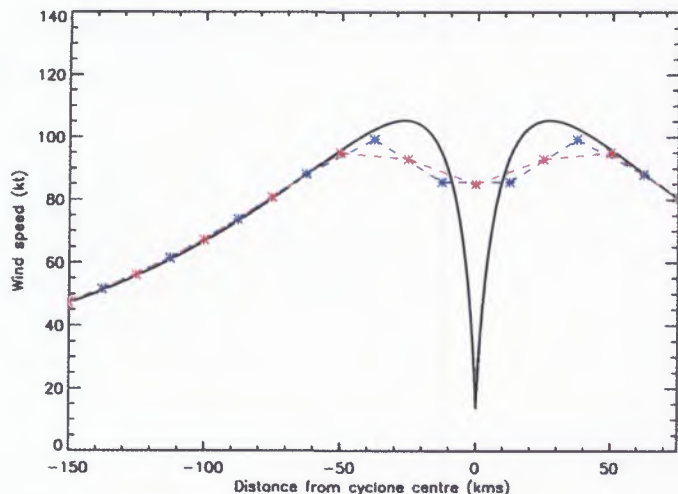


Figure 2: Theoretical model of a cyclone following (1) (black line and two different positions of the filter (red and blue stars).

3.1.2 CORRECTION OF WIND SPEED

The following step is to correct the wind speeds for values greater than 15 m/s. If we depict the bias as a function of the scatterometer wind, it seems that the curve that better fits the data is:

$$F(W_S) \equiv W_R - W_S = b_0 \cdot W_S^{b_1} \tag{2}$$

where:

- F is the scatterometer correction function
- W_R is the reported wind
- W_S is the scatterometer wind
- b_0 and b_1 are parameters that perform the very best fit.

Taking natural logarithm in (2), we can easily perform a linear fit and get the parameters b_0 and b_1 . The equation be-

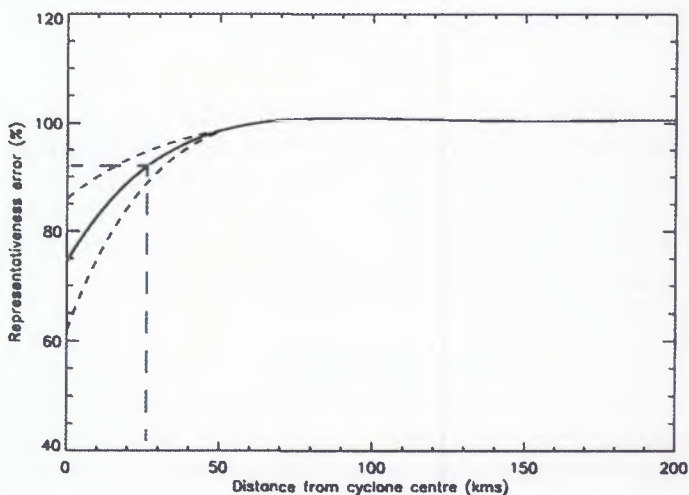


Figure 3: Representativeness error. A reported value must be situated in the graphic and the corresponding percentage value must be used in the collocation with the scatterometer.

comes:

$$\ln(F) = \ln b_0 + b_1 \ln W_S \quad (3)$$

The parameters found to fit (3) are:

ERS: $b_0 = 6.79 \times 10^{-6}$
 $b_1 = 4.91$

NSCAT: $b_0 = 2.49 \times 10^{-5}$
 $b_1 = 4.32$

Fig. 4 and fig.5 are the graphical representation of the fit to (2), using the above parameters, for both, ERS scatterometer and NSCAT respectively. For the first one, the correction is more important because the maximum retrieved wind is 23 m/s while for the second one, the range is wider and it can be found retrieved winds up to 30 m/s.

Two examples of wind pattern corrected are shown in fig. 6 and 7 for both scatterometers. The results are a more realistic shape of the cyclone structure (not perfectly circular) and a wind speed much nearer to the real one.

3.2 WIND DIRECTION

Until now, we were talking about the wind in terms of velocity but the wind direction is a feature that the scatterometers are also capable to retrieve. If we observe the direction patterns of a strong event, it is easy to see that the NSCAT data does not allow to distinguish the centre of the cyclone while the ERS Scatterometer localize it with a good precision. It seems that as the wind grows in intensity the NSCAT loses information about the direction. This is clearly shown in fig. 8 for three cyclone events of increasing strength. In fig. 8.a the maximum wind speed is 55 kt and the scatterometer captures the centre very good. Fig 8.b shows a structure with a centre location more difficult to fix (maximum winds of 95 kt) while in fig. 8.c the position of the centre becomes nearly impossible to determine (125 kt of maximum wind speeds).

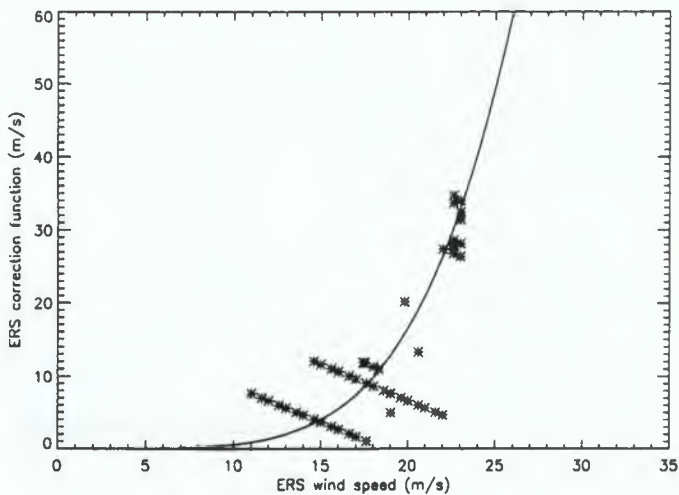


Figure 4: Correction model for ERS Scatterometer

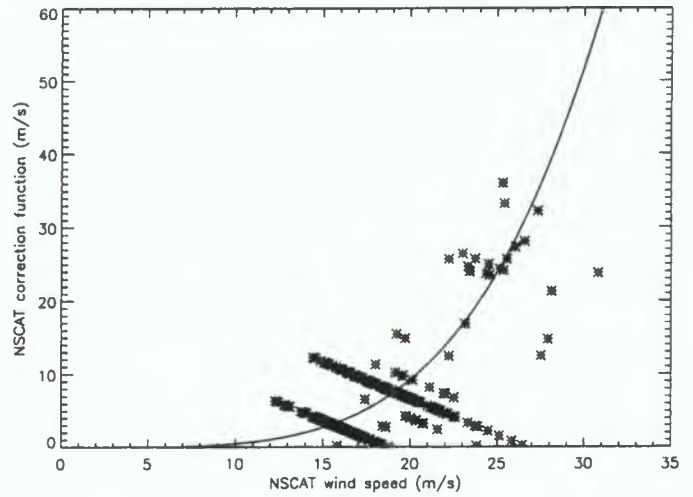


Figure 5: Correction model for NSCAT.

Fig. 9 shows a sequence of three cyclones captured by ERS-2 and similar in intensity to those of fig. 8. The centre position is always quite good localized.

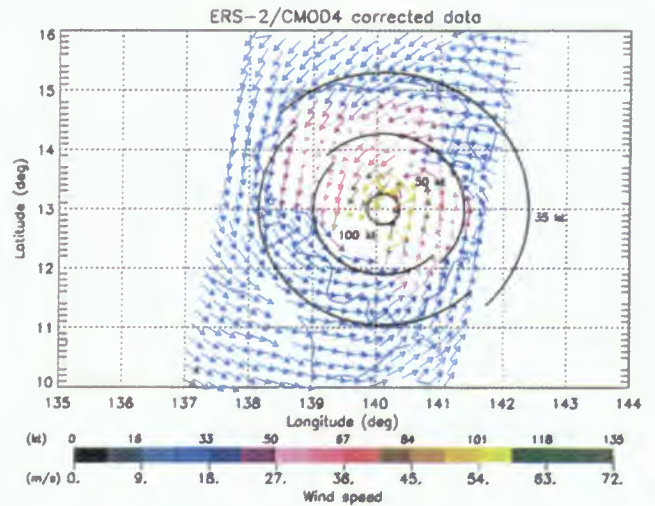


Figure 6: Cyclone ISA, 18th April, 1997. Corrected winds using model of fig. 4. Information of the OSU report is also depicted.

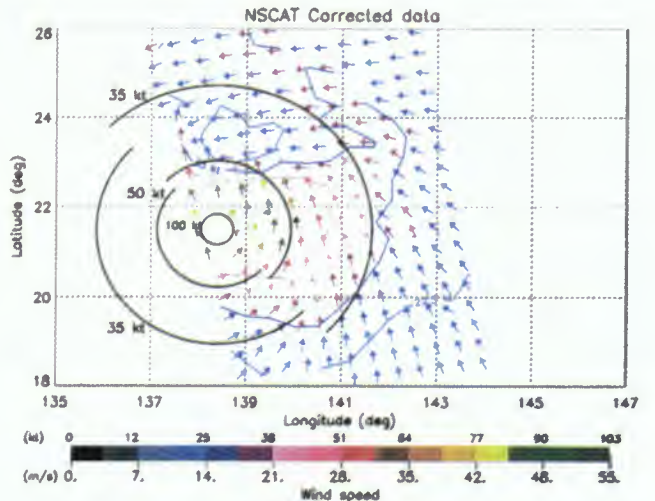


Figure 7: Cyclone ISA, 21st April, 1997. Corrected winds using model of fig. 5. Information of the OSU report is also depicted.

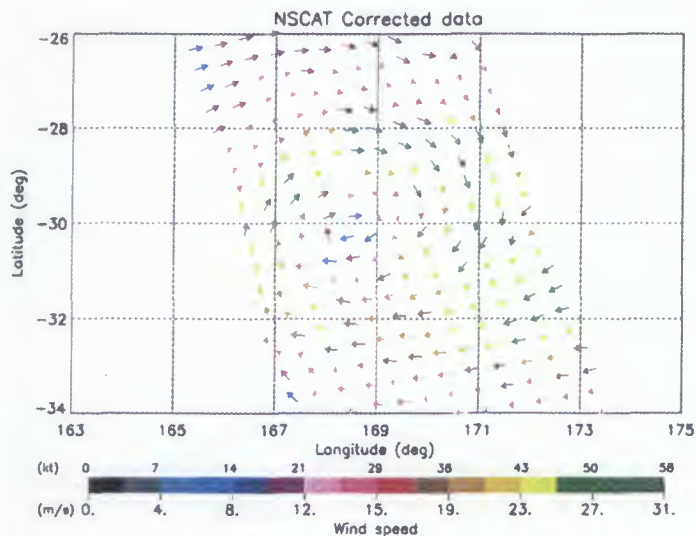


Figure 8.a: Cyclone DRENA, 9th January, 1997. Maximum sustained winds of 55 kt.

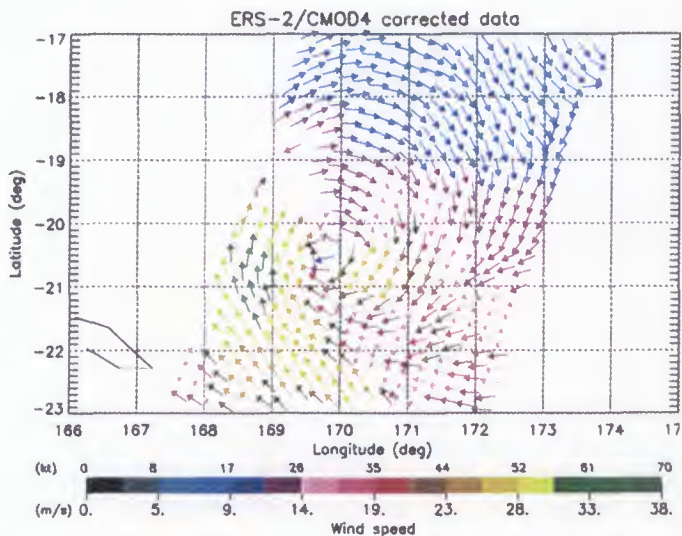


Figure 9.a: Cyclone YALI, 22nd March, 1998. Maximum sustained winds of 55 kt.

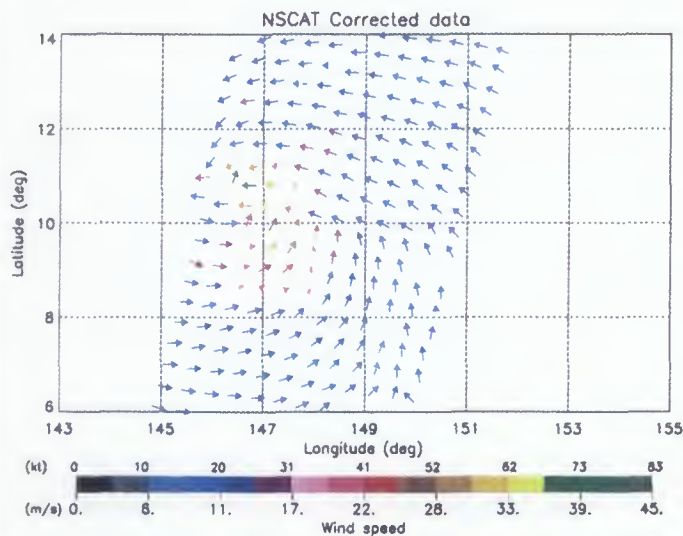


Figure 8.b: Cyclone ISA, 16th April, 1997. Maximum sustained winds of 95 kt.

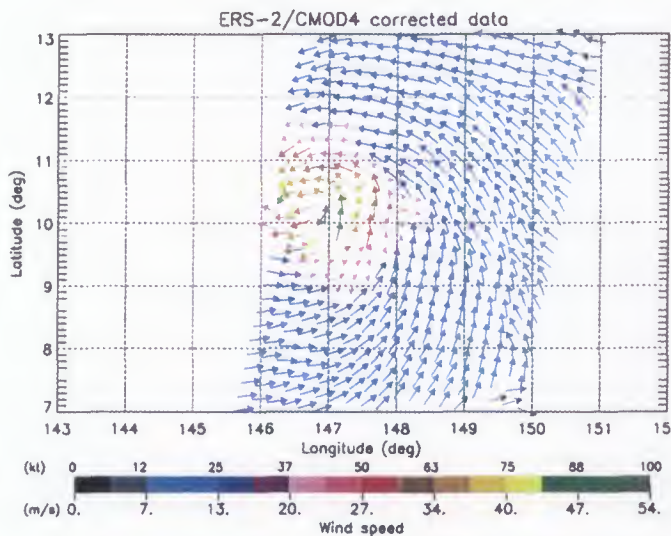


Figure 9.b: Cyclone ISA, 16th April, 1997. Maximum sustained winds of 95 kt.

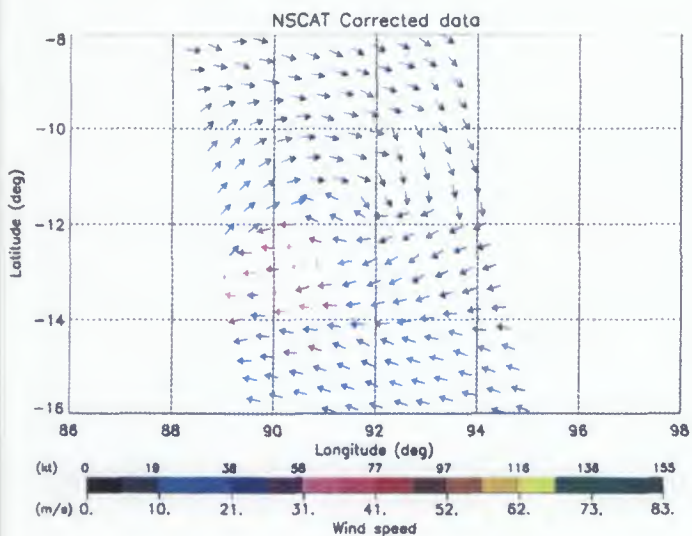


Figure 8.c: Cyclone PANCHO, 22nd January, 1997. Maximum sustained winds of 125 kt.

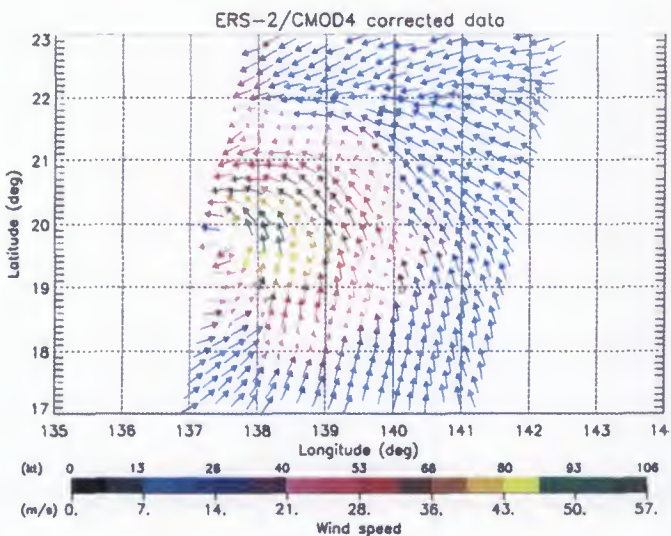


Figure 9.c: Cyclone ISA, 21st April, 1997. Maximum sustained winds of 125 kt.

4. CHARACTERISATION OF σ^0 AT HIGH WINDS

4.1 σ^0 PROFILES

In order to find the reason for this difference in direction pattern, we have analysed the σ_{00} . In normal weather conditions, the NSCAT σ_{00} are 1.5-2 db greater than ERS-2 σ_{00} (fig. 10.a & fig. 11.a). This feature could be related to the different bands of the radiated signal, C-band for ERS-2 (5.3 Ghz) and Ku-band (14 Ghz) for ADEOS Satellite. Because of that, the retrieved winds of NSCAT are 1-1.5 greater than those of ERS-2 SCATT.

In extreme weather conditions, the signals of both scatterometers are quite similar; NSCAT signal does not grow as much as the ERS-2 SCATT signal does (fig. 10.b & fig. 11.b). This could mean that the NSCAT is less sensitive in these con-

ditions, probably because the rain attenuation is more important in Ku band.

To cast light on this point, it would be interesting to go deeply into the fore and aft signal behaviours. If the phenomenon of saturation is present, the fore and aft antennae are supposed to measure the same signal and the direction information, related to their difference, would be lost. The ERS-2 SCATT, based on fig. 9, do not show a saturation behaviour while the NSCAT leads us to think that there is a possible saturation or a poor performance of the model.

4.2 FORE-AFT DEVIATION

The maps of fore minus aft differences can help us to better understand the influence of σ_{00} behaviour on the wind direction patterns.

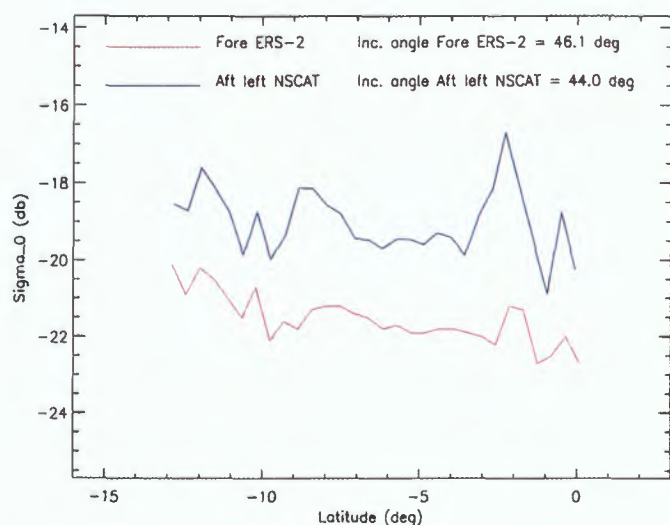


Figure 10.a: σ_{00} along the swath for both scatterometers in calm weather conditions.

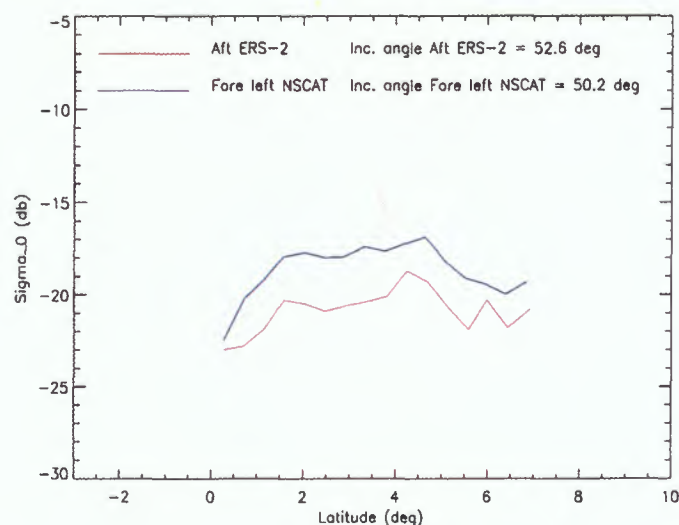


Figure 11.a: σ_{00} along the swath for both scatterometers in calm weather conditions.

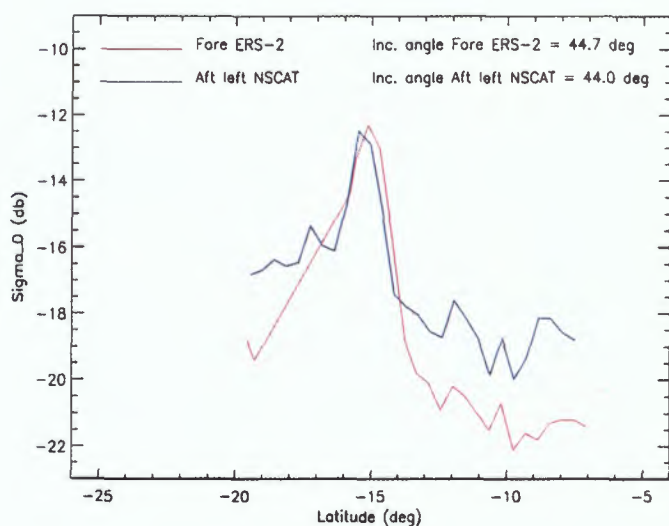


Figure 10.b: σ_{00} along track DRENA cyclone, 9th January, 1997.

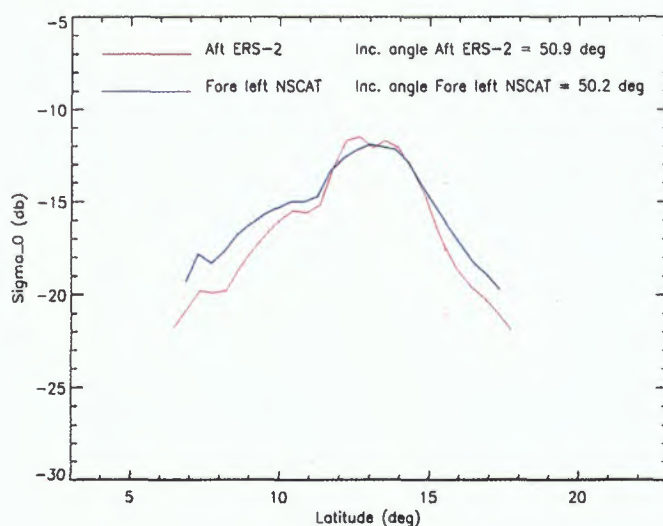


Figure 11.b: σ_{00} along track ISA cyclone, 18th April, 1997.

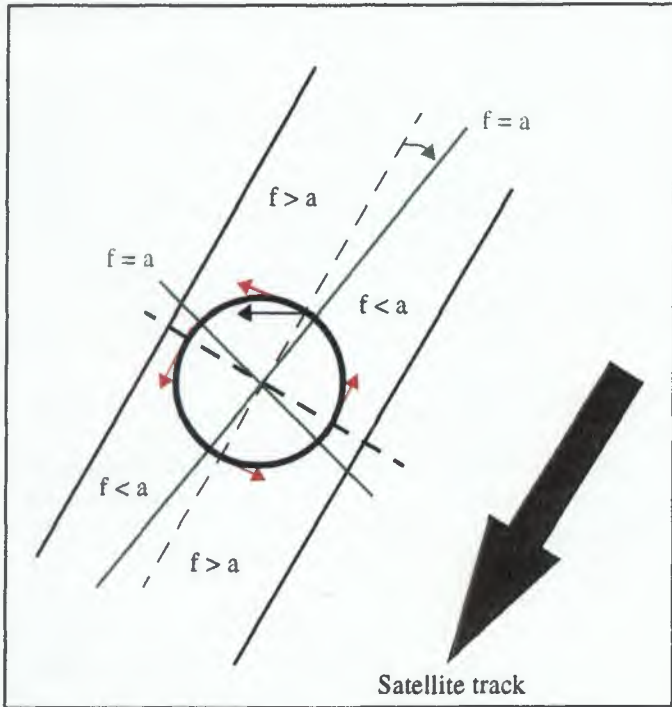


Figure 12: Diagram of fore - aft values.

What we expect to obtain is represented in fig. 12 for a cyclone with the wind blowing anti-clockwise (North Hemisphere) and a descending pass of the satellite. If the wind were tangential to the circle (red arrows), the dashed lines should represent the zone where the fore and aft antennae have the same value. As the wind is rotated 15-20 degrees (black arrow), the lines are tilted by the same angle (green lines). The zones of fore signal greater or less than aft signal depend on the upwind, downwind or crosswind direction respect to the two beams. Table 1 shows the possible combinations for the above geometry.

In fig. 13 we have evaluated the difference $f-a$ in the cyclone ISA captured by ERS-2 on 18th of April, 1997 (115 kt of maximum sustained wind). It can be seen the structure that will allow a good wind direction retrieval. However, fig. 14 (corresponding to the cyclone of fig. 8.c) does not show the same good results. The difference is clearly seen in fig. 15, where the plots are done using two colours: red for $f-a > 0$ and blue for $f-a < 0$. ERS-2 SCATT reproduce precisely the expected results given in fig. 12 whereas it is evident, for NSCAT, a deficiency of its sensitivity when measuring this kind of atmospheric events.

Table 1: Wind direction with respect to the antennae fore and aft and their relative measurements for the geometry of fig. 12.

	fore	aft
$f > a$	upwind	crosswind
$f > a$	downwind	crosswind
$f < a$	crosswind	upwind
$f < a$	crosswind	downwind

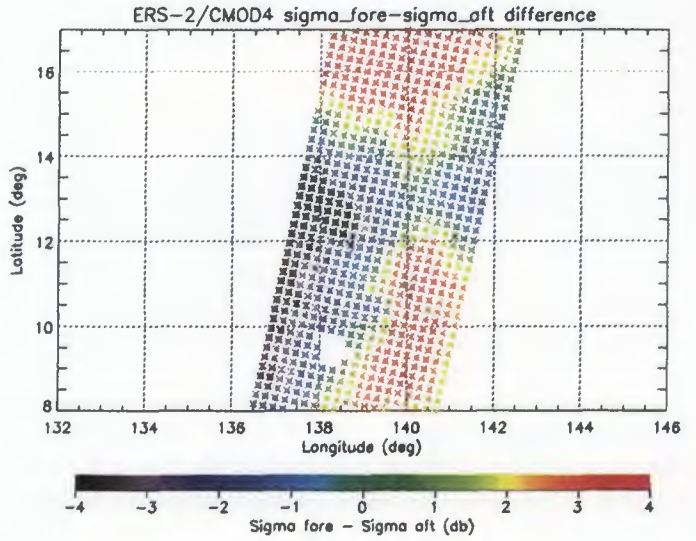


Figure 13: Graphical deviation fore minus aft ERS data for the cyclone ISA on 18th of April, 1997.

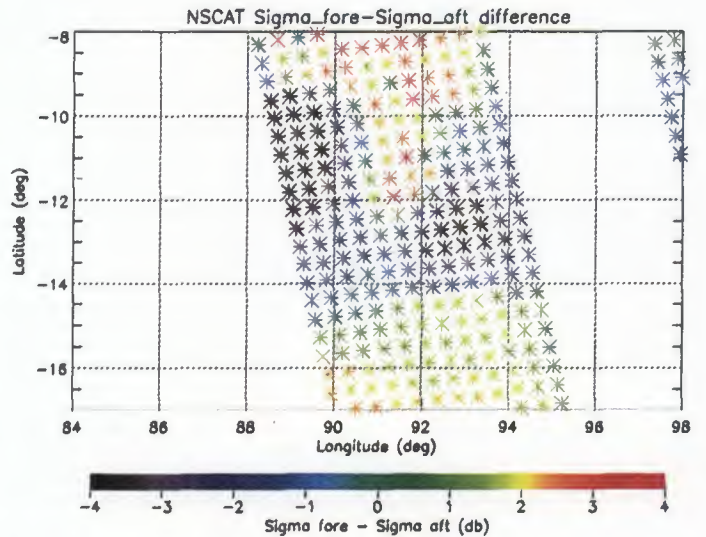


Figure 14: Graphical deviation fore minus aft NSCAT data for the cyclone PANCHO on 22nd of January, 1997.

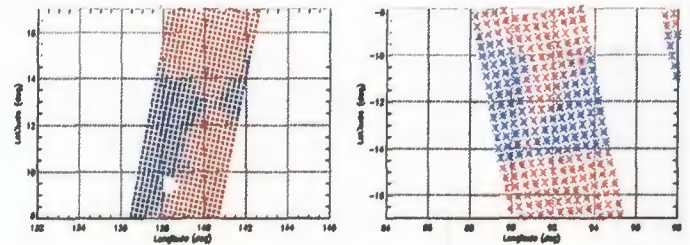


Figure 15: Same as fig. 13 (left one) and fig. 14 (right one) using two colours, red for $f-a > 0$ and blue for $f-a < 0$.

5. CONCLUSIONS

Both scatterometers far and away underestimate the wind speeds when measuring atmospheric phenomena with strong

wind fields associated. However, a supposed better calibration of NSCAT allows to obtain wind values up to 30 m/s while ERS-2 SCATT has its limit at 23 m/s. In order to correct the underestimation drawback, a preliminary model that improve the quality of high scatterometer wind speeds have been developed taking into account the effect of the instrument resolution.

The problem of the large amount of data needed to calibrate the model (mainly above 50 kt) is not solved and future data acquisition will help us to construct a more suitable data set.

A good capability of ERS-2 SCATT to measure wind direction has been observed and, because of that, it seems that no saturation is present in σ_0 signal. An expected behaviour of σ_0 fore minus σ_0 aft deviation confirm this point.

Quite the contrary, the NSCAT presents a poor direction pattern. The study of σ_0 is needed in order to check the sensibility of the instrument. The Ku-band model could also influence the observed direction winds.

In normal weather conditions NSCAT usually measures 1.5-2.0 db more than ERS-2 SCATT yielding to a wind retrieval slightly superior (about 1-1.5 m/s). As the wind increases its strength, the signals become similar. This suggests a lost of sensitivity of NSCAT, fact that is also pointed out by the behaviour of σ_0 fore minus σ_0 aft difference. Precipitation attenuation could be the main mechanism responsible for the irregular behaviour of σ_0 .

Acknowledgments.

I would like to thank Pascal Lecomte and Raffaele Crapolichio for their support and essential comments.

6. REFERENCES

C. Mejia, S. Thiria, N. Tran and M. Crépon (LODYC, UP-MC), F. Badran (Cnam-Cedric), **Determination of the geophysical model function of the ers-1 scatterometer by the use of neural networks.** J. Geophys. Res., 1997a.

K. B. Katsaros, Y. Quilfen, B. Chapron, **Tropical Cyclone Surface Winds and Waves from the Active Instrument of the ERS-1; comparison to Special Sensor Microwave Imager.**

H. Roquet, J. Poitevin, **Tropical Cyclone Monitoring using ERS-1 Scatterometer data.** Proceedings 2nd ERS-1 Symposium. Space at the Service of our Environment, Hamburg, Germany, 11-14 Oct. 1993, ESA SP-361, pp. 1133-1136 (January 1994).

Y. Quilfen, B. Katsaros, B. Chapron, **Surface Wind and Precipitation patterns in Tropical Cyclones observed with the ERS-1 Scatterometer and with the Special Sensor Microwave/Imager.** Proceedings 2nd ERS-1 Symposium. Space at the Service of our Environment, Hamburg, Germany, 11-14 Oct. 1993, ESA SP-361, pp. 1117-1122 (January 1994).

C. M. Kishtwal, B. M. Rao, P. K. Pal and M. S. Narayanan, **ERS-1 Surface Wind observations over a Cyclone System in Bay of Bengal during november 1992.** Proceedings 2nd ERS-1 Symposium. Space at the Service of our Environment, Hamburg, Germany, 11-14 Oct. 1993, ESA SP-361, pp. 1127-1131 (January 1994).

H.-H. Essen, **Scatterometer-Retrieved Winds from the Iceland-Faeroe area.** Proceedings 2nd ERS-1 Symposium. Space at the Service of our Environment, Hamburg, Germany, 11-14 Oct. 1993, ESA SP-361, pp. 1013-1016 (January 1994).

A. Bentamy, K. Katsaros, P. Queffeulou, B. Chapron, Y. Quilfen, R. Ezraty, A. Cavanie, S. Pouliquen and V. Harscoat, **IFREMER contribution to the NSCAT calibration and validation activities.**

Collocated NSCAT/ERS Products, CERSAT, Réf. NSCAT-MUT-S-01-IF, Version 1.1, 26/06/1997.

Science Data Product, User's Manual, JPL, D-12985, Version 1.1, April 1997.



2D-VARIATIONAL AMBIGUITY REMOVAL

J.C.W. de Vries

Royal Netherlands Meteorological Institute (KNMI)
Po. Box 201, 3730 AE De Bilt, The Netherlands, e-mail: jdevries@knmi.nl

ABSTRACT

A one level, two parameter (wind components) 2D variational scheme is introduced for the ERS scatterometer to remove the 180 degree ambiguity in the wind vector solution resulting from the conversion of normalised radar backscatter measurements to wind information. Implementation details of the scheme are discussed and future developments are mentioned.

Keywords: ambiguity removal, extended swath, near-surface wind field, structure functions.

1. INTRODUCTION

The retrieval of near-surface winds from scatterometer backscatter measurements consists of two main steps. The first step is the *inversion*, a procedure that converts the normalised radar backscatter measurements at each observation point into a pair of wind vectors that are approximately 180 degrees opposed in direction. The second step is the selection of the physically correct solution from the wind vector pairs. This step is called *ambiguity removal*.

In the past ambiguity removal schemes have been developed by [Cavanie & Lecomte], [Offiler] and [Stoffelen & Anderson]. Their schemes all use *a priori* information, i.e. a near-surface wind field forecast which stems from a numerical weather prediction (NWP) model. The PRESCAT statistical filter [Stoffelen] which is operational at KNMI uses a forecast for the 10m wind as first guess and selects the unambiguous wind vector as the one most likely in a statistical sense given the wind direction and speed of the surrounding unambiguous wind vectors. This scheme is sensitive to the quality of the forecast wind field. Mispositioning of low pressure systems and/or errors in the strength of the forecast wind field relative to corresponding observations can cause erroneous wind vector selection in some areas of the swath [Stoffelen]. These selection errors are likely to occur in dynamic situations like rapid cyclogenesis.

To improve the ambiguity removal skill in these cases one has to find an alternative to the local wind vector consistency constraint of current ambiguity removal schemes. In NWP analysis for the mid-latitudes the geostrophic balance between the wind field and the geopotential field provides an important constraint on the spatial structure of synoptic scale winds.

A variational approach to ambiguity removal where the structure of the forecast error covariances adheres to the approximate geostrophic balance will likely result in a meteorologically more consistent analysis for the near-surface wind field compared to current statistical schemes. This should lead to an improvement in ambiguity removal skill.

In the tropics the geostrophic balance is less pronounced and the dynamics are quite different. The focus of this research is however on ambiguity removal of scatterometer winds in the mid-latitudes.

At ECMWF ambiguous scatterometer winds are assimilated into the global NWP model in a 24 hour cycle. The ambiguity is removed implicitly in the analysis that results in the initial state for the model. Using such a model for ambiguity removal however offers no alternatives to the current ambiguity removal schemes when it comes to the near real-time application of scatterometer winds. Limited area models on the other hand could be an alternative but models with a variational scheme for the assimilation of observations are still experimental.

A one level (2D) variational scheme based on wind component analysis that attempts to fit one of the ambiguous wind vector solutions may be a good alternative. Such a 2D variational ambiguity removal scheme would work on the scatterometer swath. The swath would be extended to incorporate analysis increments outside the swath. The selected ambiguity would be the one closest to the analysis.

The proposed 2D variational ambiguity removal scheme uses only scatterometer observations. This makes it not nearly as complex and expensive to run as a current 3D-var scheme. Moreover since scatterometer observations are the only observations available over most of the world's oceans, incorporating other types of observations would add little additional information anyway.

Improved ambiguity removal skill will have added value for synoptic weather forecasting, especially in the nowcasting of storms. It may also be beneficial for the use of scatterometer winds in wave-forecast models, limited area models and ocean models.

2. IMPLEMENTATION

In a variational scheme ambiguity removal is formulated as a minimization problem [Stoffelen & Anderson]

$$\min J = J_b(\underline{x}) + J_o^{scat}(\underline{x})$$

where J is the cost function to be minimised and \underline{x} is the state vector representing the estimate of the near-surface wind field. The background term of the cost function is the quadratic form :

$$J_b(\underline{x}) = \frac{1}{2} (\underline{x} - \underline{x}_b)^T B^{-1} (\underline{x} - \underline{x}_b)$$

where \underline{x}_b is the background wind field and B^{-1} is the wind error covariance matrix. The background wind errors are considered to have a Gaussian distribution around the wind vector components. The observational cost term is specified for ERS scatterometers. It is an analytical function [Stoffelen] that incorporates both ambiguous wind vector solutions available at each scatterometer node. At each node we have

$$J_o^{scat} = \left[\frac{J_1^4 J_2^4}{J_1^4 + J_2^4} \right]^{1/4}, \quad J_i = \frac{(u - u_i)^2 + (v - v_i)^2}{\epsilon_s^2}, \quad i = 1, 2$$

where u_i, v_i are the components of the ambiguous winds and ϵ_s is the standard deviation of the scatterometer wind component error. This function is preferred over a Gaussian type cost term because it has a more pronounced separation of the minima at low wind speeds.

The optimal solution of the minimization problem is found by solving the gradient equation

$$\nabla_{\underline{x}} J = 0$$

The solution of the minimization problem is the analysed scatterometer near-surface wind field. Solving the gradient equation in practice however is not trivial and no analytical solution exists. It is solved numerically on a square grid, defined on the scatterometer swath which is extended in all directions (fig.1) to incorporate analysis increments outside the swath due to the ambiguous wind vectors on the swath. An off-the-shelf gradient type minimization scheme is used for the minimization of the cost function. In the minimization process the background field is used as the first guess which is updated with each iteration to fit one of the ambiguous wind vector solutions. The spatial structure of the covariances used to update the analysis is determined by structure functions that are

homogeneous, isotropic and flow-independent. The structure functions are derived from empirical correlations [Hollingsworth & Lönnberg]. The solution to the ambiguity removal problem is determined by the smallest wind vector difference at each node on the scatterometer swath between either of the ambiguous wind vectors and the analysed wind vector.

The 2D variational ambiguity removal scheme uses no complicated overlapping strategy to ensure continuity in the solution for the near-surface wind field. Instead it is able to handle the largest possible stretch of contiguous scatterometer messages. This strategy results in a (full) background wind error covariance matrix that becomes very large when many observations are involved. This is a problem because we require the inverse of that matrix to compute the cost function and direct inversion of the background wind error covariance matrix would make the scheme computationally expensive. We solve this problem by computing the background term in Fourier space. This allows us to express the background wind error covariance matrix as a diagonal matrix which is easily inverted.

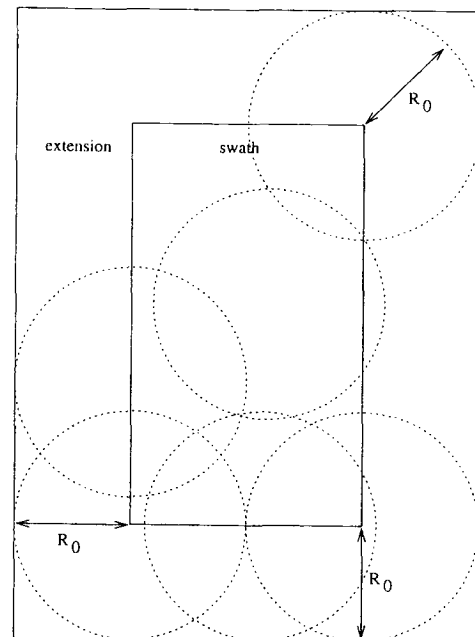


Fig. 1 The extended swath

A complicating factor when working in Fourier space is the fact that the covariance and wind error component fields have to be periodic to avoid Gibb's phenomenon. This is problematic when the distribution of ambiguous wind vectors is not homogeneous over the swath due to the presence of land masses, ice or because of quality control. We therefore make the extensions to the swath larger or equal to the de-correlation scale r_0 (fig.1) of

the structure functions. In this way analysis increments will be very small near the boundaries of the extensions.

Scatterometer measurements are available at equidistant nodes with a spacing of 25 km both in across-track and along-track direction. To avoid thinning of the measurements and perhaps losing observational information the extended 25 km grid is subdivided into coarser grids which are used cyclically in the minimization process. To obtain a scatterometer wind product based on uncorrelated measurements the 2D variational ambiguity removal scheme uses a square subgrid with a spacing of at least 50 km., i.e. a minimum of four subgrids.

3. FUTURE DEVELOPMENTS

The 2D variational ambiguity removal scheme is being implemented on the computer. It will be tested on pathological cases. It will be verified against PRESCAT and by a meteorologist.

4. REFERENCES

A. Cavanie & P. Lecomte, Vol.1 - *Study of a method to de-alias winds from ERS-1 data*. Vol.2 - *Wind retrieval*

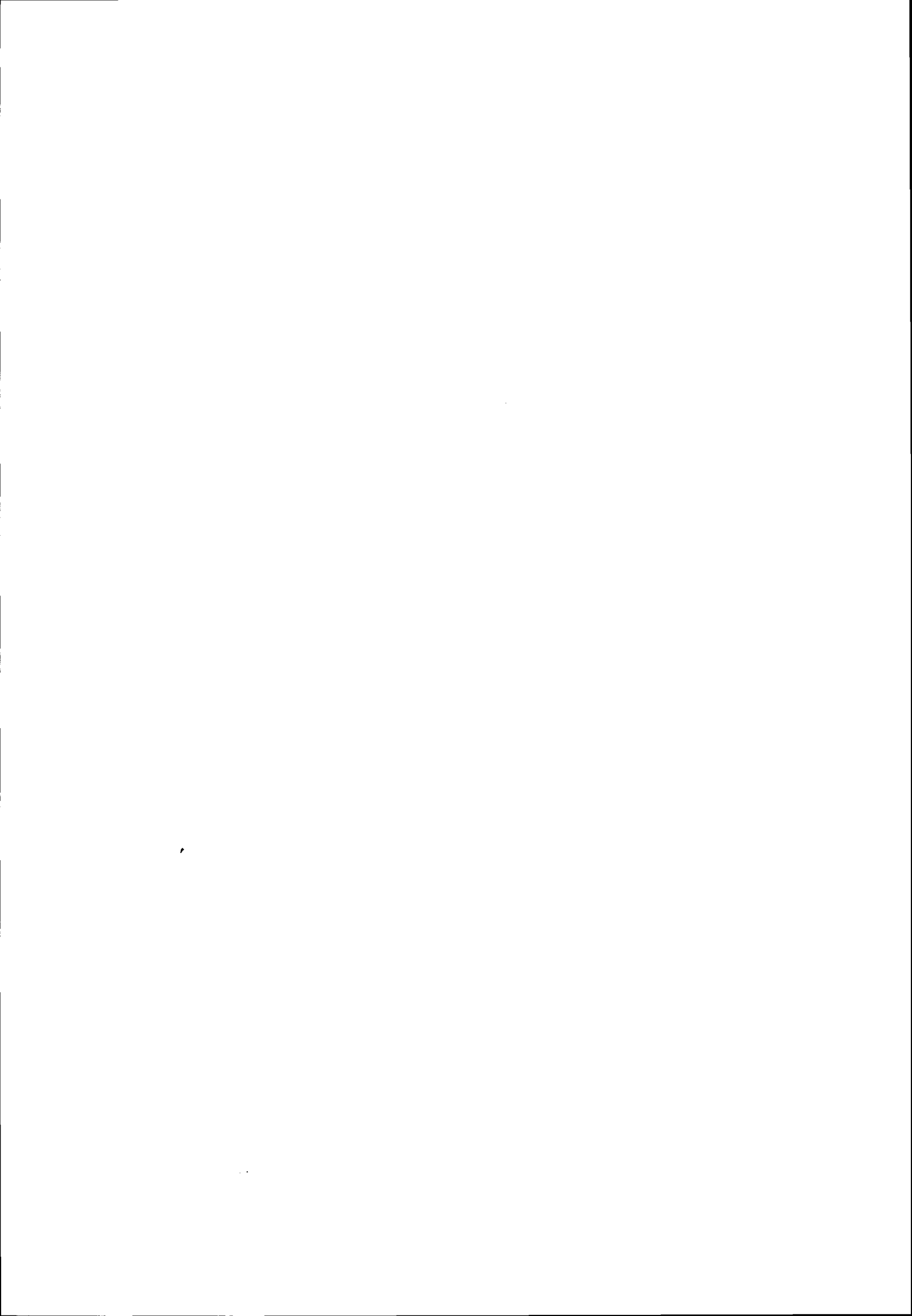
and de-aliasing subroutines. Final rep. ESA contract No 6874/87/CP-I(sc). Available from ESA Publ. Div., ESTEC Noordwijk, The Netherlands., 1987.

A. Hollingsworth & P. Lönnberg, The statistical structure of short-range forecast errors as determined from radiosonde data. Part I: The wind field, *Tellus 38 A*, pp.111-136, 1986.

D. Offiler, *ERS-1 wind retrieval algorithms*. UKMO 19 Branch Memo. No 86. Available from The National Meteorological Library, Bracknell, UK, 1987.

A. Stoffelen & D. Anderson, Ambiguity Removal and assimilation of scatterometer data, *Q.J.R. Meteorological Soc.*, pp. 491-518, 1997.

A. Stoffelen & D. Anderson, *The ECMWF contribution to the Characterisation, Interpretation, Calibration and Validation of ERS-1 Scatterometer Backscatter Measurements and Winds, and their Use in Numerical Weather Prediction Models*, ESA Contract Report, ESA contract number : 9097/90/NL/BI, 1995.



EFFECTS OF RESOLUTION AND COVERAGE IN HIRLAM DATA ASSIMILATION

Ad Stoffelen* and Paul van Beukering

KNMI, de Bilt, the Netherlands

ABSTRACT

The processing of ERS scatterometer winds is refined and interfaced to the High Resolution Limited Area Model HIRLAM. Forecast impact experiments have been carried out to assess the impact of one scatterometer, ERS-1, and of two scatterometers, ERS-1 and ERS-2, on the analyses and forecasts. Scatterometer data have a clear beneficial impact in the data assimilation cycle and on the two-day forecasts. However, scatterometer data contain much sub-synoptic scale information, and the smallest scales resolved are difficult to assimilate into a NWP model, due to general sparsity of the observing system over the ocean. Scatterometer data coverage is very important for obtaining a large impact. In that respect future scatterometer systems such as QuikSCAT, SeaWinds and METOP are promising. A fast data delivery is especially relevant for scatterometer data.

1. INTRODUCTION

After the launch of ERS-1 much improvement has been made in the interpretation of scatterometer backscatter measurements and a good quality wind product has emerged (Stoffelen and Anderson, 1997a, 1997b and 1997c). The consistency of the scatterometer winds over the swath makes them particularly useful for nowcasting purposes and several examples of the usefulness of the direct visual presentation of scatterometer winds to a meteorologist can be given. However, we will focus in this work on the data assimilation impact in numerical weather prediction (NWP) as gathered with the ERS-1 and ERS-2 scatterometer winds. As such, the scatterometer data preprocessing system (PRESCAT) has been further developed at KNMI and implemented in the High Resolution Limited Area weather forecasting Model (HIRLAM). Impact experiments are prepared to test the usefulness of the data for the analyses and for short-range forecasts up to two days. A meteorologically active period where both ERS-1 and ERS-2 scatterometer data are available has been selected to test the impact of an increased data coverage. In Stoffelen and Beukering (1997) these developments are described in detail, and here a brief summary is provided.

Accurate weather and wave forecasts are essential to monitor safety at sea for ship routing and tourism, and to issue warnings for coastal land protection in extreme wind and wave conditions. The accuracy of short-range weather and wave forecasts over Europe depends to a large extent on the real-time availability of accurate observations over the Atlantic ocean, where conventional measurements are sparse. For the medium range, the coverage over the Pacific also becomes critical. ERS-1 scatterometer data have been used to increase the data coverage over the oceans in different Numerical Weather Prediction (NWP) models and showed in general improvement in the short range weather forecasts (e.g., Stoffelen and Anderson, 1997c). In the medium range, beneficial impacts were seen particularly in the Southern Hemisphere (e.g., Bell, 1994). Furthermore, the use of NWP data, with scatterometer winds included, results in improved WAM wave forecasts (Janssen and Hansen, 1996).

In regional weather forecasting the emphasis lies on the short range and on the subsynoptic spatial scales. Wind observations with a high spatial coverage are essential to resolve these. The scatterometer provides such data, albeit only at the surface. The use of ERS-1 and ERS-2 tandem scatterometer data in HIRLAM may therefore be expected to be more beneficial than the use of only one ERS scatterometer. Also, the ASCAT scatterometer on board the future EUMETSAT METOP satellite and the NASA scatterometer QuikSCAT or SeaWinds, on board the Japanese ADEOS-II, have such an increased coverage. The HIRLAM data assimilation system at KNMI is started with a cut-off time for observations of 2 hours. Usually only 50% of the ERS scatterometer data are received within two hours. Our experiments confirm the importance for Europe of scatterometer data and suggest that a delivery of data within 2 hours would be very useful.

2. RESULTS

2.1 Calibration of ERS-2 backscatter

The ERS-2 geophysical validation strategy includes an "ocean" sigma naught calibration procedure that proved to be a reliable complement to the engineering calibration, both for the ERS-1 and ERS-2 scatterometers. In order to be able to use ERS-2

* Corresponding Author address: Ad Stoffelen, KNMI (WM/SD), Postbus 201, 3730 AE de Bilt, the Netherlands.
E-mail: stoffelen@knmi.nl

scatterometer data from before the engineering calibration, we refined the "ocean" calibration procedure, originally developed at ECMWF, resulting in new backscatter calibrations for both ERS-1 and ERS-2 that demonstrably improve the wind retrieval and the accuracy of the instrument monitoring, as described by Stoffelen (1998a). Moreover, the finding with ERS-1 that triplets of backscatter are distributed around a well-defined and curved conical surface in the three-dimensional measurement space, allows an accurate check of the distribution of the ERS-2 scatterometer sigma naught: triplets in this space. When the average distance to the conical surface as a function of node, wind speed and wind direction is the same for the ERS-1 and ERS-2 measurements than both systems have an identical calibration. Thus, it was found that the ocean calibration results in new backscatter calibrations for both ERS-1 and ERS-2 that demonstrably improve the wind retrieval and the accuracy of the instrument monitoring.

2.2 Wind Tuning

In order to avoid systematic slowing down or speeding up of the HIRLAM model by scatterometer data assimilation we adopted a careful wind validation. Gaffard and Roquet(1998) show the detrimental effect of systematic wind bias on NWP impact. The results of a wind calibration method taking into account the error characteristics of *in situ*, satellite and model winds by Stoffelen (1998b) has been used to estimate the wind biases of the HIRLAM model with respect to the scatterometer. Although scatterometer winds delivered by PRESCAT are known to be approximately 5% low, the HIRLAM first guess has a negligible bias with respect to the ERS scatterometers, and thus is also biased low with respect to the true wind. We estimate the random ERS scatterometer wind component error to be 1.8 m s^{-1} . The HIRLAM model random error is estimated to be smaller than this, i.e., 1.2 m s^{-1} .

ERS scatterometer backscatter measurements are delivered on a grid of 25 km, but have a spatial resolution of 50 km. The HIRLAM model grid distance is 50 km. In order to present the scatterometer data to the HIRLAM model in a spatial representation consistent with the model, we averaged the scatterometer data to a grid of 100 km. As is argued below, this spatial representation was still too fine to be assimilated by the HIRLAM model in some cases. Anyway, after the ocean calibration and wind tuning, PRESCAT delivers accurate ERS-1 and ERS-2 winds with much sub-synoptic scale information.

2.3 Assimilation

2.3.1 Experimental Set-up

The tandem scatterometer data assimilation experiment ran from 6-18 February 1996, a period with a disturbed westerly flow over western Europe. Since, the North Atlantic is an area with a sparse meteorological observation coverage, scatterometer data are expected to fill in this gap and thus may provide an impact on the weather forecasts over western Europe. The grid used is by approximation equidistant and 5000 by 4000 km with Dublin in the center.

The analysis is a combination of the information provided by a HIRLAM 3-hour forecast, called background, and the observations available in the 3-hour time window centered around the verification time of the forecast. The impact of observations in the analysis depends on the ratio of the estimated background over observation error. The scatterometer observation errors are assumed to be spatially uncorrelated (Stoffelen, 1996), and the spatial projection of scatterometer information in the analysis depends solely on the estimated background error structure. The typical horizontal projection scale is 250 km. The error structures are multivariate and balanced, indicating that the scatterometer wind observations will influence the pressure and temperature fields. Also will the information be projected in the vertical, e.g., a modification of the wind at the surface due to a scatterometer observation will result in a fraction 0.25 of that modification at 500 mb. From most scatterometer experiments carried out so far, it can be concluded that forecast impact can only be obtained when the upper air is improved in a consistent way with the modifications at the surface.

For the selected period in February '96 three data assimilation experiments were run

- noERS, control without scatterometer winds,
- ERS1, with only ERS-1 winds assimilated, and
- ERS12, with both ERS-1 and ERS-2 included.

2.3.2 Impact over Sea

The background wind fields of all these three experiments were verified against the scatterometer winds. Assuming that the scatterometer wind component is 1.8 m s^{-1} , it was found that both the ERS1 and the ERS12 background had a roughly 20% smaller error than the noERS background. Another, though subjective, way to test the quality of the background winds over the sea is to systematically compare the ambiguity removal skill. The ambiguity removal skill of scatterometer winds (Stoffelen and Anderson, 1997c) depends on the quality of the background field used in this process. When the solutions of the ambiguity removal were different in the experiments noERS, ERS1, and ERS12, we used other meteorological observations available to subjectively assess which experiment had obtained the best solution. We found that the ambiguity removal in experiment ERS12 worked clearly the best, followed by that of experiment ERS1, and the worst performance in experiment noERS. This suggests that phase errors of meteorological systems are smallest for experiment ERS12.

2.3.3 Impact over Land

To verify the impact over land we compared the RMS mean sea level pressure (MSLP) modifications, increments, in the analysis. Since over land the same observations are used in the three experiments, a smaller RMS increment indicates a better background MSLP. The RMS analysis increments over land in the ERS1 and ERS12 experiments were 10-20 % lower than in the noERS experiment, indicating that the background is also improved over land by the assimilation of scatterometer winds.

2.3.4 High resolution?

Although we anticipated that the HIRLAM data assimilation system would not be capable of resolving all the subsynoptic detail in the scatterometer winds, and we had averaged the winds to a 100 km resolution, we still found that the observation consistency check in the analysis rejects scatterometer winds close to sharp troughs and fronts, and substantially smoothes the winds on scales smaller than a few hundred kilometers. In other words, the small-scale information in the scatterometer winds is smoothed out by the analysis. This is due to the estimate of the spatial error correlation scale of the background error. It is determined by what spatial scales the HIRLAM model can realistically describe. Over the ocean this is not so much determined by the grid distance used by the model, but by the density of the network of meteorological observations, i.e., a decrease of the grid distance and associated with this an increase of the variability on the smaller scales would only result in a larger error, since no data is available to determine the flow on these small scales.

Scatterometer data will help improve this situation, but probably upper air wind profile observations will be needed for a substantial improvement over the oceans (ESA, 1996).

2.4 Forecast Impact

From the 00 UTC and 12 UTC analyses of all the experiments we ran two-day forecasts. The forecasts for forecast leads of 12, 24, 36 and 48 hours were systematically verified with the corresponding analyses for surface wind, pressure and temperature, and 500 mb wind and temperature. Up to a forecast lead of 24 hours, the verifications clearly depend on whether we use the noERS, ERS1, or ERS12 analyses for verification. For the 48 hour forecasts this is not the case, and our conclusions can be firm. It is clear that the ERS12 forecasts are better than the ERS1 and noERS forecasts. On the other hand, the two-day ERS1 forecasts are on average not demonstrably better than the noERS forecasts. This confirms the conclusion of Le Meur (1997) with the ECMWF NWP model that a tandem scatterometer has more than twice the impact of a single scatterometer. Scatterometer data coverage is thus important.

The average forecast impact was different for different parameters and different forecast ranges, but again we find that the forecast impact is generally similar at the surface and in the upper air, indicating that in case of positive impact the scatterometer information at the surface is well propagated in the vertical.

3. RESUME AND OUTLOOK

After the application of a backscatter calibration over the ocean the ERS-1 and ERS-2 scatterometer provide detailed subsynoptic-scale information that is relevant for nowcasting and short-range forecasting. The ERS scatterometer pre-processing system PRESCAT has been rewritten and interfaced to the HIRLAM data assimilation system. PRESCAT scatterometer

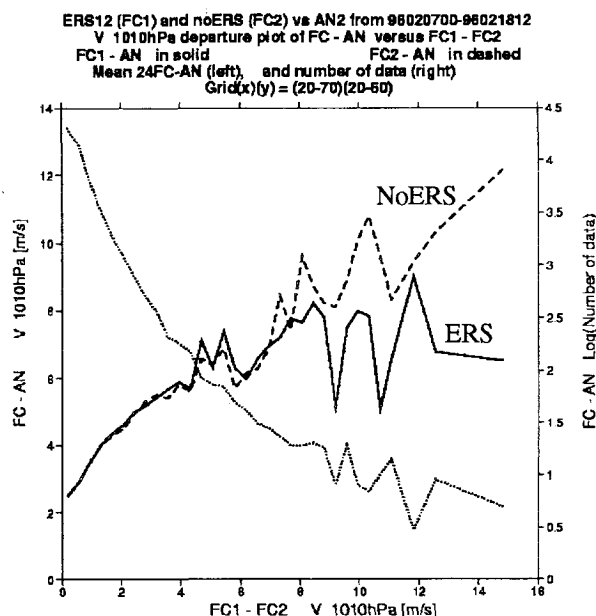


Figure 1: Plot of the ERS12 forecast minus noERS analysis vector wind difference (solid) versus the ERS12 minus noERS 48-hour forecast difference, and similarly the noERS forecast minus noERS analysis difference (dashed). The dotted line denotes the logarithm of the number of cases for each class of ERS12-noERS forecast difference. When the forecasts are significantly different, then the ERS12 48-hour forecast is better than the noERS 48-hour forecast, although the mean scores are very similar (3.13 and 3.12 $m\ s^{-1}$ resp.). Note that the noERS forecasts keep deteriorating for increasing forecast difference, whereas the ERS12 forecast is not

winds and HIRLAM winds are not biased with respect to each other, but may be both biased by roughly 5% against the true wind.

The HIRLAM analyses are clearly improved by PRESCAT winds, both over land and over sea, and both in case of one and in case of two scatterometers. However, the information provided by the scatterometer on a scale of 100 km is rejected by the HIRLAM model. Not a refinement of the grid distance of the NWP model, but an increased density of meteorological observations over the oceans, also in the upper air, is believed to be necessary in order to improve the situation.

In line with this, from our experiments it is found that scatterometer data coverage is very important to obtain forecast impact. In our particular case, we were not able to demonstrate the forecast impact of one scatterometer, but found a clear

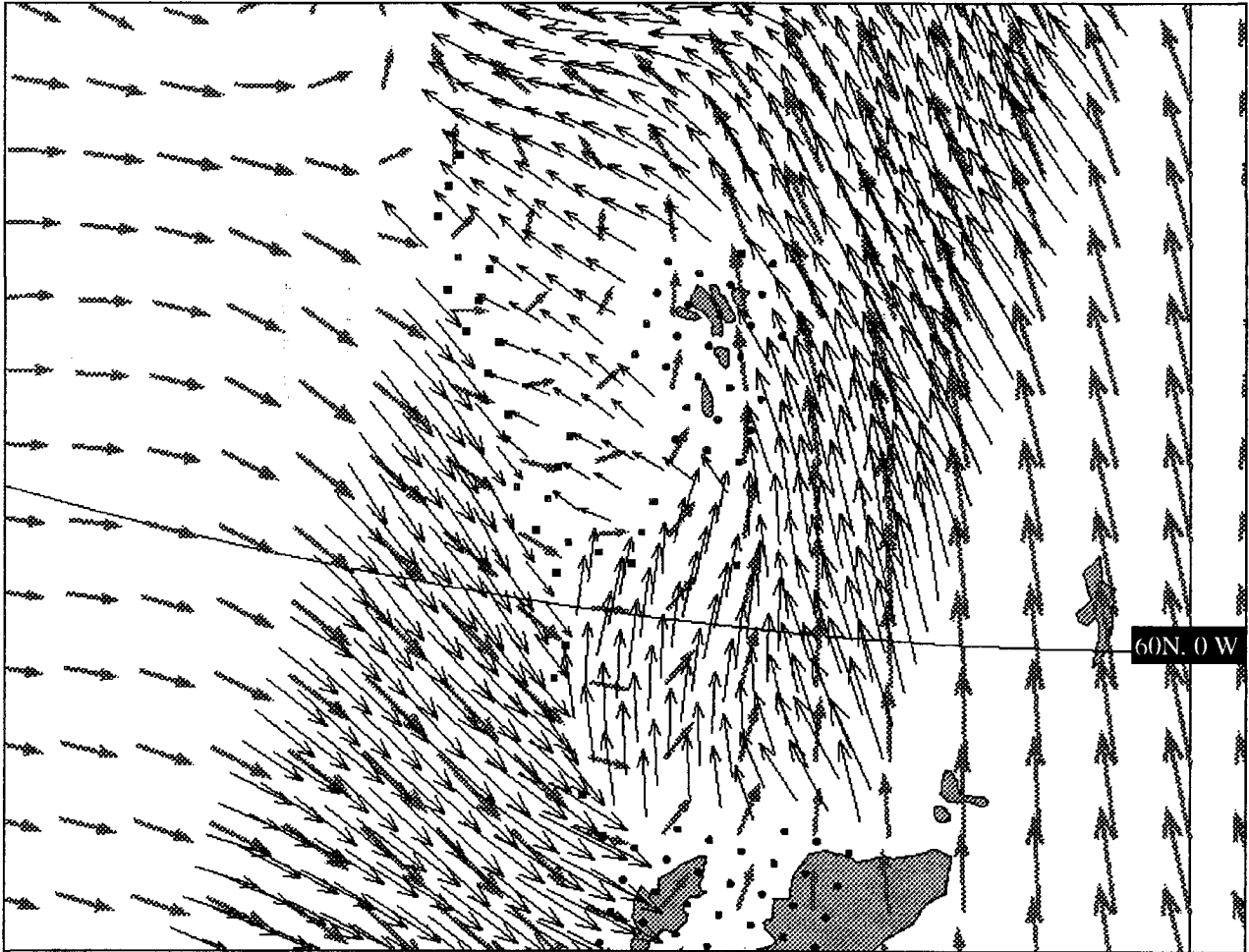


Figure 2: ERS-2 scatterometer winds (black arrows) and subsequent HIRLAM analysis (grey) for 12 UTC 6th of February to the north of Scotland. The black dots depict PRESCAT QC or land. The ERS12 analysis shows a smooth through while the scatterometer shows significant sub-synoptic scale structure.

beneficial impact in case we assimilated the ERS-1 and ERS-2 scatterometer wind data in tandem. This synergy of two scatterometers is in agreements with NWP impact studies at ECMWF (Isaksen et al, this volume).

In fact, it has been realized before that coverage is a weak point of the ERS-1 or ERS-2 scatterometer, and its successor ASCAT on METOP will obtain a threefold coverage. In preparation for METOP KNMI is developing calibration and validation tools and the wind processing chain within the EUMETSAT Ocean and Sea Ice Satellite Application Facility (Stoffelen et al, this volume). By the end of 1998, KNMI plans to have a prototype processing chain running in near real-time with ERS data, accessible from the WWW. This prototype will be based on PRESCAT. Developments on a. o. ambiguity removal (de Vries and Stoffelen, this volume) and ice screening are performed in collaboration with IFREMER.

In order to bridge the gap between the ERS scatterometer series and ASCAT on METOP, the meteorological community will have to rely on a new scatterometer concept, SeaWinds, being developed by NASA. QuikSCAT will be a dedicated scatterometer mission, carrying SeaWinds, scheduled for launch in late 1998. NOAA plans to have a near real-time distribution of the data in place by the middle of 1999. In 2000, ADEOS-II is planned for launch with also the NASA SeaWinds scatterometer on board.

Fortunately, QuikSCAT will have a large data coverage with its swath of 1800 km wide. That part of the swath that contains a similar amount of information on the full near-surface wind vector as that provided at the nodes of the ERS or NSCAT scatterometers, is of similar width than the total swath width of NSCAT or ASCAT. However, the remaining outer and middle parts of the swath will contain less information than for instance the ERS or NSCAT measurement cells. In collaboration with NASA, KNMI plans to contribute towards an effective interpretation, quality control and monitoring of the QuikSCAT and SeaWinds data to the benefit of NWP.

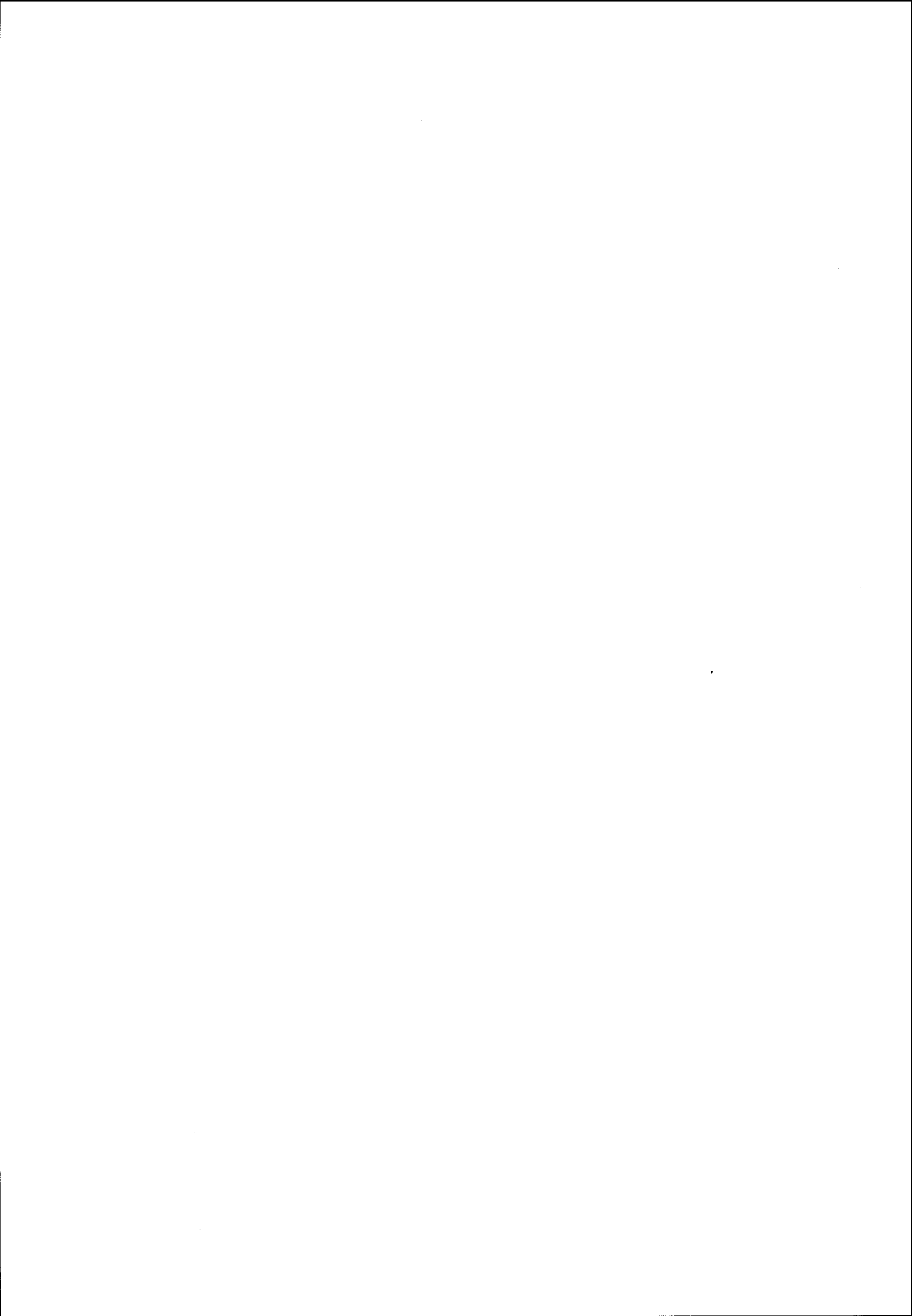
Given the importance of data coverage and the resolution of the scatterometer wind product, it may be clear that a timely data delivery has a high priority.

Acknowledgement

The Dutch Remote Sensing Council BCRS contributed funding to the experiments described in this paper.

REFERENCES

- Bell, R. S., 1994: "Operational use of ERS-1 products in the Meteorological Office", In proceedings of 2nd ERS-1 symposium - Space at the service of our environment. Hamburg 11-14 October 1993, ESA SP-361, pp. 195-200.
- Breivik, L.-A., 1993: "Assimilation of ERS-1 scatterometer wind information in a limited area model", research report from DNMI, Oslo, Norway.
- ESA, The Nine Candidate Earth Explorer Missions - Atmospheric Dynamics Mission, *Special report published by the Eur. Space Agency, ESA SP-1196(4)*, ESTEC, Noordwijk, the Netherlands, 1996.
- Gaffard, C. and H. Roquet, 1998: "Impact of the ERS-1 scatterometer wind data on the ECMWF 3D-VAR assimilation system", Submitted to Q.J.R. Meteor. Soc.
- Janssen, P. and B. Hansen, 1996: "Analysis of results from 3D-Var E-suites using the WAM model", EMWF Research Department Memorandum, available from ECMWF.
- Le Meur, D., 1996, personal communication.
- Stoffelen, Ad, 1996, "Error modeling of scatterometer, *in-situ*, and ECMWF model winds; A calibration refinement", Technical report 193, published by KNMI, Postbus 201, 3730 AE de Bilt, the Netherlands.
- Stoffelen, A., "A simple method for calibration of a scatterometer over the ocean", *J. Atmos. Oceanic Technol.*, in press, 1998a.
- Stoffelen, Ad, "Error modeling and calibration; towards the true surface wind speed", *J. Geophys. Res. (C)*, in press, 1998b.
- Stoffelen, Ad and David Anderson, "Scatterometer Data Interpretation: Measurement Space and inversion", *J. Atmos. Oceanic Technol.*, 14(6), 1298-1313, 1997a.
- Stoffelen, A. C. M. and D. L. T. Anderson, Scatterometer data interpretation: Estimation and validation of the transfer function CMOD4, *J. Geophys. Res.*, 102(C3) , 5767-5780, 1997b.
- Stoffelen, A. C. M. and D. L. T. Anderson, Ambiguity removal and assimilation of scatterometer data, *Q. J. Roy. Meteorol. Soc.*, 123, 491-518, 1997c.
- Stoffelen, Ad, and Paul van Beukering, Improved backscatter processing and impact of tandem ERS winds on HIRLAM, *HIRLAM project report nr 31*, IMET, Dublin, Ireland, 1997.



Lin, Mr., C.C.
 ESA ESTEC, APP-JPE
 Keplerlaan 1, Postbus 299
 2200 AG Noordwijk
 The Netherlands
 +31 71 565 5813
 clin@estec.esa.nl

Marshall, Mr., S.
 University of Nottingham
 Sutton Bonington Campus
 Loughborough, LE12 5RD
 U.K.
 +44 115 951-6257; ...-6251
 stewart.marshall@nottingham.ac.uk

Menard, Mr., Y.
 ESA-ESTEC, JIR
 Keplerlaan 1, Postbus 299
 2200 AG Noordwijk
 The Netherlands
 +31 71 565-4167; ...-3353
 ymenard@estec.esa.nl

Offiler, Mr., D.
 Meteorological Office
 London Road
 Bracknell, Berks, RG12 2SZ
 U.K.
 +44 1344-856 298; ...-854 026
 doffiler@meto.gov.uk

Ramseier, Dr., R.O.
 Microwave Group - Ottawa River
 3954 Armitage Ave. RR#1
 Dunrobin, Ontario, Canada
 +1 613 832-0411; ...-4166
 icedoctors@igs.net

Schmullius, Mr., C.
 DLR, Inst. of Radiofrequenztechnik
 Postfach 1116
 D-82230 Wessling
 Germany
 +49 8153 28-2337; ...-1449
 chris.schmullius@dlr.de

Skrovseth, Mr., P.E.
 Norwegian Space Centre
 Drammensveien 165
 P.O.Box 113 Skoyen
 N-0212 Oslo, Norway
 +47 2251-1800; ...-1801
 per.erik.skrovseth@spacecentre.no

Liu, Dr., W.T.
 JPL - Mail Stop 300-323
 4800 Oak Grove Drive
 Pasadena, CA 91109-8099
 USA
 +1 818-354 2394; ...-393 6720
 liu@pacific.jpl.nasa.gov

Martinez Aragonés, Mrs., S.
 ESA ESTEC
 Keplerlaan 1, Postbus 299
 2200 AG Noordwijk
 The Netherlands
 +31 71 5653401
 smartine@estec.esa.nl

Migliaccio, Prof., M.
 Istituto Universitario Navale
 Via A. Acton 38
 80133 - Napoli
 Italy
 +39 81 551-3976; ...-2884
 migliaccio@mavali.uninav.it

Oriol-Pibernat, Dr., E.
 ESA Headquarters, Metop/MSG
 8-10 Rue Mario-Nikis
 75738 Paris Cedex 15
 France
 +33 1 5369 7726
 eoriol@hq.esa.fr

Riazanoff, Mr., S.
 GAEL Consultant
 18, rue Albert Einstein
 77420 Champs-sur-Marne, France
 +33 1 6473-9955; ...-5160
 riazanoff@gael.fr

Schyberg, Dr., H.
 Norwegian Meteorological Inst.
 P.O. Box 43
 Blindern, N-0313 Oslo
 Norway
 +47 22 96 33 28
 h.schyberg@dnmi.no

Spencer, Mr., M.W.
 JPL (Jet Propulsion Laboratory)
 4800 Oak Grove Drive
 Pasadena, CA 91109-8099
 USA
 +1 818-354 1175; ...-393 5184
 mws@shiokeze.jpl.nasa.gov

Louis, Mr., J.F.
 Atmos. & Envirt. Research Inc.
 840 Memorial Drive
 Cambridge, MA 02139
 USA
 +1 617-349 2269; ...-661 6479
 jfl@aer.com

Mejia, Mr., C.
 LODYC-UPMC, T.26, 4 et.
 BC 100, 4 Place Jussieu
 75005 Paris
 France
 +33 1 4427-2709; ...-7159
 mejia@lodyc.jussieu.fr

Nobbe, Mr., E.
 NEO
 P.O. Box 341
 8200 AH Lelystad
 The Netherlands
 +31 320 28-2810; ...-2627
 nobbe@neo.nl

Pouliquen, Ms., S.
 Centre IFREMER de Brest
 BP 70
 29280 Plouzane
 France
 +33 2 9822-4492; ...-4533
 sylvie.pouliquen@ifremer.fr

Saavedra De Miguel, Ms., L.
 ESA-ESRIN, SERCO-TEC
 Via Galileo Galilei, CP 64
 00044 Frascati, Italy
 +39 6 941 80-679; ...-612
 lidia.saavedra.de.miguel@esrin.esa.it

Silvestrin, Mr., P.
 ESA ESTEC, APP-JPP
 Keplerlaan 1, PB 299
 2200 AG Noordwijk
 The Netherlands
 +31 71 565-3689; ...-4696
 psilvest@estec.esa.nl

Stephen, Mr., H.
 Asian Institute of Technology
 P.O. Box 4
 Kling Luang, Pathumthani 12120
 Thailand
 +66 2 524-6402; ...-5596
 haroon@ait.ac.th

Stoffelen, Mr., A.
KNMI
Wilhelminalaan 10, POB. 201
3730 AE De Bilt
The Netherlands
+31 30 22-06 585; ...-10 407
stoffelen@knmi.nl

Van Der Woerd, Mr., H.J.
IVM, Vrije Universiteit Amsterdam
De Boelelaan 1115
1081 HV Amsterdam
The Netherlands
+31 20 4449-555; ...-553
hans.van.der.woerd@ivm.vu.nl

Wagner, Mr., W.
EC-JRC, Space Applications Inst.
Via E. Fermi
I-21020 Ispra
Italy
+390332-786335; ...-789936
wolfgang.wagner@jrc.it

Young, Mr., N.W.
Antarctic CRC and Australian
Antarctic Division
GPO Box 252-80
Hobart, Tasmania 7001
Australia
+61 3622-62955; ...-62902
neal.young@utas.edu.au

Thiria, Mrs., S.
LODYC UPMC
BC 100, 4 Place Jussieu
75005 Paris
France
+33 1 44 2727 08
thiria@lodyc_jussieu.fr

Van Leeuwen, Dr. Ing., H.J.C.
Synoptics
Costerweg 1-k
6702 AA Wageningen
The Netherlands
+31 317-421221; ...-416146
main@synoptics.nl

Wismann, Mr., V.
IFARS
Karlastr. 81
79106 Freiburg
Germany
+49 761 2851-717; ...-719
mfars@compuserve.com

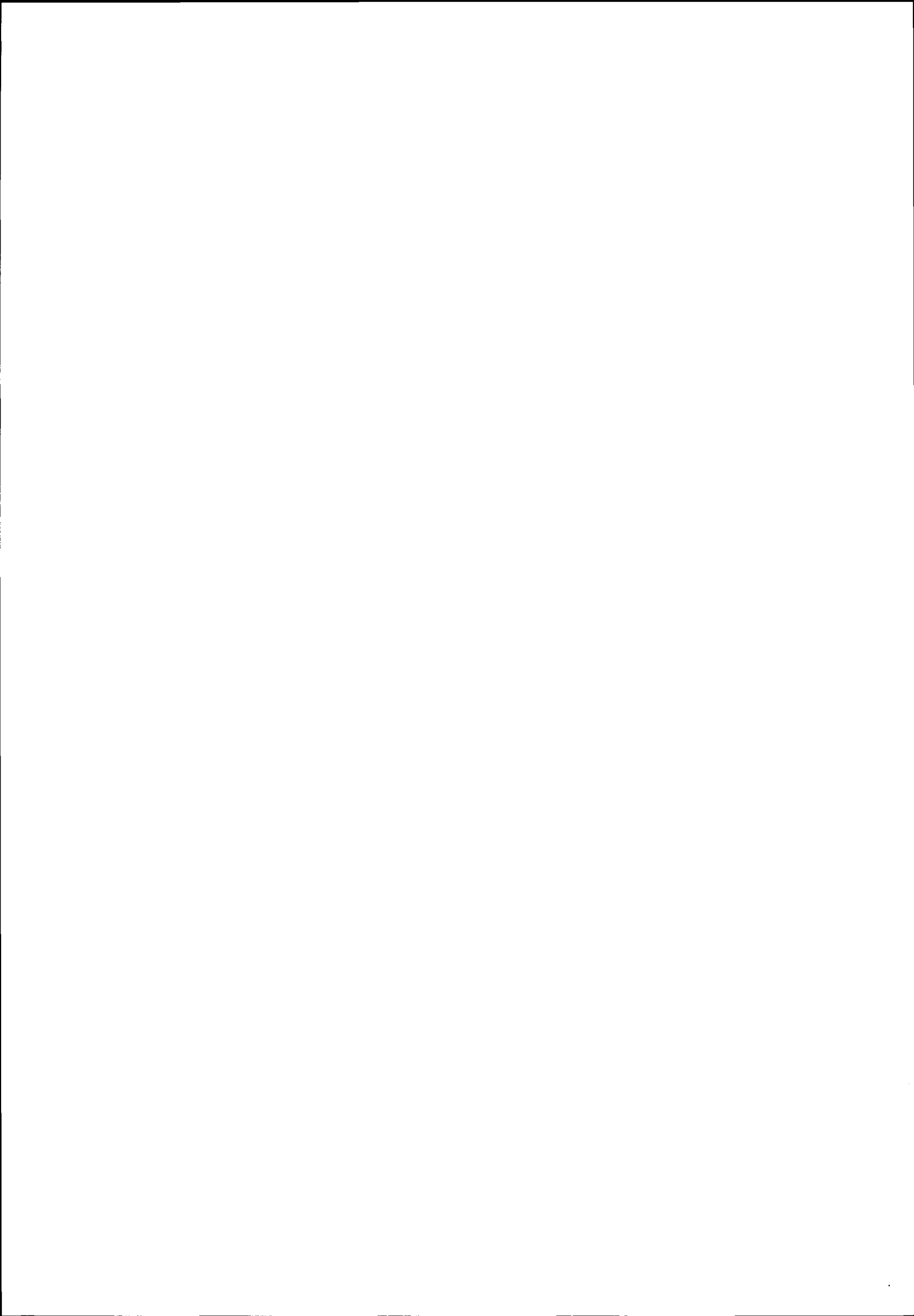
Zecchetto, Mr., S.
ISDGM-CNR
1364 S. Polo
30125 Venice
Italy
+39 41 521 6848
+39 41 260 2340
stefano@isdgm.ve.cnr.it

Tran, Mrs., N.
LODYC UPMC
BC 100, 4 Place Jussieu
75005 Paris
France
+33 1 4427-2709; ...-7159
tran@lodyc.jussieu.fr

Voorrips, Dr., A.
KNMI
Wilhelminalaan 10, POB 201
3730 AE De Bilt
The Netherlands
+31 30-2206826; ...-2210407
voorrips@knmi.nl

Woodhouse, Mr., I.
University of Dundee
Department of APEME
Dundee DD1 4HN
Scotland, U.K.
+44 1382-344933; ...-345415
i.h.woodhouse@dundee.ac.uk

Instruments & Processing



The ERS Scatterometer instrument and the On-Ground processing of its Data.

Pascal Lecomte

Directorate of Application Programmes - Remote Sensing Exploitation Division
ERS Mission Control and Product Assurance Section
ESA/ESRIN, Via Galileo Galilei, 00044 Frascati, Italy
tel: ++39-6-941 80 670, fax: ++39-6-941 80 612
Email: pascal.lecomte@esrin.esa.it

Introduction

The ERS scatterometer is a radar working at 5.3 GHz (C-Band) designed to measure the wind speed and direction. This instrument has three antennae looking 45° forward, sideways and 45° backwards with respect to the satellite's flight direction.

The radar is sensitive to the sea surface roughness which is directly related to the wind characteristics (speed and direction) near to the surface. Measuring the surface roughness, one can derive information on the wind.

More recently it has been found that scatterometer data are also very valuable for land, snow and ice applications. Parameters like surface moisture, sea ice concentrations, sea ice age and snow conditions could be successfully retrieved using scatterometer data. Particularly promising is the derivation of sea ice masks based on the polarization ratios of the scatterometer data (for NSCAT) and on the different backscatter level behaviour at different incidence angles (for ERS scatterometer), which compare well to similar products derived from SSM/I data. Over land, studies are showing the usefulness of scatterometer data to determine the impact of a lack of rain fall in sahelian areas and can help in having an early drought warning in these regions.

The scope of this document is to describe in detail the characteristics of the Scatterometer raw data when received by the ground station and of the various algorithms used during the generation of the normalised radar cross section (σ^0) and of the wind products.

The ERS Satellites

On 17 July 1991 the European Space Agency launched ERS-1 into a sun-synchronous, polar orbit at an altitude of about 780 km and an inclination of 98.5°, followed by ERS-2 launched in April 1995.

ERS-1 is an Earth Observation satellite that observes the ocean, the sea ice, the cryosphere and the land surface. The satellite (Fig. 1) carries three active microwave instruments: a synthetic aperture radar (SAR), a wind scatterometer, and a radar altimeter (RA), as well as two radiometers: an infrared-visible Along Track Scanning

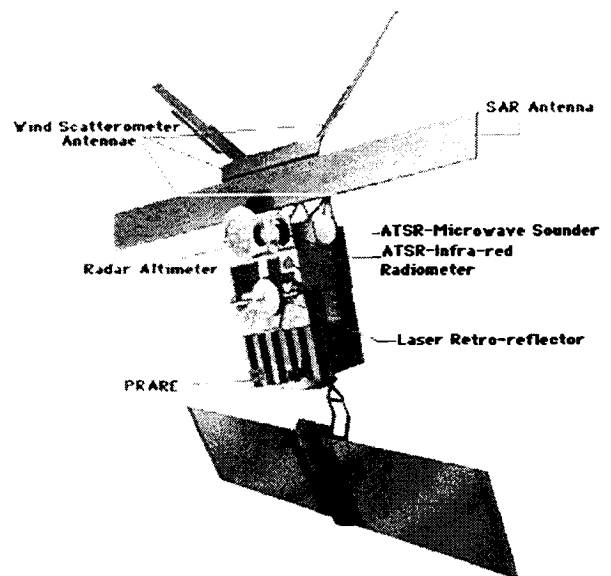


Figure 1: The ERS-1 satellite

Radiometer (ATSR) and a MicroWave Radiometer, the latter being mainly dedicated to the retrieval of atmospheric corrections for the RA. The RA and ATSR instruments collect data continuously while the Active Microwave Instrument (AMI), containing the SAR and the wind scatterometer, is configured in an alternating operation so that the SAR Wave Mode runs jointly with the wind scatterometer while the SAR Image Mode only runs with the scatterometer turned off [1].

Both ERS-1 and ERS-2 satellites have a standard orbit repeat cycle of 35 days. Two other repeat cycles of 3 days and 168 days have also been operated with ERS-1.

The Active Microwave Instrument

AMI Main Characteristics

The AMI is a radar operating at 5.6 cm wavelength at a frequency of 5.3 GHz (C-Band). It has a set of four different antennae to illuminate the Earth's surface and to receive backscattered energy. By on-board and on-ground signal processing, two-dimensional imagery is produced. In the picture elements the intensities represent the normalised radar backscattering coefficients (σ^0) and x and y coordinates correspond to the along-track

and cross-track position of the areas being observed. It is identical on both ERS-1 and ERS-2 satellites.

Areas of interest for observation include the polar ice caps, the ocean, coastal zones and the land areas. The realisation of the mission objectives for the AMI, as specified in geophysical terms, relies on the fact that the radar backscattering is affected by surface roughness, conductivity and dielectric properties of the area under observation. Consequently, surface properties can be derived from radar imagery. In the framework of the ERS mission the surface wind speed, wind direction and wave image spectra are routinely estimated from radar data in near real-time. For other applications, the radar imagery is the primary output product.

In addition to surface properties, isolated point targets (ships, icebergs, buildings, etc.) show up in the radar imagery as bright spots as long as their radar cross sections are big enough. The controlling factor is the ratio of the radar cross section of the point target to the product of the normalised radar cross section (σ^0) of the surrounding area and the radar resolution cell.

AMI Functional Description

To meet the geophysical mission objectives, the AMI has to provide imagery with different characteristics to match each application. It, therefore, has three modes of operation, namely the Image Mode, the Wave Mode and the Wind Mode.

For this, two separate radars are incorporated within the AMI. A Synthetic Aperture Radar (SAR) provides the Images and the Wave Modes of operation and a Scatterometer provides the Wind Mode operation. The operational requirements are such that each mode should operate independently. However, in addition, the Wind and Wave Modes are capable of interleaved operation, i.e. the so-called Wind/Wave Mode.

The AMI functional block diagram is shown in Fig. 2.

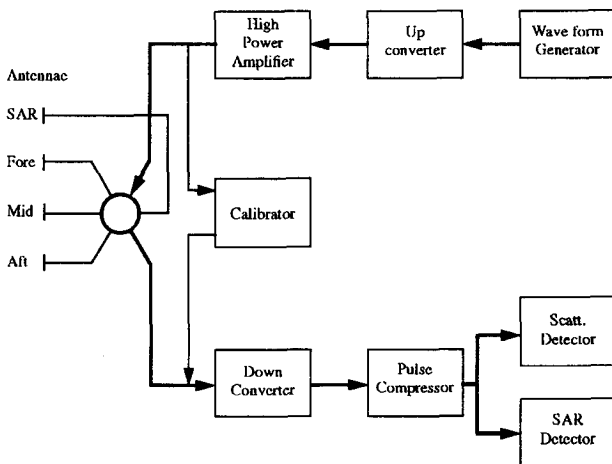


Figure 2: Active Microwave Instrument Block Diagram

The Wind Mode

The measurement objective of this mode is the determination of wind speed and direction over the ocean. Its geophysical performance is specified in Table 1.

Table 1: Scatterometer Geophysical Specifications

Swath width	500 km
Spatial resolution	50 km
Grid Spacing	25 km
Wind speed: accuracy:	0.5 to 30 m/s (s.d.) 2 m/s (bias) 0.3 m/s
Wind direction accuracy	0 to 360 ° (s.d.) 20 ° (bias) 0.8 °

The principle underlying the operation of the scatterometer is the dependence of normalised radar cross section on ocean roughness, which in turn is dependent upon the surface wind speed. In addition, the normalised radar cross section is anisotropic with respect to the angle between wind vector and incident radar beam.

The wind scatterometer is configured as a real aperture pulse radar providing three radar images of the ocean surface with a spatial resolution of 50 km and a swath width of 500 km. The three images are acquired by three different antennae: one, the mid-beam, looking to the right side of the satellite, perpendicular to the ERS ground track, one looking forward at 45 degrees azimuth projection angle, with respect to the mid-beam, and one looking backwards at 45 degrees azimuth projection angle with respect to the mid-beam, as depicted in the scatterometer radar geometry in Fig. 3.

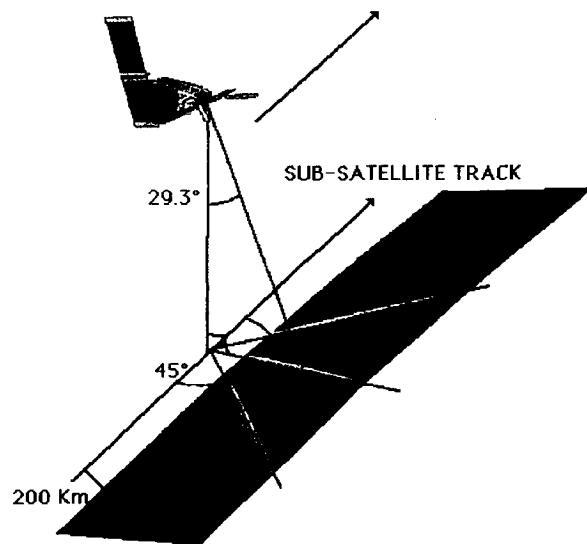


Figure 3: The ERS satellite scatterometer geometry

With the aid of these three σ^0 measurements of the same area made from different measurement directions,

wind vectors (speed and direction) can be determined. The conversion of σ^0 values into wind data is performed for each node with the aid of mathematical model, CMOD4 [2], which defines the relationship between σ^0 , wind speed and wind direction, incidence angle of the scatterometer pulse and polarisation.

The scatterometer illuminates the sea surface sequentially by RF pulses in different directions using the three antennae. The nominal look angles of these antennae are 45° fore and aft and broadside with respect to the satellite's velocity vector. This model is based on the pre-launch estimate of the radar backscattering behaviour, which was determined during a multi-year programme of experiments, using airborne radars, but 'tuned' in orbit on the basis of dedicated geophysical validation campaigns and data assimilation into numerical weather prediction models.

Radar echo is provided continuously over a 500 km wide continuous swath along the satellite ground track so wind speed and direction can be deduced at nodes which have a 25 km separation along and across the sub-satellite track within the swath.

Each node is centred within a resolution cell of $50 \times 50 \text{ km}^2$, which is determined in the range and direction by appropriate range gating of the received echo signal and in azimuth by the averaging of corresponding range-gated echo signals.

In order to achieve the correct illumination of these nodes by all three beams and to minimise Doppler shifts, the satellite is steered about its yaw axis such that the effects of Earth rotation is counteracted.

In Wind Mode, the transmit pulse is produced at the intermediate frequency by the platform generator. The IF pulse is amplified and converted to an RF signal in the up-converter unit and amplified by the High-Power Amplifier. The transmit signal is routed to the correct antenna by the circulator assembly, which in this mode is under the control of the scatterometer electronic unit.

The received signal is down-converted, amplified and routed to the scatterometer detector.

Vital to many applications of scatterometer data is absolute calibration, defined as the process by which the digital output of the instrument is converted into physical units of radar cross-section per unit area, sigma nought, with known levels of accuracy and precision. Therefore noise measurements and internal calibration are regularly performed.

For the Mid Antenna, the return echo is filtered and sampled in complex form (i.e. I and Q). Since the Doppler variation is significant over the swath width (20 kHz near swath to 140 kHz far swath from the Side antennae), a programmable Doppler compensation law is applied on the receiver signal before filtering and complex sampling.

The main engineering parameters of the AMI wind scatterometer mode are given in Table 2.

Table 2: AMI Wind mode Main Engineering Parameters

Frequency	5.3 GHz \pm 52 kHz		
Polarisation	Linear Vertical		
Swath	500 km		
Peak Power (RF)	4.8 kW		
	Fore	Mid	Aft
Antenna aspect angle	$+45^\circ \pm 0.5^\circ$	$0^\circ \pm 0.5^\circ$	$-45^\circ \pm 0.5^\circ$
Antenna length	3.6 m	2.5 m	3.6 m
Dynamic range	42 dB		
Pulse length	130 μ s	70 μ s	130 μ s
No. of pulses per 50 km	256	256	256
Radiometric resolution (Kpe)	6 %	6 %	6 %
Detection Bandwidth	25 kHz	25 kHz	25 kHz
Sampling Scheme	Complex I/Q 8 bits each		
Return Echo window duration	3.93 ms	2.46 ms	3.93 ms

Operational Constraints

The AMI image mode can be operated for up to 12 minutes per orbit. Each operation sequence must be longer than 1 minute and no more than 4 operation sequences are possible per orbit.

The AMI wind mode and wave mode can be operated separately.

Simultaneous operation of wind and wave mode is provided in the interlaced wind/wave mode. All performances and programming capabilities provided for the sequence are interrupted every 30 seconds for a duration of two cycle of Fore, Mid and Aft antenna (or FMA sequence) to permit wave operation.

The only constraint on realising the maximum duration of operation in wind, wave or interleaved modes is the on-board energy resource limitation.

Both wind and wave mode data are recorded on-board.

The Wind Scatterometer

Functional Blockdiagram

The AMI functional blockdiagram for wind mode is shown in Fig. 4.

Transmitter

A detailed block diagram of the transmitter is shown in Fig. 5. The lower and the central parts are used for Imaging and Wave modes whereas the upper and the central parts are used for Wind mode.

When operated in Wind mode, the Active Microwave Instrument (AMI) uses the same Centre frequency (5.3 GHz) and the same peak power ($\sim 5 \text{ kW}$) than in SAR imaging mode, but the type of modulation is different.

The transmit signal is a pulsed RF carrier with constant frequency (Rectangular Pulses as shown on Fig. 6) switched sequentially between the three scatterometer antennae (fore, mid and aft).

To take into account the different geometry for the side antennae (fore and aft) and for the mid antenna as

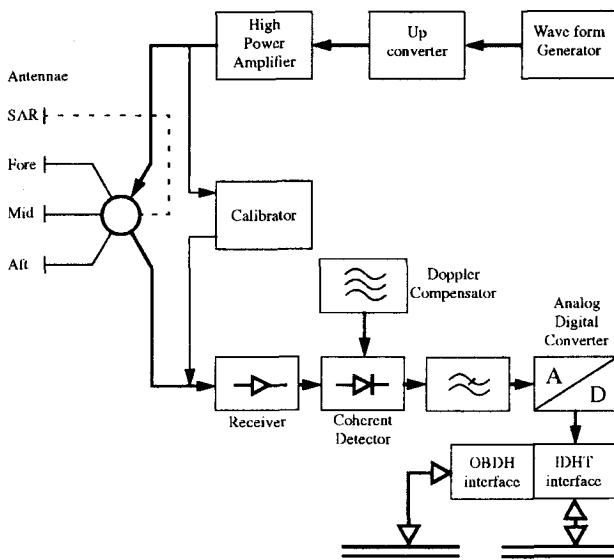


Figure 4: Scatterometer functional block diagram

frequency are the same for the side antennae but are different for the mid antenna.

A rectangular pulse of 130µs for the Side Antennae and 70 µs for the mid antenna is generated at an IF of 123.2 MHz. with a respective pulse repetition interval of 10.21 ms and 8.7 ms. The upconverter shifts this signal

20 dB / div (within pulse)

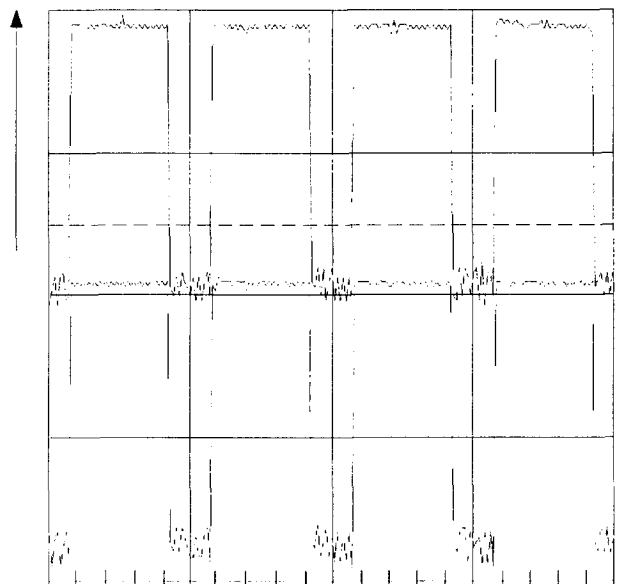


Figure 6: Example of scatterometer pulses as measured on ground during instrument testing

in frequency up to 5300 MHz. The required high RF output power is produced by the HPA (High Power Amplifier) which contains a TWT (travelling Wave Tube) as amplifying device. An automatic level control loop

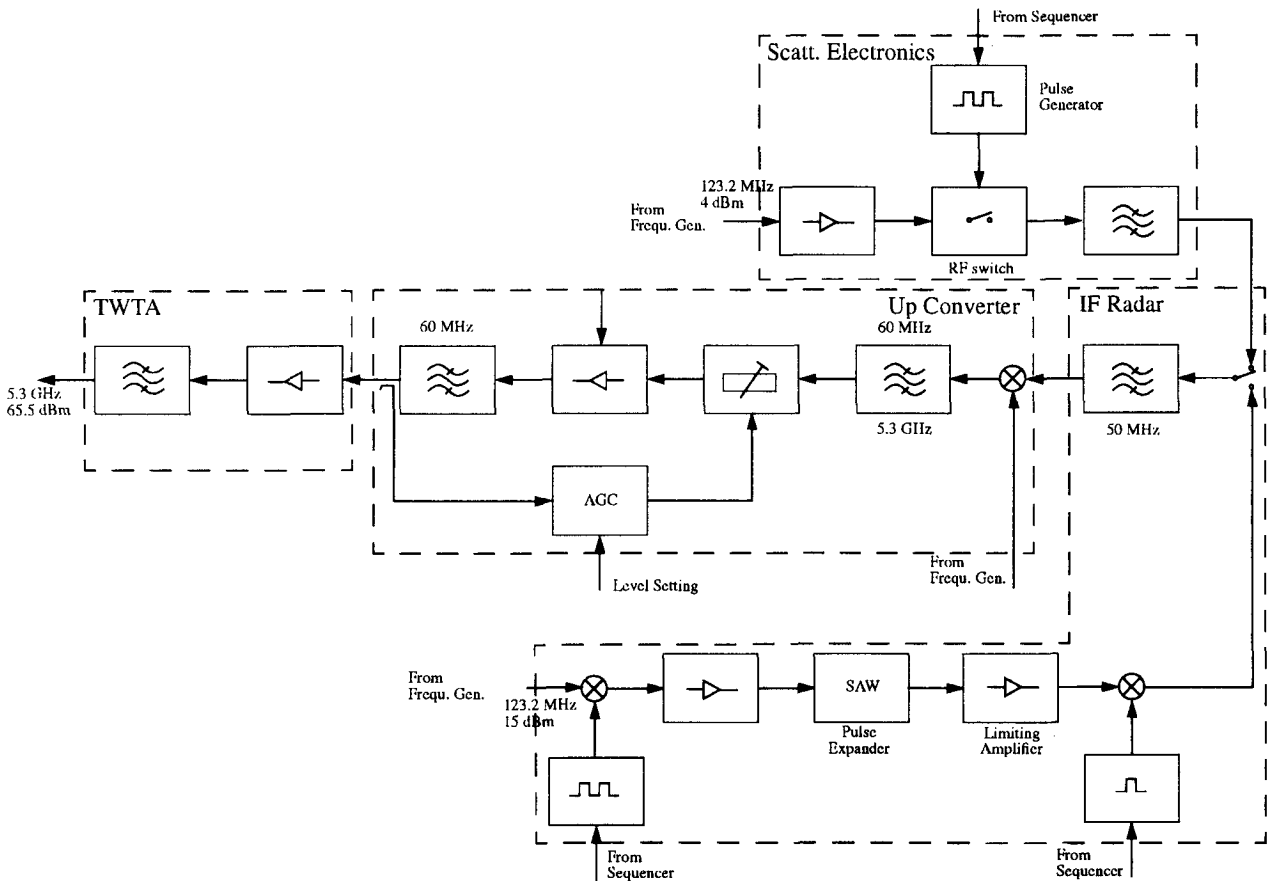


Figure 5: Transmitter blockdiagram

within the upconverter maintains the TWTA input power at a constant level adjusted to drive the TWTA just well into saturation. The mean RF output power within pulse measured at the HPA Waveguide flange is at least 65.5 dBm.

Scatterometer Antennae

The scatterometer antennae are planar waveguide arrays connected to the transmitter and the receiver via the circulator assembly (switch matrix). The measured antennae boresight gains (for ERS-2) are 30.6 dB, 28.0 dB and 30.9 dB respectively for the Fore, Mid and Aft antennae. The cross polarisation is more than 40 dB below the maximum co-polarisation for each antenna. The fore and aft antennae are identical in shape but have a different pointing, respectively 45° and 135° with respect to the flight direction.

Calibrator Sub-System

The calibrator is aimed at deriving highly stable, delayed and amplitude scaled samples of the transmitted pulses. The analysis of these calibration pulses at the receiver output permits the monitoring of the product of the transmitted power and the receiver gain, and to compensate for it (see Fig. 7) [4].

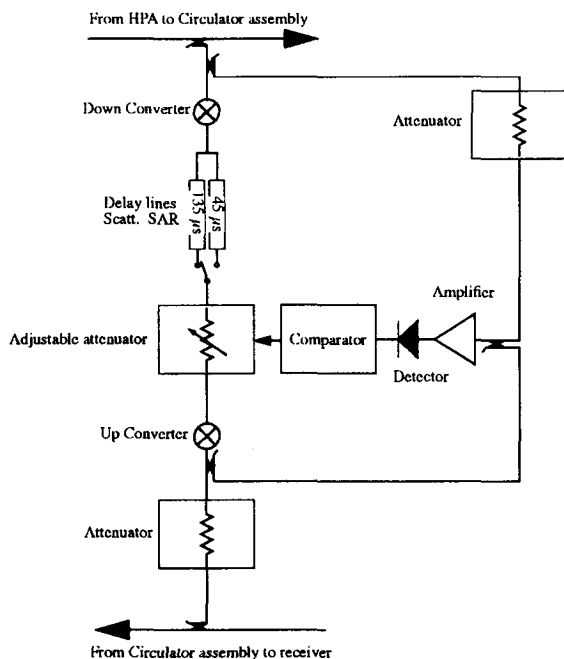


Figure 7: Basic elements of the AMI Calibration S/S

Scatterometer Measurements

After reception of the return echoes, the signal is filtered and a non-coherent detection is performed on-board still in the form of I and Q components and for each antenna separately. The doppler compensators remove the frequency shift placed upon the received signal due to the motion of the spacecraft and the beam

look direction (mainly for the fore and aft antennae). The I and Q components are converted into digital codes and telemetered to ground via the IDHT (Instrument for Data Handling and Transmission) interface. Due to the higher dynamic range requirements in Wind mode the A/D converter has a finer resolution in Wind mode (8 bits) than in Imaging mode (only 5 bits). For radiometric stability and accuracy purposes more gain drift calibration pulse and noise measurements are performed in Wind mode than in the other modes.

Timelining

The three scatterometer antennae, fore (F), mid (M) and Aft (A), are operated in sequences of 32 Radio Frequency pulses each, starting with the fore antenna as shown in Fig. 8. The Pulse Repetition Interval (PRI)

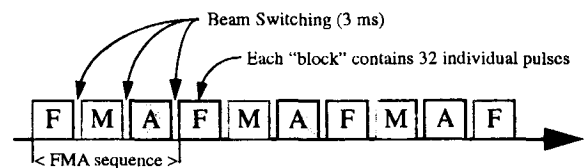


Figure 8: Scatterometer Beam Switching sequence

being of 10.21 ms for the side antennae and of 8.7 ms for the mid antenna, the total length of a repeat cycle called a FMA sequence is 940.84 ms as summarised in Table 3.

Table 3: Timelining Diagram for Wind mode

Fore Antenna	32 x 10.21 ms	326.72 ms
Switching		3.00 ms
Mid Antenna	32 x 8.70 ms	278.40 ms
Switching		3.00 ms
Aft Antenna	32 x 10.21 ms	326.72 ms
Switching		3.00 ms
Total of one FMA sequence		940.84 ms

Four FMA sequences last 3.763 seconds and correspond to 25 km along the sub-satellite track when the satellite is at an altitude of 785 km and is continuously repeated in the Wind mode with any gaps.

The fixed duration of this sequence means that it does not always correspond exactly to 25 km along the sub-satellite track as the satellite altitude varies over the total ERS orbit from 769 km to 825 km, and with the altitude, the relative velocity of the spacecraft to the ground.

Gain drift calibration pulse measurements or noise measurements are taken after each transmit pulse before the echo signal returns. During each beam sequence of 32 pulses, 4 gain drift calibration pulses and 28 noise signals are measured (see Fig. 9). In the calibration unit, the gain drift calibration pulse is delayed by 135 μs rela-

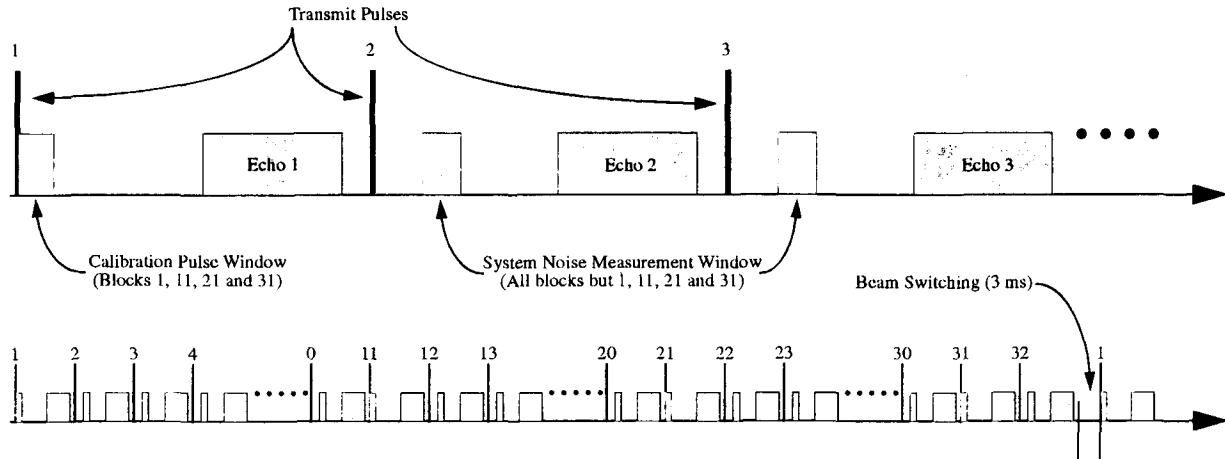


Figure 9: Sequence of 32 Scatterometer transmissions

tive to the transmit pulse in order to fall in the Calibration window.

Table 4 summarises all the pulse and sampling characteristics.

Table 4: Pulse and sampling windows characteristics in Wind mode

Parameter		Fore and Aft beams	Mid Beam
Pulse Shape		Rectangular	Rectangular
Pulse width		130 μ s	70 μ s
Pulse Repetition Interval		10.210 ms	8.700 ms
Sampling rate		30 kHz	30 kHz
Number of bits for I & Q		8 bits	8 bits
Number of samples	Echo Signal	118	74
	Cal. Pulse	30	30
	Noise	32	32
Calibration Window start		100 μ s	100 μ s
Calibration Pulse Delay		135 μ s	135 μ s
Length of Cal. Window		1.000 ms	1.000 ms
Noise Window start		1.500 ms	1.500 ms
Length of Noise Window		1.030 ms	1.030 ms
Echo Window start		5.400 ms	5.200 ms
Length of Echo Window		3.910 ms	2.440 ms

Doppler Compensation

The radar echo from a target on the earth's surface doesn't always have the same frequency as the transmitted signal because of doppler shifts, due to the relative motion between the satellite and the target. This motion depends on satellite velocity, antenna look angle and earth rotation.

The range of the doppler shift is 50 - 150 kHz for the side antennae and 0 - 10 kHz for the Mid antenna. By yaw - steering the satellite, the doppler shifts in the mid - antenna are minimised but not entirely eliminated. It follows from the above that continuous frequency tuning of the scatterometer receiver is required to keep the echo signals within the 25 kHz on-board bandwidth.

The frequency deviation is not only function of the echo time delay, but varies also over the orbit due to geometrical effects and earth rotation.

Nominally, every 15 s the on-board doppler correction is updated, but provisions are made that no update takes place during a 32 pulses sequence of a single beam.

The required tuning signal is synthesised on-board by the scatterometer electronic module, using a time dependent algorithm with coefficient provided to the instrument by macrocommand.

The accuracy with which the received signals are actually centred within the receiver band depends on the pointing errors, the receiver hardware errors, the computational and curve-fitting errors (for the on-board compensation), as well as the uncertainties introduced by the geometry such as earth and orbit modelling.

These errors have an effect on instrument radiometric stability. The on-board errors are partly compensated by the on-ground filter and fine tuning algorithms of the Wind mode processor. The actual receiver tuning errors are limited to a small fraction of the 25 kHz receiver bandwidth.

The blockdiagram of the scatterometer detector and doppler compensator is shown in Fig. 10.

Receiver gain Setting

The receiver Gain is set differently for the Side and the Mid antennae in order to take into account the different bandwidth of the signal due to the geometry of the system.

The nominal receiver gain, both for ERS-1 and ERS-2 is -111.7 dBW for the Side beams and -106.6 dBW for the Mid beam. Because of the reduce transmitted power required for ERS-2 the Receiver gain was respectively set to -112.6 for the Side antennae and -107.91 for the Mid antenna.

Sampling

The echo, as well as the calibration pulses and the noise, are sampled at 30 kHz. The Analogical to Digital

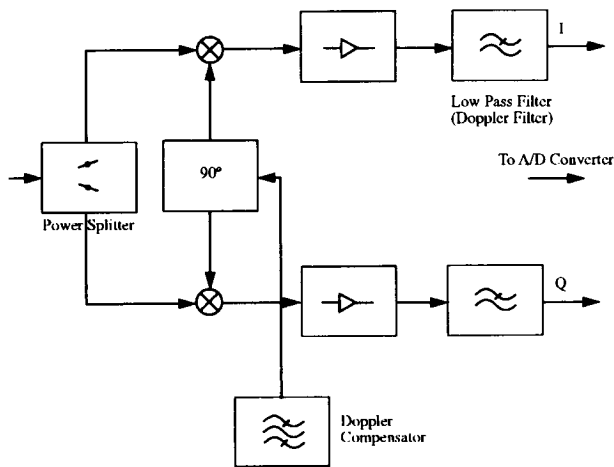


Figure 10: Scatterometer Detector / Doppler

converter is making instantaneous measurement of the input signal. This sampling rate corresponds to roughly 5.2 km at 18° incidence angle (Mid beam, inside the swath) and 13.3 km at 68° incidence angle (side antennae, far swath).

Interface to the Instrument for Data Handling and Transmission

All echo and calibration data are directly transferred to the IDHT without any on-board processing, whereas the noise data are pre-processed on-board by software. In fact all noise samples are averaged over each 32 shot sequence. This means that the 32 noise samples per sampling window multiplied by the 28 noise sample windows, which results in 896 noise samples are averaged on-board. The averaging is made separately for the I and the Q channel. The averaged noise data is then included as a 16 bit word for I^2 and for Q^2 as part of the auxiliary data stream.

The data are transferred to the IDHT in form of source packets. Each source packet includes the data collected during a 32 shot beam sequence. The generation time for a source packet is therefore 326.72 ms for the side antennae and 278.40 ms for the mid antenna. The IDHT will read out at a mean data rate of 1.09 Mbit/s one source packet in a time not greater than 280 ms. The IDHT stores and transmits the measurement data in the same sequence in which it was sampled.

It is important to note that the Mid antenna source packet differs from those of the Fore and Aft antennae by the fact that less echo data are present (74 instead of 118). To obtain three source packets of the same size, 7860 bytes, dummy data are inserted at the end of the Mid packet.

Source Packet Description

Each source packet is composed of three parts, the primary and secondary headers and the measurement data field.

The primary header contains three fields:

- the Packet Identifier containing in particular the antenna id and the operation mode (Wind, Wind/Wave or calibration mode).
- the Packet Sequence Control coded over two bytes. This parameter is restarted after each switch-on in that mode and labels each individual FMA sequence. Then after switch-on the Source packets will be labelled 0, 0, 0, 1, 1, 1, 2, 2, 2, ... etc...
- The source packet length fixed to 1EAD (HEX) which correspond to 7854 bytes (from 0 to 7853) and doesn't include the 6 bytes of the primary header.

The secondary header contains the time code given by the ICU (Instrument Control Unit) and the auxiliary data.

The time data included in a source packet shall have a known relationship to the actual time at which the data contained in that packet is sampled with an accuracy of $\pm 1 \mu\text{s}$. The time data is sampled 10.210 ms (-1, + 250 μs) for the side antennae and 8.700 ms (-1, + 250 μs) for the Mid antenna after the last RF transmit pulse leading edge (Fig. 11).

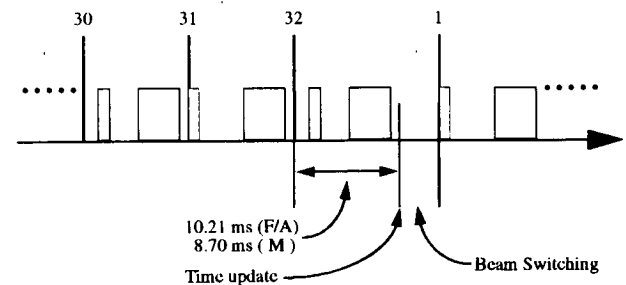


Figure 11: Sampling of the time code

The auxiliary data supply the additional information needed for the interpretation and the processing of the measurement data. In particular the following information is included:

- Scatterometer time from the ascending node (the resolution is $1/256 = 3.90625 \text{ s}$). Reset to zero at each ascending node.
- Scatterometer Calculation time used for the on-board doppler compensation. Updated every 15 s.
- The orbit period used to reset the scatterometer and the scatterometer calculation times.
- All the instrument setting (gains, modes Attenuations, doppler coefficients).
- The noise measurements for I^2 and Q^2 coded over 16 bits.

The measurements data is simply all the I and Q samples coded over 1 byte for the following measurements:

- 1st Calibration Pulse
- 1st to 10th Echoes
- 2nd Calibration Pulse
- 11th to 20th Echoes
- 3rd Calibration Pulse
- 21st to 30th Echoes
- 4th Calibration Pulse
- 31st to 32nd Echoes

Which corresponds to 7792 bytes for the Fore and Aft antennae and 4976 bytes for the Mid antenna.

2816 bytes of dummy data are added to the Mid antenna source packet in order to obtain a total of 7796 for the measurement data field.

Scatterometer Data Characteristics

It is interesting to have a description of the three major parameters included in the source packets, namely the noise measurement, the calibration pulse and of course the echoes. These measurements are given in ADC units which correspond to one step of the Analog to Digital Converter.

The noise measurements

Each source packet contains one average of the I^2 and Q^2 noises estimated from the $32 \times 28 = 896$ I and Q noise samples retrieved during one measurement block. Typically this value is 1 ADC step for the Fore and Aft antennae and 0 for the Mid Antenna as shown on Fig. 12. The averaged values since ERS-2 scatterometer started operation are stable as summarised in Table 5.

Table 5: ERS-2 Scatterometer I and Q noise value

Fore Antenna		Mid Antenna		Aft Antenna	
I	Q	I	Q	I	Q
0.97403	0.88831	0.00000	0.00000	0.92508	0.81170

The instrument noise is so low that it never exceeds one quantisation step for the side antennae and is always set to 0 for the Mid beam. This fact is confirmed on Fig. 13 which shows the evolution of the noise levels during the overall ERS-2 scatterometer operation (23 November 1995 - 17 August 1998).

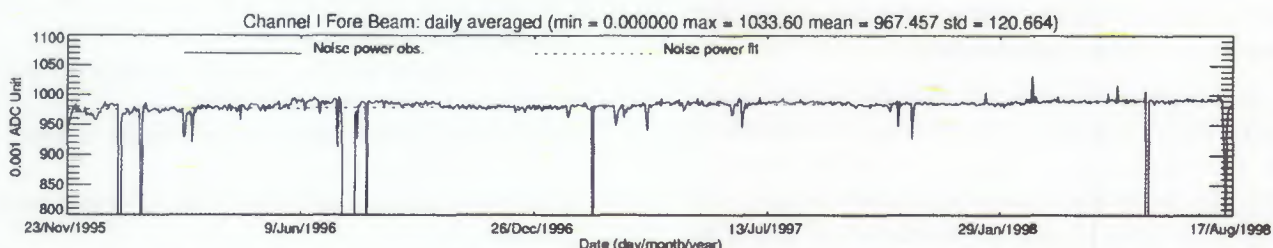


Figure 13: ERS-2 scatterometer noise level evolution since the beginning of the mission (23 Nov. 1995 - 17 Aug. 1998)

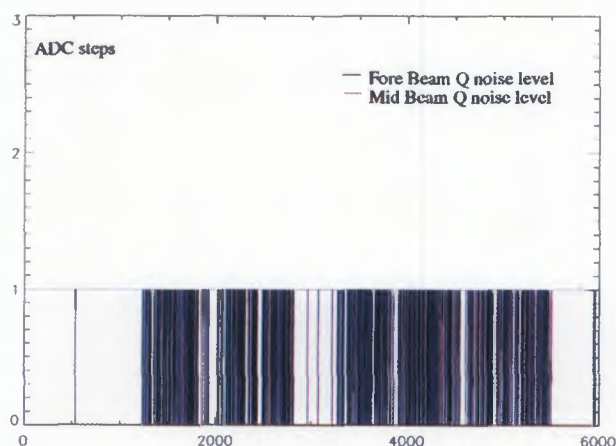


Figure 12: Typical Fore and Mid noise measurements for a complete orbit every FMA sequence (every 904.8 ms).

When this level of noise is compared to the level of the echoes (Fig. 18 and Fig. 19), the reason why no negative values of the σ^0 are ever extracted from the ground processor, especially after the spatial filtering (see the related paragraph hereafter), becomes very clear.

Another discussion on the overall system noise can be found in [15], included in this workshop proceedings.

The calibration pulses

The calibration pulse is an image of pulse sent toward the ground. It is an important element of the data for two reasons. First, it is used to normalise the returned echo in order to correct for any short term or long term evolution of the High Power Amplifier. Second, it is permanently and very closely monitored in order to anticipate instrument ageing and to detect anomalies.

Table 4 gives the main characteristics of the calibration pulse (130 μ s and 70 μ s respectively for the Side and Mid antennae, delayed by 135 μ s) and of the Calibration window (it starts 100 μ s after the pulse and it is sampled at 30 kHz). A schematic of the pulses (Side and Mid antennae) at the output of the HPA, of the calibration pulses delayed in the calibration sub-system and low pass filtered and of what would be the sampling of this later pulses is given in Fig. 14 and Fig. 15. The comparison with typical pulses actually measured is shown on Fig. 16.

If the sampling of the calibration pulses doesn't allow for a detailed analysis of the pulse shape or of the low

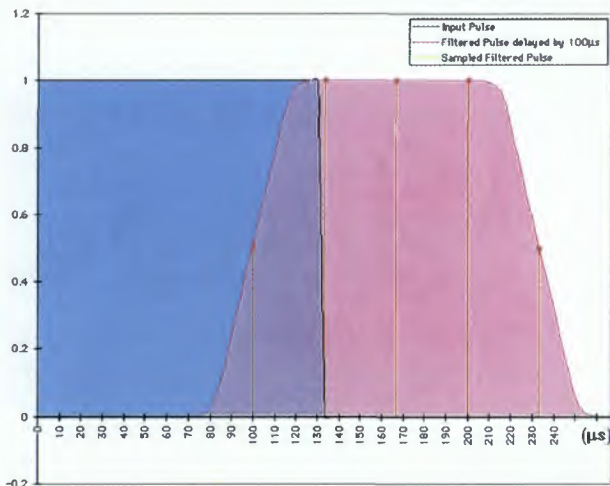


Figure 14: Fore Calibration Pulse Timing and sampling

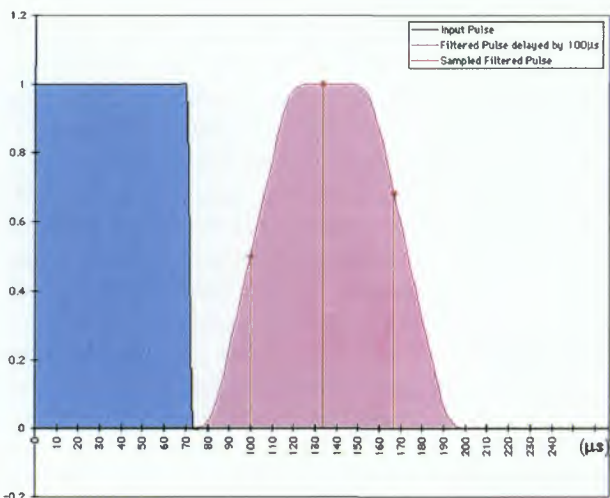


Figure 15: Mid Calibration Pulse Timing and sampling

pass filter, it certainly allows to monitor the HPA power and the instrument timing.

It is important to remember that, due to the reduction of power required to operate the ERS-2 AMI, the TWTA

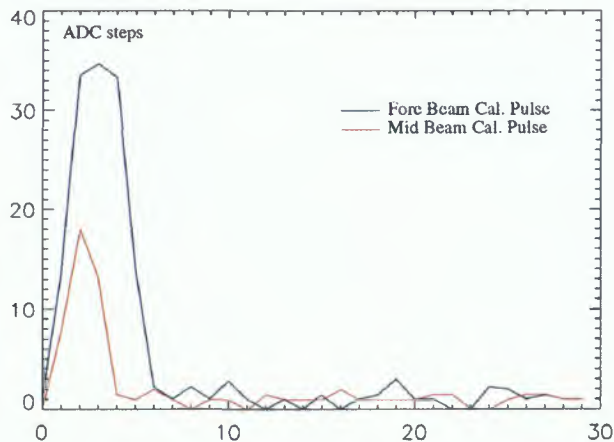


Figure 16: Typical Fore and Mid Beam Calibration Pulse

is not working in saturation. Therefore, any variation of the pulse's power (due to pulse generator for example) will be seen in the transmitted pulse and in the echo.

In this context it becomes very important to monitor very closely the ERS-2 Calibration pulse power in order to assess any degradation of the transmission part of the instrument. The same monitoring for ERS-1 never showed any evolution of this part of the instrument.

Fig. 17 shows the evolution of the Calibration Pulse power evolution since the beginning of the ERS-2 AMI mission (23 November 1995 - 17 August 1998). It is clear that the power is decreasing by roughly 0.14 dB per cycle since the Calibration Sub-System B is operationally used (August 1996). It seems that the slope was slightly smaller when the sub-system A was selected. This power decrease is automatically corrected for during the on-ground processing.

The echoes

The returned echoes are sampled at a rate of 30 kHz which corresponds to roughly 10 km on ground (see Sampling), after the doppler compensation and the low pass filter.

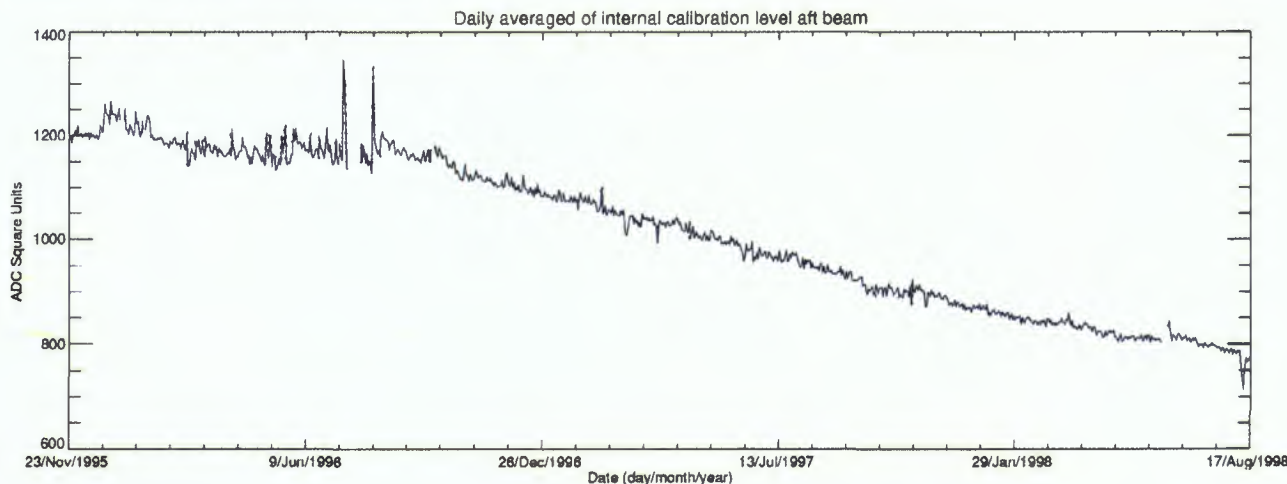


Figure 17: ERS-2 scatterometer calibration pulse power evolution since the beginning of the mission

Fig. 18 and Fig. 19 are respectively showing Fore and Mid antenna echoes over ocean (East Tropical Pacific) before any processing on ground and for comparison, Fig. 20 and Fig. 21 are showing a Fore and mid antenna echo over ice (North of Alaska during the winter 97-98).

Because of the different size of the Side and Mid antennae (respectively 3.6 m and 1.8 m length) and also for a small part because of different gains used, the power level of the Mid beam is roughly half than of the Side beams.

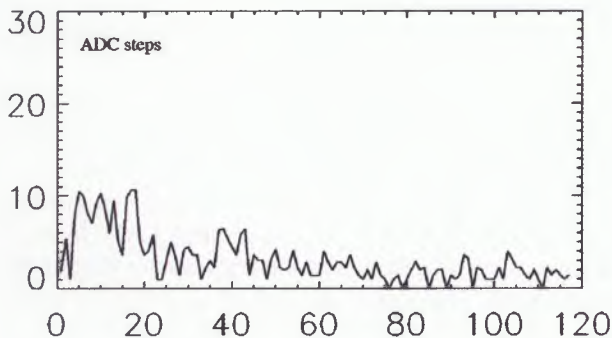


Figure 18: Typical Fore Beam echo over ocean

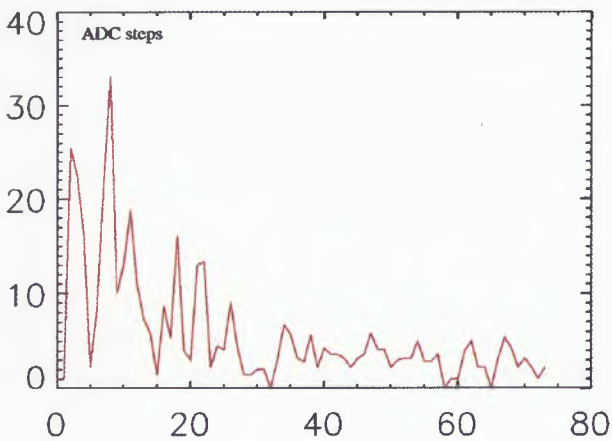


Figure 19: Typical Mid Beam echo over ocean

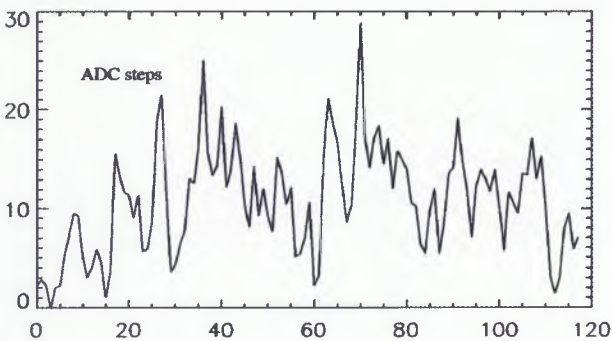


Figure 20: Typical Fore Beam echo over ice

Scatterometer Processing to σ^0

Performances

The performance of the scatterometer is defined in terms of:

- swath coverage
- localisation
- σ^0 measurement range and stability
- output signal response to a fictive point target (both in time and frequency domain)

In order to achieve the required overall performances, the measurement data delivered by the instrument have to be processed on-ground using externally supplied data (orbit and attitude information) and the characteristics of the instrument (instrument characterisation data).

Input Data

The input to the processing are of three major types: the instrument delivered data (target data, noise, internal calibration and time information), the data delivered by the orbit propagator and the external data containing the relevant information on the instrument characteristics, the system geometry and the ground processing.

The instrument data have been described in the previous chapter. The orbit propagator is included in the processor and is used to relate acquisition times and satellite and targets localisation around the earth using the Goddard Earth Model (GEM6) for earth surface modelling.

Generally, other external data not computed with the orbit propagator are provided as Look-Up-Tables as either a scalar or an array and can be updated, if the need arises, in particular in case of new calibration coefficient, antennae pattern or orbit characteristics. These tables may depend on the beam activated and may be indexed by the orbit time and the pulse time.

All these tables are provided by using the Scatterometer Simulator System (SSS). An important part of the scatterometer data processing is done before hand in the SSS and is passed to the real-time processor via these Look-Up-Tables. This includes mainly the Doppler compensation phases, the normalisation factors used to convert the powers into σ^0 (both for the echo and for the noise) which are computed using the antenna patterns, the incidence and look angles.

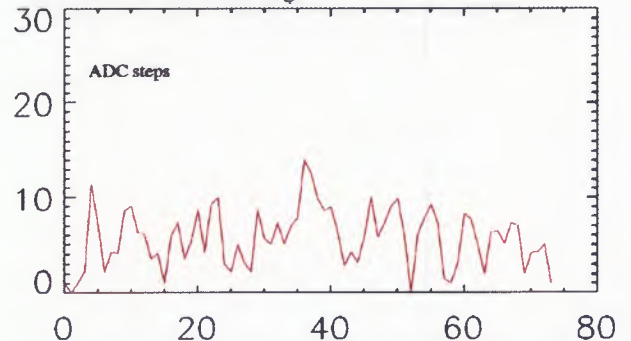


Figure 21: Typical Mid Beam echo over ice

Output Data

The output data includes:

- the node characterisation data
- the σ^0 values
- the k_p values (standard deviation of each σ^0 estimate)
- the product confidence data (monitoring parameters and processing flags)

The node characterisation data comprises the node position in latitude and longitude, directly computed using the orbit propagator, and the node incidence and look angles, derived from the Look-Up-Tables.

The σ^0 are the primary output from the scatterometer ground processing. In fact, if they are the main input to the σ^0 to wind conversion, they are also directly used for land and ice applications.

The standard deviation k_p of each σ^0 estimate computation is based on the following assumption. This parameter is dominated by the instrument noise and not by the speckle, an approximation to within 20% is adequate.

The product confidence data are used to monitor the system behaviour (power spectrum monitoring, I/Q imbalance monitoring, internal calibration level monitoring) as well as processing flags (valid/invalid, arcing, ...etc...).

Main processing steps

A functional block diagram of the scatterometer Ground Processing is shown on Fig. 22.

The main processing steps to be performed are listed in sequence below:

- Resampling and filtering of the measurement data delivered by the instrument to avoid aliasing during later processing steps and to compensate for the on-board filtering,
- Doppler compensation to shift the spectrum of the received signal into the low pass filter passband,
- Low pass filtering to improve the signal to noise ratio,
- Envelope detection to get a measure for the signal power,
- Block averaging to reduce both the data throughput for the following steps and the variance of the signal power samples,
- ADC-non linearity correction
- Noise correction to increase the measurement accuracy,
- Internal calibration correction to compensate for the transmitter and the receiver fluctuations,
- Power to σ^0 (radar Backscattering coefficients per unit area) conversion to relate the measured signal power to the wanted quality σ^0 ,
- Spatial integration both to increase the measurement accuracy (radiometric resolution) and to give the desired point target response,
- Output signal characterisation (including the estimation of the k_p) to allow the determination of wind

characteristics from the ground processing output data,

- Product confidence check to monitor the accuracy of the on-board and the on-ground doppler compensation process, the I/Q channels imbalance and the internal calibration time delay.

Description of the main processing steps

Resampling and Refiltering

The target data entering the ground processing in form of I and Q components, are sample values of a continuous time function. In order to avoid aliasing (Nyquist's criterion), the sampling frequency is chosen higher than twice the highest component contained in the spectrum of the input function.

The next step in the processing is the doppler compensation which consists in a multiplication in the time domain. Depending on the Doppler compensator frequency, this multiplication can cause a slight frequency spread. In order to avoid aliasing in case the sampling frequency is just adequate for sampling the input function, the signal should be resampled at an increased rate before the doppler compensation function is called.

It was chosen to perform the resampling in the frequency domain with the help of two Fourier transforms. The correction for the on-board filter ripples, the resampling step is combined with a refiltering, which is performed by multiplying the signal spectrum with the appropriate filter transfer function.

The spectral shift which could occur during the extension of the complex spectrum and the refiltering is avoided by using two real-to-complex and complex-to-real FFT's instead of single complex-to-complex FFT's.

Doppler Compensation

The Doppler compensation aims at compensate for the Doppler shift introduced on the received signal due to the motion of the spacecraft and to the earth rotation. Most of the original doppler shift of the echo signal is compensated on-board, in a dedicated mixer stage within the instrument, by the application of a suitable time dependant local oscillator signal. The Doppler compensation itself is simply a multiplication in the time domain. The difficulty associated with Doppler compensation is the complicated law governing the Doppler frequency versus echo time behaviour and its change over the orbit due to:

- non-circular orbit,
- rotating oblate earth,
- spacecraft attitude steering,
- on-board compensation Doppler law.

The Doppler compensation information is contained in an externally supplied 2-dimensional Look-Up-Table. In order to reduce the computational load on the ground processing, this Look-Up-Table contains the phase rota-

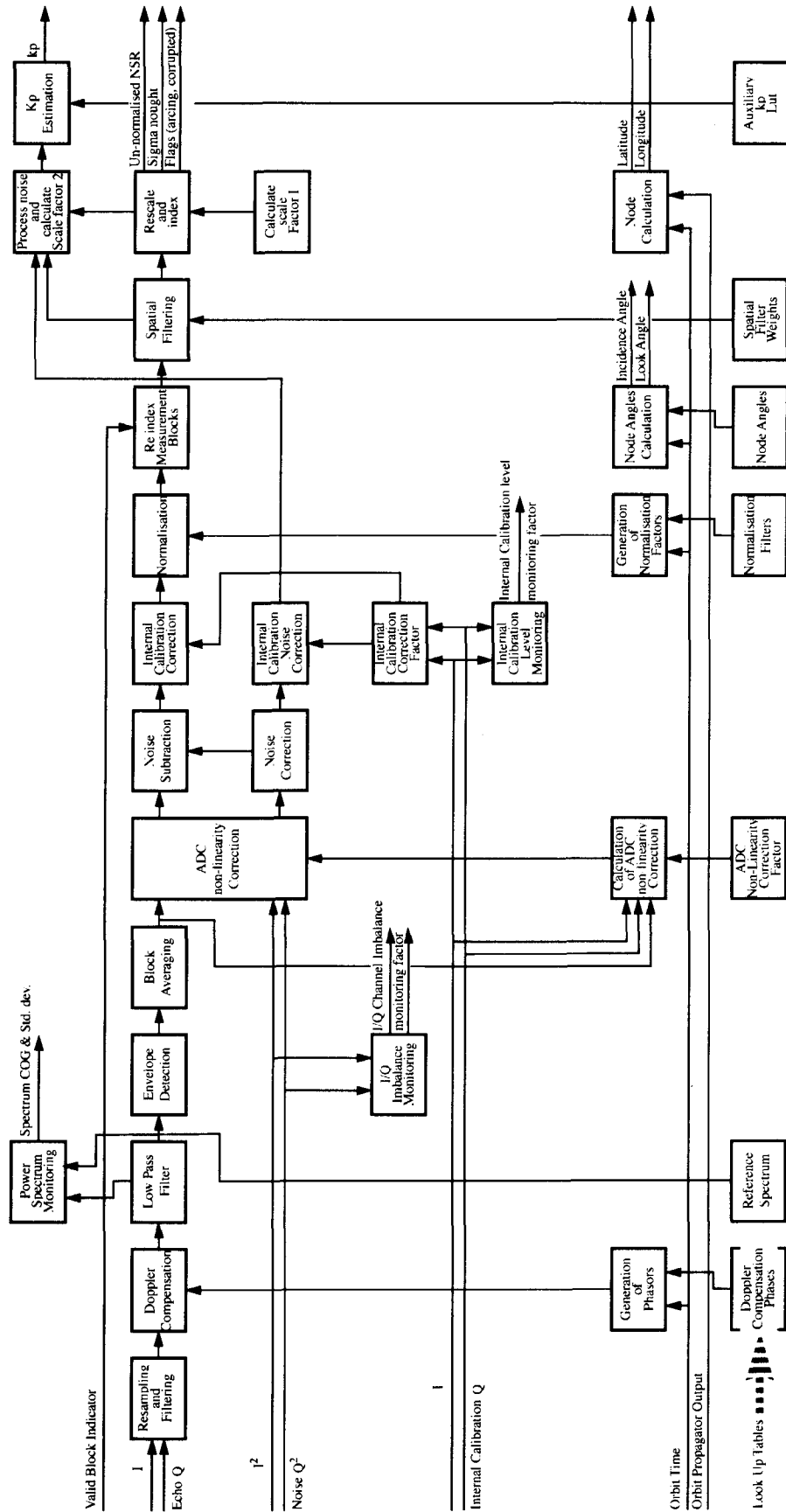


Figure 22: ERS-2 scatterometer Ground processing Functional Block Diagram

tion to be applied to the signal samples rather than the residual Doppler frequency shifts.

Low Pass Filtering

The aim of the low pass filter after the Doppler compensation, is to match the overall system bandwidth of the received signal in order to optimise the signal to noise ratio. The signal bandwidth is changing with the time along the echo (see Sampling above) and the position along the orbit, but the effect is relatively small and therefore the filter function is defined time-independent. As the filter function is defined in the frequency domain, to the most effective way is to perform the low pass filtering by using FFT's and multiplication in the frequency domain. During this operation, it was taken care of avoiding any aliasing in the time domain due to insufficient sampling in the frequency domain and to the extension of the signal in time caused by the low pass filtering.

Envelope detection

Up to the output of the low pass filter, the signal is represented as I and Q (in phase and in quadrature) signals. The instantaneous power is calculated by summing the square of each I and Q samples.

Block Averaging

The duration of a measurement block is roughly 300 ms (see Table 3), and the corresponding distance measured on the sub-satellite track is roughly 2 km. This distance is small compared to the diameter of the spatial integration area (in the order of 100 km) and therefore corresponding target samples (those with identical echo time) can be averaged over the 32 echoes before further processing in order to reduce the data throughput.

The time instant appointed to the block signal is the average of the time instants for the 1st and the 32nd pulses of the block. It has to be noted that these times are not directly provided in the raw data, but are derived by using the information illustrated on Fig. 10.

ADC Non-linearity Correction

In principle, the signal power (both echo and noise) at the ADC can be such that a significant proportion of samples exceeds the ADC maximum level, or is below the least significant bit level. In such a situation, a significant sampling error would occur. This is not reduced by sample averaging and there is a resultant power transfer non linearity. These value of non linearity are comparable with the required radiometric stability, and will have to be corrected for during the ground processing. Since this is a statistical correction to the power, it should be applied after the power detection and the block summation.

In practice, the echo is fairly low in the ADC (less than 40 ADC steps) and the noise is always 0 or 1 ADC

step (see Chapter on Scatterometer Data Characteristics).

This ADC non-linearity correction is performed for both the block averaged target echo and the noise averages.

The Analogical to Digital Converter non-linearity is characterised on-ground and provided to the ground processing via a Look-Up-Table, which for a given ADC output power gives a correction factor to be applied in order to retrieve the expected input power.

For ideal correction, the output power used to determine this correction factor should be obtained immediately after the ADC. In order to reduce the stochastic variance of individual power samples a running average over the corresponding echo power samples of the last 8 measurement blocks of the same beam is performed.

A more precise value of the correction factor is derived by linear interpolation between two successive readings of the LUT.

The correction factor for the noise power correction is based on the actual averaged noise power only.

Noise correction and subtraction

The target signal is masked by the receiver noise, or more precisely, the signal power which is measured is the signal power plus the receiver noise power. To improve the instrument accuracy, the receiver noise power is measured separately and then subtracted from the sum of both. The processing required for noise subtraction is partly performed on-board (see The noise processing above). The I and Q channel averages (I^2 and Q^2 averages) are added on-ground to derive a single noise power estimate. This noise sample is used to correct each individual target sample of the corresponding measurement block by simple subtraction. Just before the subtraction, the noise is multiplied by a constant which takes into account the different ways of noise processing in the target measurement chain and the noise chain. This constant depends on

- the receiver pre-doppler compensation transfer function,
- the frequency offset applied by the on-board Doppler compensation for the noise alone measurement,
- the on-board low pass filter,
- the on-ground detection filter.

This constant is supplied externally.

Internal Calibration Correction and HPA monitoring

During internal calibration, a small fraction of the transmit signal is directly routed into the receiver low noise amplifier via a calibrator. The main function of the calibrator when the AMI is in scatterometer mode is to delay the transmit signal a little bit more than the transmit pulse length to allow sampling of the delayed signal at the output of the receiver. During each measurement block, four calibration measurements take place after transmit pulses 1, 11, 21 and 31. Within the receiver, the

samples taken during the calibration window are handled in the same way as the target samples. They are transferred to the ground as I and Q components. After proper processing on-ground, they are used to correct for gain variations and to monitor power level variations of the instrument.

No on-ground Doppler compensation and no low pass filtering are required for the internal calibration signal. After forming the envelope squared of the signal ($I^2 + Q^2$), gain information is extracted. In order to reduce quantisation noise, the result is low pass filtered by an exponential filter.

As the envelope squared of the signal is rather sensitive to deviations of the characteristics of the I and Q channels from the ideal case, a possibility to correct the calibration signal samples for these I/Q imperfections, based on an externally provided characterisation, is foreseen.

The gain correction information is derived as a multiplicative correction factor which is applied to the noise corrected signal samples. This factor is the ratio of the actual low pass filtered internal calibration signal energy and a reference energy valid for that system configuration which was used to derive the normalisation factors.

Noise correction is not required for the calibration signal due to the high signal to noise ratio.

The averaged energy of the four calibration pulses of each measurement block is used to detect missing transmit pulses due to the arcing of the High Power Amplifier (HPA). If HPA arcing occurs the HPA is switched down and automatically restarted after a few seconds, unless the number of arcing exceeds a certain threshold, which leads to an error condition of the AMI. During HPA switch down, no transmit pulses and hence no internal calibration pulses are generated and therefore only noise is recorded during the internal calibration and echo sampling windows. The σ^0 derived from these echo samples are invalid and have to be flagged accordingly. As the noise energy is much below the internal calibration pulse energy, HPA switch down can be detected by comparing the averaged energy of the samples of the calibration pulses of a measurement block with a threshold value and raising a flag for those measurement blocks, for which the averaged energy is below the threshold. These flags are used during the spatial filtering to determine the nodes affected.

Power to σ^0 Conversion - Normalisation

The target signal at the output of the envelope detection is proportional to the instantaneous power. The quantity to be measured is the backscattering coefficient σ^0 . In order to perform the desired spatial integration of the σ^0 values around the node, the measured power needs to be converted into σ^0 .

The normalisation factor is defined as the instantaneous power at the input of the normalisation block for a uniform reference backscatter coefficient equal to 1 on

the earth surface everywhere in the swath. Due to the changing geometry with the time of the echo (beam range) and along the orbit, this normalisation factor for a given antenna, is a function of both variables.

Initially, provision was made to correct for the variation of the scatterometer antennae temperature around the orbit, which would have caused a mechanical distortion of the antenna and a modification of the antenna pattern. Practically this capability was never used and a unique set of normalisation factors were used (for a given orbit characteristic and antenna pattern).

The ERS scatterometer system is far from being simple from the point of view of the geometry as well as from the point of view of the instrument.

These normalisation factors are supplied externally as Look-Up-Tables indexed by the orbit time and the echo time. The values not contained in the LUT's are calculated by bi-linear interpolation.

Spatial Filtering

The spatial filtering process consists of two different steps:

- Calculation of the node positions on the earth's surface in an adequate coordinate system,
- weighted integration of samples belonging to an area around these nodes (integration area).

The weighting function used and the size of the integration area are mainly determined by the scatterometer system requirements in terms of the instrument response to a point target on ground, specified both in the time domain (impulse response) and in the frequency domain (modulation transfer function). The integration process acts like a two-dimensional filter, hence the name "Spatial Filtering".

The calculation of the node position is based on the Mid antenna measurement blocks.

The position of the central node of the swath (node 10) is at the intersection of the Mid antenna line of sight with the earth (defined by GEM6) (see Fig. 23). The other nodes are localised along the intersection of the plane defined by the centre of the earth, the satellite and the Mid antennae line of sight every 25 km in both directions. A total of 19 nodes are localised like that for a given Mid antenna measurement block. This is repeated every four measurement blocks (equivalent to four FMA sequences), which corresponds to 3,763.36 ms or roughly 25 km on ground. It has to be noted that because of the oblateness of the earth, these successive line of nodes are not exactly parallel.

The results of this process are shown on Fig. 24. Samples taken by the three antennae within a certain area around each node are averaged. The averaging process gives a high weight to the samples near the node and a low weight to those far from the node (weighted averaging). The contributions of the pulses from this area are weighted by a Hamming function which takes the following form:

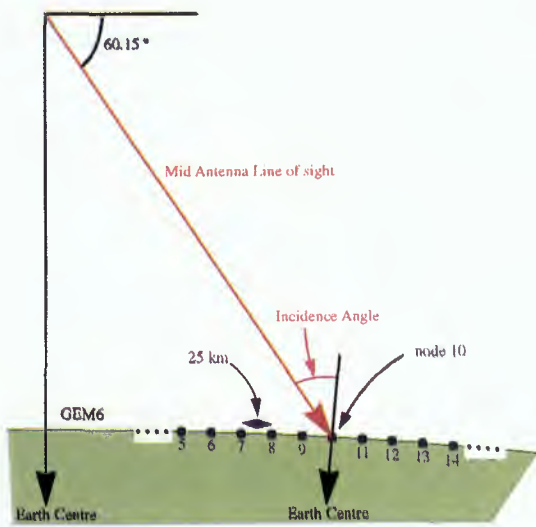


Figure 23: Definition of the node localisation

$$w(n) = \alpha + (1 - \alpha) \cos\left(\frac{2\pi n}{N}\right) \quad \text{eq: 1}$$

where,

$$|n| = \frac{N}{2} \quad \text{eq: 2}$$

The main concept of the spatial filtering is shown on Fig. 25.

By using trigonometric relations it can be shown that this equation is a cosine squared function which sits on a pedestal above the zero level. More often the Hamming window is designed to have a Fourier transform with low sidelobes. The value of α (which can vary between 0 and 1) used in the scatterometer weighting function is set to 0.54. This value produces the optimum level

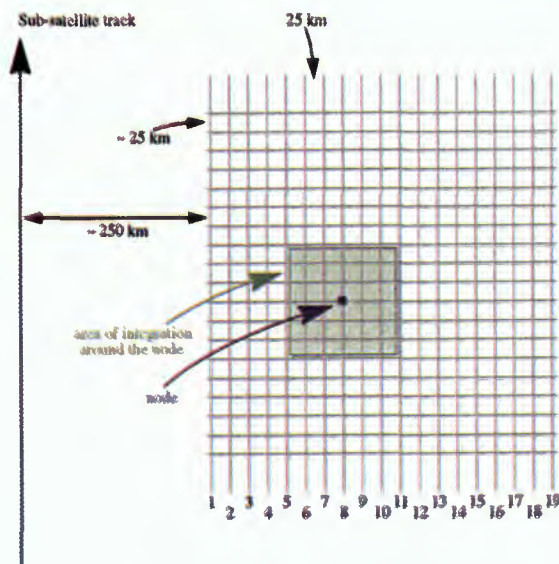


Figure 24: Node localisation

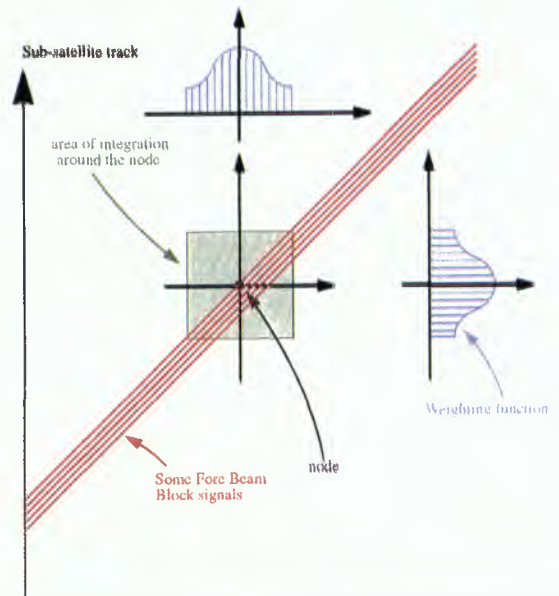


Figure 25: Weighted integration and Hamming function

of sidelobe suppression, such that the highest sidelobe is -43 dB below the peak value.

The Hamming function used in the spatial averaging process will dominate the form of the scatterometer impulse response function. The special properties of this function are important when considering whether the scatterometer data can be regarded as being adequately or inadequately sampled.

The size of the Hamming function is 84.5 km by 84.5 km across and along track respectively for the Side antennae, and 86.0 km by 86.0 km for the Mid antenna.

This part of the processing impacts a lot the characteristics of the σ^o and in particular the resolution.

Kp Calculation

In order to allow an optimised wind field extraction algorithm, each σ^o value has to be characterised by the accuracy to which it has been measured. Taking into account speckle and receiver noise contributions only and assuming that the noise subtraction process gives only a negligible contribution (noise signal integration time is comparable with the target signal integration time, which is true for ERS), the standard deviation Kp of the σ^o can be written as:

$$Kp = \frac{1}{\sqrt{M}} \left(1 + \frac{\sigma^o_{noise}}{\sigma^o} \right) \quad \text{eq: 3}$$

where M is the number of independent σ^o measurements and σ^o_{noise} is the σ^o equivalent of the receiver noise power. As the Kp value is only used as a weighting factor during further processing, a limited accuracy is acceptable for M and σ^o_{noise} .

During this step of the processing M and the noise normalisation factor are extracted from Look-Up-Tables.

Monitoring Parameters

The last steps of the processing consist of the computation of the Power Spectrum characteristics (Centre of Gravity and Standard Deviation), I and Q channels imbalance factors and the Internal Calibration Level. These parameters are provided in the Source Packet Headers for monitoring purpose.

Wind / Wave mode

The algorithms described in the previous paragraphs were proposed between 1985 and 1986, a long time before the actual launch of ERS-1 on July 21, 1991. In parallel to the progress in the design of this processor, the Scatterometer Simulator System was developed. In the context of this note, the main task of the SSS is the generation of the Look-Up-Tables.

At that time the nominal mode for the scatterometer operations was the Wind mode. An experimental mode called the Wind/Wave mode was proposed, but not supposed to be scheduled nominally.

The Wind/Wave mode consists of interrupting the Scatterometer measurements every 200 or 300 km for a time period corresponding to 2 FMA sequences (1 881.68 ms) in order to acquire a small SAR imagette.

Practically ERS-1 was operated in Wind mode only three days during the commissioning phase, and ERS-2 is operated in Wind mode over land only to allow ATSR High Rate data on-board recording (because of the SAR imagettes, the Wind/Wave mode has a relatively high data rate which doesn't allow the ATSR HR operation at the same time). All data over the ocean (excepted the three days in 1991) were acquired with ~2 s interruption every 200 km for Sar imagettes acquisition.

Basically in Wind/Wave mode, two source packets are permanently missing in the Side antennae spatial filter, and are missing half of the time for the Mid Antenna (see Fig. 26 and Fig. 27).

The impact on the σ^0 is due to a combination of the size of the Hamming function used for the Spatial Filtering which is a bit less than 100 km (see Spatial Filtering) and of the fact that the σ^0 is not uniform across the averaging area due to the evolution of the incidence angle (the σ^0 decreases when the incidence angle increases) as illustrated on Fig. 28.

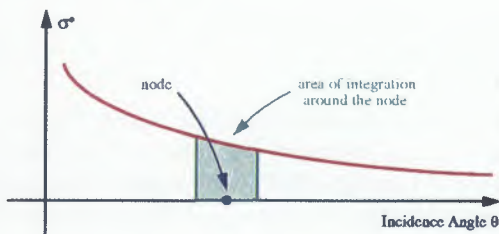


Figure 28: σ^0 evolution across the swath

If the geophysical phenomena to be measured is uniform, the impact on the Mid σ^0 is negligible as, the same

number of samples are missing inside the integration area at low and at high incidence angle. For the fore and Aft beams the samples are in general not missing in a uniform manner across the node. Fig. 26 shows a situation where high σ^0 (low incidence angle) samples are missing, therefore the averaged σ^0 will be slightly lower than what it should have been if all samples were present.

A study was carried out to estimate the impact on the σ^0 [7]. In case there is no marked structure inside the integration area (well marked meteorological front for example), the error on the Side antennae σ^0 is lower than

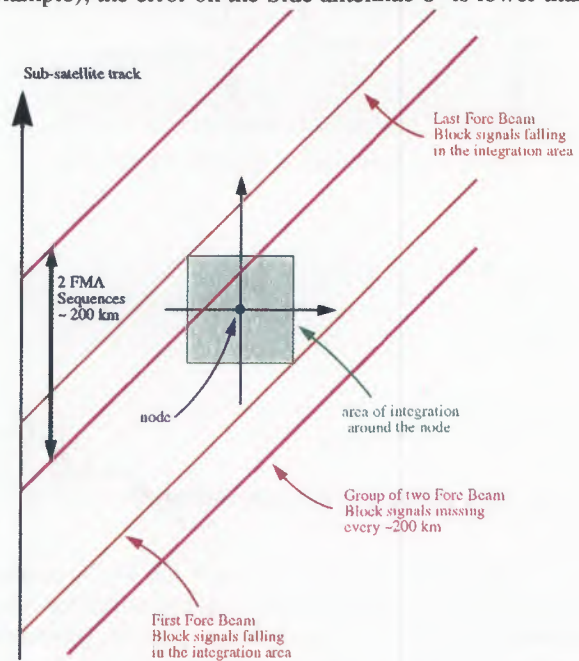


Figure 26: Fore missing Source Packets in Wind/Wave

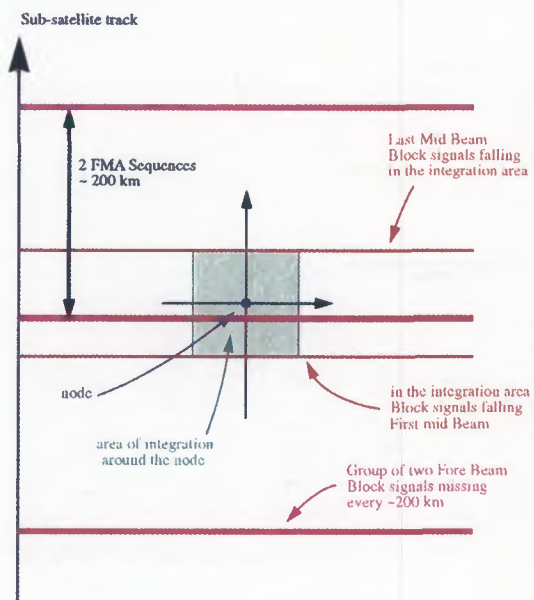


Figure 27: Mid missing Source Packets in Wind/Wave

4% of the nominal σ° value. For the Mid antenna this error is less than 0.1% as expected.

As the normalisation factors are computed in the SSS before hand without knowing the position of the missing source packets, it is impossible to correct this anomaly without modifying completely the actual Ground Processing chains.

σ° to wind processing

This part of the processing chain is the result of various studies carried out by scientific groups in France, United Kingdom and Germany. There are three elements to clearly distinguish. Two are algorithms called Wind Retrieval and Ambiguity Removal and the third element is the model used to relate the σ° and the wind as measured at 10 m altitude. The model used today in the ESA Ground Segment for Real-Time data processing is called CMOD-4 [2]. Very often the quality of the algorithms is confused with the quality of the model when these elements are linked to two different aspects, software engineering on one side, physics of the interaction of the microwave with the sea surface on the other side.

One could propose to use different C-Band models for different type of applications.

It is not our intention to discuss in this document the respective merit of the various existing models; therefore only the algorithms will be presented.

The Wind Retrieval - Principles

This step of the processing is easier to understand when it is represented in the σ° measurement space, defined by the $\sigma^\circ_{\text{fore}}$, $\sigma^\circ_{\text{aft}}$ and $\sigma^\circ_{\text{mid}}$. In this space the C-Band model looks like a double cone as shown on Fig. 29 in an artistic representation and on Fig. 30 as a cut by a plane defined by $\sigma^\circ_{\text{fore}} + \sigma^\circ_{\text{aft}}$ equal a constant value [8].

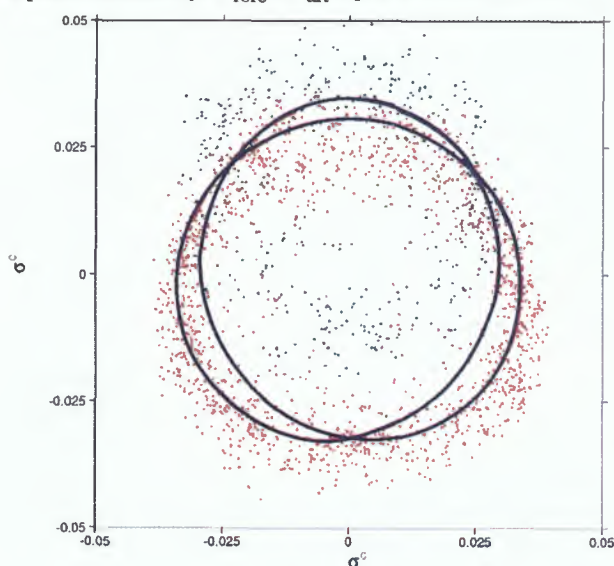


Figure 30: Representation of CMOD 4 (in blue) with ERS-1 and ERS-2 data (respect. in red and in green).

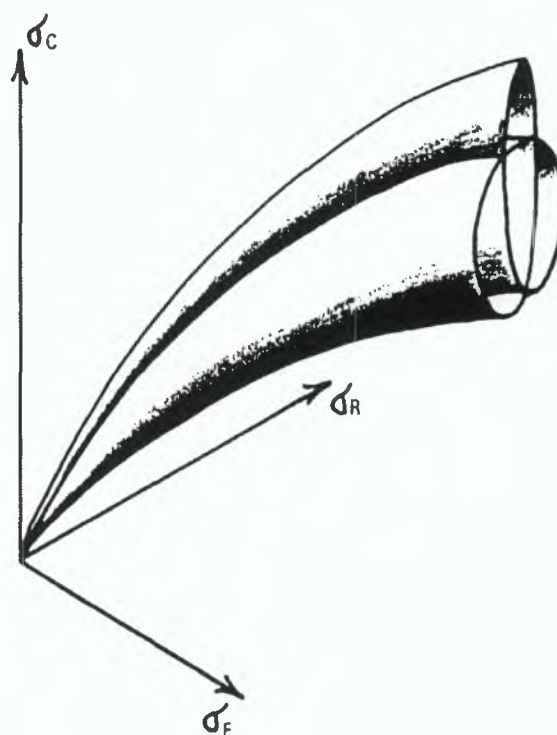


Figure 29: Artistic representation of the C-Band model

This part of the processing consists in finding the minima in the σ° space, of the distance between the σ° triplet measured and this cone.

Historically two definitions of the distance were used.

The first one corresponds to the maximum likelihood distance which assumes that each measurement has a gaussian noise of standard deviation kp (see paragraph on kp calculation):

$$M = \sum_{i=1}^3 \left(\frac{\bar{\sigma}_i - \sigma_i}{kp_i} \right)^2 \tag{eq: 4}$$

The second one is simply the Euclidian distance:

$$E^2 = \sum_{i=1}^3 (\bar{\sigma}_i - \sigma_i)^2 \tag{eq: 5}$$

In these equations i is the antenna, $\bar{\sigma}$ is the measured σ° triplet and σ is the theoretical σ° triplet defined by the C-Band model. The later can be parametrised with the Wind speed v and Wind direction ϕ for a given look angle ψ and the incidence angle θ , these two last variables depending on the antenna.

$$\sigma_i = \text{Model}(v, \phi, \psi, \theta_i) \tag{eq: 6}$$

The model can be internally represented as a Look-Up-Table or an analytical formula. Both representations have been implemented but only the Look-Up-Table was used operationally because of the throughput operational requirement.

The first implementation was based on equation 4, and was giving up to six minima for each σ^0 triplet. It was later shown that, because of the non-linearity of the model, the component of the noise parallel and perpendicular to the model were not gaussian, and that there was no real justification for using a maximum likelihood distance.

A new implementation of the wind retrieval algorithm was made based on equation 5. Typically this method returns up to four solutions (see Fig. 31).

The Wind Retrieval - Algorithm Description

The Wind retrieval algorithm is made of four steps:

- Calculation of a realistic Wind Speed as a starting point for the minimisation process.
- Minimisation with a variable wind speed and a fixed wind direction using a Newton-Raphson technique. This minimisation is performed every 10° in wind direction with 0.5 m/s precision if the Look-Up-Table is used and 5° and 0.1 m/s precision if the analytical form of the model is used. 36 (or 72) triplets of speed, direction and distance are calculated. It is important to note that the various solutions have not only different wind directions but also different wind speed.
- Retrieval of the up to six minima (only four are actually retrieved since the Euclidian Distance method was implemented)
- Ranking of the minima from the smallest distance to the largest (Rank 1 to 6).

When the C-Band model is modified, the convergence of the Newton-Raphson minimisation has to be checked. A trade-off has to be found between the operational requirements (throughput, memory and processing power available) and the size of the Look-Up-Table. When this algorithm was installed for ERS-1, the best trade-off was 10° and 0.5 m/s resolution, these specifica-

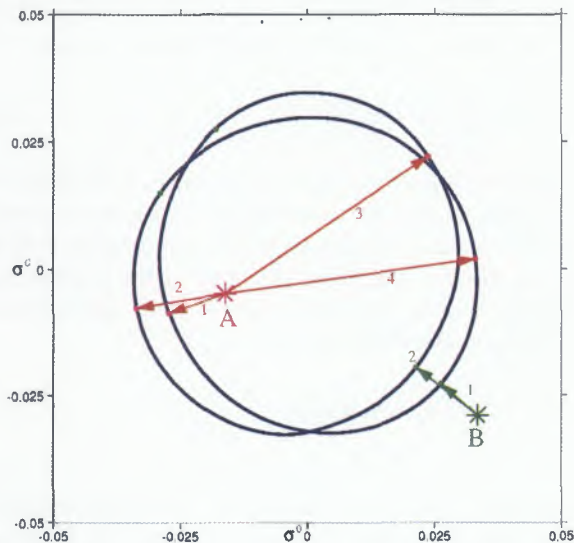


Figure 31: Illustration of an example of wind solutions retrieval (A and B have respectively 4 and 2 solutions)

tions were never changed even if the hardware was upgraded twice (once just before ERS-1 launch and a second time just before ERS-2 launch).

The output of this part of the processing is the up to four solutions (wind speed and direction) and the distance from the solution to the cone.

The Ambiguity Removal

The ambiguity removal consists in choosing the right solution within the up to four computed by the Wind retrieval.

The capacity of choosing the right solution in an autonomous way (i.e. without any external support from analysis or forecasts) depends directly on the relative distance between the two sheets of the cone and the measurement noise. In other words, if the noise doesn't "move" the measurement point from the cone further than half the distance between the two sheets, the rank one solution is most of the time the correct one.

In C-Band, we are not in that situation, in fact Fig. 30 indicates clearly that the noise and the distance between the two sheets are of the same order of magnitude. The quality of the C-Band model is also very important. Errors in the model description will lead directly to errors in the distances and eventually to the wrong solution.

Practically the algorithm implemented uses two methods, an autonomous one which works only in certain conditions (high uniform winds with a direction which corresponds to an area of the cone where the two sheets are well separated) and a second method which uses the support of forecasts produced by ECMWF.

Due to operational reasons (generation and transmission time), the forecasts used are 18, 24, 30 and 36 hours forecasts valid for ambiguity removal for a period of 6 hours from -3 to +3 hours around the nominal time. This will be improved soon, as ECMWF produces these forecasts twice a day (and not only once as before). Starting in October 1998 only 18 and 24 hours forecasts are used twice a day.

In both cases the algorithm uses a statistical approach. Based on the first two solutions for each node (rank 1 and 2) two coherent wind fields are constructed, where each node in one of the field is 180° apart of the same node in the other field ("opposite" wind fields). By counting the number of rank 1 solution in each field (autonomous method) or by computing an averaged directional distance between each field and the meteorological forecast (meteorological method), the best field is chosen.

In order to optimise the use of the hardware capacity and to avoid to propagate ambiguity removal errors, it has been decided to work on continuous segment of the swath up to 3000 km (6 products) long.

New ambiguity removal methods using in particular 2 dimensional variational techniques are being studied and

made available. The possibility of implementing such a technique is being investigated.

The Ambiguity Removal - Algorithm Description

Five main steps are presents in both methods.

- Select six consecutive products
- Define continuous zones within the selected 6 products (these zones are interrupted by land, no wind area)
- Using rank 1 and rank 2 solutions build two "opposite" wind fields for each of the zones. The algorithm in place works by continuity, choosing the solution which has a direction close to the average direction of the previous two nodes. In order not to cross the centre of low pressures which are characterise by a lower wind speed, a lower threshold of 4 m/s is given to a node to be ambiguity removed.
- Select by using the autonomous and/or the meteorological method the "best" wind field.
- Introduce rank 3 and 4 solution by checking if they make the retrieved wind field smoother.

Postface

The purpose of this document is to give enough details for the scientific and application users to understand how the scatterometer operates and how the various parameters (σ^0 and wind information) are retrieved.

On its own, this document doesn't cover all the important aspects to be taken into account to use the scatterometer products. In fact it shall be completed with a description of the products (format) and a detailed review of the instrument operations also presented in this workshop [13] and [14]. Of course it doesn't include any description of all the applications which were developed using the scatterometer data.

When this document was written, assumptions were made on which information is required or usefull to use the scatterometer data. These assumptions may be reconsidered on request and some chapters and paragraphes could be reviewed accordingly.

References

- [1] Attema E., "The Active Microwave Instrument On-Board the ERS-1 Satellite", Proc. IEEE, Vol. 79, No 6, pp. 791-799, June 1991.
- [2] Lecomte P., "CMOD4 Model Description", ESA technical note, issue 1.2, March 1993.
- [3] T.D. Guyenne, "Engineering Achievement of ERS-1", ESA SP-1176/III, October 1997.
- [4] Pulliainen J., J. Grandell, M. Hallikainen, M. Virtanen, N. Walker, S. Metsaemaeki, J.P. Ikonen, Y. Sucksdorff, T. Manninen, "Scatterometer and Radiometer Land Applications", ESRIN Contract: 11122/94/I-HGE(SC), 253 p., April 1996
- [5] Cavanié A., P. Lecomte, "Study of a method to dealise winds from ERS-1 data", ESA contract 6874/87/GP-I(sc), 1987.
- [6] Wuttge S., H. Munz, "Effect of Gaps in Scatterometer Raw Data on σ^0 -Triplets", ER-TN-DSF-FL-0001, May 1995.
- [7] Cavanie A., J. Demurger and P. Lecomte, "Evaluation of the different parameters in Long's C-band model" Proceedings of a Workshop on ERS-1 Wind and Wave Calibration, Schliersee, FRG, 2-6 June, 1986 (ESA SP-262, Sept. 1986), pp 47-51.
- [8] Long A.E., "Toward a C-Band Radar Sea Echo model for the ERS-1 Scatterometer", Proc. of the Third international Colloquium on Spectral Signature of Objects in Remote Sensing, les Arcs 1985, (ESA SP-247).
- [9] Long A.E., "ERS-1 C-Band and Sea-Echo Models", ESA internal Report ESTEC/WMA/9104, Rev. 1. April 1991.
- [10] Offiler D., "Validation of ERS-1 Scatterometer Winds; An appraisal of Operational Backscatter Model Performances from launch to Present", NOAA/NESDIS Workshop Proceedings, Alexandria, VA, USA, April 1996.
- [11] Stoffelen, A.; "Improvement and Quality Assurance of the scatterometer Wind Product in the Backscatter Domain." Proceedings of the CEOS Wind and Wave Validation Workshop, ESA WPP-147, 159-160, 1997.
- [12] Stoffelen, A., D. Anderson, "Characterisation of ERS-1 Scatterometer measurements and wind retrieval." Proc. of the Second ERS-1 Symposium - Space at the service of our environment, Hambourg 1993, ESTEC, Noordwijk. The Netherlands, (ISBN 92-9092-286-9).
- [13] Lecomte P., "ERS wind product specifications", Proc. of this workshop.
- [14] Crapolicchio R., P. Lecomte, "The ERS Wind Scatterometer mission: routine monitoring activities and results", Proc. of this workshop.
- [15] Lecomte P., W. Wagner, "ERS Wind Scatterometer Commissioning and in-flight Calibration", Proc. of this workshop.

Other various References

- [16]Attema E. "Estimating Satellite Pointing Biases from Scatterometer transponders Measurements - An exact Solution", ORM/3078/EA/sml, 14 March 1989.
- [17]Attema E., "The Design, Calibration and System Performances of the ERS-1 and ERS-2 Wind Scatterometer", NOAA/NESDIS Workshop Proceedings, April 1996, Alexandria, VA, USA.
- [18]Graham R. et Al., "Evaluation of ERS-1 Wind Extraction and Ambiguity Removal Algorithms", ESA Contract, January 1989.
- [19]Guyenne D. ed., "ERS-1 A new tool for global environmental monitoring in the 1990's", ESA BR-36, November 1989, ESTEC, Noordwijk. The Netherlands, (ISBN 92-9092-019-X).
- [20]Lecomte P. et Al., "ERS product Assurance and Quality Control", ESA Bulletin 82, May 1995, ESTEC, Noordwijk, The Netherlands, (ISSN) 0376-4265).
- [21]Lecomte P., Attema E.P.W., "Calibration and Validation of the ERS-1 Wind Scatterometer", Proc. First ERS-1 Symposium, 4-6 November 1992, Cannes, France.
- [22]Longdon N. ed., "ERS-1 Data Book", ESA BR-75, April 1991, ESTEC, Noordwijk. The Netherlands, (ISSN 0250-1589).
- [23]Mestre O., "Réponse du diffusiomètre d'ERS-1 en fonction de l'angle d'incidence", note de travail de L'ENM 462, 1993.
- [24]Vass P., B. Battrick ed., "ERS-1 System", ESA SP-1146, September 1992, ESTEC, Noordwijk. The Netherlands, (ISSN 0379-6566).
- [25]Wooding M. ed., "ERS-1 Geophysical Validation, Workshop Proc.", ESA WPP-36, August 1992, ESTEC, Noordwijk. The Netherlands.
- [I-1] ERS-2 Satellite to ground Segment Interface Specification - ER-IS-ESA-GS-0002 - Issue 1.1, 02.12.1993
- [I-2] Kiruna Station Requirements Specification - ER-RS-DSF-GS-0002
- [I-3] ERS-2 AMI Flight model Characterisation Data - ER-TN-ESA-GS-0447 - Issue 1.0, 17.03.1995
- [I-4] Wind Scatterometer Ground Processing Requirements up to σ^0 - ER-RP-DSF-SY-0006 - Issue 4, 18.12.1987, hand write updated June 1990.

Documentation

This paper was written using intensively internal documentation released by industry during the ERS Active Microwave Instrument development on one side and during the various studies in preparation for the ground processing and for its development on the other side. This documentation cannot be made available to external users.

ERS Wind Scatterometer Commissioning and in-flight Calibration

Pascal Lecomte

Directorate of Application Programmes - Remote Sensing Exploitation Division
ESA / ESRIN, Via Galileo Galilei, 00044 Frascati, Italy
tel: ++39-6-941 80 670, fax: ++39-6-941 80 612
Email: pascal.lecomte@esrin.esa.it

Wolfgang Wagner

Space Application Institute,
EC Joint Research Centre, TP 440, 21020 (VA), Italy
tel: ++39-332-78-6153, fax: ++39-332-78-9074
Email: wolfgang.wagner@jrc.it

Abstract

On the 26th March 1996, the ERS-2 Scatterometer Commissioning Phase Working group declared that ERS-2 Scatterometer data were ready for distribution to end-users.

This was the last step after nearly one year of work, firstly to find a way to recover the scatterometer, and secondly to perform in-flight characterisation of the instrument.

Since then, the AMI instrument suffered some anomalies and is under constant scrutiny to continuously assess the data quality, developing when required new methods.

The scope of this paper is to present the objectives of the calibration and validation activities, to detail the methods used to fulfil these objectives, and to present a method for estimating the spatially variable noise level over land surfaces.

Introduction

On the 21st April 1995, some three years ago, the second European Remote sensing Satellite, ERS-2 was launched from Kourou in French Guyana (see Fig. 1).

A C-band Scatterometer is part of the payload of the two European Remote sensing Satellites ERS-1 and ERS-2. It has been primarily designed for the derivation of wind speed and direction information over the oceans, but it is also a powerful sensor for the study of land surface processes. Over land, large-scale terrain features, and to a lesser extent build-up areas and inland waters, are causing modest azimuthal effects in the ERS Scatterometer data. As these effects do not contain important information, it is proposed to consider them as a noise to be added to the instrument noise and to the speckle. After a discussion on the calibration and validation tools already in use at the European Space Agency, a user-friendly method is presented that allows to estimate the spatially variable standard error of ERS Scatterometer measurements due to these error sources over land (Wagner et al., 1998). The method described, allows a consistent assessment of the quality of ERS Scatterometer derived data products.

The ERS Scatterometer

The scatterometer on ERS satellites is combined with a Synthetic Aperture Radar (SAR) into a single Active Microwave Instrument (AMI). This instrument is operated in either SAR or scatterometer mode. Most of the time, the instrument is operated in wind/wave mode which consists of nominal Scatterometer operation interrupted every 30 seconds by a couple of seconds of short SAR operation in order to acquire small SAR imagettes from which the wave spectra can be derived. This wind wave mode of operation is interrupted for SAR images acquisitions on end user request.

The ERS Scatterometer is a vertically polarised radar operating at 5.3 GHz (C-band). Since the launch of ERS-1 in 1991 it has been providing world-wide coverage with a spatial resolution of 50 km. It illuminates a

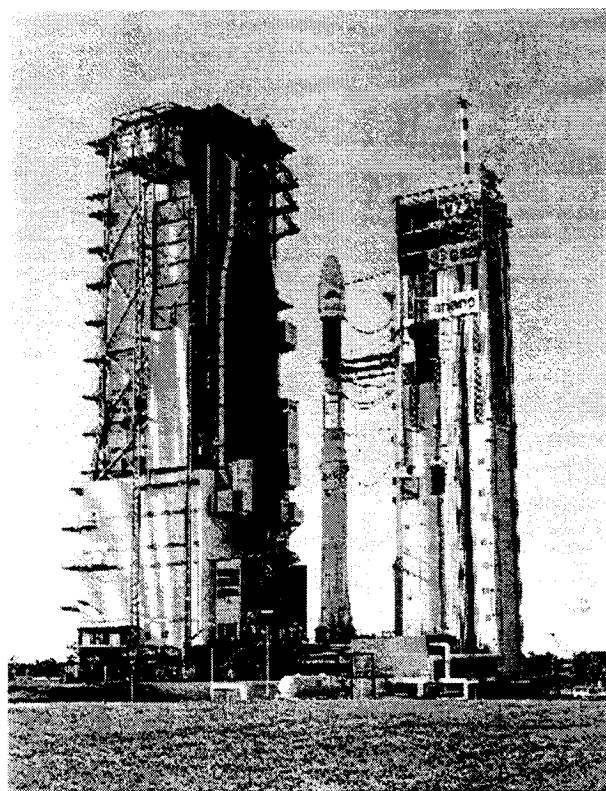


Figure 1: 21 April 1995: ERS-2 on the launch pad

500 km wide swath corresponding to an incidence angle range of 18° to 59°. Its three sideways looking antennas measure the backscattering coefficient from three different viewing directions. One antenna is looking normal to the satellite track, one is pointing 45° forward and one 45° backward with respect to the satellite track. Over ocean surfaces backscatter is modified by wind-driven ripples and the information acquired by looking from three different azimuth angles onto these ripples allows to derive wind speed and wind direction. ERS Scatterometer wind data are used operational by meteorological offices (Stoffelen et al., 1993) for wind and wave forecasting and to support offshore operations and ship routing.

The ERS Scatterometer can also be used for monitoring land surface processes. Potential applications are soil moisture monitoring (Pulliainen et al., 1996; Wagner et al., 1996; Magagi and Kerr, 1997; Wagner, 1998), production of global vegetation maps (Frison and Mougin, 1996a and 1996b), and soil state monitoring in permafrost regions (Boehneke and Wismann, 1996). It is foreseen that one or the other application will become operational. To ensure high-quality geophysical data products the absolute radiometric calibration and the relative noise level of ERS Scatterometer measurements must be known.

First Scatterometer data

During the initial testing of the ERS-2 spacecraft, the first attempt to switch on the AMI resulted in a serious anomaly causing the instrument to shut down, both in SAR and Scatterometer modes. It was soon discovered that the instrument was prevented from working at nominal power. By reducing the output power to the minimum, engineers succeeded in acquiring the first SAR image on the same day, but it was still not possible to run the instrument in Wind mode.

Many tests were made to determine the cause and possible solutions to the problem. For more than six months the only data received from the scatterometer was limited to few calibration pulses and echoes at each test, with no more than six echoes in a row before the instrument shut down.

On the 29th September 1995 more echoes were received than during all the months since launch, when the instrument was operated for an entire orbit.

The anomaly was resolved by setting the redundancy switch at the input to the High Power Amplifier to an intermediate position, thereby using it as a voltage splitter. The output power was reduced by a factor of two, and, for the first time some wind measurements could be made.

After the resolution of a few minor problems involving the system stability in the new configuration, the instrument went into the everyday satellite operations plans on the 2nd of November 1995.

The Calibration subsystem

After few months of nominal operation, a new anomaly affected the ERS-2 Scatterometer operations. The relay used to switch on and off the Calibration subsystem was not latching properly and more and more often the instrument was shutting down following a relay failure. On the 6th of August 1996 it was decided to operate the instrument with the redundant unit of the Calibration subsystem.

This change of configuration implied directly the necessity of re-calibrating the AMI in both SAR and Scatterometer mode. The detailed Analysis of the data before and after the switch showed two features, a bias which was initially measured to be around -0.16 dB and a power decrease of -0.24 dB per cycle since the instrument was operational. The bias had to be corrected by changing the level of the reference Calibration Pulse in one of the processing Look-Up-Tables. The drift was not expected as nothing like that was never experienced with ERS-1.

It was first necessary to characterise which elements of the chain were producing this power decrease and in particular if the Calibration sub system was not directly involved. After a long analysis it was finally confirmed that the drift is entirely due to pulse generation and amplification part of the AMI, and that the Calibration sub/system is not contributing to it. This means that the same drift is observed in the echo and the Calibration pulse and that the final σ^0 is free of any drift as the echo is normalised by the Calibration pulse during the processing.

On the 18th June 1997, the Reference Calibration Pulse was corrected by 0.2 dB, 0.16 dB to correct for the different characteristics of the two Calibration sub-systems and 0.04 dB to correct the fact that ERS-2 was a bit low with respect to ERS-1.

Absolute and Relative Calibration

At the engineering level, the result of processed scatterometer data are radar backscattering coefficients, σ^0 , across the range of incidence angles of the instrument, for each of the three beams. These are then used to derive wind speed and direction using a backscatter to wind model (inversion).

The objectives of engineering calibration are to ensure that the σ^0 which is expected from a known target, is measured by the instrument (absolute calibration), and that the variation over the range of incidence angles of the instrument is unaffected by the local attenuation from the antennae (relative calibration).

When ERS-1 was launched, it was agreed that an absolute radiometric calibration of 0.7 dB was enough to satisfy the geophysical data quality requirements in terms of wind speed and direction (Instrument specification). Following the Calibration subsystem anomaly it

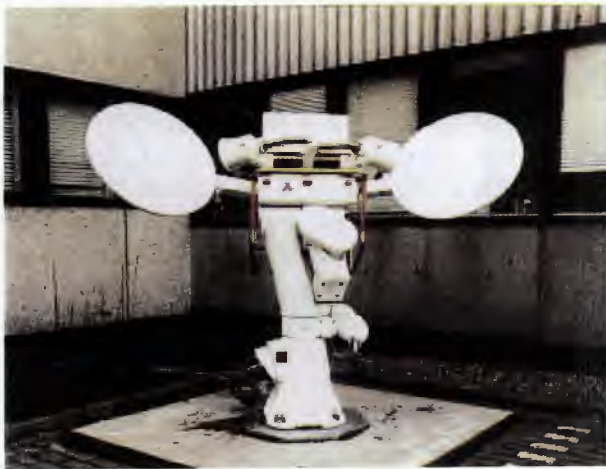


Figure 2: Scatterometer Transponder during testing at Estec

became clear that the meteorologist can detect in the wind fields a bias corresponding to less than 0.2 dB.

This requirement is translated into three elements:

- the radiometric stability
- the absolute calibration
- the relative calibration across the swath for a given antenna (antenna patterns) and between the different antennae

This is achieved by using a combination of internal (for the radiometric stability) and external references (Lecomte and Attema 1992). Two different types of external references are used, point targets (transponders) and distributed targets (areas of known, constant backscatter), addressing respectively the absolute and the relative calibration.

Three transponders, one of them shown on Fig. 2 during testing at Estec, are installed in the South of Spain (Fig. 3). This position facilitates measurements at two or more incidence angles every three days. They are arranged in a line, spaced over hundreds of kilometres, such that all three may be illuminated by each scatterom-



Figure 3: Scatterometer Transponder Location South of Spain

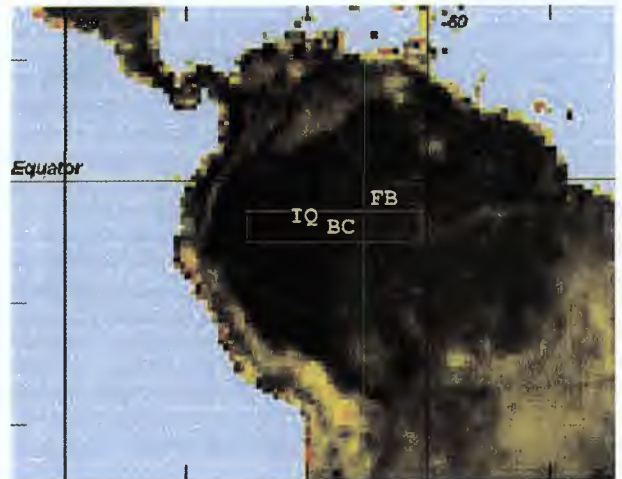


Figure 4: Amazonian Forest: Test area

eter beam during an ascending or a descending pass. Additionally, passes where two transponders are illuminated by one or more beams are used.

Each pass over a transponder allows the measurement error in backscatter at a particular incidence angle, to be computed from the power of the returned signal, and that measured at the transponder. The observation time of the transponders (in range and in azimuth) is used to verify proper antennae pointing.

After ERS-2 commissioning, two transponders will remain for monitoring purposes.

Although the transponders give accurate measurements of antenna attenuation at particular points within the antenna pattern, they are not adequate for fine tuning across all incidence angles, as there are simply not enough samples. This could be solved by deploying and operating a large number of transponders, so that many measurements can be made across the entire swath. Fortunately this enormous expense can be avoided by making use of large scale natural targets with a known response.

The tropical rain forest in South America has been used as a reference distributed target. The target is assumed to be isotropic and time invariant. Radar backscatter from the rain forest is shown on Fig. 4, as it was imaged by the ERS-2 Scatterometer. This image shows the σ^0 of the rain forest corrected for the effect of illuminating the scene over a range of incidence angles. This demonstrate clearly the uniform rain forest radar backscattering signature. Rivers, towns and mountains have a lower or higher σ^0 and consequently show up as dark or bright patches in the image.

The primary goal of the ERS-2 Scatterometer calibration was to provide continuity to the users of the ERS-1 Scatterometer data. It was assumed that once the engineering calibration was complete, in terms of σ^0 , that the wind derivation, and in particular the C-Band model used to compute the wind from the σ^0 , was identical

Prior to the launch, the engineering parameters such as the antenna pattern or the on-board gain, were set using the results of the on-ground characterisation of the instrument. Following launch, and the subsequent recovery of the instrument, the transmit power was lower, due to the initial anomaly.

The commissioning phase activities were then limited to the following activities:

- Set the on-board receiver gain,
- Derive the antenna pattern correction for the three antennae from the rain forest and transponder measurements,
- Compute the antennae mispointing,
- Compute the calibration coefficients, and generate the associated Look-Up-Tables,
- Verify the stability of ERS-2 raw data (monitoring of the Long Term Stability of the instrument),
- Compare the ERS-1 and ERS-2 response over rain forest and transponders.

Receiver Gain Setting

ERS-1 on-board gains were optimised to ensure maximum use of the dynamic range of the analog to digital converter (ADC), whilst avoiding saturation. The initial ERS-2 on-board gains were set to the same level as for ERS-1.

The operational ERS-2 transmit power is approximately half the original setting, and also that of ERS-1. The configuration of the on-board receiver gain was not changed at the beginning of the commissioning phase. This allowed the stability of the instrument to be monitored for a number of months after operation began.

The ERS Scatterometer processing is independent of the receiver gain setting, and small variations in on-board transmit power. This is achieved by scaling the incoming echoes by the ratio of the expected calibration pulse level, against the calibration pulse measured on-board at the same moment. Thus changing the receiver gain, result in an increase or decrease in the echoes, and a similar effect in the measured calibration pulses.

Once the first corrections to the antenna patterns were made, and the stability of the instrument verified, the receiver gain was modified from 18 to 21 dB to take full advantage of the ADC dynamic range.

Antennae Mispointing

Two of the three scatterometer antennae on ERS are mechanically deployed. Small mispointing errors of the antennae may be corrected for in the ground processing. The orientation of the normal of each antenna plane can be determined using the transponders, by measuring the difference between the time the peak signal of each beam is observed, and when they are expected.

This analysis performed on ERS-2 Scatterometer data shows that the mispointing is negligible.

Antenna patterns

The in-flight antenna patterns are characterised using a combination of single point measurements from the transponders, and measuring the response over a known, stable distributed target.

For C-Band microwaves (5.3 GHz) tropical rain forests may be regarded as pure volume scatterers for which the incoming signal is equally scattered in all directions. Consequently, for the angle of incidence used by the ERS Scatterometers, the normalised backscattering coefficients σ^0 will depend only on the surface effectively seen by the instrument.

This surface S' is directly linked to the incidence angle by the relation

$$S' = S \cdot \cos\theta \quad 1$$

Definition of γ^0

One can define the following formula:

$$\gamma_{linear}^0 = \frac{\sigma_{linear}^0}{\cos\theta} \quad 2$$

Using this relation, the γ^0 backscattering coefficients over the rain forest are independent of incidence angle, allowing the measurements from each of the three beams to be compared.

Thus if the assumptions of this relation are correct, then the γ^0 over such a target should be flat across the entire swath, and equal in all beams.

An area was chosen, shown in Fig. 4, which exhibits:

- Flat topography. (The incidence angle θ is computed with respect to the ellipsoid GM6, and not with respect to the real topography).
- No large scale deforestation.
- No large rivers, lakes or towns.
- Stable climate. (Rain and humidity influence the backscattered signal).

This test area is located between 2.5°S and 5.0°S in latitude and 60.5°W and 75.0°W in longitude. This area is not touched by deforestation and has limited urbanisation, lies south of the Amazon, and north east of the main mountain ranges of South America. Furthermore, this area has a low rain variation over the year. In fact the comparison of the annual rain fall over the stations of Fonte Boa, Iquitos and Benjamin Constant ("FBV", "IQ" and "BC" in Fig. 4) and other stations, shows that the annual variation is lower over the test area. Still, this variation is not negligible as the annual variation is higher than 200 mm at Benjamin Constant. At this station, the annual minimum is during the period June to September.

Analysis of γ^0

The Fig. 5 shows a comparison of the γ^0 with respect to the incidence angle θ for the three beams of the ERS-

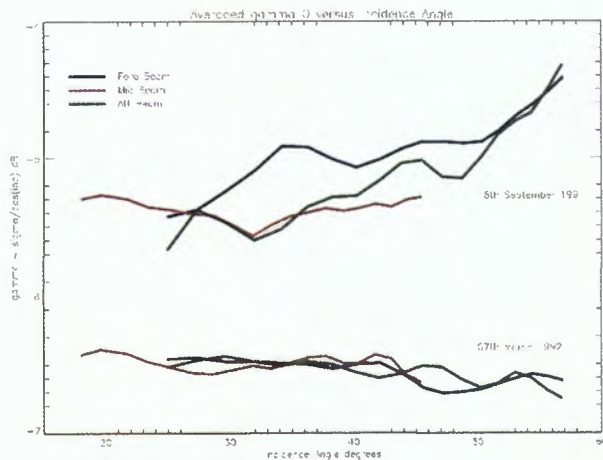


Figure 5: Average γ^0 over rain forest, before and after engineering Calibration

2 Scatterometer, before and after the instrument calibration.

The two side antennae (fore and aft) have nearly identical patterns. The deviation between the two curves are less than 0.3 dB. A more careful analysis of this data shows that the oscillation observed in these two curves can also be seen in the mid beam at an incidence angle 10° less. Thus it can be surmised that these anomalies correspond to the target and are probably due to small heterogeneity of the test area.

The second and the third nodes of the mid beam, which correspond respectively to an incidence angle of 19.6° and 21.7° , show a different effect. These two measurements give a value of γ higher than that measured by the two other beams.

The deviation, +0.2 dB, is systematic and does not depend either on the period of the year, nor on the test area chosen. This may point to an anomaly in the characterisation of the mid antenna pattern.

The initial ERS-2 pattern corrections have produced satisfactory results, and a fine tuning is under way.

Instrument stability

The instrument calibration pulses are used to measure the stability of the transmit/receive chain on-board. As mentioned above, the scatterometer processing automatically corrects for any variation measured by the calibration pulses. Changes in the antenna patterns over time may also occur, in the long term due to temperature variation around the orbit, and throughout the year.

As γ^0 is independent of incidence angle, a histogram of γ^0 over the rain forest is characterised by a sharp peak. Monitoring the position of the peak over time is one method to check the stability of the calibration.

Histograms are produced, one for each antenna ("Fore", "Mid", and "Aft") and one combining all measurements ("Fore/Mid/Aft"). The histogram bin size is 0.02 dB. The mean and the standard deviation are com-

puted directly from each distribution. The peak position is computed by fitting the histogram with a normal distribution added to a second order polynomial.

$$F(x) = A_0 \cdot \exp\left(-\frac{z^2}{2}\right) + A_3 + A_4 \cdot x + A_5 \cdot x^2 \quad 3$$

$$\text{with } z = \frac{x - A_1}{A_2} \quad 4$$

In this formulation, the normal distribution has a mean equal to A_1 and a standard deviation equal to A_2 . The parameters A_0 to A_5 are computed by using a non linear least square method called "gradient expansion" [Bevington, 1969].

The position of the peak is given by the maximum of the function F .

This method gives much more precise results than a simple filtering method.

The histograms (Fig. 6) computed for ERS-2 with one of the first set of calibrated data acquired at the beginning of April 1996 over the test area show the following points:

- Unique peak,
- The peak positions for all beams are nearly identical,
- The widths of the distributions are small (the standard deviations are lower than 0.35 dB).

The following table summarises the results for the end of March 1996.

γ^0	Mean	Peak position	Standard deviation
Fore	-6.48 dB	-6.44 dB	0.29 dB
Aft	-6.46 dB	-6.44 dB	0.28 dB
Mid	-6.61 dB	-6.56 dB	0.32 dB
All	-6.51 dB	-6.48 dB	0.30 dB

Table 1: ERS-2 γ^0 mean, peak position and standard deviation for end of March 1996

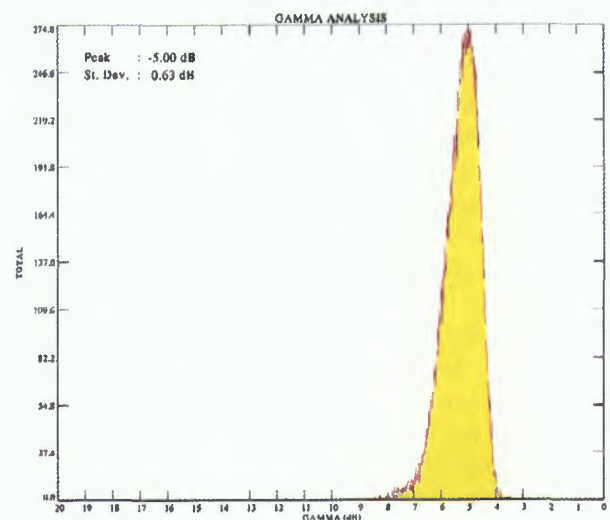


Figure 6: ERS-2 γ^0 distribution beginning of April 1996

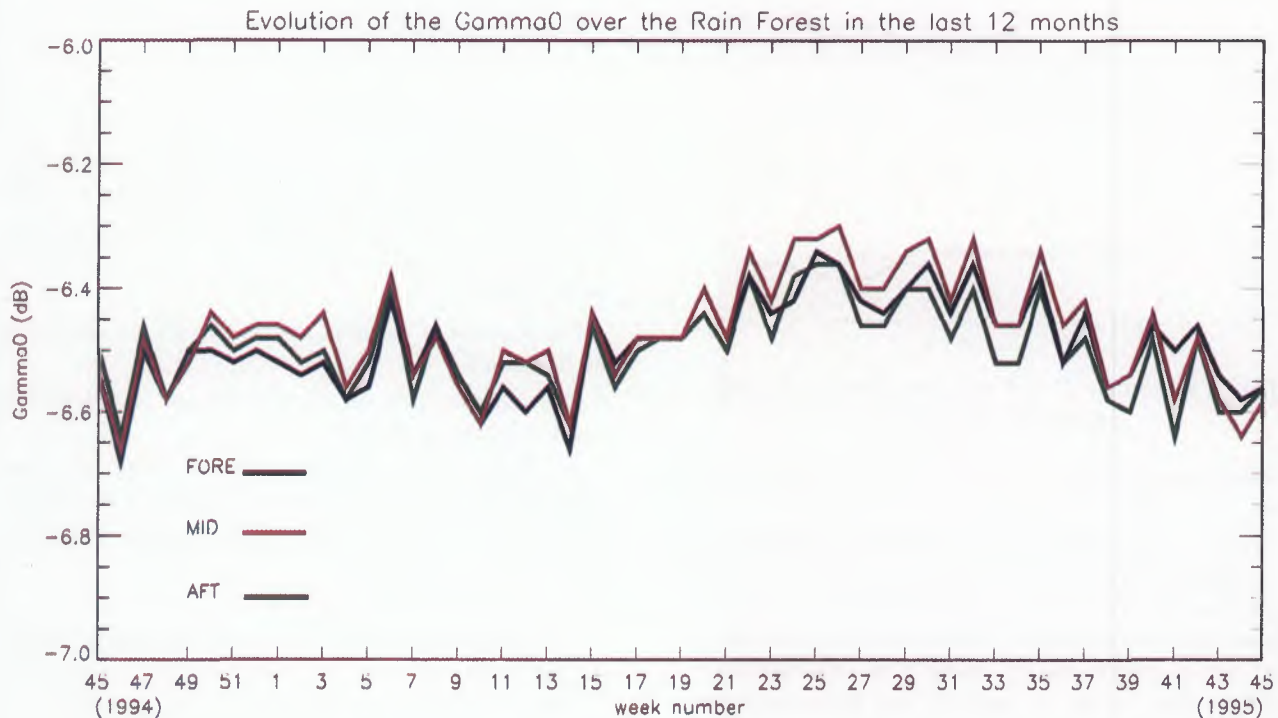


Figure 7: ERS-1 γ^0 distribution peak position time-series.

This demonstrates that the assumptions of the γ^0 have some foundation, and that γ^0 is useful as a comparison of the measurements made with the three antenna without having to take into account the incidence angles.

The following conclusions can be drawn:

- There is a slight deviation between the peak position and the mean of the distribution; i.e. that the distributions are not symmetrical.
- The standard deviation of the mid beam is higher than the two other antennae. This can be due to two reasons: first the noise on the mid beam is slightly higher. Secondly the higher γ^0 measured on the mid beam at low incidence angles (node two and three) is not corrected for when constructing the histograms and introduces noise in the γ^0 distribution.
- Taking into account the noise observed in the measurements, the peak position for the Fore and Aft antennae are equal; the mid beam has a slightly higher signal (+0.1 dB).

ERS-1 Annual stability

The Long term stability of the scatterometer is an important element of the Calibration activities. It has to be seen as the extension of the commissioning phase across the entire life time of the instrument.

For the ERS missions, the peak position of the γ^0 distribution is weekly monitored in parallel to the transponder activities.

The Fig. 7 shows the ERS-1 peak position time series for the three antennae over the period November 1992 to November 1993.

The analysis of these curves demonstrate the stability over the whole period, even if a small oscillation can be detected. It is also noteworthy that the three antennae have very similar responses. One can see a seasonal variation in all three antennae. This signal has an amplitude of 0.2 dB.

Comparisons of the γ^0 time-series with the rain fall measurements at Benjamin Constant show that the data do not correspond. The maximum γ^0 is separated by three months from the minimum rainfall.

Noise Level over Land Surfaces

σ^0 Azimuthal Dependence

Backscatter from water surfaces and ice sheets depends on the azimuthal look direction. In the case of water the orientation of the water ripples with respect to the look direction of the sensor is important and in the case of ice the morphology of the surface and the top few meters of the snow and ice volume (Rott et al., 1993). On a field scale backscatter from vegetation might also exhibit an azimuthal dependence, but on larger scales these effects are not important. Nevertheless, azimuthal effects have been observed in the ERS Scatterometer data also over land surfaces (Wismann and Boehnke, 1994; Wagner, 1996). To investigate these effects in more detail the data acquired with the forward and backward looking antennas are analysed. These two antennas look at the surface with the same incidence angle, but from two different azimuth angles. Let us denote the backscattering coefficients acquired with the

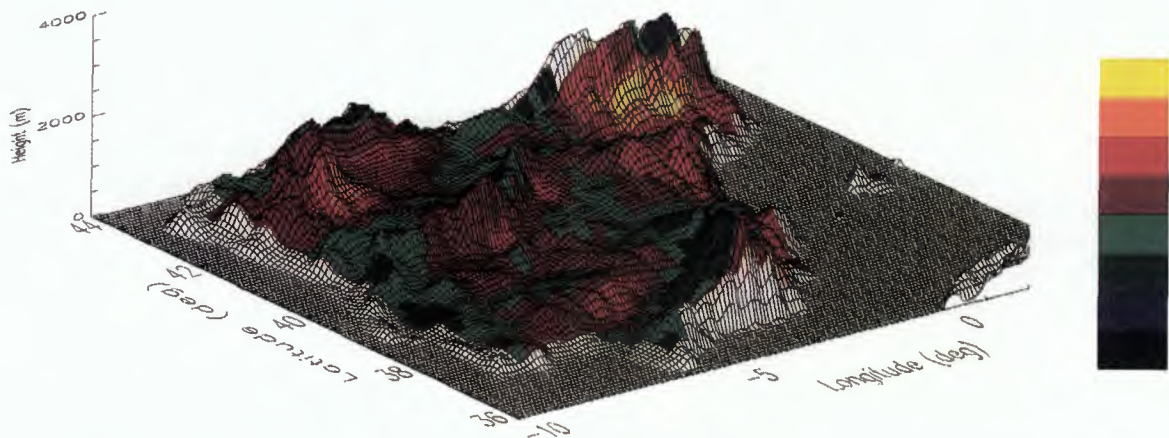


Figure 8: Overlay of δ (averaged value over ERS-1 mission) in dB for ascending passes over the DEM of the Iberian Peninsula

fore- and the aft-beam antennas with σ_{fore}^0 and σ_{aft}^0 respectively and let us take their difference:

$$\delta = \sigma_{fore}^0 - \sigma_{aft}^0 \quad 5$$

Since σ_{fore}^0 and σ_{aft}^0 are measured at the same incidence angle the difference δ depends on the noise level of individual σ^0 measurements and on the azimuthal dependence of σ^0 , but not on the backscattering characteristics of the target. If a large number of measurement pairs σ_{fore}^0 and σ_{aft}^0 are available then the noise can be averaged out and the resulting mean value of δ shows the magnitude of azimuthal effects. In Fig. 8 the average value of δ for ascending passes can be seen for the Iberian Peninsula. In the view of this figure, the look direction of the fore-beam antenna is approximately perpendicular to the plane of the page (south-west to north-east) and the look direction of the aft-beam antenna is approximately in the plane of the page from the left to the right (north-west to south-east). It can be observed that δ is positive over southward facing slopes where the local incidence angle of the forward looking antenna is smaller than the incidence angle of the backward looking antenna. The difference is positive because σ^0 is in general decreasing with the incidence angle and thus σ_{fore}^0 is larger than σ_{aft}^0 . Over northward facing slopes the reverse is true. Such it is clear that azimuthal effects as observed with the ERS Scatterometer are in reality incidence angle effects. Over the Iberian Peninsula the highest values of δ are around 0.4 dB. Over the Canadian Prairies δ is observed to be as large as 0.6 dB (Wagner, 1996).

Estimating the Noise Level

The three antennas of the ERS Scatterometer measure σ^0 from six different azimuth angles, three for the ascending and three for the descending node respectively. Over land the variation of σ^0 with the azimuth angle does not convey important information and thus

one may treat these rather modest variations as noise and the azimuth angle as "unknown". Let us assume that in the logarithmic range σ_{fore}^0 and σ_{aft}^0 are normally distributed variables with equal means and with a standard deviation $s(\sigma^0)$. The means of σ_{fore}^0 and σ_{aft}^0 are determined by target characteristics and the standard deviation is due to all possible noise sources. The most important noise sources are speckle and instrument noise (Wuttge and Munz, 1995) and, in the present model, azimuthal effects. If we blindly take the difference $\sigma_{fore}^0 - \sigma_{aft}^0$ or $\sigma_{aft}^0 - \sigma_{fore}^0$ from both ascending and descending passes then we simulate the impact of an "unknown" azimuth angle on σ^0 . The standard deviation of the resulting values which are stored in the random variable ϑ is

$$s(\vartheta) = \sqrt{2} \cdot s(\sigma^0) \quad 6$$

because the variance of a linear combination of mutually independent, normally distributed variables is the sum of their variances. The observation that ϑ is normally distributed in the logarithmic range is the justification for assuming that σ_{fore}^0 and σ_{aft}^0 are normally distributed (Fig. 9).

Since, in reality, the azimuth angle is not random but is determined by the orbit characteristics of the ERS satellites, Equation 6 is not entirely correct. To express this fact we call the derived value for the standard deviation of σ^0 the estimated standard deviation, $\widehat{s}(\sigma^0)$:

$$\widehat{s}(\sigma^0) = \frac{s(\vartheta)}{\sqrt{2}} \quad 7$$

In Equation 10, an overlay of $\widehat{s}(\sigma^0)$ over a DEM of the Iberian Peninsula is shown. About half of the values of $\widehat{s}(\sigma^0)$ - which can mainly be found in more gently sloping terrain - are in the range 0.15 - 0.2 dB and the other half is above 0.2 dB with the highest values found in the Pyrenees.

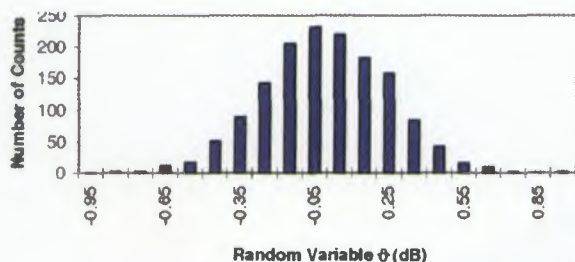


Figure 9: Histogram of the random variable ϑ which has been calculated by first calculating the difference $\delta = \sigma^0_{\text{forc}} - \sigma^0_{\text{aft}}$ for both ascending and descending passes and then multiplying δ by +1 or -1 in a random fashion. Data for this example were taken from a region in Southern Portugal

Influence of Land Cover on Noise Level

Experience has shown that $\widehat{S}(\sigma^0)$ is not only related to large-scale terrain features but also to land cover. For example, $\widehat{S}(\sigma^0)$ is in general smaller over forested areas than over regions with low vegetation cover. This is because azimuthal effects are in principle incidence angle effects and consequently $\widehat{S}(\sigma^0)$ is lower over forested areas where σ^0 decreases more slowly with the incidence angle than over grass- and agricultural land. Also, $\widehat{S}(\sigma^0)$ is observed to be high over areas with large water bodies. To investigate the dependency of $\widehat{S}(\sigma^0)$ on land cover in more detail a multiple correlation analysis between $\widehat{S}(\sigma^0)$ and the area occupied by CORINE land cover classes within one ERS Scatterometer pixel is conducted. The CORINE Programme (Co-ordination of Information on the Environment) has been realised by the European Commission and one of its major tasks is the establishment of a computerised inventory on the land cover. On the most detailed level the CORINE land cover consists of 44 class. For the present analysis a subset of these 44 classes was taken and was grouped into only four class: artificial surfaces including urban areas and other build-up areas, inland waters, open spaces with little or no vegetation, and low

vegetation including agricultural- and grassland (Table 2). To make inferences about the dependency of $\widehat{S}(\sigma^0)$ on these four classes a multiple regression together with a one-sided t-test for each regressor is performed. The multiple coefficient of determination is low ($R^2 = 23\%$) but significant. For all classes the null hypothesis that the regressor is equal to zero can be rejected with high confidence, at the $\alpha = 0.5\%$ level for the "inland water" class and at the $\alpha = 0.05\%$ level for the other three classes. Thus it can be concluded:

1. Most of the variation of $\widehat{S}(\sigma^0)$ is caused by terrain effects but also land cover classes are important for the explanation of $\widehat{S}(\sigma^0)$.
2. The magnitude of azimuthal effects depends on how fast σ^0 decreases with the incidence angle because, as shown previously, azimuthal effects are in reality incidence angle effects. Since σ^0 decreases quickly with the incidence angle over sparsely vegetated areas, $\widehat{S}(\sigma^0)$ tends to be higher over areas with sparse or low vegetation cover than over forested regions.
3. The noise level increases with the percent area occupied by build-up areas and water bodies. This is because both surface types show azimuthal behaviour

Classes	CORINE class	% of total area of the Iberian Peninsula
Artificial surfaces (%)	1.	1.3
Inland waters (%)	5.1.	1.3
Open spaces with little or no vegetation	3.3	6.7
Arable land and natural grassland	2.1.1 + 3.2.1	24.6

Table 2: CORINE classes used for multiple regression analysis



Figure 10: Overlay of the estimated standard deviation of σ^0 , $\widehat{S}(\sigma^0)$, in dB over the DEM of the Iberian Peninsula.

Estimating the Noise Level due to Instrument Noise and Speckle

Because $\widehat{\sigma}(\sigma^0)$ can be as low as 0.15 dB the standard deviation of σ^0 due to instrument noise and speckle effects alone must be even better than that. This value is on the low side of specifications found in the literature. To investigate the noise level of ERS Scatterometer measurements it is generally assumed that backscatter from tropical forests is stable. For example, by analysing σ^0 separately for each antenna and separately for ascending and descending passes Frison and Mougin (1996b) found that σ^0 is stable with an estimated standard deviation smaller than 0.22 dB for all beams and passes. However, even over tropical rain forests, σ^0 shows variations in the magnitude of 0.5 dB to 1 dB due to precipitation (Fig. 7, Wismann et al., 1996) and other environmental effects. Therefore this classical approach overestimates the relative noise level of ERS Scatterometer measurements. On the other side, environmental factors play no role in the calculation of $\widehat{\sigma}(\sigma^0)$ thus allowing a better estimate of the standard deviation of σ^0 due to instrument noise and speckle. Azimuthal effects are not important over tropical forests because σ^0 decreases only slightly with the incidence angle. As can be seen in Fig. 11 which shows over the african rain for-

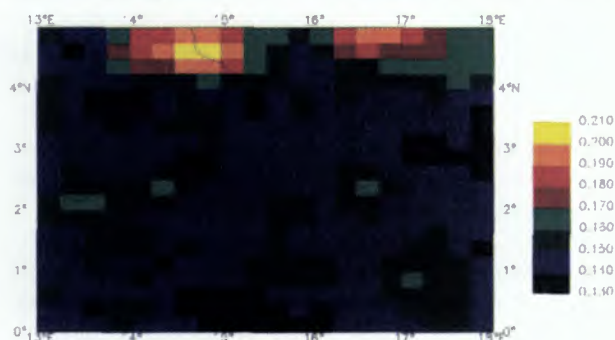


Figure 11: The estimated standard deviation of σ^0 , $\widehat{\sigma}(\sigma^0)$ in dB over the tropical forest in Africa. The area shown covers partly Congo, Cameroun, Central African Republic and Gabon.

est the standard deviation of σ^0 due to instrument noise and speckle is about 0.13 dB. Any increase over this value is due to azimuthal effects.

Given that $\widehat{\sigma}(\sigma^0)$ may be as large as 0.5 dB it becomes clear that azimuthal effects are important and must be considered in any error analysis of ERS Scatterometer land data. $\widehat{\sigma}(\sigma^0)$ itself can be used in various ways, e.g. to define criteria to reject invalid ERS Scatterometer measurements which might occur during instrument switching operations (Wuttge and Munz, 1996) or to provide an error estimate of any geophysical product derived from ERS Scatterometer data.

Conclusions

In this paper it was described how high quality ERS Scatterometer products can be ensured. While an absolute calibration and validation of ERS Scatterometer data is carried out by ESA, product developers may assess the relative noise level of these data by themselves. As shown in this paper azimuthal effects caused by large scale terrain features, inland waters, and build-up areas have an impact on ERS Scatterometer measurements. A simple method was presented that allows to assess the relative noise level of σ^0 due to instrument noise, speckle, and azimuthal effects. The method is unique in that no external data sets are required. The procedures introduced here can also be applied for future scatterometers like the planned Advanced Scatterometer (ASCAT) on METOP.

References

- [1] Amans V. (1996) ERS Wind Scatterometer Quality Control, NOAA/NESDIS Workshop Proceedings, April 1996, Alexandria, VA, USA.
- [2] Attema E. (1989) Estimating Satellite Pointing Biases from Scatterometer transponders Measurements - An exact Solution, ORM/3078/EA/sml, 14 March 1989.
- [3] Attema E. (1996) The Design, Calibration and System Performances of the ERS-1 and ERS-2 Wind Scatterometer, NOAA/NESDIS Workshop Proceedings, April 1996, Alexandria, VA, USA.
- [4] Boehnke K., V. R. Wismann (1996) ERS Scatterometer Land Applications: Detecting Soil Thawing in Siberia, Earth Observation Quarterly, N°52.
- [5] Cavanié A., P. Lecomte (1987) Study of a method to dealise winds from ERS-1 data, ESA contract 6874/87/GP-I(sc), 1987.
- [6] Frison P. L., E. Mougin (1996a) Monitoring global vegetation dynamics with ERS-1 wind Scatterometer data, Int. J. Remote Sensing, Vol. 17, No. 16, pp. 3201-3218.
- [7] Frison P. L., E. Mougin (1996b) Use of ERS-1 Wind Scatterometer data over Land Surfaces, IEEE Trans. Geosc. Remote Sensing, Vol. 34, No. 2, pp. 550-560.
- [8] Graham R. et Al. (1989) Evaluation of ERS-1 Wind Extraction and Ambiguity Removal Algorithms, ESA Contract, January 1989.
- [9] Guyenne D. ed. (1989) ERS-1 A new tool for global environmental monitoring in the 1990's, ESA BR-

- 36, November 1989, ESTEC, Noordwijk. The Netherlands, (ISBN 92-9092-019-X).
- [10] Lecomte P. et Al. (1995) ERS product Assurance and Quality Control, ESA Bulletin 82, May 1995, ESTEC, Noordwijk, The Netherlands, (ISSN) 0376-4265).
- [11] Lecomte P., Attema E.P.W. (1992) Calibration and Validation of the ERS-1 Wind Scatterometer, Proc. First ERS-1 Symposium, 4-6 November 1992, Cannes, France.
- [12] Lecomte P. (1993) CMOD4 Model Description, ESA technical note ER-TN-ESA-GP-1120, Rev. 1.2, March 1993.
- [13] Long A.E. (1985), Toward a C-Band Radar Sea Echo model for the ERS-1 Scatterometer, Proc. of the Third international Colloquium on Spectral Signature of Objects in Remote Sensing, les Arcs 1985, ESA SP-247, ESTEC, Noordwijk. The Netherlands, (ISSN 079-6566).
- [14] Long A.E. (1991) ERS-1 C-Band and Sea-Echo Models, ESA internal Report ESTEC/WMA/9104, Rev. 1. April 1991.
- [15] Longdon N. ed. (1991) ERS-1 Data Book, ESA BR-75, April 1991, ESTEC, Noordwijk. The Netherlands, (ISSN 0250-1589).
- [16] Magagi R.D., Y.H. Kerr (1997a) Retrieval of soil moisture and vegetation characteristics by use of ERS-1 wind Scatterometer over arid and semi arid areas, *J. Hydrology*, No. 188-189, pp. 361-384.
- [17] Mestre O. (1993) Réponse du diffusiomètre d'ERS-1 en fonction de l'angle d'incidence, note de travail de L'ENM 462.
- [18] Offiler D. (1996) Validation of ERS-1 Scatterometer Winds; An appraisal of Operational Backscatter Model Performances from launch to Present, NOAA/NESDIS Workshop Proceedings, April 1996, Alexandria, VA, USA.
- [19] Pulliainen J., J. Grandell, M. Hallikainen, M. Virtanen, N. Walker, S. Metsaemaeki, J.P. Ikonen, Y. Sucksdorff, T. Manninen (1996b) Scatterometer and Radiometer Land Applications, ESRIN Contract: 11122/94/I-HGE(SC), 253 p.
- [20] Rott H., H. Miller, K. Sturm, W. Rack (1993) Application of ERS-1 SAR and Scatterometer Data for Studies of the Antarctic Ice Sheet, Proc. Second ERS-1 Symposium - Space at the service of our environment, Hambourg 1993, ESTEC, Noordwijk. The Netherlands, (ISBN 92-9092-286-9).
- [21] Stoffelen, A. (1997); Improvement and Quality Assurance of the scatterometer Wind Product in the Backscatter Domain. Proceedings of the CEOS Wind and Wave Validation Workshop, ESA WPP-147, 159-160.
- [22] Stoffelen, A., Gaffard, C. and D. Anderson (1993): ERS-1 Scatterometer data assimilation. Proc. of the Second ERS-1 Symposium - Space at the service of our environment, Hambourg 1993, ESA SP-361, ESTEC, Noordwijk. The Netherlands, (ISBN 92-9092-286-9).
- [23] Stoffelen, A., D. Anderson (1993): Characterisation of ERS-1 Scatterometer measurements and wind retrieval. Proc. of the Second ERS-1 Symposium - Space at the service of our environment, Hambourg 1993, ESTEC, Noordwijk. The Netherlands, (ISBN 92-9092-286-9).
- [24] Vass P., B. Battrick ed. (1992) ERS-1 System, ESA SP-1146, September 1992, ESTEC, Noordwijk. The Netherlands, (ISSN 0379-6566).
- [25] Wagner W. (1996) Change Detection with the ERS Scatterometer over Land, EWP N°1896, ESA ESTEC, Noordwijk, 143 p.
- [26] Wagner W. (1998) Vegetation Cover Effects on ERS Scatterometer Data, Technical Note No. 1.98.05, Space Applications Institute, EC Joint Research Centre, Ispra, Italy, 193 p.
- [27] Wagner W., M. Borgeaud, J. Noll (1996) Soil Moisture Mapping with the ERS Scatterometer, *Earth Observation Quarterly*, N°54, pp. 4-7.
- [28] Wagner W., J. Noll, M. Borgeaud, H. Rott (1998) Monitoring Soil Moisture over Canadian Praires with the ERS Scatterometer, *IEEE. Geosc. Remote Sensing*, in press.
- [29] Wismann V. R., K. Boehnke (1994) Land surface monitoring using the ERS-1 Scatterometer, *Earth Observation Quarterly*, N°44, pp. 11-15.
- [30] Wooding M. ed. (1992) ERS-1 Geophysical Validation, Workshop Proc., ESA WPP-36, August 1992, ESTEC, Noordwijk. The Netherlands.
- [31] Wuttge S., H. Munz (1995) Effects of Gaps in Scatterometer Raw Data on s0- Triplets, ESA, Doc. No. ER-TN-DSF-FL-0001, 95 p.
- [32] Wismann V., K. Boehnke, A. Cavanié, R. Ezraty, F. Gohin, D. Hoekman, I. Woodhouse (1996) Land Surface Observations using the ERS-1 Windscaeterometer, Part II, ESA ESTEC, Contract No. 11103/94/NL/CN, 59 p.

ERS Wind product specifications.

Pascal Lecomte

Directorate of Application Programmes - Remote Sensing Exploitation Division
 ESA / ESRIN, Via Galileo Galilei, 00044 Frascati, Italy
 tel: ++39-6-941 80 670, fax: ++39-6-941 80 612
 Email: pascal.lecomte@esrin.esa.it

Introduction

This paper describes the wind products generated in real time in the ESA Ground Stations. It is based on a document available for distribution "ERS Ground Stations Products specification", ER-IS-EPO-GS-0201. The issue available today is the issue 3/1 and will be referenced [1] in this paper.

A major revision of this document is in preparation and will be issued by the end of the year 1998.

If most of the generic information can be found in [1], more details and explanation are added in particular in reference to "The ERS Scatterometer instrument and the On-Ground processing of its Data" presented during this workshop [2].

The ERS Ground Stations

The ERS ground stations at Kiruna, Fucino, Maspalomas, Gatineau and Prince Albert acquire, process and distribute data from the two European Remote Sensing satellites ERS-1 and ERS-2.

The Kiruna Station, having also Tracking, Telecommand and Control (TTC or TT&C) capability for the ERS satellites, is controlled by the Mission Monitoring and Control Centre (MMCC) at ESOC (Darmstadt). All parameters and commands to Kiruna Station will be originating from MMCC and will be processed in the Data Processing Monitoring and Control (DPMC), subsystem.

All other ERS Ground Stations are controlled by the Esrin ERS Central Facility (EECF) at Esrin (Frascati). The processing parameters and commands will be processed by the Control and Monitor Subsystem (CMS) at the Ground Stations.

Fig. 1 presents the block diagram for the ERS ground segment and shows the main product data flow from the acquisition subsystem to the dissemination to EECF.

The ERS telemetry consists of two parts: High Bit Rate data and Low Bit Rate data (respectively (HR and LR). Kiruna, Fucino and Maspalomas acquire HR data. Kiruna, Maspalomas, Gatineau and Prince Albert acquire LR data.

Due to its geographical position the Kiruna station acquires 10 out of 14 1/3 ERS-2 orbits per day. Fucino

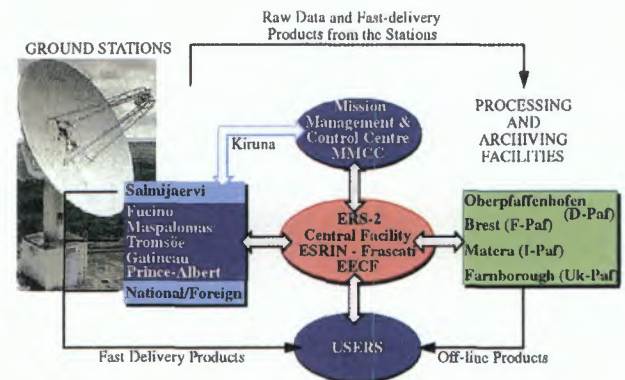


Figure 1: ERS Ground Segment Block diagram

covers the southern Europe and Mediterranean area for 4 to 5 passes of HR data acquisition per day. The acquisition of 3 orbits of LR data are shared between Maspalomas and Gatineau. Prince-Albert takes care of the acquisition of the 14th orbit of LR data.

Kiruna, Maspalomas and Gatineau station have the capacity to process the LR data in real time. This data is sent to EECF (via MMCC for Kiruna) and disseminated in less than three hours to the users. Prince-Albert doesn't have that capacity.

In Prince-Albert, the data are recorded on HDDT which are shipped to Gatineau for processing, transcription and dissemination to EECF and the users. The delay introduced by the shipment of the tape is 3 to 5 days.

Prince-Albert is being upgraded to ingest directly on disk the data acquired and to transmit it to Gatineau via land line in order to be processed in near real time. This capacity of real time processing of the last orbit should be made available by the end of the year 1998.

This upgrade will not only make available in near real time the orbit acquired in Prince-Albert, but will also make possible an optimisation of the station acquisition plan as it will give the possibility to distribute better the different passes between Gatineau, Prince-Albert and Kiruna and to improve the descoping strategy.

Product generation and distribution

The products are generated and distributed accordingly to a strategy based on the High Level Operation Plan (HLOP) approved at delegations level and detailed in the Mission Operation Plan (MOP).

The MOP takes into account all the Space and Ground segment technical constraints and is the basis for MMCC and EECF mission planning, station scheduling and data dissemination and archiving.

These schedules, which are elaborated, based on the MOP, by MMCC for Kiruna and EECF for the other stations, contain separate commands to generate, transcribe and disseminate the products.

The ground stations were completely upgraded in 1994 in preparation for ERS-2. This major upgrade was the opportunity not only to install more performant hardware, but also to install new algorithm, to integrate the transcription facility in the LRDPF and to prepare the installation of the SAR Wave processing in the LRDPF. This last step was done in 1997. The following two paragraphs give a description of the station setup before and after this major upgrade.

Initial Ground Station Setup

The products were generated by the three Fast Delivery Processors (FDP's), SARFDP 1, SARFDP 2 and LRDPF. Once completed, the products were sent to the DPMC or the CMS, which provides temporary storage on disk until the products are disseminated to EECF (through MMCC for Kiruna) and from there to the users.

In the original station design (Fig. 1), the two SAR Fast Delivery Processors, (SARFDP), were producing AMI Image and AMI Wave products. All other products (wind and Radar Altimeter) were produced by the Low bit Rate Data Processing Facility (LRDPF).

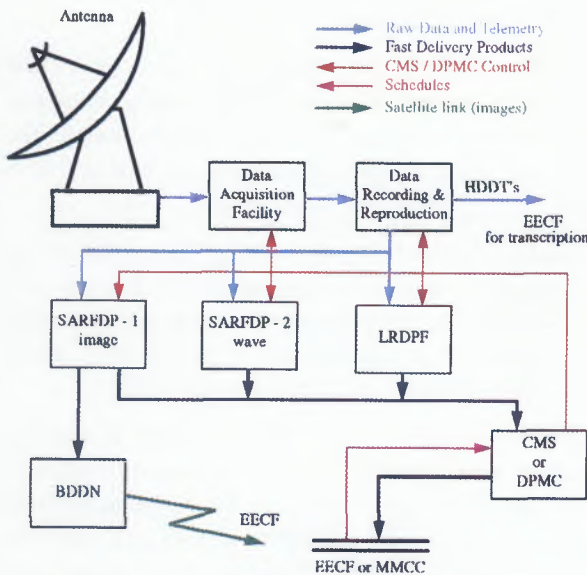


Figure 2: ERS-1 Ground Station Block diagram

The Low Bit Rate Transcription Facility (LRDTF) was installed at Fucino to transcribe all ERS-1 LR raw data (wind, wave, Radar Altimeter, Microwave and ATSR) from HDDT to Optical disk and Exabyte. This facility worked off-line from any other system.

Upgraded Ground Station Setup

In the newstation design (Fig. 1), the two SAR Fast

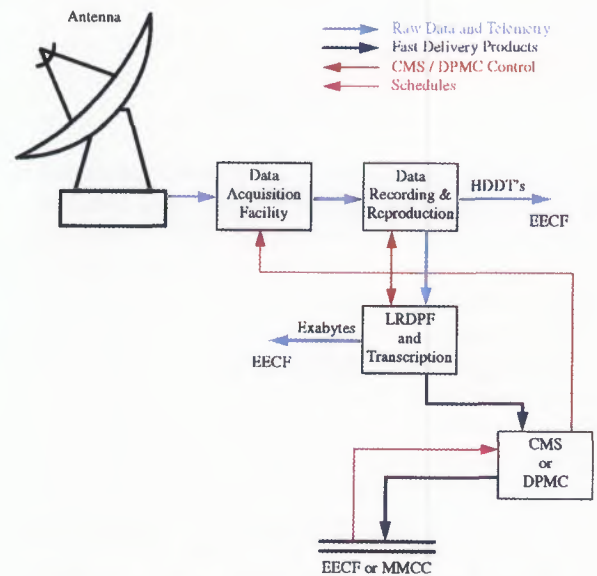


Figure 3: ERS-2 Ground Station Block diagram

Delivery Processors have been dismissed as there was no user for the Images produced in real time, and the AMI Wave processor has been ported into the LRDPF. Therefore, all real-time products are now generated by the Low bit Rate Data Processing Facility (LRDPF).

All Low Bit Rate data for ERS-2 is transcribed to Exabyte directly at the receiving station by the second generation of the LRDPF system. If necessary (e.g. failure of an exabyte drive during transcription, or lost of an exabyte) these transcribed Exabytes can be copied in a Copy Utility runned on the same hardware as the LRDPF but off-line from the rest of the station.

Fig. 1 shows the complete product distribution scheme as of today. The inclusion of the Direct Ingest system at Prince-Albert will allow the substitution of the tape shipment from Prince-Albert to Gatineau for Processing by a Land line. It is important to note that on this line no product will be disseminated but raw data which will be processed at Gatineau.

Product types

This section gives a description of all products generated in the ESA ERS Ground Stations at Kiruna, Fucino, Maspalomas and Gatineau.

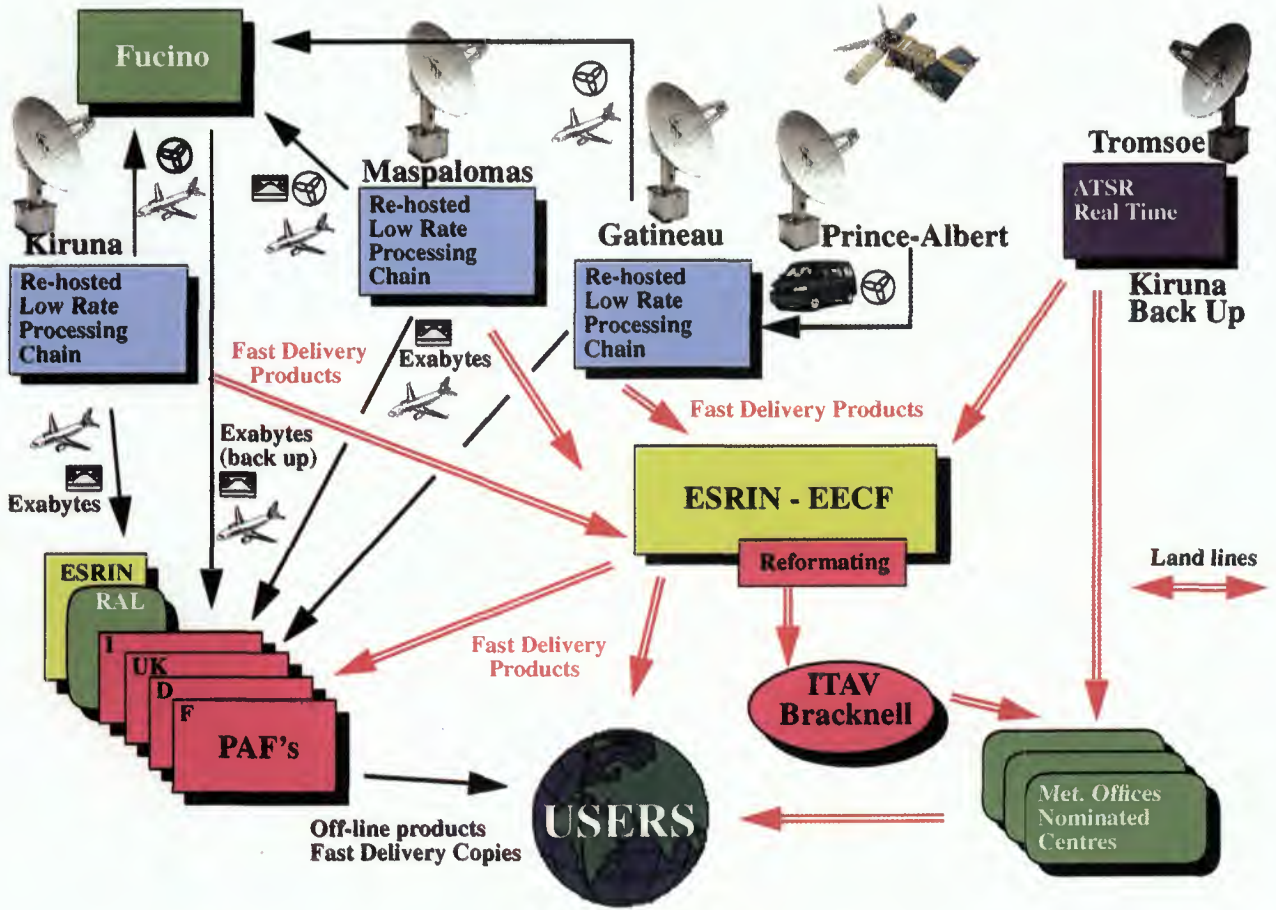


Figure 4: ERS Ground Segment - Product Distribution

The products fall into five categories:

- Fast Delivery Products addressed to the Users, acronym starting with 'U'.
- Intermediate Products, acronym starting with 'I'.
- Extracted products generated for Calibration purpose, acronym starting with 'E' and ending with 'C'.
- Extracted General and Instrument header products, acronym starting with 'E' and ending with 'I'.
- Text products, acronym starting with 'T'.

On top of that list, one should add the Raw Data on HDDT which are not product as such, but raw telemetry.

One product was called RATSr (Extracted ATSR-1 Raw Data) in the initial ground station setup. It corresponds to a product called EATC1 for better homogeneity of the Ground segment when the stations were upgraded.

The list of ERS ground station products and their size is given in Table 1.

Product Format

All products, with the exception of the raw data products stored on HDDT, have the same structure, which consists of three parts as shown on Fig. 5.

Main Product Header	
Specific Product Header	<i>Optional</i>
Data Set Record #1	
Data Set Record #2	
...	
...	
Data Set Record last	

Figure 5: Product Structure

The Main Product Header (MPH) has a single 176-byte record with an identical format for all products. The format of the MPH record is given in Table 4. The MPH contains information applicable to all processing chain products.

The Specific Product Header (SPH) is optional. The number and length of the record varies by product type.

All products have a product data set, consisting of one or more records. Length and number of records is determined by the product type and is given in the Main Product Header together with the size of the Specific Product Header.

Table 1: ERS Ground Station Product Sizes

Products		SPH Size in Bytes	DSR Size in Bytes	Number of DSR	Product Size in Bytes
EATC1	ATSR-1 Extracted Calibration data (identical to RATSr)	282	4004	1	4462
EATC2	ATSR-2 Low rate Extracted Calibration data	282	6804	1	7262
EATC2	ATSR-2 High rate Extracted Calibration data	282	6804	2	14066
EATI1	ATSR-1 Instrument Headers	40	4004 ¹	N ²	1500000 ³
EATI2	ATSR-2 Instrument Headers	40	6804 ¹	N ²	1500000 ³
EEP	Ephemeris Data	N/A	388	1	564
EGH	General Headers	N/A	260	16	4336
EGOC	GOME Extracted Calibration data	303	8004	1	8483
EGO1	GOME Instrument Headers	40	8004 ¹	N ²	1500000 ³
EIC	AMI Image Extracted Calibration data Calibration Data	N/A	11466	1	11642
EII	AMI Image Instrument Headers	40	234 ¹	N ⁴	1500000 ³
EMWC	Microwave Sounder Extracted Calibration data	315	900	1	1391
ERAC	Radar Altimeter Extracted Calibration Data	282	3136	1	3594
ERAI	Radar Altimeter Instrument Headers	40	3136 ¹	N ²	1500000 ³
EWAC	AMI Wave Extracted Calibration data Calibration Data	4480	4332	299	1299924
EWAI	AMI Wave Instrument Headers	40	108 ¹	299	1500000 ³
EWIC	AMI Wind Extracted Calibration data Calibration Data	282	7864	1	8322
EWII	AMI Wind Instrument Headers	40	72 ¹	N ²	1500000 ³
II16	AMI Image Intermediate Products	600	10004	6300	63025976
IWA	AMI Wave Intermediate Products, OGRC	260	16004	17	272504
IWA	AMI Wave Intermediate Products, OBRC	260	24004	17	408504
RH	High rate raw data on HDDT	N/A	N/A	N/A	N/A
RL	Low rate raw data on HDDT	N/A	N/A	N/A	N/A
TP	Text Product	N/A	84	1	260
UI16	AMI Image 16-bit Fast delivery	260	10004	6300	63025636
UI8	AMI Image 8-bit Fast delivery	260	5004	6300	31525636
UIC	AMI Image Chirp Replica	N/A	1540	2	3256
UIND	AMI Image Noise Statistics and Drift Calibration	28	1540	4	6364
UILR	User Image Low Resolution Image	260			
URA	Radar Altimeter Fast delivery	56	88	77	7008
UWA	AMI Wave Fast delivery	260	148	1	584
UWAC	AMI Wave Chirp Replica	N/A	1540	1	1716
UWAND	AMI Wave Noise Statistics and Drift Calibration, OGRC	28	1540	4	6364
UWAND	AMI Wave Noise Statistics and Drift Calibration, OBRC	28	124	4	700
UWI	AMI Wind Fast delivery	166	46	361	16948

Notes: 1 Maximum number of bytes per record depending on which data is extracted from the raw data

2 Maximum number of Data Set Records. This number corresponds to the number of source packets in 110 minutes of raw data.

3 Maximum product size.

4 Variable number of records depending on the number of source packets

Data Types

Table 2 shows the simple common data types in the ERS Ground station products.

There are two important complex data types as well: the `prod_type_list` and the `utc_time_m`. The first speci-

fies a list of product types for a command, the second gives the time in two integers.

Table 2: Data types in the ERS Ground station products

Data Type	Meaning
I1	1-byte unsigned integer
I2	2-byte integer in DEC format
I4	4-byte integer in DEC format
A	ASCII
B	1 byte or bits (flags)
S	Special format, as defined in description field

Data type `prod_type_list`

The `prod_type_list` data type is an array of 50 Bytes. Each byte indicates one product type. Several product

types can be indicated. Table 3 shows the indices for each product type. The processing subsystems read this list from the parameters in the commands and interprets which products they have to process, for example `transcrib_list [15] = 0` in the `C_Config_Trans` command means that product type 15, ERAC, will be transcribed.

In that particular case, the logic behind is that by default all products are transcribed (all flags set to zero). The flag corresponding to the product which shall not be transcribed have to be set to 1.

Table 3: Product types

Type	Product	
0	RATSR	ATSR-1 Extracted Calibration data
1	UI16	AMI Image 16-bit Fast delivery
2	UI8	AMI Image 8-bit Fast delivery
3	UIND	AMI Image Noise Statistics and Drift Calibration
4	UIC	AMI Image Chirp Replica
5	UWA	AMI Wave Fast delivery
6	UWAND	AMI Wave Noise Statistics and Drift Calibration
7	UWAC	AMI Wave Chirp Replica
8	UWI	AMI Wind Fast delivery
9	URA	Radar Altimeter Fast delivery
10	IWA	AMI Wave Intermediate Products
11	IUI6	AMI Image Intermediate Products
12	EIC	AMI Image Extracted Calibration data Calibration Data
13	EWAC	AMI Wave Extracted Calibration data Calibration Data
14	EWIC	AMI Wind Extracted Calibration data Calibration Data
15	ERAC	Radar Altimeter Extracted Calibration Data
16	EII	AMI Image Instrument Headers
17	EWAI	AMI Wave Instrument Headers
18	EWII	AMI Wind Instrument Headers
19	ERAI	Radar Altimeter Instrument Headers
20	EGH	General Headers
21	EEP	Ephemeris Data
22	TP	Text Product
23	UILR	User Image Low Resolution Image
30	VI	Verification Image
31	VIC	Verification Image Calibration
32	VWA	Verification Wave
33	VWAC	Verification Wave Calibration
34	EGOC	GOME Extracted Calibration data
35	EGOI	GOME Instrument Headers
36	EATI2	ATSR-2 Instrument Headers
37	EATI1	ATSR-1 Instrument Headers
38	EATC2	ATSR-2 Low rate Extracted Calibration data
39	EMWC	Microwave Sounder Extracted Calibration data
40	EICM	Multiple AMI Image Calibration Data

Data type `utc_time_m`

The data type `utc_time_m` contains the Julian day and time format in two four byte integers. The first integer gives the number of days since January 1, 1950. The

second shows the number of milliseconds the actual day.

Nonvalid Fields

If a Ground Station does not have a value for a field, either because the field is not applicable or a value is unavailable the field is set according to the following table:

Field value	Used for data type
0	for integer numbers
space	for ASCII
0	for bit fields within a byte
0	for special format. Note that there may also exist a 'non-value' definition by special format itself.

If a value exceeds the range of a type, the positive or negative maximum is given.

Byte and Bit Order

Data which are stored in Digital Equipment Corporation (DEC) internal storage formats have the following layout: 16-bit or 32-bit integer numbers have the Least Significant Byte first; for example:

Byte		
1	Least significant byte	Integer 1 (32 bits)
2	.	
3	.	
4	Most significant byte	
5	Least significant byte	Integer 2 (32 bits)
6	.	
7	.	
8	Most significant byte	
9	Least significant byte	Integer 3 (32 bits)
10	.	
11	.	
12	Most significant byte	
...
...

Data addressed on bit level; for example, Product Confidence Data (PCD), have the bit addresses starting at the least significant bit of a byte and increase to the most significant bit in the byte, i.e. the data item with the following description:

Bit	Meaning
bit 1 - 3	PCD_A
bit 4	PCD_B
bit 5 - 7	PCD_C
bit 8 - 10	PCD_D
bit 11 - 16	PCD_E

These bits are stored in two bytes as follows: a bit is defined to be set if the bit has a value 1.

	byte 1	byte 2
bit number:	8 7 6 5 4 3 2 1	16 15 14 13 12 11 10 9
bit position:	7 6 5 4 3 2 1 0	15 14 13 12 11 10 9 8
storage of PCD:	D C C C B A A A	E E E E E E D D

Main Product Headers

Table 4 describes the Main Product Header valid for all products. This MPH is not used for raw data products stored High Density Digital Tapes (HDDT) .

Table 4: Main Product header Detailed Description

Field	Bytes	Type	Description
1	17	A/I	Product identifier (for ESA internal operational use only), i.e. a set of characters and integers which form a unique identifier. The set of 17 Bytes is defined as follows: Byte 1: Originator of logical schedule (for ESA internal use only) e.g.: I: MMCC/EECF, Immediate Command M: MMCC/EECF, Logical Schedule J: Local operator, Immediate Command K: Local operator, Logical Schedule Byte 2-5: Sequential Counter of Logical Schedule Byte 6-9: Unique Identification or Schedule Offset Byte 10-13: Not used, set to 0 Byte 14-17: Sequential Number of Currently Generated Product
2	1	I1	Type of Product, see Table 3
3	1	I1	Spacecraft 1: ERS-1 2: ERS-2
4	24	A	UTC time of subsatellite point at beginning of product. Format in ASCII: DD-MMM-YYYY hh:mm:ss.itt For example: 30-JAN-1987 14:30:27.123
5	1	I1	Station ID, where data was processed 1: Kiruna Station (KS) 2: Fucino Station (FS) 3: Gatineau Station (GS) 4: Maspalomas Station (MS) 5: EECF Station (ES) 6: Prince Albert Station (PS)
6	2	B	Product Confidence Data bit 1 PCD Summary Flag 0: product correctly generated 1: at least one of the remaining 15 bits of the PCD in the MPH is set. bit 2 - 3 spare bit 4 - 5 Downlink Performance and X-Band acquisition chain. This value summarizes the PCD snapshots rel. to the products. 0: performance better than MMCC/EECF-supplied minimum threshold 1: performance equal to or worse than threshold 2: performance unknown bit 6 - 7 HDDT Summary. This value summarizes the PCD snapshots rel. to the product. 1: performance equal to or worse than threshold 2: performance unknown bit 8 - 9 Frame Synchronizer. This value summarizes the PCD snapshots rel. to the product. 0: performance better than MMCC/EECF-supplied minimum threshold 1: performance equal to or worse than threshold 2: performance unknown bit 10 - 11 FS to Processor I/F The LRDPF and SARFDP reads the status of the FS interface. 0: no parity error detected 1: at least one parity error detected 2: performance unknown bit 12 - 13 Checksum Analysis on LR Frames. The percentage of source packets, featuring a checksum error, and used in the actual product is compared to a MMCC/EECF given threshold. 0: lower than threshold 1: greater than threshold 2: performance unknown bit 14 - 15 Quality of Downlinked Formats and Source Packets. The RA product is based on using 80 consecutive source packets. The percentage of erroneous ones is determined and compared to a MMCC/EECF given threshold. 1: greater than threshold 2: performance unknown bit 16 Existence of Auxiliary Data. 0: auxiliary data and/or chirp correctly extracted 1: not all auxiliary data extracted
7	24	A	UTC time when MPH was generated; Format as in field 4.
8	4	I4	Size of Specific Product Header: Record in Bytes
9	4	I4	Number of Product Data Set Records
10	4	I4	Size of each Product Data Set Record in Bytes
11	1	B	Subsystem that generated the product. 0: SARFDP 1 1: SARFDP 2 2: LRDPF 3: VMP 4: LRDTF

Table 4: Main Product header Detailed Description

Field	Bytes	Type	Description
12	1	B	OBRC flag used for SAR products only bit 1 - 2 0: not used 1: OGRC data 2: OBRC data
13	24	A	UTC reference time. Time relation used to convert from satellite to ground, used together with the next two fields.
14	4	I4	Reference binary time of satellite clock (32-bit unsigned integer)
15	4	I4	Step length of satellite clock in nanoseconds
16	8	I2	Processor software version used to generate product. Format as defined by MMCC/EECF. 8 bytes = 4 words of integer x 2
17	2	I2	Threshold table version number.
18	2	B	Spare
19	24	A	UTC time of ascending node state vector
20-25	24	6I4	Ascending node state vector in earth-fixed reference system
20	4	I4	State vector; X in 10-2 m
21	4	I4	State vector; Y in 10-2 m
22	4	I4	State vector; Z in 10-2 m
23	4	I4	State vector; X velocity in 10-5 m/s
24	4	I4	State vector; Y velocity in 10-5 m/s
25	4	I4	State vector; Z velocity in 10-5 m/s

Product Quality Control

In case there is a loss of data between products, null products may be generated. The interval between null products is determined by the PCD update rate (nominally 2.5 seconds) during ingestion. In terms of satellite time, the interval between null products will be:

Low Rate Real-time data: 1.25 seconds

Low Rate Playback data: 17.1 seconds

High Rate data: 0.078 seconds

This difference is due to the difference between the record speed and the speed of data reproduction during the ingestion.

Wind Scatterometer Error Handling.

In the LRDPF, the error handling is performed on a product-type basis. This section describes the error handling strategy for the User Wind Product only.

Wind Scatterometer Fast Delivery Products will always be generated for the complete specified processing time interval with reference to the mid-beam.

Each product will correspond to an array of 19 nodes across-track by 19 nodes along-track with a node spacing of about 25 km.

For each node within the processing interval, the processor will attempt to find and process the corresponding satellite telemetered data of each beam (fore, mid and aft). For each beam and each node, the processor will calculate the corresponding sigma-nought value only if sufficient valid data are available for this node calculation.

The wind extraction algorithm will not be attempted for nodes not having the nominal 3σ calculated. For each of the product record generated within the processing time interval, the appropriate data fields will be

filled or flagged according to the number of processed beams and the possibility of wind vector extraction.

If a source packet is valid but not error-free, then calibration values contained in the auxiliary data of the packet will be ignored and the previous values, obtained from the last error-free source packet, will be used.

If at the end of the processing time interval, the last product is incomplete, it will be completed either by processed data or by blank records to make a complete product.

Product Confidence Data

All products disseminated from the ESA Ground Stations contain information on the quality of the content. This data is referred to as Product Confidence Data (PCD). Six areas are covered:

- Performance of downlink and X-Band acquisition chain;
- Checksum analysis on LR frames;
- Quality of downlinked formats and source packets;
- Quality of auxiliary data;
- Performance and status of processing chain equipment;
- Quality assessment performed during product generation.

In the context of the direct ingestion system which is being installed at Prince-Albert some PCD will have no meaning (e.g. performance of the High Density Tape Recorders).

Location of Product Confidence Data in Product Format

Product confidence data are stored in several places throughout a product. As a general rule, acquisition-related information is stored in the MPH, processing

information covering the entire product is given in the SPH, and information affecting the quality of individual cells is recorded on a cell basis together with the other cell contents. The location of the PCD in a product is as follows:

- Main Product Header: Within the main product header (same format for all products), 16 bits provide a summary of all checks performed before product dissemination;
 - PCD summary flag;
 - performance of downlinked and X-Band acquisition chain;
 - performance and status of processing chain;
 - checksum analysis on LR frames;
 - quality of downlinked formats and source packets;
 - quality of auxiliary data;
- Specific Product Header (FD and intermediate products):
 - product processor hardware equipment;
 - quality of downlinked formats and source packets (image and wave products only);
 - performance during product generation;
- Data Set Cell (RA and Wind products only):
 - quality assessment performed during product generation.

All PCD collected during acquisition and product generation are summarized in a single flag, the PCD summary flag. This flag is stored in the MPH of every product.

Performance of Downlink and X-Band Acquisition Chain

During acquisition, the following PCD is collected from the demodulator/bit synchronizer:

- Bit Error Rate (BER) estimate;
- Downlink channel signal strength (through the automatic gain control);
- I and Q bit synch lock status;
- Demodulator lock status.

These PCD, called PCD_DEMOD, are passed via the Time Code Generator (TCG) Interface to the TCG, to be embedded in the IRIG time code and passed on to the Data Path Switcher (DPS). The DPS outputs the downlinked data in parallel with the time code for recording on HDDT. When data are read back from the HDDT for processing, the DPMC collects the PCD_DEMOD from the time code. It checks the PCD_DEMOD against limits, and passes the result as PCD flags (correct, incorrect, unknown) every 2.5 seconds on to the LRDPF and SAR FDP. The LRDPF and the SAR FDPs attach the PCD flags to all products which are generated from the downlinked data associated with the PCD_DEMOD.

Checksum Analysis on Low Rate Frames

The LR transfer frame checksums are analyzed by the Frame Synchronizer. Any detected errors are flagged by the Frame Synchronizer. The LRDPF takes action by replacing the noise and calibration pulse data with defaults, and by flagging the event in the MPH. A count of checksum errors is maintained and a flag in the MPH set if the ratio of erroneous frames to total frames exceeds a threshold.

Quality of Downlinked Formats and Source Packets

The performance of instrument formats and source packets is monitored by the SAR FDPs and the LRDPF through analysis of the data from the Frame Synchronizer. If a source packet (LR) cannot be reassembled; it is totally disregarded (AMI wind and RA products). In addition, a flag is set accordingly in the MPH, the SPH and the DSR.

Quality of Auxiliary Data

Auxiliary data in the header of the downlinked source packets are checked by the processors against predefined limits. If a processor is unable to extract the auxiliary data needed for product generation, a flag is set accordingly in the MPH or in the DSR.

Performance and Status of Processing Chain Equipment

The following equipment is monitored during product generation:

- High Density Digital Recorders (HDDR)
- Frame Synchronizers (FSs)
- Frame Synchronizer to product processor interfaces
- SAR FDP and LRDPF processor status

The HDDRs are monitored by the DPMC/CMS, which collects status information generated by the Tape Search Units (TSUs). The DPMC/CMS also collects Synch Lock status via the Tape Search Units every 2.5 seconds, checks the parameters against predefined limits, and passes the resulting flag (correct, incorrect, unknown) every 2.5 seconds on to the LRDPF and the SAR FDPs.

During the replay of the recorder, the Frame Synchronizers monitor the Bit Error Rate, and the Lock status of the downlinked data. The DPMC/CMS samples the Frame Synchronizer status every 2.5 seconds, checks the parameters against predefined limits, and passes the resulting flag (correct, incorrect, unknown) every 2.5 seconds on to the LRDPF and the SAR FDPs. The Frame Synchronizers to processor interfaces are monitored in the SAR FDPs and the LRDPF. The processors check the parity bit in the incoming data from the Frame Synchronizer. Performance below a certain threshold is recorded in the MPH of the related products.

Generally, the processing hardware is checked out in the daily or in the prepass test. Each test usually pro-

duces a Pass or Fail result, which is reported to MMCC and EECF in the relevant test report. In certain ambiguous cases, where processing is done with uncertain hardware conditions, a flag is set in the SPH of each product.

Performance during Product Generation

During product generation, algorithm-specific data for product confidence parameters are generated. Depending on whether a PCD applies to an entire product or a product cell, the PCD is stored in the SPH or in the DSR PCD.

Fast Delivery Product Descriptions

Fast Delivery products include all products which are disseminated over an electronic telecommunication link from the Stations or from EECF. This includes the following products:

- AMI Image-16-bit (UI16)
- AMI Image-8-bit (UI8)
- AMI Image Noise Statistic and Drift Calibration (UIND)
- AMI Image Chirp Replica (UIC)
- AMI Wave (UWA)
- AMI Wave Noise Statistic and Drift Calibration (UWAND)
- AMI Wave Chirp Replica (UWAC)
- AMI Wind (UWI)
- Radar Altimeter (URA)

Only AMI Wind product is described in this document.

Users Wind Product (UWI)

Product Description

This product includes the intermediate and final results of the wind product generation. It consists of an array of wind vectors expressed in wind speed and direction. The product corresponds to a 500 x 500-km area. This area is represented by a 19 x 19 array of cells, with nominal 25-km spacing.

The produced wind field corresponds to an equivalent neutral stability wind field, referenced to a height of 10 m. For each cell a wind vector is given together with latitude and longitude. The sigma nought and other information needed to convert these to wind fields are also provided for each cell. Roughly 70 products are generated per orbit.

Format

One product includes:

- Main Product Header (already described in Table 4)
- Specific Product Header
- 361 Product Data Set Records: One cell is stored in one record.

The following two tables, Table 5 and Table 6 are describing the User Wind Product SPH and DSR.

Table 5: Specific Product Header for User Wind Product (UWI)

Field	Bytes	Type	Description	Units
1	2	B	Product Confidence Data for Processing bit 1 & 2: Processing equipment status 0: equipment working 1: some problems with equipment 2: equipment failed during product generation bit 3: Spare bit 4: I/Q Imbalance Flag 0: all beams better than MMCC/EECF-defined threshold 1: any beam above or equal to MMCC/EECF-defined threshold bit 5: Internal Calibration level flag 0: all beams within MMCC/EECF-defined level window 1: any beam out of MMCC/EECF-defined level window bit 6: Blank Product Flag 0: data available 1: no data available bit 7: Doppler Compensation: Center of Gravity flag 0: all beams below MMCC/EECF defined threshold 1: any beam above or equal to MMCC/EECF-defined threshold bit 8: Doppler Compensation: Standard Deviation flag 0: all beams below MMCC/EECF defined interval 1: any beam outside MMCC/EECF-defined interval bit 9 - 16: Spare	N/A
2	4	I4	Geodetic latitude of Product Center; A negative value denotes South latitude, and a positive value denotes North latitude.	10 ⁻³ deg
3	4	I4	East longitude (i.e. 0-360°) from Greenwich to East	10 ⁻³ deg
4	4	I4	Subsatellite Track Heading w.r. to North, turning clockwise 0at time of product center	10 ⁻³ deg
5	2	I2	Mean distance between two successive along track nodes at product center	meter
6	2	I2	Center of Gravity of averaged power spectrum (forebeam)	2.344 Hz
7	2	I2	"Standard Deviation" of averaged power spectrum (forebeam)	2.344 Hz
8	2	I2	Center of Gravity of averaged power spectrum (midbeam)	2.344 Hz
9	2	I2	"Standard Deviation" of averaged power spectrum (midbeam)	2.344 Hz

Table 5: Specific Product Header for User Wind Product (UWI)

Field	Bytes	Type	Description	Units
10	2	I2	Center of Gravity of averaged power spectrum (aftbeam)	2.344 Hz
11	2	I2	"Standard Deviation" of averaged power spectrum (aftbeam)	2.344 Hz
12	4	I4	I Mean Noise Power, forebeam	10^{-3} ADC units
13	4	I4	Q Mean Noise Power, forebeam	10^{-3} ADC units
14	4	I4	I Mean Noise Power, midbeam	10^{-3} ADC units
15	4	I4	Q Mean Noise Power, midbeam	10^{-3} ADC units
16	4	I4	I Mean Noise Power, aftbeam	10^{-3} ADC units
17	4	I4	Q Mean Noise Power, aftbeam	10^{-3} ADC units
18	4	I4	Internal Calibration level monitoring factor, forebeam	10^{-3} ADC units
19	4	I4	Internal Calibration level monitoring factor, midbeam	10^{-3} ADC units
20	4	I4	Internal Calibration level monitoring factor, aftbeam	10^{-3} ADC units
21	2	B	Mode of operation - set by the first midbeam source packet contributing to spatial filtering for the first node (near swath) in the center row of a product. bit 1 and 2: 0: windmode 1: wind/wave mode 2: no data found to identify mode bit 3 - 16: Spare	N/A
22-71	82	I2	Parameter Table ID. Details as follows:	N/A
22	2	I2	Global threshold Parameter Table ID	N/A
23	2	I2	Static parameter Parameter Table ID	N/A
24	2	I2	Dynamic parameter Parameter Table ID	N/A
25	2	I2	$F R_b(n)$ Parameter Table ID	N/A
26	2	I2	$T_{orbit,ref,D}$ Parameter Table ID	N/A
27	2	I2	$*F$ Parameter Table ID	N/A
28	2	I2	$*M$ Parameter Table ID	N/A
29	2	I2	$*A$ Parameter Table ID	N/A
30	2	I2	$F T_b(n)$ Parameter Table ID	N/A
31	2	I2	$C_{ADC,b(n)}$ Parameter Table ID	N/A
32	2	I2	$T_{orbit,ref,N}$ Parameter Table ID	N/A
33	2	I2	$F_{N,I}$ Parameter Table ID	N/A
34	2	I2	$F_{N,M}$ Parameter Table ID	N/A
35	2	I2	$F_{N,F}$ Parameter Table ID	N/A
36	2	I2	$*_{N,b(j,k)}$ Parameter Table ID	N/A
37	2	I2	$*_{N,b(j,k)}$ Parameter Table ID	N/A
38	2	I2	$M_{eff,b(j,k)}$ Parameter Table ID	N/A
39	2	I2	$N(j,k)$ Parameter Table ID	N/A
40	2	I2	Wind extraction software configuration Table ID	N/A
41	2	I2	$LA_b(i_r, i_c)$ Parameter Table ID	N/A
42	2	I2	$LZ_b(i_r, i_c)$ Parameter Table ID	N/A
43	2	I2	LN_b Parameter Table ID	N/A
44	2	I2	MA_b Parameter Table ID	N/A
45	2	I2	MS_b Parameter Table ID	N/A
46	2	I2	$NA_F(*, i_c)$ fore Parameter Table ID	N/A
47	2	I2	$NA_M(*, i_c)$ mid Parameter Table ID	N/A
48	2	I2	$NA_A(*, i_c)$ aft Parameter Table ID	N/A
49	2	I2	$NS_F(*, i_c)$ fore Parameter Table ID	N/A
50	2	I2	$NS_M(*, i_c)$ mid Parameter Table ID	N/A
51	2	I2	$NS_A(*, i_c)$ aft Parameter Table ID	N/A
52	2	I2	$NN_F(*, i_c)$ fore Parameter Table ID	N/A
53	2	I2	$NN_M(*, i_c)$ mid Parameter Table ID	N/A
54	2	I2	$NN_A(*, i_c)$ aft Parameter Table ID	N/A
55	2	I2	I_{ref} Parameter Table ID	N/A

Table 5: Specific Product Header for User Wind Product (UWI)

Field	Bytes	Type	Description	Units
56	2	I2	$a_f(*, i_c)$ fore Parameter Table ID	N/A
57	2	I2	$a_M(*, i_c)$ mid Parameter Table ID	N/A
58	2	I2	$a_A(*, i_c)$ aft Parameter Table ID	N/A
59	2	I2	$av_f(k, i_p, i_c)$ fore Param. Table ID	N/A
60	2	I2	$av_M(k, i_p, i_c)$ mid Parameter Table ID	N/A
61	2	I2	$av_A(k, i_p, i_c)$ aft Parameter Table ID	N/A
62	2	I2	i_b Parameter Table ID	N/A
63	2	I2	Spare	N/A
64	2	I2	Spare	N/A
65	2	I2	Meteo Table ID (table type 83, Forecast F18)	N/A
66	2	I2	Meteo Table ID (table type 84, Forecast F24)	N/A
67	2	I2	Meteo Table ID (table type 85, Forecast F30)	N/A
68	2	I2	Meteo Table ID (table type 86, Forecast F36)	N/A
69	2	I2	Spare	N/A
70	2	I2	Spare	N/A
71	2	I2	Spare	N/A

The power spectrum, noise and calibration level parameters included in the SPH of each User Wind products are the mean or the standard deviation computed over all the Source Packets having contributed to at least one cell included in the product (typically 2432 for the Mid beam and 4864 for the Fore and Aft beam). In order to have a correct representation for these parameters the units are 1/100 or 1/1000 of the sampling units (i.e. 2.344 Hz for the frequencies which are digitalized every 234.4 Hz and 10^{-3} ADC units for the other parameters).

The meteo table used in support to the ambiguity removal algorithm are selected at the beginning of the processing of the pass (C-GEN command). The table chosen is less than 3 hours from the first source packet used in the processing. In some cases (i.e. when the first Source Packet is just few second less than the 3 hours limit, this meteo table is chosen, even if the pass can finish more than 1.5 hours later. The meteo tables available are only forecasts. In fact the analysis are available only several hours after their validity time, and the forecast are following the analysis. Typically, the meteo tables (forecasts) computed on the basis of an analysis valid at 12:00 arrive at the station 10 hours later around 22:00. Therefore, taking into account that a forecast is used in the processing from 3 hours before to 3 hours after its validity time, only the 18, 24, 30 and 36 hours forecasts are used.

Recently, ECMWF duplicate its processing capacity to produce such forecasts twice a day at 00:00 and 12:00 UTC and not only at 12:00 UTC. The dissemination of the corresponding four forecasts to the stations twice a day is in place. As soon as the test are finished successfully, the LRDPF will have at disposal the same four tables but twice a day and will nominally use only 18 and 24 hour forecasts.

Remarks on the SPH parameters and flags

Equipment status flag (bits 1 and 2): This flag is always zero in the current implementation.

I/Q Imbalance flag (bit 4): Input statistics of noise channels, per beam: The I/Q imbalance monitoring factor is calculated by averaging the I and Q noise power, over a given number of consecutive F/M/A sequences. This number (nominally 8), is an external parameter. The respective quantities; I mean noise power and Q mean noise power for each beam are reported on fields 9 to 14. The given values are computed before any bias correction.

Flag on mean power on I and Q: For each beam the I/Q imbalance is estimated by forming the ratio: mean I power / mean Q power. However, these two values are separately checked against a threshold, without forming the ratio. Therefore $3 * 2 = 6$ thresholds are used. The flag is set when any of the I or Q channels parameter exceeds its threshold.

Internal Calibration level (bit 5): This calculation is performed for every beam, once per product.

Blank Product flag (bit 6): When no source packet is found in the time interval corresponding to a product, a dummy product is generated and this flag is set. This also means that if at least one source packet has been found, this flag is not raised.

Doppler compensation flags (bits 7 and 8): The on-board Doppler compensation is refined on ground. The overall performance of the Doppler compensation scheme is measured by taking the resulting signal power spectrum, averaged over a number of L1 measurements blocks and comparing its Center of Gravity and 'Standard Deviation' with those of an externally specified reference spectrum corresponding to an ideal Doppler compensation. This is done for all beams and per product.

When no beam and no estimate is available, the following default values are used (as shown in the table. In case of lack of input data, the standard deviation fields should not be filled with the best case values.

Fields 6,8,10	Averaged power spectrum Center of Gravity	999
Fields 7,9,11	Averaged power spectrum Standard Deviation	-1
Fields 12-17	I/Q Mean Noise power	-1
Fields 18-20	Internal Calibration level	-1

Table 6: Data Set Header for User Wind Product (UWI)

Field	Bytes	Type	Description	Units
1	4	I4	Data record number, starting with 1.	Count
2	4	I4	Geodetic latitude of Node. A negative value denotes South latitude, and a positive value denotes North latitude.	10 ⁻³ deg
3	4	I4	East longitude (i.e. 0-360* from Greenwich to east)	10 ⁻³ deg
4	4	I4	σ° of forebeam	10 ⁻⁷ dB
5	2	I2	Incidence Angle for forebeam	0.1 deg
6	2	I2	Look Angle of forebeam clock- wise w.r.t. North at grid point	0.1 deg
7	1	I1	Kp Value of forebeam, set to 255 if the calculation is not possible.	%
8	1	I1	Counter of forebeam corrupted or missing source packets	Count
9	4	I4	σ° of midbeam	10 ⁻⁷ dB
10	2	I2	Incidence Angle of midbeam	0.1 deg
11	2	I2	Look Angle of midbeam clock- wise w.r.t. North at grid point .	0.1 deg
12	1	I1	Kp Value of midbeam, set to 255 if the calculation is not possible.	%
13	1	I1	Counter of midbeam corrupted or missing source packets	Count
14	4	I4	σ° of aftbeam	10 ⁻⁷ dB
15	2	I2	Incidence Angle of aftbeam	0.1 deg
16	2	I2	Look Angle of aftbeam clock- wise w.r.t. North at grid point.	0.1 deg
17	1	I1	Kp Value of aftbeam, set to 255 if the calculation is not possible.	%
18	1	I1	Counter of aftbeam corrupted or missing source packets	Count
19	1	I1	Wind speed (set to 255 if wind extraction is not possible)	0.2 m/s
20	1	I1	Wind direction with respect to North turning clockwise at grid point (set to 255 if wind extraction is not possible)	2 deg.
21	2	B	Product Confidence Data bit 1 Summary PCD factor 0: processing of cell according to full specification 1: result to be viewed with limitation, i.e. one of the PCD flags listed below is not 0 (except bits 11-13). bit 2 Forebeam Flag 0: beam OK 1: no forebeam calculation bit 3 Midbeam Flag 0: beam OK 1: no midbeam calculation bit 4 Aftbeam Flag 0: beam OK 1: no aftbeam calculation bit 5 Forebeam Arcing Flag 0: no arcing detected on forebeam 1: arcing detected on forebeam bit 6 Midbeam Arcing Flag 0: no arcing detected on midbeam 1: arcing detected on midbeam bit 7 Aftbeam Arcing Flag 0: no arcing detected on aftbeam 1: arcing detected on aftbeam bit 8 Limit of Kp value 0: all beams below MMCC/EFCF-supplied threshold 1: any beam above or equal to MMCC/EFCF-supplied threshold bit 9 Land-Sea Flag 0: Sea 1: Land bit 10 Rank one solution flag . 0: Ambiguity removed 1: No ambiguity removal performed or ambiguity removal not successful See Note 6. bit 11-12 Ambiguity Removal Method . 0: ambiguity removed autonomously 1: use of meteorological tables after failure of autonomous ambiguity removal 2: ambiguity removed using meteorological data only 3: no ambiguity removal attempted bit 13 Maximum likelihood distance flag . 0: Maximum Likelihood Distance M of the rank 1 solution is less than or equal to a threshold 1: Maximum Likelihood Distance M of the rank 1 solution (i.e. solution of minimum residual) is greater than a threshold (see note 9). bit 14 Frame Checksum Flag 0: Checksum correct 1: Checksum error detected, noise and calibration replaced with default bit 15 and 16 Spare	N/A

Remarks on the DSR parameter fields

Each of the 19 x 19 cells are stored in ascending time order within each cell line across-track; cells closer to the satellite track precede farther cells.

The σ° values (fields 4, 9 and 14) are derived from the linear values using the following formula:

$$\sigma^\circ_{dB} = 10 \cdot \log_{10} \sigma^\circ_{linear} \quad |$$

If the σ° is not available, -999 999 999 dB is returned.

The look angles for the three beams (fields 6, 11 and 16) are defined as the angle between the unit vector tangential to the local meridian and pointing North at the centre of the node and the projection of the vector from the centre of the node to the satellite onto the local tangential plane, counting clockwise.

The counter of corrupted or missing source packets (fields 8, 13 and 18) is multiplied by -1 when the instrument is operated in Wind/Wave mode to recognise the mode of operation. In Wind/Wave mode, the absolute value of the counter is always greater than 2 because of the missing source packets due to wave image acquisition.

The kp is given in %. A new version of the software to be implemented by the end of 1998 will give the kp in 1/10 of %. In that case, a kp higher than 25.4 % will be considered as invalid. It has to be noted that values higher than 10 % have never been reported.

It is important to note that the wind speed is reported in units of 0.2 m/s (a value of 64 corresponds to 12.8 m/s). Therefore it may lie in the range 0 to 50.8 m/s. The value of 51.0 m/s (field value of 255) is reserved to indicate that no invalid wind speed was determined. When no wind extraction is possible, the product is written with the following default values: Wind speed = 255, Wind direction = 255

In the same way the wind direction is reported in unit of 2 degrees (a value of 64 corresponds to 128 degrees). The wind direction is given at the centre of the node using the meteorological definition (the wind direction is defined as the angle between the North and the vector pointing toward the point where the wind is blowing from, measured clockwise) as shown on Fig. 6.

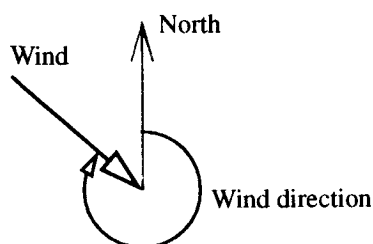


Figure 6: Wind direction definitions

It is important to note that the wind direction reported in the product generated by version of the LRDPF older

than 2.502 (in use up to October 15th, 1991) was 180° off with respect to the actual definition.

During the wind retrieval the wind direction is calculated with a resolution of 5° (from 0° to 355° with respect to the satellite velocity vector). Then, in order to report the wind direction with respect to the North, the satellite heading which is given with a precision of 10⁻³ degree is subtracted. This parameter, when reported in the product has a resolution of 2 degrees.

Remarks on the DSR PCD fields

Forebeam, Midbeam and Aftbeam Flag (bits 2,3 and 4): If a source packet is incomplete or too long, it is disregarded. During the calculations of the 3 σ° values, the number of missing or erroneous packets is counted. This flag is set when no source packet contributing to a node has been found, for this beam. This means that when at least one source packet, out of a maximum number of 36, is found, the spatial filtering is performed.

Forebeam, Midbeam and Aftbeam arcing flag (bits 5,6 and 7): A possible arcing of the Travelling Wave Tube (TWT) leads to an automatic switching off of the Pulse transmission. As a new transmission is not attempted before few seconds, an arcing results in loss of data. These missing data are identified by looking at the statistics of the received data; as no transmission occurs, received data feature noise statistics. The corresponding beam data for a given node are flagged.

Limit of Kp value (bit 8): Before the wind extraction, the Kp value for each beam, for a given node is estimated. For every beam the actual value is compared to a given limit (e.g. 20%), and this flag is raised in case at least one exceeds this limit. In case this flag is raised no wind extraction is attempted for that node.

Land / sea flag: in order to avoid any land contamination, the land/sea flag is pessimistic in the sense that every node which has land within 50 km from the node centre is declared land.

The flags in PCD bits 10 to 13 are set by the ambiguity removal algorithm.

The flag 10 indicates if the ambiguity removal was successful or not. In case the ambiguity removal was not successful, the rank one solution is reported (solution with the lowest distance to the C-Band model).

Flags 11 and 12 are indicating which ambiguity removal method was used.

The flag 13 indicates if the distance between the sigma nought triplet and the C-Bands model is greater than a threshold. If this flag is set no ambiguity removal is attempted and the rank 1 solution is reported as indicated by flag 10.

Fig. 7 summarizes the logic for setting flags 10 to 13 of the DSR PCD's.

The Ambiguity removal runs on a set of 6 products. In order to increase the confidence in the results, only 4 products are disseminated at the end of the processing and four new products are loaded to create a new set of

References

- [1] "ERS Ground Stations Products specification", ER-IS-EPO-GS-0201, issue 3/1.
- [2] Lecomte P., "The ERS Scatterometer instrument and the On-Ground processing of its Data", Proc
- [3] Albani M., V. Beruti & S. D'Elia, "Evolution of the ERS-2 Data Processing Ground Segment", ESA Bulletin Nr. 83, August 1995.

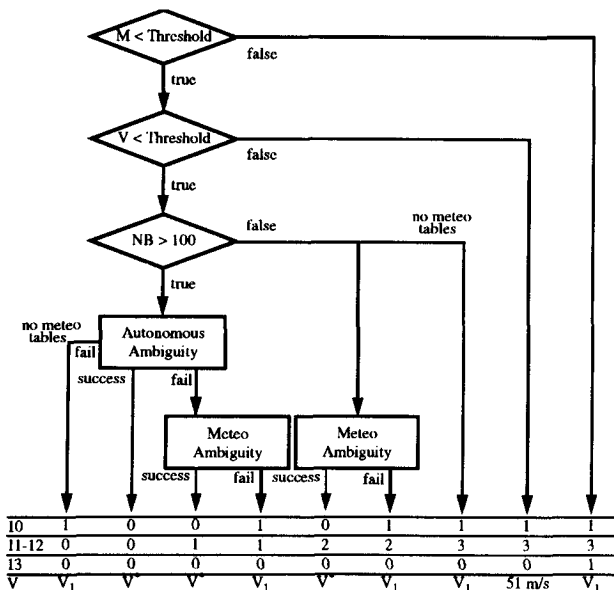


Figure 7: PCD flags for User Wind Product with respect to ambiguity removal

six products (including the two products which were kept). If the second ambiguity removal attempt on the nodes of the two products which were processed twice is successful or identical to the first attempt, the flags are set as processed the second time. If the second attempt fails when the first one succeeded, the first results are kept and the flags are set as follows:

- bit 10 = 0,
- bit 11-12 = 3,
- bit 13 = 0.

Flag on frame checksum (bit 14): For every source packet contributing to a node (up to 36), there is an input flag set by the frame synchronizer. This flag is set whether at least one out of these 36 input flags has been set by the frame synchronizer. If a checksum error happens, the calibration and noise data are replaced with defaults.

Product distribution

The ERS ground stations use a number of different media to distribute their products. The products can either be distributed via telecommunication links or on some magnetic or optical media.

The User Wind Product is in practice only distributed via telecommunication links from the Ground stations to EECF where they are :

- Sent to the PAF for archiving. Copies of these fast Delivery Products can be requested on tapes.
- Put on a FTP server for immediate delivery to some users,
- Converted in BUFR format for immediate dissemination to the Meteorological users.

The ERS Wind Scatterometer mission: routine monitoring activities and results.

Raffaele Crapolicchio, Pascal Lecomte

Directorate of Application Programmes - Remote Sensing Exploitation Division

ESA / ESRIN, Via Galileo Galilei, 00044 Frascati, Italy

tel: ++39-6-941 80 693/670, fax: ++39-6-941 80 612

Email: raffaele.crapolicchio@esrin.esa.it, pascal.lecomte@esrin.esa.it

Abstract

This paper summarizes the major events occurred since the launch of ERS-1 and ERS-2 Wind Scatterometer, and shows the results from the monitoring of the instrument by looking at the telemetry data stream (e.g. working modes, currents, voltages and temperatures of AMI instrument) and the fast delivery product (e.g. doppler, noise and calibration information). The latter allows also the monitoring of the On-Ground Processing and the geophysical validation of the products. This paper also reports the results of the commissioning phase and describes the calibration status of both ERS-1 and ERS-2 Wind Scatterometer.

This monitoring activity is conducted within the Product Control Service (PCS) at ESRIN.

Introduction

A remote sensing mission involves many aspects: the mission scenario, the instrument calibration and maintenance, the data quality control. In order to monitor these different aspects in the ERS ground segment the Mission Coordination and Product Assurance Section at ESRIN is in charge of ensuring the operational integrity of the overall ERS mission and in particular, the quality of the data products provided to users. The strategy adopted to meet this objective is to regularly monitor both the ERS sensors performance and the ground segment operations by analysing the quality of the ERS products.

The scope of this monitoring activity which is an important task which runs in the background, is two-fold: first to maintain the quality of the results obtained during the commissioning phase, to assess the evolution of the instrument quality due to ageing or to human action commanded from ground and to take all corrective actions necessary to restore the initial quality.

At this time we have five years of ERS-1 Wind Scatterometer mission (from July, 21st 1991 to June, 3rd 1996 ERS-1 where instruments were put in stand-by) and more than three years of ERS-2 Wind Scatterometer mission since the launch of the ERS-2 satellite on the 21st April 1995. At this point, it is useful to outline the differences between the ERS-1 and ERS-2 Wind Scatterometer missions in terms of events, operations and per-

formance. Moreover it is important to assess the continuity in the sigma nought calibration and in the validation of the geophysical parameters retrieved: the wind speed and direction.

The paper is structured in the following chapters:

- Events since launch.
- Instrument operation modes
- Calibration objectives.
- Commissioning phase activities and results.
- Calibration performance.
- Instrument performance.

Events since launch

The events since launch can be grouped into three main categories.

- Every event linked to the satellite itself; these events are not related to the AMI or to the Ground processing, but do affect the data quality for a certain period of time. In this table we didn't include the orbit manoeuvres which are occurring roughly every month.
- The instrument anomalies which generally affect the data for a short period (time needed for being alerted and to take the appropriate action). In few cases these anomalies are more difficult to overcome and the data quality could be slightly degraded until the definitive solution is implemented.
- Ground segment events which are mostly installation of scatterometer data processing chain upgrades and Look-Up-Tables loading in the stations.

Table 1, 2 and 3 are covering these three categories of events in reference to ERS-1, table 4, 5 and 6 are relative to ERS-2.

Table 1: ERS-1: Satellite events

13rd July 1991	ERS-1 Launch.
25th July 1991	Phase A: commissioning. 3 days repeat cycle.
28th December 1991	Phase B: 3 days repeat cycle.
14th April 1993	Phase C: 35 days repeat cycle.
6th December 1993	IDHT failure (HR amplification tube).

23rd December 1993	Phase D.: 43 days repeat cycle.
10th April 1994	Phase E/F: 168 days repeat cycle.
21st March 1995	Phase G. 35: days repeat cycle.
3rd June 1996	ERS-1 instruments in stand-by. Check-up period every two 35-days cycle.
29th December 1997	solar panel partial failure: the instruments cannot be powered-on all at the same time.

Table 2: ERS-1: Active Microwave Instrument events

	none.
--	-------

Table 3: ERS-1: Ground segment events related to scatterometer data

19th September 1991	Scaling by 1.3 dB of all beams. Coarse mid beam correction.
29th October 1991	Gain tuning.
4th November 1991	Coarse Fore and Aft beam correction.
15th January 1992	Sampling correction.
1st March 1992	Final antenna pattern.
1st June 1992	LRDPF 3000
10th June 1992	CMOD3
26th June 1992	LRDPF 3010
24th February 1993	LRDPF 4000 + CMOD4
24th December 1993 14th January 1994	Data reprocessed in backlog with correct tables.
24th March 1994	LRDPF 4100
10th March 1995	SGI LRDPF 6210 (transcription)
22nd March 1995	LRDPF 4200
27th April 1995	LRDPF 4210
3rd October 1995	SGI LRDPF operative at Maspalomas and Gatineau stations.

The AMI instrument on board ERS-1 has not been affected from serious anomaly, on the contrary, the ERS-2 AMI has a different history.

During the initial setting of the ERS-2 spacecraft, the first attempt to switch on the AMI resulted in a serious anomaly causing the instrument to shut down, both in SAR and Scatterometer modes. It was soon discovered that the instrument was prevented from working at nominal power. By reducing the output power to the minimum, engineers succeed in acquiring the first SAR image on the same day, but it was still not possible to run the instrument in Wind mode.

Many test were made to determine the cause and possible solutions to the problem. The anomaly was resolved by setting the redundancy switch at the input to the High Power Amplifier to an intermediate position,

thereby using it as a power splitter. The output power was reduced by a factor of two, and, for the first time some wind measurements could be made (November, 16th 1996).

After few months of nominal operation, a new anomaly affected the ERS-2 Wind Scatterometer instrument. The relay used to switch on and off the calibration subsystem was not latching properly and more and more often the instrument was shutting down following a relay failure. On August, 6th 1996 it was decided to operate the instrument with the redundant unit of the calibration subsystem.

Also in August 1996 a major failure of the Scatt electronics required to switch to the redundant unit.

Table 4: ERS-2: Satellite events

21st April 1995	ERS-2 Launch. ERS-2 orbit is approximately 30 minutes behind ERS-1 with a 35 days repeat cycle.
26th January 1996	Attitude and Orbit Control System depointing anomaly.
14th February 1997	Gyroscope anomaly.
3rd June 1998	Depointing anomaly

Table 5: ERS-2: Active microwave instrument events

1st May 1995	Switch-on of the AMI was attempted and failed due to activation of the receiver overload protection circuit.
	Reducing the RF drive level to the HPA. Output power reduction of 1.7 dB.
	AMI Image and Wave mode switch on.
	Attempt to operate in Wind mode failed.
16th November 1995	By use of an updated beam current command the input redundancy switch control circuit was set in an intermediate condition (Power split function).
15th - 25th July 1996	Scatterometer unavailability due to calibration DC converter switch off.
26th July 1996	Switch to Scatterometer electronics side B.
26th July to 5th August 1996	Scatterometer unavailability due to calibration DC converter switch off.
6th August 1996	Switch to calibration subsystem side B.
23rd September 1996	AMI Scatterometer test.
24th September 1996	Calibration DC converter test. Operation without calibration subsystem.
26th September 1996	No doppler information on board after the test.
31st October 1996	AMI Scatterometer test.

December 1997	SBT and noise field corruption
6th June 1998	No doppler information on board after the depointing anomaly.

Table 6: ERS-2 Ground segment events related to scatterometer data

24th April 1995	Installation of SGI LRDPF version 6210.
3rd October 1995	SGI LRDPF version 6300 in operation at Maspalomas and Gatineau stations.
22nd November 1995	Wind mode was introduced as part of the nominal Mission Operation Plan.
15th January 1996	Start of the scatterometer commissioning phase.
19th March 1996	End of the scatterometer commissioning phase. Gain setting, final antenna pattern, new set of LUT in the ground stations.
16th April 1996	Wind scatterometer data distributed.
12nd August 1996	Update of the reference calibration pulse (new Look-Up-Table).
18th March 1997	Installation of SGI LRDPF version 7100.
18th June 1997	Updated of the value of internal calibration reference energy
March 1998	Installation of SGI LRDPF version 8200.
end of 1998	Fast delivery dissemination of data acquired at Prince Albert station

Instrument operation modes

The Wind Scatterometer is part of ERS payload and is combined with a Synthetic Aperture Radar (SAR) into a single Active Microwave Instrument (AMI). This instrument is operated in either SAR or Wind mode. The SAR mode is planned as consequence of users' request and priority is given to descending passes. Another possible working mode is the Wind/wave mode which consist of nominal Scatterometer operations (Wind mode) interrupted every 30 seconds (roughly 200 Km) by a couple of seconds of a short SAR operation in order to acquire small SAR imagerettes of roughly 6 x 6 Km from which the wave spectra can be derived. The Wind/Wave mode is the default mode for the AMI on board ERS-1. The different mode of operation has a constraint that comes also from the presence of other instruments on-board. These constraints and rules have consequences on the scatterometer data availability.

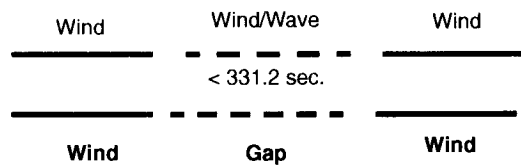
The constraints for AMI operations

The Wind mode and Wind/Wave mode have the following constraints:

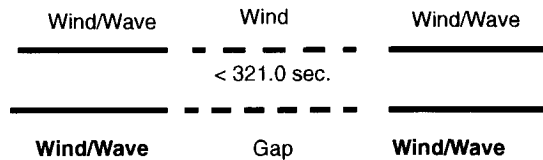
- 8 seconds (~ 53 km) are needed to switch from Wind Only to Wind/Wave or vice versa.



- The instrument is switched to Gap mode (no operation) if a Wind/Wave segment is less than 331.200 seconds (~ 2206 km).

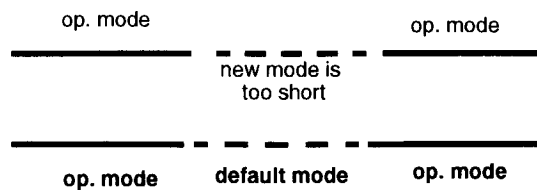


- The instrument is switched to Gap mode (no operation) if a Wind Only segment is less than 321.000 seconds (~ 2138 km).

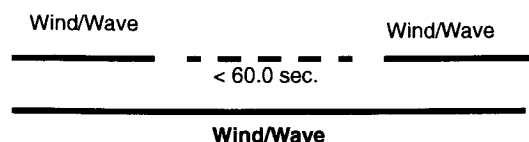


in order to avoid the Gap mode the following rules has been added

- If the AMI cannot switch because the segment is too short, less than 331.200 in Wind/Wave or less than 321.000 in Wind only, the instrument is switched in a default mode (which could be Wind/Wave or Wind Only).



- If two segments of the same mode are separated by less than 60 seconds (~ 400 km) the gap is filled by leaving the instrument in the same mode and these two segments are merged.



- On ERS-2, there is an other constraint. Because of the data rate, the on-board recorder cannot handle at the same time, both the ATSR-2 in High Rate mode (twice the data flow of the same instrument in Low Rate mode) and the AMI in Wind/Wave mode.

The rules from the Mission Operation Plan

In order to optimise the satellite potentiality and to satisfy all user communities, the following rule have been defined:

- Over the Ocean the AMI is in Wind/Wave mode and the ATSR-2 in Low Rate. Over Land the AMI is in Wind mode to allow the ATSR-2 to be switched in High Rate. This strategy preserves the Ocean mission.

The consequences

To satisfy the ATSR community, the ERS-2 AMI is switched from Wind/Wave to Wind Only when the satellite crosses the coast line inland, and back to Wind/Wave when it is back over Ocean. This allows the switching of the ATSR-2 to High Rate mode.

The first consequence is that each time the AMI crosses the coast line, there is a gap in the data of 8 seconds (~53 km). The main problem is between Antarctica and Australia or South America where the distance over the ocean is less than 2206 km. For example: Over Australia, the instrument is in Wind Only mode. When it crosses the coast line it tries to switch to Wind/Wave for a segment less than 331.200 seconds which is not allowed. Then it tries to switch in the default mode which today is also Wind/Wave, and therefore the switch is not allowed too. Then the instrument is switched in Gap mode. The merging doesn't work because the gap is bigger than 60 seconds. A way to solve this problem would be to change the default mode from Wind/Wave to Wind Only. This moves the problem from over ocean, to over Australia which is less than 321.000 seconds long. The only solution to avoid these gaps is to change the land mask over Antarctica in order to have an Antarctic Ocean larger than 2206 km.

Figure 1 and Figure 2 show the 501 orbits for one cycle (35 days) of the ERS-1 and ERS-2 satellite respectively.

Each orbit's segment has a different colour depending on the instrument mode: brown for Wind mode, blue for Wind/Wave mode and green for image mode (SAR). The red and yellow colours correspond to gap modes (no data acquired). For ERS-1 the last cycle was selected (cycle 156). The default mode for the AMI was Wind mode. During this period the AMI activity is summarised in the table 7.

For ERS-2 satellite the loss of data due to the AMI in gap mode, over the ocean between Antarctica and Australia or South America or Africa is clear show in Figure 2.

Table 7: ERS-1 AMI activity cycle 156

AMI activity	ascending	descending
Wind or Wind/wave	92.0	79.0
Image	3.5	13.5
Gap	2.4	4.4
Other	2.1	3.1

During this period (cycle 30) the ERS-2 AMI activity is as shown in table 8

Table 8: ERS-2 AMI activity cycle 30

AMI activity	ascending	descending
Wind or Wind/Wave	91.0	82.0
Image	1.4	8.0
Gap	5.3	8.7
Other	2.3	1.3

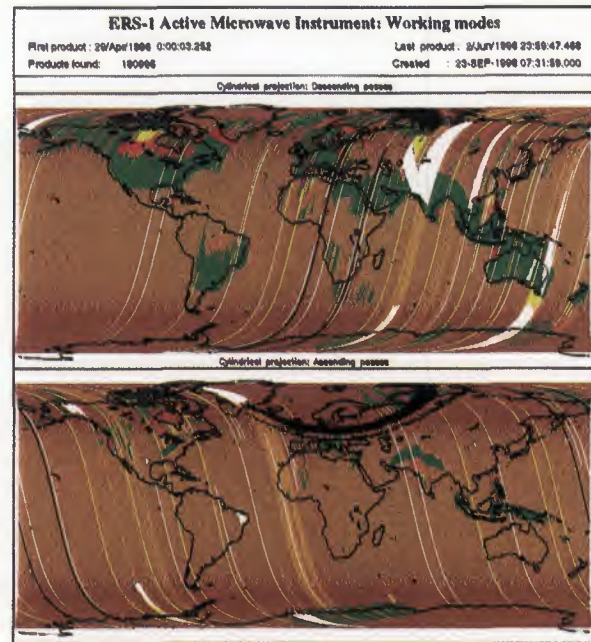


Figure 1: ERS-1 AMI instrument working modes.

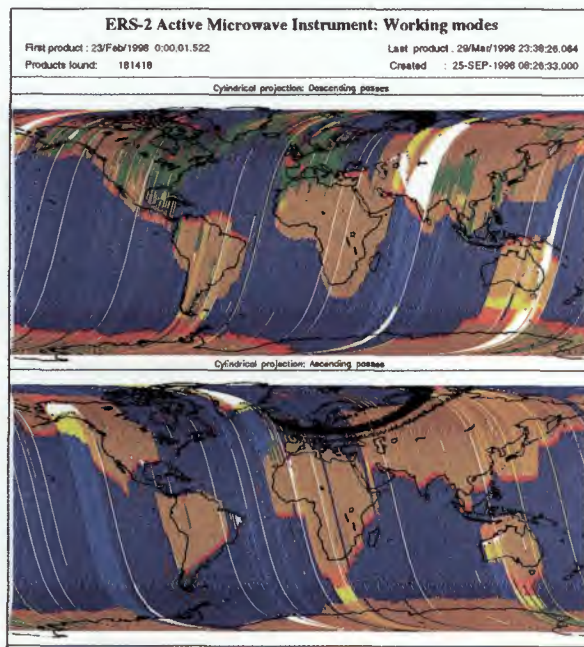


Figure 2: ERS-2 AMI instrument working modes.

Calibration objectives

The most important objective during the commissioning phase was to ensure that the system response is absolutely calibrated in terms of the radar backscattering coefficient (sigma nought) over the range of the incident angles of the instrument. This is achieved using a combination of internal and external references.

Internal reference

The internal reference is the calibration pulse. During the nominal operations, 32 pulses are transmitted on a given beam, followed by 32 pulses on the next beam, and so on. The 1st, 11th, 21st and 31st pulses are directly injected via the calibration subsystem which provides an attenuation and a delay of the pulses, into the receiver. This allow us a monitoring of the instrument stability (e.g. the transmitted power and the receiver chain gain).

External reference

Two different type of external references are used, point targets (transponders) and distributed targets. The difference between these is that point targets provide high accuracy but do not take into account the antenna pattern, while the distributed targets provide the necessary antenna pattern information. These references allow us to ensure that the sigma nought which is expected from a known target, is properly measured by the instrument (absolute calibration), and that the variation over the range of incident angles of the instrument is unaffected by the local attenuation from the antennae (relative calibration).

The transponders

For the ERS Wind Scatterometer mission three calibration transponders are used. These transponders are located in the south of the Spain on a line almost perpendicular to the ground track of ascending as well as descending passes. The transponders have a varying (with transponder electronics temperature), but accurately measured Radar Cross Section (RCS) according to which received Radio Frequency pulses are re-transmitted to the spacecraft. Every time the ERS Wind Scatterometer over-flies the three transponders, it is configured in wind calibration mode and radio Frequency (RF) pulses are transmitted to the three transponders by the fore, mid and aft antennae during periods of 120, 40 and 120 seconds, respectively.

The basic idea of the calibration is to compare the echo data from transponder with simulated data which are generated by the Scatterometer System Simulation (SSS) by using the most accurately known model of the instrument and the actual scenario, in particular the transponder RCS, as input. By comparing the actual and simulated data, the model of the instrument can be update in terms of echo power level. The result of the whole process is the gain constant which is simply the simulated power divided by the actual power. When the model has been updated so the actual and the simulated data agree within a desired accuracy, the updated model is used by the SSS to generate the Look Up Tables (LUT). These LUT are used in the ground processing in order to produce from the echo data the correct sigma nought value.

The rain forest

The tropical rain forest in South America has been used as a reference distributed target. The target at the working frequency (C-band) of ERS-2 Scatterometer acts as a very rough surface, and the transmitted signal is equally scattered in all directions (the target is assumed to follow the isotropic approximation). Consequently, for the angle of incidence used by ERS Wind Scatterometer, the normalised backscattering coefficient (sigma nought) will solely depend on the surface effectively seen by the instrument:

$$S^0 = S \cdot \cos \theta$$

With this hypothesis it is possible to define the following formula:

$$\gamma^0 = \frac{\sigma^0}{\cos \theta}$$

Using this relation, the gamma-nought backscattering coefficient over the rain forest is independent of the incident angle, allowing the measurements from each of the three beams to be compared. The reference area used by

the PCS is located between 2.5 degrees North and 5.0 degrees South in latitude and 60.5 degrees West and 70.0 degrees West in longitude.

Commissioning phase activities and results

The commissioning phase activities were then limited to the following points:

- Set the on-board receiver gain
- Derive the antenna pattern correction for the three antennae from the rain forest and transponder echoes,
- Compute the antennae mispointing,
- Compute the calibration coefficients, and generate the associated Look_Up_Tables,
- Verify that the ERS X-Band data are stable (monitoring of the Long Term Stability of the instrument),
- Compare the ERS-1 and ERS-2 response signal over rain forest and transponders.
- Validate the geophysical products.

Gain setting

ERS-1 on-board gains were optimised to ensure maximum use of the dynamic range of the analog to digital converter (ADC), whilst avoiding saturation. For the ERS-2 the operational transmit power is approximately half the ERS-1. The initial ERS-2 on-board gains were set to the same level as for ERS-1. Once the first corrections to the antenna patterns were made (March 1996), and the stability of the instrument verified, the receiver gain was modified from 18 to 21 dB to take full advantage of the ADC dynamic range.

Antenna patterns

The antenna patterns have been computed over the reference area during the month of May 1996 when both ERS-1 and ERS-2 Wind Scatterometer were operating. The results are shown in Figure 3 and Figure 4 for the ERS-1 and ERS-2 respectively and are very close.

The antenna profiles are flat within 0.3 dB in particular for the fore and aft antenna. The mid antenna shows a ripples which is not found in the fore and in the aft antenna. A small diffracted signal due to the presence of the SAR antenna edge close to the Mid antenna is suspected to be the reason for this. Figure 5 shows the ERS-2 antenna patterns before the commissioning phase. It is clear from the figure the efficiency of the new set of LUT installed in the ground processing on March 1996.

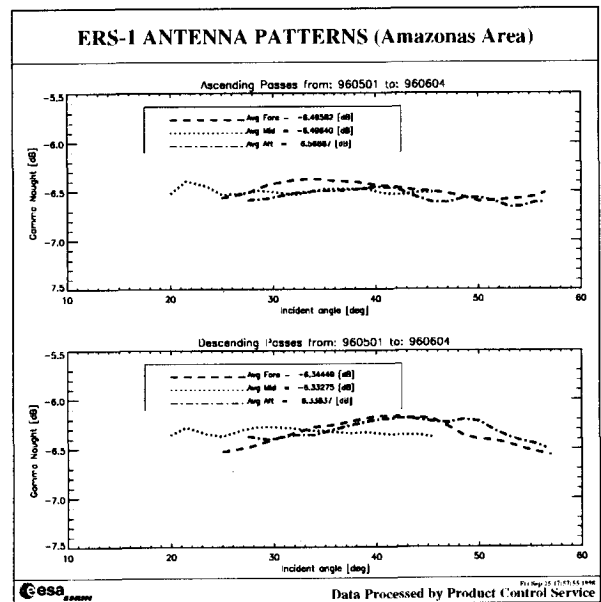


Figure 3: ERS-1 Scatterometer: Antenna pattern over Brazilian rain forest (May 1996).

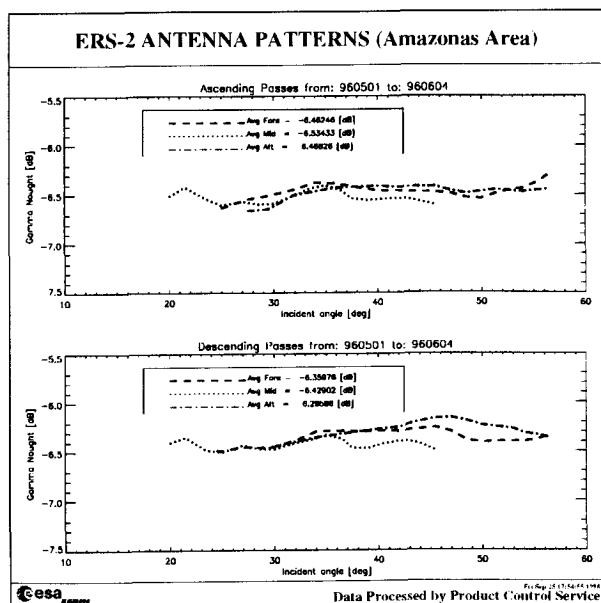


Figure 4: ERS-2 Scatterometer: Antenna pattern over the Brazilian rain forest (May 1996).

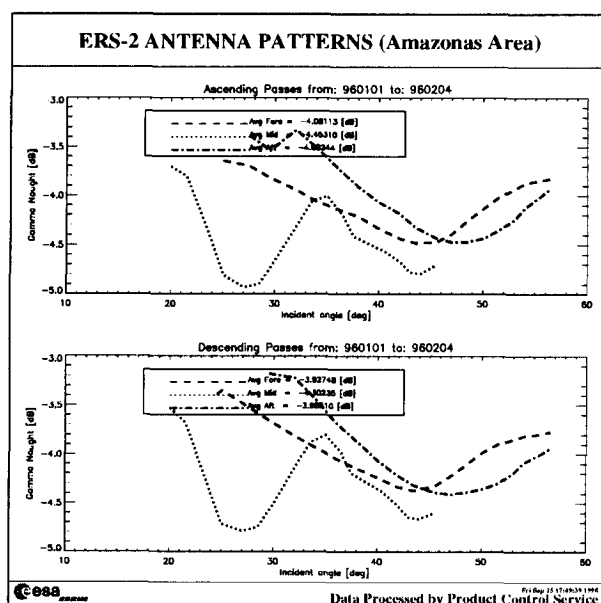


Figure 5: ERS-2 Scatterometer: Antenna pattern over Brazilian rain forest (January 1996 before the commissioning phase).

ERS-1 and ERS-2 signal over rain forest

As the gamma-nought is independent from the incidence angle, the histogram of gamma-noughts over the rain forest is characterised by a sharp peak as shown in Figure 6 and Figure 7.

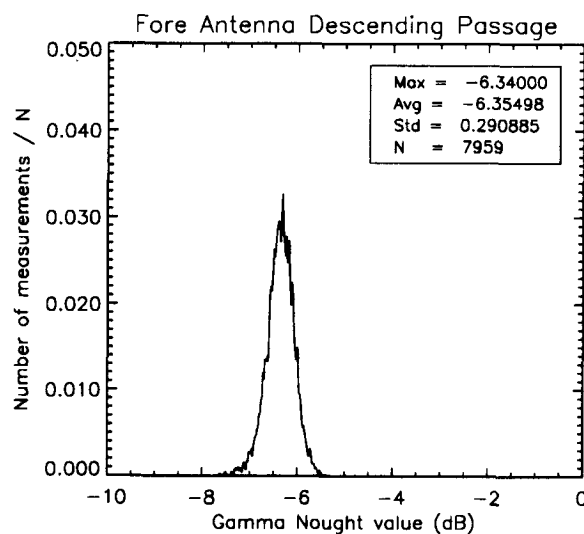


Figure 6: ERS-1 Scatterometer: Gamma nought histograms Fore beam (May 1996).

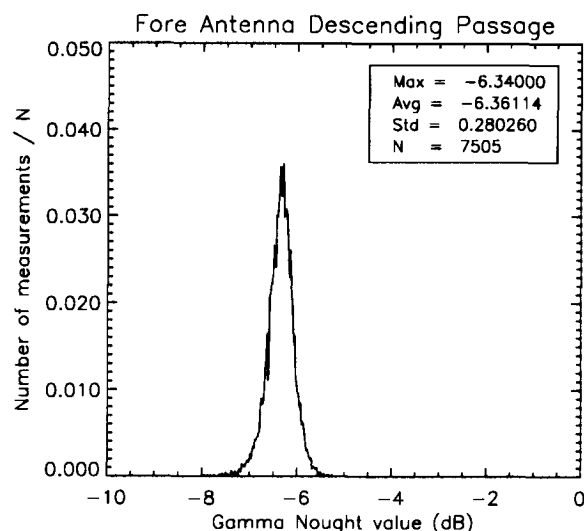


Figure 7: ERS-2 Scatterometer: Gamma nought histograms Fore beam (May 1996).

The peak position allows us to make comparisons among the signal received from the three antennae and between the ERS-1 and ERS-2 Wind Scatterometer.

The position of the peak is computed by fitting the histogram with a normal distribution added to a second order polynomial:

$$F(x) = A_0 \cdot \exp\left(-\frac{z^2}{2}\right) + A_3 + A_4 \cdot x + A_5 \cdot x^2$$

$$\text{where: } z = \frac{x - A_1}{A_2}$$

The parameters are computed using a non linear least square method called "gradient expansion". The position of the peak is given by the maximum of the function $F(x)$. Table 8 and Table 9 show the results from the reference area for ERS-2 and ERS-1 Wind Scatterometer respectively.

Table 9: ERS-2 Gamma nought peak position, mean and standard deviation (descending passes, May 1996).

antenna	gamma nought peak position (dB)	gamma nought mean (dB)	gamma nought standard deviation (dB)
fore	-6.34	-6.36	0.28
mid	-6.42	-6.44	0.29
aft	-6.28	-6.30	0.29

Table 10: ERS-1 Gamma nought peak position, mean and standard deviation (descending passes, May 1996).

antenna	gamma nought peak position (dB)	gamma nought mean (dB)	gamma nought standard deviation (dB)
fore	-6.34	-6.35	0.29
mid	-6.32	-6.34	0.27
aft	-6.32	-6.33	0.29

From tables 8 and 9 it is clear that the assumptions for the gamma nought have some foundation, and that gamma nought is useful as a comparison of the measurements made with the three antennae and with the two Wind Scatterometer without having to take into account the incidence angles. The accuracy of the calibration over the rain forest is within 0.3 dB, the signals from both ERS-1 and ERS-2 Wind Scatterometer are very close. For the ERS-2 the mid beam signal over the rain forest is roughly 0.1 dB less than the one measured with the ERS-1.

Antennae mispointing

Two of the three scatterometer antennae on ERS are mechanically deployed. Small mispointing errors of the antennae may be corrected in the ground processing. The orientation of the normal of each antenna plane can be determined using the transponders, by measuring the difference between the time of the peak's signal (in range and azimuth) of each antenna and when it is expected (using a geometrical model and the orbit propagator). This analysis performed on ERS Wind Scatterometer data shows that the mispointing is negligible.

Gain constant

The plots in Figure 6 show the value of the Gain Constant for ERS-2 Wind Scatterometer computed since January 1996 for the three beams and for ascending, descending and all passes. The data before the commissioning phase was re-processed using the updated set of LUT. The measurements are performed at fixed incidence angle and we have from 3 to more than 10 values for each angle. The plots show an accuracy of 0.5 dB. The bias among the three antennae suggests the introduction of a scaling factor of roughly 0.2 dB, -0.3 dB and 0.2 dB for the fore, mid and aft antenna respectively. This scaling factor has not implemented in the ground station because the results from the Brazilian rain forest do not confirm this bias and because the initial pattern corrections have produced satisfactory results. A fine tuning is an on-going activity.

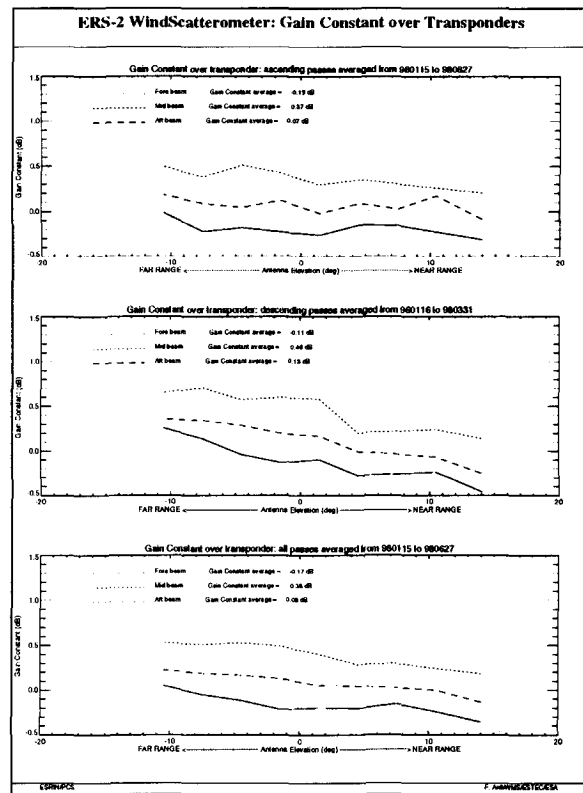


Figure 8: ERS-2 Gain Constants over transponders since January 1996.

Impulse response function

The raw data acquired during skim over the transponders are processed by the Scatt Calibration Processor. The output of this processing is a set of calibration files from which is computed the Wind Scatterometer Impulse Response Function.

Figure 8 and Figure 9 show the along track IRF (fore antenna) for ERS-1 and ERS-2 Wind Scatterometer respectively. The result is that in both cases the spatial resolution defined as the -3.0 dB width is within the nominal resolution (50 Km).

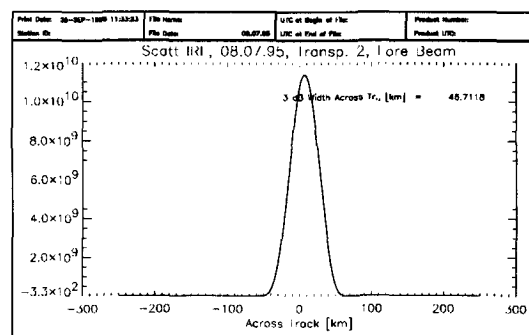


Figure 9: ERS-1 Wind Scatterometer fore beam: impulse response function along track.

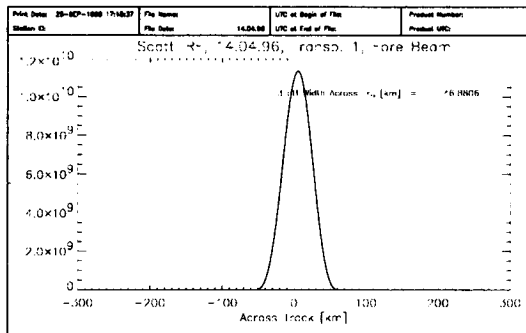


Figure 10: ERS-2 Wind Scatterometer Fore beam: impulse response function along track.

Geophysical products performance

As the output of the Wind Scatterometer is a set of geophysical variables: the wind speed and the wind direction, it is important to check the quality of this variables after the commissioning phase. The quality of the ERS wind speed and direction are everyday monitored in the PCS. The ERS measurements are compared with the ECMWF forecast (24 hours). The result is shown in Figure 11 for the ERS-1 Wind Scatterometer (from 1st August 1996 to 30th May 1996) and in Figure 12 for the ERS-2 Wind Scatterometer (from 23rd November 1995 to 21st September 1998).

The first plot in Figure 11 and 12 shows the percentage of nodes whose ambiguity removal works successfully. The second and third plot in Figure 11 and 12 show the wind speed deviation: bias and standard deviation.

The results for ERS-1 and ERS-2 Wind Scatterometer are comparable. In both cases the ambiguity removal works properly for the 93% of nodes and the wind speed bias is within 0.5 m/s.

One can note three important changes in the wind speed bias for the ERS-2 Wind Scatterometer. The first in the month of March 1996 at the end of the commissioning phase when the new calibration set was installed in the ground processing, the second on 3rd June 1996 when the ERS-2 data were assimilated into the meteorological model and the third at the beginning of September 1997 when important changes were made in the ECMWF algorithms.

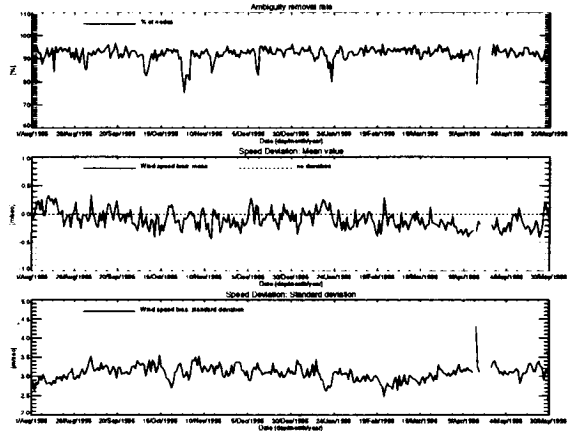


Figure 11: ERS-1 Geophysical validation performance: from 1st August 1995 to 30th May 1996.

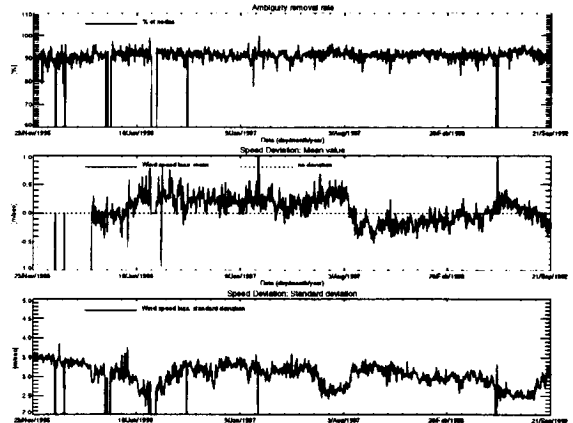


Figure 12: ERS-2 Geophysical validation performance: from 25th November 1995 to 21st September 1998

Calibration performance

The long term stability of the ERS Wind Scatterometer is an important element of the calibration activities. It has to be seen as the extension of the commissioning phase across the entire life time of the instrument. For the ERS mission, the peak position of the gamma nought distribution is weekly monitored.

The Figure 13 shows the evolution of the histograms peak position since January 1996 for the ERS-2 Wind Scatterometer. The step shown in March 1996 is due to the end of commissioning phase when a new Look Up Table was used in the ground stations for Wind fast Delivery products generation.

It is important to note the decrease of roughly 0.2 dB from August 1996 to June 1997. This is linked to the switch of the Scatterometer calibration subsystem from A to B on 6th of August 1996. This new setting caused a little change in the instrument calibration which was corrected on 19th of June 1997 with a new calibration LUT used in the ground processing.

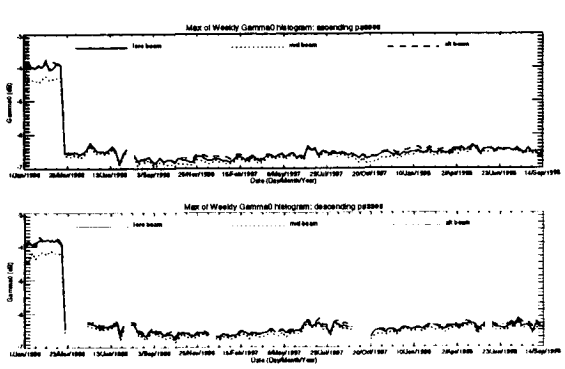


Figure 13: ERS-2 Wind Scatterometer: weekly evolution of gamma nought histogram peak position. From up to down: ascending passes, descending passes.

The analysis of the curve in Figure 13 demonstrates the stability over the whole period, even if a small oscillation can be detected. It is important to outline that the three antennae have very similar response in particular for the fore and aft antenna. One can see a seasonal variation in all three antennae; this signal has an amplitude of roughly 0.2 dB. The stability achieved is within the 0.3 dB.

The result for the ERS-1 Wind Scatterometer is similar to the ERS-2 case.

When ERS-1 was launched, it was agreed that an absolute radiometric calibration of 0.7 dB was enough to satisfy the geophysical data quality requirements in terms of wind speed and direction (instrument specification).

This analysis proves that this target has been reached in the ERS Wind Scatterometer mission. The change of the calibration subsystem from side A to side B in the ERS-2 Wind Scatterometer has also proved that the meteorologist can detect in the wind fields a bias corresponding to less than 0.2 dB, and this led to a re-calibration of the ERS-2 Wind Scatterometer.

Instrument performance

The results reported are a summary of the daily data quality control made within the PCS at ESRIN. This monitoring work has led to continuous upgrade of the instrument status and on the other side a good detection of the instrument problems.

The instrument status is checked by monitoring the following parameters:

- Centre of Gravity and standard deviation of the received signal spectrum.

This parameter is useful for the monitoring of the orbit stability, the performances of the doppler compensation filter, the behaviour of the yaw steering mode and the performances of the devices in charge for the satellite attitude (e.g. gyroscopes, earth sensor).

- Noise power I and Q channel.

- Internal calibration pulse power.

The latter is an important parameter to monitor the transmitter and receiver chain, the evolution of pulse generator, the HPA, the TWT and the receiver.

These parameters are daily extracted from the Fast Delivery products (UWI).

The following parameters are daily extracted from the telemetry data (EGH product):

- Calibration subsystem input and output peak power.
- Travelling Wave Tube (TWT) currents and voltages
- AMI hardware temperatures (only ERS-2).

In the case of ERS-2 AMI the analysis is splitted for the different AMI working modes.

Centre of gravity (CoG) and standard deviation of received power spectrum

Figure 14 shows the evolution of this two parameters (ERS-2 Wind Scatterometer) for each beam. The tendency since the beginning of the mission is a slight increase of the Centre of Gravity (CoG) of the signal spectrum for the three antennae while the result for the standard deviation is more stable, in particular for the mid antenna.

The two steps observed on the plots of the CoG are due to a change in the pointing subsystem (DES reconfiguration) side B instead of side A. The first from 24 January 1996, 09:10:03 to 14 March 1996, 10:22:50, the second from 14 February 1997, 01:25:44 to 22 April 1997, 10:27:30. During these periods side B was switched on. The large deviation from nominal values in the plots of the CoG of the fore and aft beams shown on 26th September 1996 is due to missing doppler compensation information on board of the satellite (no yaw steering mode).

A depointing anomaly occurred on ERS-2 from 03-June-1998 14:43:53 to 06-June-1998 12:47:40; this explains the data gap shown in the plots of Figure 12. After the anomaly the Yaw Steering Mode (YSM) transition was achieved on 07-June-1998 00:48:00 so the daily average of the doppler compensation parameters shows a large deviation from nominal values for the days June, 6th and 7th 1998. After the depointing anomaly, the CoG had an increase of roughly 100 Hz for the three antennae and it stayed stable.

The peaks shown in the plot of mid beam CoG standard deviation are linked to the satellite manoeuvres and the DES reconfiguration.

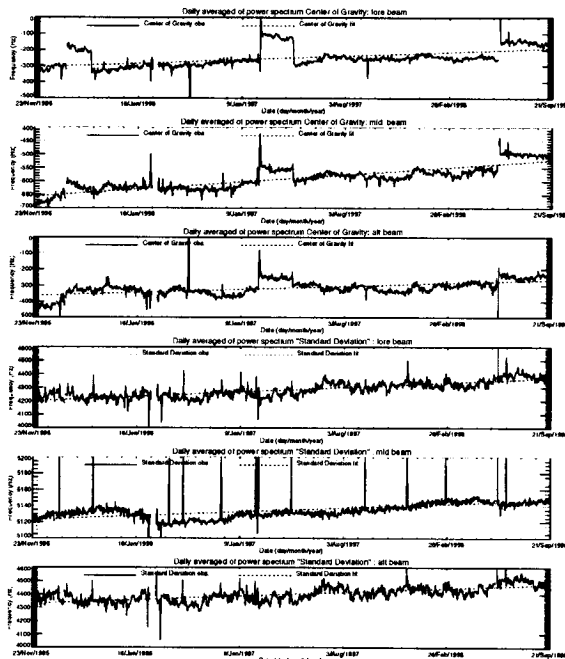


Figure 14: ERS-2 Scatterometer evolution of the doppler compensation from January, 1st 1996 to September, 21st 1998.

Table 9 summarizes the doppler performance of the ERS-2 Wind Scatterometer since the beginning of the mission (mean values).

Table 11: ERS-2 Doppler compensation performance

Antenna	CoG (Hz)	CoG standard deviation (Hz)
fore	-306.5	4198.9
mid	-654.5	5123.0
aft	-361.5	4329.1

Figure 15 and Figure 16 show the evolution of the CoG and its standard deviation for the ERS-1 WindScatterometer since June 1993. The mid beam CoG is roughly 400 Hz greater than the ERS-2 one, the fore and aft CoG are roughly 100Hz less than the ERS-2 ones. The CoG standard deviation is roughly 500 Hz less than the ERS-2 for the three antennae. The variations of the COG reported in Figure 15 are related with the different ERS-1 operational phases.

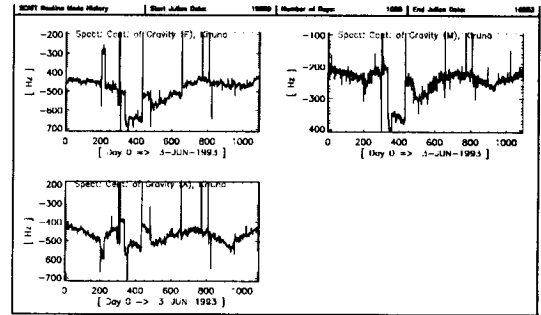


Figure 15: ERS-1 Scatterometer evolution of the COG (mean) from June, 3rd to the end of mission.

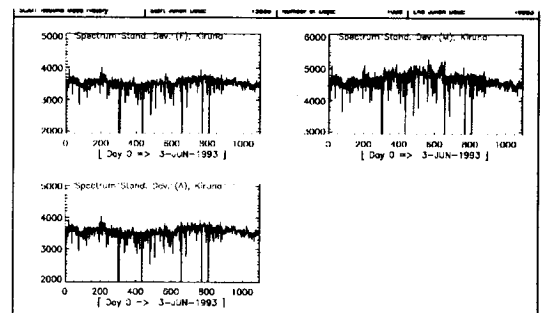


Figure 16: ERS-1 Scatterometer evolution of the COG (standard deviation) from June, 3rd to the end of mission

Noise power level I and Q channel

The results of the monitoring are shown in figure 17 for the ERS-2 Wind Scatterometer. The first set of three plots presents the noise power evolution for the I channel while the second set shows the Q channel.

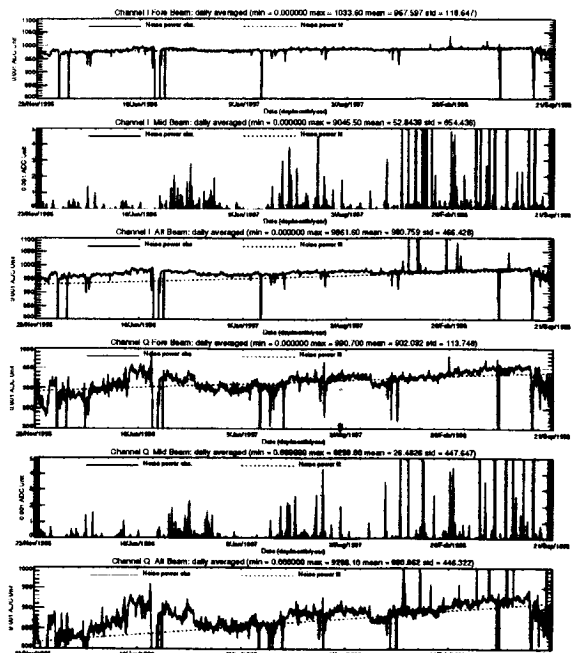


Figure 17: ERS-2 Scatterometer evolution of the noise power from January, 1st 1996 to September, 21st 1998.

The noise level is less than 1 ADC Unit for the fore and aft signals and is negligible for the mid one. From the plots one can see that the noise level is more stable in the I channel than in the Q one.

Since 5th December 1997, some peaks appear in the plots. These high values for the daily mean are due to the presence for these special days of a single UWI product with an unrealistic value in the Specific Product Header noise power field. The analysis of the raw data used to generate these products lead in all cases to the presence of one source packet with a corrupted value in the noise field stored into the source packet Secondary Header.

The reason why noise field corruption began on 5th December 1997 and is going on is at present unknown. It is interesting to note that at the beginning of December 1997, we started to get as well the corruption of the Satellite Binary Times (SBTs) stored in the EWIC product. The impact in the fast delivery products was the production of blank products starting from the corrupted EWIC until the end of the scheduled stop time. A change in the ground station processing in March 1998 overcame this problem.

Since August, 9th 1998 an instability has affected the noise power level (channel I and channel Q); this explains the small decrease in the noise power level shown in Figure 15. Investigations to better understand the case are on-going.

The result from ERS-1 Wind Scatterometer is shown in Figure 18 for the I channel, the Q one is very similar.

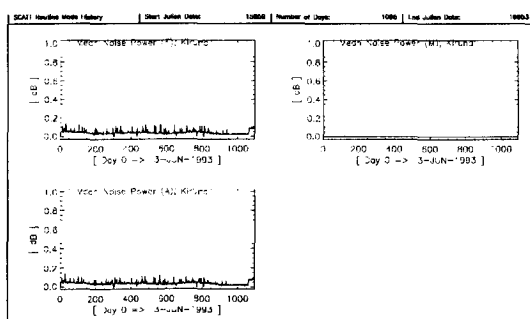


Figure 18: ERS-1 Scatterometer evolution of the noise power level (I channel) from June, 3rd to the end of mission

The noise power is 0 ADC unit for the mid antenna while is roughly 0.1 ADC unit for the fore and aft antenna. In comparison with ERS-2, the ERS-1 Wind Scatterometer has a lower noise level.

Power level of internal calibration pulse

Figure 19 shows the evolution of the internal calibration level for the ERS-2 Wind Scatterometer.

The high value of the variance in the fore beam (see Figure 17) until August,12 1996 is due to ground processing. In fact, all the blank source packets ingested by the processor were recognized as fore beam source packets with a default value for the internal calibration

level. The default value was applicable for ERS-1 and therefore was not appropriate for ERS-2 data processing. On August 12, 1996 a change in the ground processing LUT overcame the problem.

Since the beginning of the mission a power decrease is detected. This drift was unexpected. Nothing like that was never experienced with the ERS-1 Wind Scatterometer as shown in Figure 20 and Figure 22.

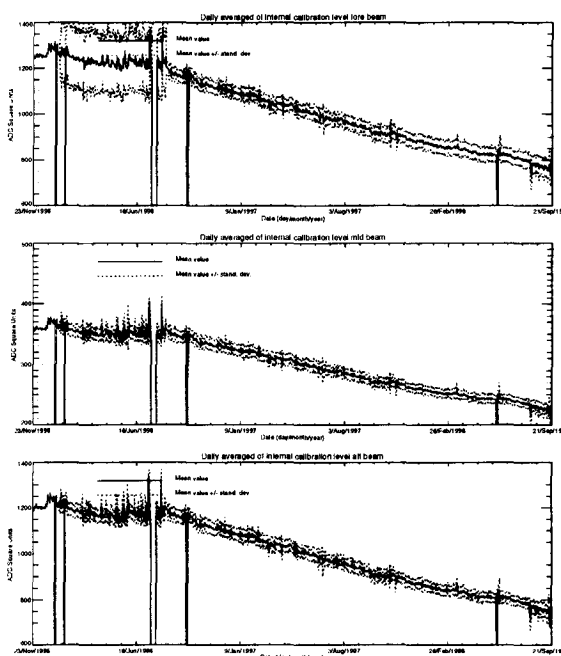


Figure 19: ERS-2 Scatterometer evolution of the internal calibration level: from January, 1st 1996 to September, 21st 1998.

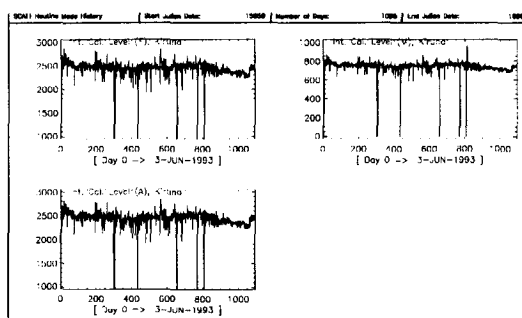


Figure 20: ERS-1 Scatterometer evolution of the internal calibration level from June, 3rd to the end of mission.

It was first necessary to characterise which elements of the chain were producing this power decrease and in particular if the calibration sub-system was not directly involved.

After a long analysis it was finally confirmed that the drift is entirely due to the variability of the input signal to the TWT.

This means that the same drift is observed in the echo and in the calibration pulse and that the final sigma nought is free of any drift as the echo is normalised by

the calibration pulse during the processing. The efficiency of the internal calibration to keep the absolute calibration level stable is proved with the monitoring of the gamma-nought level over the Brazilian rain forest. In fact, no drift is noted (see calibration performance paragraph).

In the ERS-2 case the TWT is not working in saturation, so that a variation in input signal is visible in output.

The variability of the input signal can be two-fold: the evolution of the pulse generator and the tendency of the switches between the pulse generator and the TWT to reset themselves into a nominal position.

These switches were set into an intermediate position in order to put into operation the scatterometer instrument (on 16th November 1995). The decrease is estimated to be about 0.0025 dB per day, 2.2 dB since the beginning of the mission.

The power decrease is regular and affects the AMI when working in wind-only, wind/wave and image mode indifferently.

This is clearly shown in figure 19 where the daily average of the input and output calibration subsystem peak power are plotted.

These data are daily extracted from the AMI telemetry (EGH products). The results are split for the different AMI working modes: brown for wind-only, blue for wind/wave.

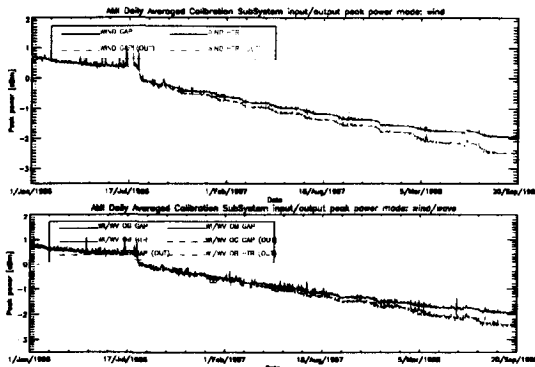


Figure 21: ERS-2 AMI Calibration subsystem input and output peak power from January, 1st 1996 to September, 21st 1998. Wind mode (up) and Wind/Wave mode (down).

Figure 22 shows the calibration subsystem input/output peak power for the ERS-1 Wind Scatterometer. In this case the daily average is relative to the all AMI working modes.

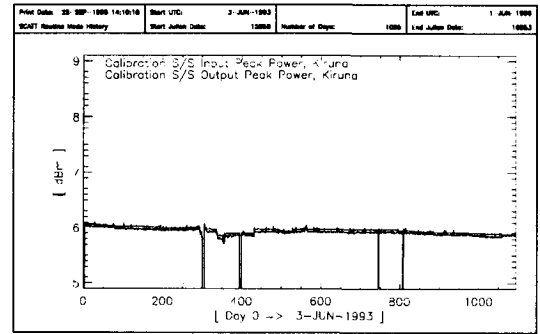


Figure 22: ERS-1 AMI Calibration subsystem input and output peak power: from June, 3rd 1993 to end of mission.

Telemetry results

Figure 23 shows the daily average (all modes) for the TWT average body current, the TWT filament current, the TWT beam current and the TWT collector voltage of the AMI on board ERS-1.

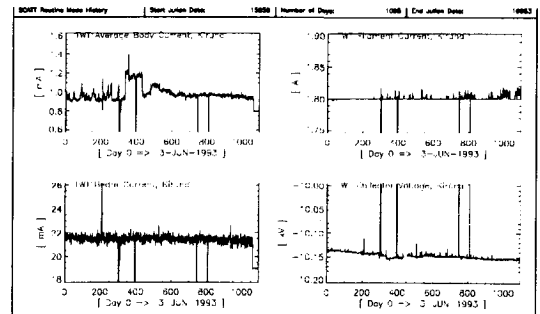


Figure 23: ERS-1 AMI TWT currents and voltages: from June, 3rd 1993 to the end of mission.

Figure 24 shows the same parameters plus the TWT cathode voltage for the AMI on board ERS-2 when AMI is in wind only mode.

In the case of ERS-2 AMI the drift that affects the transmission chain is clear.

Figure 25 shows the temperatures of the main devices (side A) of the ERS-2 AMI instrument when it is operated in wind-only mode. The plots shown a stable evolution of those temperatures.

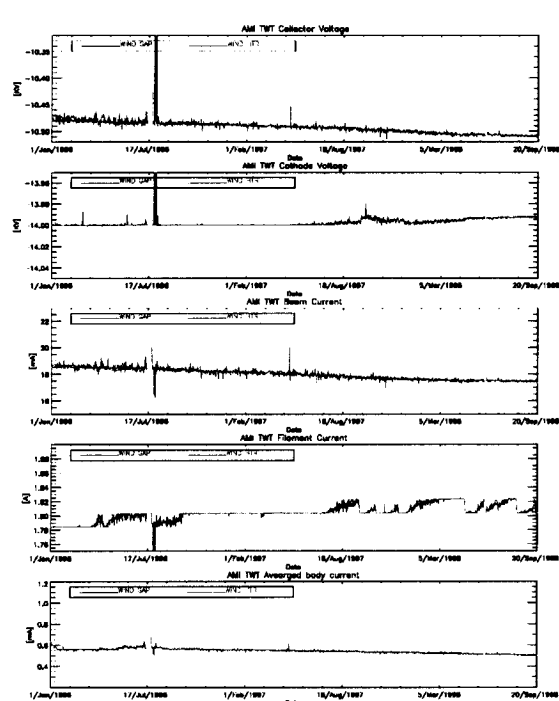


Figure 24: ERS-2 AMI TWT currents and voltages from January, 1st 1996 to 21st September 1998 (only wind mode).

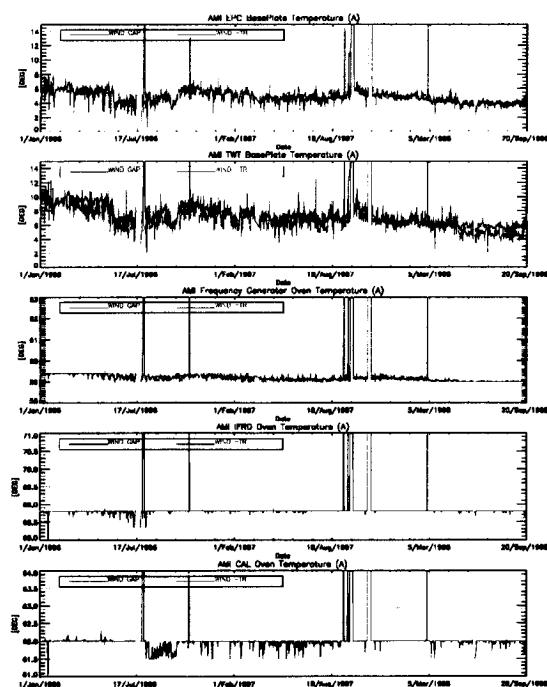


Figure 25: ERS-2 AMI Temperatures (side A): from January, 1st 1996 to 21st September 1998 (wind mode).

Conclusions

During the 5 years of ERS-1 Wind Scatterometer mission no important problems have affected the AMI

instrument, on the contrary after the launch of ERS-2 on 21st April 1995 a serious anomaly caused the AMI instrument to shut down. The anomaly was resolved by setting the switch at the input to the HPA to an intermediate position and reducing the power output by a factor or two. This allowed to get wind data since November 1995.

Although the ERS-1 Wind Scatterometer and ERS-2 Wind Scatterometer work with a different level of output power the quality of the measured backscattering is very high and allow the users to have a comparable set of data (a difference of 0.1 dB between the ERS-1 and ERS-2 mid antenna's signal can be underline).

The efficiency of the internal calibration to keep the absolute calibration level stable is verified in the case of ERS-2 Wind Scatterometer. In fact for this instrument a power decrease of roughly 2.2 dB is detected since the beginning of the mission but as waited for no drift is visible in the signal measured over the Brazilian rain forest that is the reference natural calibration target.

The level of the noise is 1 ADC unit for the ERS-2 Wind Scatterometer (fore and aft antenna) while it is very close to 0 ADC unit for the ERS-1 case. The noise for the mid beam antenna is 0 ADC unit for both the ERS-1 and ERS-2 Wind Scatterometer.

The antenna patterns show a flat profiles, within 0.3 dB for both ERS-1 and ERS-2 Wind Scatterometer.

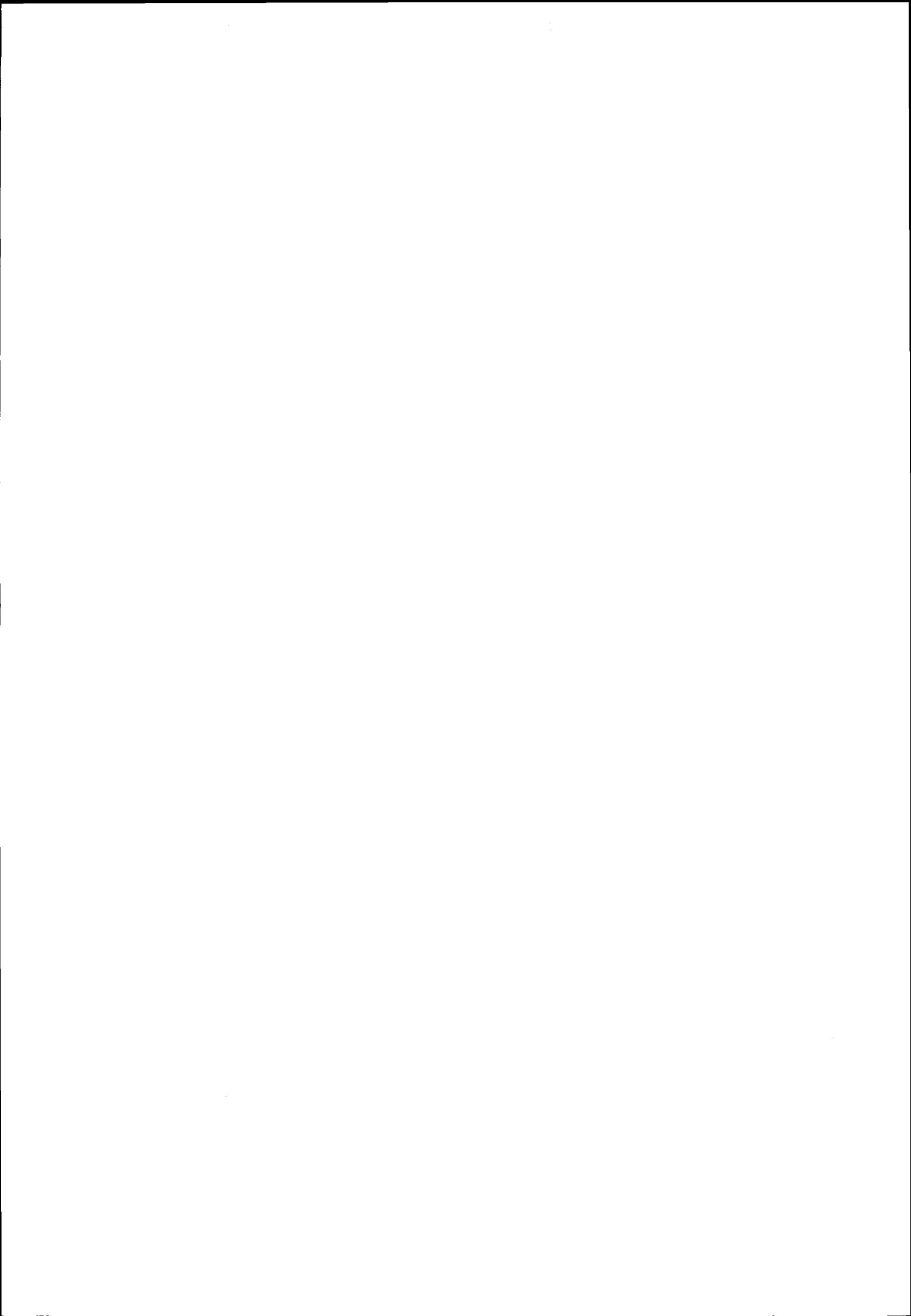
The different operational mode between the ERS-1 and ERS-2 Wind Scatterometer has an impact in the data availability. In particular for the ERS-2 mission the use of the ATSR-2 in high rate mode over the land force the AMI to switch from wind/wave mode to wind only mode when the satellite flies over the land. Due to operational constraint this involve a small amount of data between Antarctica and Australia or South America or South Africa.

The output geophysical variables, wind speed and wind direction, of the ERS-1 and ERS-2 Wind Scatterometer have a comparable quality. In particular the actual ERS-2 wind speed has a bias within 0.5 m/s and a standard deviation of 3.0 m/s with reference to the ECMWF forecast (24 hour); a bias of -0.5 m/s and a standard deviation of 1.6 m/s with reference to the First Guess (FG) analysis; a bias of -0.3 m/s and a standard deviation of 1.6 m/s with reference with the 4D-Var analysis performed by ECMWF.

References

- [1] V. Amans, 1996 ERS Wind Scatterometer Quality Control, NOAA/NESDIS Workshop Proceedings, April 1996, Alexandria VA USA.

Participants



Participants

Abdel Messeh, Mr., M.
University of Sheffield
The Hicks Building
Hounsfield Road S3 7RH
Sheffield
U.K.
+44 114-222 3705; ... -222 3739
m.messeh@sheffield.ac.uk

Attema, Mr., E.
ESA ESTEC
SCI-VRS
Keplerlaan 1
2200 AG Noordwijk
The Netherlands
+31 71 565-4461; ... -5675
eattema@estec.esa.nl

Breivik, Mr., L.A.
Norwegian Meteorological Inst.
P.O. Box 43
Blindern - N-0313 Oslo
Norway
+47 2296-3333; ... -6355
l.a.breivik@dnmi.no

Carpay, Mr., J.G.H.
NIVR
Kluyverweg 1
P.O. Box 35
2600 AA Delft
The Netherlands
+31 15 2782015; +31 15 2623096
j.carpay@nivv.nl

Crapolicchio, Mr., R.
ESA-ESRIN, SERCO TEC
Via Galileo Galilei, CP 64
00044 Frascati
Italy
+39 6 94 180 693; +39 6 94 180 612
raffaele.crapolicchio@esrin.esa.it

De Vries, Mr., J.C.W.
KNMI
Wilhelminalaan 10
3730 AE De Bilt
The Netherlands
+31 30 220 6771; +31 30 2210407
jdevries@knmi.nl

Agter, Ms., R.
SRON
Sorbonnelaan 2
3584 CA Utrecht
The Netherlands
+31 30-2538593
+31 30-254 0860
r.agter@sron.nl

Barlag, Mrs., S.J.M.
KNMI-Koninklijk Nederlands
Meteorologisch Instituut
Postbus 201
3730 AE de Bilt
The Netherlands
+31 30-2206344; ...-2210407
barlag@knmi.nl

Caparrini, Mr., M.
ESA ESTEC
TOS-ETP
Keplerlaan 1
2200 AG Noordwijk
The Netherlands

Cavanie, Mr., A.
Centre IFREMER de Brest
BP 70
29280 Plouzane
France
France
+33 2 98224410; +33 2 9822 4533
cavanie@ifremer.fr

Crepon, Mr., M.
LODYC - UPMC
4 Place Jussieu, T.26, 4e ét., BC 100
75005 Paris
France
+33 1 44 27 72 74; ... 1 44 27 71 59
mc@hermes.lodyc.jussieu.fr

Drinkwater, Dr., M.R.
JPL - mail stop 300-323
4800 Oak Grove Drive
Pasadena, CA 91109-8099
USA
+1 818 354 8189; +1 818 393 6720
mrd@zpacific.jpl.nasa.gov

Alvarez Perez, Mr., J.L.
University of Nottingham
The Elms
Sutton Bonington Campus
Loughborough LE12 5RD
U.K.
+44 115-9515151; ...-9516261
sbxjla@sbn2.nott.ac.uk

Borgeaud, Mr., M.
ESA ESTEC
TOS-EEP
Keplerlaan 1
2200 AG Noordwijk
The Netherlands
+31 71 565-4830; ...-4999
maurice@xe.estec.esa.nl

Carnall, Mr., J.
Honeywell Inc.
13350 US Highway 19N
33764-7290
Clearwater, Florida, USA
+1 813 539-5675; ...-2183
jjcarnall@space.honeywell.com

Courtier, Mr., P.
LODYC UPMC
BC 100
4 Place Jussieu
75005 Paris
France
+33 1 44 27 7073
courtier@lodyc.jussieu.fr

D'Amelio, Ms., C.
Telespazio SpA
Via Tiburtina 965
00156 Roma
Italy
+39 06 4079-3714; ...-6202
claudia_damelio@telespazio.it

Duchossois, Dr., G.
ESA Headquarters
8-10 Rue Mario Nikis
75738 Paris Cedex 15
France
+33 1 5369 7284;
+33 1 53 69 7674

Edwards, Mr., P.
ESA-ESRIN
Via Galileo Galilei
CP 64
00044 Frascati

Italy

Frison, Mr., P.-L.
CESBIO/CNRS/Univ. Paul Sabatier
18, Av. E. Belin
F-31401 Toulouse Cedex 4
France
+33 61 55-8537; ...-8500
frison@cesbio.cnes.fr

Grima, Mr., N.
LODYC UPMC
UMR 7617 CNRS/ORSTOM
BC 100, 4 Place Jussieu
75005 Paris
France
+33 1 4427-2711; ...-7159
nglod@ipsl.jussieu.fr

Habermeyer, Mr., M.
DLR, Inst. für Hochfrequenztechnik
Postfach 1116
D-82230 Wessling
Germany
+49 8153 28-2331; ...-1449
Martin.Habermeyer@dlr.de

Isaksen, Mr., L.
ECMWF
Shinfield Park
Reading Berkshire RG2 9AX
U.K.
+44 118-949 9852; ...-986 9450
mpi@ecmwf.int

Kerkmann, Mr., J.
Eumetsat
Am Kavalleriesand 31
64295 Darmstadt
Germany
+49 6151 807-514; ...-555
kerkmann@eumetsat.de

Figa, Ms., J.
KNMI
Wilhelminalaan 10, P.O. Box 201
3730 AE De Bilt
The Netherlands
+31 20-2206585; ...-2210843
figa@knmi.nl

Grandell, Mr., J.
Finnish Geodetic Institute
Geodeetinrinne 2
SF- 02430 Masala
Finland
+358-40 548 3858; ...-9 295 55 200
jochen.grandell@hut.fi

Guijarro, Mr., J.
ESA ESTEC
Keplerlaan 1
Postbus 299
2200 AG Noordwijk
The Netherlands
+31 71 565 4435
jguijarro@estec.esa.nl

Halpern, Dr., D.
JPL - Caltech
4800 Oak Grove Drive
Pasadena, CA 91109-8099
USA
+1 818-354 5327; ...-393 6720
halpern@pacific.jpl.nasa.gov

Jarlan, Mr., L.
CESBIO
18, Av. E. Belin
F-31401 Toulouse Cedex 4
France
+33 561558537
lionel_jarlan@cesbio.cnes.fr

Lecomte, Mr., P.
ESA-ESRIN, Remote Sensing Div.
Via Galileo Galilei, CP 64
00044 Frascati
Italy
+39 6 94 180-670; ...-612
pascal.lecomte@esrin.esa.it

Flament, Mr., P.
U. of Hawaii, Dept. of Oceanography
1000 Pope Road
Honolulu, Hawaii 96822
USA
+1 808 956-6663; ...-9225
pierre@soest.hawaii.edu

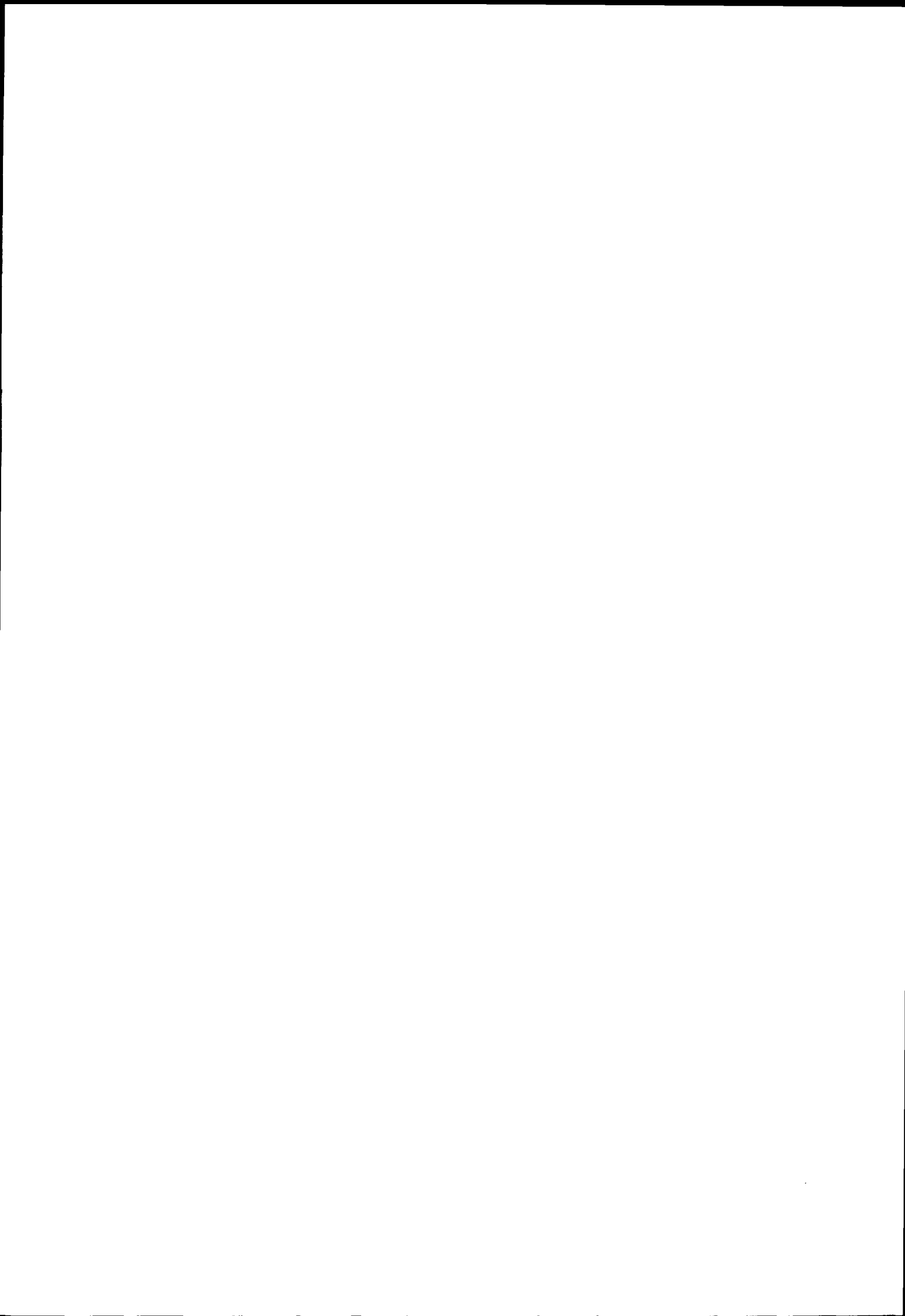
Grassotti, Mr., C.
Atmospheric & Environmental
Research Inc.
840 Memorial Drive
Cambridge, MA 02139, USA
+1 617-547 6207; ...-661 6479
jlouis@aer.com

Guyenne, Mr., T-D.
ESA ESTEC
Keplerlaan 1
Postbus 299
2200 AG Noordwijk
The Netherlands
+31 71 565-3403; ...-5433
tguyenne@estec.esa.nl

Ille, Mr., E.
Honeywell Inc.
13350 US Highway 19N
33764-7290
Clearwater, FL, USA
+1 813 539-3264; ...-2183
eille@space.honeywell.com

Johannessen, Mr., J.
ESA ESTEC, SCI-VRO
Keplerlaan 1, PB 299
2200 AG Noordwijk
The Netherlands
+31 71 565-5959; ...-5675
jjohanne@jw.estec.esa.nl

Leidner, Mr., S.M.
Atmos. & Envirt. Research Inc.
840 Memorial Drive
Cambridge, MA 02139
USA
+1 617-547 6207; ...-661 6479
leidner@aer.com



European Space Agency
Agence spatiale européenne

Contact: ESA Publications Division
c/o ESTEC, PO Box 299, 2200 AG Noordwijk, The Netherlands
Tel (31) 71 565 3400 - Fax (31) 71 565 5433